Numerical study of evaporators in power plants for improved dynamic fl exibility

Johansen, Axel Vodder Ohrt

Publication date:
2013

Document Version
Publisher's PDF, also known as Version of record

Numerical study of evaporators in power plants for improved dynamic flexibility

PhD Thesis

$$(EIv'')''=q-\rho A\ddot{v}$$

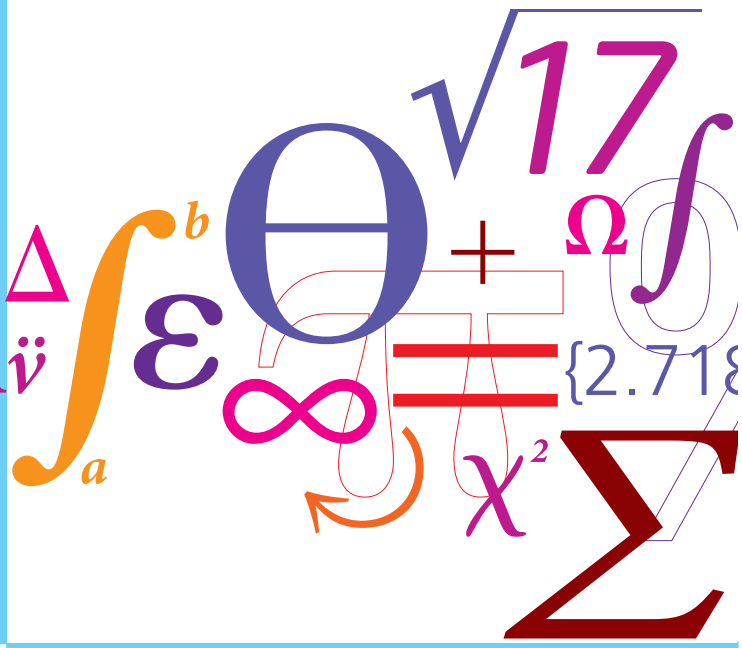

Axel Ohrt Johansen
DCAMM Special Report No. S165
March 2013

DTU Mechanical Engineering
Department of Mechanical Engineering

Preface

This thesis was prepared at the Section of Thermal Energy Systems, Department of Mechanical Engineering, Technical University of Denmark (DTU) and at DONG Energy - Thermal Power A/S Frederica. It was submitted in partial fulfilment of the requirements for acquiring the Ph.D. degree. The work is carried out from February 2009 to March 2013, with leave of absence in two periods a total of 13 months. The project was under the supervision of Associate Prof. Brian Elmegaard (DTU), Senior engineer Torkild Kristensen (DONG Energy - Thermal Power) and the co-supervision of Ph.D. Professor Jens Nørkær Sørensen (DTU). The project was financed by the Danish Agency for Science, Technology and Innovation, under the industrial Ph.D. program and by DONG Energy - Thermal Power. The thesis is written as a monograph, and it contains various analyses of the evaporator tubes based on both traditional smooth inclined boiler tubes and vertical internally rifled boiler tubes. Numerical models of varying complexity are used to illuminate the dynamic behaviour of the heated boiler tubes. Furthermore, the thesis describes the development and implementation of the numerical models used in this work, which are written in the programming language C++.

Lyngby, March 2013

Axel Ohrt Johansen

Acknowledgements

I owe gratitude to many people who have been involved in various ways during the work on this research project. First of all I would like to thank my principal supervisor, Brian Elmegaard; I have a debt of gratitude for his support, advice, guidance and encouragement that have shaped this project and thesis. Also thanks to my co-supervisor, Torkild Christensen, for his encouragement and his experienced guidance with respect to discussing the model setup, simulation cases and solving problems up front. I would also like to thank my co-supervisor, Jens Nørkær Sørensen, for always being available for questions and discussions about the fluid mechanical as well as numerical aspects.
An industrial Ph.D. project is not an easy task always balance on the borderline between the interests of industry and academia. The task of writing a thesis with the right level of detail for various readers with different backgrounds and interests is challenging. I would like to thank many people for helping me produce this thesis and for getting me through the industrial Ph.D. program. I am grateful to Rudolph Blum and Tommy Mølbak for providing me with the opportunity to work at DONG Energy - Thermal Power A/S and apply for the industrial Ph.D. program. I would like to give special thanks to all my colleagues at DONG Energy - Thermal Power A/S for providing an inspiring work environment, and a special thanks to the staff at DONG Energy for providing me with the measurements from Skærbækværket Unit 3. In the same way I thank all my colleagues at the Section of Thermal Energy Systems at DTU and also a special thanks to Allan Peter Engsig-Karup at IMM DTU, for our fruitful discussions of numerical subjects. Last but not least, I thank my family for supporting and encouraging me always. They deserve the credit for my achievements. I am especially thankful to my wife Jeanette, for her support and understanding even during the most stressful parts of the project. Thanks for making it possible for me to pursue this Ph.D. Thanks for keeping me mindful of life besides work. And to our two sons, Andreas, and Rasmus for being so kind and for giving me so much joy in life.

Abstract

The main objective of this Ph.D. thesis is to describe and analyse the most recent knowledge about operational flexibility in steam power plant evaporators, based on mathematical / numerical methods. The thesis addresses a mathematical study of steam power plant evaporators and involves the reader in many of the complex considerations-, that are necessary to initiate such a study of thermal-hydraulic two-phase flows. The model complexity is increased with the transport of a fluid that changes phase from a sub-cooled liquid state, to a superheated vapour through the evaporator. The mathematical models include analysis of static stability, in the form of studies of mal-distribution in panel walls and Ledinegg stability. Additionally dynamic studies of start-up conditions and load control examples are performed. The choice of the numerical scheme has focused on a higher-order scheme, which can handle steep gradients, discontinuities and shock in the solution and can handle dynamic effects through boundary conditions and initial fields. Furthermore, the thermodynamic properties associated with the flowing media are modelled as a fast look-up table, which in this case is water/steam. The reader will be introduced to basic concepts in the power sector, including lifetime terms, such as corrosion, creep and fatigue, related to the evaporator tubes, which are responsible for the transfer of energy from the boiler to the water / steam circuit of a power plant. New evaporator technologies are briefly described, followed by a simulation of a steam power plant evaporator of Skærbækværket (SKV3), which is one of DONG Energy's ten central CHP plants, built in 1998 and located in Skærbæk at the mouth of Kolding Fjord in Denmark. Here different heating profiles of the evaporator are investigated, as well as an examination of the consequences of a feed water preheater outfall and reduced evaporator pressure, which are some among many other actions that can be analysed to adjust the thermal power stations to the new market conditions requiring increased green energy. The numeric scheme is particularly well suited to handle strong oscillations and slugs in relation to the two-phase flow, and in spite of the associated water / steam library being designed as a fast bilinear 'look-up' table, the calculation time is long. The structure of the application is generic in the sense that other fluids can be used. The simulation tools are implemented in C++ and can communicate with various commercial tools, for the purpose of post processing of the calculation results.

Resumé

Formålet med denne afhandling er at beskrive og analysere driftsfleksibilitet i fordampere, baseret på matematiske / numeriske metoder. Afhandling omhandler matematiske studier af fordampere og inddrager læseren i mange af de komplekse overvejelser, som er nødvendige for at kunne indlede et studie af thermo-hydrauliske to-fase strømninger. Model kompleksiteten forøges af, at vi har at gøre med transport af en fluid, som ændre fase undervejs, fra en tilstand som underkølet vædske ved indløbet til fordamperen og til overhedet damp ved udløbet af fordamperen. De matematiske modeller omfatter både en analyse af statisk stabilitet i form at undersøgelser af flow fordeling i panelvægge og Ledinegg stabilitet samt dynamiske studier af opstartsforhold og lastregulerings eksempler. I valget af numerisk skema er der lagt vægt et højere ordens skema, som kan håndtere store lastspring, diskontinuiteter og shock i løsningen samt kan håndtere dynamiske påvirkninger via randbetingelser og initialfelter. Desuden er der modelleret passende udtryk for de termodynamiske tilstandsstørrelser som knytter sig til det strømmende medie, som i dette tilfælde er vand/damp. Læseren vil blive introduceret til grundlæggende begreber inden for kraftværkssektoren, herunder levetidsbegreber som korrosion, krybning og udmattelse, som kan relateres til fordamperrøret, som er ansvarlig for overførsel af energi fra fyrrummet til vand/damp kredsløbet i et termiske kraftværk. Nye fordamper teknologier er kort blevet beskrevet, efterfulgt af simuleringer af en kraftværksfordamper fra Skærbækværket (SKV3), som er beliggende ved Kolding Fjord. Her analyseres forskellige driftsforhold på fordamperen med hensyn til fyringsprofil. Endvidere undersøges konsekvensen af udfald af en fødevands forvarmer samt reduceret fordampertryk, som er nogle blandt mange af de tiltag, som kan anvendes til at tilpasse de termiske kraftværker til de nye markedsvilkår med øget grøn energi. Det numeriske skema viser sig særdeles velegnet til at håndtere kraftige oscillationer og slugs i relation til to-fase strømninger. Det tilhørende vand/damp biblioteket er opbygget som en hurtig bilineær 'look up' table som har reduceret beregningstiden betydeligt. Applikation er generisk opbygget, således at andre fluider kan anvendes. Simuleringsværktøjerne er implementeret i C++ og kan kommunikere med forskellige kommercielle værktøjer, med henblik på post processering af beregningsresultaterne.

Papers included in the thesis

Journal papers (not reviewed yet):

Johansen, A. O, Elmegaard B. and Sørensen, J. N, 2012a, Implementation and test of a higher order hybrid solver for hyperbolic and parabolic balance laws. International Journal for Computers & Mathematics with Applications,1-32.

Johansen, A. O. and Elmegaard B, 2012b, Finite Element Method Implementation Scheme for Fast Calculation of Water Steam Properties., Journal of Computational Physics, 1-26.

Johansen, A. O. and Elmegaard B, 2012c, A homogeneous two-phase flow model of a vertical evaporator, Modelled by a fifth order Central WENO scheme for solving hyperbolic balance laws, Applied Thermal Engineering, 1-33.

Peer-reviewed conference papers:

Johansen, A. O. and Elmegaard B,2012d, A homogeneous two-phase flow model of an evaporator with internally rifled tubes, modelled by a fifth order Central WENO scheme for solving hyperbolic balance laws, Proceedings, SIMS 2012, Reykjavik, Iceland.

Papers included in the thesis

Contents

Nomenclature

Symbol	Description	Unit
A	Cross-sectional flow area of pipe	m^2
Bo	Boiling Number (A.2)	–
Br	Brinkman Number (A.2)	–
Bc	Buoyancy Modulus (A.2)	–
a	Acceleration due to swirl (centrifugal forces)	m/s^2
c	Volume fraction of layer	–
c_p	Specific heat capacity (fixed pressure)	kJ/kg^oC
c_v	Specific heat capacity (fixed volume)	kJ/kg^oC
C	Virtual mass force coefficient	–
e	Specific energy	m^2/s^2
Ec	Eckert Number (A.2)	–
Eo	Eötvö Number (A.2)	–
Eu	Euler Number (A.2)	–
F	Force	N
Fr	Froude Number (A.2)	–
f	Shear stress (friction force)	N/m^2
g	Acceleration due to gravity	m/s^2
G	Mass flux	kg/m^2s
Gr	Grashofs Number (A.2)	–
h	Enthalpy	kJ/kg^oC
Ja	Jakob Number (A.2)	–
k	Thermal conductivity	w/m^oC
l	Length of pipe/geometry/film	m
$\dot{m}$	Mass flux	kg/m^2s
$\dot{M}$	Mass flow rate	kg/s
Nu	Nusseltl Number (A.2)	–
P	Pressure of fluid	Pa
Pr	Prandts Number (A.2)	–
q	heat flux	w/m^2
Q	heat uptake	w
R	Radius of pipe	m
Ra	Rayleigh Number (A.2)	–

Continued on next page...

Symbol	Description	Unit
Re	Reynolds Number (A.2)	–
Ri	Richardson Number (A.2)	–
S	Perimeter wetted	m
Sh	Sherwood Number (A.2)	–
St	Stanton Number (A.2)	–
t	Time coordinate	s
T	Temperature (absolute)	^{o}C
u	Axial flow	m/s
v	Redial flow velocity	m/s
x	Dryness (steam quality)	–
z	Spatial coordinate	m
Greek letters		
α	Thermal diffusivity	m^2/s
β	Volumetric thermal expansion coeff. (A.2)	$^{o}C^{-1}$
δ	Difference between two terms	–
Δ	Difference between two terms	–
ε	void (presence) fraction	–
γ	angle of fins	rad
Γ	phase change rate	kg/m^3s
λ	Eigenvalues to homogeneous transport equations	m/s
Λ	Vector of eigenvalues to transport equations	m/s
ω	frequency of fluid rotation	s^{-1}
τ	shear stress / time constant in pipe wall	Pa / s
θ	pipe inclination to horizontal plane	rad
ρ	density of fluid	kg/m^3
μ	dynamic viscosity	kg/ms
σ	surface tension	N/m
φ	angle of rotation (fluid element)	rad
ϕ	bubble entrainment and disengagement rates	kg/m^3s
Φ	droplet entrainment and deposition rates	kg/m^3s
δ	layer thickness	m
ζ	pipe length over pipe diameter	–
Subscripts		
b	bubbles	

Continued on next page...

Symbol	Description	Unit
c	centre / critical / acceleration due to centrifugal force (swirl).	
d	centers	
e	evaporation	
f	fins	
g	gas	
i	Interface	
k	phase (l,g,d or b)	
l	liquid	
p	position on a circular helix	
s	superficial velocity	
s_1	slip between bubbles and continuous liquid	
s_2	slip between droplets and continuous gas	
z	length of heat pipe element	
1	field 1	
2	field 2	
j	element j (cell)	
∞	Bulk	
$-$	Averaged value	
$*$	Actual value (variable is intended to solve)	
s	Saturation	

Abbreviations	
$AVV1$	Avedøreværket Unit 1
$AVV2$	Avedøreværket Unit 2
BWE	Burmeister & Wain Energy A/S
CCS	Clean Coal technology
CD	Central Differencing scheme
CFD	Computational Fluid Dynamics
CFL	Courant-Friedrichs-Lewy
CG	Conjugated Gradient
CV	Control Volume
DCS	Distributed Control System
DNB	Departure from nucleate boiling
$DONG$	Danish Oil and Natural Gas
EES	Engineering Equation Solver
ENO	Essentially Non-Oscillatory
EOS	Equation Of State (Properties of fluids)

Continued on next page...

Symbol	Description	Unit
FD	Finite Difference	
FEM	Finite Element Method	
FV	Finite Volume	
$IRBT$	Internal Rifled Boiler Tubes	
LB	Left Bottom	
LHS	Left Hand Side	
LT	Left Top	
LTF	Lifetime Fraction	
LTI	Linear Time Invariant	
$NJV3$	Nordjyllandsværket Unit 3	
OFI	Onset of Flow Instability	
PDE	Partial Differential Equations	
$PF-USC$	Pulverised coal-fired USC boiler	
$PFBC-USC$	Pressurised Fluidised Bed Combustion	
RB	Right Bottom	
RHS	Right Hand Side	
RT	Right Top	
SBL	System of Balance Laws	
SCL	System of Closure Laws	
$SKV3$	Skærbækværket Unit 3	
$SLMF$	Siemens Low Mass Flux	
$SSP-RK$	Strong Stability Preserving - Runga Kutta	
TSO	Transmission System Operator	
TVD	Total Variation Diminishing	
UD	Upwind Differencing scheme	
USC	Ultra Super-Critical	
$WENO$	Weighted Essentially Non-Oscillatory	
$YPGL$	Yaomeng Power Generation Ltd	
$1D$	One-Dimensional	
$2D$	Two-Dimensional	

1. Introduction

The deregulation of electricity markets and the massive investments in renewable energy in Europe have increased the request for flexibilization of large central power plants. Denmark was the first country really to experience the challenges that the stochastic nature of wind impose on the electricity systems. The challenges with renewable sources began in west Denmark as early as around the year 2000 and have ever since just increased as more wind farms have been commissioned. The average generation from renewables in Denmark is some 28.1% by 2011, according to the annual energy statistics from the Danish Energy Authority, [1]. Denmark plans to increase renewable energy with an additional 2000 MW by 2020. Looking beyond Denmark's borders, Germany is about to impose even greater challenges up on themselves and their thermal power plants. They have invested massively in renewables, both wind and photovoltaic generation, and plan to have all nuclear generation phased out by 2023. Both Denmark and Germany already have massive challenges with the momentarly balancing of power consumption and generation which is a prerequisite for a stable power system. To balance consumption and generation it is necessary to operate the thermal power plants 'as the wind blows and the sun shines'. The flexibility requirements impose on thermal units are especially:

- The request for lower minimum load such that the units are ready to ramp up if the generation from renewables suddenly fails (e.g, forecast errors)
- The request for faster start-up (again typically forecast errors)
- The request for larger ramping rates (typically because fewer units are in operation but the total demanded load gradient remains the same)

All three flexibilization initiatives mentioned above are important for the inclusion of even more renewables. However, if one digs further into the technical challenges, it becomes clear that the lower stable minimum boiler load is one of the most important issues for the flexibility-optimisation and thus the integration of renewables. This is discussed below:

The number of thermal power plants in daily operation (in both Denmark and Germany) have already been reduced to a minimum. This minimum is either defined by power transmission stability requirements set forth by the TSO, or by district heating requirements. In general, it is thus not possible to shut down the remaining units in operation; they must be kept in operation and so to speak run

idle and be ready for high load operation in case of forecast errors, incidents and the like. When an incident occurs, a high ramping rate is of course desired in order to respond and balance the grid as quickly as possible.

DONG Energy has put much effort in reducing the minimum load on the larger 400 MW Benson-type, or once-through boiler, power units during the last one to two decades. Most of the units today are operated smoothly down to 20% boiler load and some even to a significantly lower load. However, the Benson boilers are here operated in boiler start-up mode, which means that not all feed water entering the evaporator furnace walls is evaporated. The boiler is in fact operated as a drum boiler at this low load. One consequence of this 'boiler start-up operation mode' is, that the unit efficiency drops and steam temperatures decrease, and this again has a negative impact on the fatigue of thick-walled components downstream the evaporator, when the boiler load e.g, one hour later, is rapidly increased again. During high wind periods, in order to save fuel and reduce material life-time consumption, it is thus desirable to seek to reduce the boiler load where transition from once-through operation (with high ramping rates) to boiler start-up mode (with lower ramping rate) takes place. The challenges to this issue are many, notably the following aspects: (1) evaporator flow stability and adequate cooling of furnace walls with feed water; (2) burner/flame stability; (3) flue gas inlet temperature to DeNox; (4) boiler control.

Approximately in 2006 DONG Energy decided to build and operate two 800 MW hard coal-fired units, located near the city of Greifswald in northern Germany. During the design phase of the boiler and turbine, much effort was put into optimizing the flexibility of the entire unit. Some of the most important issues that were addressed during the design phase, were to achieve as low stable minimum load and as high ramping rates as possible. The boiler furnace was designed with internal rifled vertical evaporator tubes instead of the traditional spiral wound furnace wall tubes. This Siemens Low Mass flux principle (SLMF) concept made it possible to operate the boiler stable in once-through mode down to some 20% of boiler base load. The traditional spiral wound tube concept normally only allows once-through operation down to approximately 35-40%.

DONG Energy had little knowledge on the thermo-hydraulics of the vertical arrangement. It was thus desirable to initiate this Ph.D project in order to achieve a fundamental comprehension of the thermo-hydraulics and load dynamics that we would face in daily operation at Greifswald, when the unit went into operation.

Unfortunately, due to the economic crisis that Europe faced by 2008, the Greifswald project was canceled by 2009. Knowing that the dynamics of evaporator

processes are vital for low load boiler operation, focus in this Ph.D. project was changed towards a more general understanding of the dynamics of evaporator processes.

1.1. A brief review of boiler technologies

A power plant boiler is a heat exchanger which includes several units: economizer, evaporator, superheaters, reheaters and air preheater. The more general boiler design will not be touched on here, as this is assumed to be known. Also, focus is entirely on the furnace and water walls, or the evaporator part. In the evaporator part, the fuel is burned on the furnace side and the combustion product is a hot flue gas exchanging radiant heat to the water on the other side of the heat exchanger. The boiler is traditionally built as a tower: inside the hot gas is produced, and the walls of the boiler are made of pipes welded together in which the water flows.

Most of the power plants are nowadays built as super-critical power plants, in order to obtain maximum efficiency, meaning that they are sized to operate in the super-critical region during high load operation, but in low load operation they will enter the sub-critical region. The difference between a super-critical and a sub-critical boiler is, that the latter is equipped with a drum boiler operating below the critical pressure. The drum acts as a water/steam separation unit. For the super-critical boiler, this part has become superfluous. Contrary to a drum boiler, where the water may pass the evaporation zone several times before it leaves for super-heating, the omission of the drum means that the water evaporates in one pass. For this reason, a super-critical boiler is called a *Once-through boiler*. The simplest of these is called the Benson boiler after its inventor. For Benson boilers there is a challenge at low load; at this working point the water does not fully evaporate, thus it is necessary to divert the outlet flow into a cyclone to separate the steam from the liquid. The liquid is finally collected and pumped back into the main feed water circuit. The outlet steam goes through a cyclone. That device is called a *connecting vessel* and typically consists of a high cylinder with a small diameter.
The super-critical power plants, operated in sliding pressure mode, which have been built over the last many years, are characterized by having high efficiency and improved load dynamics compared to drum boilers.
The heat flux in the central part of the furnace of a coal-fired power plant evaporator is approximately 200-400 [kW/m^2] and appears as radiation. In a gas-fired plant, the combustion zone is more controlled; therefore the temperature of the vapor leaving the approximately 200 parallel evaporator tubes is more stable, which is illustrated in figures (1.1) and (1.2).
Both figures show enthalpy measurements at separator vessel versus pressure

from SKV3 and NJV3. The coloured dots (cyan, red, green and blue) refer to the thermodynamic state after the four panel walls; front, back, right and left, all measured [2]. Note that the outlet enthalpy at SKV3 is much less stratified than at NJV3. The two units are geometrically identical, but SKV3 is gas-fired and NJV3 hard coal-fired, which apparently makes a significant difference in the heat uptake of the evaporator. The super-critical once-through boilers, built in

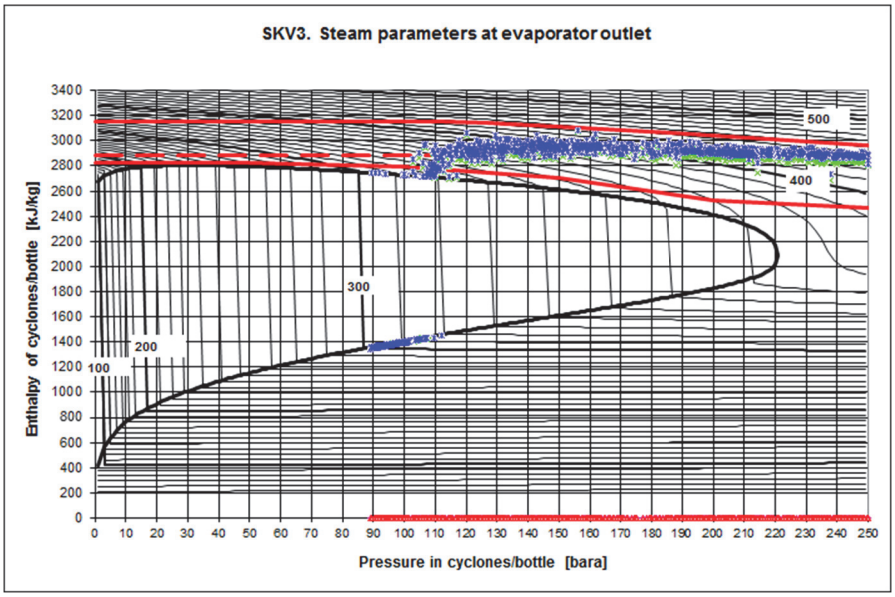

Figure 1.1.: Enthalpy at cyclones (evaporator outlet) versus pressure at cyclones. Readings from SKV3. Black thick line is lower and upper saturation curve. Red lines are enthalpy set point (dotted) and min/max enthalpy curves. From MOBE project [2].

Denmark, are all of the Benson type. They are partly characterized by requiring a minimum flow rate,which secures a relatively uniform flow rate through all parallel water tubes. The mass flux flow rate at base load is in general approximately 2200-2500 [kg/s/m^2]. The mass flux flow rate decreases linearly with boiler load and is approximately 800 [kg/s/m^2] at minimum load. This corresponds to an evaporator flow rate (ECO minimum flow) at SKV3 at some 90 [kg/s]. The Benson boilers at SKV3 and NJV3 are operated in sliding pressure mode down to approximately 35% load. Here below the evaporator pressure is kept constant at approximately 90 [bar]. Lower pressure than 90 [bar] increases the risk of flow oscillations. If possible, it is desirable to reduce both the pressure and flow further, so DONG Energy's boilers are operated in ultra-low load ("micro load"). By reducing the ECO minimum flow in an evaporator, it is possible to lower the Benson minimum, and thus increase the ramp rate at low load.

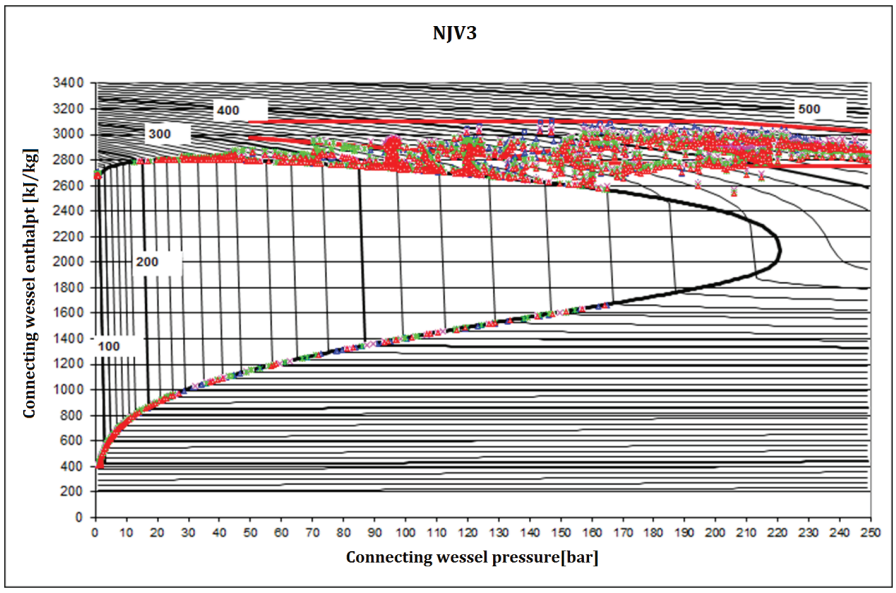

Figure 1.2.: Enthalpy at cyclones (evaporator outlet) versus pressure at cyclones. Readings from NJV3. Black thick line is lower and upper saturation curve. Red lines are enthalpy set point (dotted) and min/max enthalpy curves. From MOBE projekt [2].

One of the easier interventions for rapid load control, is to close down one or more of the high-pressure feedwater preheaters, whereby the amount of steam through the turbine train is increased, and thus the electricity production. The negative effect is reduced unit efficiency and a considerable stress on the economiser and evaporator due to reduced inlet temperatures. This can be compensated for by controlling the feed water flow quickly.
Siemens has invested years in developing a new evaporator concept where the Benson minimum can be reduced even further, see; [3]. The evaporator is constructed with vertical boiler tubes lined with internal rifles (SLMF). These can be used for very specific evaporator systems. The advantages of using SLMF are that the boiler's primary operating area (the Benson minimum) can be moved from the traditional 35-40 % load to around 20 % load. The Benson transition point which often must be passed at low ramping rate due to swelling and large material temperature gradients, is thus moved to a lower load. This allows the boiler to be 'parked' at low load with very low fuel consumption and be immediately available when market conditions again become attractive. There is limited literature on the subject, and there is a modest material relating to the mathematical description of the heat transfer and pressure drop in rifled boiler tubes. Foster Wheeler have

constructed a boiler for Longview Power in the US, which was in commercial operation in 2011. Finally, a unit in China was retrofitted (Yaomeng), but this boiler is operated at sub-critical condition. There is very limited operating experience with the SLMF principle.

1.2. Motivation

As discussed in previously, one of the primary areas of interest concerning flexibility optimization is the reduction of minimum load on the power plant, for both existing and new power plants. A reduced minimum load of the unit will (1) reduce fuel cost during periods when the unit is not in operation, and (2) keep the unit in operation such that it can be ramped up when the market conditions again are favorable. In other words, the power plant is available for load dispatch many more hours a year. This will improve the possibilities for enhanced revenue.

In recent years the market conditions for new power plants in Europe have become dramatically poor. Consequently the focus has changed, and today the flex-optimization of older power plants is of primary interest. Thus, it is not only interesting to study the thermo-hydraulic conditions in new plants, like the flow in vertical internal rifled evaporator tubes, but also certainly the dynamical thermo-hydraulic behaviour in existing power plants with the traditional spiral wound furnace wall tubes.

Danish central power plants are all once-through boilers of the Benson type. The water walls are typically constructed of some 200 tubes connected in parallel, running from hopper to furnace outlet with an inclination angle of approximately 15 degrees. Each of these tubes must at any instant be sufficiently cooled at any location along the tube. Normally this corresponds to a tube mass flux rate of 700-800 [kg/s/m^2] at minimum stable generation and 2000-2500 [kg/s/m^2] at rated capacity (Effenberger, [4], p. 518). If cooling fails for a certain time, the tube in question will be damaged (material creep and cyclic hoop stress) and eventually burst. Consequently, each power plant has a minimum feed water flow rate, which must be respected in order to avoid trip of the plant. Typically, the boiler is tripped after only 10 seconds, if the flow rate is too low. This trip criterium is very problematic and imposes huge challenges for the control engineer at low load operation, for example, during start-up/shut-down of the second feed pump or during swelling.

There is presumably a 'however': that the plants were designed for base load during the 1980-1990 when extreme low load was not an issue at all, and this leads to the belief that further low load optimization is possible. Based on other

basic flexibility challenges in power plants, solved with success, it is our belief that a thorough understanding of the thermo-hydraulic problems - paired with our existing knowledge on material creep and fatigue (FEM calculations), furnace load (CFD calculations) and more intelligent furnace control of the feed water, fuel and combustion control systems, restricted by an intelligent distributed control system (DCS) - will make it possible to further improve the low or micro load properties of a plant, which again eventually will lead to enhanced low load operation. This again may allow for further penetration of renewables like wind and photovoltaic. All aspects related to this optimization, except for the thorough comprehension of the thermo-hydraulics of the water walls, have already been thoroughly studied by DONG Energy Thermal Power during the past decade.

The purpose of this Ph.D. study is to demonstrate that it is possible to develop a robust numerical model able to dissolve the excessive dynamics that occur in connection with an evaporation process, taking place at varying feed water inlet conditions, evaporation pressures (fixed or sliding pressure operation) and heat flux rates and profiles along the pipe. If we can achieve a better understanding of the processes, mechanisms and boundary conditions that affect the dynamic evaporation process in a power plant boiler, then we have the fundamental basics for any further flex-optimization.

DONG Energy - Thermal Power A/S require a comprehensive description of the evaporator stability, in order to optimize the dynamic flexibility on the large central power plants in Denmark. Therefore, there are some added chapters to this thesis, which do not have the character of research efforts, but are included to provide a better understanding of the overall picture of the operational flexibility of power plants. This is particularly related to the CFD analysis of the boiler room, temperature profiles in the tube wall associated to its life cycle assessments in Chapter (4) and a description of the equation of states for water / steam (EOS) in Chapter (6). The novelty of the report is to be found in the section on flow distribution and dynamic stability, including interpolation and the use of the latest numerical techniques in connection with dynamic evaporator modeling.

1.3. Literature review

Much effort has been put into modelling evaporators. Focus was especially on the dynamic regulatory technical features of the power plant boilers, but there is not much literature on dynamic modelling of the evaporation process in the power plant boiler and the consequent load limits. There are some references

about experimental studies of evaporators, and much of this material is based on standards and is well documented in [5]. In [6] there is the modeling of a complete circuit distribution of a flow network system in a water wall of an ultra-supercritical boiler with vertical tubes. The model is steady, state and good agreement is achieved between the calculated mass flux distribution in the lower front wall and the plant data; the maximum relative difference is between 5.6 and 9.7 %. A dynamic evaporator model, which is able to simulate the entire vaporization process, including the sub-cooled liquid at the entrance and super-heated fluid at the outlet, has not been seen in published literature, due to the complexity around the saturation curve, which basically includes a singularity in the gradient of the density. With respect to internal rifled boiler tubes (IRBT), Harald Griem, [7] wrote back in 1985 on the subject, and both KEMA, [8] and Siemens have performed considerable experimental work that is considered properietary information, see [3] and [9]. Other authors have dealt with the experimental topic, with special focus on internal rifled boiler tubes; see [10], [11], [12] and [13]. Here consistent algebraic function terms are developed for the frictional pressure drop and heat transfer in IRBT. A thermo-hydraulic analysis of an ultra-supercritical boiler at full load is performed in [6], but no studies of part load conditions. Since this thesis deals with many specific subject areas, there is a detailed literature review in each individual chapter and literature references related to the topics discussed, and each subject is supported by literature references in relation to the articles developed in this study; see [14], [15], [16] and [17].

1.4. Thesis statement

Evaporator stability is very much related to the increased request for flexibilization of large central power plants. Therefore it is crucial to understand the basic concepts, related to the stability of a power plant evaporator, which is the absolute largest component in a thermal power plant, where the steam is used in both the production of electricity and district heating. In principle it is a questionof understanding the physics associated with an evaporation process and understanding the mechanisms which impose restrictions on large load dynamics.There are many factors to be illuminated in this context, such as the circumstances of combustion in the furnace related to the strength of the heat flux, materials technology, design of boiler tubes, an in-depth understanding of the physics that describe both the heat absorbed and pressure drop in the evaporator tubes, and finally an understanding of the market conditions of today. In addition, it is important to understand the fluid dynamic conditions prevailing in the evaporator tubes as well as selecting the correct mathematical/numerical methods to simulate the dynamic conditions in the evaporator. It is believed that the key for a more flexible energy

production is hidden in the understanding of the stability conditions of a power plant boiler, both static as well as dynamic.

1.4.1. Objectives and hypothesis

The main hypothesis of this study is linked to the idea of being able to model the temperature fluctuations that occur in the evaporator tubes. These temperatures are initiated by fluid temperatures as well as the heat flux from the furnace. Therefore a basic understanding of the fluid dynamics as well as material conditions in the form of heat transfer and lifetime analysis are essential in this work. The main objective of this Ph.D. thesis is to describe and analyse the up-to-date knowledge about operational flexibility in steam power plant evaporators, based on mathematical / numerical methods. More specifically, the Ph.D. thesis aims to:

- Examine the advantages and disadvantages in using internal rifled boiler tubes (IRBT) in steam power plants.
- Give a description of the furnace conditions, time dynamics of the heat tube material for power plant evaporators and the corresponding methods for estimating the lifetime of boiler tubes due to fatigue and creep.
- Obtain a detailed understanding of the phenomena leading to flow maldistribution and Ledinegg stability under different operation pressures including flow regime maps for the flowing fluid.
- Outline the various equations of states (EOS) for modelling tasks and specify concrete implementation proposals, which adequately take into account both the accuracy and calculation speed.
- Map the dynamic response of the power plant evaporators especially for the start-up of a plant.
- Describe and implement a robust numerical solver for handling the very strong thermal-hydraulic transients that can occur in a power plant evaporator. Point out the numerical challenges and choose methods for implementing a dynamic solver, tested on a homogeneous thermo-hydraulic flow model.
- Develop mathematical models for simulating the dynamics of power plant boilers in order to understand the mechanisms that occur in an evaporation process and point out some coupling examples, which can lead to increased operational flexibility in power plants.

1.4.2. Methodology

This thesis develops mathematical models for simulating power plant evaporators, in order to answer the above questions and meet the objectives. The steady state models are implemented in the EES software package, while the dynamic model is based on a new numerical scheme (WENO). The dynamic modesl are implemented in C++ in order to optimise the performance of the application. The equations of state are based on IAPWS-97 (International Association for the Properties of Water and Steam) and are implemented in an interpolation scheme in order to speed up the simulation. However, we have been given access to readings from the control system of Skærbækværket, and have focused on four stable and common load situations. The measurements did not quite satisfy high time resolution, but we can use the measured data for model calibration. We will primarily model traditional spiral wound furnace wall tubes with smooth boiler tubes, which are totally dominant in the Danish energy market, but will also perform simulations of the IRBT, which in size corresponds to a SKV3 boiler.

1.4.3. General delimitations

DONG Energy-Thermal Power have several different modelling tools for subsequent analysis of more complex energy systems, where the boiler is integrated with other control systems and turbine components. These systems, however, suffer from the weakness of not having advanced boiler models, or rather a spatial discretization of an evaporator tube, so we lack a general understanding of how an evaporator behaves in a dynamic context. In order to reduce the complexity and computation time, we analyse only the evaporator, and we force our numerical models with conservative downstream boundary conditions, especially in terms of pressure, which is assumed to be a fixed boundary condition at tube outlet. This is a truth with modifications, as the pressure in general is determined by the swallowing capacity of the downstream steam turbine, thereby building up a pressure level, which initially is fixed at the condenser and / or district heating condenser. This pressure build-up through the turbine train causes a form of compressibility and elasticity of the downstream boundary condition on the evaporator. Therefore, the dynamic response represents a worst case scenario in the case of forcing the model with fixed upstream pressure boundaries.

Another limiting factor is the introduction of artificial diffusion in sub-areas, where the equation of state (EOS) for water/steam provides dedicated singularities in the first derivative of the fluid density. Here the artificial diffusion is introduced, scaled from relations derived from a Boussinesq approximation of thermal-hydraulic fluid flow. The intention is to attenuate unwanted pressure waves initiated from the above-mentioned singularities.

1.5. Thesis outline

The thesis is organized in the following way and contains 12 chapters and 17 appendixes. The contents are as follows:

Chapter 1 is the introduction which contains the thesis statement, motivation, an overall literature review, objectives, approach and an introduction to the background and fundamental aspects of the commercial energy market in Denmark.

Chapter 2 provides an introduction to power plant boiler technology and corresponding loading conditions. The internal rifled boiler tubes are introduced.

Chapter 3 presents a case study of Skærbækværket (SKV3) with a brief plant description and discussion of corresponding measurements.

Chapter 4 describes the heat flux distributions in the furnace of SKV3, modelled by CFD, and discusses the corresponding furnace tube wall (panel wall) conditions together with a tube lifetime description.

Chapter 5 presents the physical mechanisms of the most common flow instabilities; among these phenomena, we choose and analyse those that can trigger an oscillation. Various flow regimes are described in relation to the heat transfer calculations. Primarily focus is on mal-distribution, based on an optimisation problem of mal-distribution, as a function of heat uptake on two parallel tubes, for varying samples of measurements and an Ledinegg stability analysis in panel walls including gravitational pressure drop. The chapter ends with a brief conclusion on the static stability and what we need to focus on when designing a steam power plant evaporator.

Chapter 6 presents the most common equation of state (EOS) for the water / steam media, for use in multi-layer models. Here the liquid and the gas (steam) phases are typically separated.

Chapter 7 deals with compact numerical interpolation schemes, for fast calculation of the thermodynamic properties, based on the IAPWS-97 (International Association for the Properties of Water and Steam). These methods are based on linear, bilinear and second-order interpolation elements. The accuracy and computing speed of the interpolation schemes have been compared to the IAPWS-97 standard, which is the reference application in this work.

Chapter 8 presents a two-phase flow model for predominantly one-dimensional

flow. The model can be adapted to different flow regime patterns (vertical as well as horizontal stratification) and handle tubes with or without rifling. The model uses a non-equilibrium approach and consist of two continuity equations, two momentum equations and two energy equations. Phenomena such as relaxation terms in the context of Riemann surfaces and discontinuities are briefly described and various eigenvalue analysis of the system Jacobians of two phase systems are presented as well as relations for the speed of sound in the two phase fluid for different flow regimes. A homogeneous model, based on the two layer approach is outlined. Finally a four-field model for detailed description of flow regimes in two-phase flow is mentioned.

Chapter 9 deals with solving hyperbolic systems of partial differential equations and contains a brief introduction to some of the fundamental concepts and an overview of the primary challenges in solving hyperbolic partial differential equations. The WENO approach is outlined and tested against the most common test cases from the literature.

Chapter10 gives a general overview of the dynamic flow stability in boiler systems. A homogeneous two-phase model is setup and is configured in order to simulate the impact of four different heat flux profiles during a start-up situation. Also effects of a high-pressure preheater failure on SKV3 is modelled and finally the low-pressure operation (turbine bypass) of a power plant evaporator is clarified, in order to generate district heat at the expense of the electricity production.

Chapter11 contains a discussion of the principal areas of work.

Chapter12 covers the conclusions of the thesis and the recommendations for further research and product development.

Appendix A is a detailed description of the dimensional analysis with the most common constants in fluid mechanics and thermodynamics.

Appendix B includes a list of static cycle calculations of the thermal power plant SKV3. The calculations are based on the consolidated simulation tool Turabs 2, developed by DONG Energy-Thermal Power A/S. The simulations have the aim of identifying a complete operating range in terms of both heat and net electricity production. The output from calculation results is a so-called PQ diagram.

Appendix C outlines the net cross-section area of an internal rifled boiler tube (IRBT).

Appendix D outlines the net cross-section area of an internal rifled boiler tube (IRBT).

Appendix E is a derivation of the classical formula that reflects pressure drop and heat transfer for internal two-phase flows in pipes.

Appendix F contains four sets of measurements (samples 1-4) from October 2011 at the power plant SKV3. Measurements are recorded in the control system of the power plant and processed further into a InSql® database where data can be treated. Measurement data covers typical operating situations where the boiler is operated in Benson or circulation mode.

Appendix G contains a brief description of the estimation of lifetime in heated tubes with respect to fatigue and creep.

Appendix H includes additional curves due to mal-distribution analysis, showing the correlation between the relative friction pressure, mass flow and outlet enthalpy as a function of the relative distribution of heat between two heat pipes.

Appendix I provides a comparison of three different setups of interpolation maps of IAPWS-97 from the analysis performed in Chapter (6).

Appendix J is a brief description of algorithms for solving an implicit given linear system of equations created by discretization of partial differential equations. The solver is based on a fast sparse technique, and is used in solving the poisson equation of heat conductivity in heat pipe walls.

Appendix K lists the most important partial derivatives describing the equations of state for the one-phase and two-phase regions of a fluid.

Appendix L deals with the fluent combustion model and describes both the flow model as well as the combustion reaction and gas phase reaction models.

Appendix M presents a four-layer incompressible flow model with a time-averaging of the velocity fluctuations. For vertical flow, a non isotherm stratification of the flow fields is caused by a swirl initiated by the IRBT. The model is able to describe different flow regimes.

Appendix N presents a journal paper (Computers and Fluids); Implementation and test of a higher order hybrid solver for hyperbolic and parabolic balance laws.

Appendix O presents a journal paper (Applied Thermal Engineering); Finite Element Method Interpolation Scheme for Fast Calculation of Water/Steam Properties.

Appendix P presents a journal paper (Heat and Fluid Flow); Homogeneous two-phase flow model of a vertical steam evaporator implemented in a fifth order Central WENO scheme for hyperbolic balance laws.

Appendix Q presents a conference paper (SIMS 2012, Reykjavik, Iceland); A homogeneous two-phase flow model of an evaporator with internally rifled tubes, modelled by a fifth order Central WENO scheme for solving hyperbolic balance laws.

2. Power plants

This chapter provides an introduction to the power plant boiler technology and the corresponding loading conditions. Here is a brief description of a specific power plant (Skærbækværket Unit 3) with the boiler and the loading regulatory aspects in relation to the technical limitations that exist in power plant technology.

2.1. Furnace design

This section will outline two types of furnace designs in relation to the Benson once-through technology, the traditional spiral wound furnaces and the new boiler concept with vertical, internal rifled boiler tubes. Both technologies have advantages and disadvantages, and these will briefly be highlighted below. The operation experience gained at Yaomeng Unit 1, which underwent a retrofit in 2002 and was converted to low mass flux boiler technology, will be highlighted, too.
The ideal furnace design would be able to support its own weight and be capable of variable pressure operation over the load range while exhibiting natural circulation flow characteristics with flow increasing as heat absorption increases, thus preventing high temperature differentials between adjacent tubes. The boiler ramp rates today are a very important issue due to the deregulation of the electricity market.

2.1.1. Spiral tube furnace design

Spiral wound furnaces have tubes that are wound at an angle of 10^o to 25^o around the furnace perimeter from the lower furnace inlet headers to above the burner zone; see figure (2.1). This arrangement allows each tube in the furnace to pass through the various heat zones so that the heat absorption for adjacent tubes is reasonably uniform. By wrapping each furnace enclosure tube through each of the four furnace enclosure walls, each tube goes through approximately the same variation in heat absorption, both axially and radially. A high mass flux is required to maintain effective heat transfer across the boiler load range as well as to avoid stratification of the two phases of water and steam at minimum load. The danger of stratification or inadequate heat transfer at low loads limits the minimum once-through load (*Benson load*) of spiral furnaces. Also the high mass flux causes a high pressure drop in the tubes, which means feed water pump power is correspondingly high, again leading to a high dynamic friction loss compared to

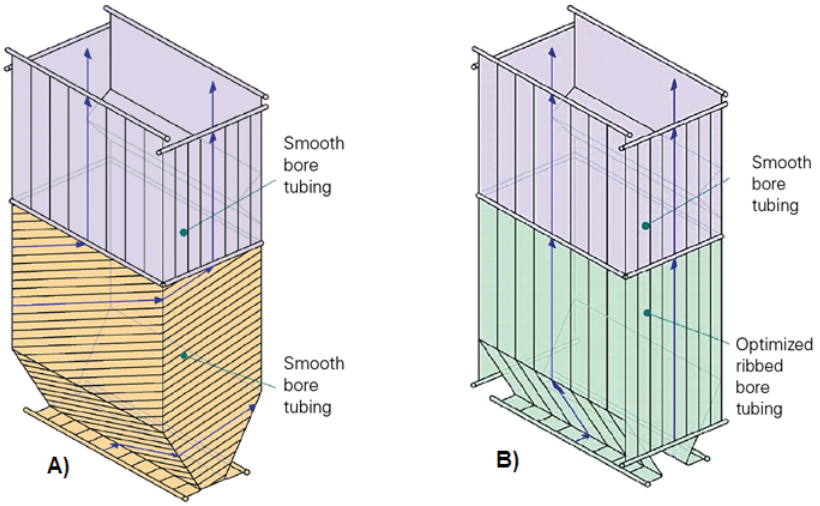

Figure 2.1.: A: Spiral furnace. B) Vertical tube low-mass-flux furnace. see [18]

the static pressure loss (hydrostatic loss). Additionally the spiral wound furnace has negative flow response characteristics for a high mass flux system. The water flow must decrease with higher heat input to maintain the system pressure loss, which illustrates that the furnace wall tube metal temperature is adversely affected, as tube flow is reduced when there is an above-average heat supply. The ramping rate of spiral wound furnaces is restricted by the construction of the furnace. Because spiral wound tubes cannot support their own weight, vertical support straps are required on the outside of the furnace. This leads to thermal stresses between tubes and support straps during dynamic load conditions, which limits the start-up speed of the boiler as the strap temperature lags behind the tube temperature.

2.1.2. Vertical tube furnace design

The use of vertical internal rifled boiler tubes is the key to a low mass flow boiler design, because the spiral ribs force the heavy fluid phase (water) to the tube wall, thus maintaining the water film up to a higher steam quality. Figure (2.3) illustrates the dry-out boiling crises for both the ribbed and the smooth boiler tube. The ribbed tubes postpone the dry-out so it occurs at higher steam qualities. One of the major benefits of a vertical tube furnace design is the positive flow response characteristics for a low mass flux system. The tube characteristics are positive, which means that the water flow must increase with higher heat input to maintain the system pressure loss. These characteristics of a once-through boiler furnace design are highly desirable. An advantage of the low mass flux system is also a general reduction in pressure loss through the furnace, so the feed pump power is

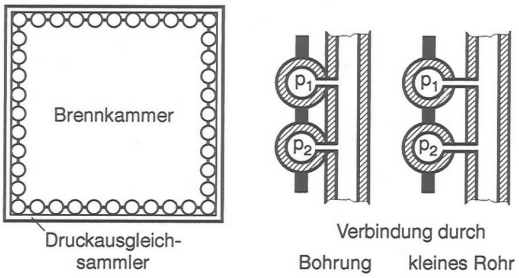

Figure 2.2.: Pressure equalizing zones between panel wall and pressure wessel, from [4].

reduced and the cycle efficiency is correspondingly increased. One of the major disadvantages is that the flow distribution through the vertical boiler tubes is very sensitive to the heat flux distribution in the boiler and to a uniform distribution of feed water to each tube from the inlet headers, result in varying heat uptake through the panel walls, which can result in local instability in the flow field lead to very low or zero flow conditions and departure from nucleate boiling *DNB* or in the worst case a melting tube wall. To prevent this phenomenon, some boiler manufacturers have built in pressure equalizing zones or even temperature mixing vessels in the evaporator at approximately half height; this was considered for the Griefswald boiler. This is done to reduce the temperature disparity in the evaporator, thereby ensuring a more uniform flow through the evaporator. One example of a general pressure equalizing zone is illustrated in figure (2.2). According to reference [19], there are obvious structural benefits to using SLMF technology. The Low Mass Flux furnace design for a typical 800 MWe boiler is lighter by approximately 300-400,000 kg, has about 4,000 fewer welds, and will require close to 50,000 fewer construction hours to erect than a typical 800 MWe universal pressure boiler. The vertical wall panels are also much easier to fabricate, thereby reducing manufacturing cost. Another advantage is that the Benson load can be reduced to some 20 % boiler load for a Low Mass Flux boiler, which leads to smaller start-up systems. This could, e.g, eliminate the need for a recirculation pump.

2.1.3. Operating experience with the low mass flux boilers

The Yaomeng Power Plant is situated in the central southern area of Henan Province of China. The plant consists of four 300 MWe sub-critical boiler units. The original boilers consist of traditional spiral wound furnace wall tubes with smooth boiler tubes, once-through units designed for base load operations. The success of the retrofit of Unit 1, which began in May 2000, can clearly be seen through the improved availability and the unit's ability to change load rapidly.

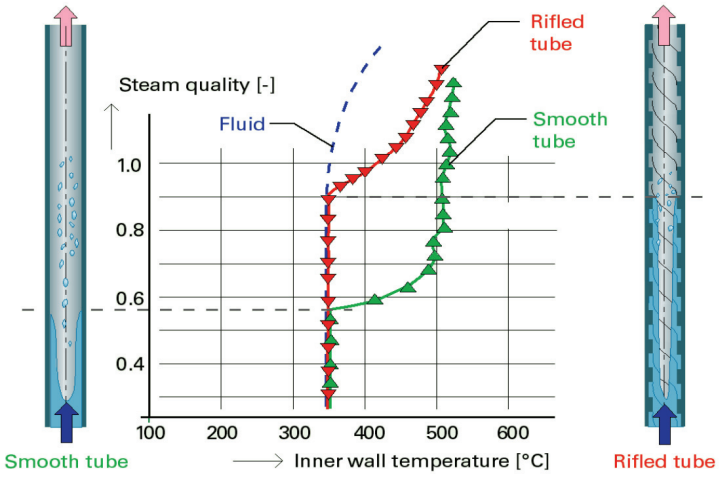

Figure 2.3.: Comparing the dryout characteristics of ribbed and smooth boiler tubes the ribbed tubes postpone dryout which then occurs at higher steam qualities; see [19].

Before the retrofit in 2000, the unit availability was 88.7 % and after the retrofit it is 95 % according to [19]. The boiler ramp rate is improved from 1 %/min. to 3 %/min. Even though Yaomeng Unit 1 was the first low mass flux Benson boiler unit in China, there have been no ribbed tube failures, caused by overheating or high temperature differentials of adjacent tubes in its seven years of operation. Furnace temperature and metal temperatures in the panel walls are simultaneous recorded. The temperature difference between adjacent tubes has been reduced from 70^oC to between 20^oC and 30^oC. As a result, no boiler wall tubes have failed, and the unit can now reduce the load to 40 % without oil-firing assistance - something never achieved with the original boiler.
In the Yaomeng Unit 1 boiler, the once-through boiler has its basic evaporator zone in the low heat flux region, where the tube metal temperature is minimized. The water purity has to be high to avoid corrosion, deposition, and carry over of dissolved solids. As the ribbed boiler tubes have an optimized profile, Yaomeng Power Generation Ltd (*YPGL*) questioned how the positive flow response would be affected by the potential deposit build-up on the inside of the tubes. It can be inferred that the positive flow response is still active, if it can be shown that the metal temperature has not risen above material limits and that tube failures caused by adjacent tube temperature differences do not occur, even if there is a high deposit weight density. Tube samples containing internal deposits were removed from the high flux heat areas of the furnace to determine deposit thickness in

July 2008. The tubes were then arranged by firing side and nonfiring side, which clearly shows deposit build-up on the ribs of the furnace wall tubes before acid cleaning. The build-up on the non firing side shows a more uniform distribution of deposit. The deposit was analysed during every outage to determine the weight density. The results show an increase in deposit weight density is also apparent on the non-firing side, but the increase is less uniform over time.
The major conclusions of the retrofit of Yaomeng Unit 1 plant are, according to [19], that the new boiler steam output as well as thermal efficiency have both met the guaranteed conditions and peak levels in steam production. Major environmental improvements are achieved, where NOx levels are reduced and unburned carbon has decreased with approximately 75 % as well as the particulates issued from the chimney have been reduced approximately by 90 %. The customer *YPGL*, has expressed satisfaction with the results of the retrofit. As has been demonstrated, the full scale heat transfer and pressure loss test data, on which the Yaomeng design was based, extends to super-critical pressure conditions. Thus the technology for super-critical plants is available now, and there is every reason to believe that the move towards higher pressures will be equally if not more successful.

2.2. Geometry of boiler tubes

One parameter that determines the single-phase heat transfer rate on the inside of a heat pipe, is the fluid velocity near the inner pipe wall. If the velocity can be increased without increasing the net mass flux through the boiler, the heat transfer rate can be increased. With that assumption it is possible to build a more compact boiler, without taking the theory of combustion into account. Internally rifled boiler tubes (IRBT) are an attempt to speed up the velocity at the wall without leaving the vertical tube of a boiler construction. The mass flux through the IRBT is usually in the range of 1000 $[kg/m^2s]$ at base load and is less than the half as seen in traditional Benson boiler panel walls, with a moderate pipe inclination. In addition to the rise in heat transfer, the IRBTs are characterised by an excellent performance concerning two-phase flow. The swirl is very good for separat liquid from gas. The centrifugal force increases the rate of light fluid to the centre of the pipe and forces the heavy fluid components to near the wall, improving the cooling of the pipe and thereby increasing the heat transfer and decreasing the wall temperature of the pipe. Additionally the IRBT has the following advantages: the rifles will enlarge the surface of convective heat transfer, increasing the turbulent intensity in the boundary layer and increasing the relative velocity between the wall and the core fluid by the rotational flow.

The advantages of the IRBT have a price. The relative pressure loss is higher

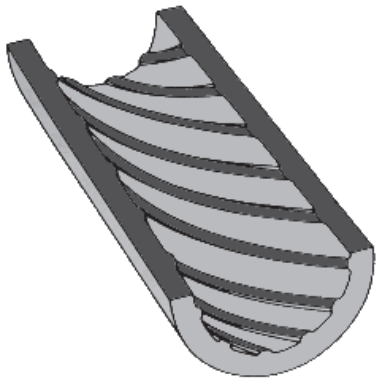

Figure 2.4.: Center cutting of an internal rifled boiler tube

than that in the traditional boiler tubes, but it can be used in a constructive way. When super-critical boilers are partly loaded, stability problems can occur. The problem is usually solved by inserting orifices in the tubes that adjust the pressure loss of each individual tube. Thus the increased pressure loss in the IRBT can be utilized to replace the traditional built in pressure loss and thereby not increase the pumping power. The wall shear stress in an internal rifled boiler tube is given by

$$\begin{aligned}\tau_w &= f_w \xi \bar{\rho} \frac{U \cdot |U|}{2} \\ &= f_w \xi \frac{G \cdot |G|}{2\bar{\rho}}\end{aligned} \tag{2.1}$$

where the term f_w is the friction coefficient under single-phase flow, and ξ is the dimensionless friction coefficient based on the single-phase frictional coefficient in heated rifled tubes:

$$\xi = \frac{a}{Re^b} + c. \tag{2.2}$$

In table (2.1) we propose coefficients based on the Blasius formulation given by [7], for different rifled profiles. In [11] the same formulation of ξ is used, and an absolute relative error less than 6.3 % is reported by the author for specific rifled tubes. In two-phase flow the friction loss can be expressed by (2.1), where f_w is adjusted by the two-phase multiplier given by equation (E.42) in Appendix E. The cross-section area of a fin is illustrated in figure (C.1) and can be calculated by using equation (C.6).

Table 2.1.: Algebraic relations of f_w for different profiles. [7]

type	RR6	RR5	RR4	RR2
a	1702	0.56	16.26	1.65
b	1.18	0.32	0.71	0.44
c	0.032	0.01309	0.01509	0.02344

2.2.1. Summary

In this chapter we have described the benefits of using IRBT compared to a traditional spiral wound furnace. In brief the advantages are of both a constructive and a fluid mechanical nature, as there are obvious structural benefits of using SLMF as the boiler is lighter and becomes a self-supporting structure without requiring straps that affect the dynamic response. Furthermore, the low mass flux boiler has a completely different operating profile, by having a positive flow response characteristic, in the sense that the tube flow response requires the water flow to increase with higher heat input to maintain the system pressure loss, while the spiral wound furnace has a negative flow response characteristic for a high mass flux. The dry-out characteristics of ribbed boiler tubes occurs at higher steam qualities, which gives a much better cooling of the tube wall. Last but not least, the Benson load can be lower for a low mass flux boiler, which leads to smaller start-up systems that could eliminate the need for a recirculation pump. One of the major disadvantages of vertical evaporator tubes is that the flow distribution through the vertical boiler tubes is very sensitive to the heat flux distribution in the boiler, resulting in varying heat flux through the panel walls, which in the worst case can result in local instability in the flow and ultimately cause a melting tube wall. In the spiral wound furnace, each tube passes through each of the four furnace enclosure walls, and goes through approximately the same variation in heat absorption, both axially and radially, but at low load there is a potential of stratification or inadequate heat transfer, limits the minimum once-through load (the Benson minimum load).

3. Case study - Skærbækværket

This chapter describes the design and layout of Skærbækværket (SKV3) thermal power plant complemented by measurement campaigns taken from its control systems. Skærbækværket is one of DONG Energy's ten central CHP plants, built in 1998, with a capacity of 392 [MW] and located in Skærbæk at the mouth of Kolding Fjord. The utilisation of natural gas entails that the environmental impact is reduced to a minimum. By firing natural gas, the power plant ensures that no particles, fly ash or considerable amounts of sulphur are produced during operation. The use of low-NOx burners reduces the formation of nitric oxides in the flue gas. The heat and power production at SKV3 is primarily based on natural gas, and the production is made with a strong focus on the environment and cost effectiveness. The combined heat and power production at SKV3 means optimum utilisation of fuel, ensuring an advantage in terms of savings in resources and protection. An identical power plant based on coal combustion is located in Aalborg in northern Jutland. The plant is named Nordjyllandsværket Unit 3 (NJV3).

3.1. Plant flexibility

According to the immediate production requirements, the steam may either be taken out on its way through the turbine steps and used for district heating production in the heat exchangers - or it may be used for maximum power production in which case the steam leaves the turbine after the LP part to be cooled in the condenser. The SKV3 Unit 3 is a combined heat and power plant which both produces power for the high voltage grid and supplies district heating to the Triangle Region Denmark. Figure (3.1) shows a PQ-diagram, indicating the entire operational flexibility range for SKV3 with respect to power (P) and district heating (Q). The C_v-value is a frequently used figure for the pricing of district heating production, which expresses a relation between loss in power production caused by district heat production and the actual district heat production:

$$C_v = \frac{P_{cond} - P_{actual}}{Q_{DH}}. \tag{3.1}$$

Here P_{cond} is the net power production in condensed mode and P_{actual} is the net power production for the same boiler load, but with district heating (Q_{DH}). Corresponding simulated PQ diagrams provide DONG Energy with a continuous picture of the fuel amount and the C_v-value within the operating areas of all power

stations, which enables optimisation of the mutual operation of the power station units. The PQ-diagram are based on the simulations performed in tables (B.2) and (B.3). The corresponding abbreviations are listed in table (B.1). The design model of SKV3 is illustrated in figure (3.4) and covers only the water / steam circuit of SKV3. The model forms the basis of the displayed PQ diagram with associated tables (B.2) and (B.3). The design model consists of approximately 850 unknown variables (Principal DOFs) and 2000 secondary DOFs.

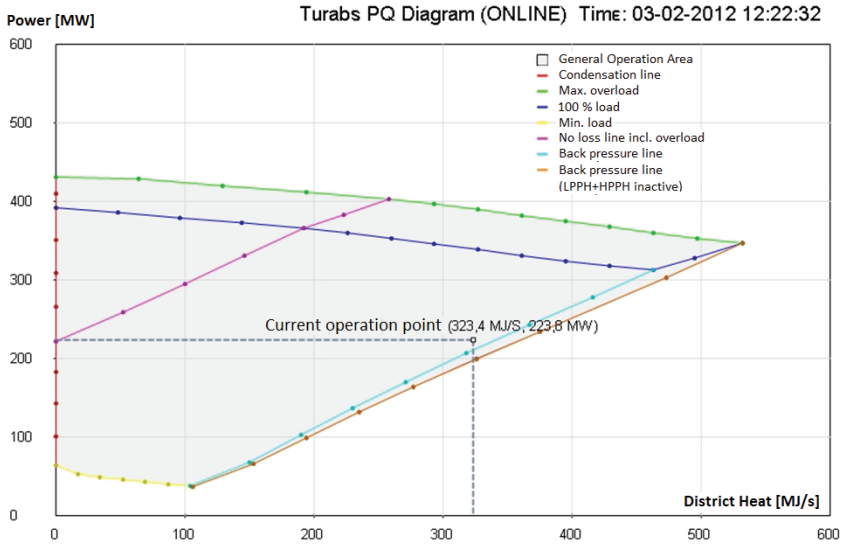

Figure 3.1.: Operational area for SKV3 with respect to district heat and power, based on tables (B.2) and (B.3).

3.2. Description of the SKV3 plant

Over time Denmark has been dependent on foreign fuel resources, and this has been a continuous incentive to try to obtain higher efficiency at power stations. It was therefore a natural consequence to build a unit with double reheat and super-critical steam data. The efficiency is thus 48% at SKV3 in condensing mode with a fuel utilisation of up to 93% by combined heat and power production. The overall efficiency of the unit is up to 49% by installation of an expansion turbine, which by reducing the pressure of the natural gas, supplies a net output to the power production of 4 [MW] at full load. Unit 3 consists of a 90 m high boiler house, a 32 m high turbine building, a 48 m high district heat storage tank and a 120 m high stack. The boiler is built as a 75 m high tower boiler with a furnace volume of 59,000 $[m^3]$.
The unit is equipped with an Alstom ® turbine extraction unit, designed with

maximum capacity for district heat production. The turbine plant comprises five turbine parts:

- A very high-pressure turbine with 14 stages.
- A compact module with a high-pressure and an intermediate pressure part (HP/IP0) with 6 and 9 stages, respectively.
- An asymmetric intermediate-pressure part IP1 and IP2 with 5 and 7 steps, respectively. Steam extraction for two serial connected district heat exchangers from the first (IP1) and the second (IP2) part, respectively.
- Two double-pass (butterfly) low-pressure turbines (LP1 and LP2).

The steam is reheated to 580°C both after the very high-pressure turbine (VHP) and after the high-pressure turbine (HP). The double reheat results in the efficiency of the plant being increased by approximately 1 percentage point compared to a plant with single reheat. The turbine plant is throttle-controlled and is normally run in slide pressure mode, which results in the best available efficiency. Due to the slide pressure mode, the up or the down throttle of the plant takes place based on the boiler pressure while the control valves of the turbine are wide open. The live steam pressure varies from 285 [bar] at full load to 90 [bar] in circulation mode. The outlet pressure from the VHP turbine is 78 [bar]. In the high-pressure turbine the steam is expanded from 76 [bar] to 20.5 [bar] and in the first intermediate-pressure turbine (IP0) it is expanded from 19 [bar] to 7 [bar], after which the steam is led to the asymmetrical IP1/IP2 turbine. Here the steam is expanded to a pressure of 2.3 [bar] by outlet from IP1 and to approximately 1 [bar] by outlet from IP2. From here the steam is led either to the district heat exchangers or to LP1 and LP2, respectively, and further on to the condenser. The regulation capacity of the plant is according to DONG Energy's load gradient requirement of maximum 8 % of maximum continuous capacity (MCR) per minute, see figure (3.2). The marked red line in figure (3.2) illustrates the transition area where the boiler is moves from circulation-mode to Benson-mode. The last 10% load, from 90% to 100% is reduced to only 3 [%/min] to ensure stable temperature and calm operating conditions at full load range, where the temperature is 582 [°C], which is close to the material limits that super-heater material like Esshete 1250 and fine-grained, austenitic steel TP-347 H FG dictates. By running down the plant through the transition region from Benson to circulation mode, a corresponding reduction of the load gradient is seen (from 8 to 3 [%/min]) to avoid major temperature fluctuations in the bottle and thick-walled components caused by the sliding pressure curve and low flow rates.

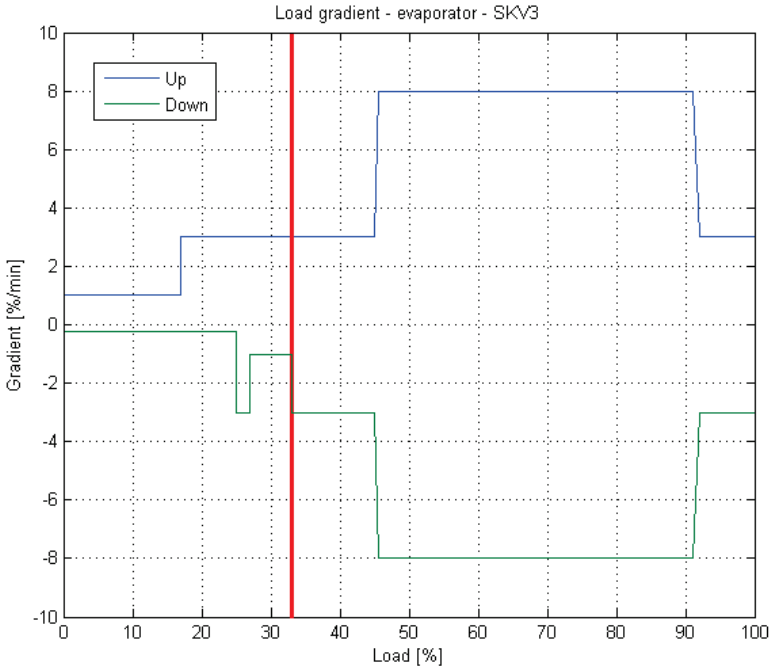

Figure 3.2.: DONG Energy's load gradient requirements for SKV3.

3.2.1. Main cooling-water system

The plant is cooled using seawater, and the main cooling-water system is optimised for an inlet temperature of 10 [°C]. The condenser at the cooling-water side is divided into two parts. Operation can thus be maintained while one part is cut off. The condenser pipes and the tube plates are made of titanium to avoid corrosion at the seawater side. Cooling water is taken in from Kolding fiord and led through two 50% main cooling pumps to the cooling-water intake structure with automatic cleaning grating and on through two mussel filters to the condenser. The total amount of cooling water for supply of the main cooling system is 14,000 [kg/s] at 100% load.

3.2.2. District heating

District heating is supplied to the surrounding towns with a total population of approximately 250,000 inhabitants. At SKV3 steam for the district heat production is extracted at two outlets of the asymmetrical double-current intermediate-pressure turbine and led to the two heat exchangers. These heat exchangers are serially connected in order to achieve the best possible reduction of the power production combined with heat production. The outlet pressure and the temperature are 1.34 [bar] and 220 [°C] and 0.46 [bar] and 113 [°C], respectively. The district

heating water is heated to a forward temperature of 105 to 120 [°C]. The return temperature is normally 48 [°C]. The maximum district heat production is 465 [MJ/s] in back pressure mode only (and up to 530 MJ/s in overload condition). The local area can at most take 400 [MJ/s] district heating. The remaining production capacity can be used for storage in a district heat storage tank balancing economy and energy in relation to heat and power production. The district heat production can be regulated from zero to the required output, being subject to, however, the usual interdependence between power and heat production. The district heat storage tank holds 25000 $[m^3]$ and can instantaneously release a power production capacity of approximately 60 [MW].

3.2.3. Boiler system

The boiler is a super-critical once-through tower boiler of the Benson type with double reheat, and the boiler efficiency is 95.7% by gas-firing. The furnace walls are with helical tubing. By using special materials, it has been possible to design the plant to very advanced steam data. Below 540 [°C] the following materials are used for the super-heater and reheater tubes: 15Mo3, 13CrMo44 (T11), 10CrMoV910 (T22) and X20CrMoV121. For the final super-heater and the reheaters, Esshete 1250 and fine-grained, austenitic steel TP-347 H FG are used to guarantee good control of the steam side oxidation and high temperature corrosion on the flue gas side of the tubes. For the headers and external piping in the HP system, martensitic steel P 91 is used from the HP 1 outlet header and above. Flue gas recirculation, including the reheating of the flue gas in a special sector in the quad sector rotating air heater, is installed as part of the control of the IP outlet temperature. The once-through boiler is designed by Danish Burmeister & Wain Energi (BWE).
The firing is tangential with low NOx burners and staged combustion. The main steam is controlled by sliding pressure operation and fully open turbine valves. The top of the boiler house is some 90 m above ground level for the double reheat cycles. Figure (3.3) shows a schematic view of the boiler for SKV3. The water walls are spirally wound up to approximately 40 m above the bottom of the boiler, and special attention has been given to the choice of materials for the water walls, the final super heaters, the high-pressure outlet header and the pre-separator. The well-known 13CrMo44 (T11) has been foreseen for the water wall tubes, but further improvements of steam parameters will need better steel for the water walls.

3.2.4. Control system

The control system performs all the tasks of control, regulation, supervision and protection of the boiler, turbine, generator, and condensate system, including auxiliary systems and district heating and system consumption. The operating

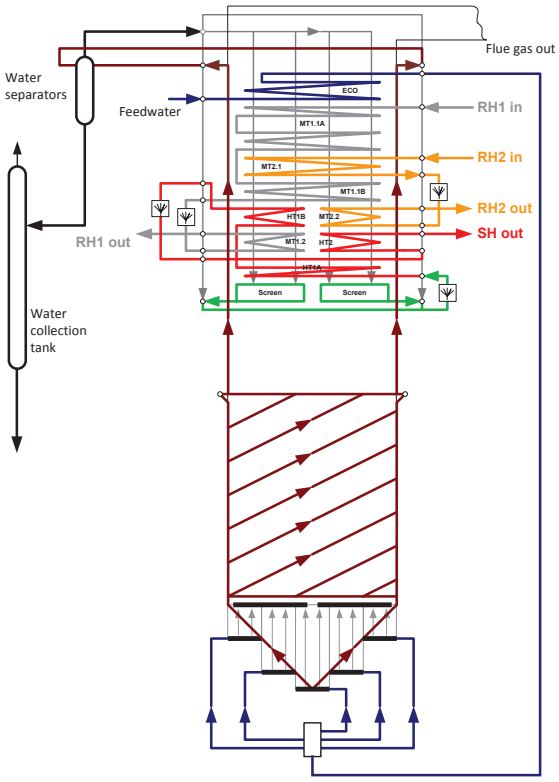

Figure 3.3.: Schematic view of the boiler for SKV3.

situation and the development in the efficiency of the individual plant components are continuously supervised by means of calculations in the control system. Results of this supervision and measuring signals from several parts of the process make up around 6000 tags per plant, which are transferred to a central InSql® database where data can be compared and analysed over time to obtain optimum operation both financially and technically, based on online performance simulations (Turabs Online); see [20]. It is also possible to compare operational results from DONG Energy's other power stations as all control systems send data to the central InSql® database.

3.3. Steady state modelling

Numerical modelling of SKV3 is performed by Turabs II. Turabs II is a simulation programme developed by DONG Energy - Thermal Power A/S for calculation of turbine and water/steam circuits in general. Turabs II is the result of more than

15 years of continuous development and is tuned through the experience gained from energy projects worldwide. The system is a static calculation programme, which with a comprehensive component library and advanced water/steam and gas library, can be used for design and consequence calculations of power station units. Turabs II equips engineers to carry out accurate pressure, temperature and flow analysis from a position of knowledge, and rapidly achieve an optimised design. This cuts production costs and improves product quality. The system runs on a Windows platform and comprises a pre-processor, which can run in a design and in an off-design mode so that based on a design calculation, consequence calculations can quickly be established in the form of off-design calculation. Turabs II includes a multi-stage equation solver (search directions), which numerically is very robust. Turabs II solves (minimises a functional) a constrained non-linear equation system by establishing a Jacobiant matrix which is solved iteratively by means of a modified Newton Rapson algorithm. A Cholesky decomposition [21] is used in connection with an iterative solution of the equation system and at the same time a Cuthil McKey re-numeration of the equation system is used. The solution vector is accepted during an iteration process when the Euclidean norm is less than a user specified accuracy, which is the convergence criterion. The solution vector is supervised by a control routine, ensuring that the solution will always be within a predefined definition interval. The following solver algorithms (search directions) are available:

- The Line Search Method, [22] page 116.
- The Double Dog Leg Step Method, [22] page 139.
- The Locally Constrained Optimal Hook Step Method, [22] page 134.
- The Method of Bisection, [22] page 25.

The various solvers are extensively described in [22]. The Turabs II system includes an algorithm, which utilises a hierarchic priority of the above search directions dependent on the convergence speed of the equation solver at the actual operating point. The hierarchy indicates how fast the line search and the dog leg methods are compared to the method of bisection. The method of bisection is not used until it is absolutely necessary. Moreover Turabs II includes a comprehensive component library of turbines, generators, condensers, pre-heaters, pipes, valves and controllers which are all implemented in the Turabs II code. In general the involved components are very detailed and fulfil the above descriptions of the actual plant. A comprehensive modified water/steam (IAPWS 97) and gas library [23] is connected covering the pressure range from 0 to 800 [bar] and the temperature range from 0 to 1000 [°C]. The application runs on a wide range of high performance PCs including MS Windows 7, 64 bit.

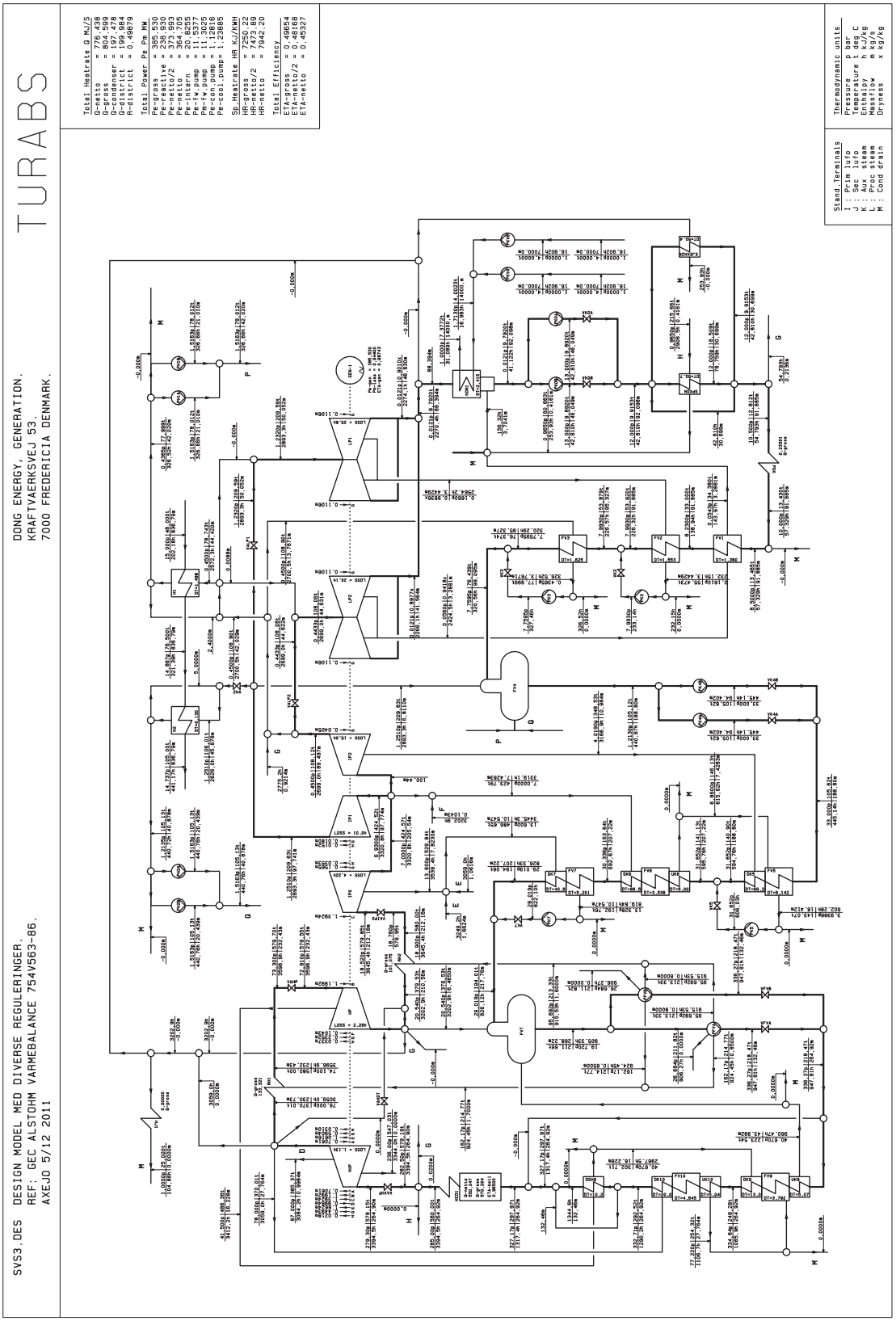

Figure 3.4.: Design model of water / steam circuit of SKV3, performed by Turabs II.

3.4. Measurements - SKV3 evaporator

A measurement campaign has been established in order to identify the tube wall temperature of the panel walls of the evaporator of SKV3. The measurement campaign matches the requirement to cover both a stationary period as well as a dynamic period where there is a jump in temperature, mass flow and pressure. A total of four measurement campaigns are listed in table (3.1). The data are measured every second, and the resolution of the data is subject to a measurement signal window for determination of when changes to the measurement data logged. This is to save disk space, so that data volumes are not too extensive. Every second 6000 data are measured on SKV3. Unfortunately, we find that this measurement window is disadvantageous placed for many of the pipe wall temperature measurements that we measure, because data is only applicable as a signal value for any alarm for high tube wall temperature. We have chosen to log the metal temperature at the panel wall every second. These wall temperatures are found in figures (F.3) to (F.6), (F.9) to (F.12), (F.15) to (F.18) and (F.21) to (F.24). The measurements are located physically by their KKS number-

Table 3.1.: Measurement campaigns.

Sample nr.	Date	t_{start}	t_{end}	Description	Sentence of burners
1	17.10.2011	07 : 55 : 00	08 : 10 : 00	Benson mode	Full
2	17.10.2011	11 : 25 : 00	11 : 40 : 00	Benson mode	Full
3	29.10.2011	17 : 30 : 00	17 : 50 : 00	Transition to Benson mode	High
4	30.10.2011	17 : 00 : 00	17 : 20 : 00	Boiler circulation mode	High

ing system, which is an unique identification number based on the **K**reftwerke **K**ennzeichnen **S**ystem; see [24]. From each sample period it is possible to calculate the entire heat production in the boiler, which is illustrated in figure (3.5). The measurement tags are defined for each panel section (X = 1 to 4), *front*, *rear*, *left* and *right* sections, where signals for pressure and temperature before and after the evaporator are given by the following KKS numbers: HAD3XCP02, HAD3XFT001, HAD1XCP001 and HAD1XFT001. Furthermore, a mass flow measurement before the economiser and an enthalpy measurement upstream the bottle are registered so that a complete energy balance can be made for the entire evaporator. Hence the power absorbed in the wall panel and hub can be calculated and is illustrated in figure (3.5). The corresponding averaged data for the four samples can be summarised in the following table (3.2). Depicting the pressure drop curve for the SKV3 boiler is attempted on figure (3.7) on the basis of the four samples showing immediately a linear correlation, with an overall correlation coefficient of 0.99562. Taking into account the hydrostatic pressure, a non-linear relationship is indicated between Δp and mass flow. The hydrostatic

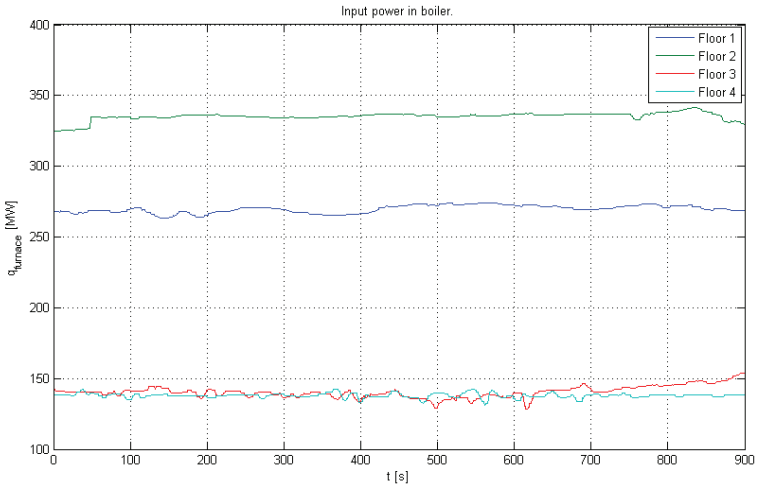

Figure 3.5.: Power input in the boiler for samples 1 to 4.

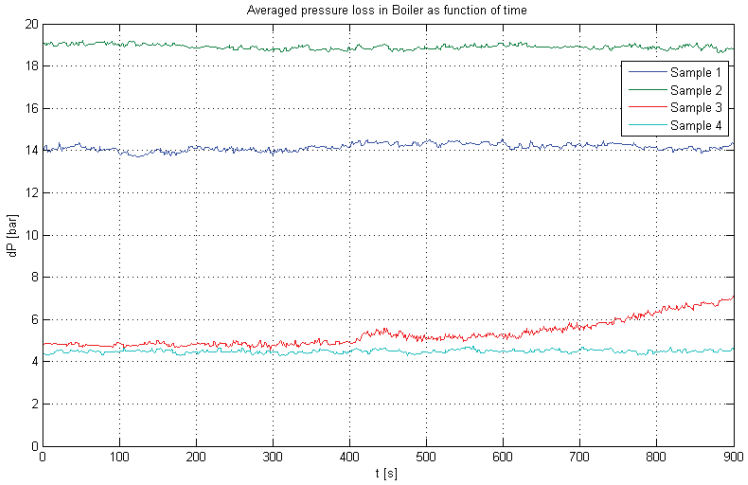

Figure 3.6.: Pressure drop in the boiler for samples 1 to 4.

Sample nr.	$\dot{m}$	h_{in}	h_{out}	$\dot{q}$	P_{in}	P_{out}	ΔP	Load
Units	$[kg/s]$	$[kJ/kg]$	$[kJ/kg]$	[MW]	[bar]	[bar]	[bar]	[%]
1	195.46	1514.27	2894.32	269.75	244.20	230,05	14.15	80.5
2	258.11	1566.09	2835.05	335.27	325.20	306.29	18.91	100.0
3	89.54	1169.20	2819.71	140.48	110.89	105.58	5.31	41.9
4	90.04	1187.70	2720.25	137.99	96.87	92.38	4.49	41.2

Table 3.2.: Mean values for heat and pressure balance for the four samples.

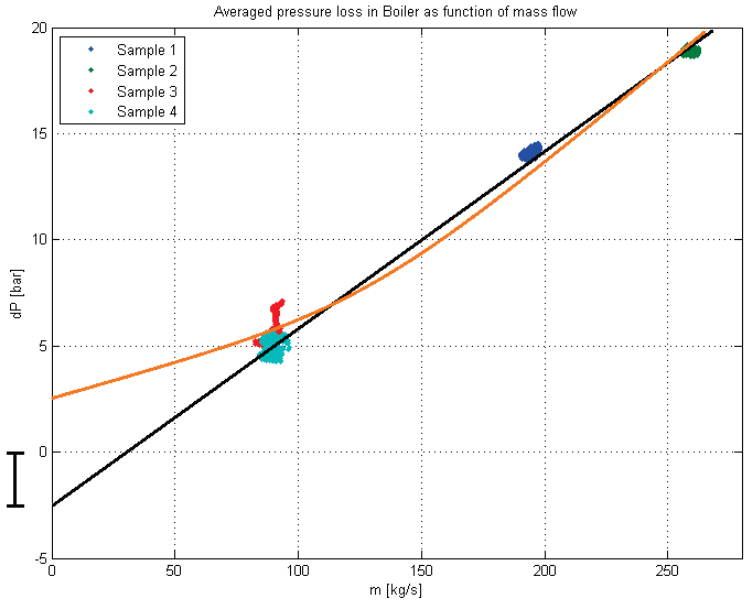

Figure 3.7.: Pressure drop as a function of mass flow in the boiler for samples 1 to 4.

pressure Δp_{geo} is estimated to be approximately 2.5 [bar], corresponding to the hydrostatic pressure drop in the evaporator. Assuming an average density of approximately 700 [kg/m^3] at 90 [bar] and a bottle operation flow of approximately 90 [kg/s] corresponding to the ECO minimum flow at low load, the geodetic height can be estimated to 35 [m], which is consistent with project drawings for the boiler plant. Measurement data from SKV3 are obtained from the plant control systems, where the sampling frequency is lowered. One of the major challenges in a Benson boiler is to ensure uniform flow distribution to each of the evaporator tubes. Normally, a certain degree of sub-cooling is needed, in order to ensure a single-phase flow; otherwise having resistors incorporated is necessary to ensure a uniform flow to the individual orifices. The thermo sensors provided on the panel walls are of type N (thermocouple), welded to the panel wall. It is therefore difficult to calibrate the gauges, but the supplier of thermo couples provide the information that they are constructed from the same roll of wire; hence we assume that their temperature characteristics and tolerances are largely identical. Normally we expect a temperature tolerance of 1-2 [^{o}C] for the calibrated type N thermo sensors. If we only want to look at differences in temperature between the evaporator tubes, we can ignore the temperature offsets of the thermo-elements and only look at the temperature difference relative to the mean temperature within a batch of, e.g seven thermocouples. The thermo sensors provided on the panel walls are located in a reference elevation of 43.2

[m] above mean sea level, which corresponds to a position immediately above the top burner floor. The other thermocouples used in this measurement campaign are also based on the type N, which can operate in a temperature range from -180 [^{o}C] to 1300 [^{o}C]. Measurement uncertainty is here stated to be below 1-2 [^{o}C]. Pressure transducers are calibrated each year, and according to the certificates, the measurement uncertainty is found below 0.3% on all transducers.

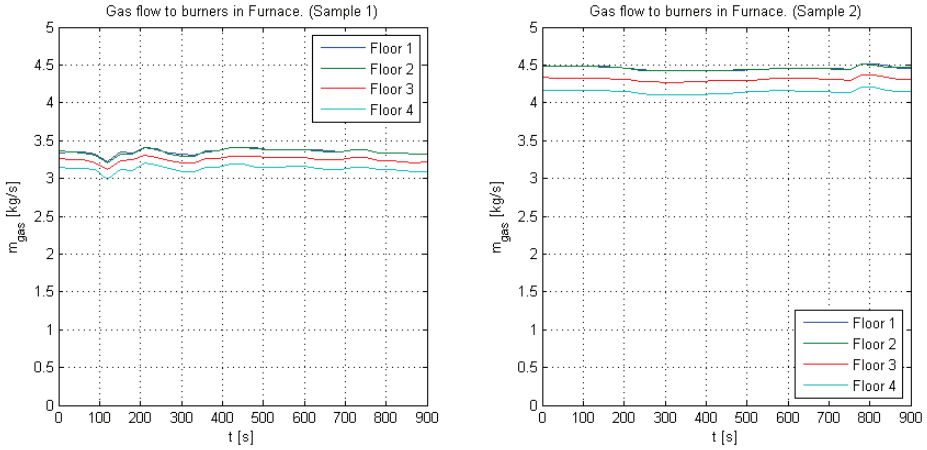

Figure 3.8.: Burner load - SKV3 samples 1 and 2.

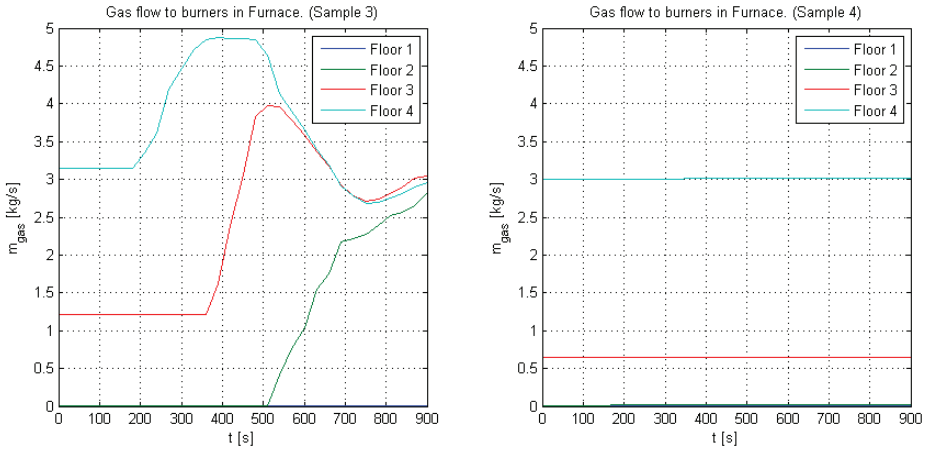

Figure 3.9.: Burner load - SKV3 samples 3 and 4.

The thermo sensors are located on the back of the evaporator tubes, thus located on the cold side and are in principle measuring the surface temperature of

the heat pipe. The KKS numbers are named HAD21CTXXR, HAD22CTXXR, HAD23CTXXR and HAD24CTXXR, corresponding to the left side, back wall, front wall and right side, respectively. XX is the pipe number on each side, starting from 01 to 55. Only every second pipe is included in this measurement campaign.
In table (3.3) is an overview of the five measurement campaigns. The measurements are grouped into four sections, each consisting of seven heat pipes and are available as a time series of 15-20 minute sampling periods (Samples 1-4). Mean values for each group (of seven measurements) are analysed, and the maximum deviation from the mean value in each group (signed) are shown in table (3.3) for groups: 1-13, 15-27, 29-41 and 43-55. Furthermore, the absolute maximum and minimum deviation of all measurements (1-55) are located in column 'Max' and 'Min', and the corresponding standard deviation is shown in column 'S.Dev'.

Sample nr.	Panel	1-13	15-27	29-41	43-55	Max.	Min.	S.Dev.
1	Front	4.167	-5.350	5.628	7.211	7.211	-5.350	3.344
	Right	-4.525	-2.676	12.934	-9.419	12.924	-9.419	4.270
	Back	6.926	5.691	4.933	4.508	6.926	-5.962	2.833
	Left	-4.666	8.597	5.671	-5.327	6.152	-8.597	2.930
2	Front	1.804	4.204	2.877	4.231	4.231	-4.131	2.019
	Right	-3.685	-4.324	8.151	-5.692	8.151	-5.692	2.951
	Back	-3.774	4.129	3.045	-3.318	4.129	-3.774	2.073
	Left	-2.220	-5.760	3.131	-4.123	3.477	-5.760	1.953
3	Front	12.336	22.606	36.260	27.167	36.260	-29.027	15.725
	Right	-24.446	-29.676	-39.644	-29.525	34.396	-39.644	17.770
	Back	26.839	-24.885	8.705	6.769	26.839	-26.201	10.827
	Left	-2.585	2.827	3.360	3.832	3.832	-2.686	1.283
4	Front	-0.400	-0.710	-0.359	0.743	0.743	0.710	0.278
	Right	0.193	-0.256	1.205	0.666	1.205	-0.832	0.376
	Back	-0.385	0.478	0.722	-0.298	0.722	-0.450	0.234
	Left	-0.356	0.572	0.823	0.552	0.823	-0.615	0.288

Table 3.3.: Measurements of panel wall temperature differences.

3.5. Summary

The calculated temperature imbalances in the different sequential sections (1-13, 15-27, 29-41 and 43-55) are illustrated in table (3.3). What immediately catches the eye is sample 4, which is very homogeneous in the temperature level. The maximum deviation relative to the mean value is approximately +/- 1 [^oC], which is a steady state situation with a pressure loss of approximately 5 [bar] over the boiler, running in circulation mode. On the other hand we have sample 3, which is distinguished by intense temperature gradients between the tube elements in the panel wall. Here is recorded up to +36 [^oC] and -39 [^oC] difference in relation to the mean temperature in each group of seven tubes. This is a dramatic deviation

and can be a result of an asymmetric flow distribution in the panel walls. In sample 3, the boiler is in a transition phase, from circulation operation to Benson operation, and this results in substantial imbalances in the flow distribution, because some tubes contain more steam than others, so that the total pressure of the evaporator dictates the flow distribution in the panel wall. This is a dynamic phenomenon, which will stabilize when the boiler gets into a stationary operation again, as seen in sample 3. It is exclusively a dynamic phenomenon, that is initiated by the transition point from circulation to Benson operation. Generally, there is not much difference in the thermal imbalances in the various panels ('Front', 'Right', 'Back' and 'Left'), apart from sample 3, where the gaps are remarkably higher, than in the other panels. For example, there are disparities in the order of +/- 30 [^oC] in the 'Front', 'Right' and 'Back' panels, while in the 'Left' panel there only occurs a bias of +/- 3 [^oC]. This may be due to that the fluid here exists in the two-phase region and thus is not subject to local superheating of steam. Another possibility is the burner composition, which stabilizes the flow of the Left panel. At high load steady state operation, we see insignificant fluctuations in the panel wall temperature, where the maximum/minimum temperature deviation is approximately +/- 10 [^oC] from the average temperature at 80 % load and only +/- 5 [^oC] from the average temperature at 100 % load. In both high load cases, a uniform behaviour is observed for all panels.

In figure (3.5) time series of the power absorbed in the panel walls is calculated. It is only in sample 3 that significant variations in the load may be registered, in the form of higher departure enthalpy (temperature). The superheated steam contributions are confined to the total enthalpy departure, because the latent heat is so large at part load. The inlet condition to the evaporator is depicted in figure (F.2), (F.8), (F.14) and (F.18), where samples 1 and 2 are operating above the critical point, while samples 3-4 are sub-critical. It appears from the sub-critical scenarios, that the inlet conditions are sub-cooled water and the outlet conditions from the evaporator are typically super-heated steam, apart from sample 4, where super heating is found at the end of the measurement period; otherwise the exit conditions are in a two-phase region by circulating operation.

4. Heat flux and wall temperature distribution

In this paragraph, an attempt is made to clear out the effect of heat flux profiles on the stability of a boiler system as well as describe the temperature cross-section profile of a heat tube wall in relation to creep and fatigue phenomena. Our starting point is the boiler geometry as described for SKV3. Therefore, we can ask if the hypothesis of constant heat flux is realistic. A certain residence time in the combustion zone, which creates a time delay, is required in order to obtain a complete combustion. Therefore, we must assume some bias in heat flux profile, centred, with a maximum, in the middle of the furnace. The burners are combined in a ring on each floor around the combustion chamber. When the load is changed, the heat flux profile can vary according to the order in which the burners are turned off and affect the temperature distribution in panel walls drastically.

4.1. Heat flux profiles in the SKV3 furnace

For the simulation of combustion processes in the SKV3 power plant boiler FLUENT® 13.0 is used. The application is able to handle a 3D thermo hydraulic-simulation, combined with a complex internal combustion model. DONG Energy - Thermal Power has extensive experience in the use of CFD simulation and optimization of combustion processes in power plant boilers, and therefore used this tool to estimate the flux distributions in the power plant boiler on SKV3, rather than use a technical measuring approach that is both more costly and time-consuming and not necessarily more precise. Heat fluxes are one outcome of the simulations that can be determined along the surfaces and some lines specified by the user. These flux profiles can give us an idea of what kind of heat profile is realistic to use on an evaporator model. Below is a brief description of the assumptions, that form the basis for determining the heat flux along the typical heating surface elements of a power plant boiler like SKV3, which in this case is gas-fired. The governing fluid dynamic equations and the corresponding combustion processes are described in Appendix L. For further details, see the user documentation of FLUENT® 13.0.

4.1.1. Model setup

The SKV3 boiler is modelled using only half of the furnace volume, because the furnace approximately can be treated as being axi-symmetric around the x-z plane. In the following setup a standard air mixture is taken as the fluid and is assumed to be incompressible. Bulk axial velocity in the upper portion of the

boiler, before flue gas entry into the super-heater section, is around 18 [m/s] at base load. The flue gas temperature in the same region is around 1875 [K] leading to an approximate Reynolds number of 6.0e+5, meaning turbulent flow. The model is forced by fixed thermal boundaries to absorb the heat produced during the combustion processes. The model is constructed by mainly hexahedral cells except for the central part of the boiler volume which has been meshed using polyhedral cells. This has been necessary to interface the mesh structure of the circular concentric burners while maintaining a high mesh quality. The model geometry is generated by the pre-processor of FLUENT® 13.0, and a total of 2.44 million computational cells are used to resolve the modelled geometry. The average cell volume differs in the various parts of the model and is listed in table (4.1).

Table 4.1.: Average cell volumes in various parts of the SKV3 model.

	Average volume	**Average side length**
Section	$[cm^3]$	[cm]
Burners	85	4
Main furnace (combustion volume)	2200	13
OFA volume	2600	14
SH volume	4750	17
Top of boiler	6800	19
Bottom of furnace	9000	21

4.1.2. Boundary conditions

Boundary conditions for burner registers (air and gas), OBA (Over Burner Air) and OFA (Over Fire Air) nozzles are assumed to be uniform across the designated inlet cross-sections. This applies to all fields (velocity, temperature and species concentrations). To simplify the combustion chemistry, the fuel is assumed to consist of methane, and the mass flow of gas is adjusted accordingly to ensure correct thermal input. The final part of the gas burners has been geometrically resolved, as is seen in figure (4.1). The model describes a half boiler, which is symmetric in the x-z plane, so that the flux distribution is symmetrical in this plane. The wall boundary conditions applied for the boiler simulation are steam side temperatures supplemented by the thermal resistance of the pipe wall, where only the one-dimensional heat transfer component normal to the pipe wall is taken into account. The steam side temperature variation is assumed to vary (approximately) linearly as a function of the exposed surface area, as illustrated in figure (4.2). In other words, the coupled problem is not solved directly, since the computed local heat flux is not allowed to alter the assumed steam side temperature. Instead, the integral heat uptake for the evaporator is calibrated to

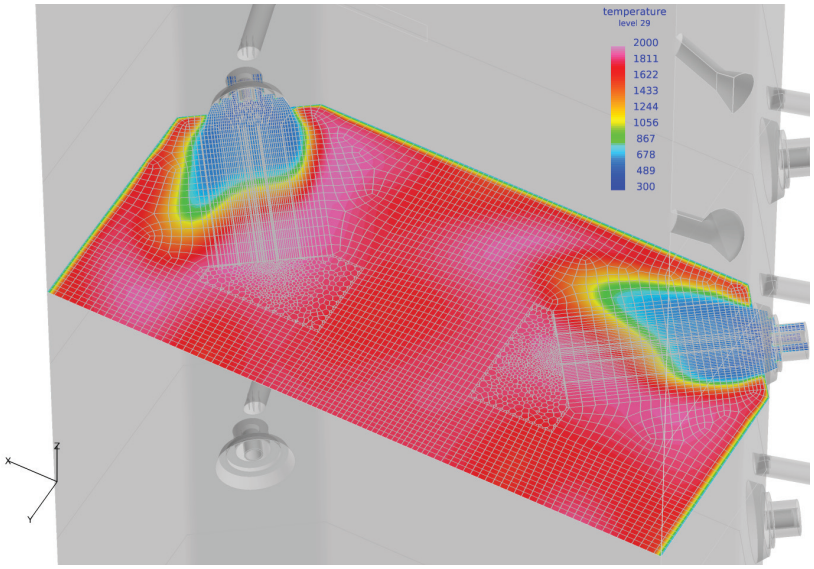

Figure 4.1.: Plot showing geometry and mesh structure around the burners of SKV 3. The temperature field is shown on the coordinate plane illustrated.

fit actual evaporator uptakes, by changing radiate and heat resistive properties of the wall (the wall emissivity and the wall thickness). The wall thickness is varied only as a convenient way to modify the overall heat transfer coefficient, which is a function of the furnace side fouling, steal properties, steam side fouling and the steam convective heat transfer coefficient.

4.1.3. Simulation results

The simulation result is a steady state picture of the thermal-dynamic and hydrodynamic flow condition, balanced with the inflowing species as source terms, combusted by the chemical reaction given in (L.12). Our goal is to get a qualified estimate of the heat flux perpendicular to the evaporator surface, as this will be the boundary condition for the two-phase tube model. The heat flux, given in $[W/m^2]$, is illustrated as a 3D illustration in figure (4.3), and the corresponding line series of heat fluxes as vertical lines along the boiler surface are illustrated in figure (4.5), with the positions of the vertical line series indicated in figure (4.4). The 100 % load simulation shows clearly that the radiation flux varies a lot along the vertical z-axis of the boiler, despite the fact that all burners are active. A comparison of the heat flux distribution along line 1 versus line 4 and line 2 versus line 6 is reasonably symmetrical along the y-z plane and x-z plane. It is therefore reasonable to project the flux distribution onto the individual tubes, which we model in this project.

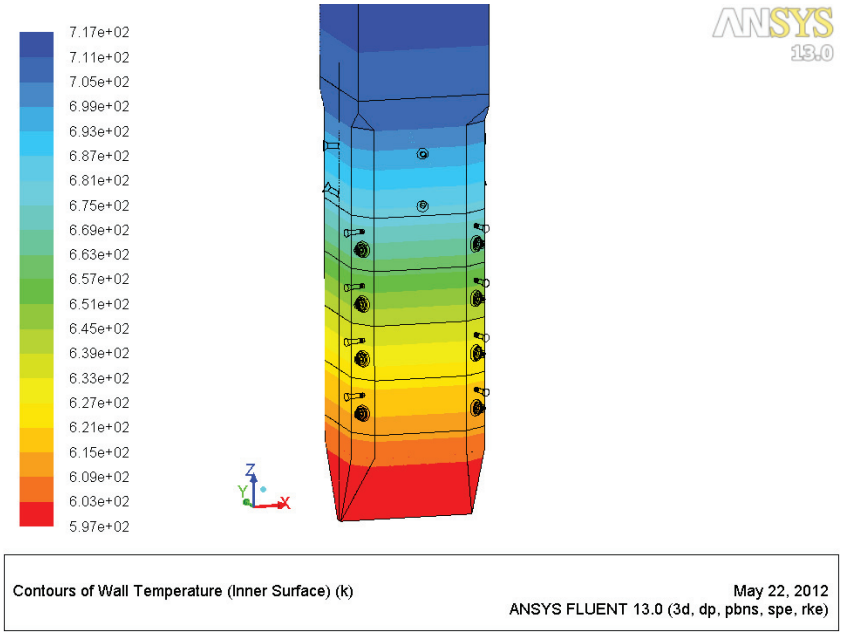

Figure 4.2.: Steam side wall temperature variation assumed for the SKV3 full boiler thermal load case.

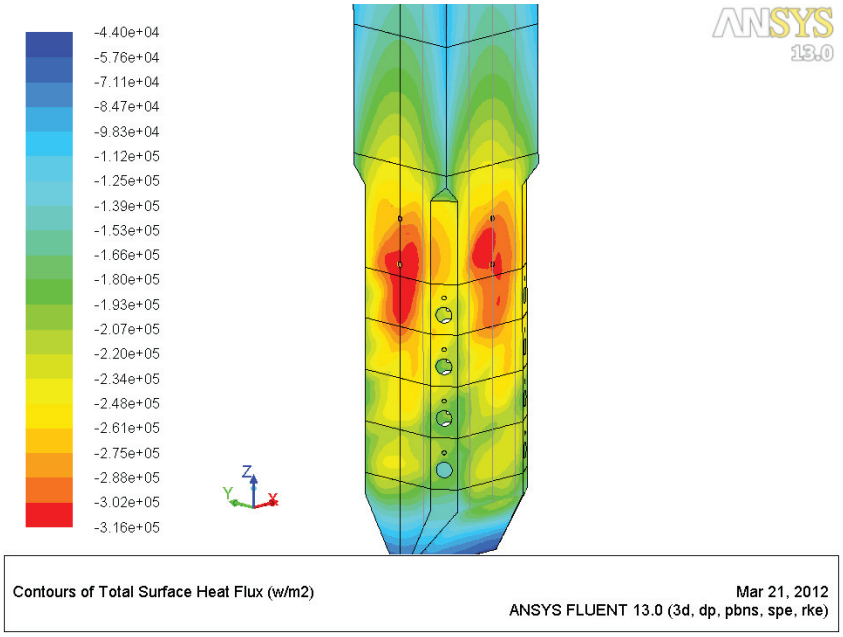

Figure 4.3.: ANSYS CFD simulation of surface heat flux at SKV3 furnace (100% load).

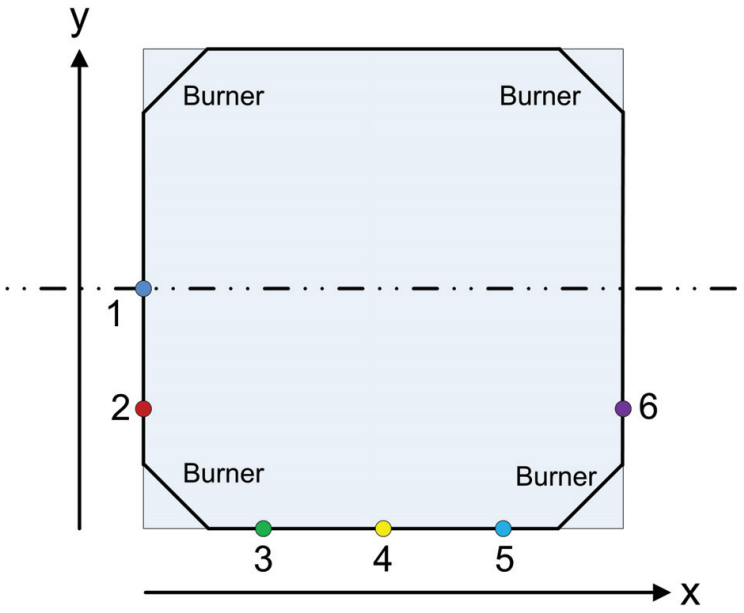

Figure 4.4.: Cross-section of SKV3 furnace with indication of Flux line series as vertical lines.

4.1.4. Summary

The model is a steady state model, running until a converge criterion is fulfilled (approximately 0.1 % in absolute flow). The model ensures mass balance, so that the velocity distribution on the downstream edge, just matches the fuel and airflow into the boiler. The total power input must be balanced by the heat uptake, which takes place in the water / steam circuit. Hence there are two conditions that must be met - the mass and energy balances. The heat flux distributions on the panel walls can be projected onto the evaporator tubes, which are wound at an angle of 10^o to 12^o around the furnace perimeter from the lower furnace inlet headers to above the burner zone; see figure (2.3) and provide the necessary heat uptake. We can see a high degree of symmetry in the heat flux distribution, as lines 1 and 4 largely coincide; lines 2 and 3 and lines 5 and 6 also coincide. The flux distribution on slightly rising heat pipes in the evaporator, which embraces the whole boiler room, can be reasonably assumed to follow the trend of a heat flux distribution function with a maximum heat flux in the middle of the boiler room. Therefore, we assume the flux distribution along a heat pipe follows the distribution line which is estimated along the lines 1 and 4. These results will be used in section 10.4 in the form of a parabolic heat flux profile of the evaporator tubes, in order to analyze the effects of different heating profiles in the boiler.

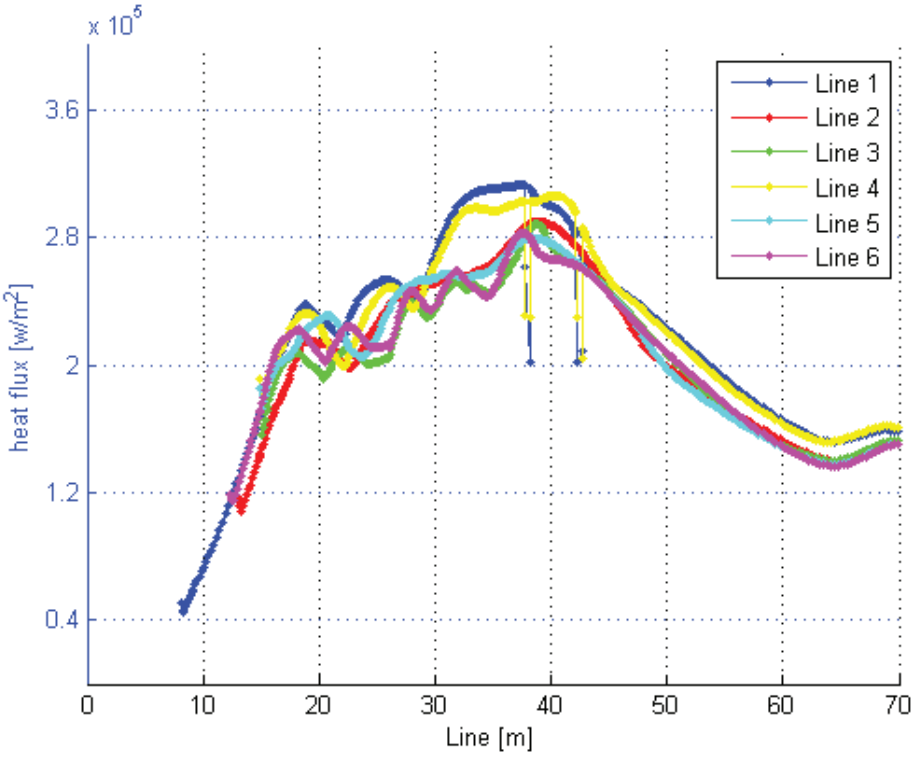

Figure 4.5.: Line series of surface heat flux along line 1 to line 6 at the SKV3 furnace (100% load).

4.2. Pipe conditions

Modern Benson boilers have a working pressure which exceeds the critical steam pressure. Therefore the pipe wall thickness is of such size that the heat capacity is essential for the dynamic flow response. The temperature distribution through a pipe wall in a uniform radial pipeline (heat pipe) is developed for a dynamic point of view.
An evaporator tube is a passive device that is constructed in such a way that it acts as though it has extremely high thermal conductivity, to ensure an optimal heat transfer in a furnace.Some considerations follow about the time constants in the heat pipes exposed to dynamic loads, so that qualitative terms can be evaluated on the dynamic effects, for the study of creep and fatigue in boiler tubes and evaporator tubes.

4.2.1. Heat conduction

Heat conduction may occur under static and dynamic conditions. The steady state conduction has a constant temperature difference, driving the conduction so that after an equilibration time, the spatial distribution of temperatures (temperature field) in the conducting object does not change any further. In steady state conduction, the amount of heat entering a section is equal to the amount of heat coming out. In steady state conduction, the law of direct current electrical conduction can be applied to 'heat currents'. In such cases, it is possible to take 'thermal resistances' as the analogy to electrical resistances. Temperature plays the role of voltage, and heat transferred is the analogy of electrical current.
The non-steady-state situations are those in which the temperature drop or increase occurs more drastically, such as when a thermal boundary condition (inlet condition to panel wall in furnace) is rapidly changed from low to high temperature (pressure). Here the temperature field within the object changes as a function of time, and the interest lies in analysing this spatial change of temperature within the object over time. This mode of heat conduction can be referred to as transient conduction. An interesting aspect in this context is the fatigue of steel, due to thermal fluctuations in the material. Analysis of these systems is more complex and (except for simple shapes) calls for the application of approximation theories, and/or numerical analysis by computer.

The following assumptions are made:

- No internal heat generation
- Symmetric geometry with isotropic material properties (k_w and c_p are assumed constant and the internal rifles are ignored)

4.2.2. Pipe model theory

The law of Heat Conduction, also known as Fourier's law [25], states that the time rate of heat transfer through a material is proportional to the negative gradient in the temperature and to the area at right angles, to that gradient, through which the heat is flowing. We can state this law in two equivalent forms: the integral form, in which we look at the amount of energy flowing into or out of a body as a whole, and the differential form, in which we look at the flows or fluxes of energy locally.
Consider a cylinder as in figure (4.6), whose inner and outer surfaces are exposed to fluids at different temperature. For dynamic conduction, with no heat generation, the appropriate form of the heat equation is given with the differential form

$$\frac{1}{r}\frac{\partial}{\partial r}\left(k_w r \frac{\partial T}{\partial r}\right) + \frac{\partial}{\partial z}\left(k_w \frac{\partial T}{\partial z}\right) = \rho c_p \frac{\partial T}{\partial t} \tag{4.1}$$

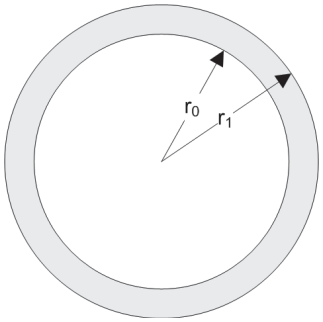

Figure 4.6.: Cross section of pipe wall

where r $\in [r_0,..,r_1]$, z $\in [0,..,l_z]$ and t $\in [0,..,\infty[$. Equation (4.1) has to be supplied with four boundary conditions belonging to the outer and inner diameter respectively, and the pipe inlet and outlet cross-sections, respectively (z=*0* and z=l_z). The boundary conditions could be:

1. Neumann boundary condition, where a heat flux q(z,t) (radiation) is forced at the out-side of the pipe wall.

2. Robinson boundary condition, where the heat transfer $h(T - T_0)$ is modelled at the pipe inner wall.

3. Dirichlet boundary condition, where the surface temperature T_0 and/or T_1 is specified.

The solution domain is illustrated in figure (4.7) and consists of a normalized Cartesian grid. The axial direction is represented by the $z^{'}$ axis, and the radial axis is given by $r^{'}$. The discretization of the model is discretised in n_x and n_r computational cells with a grid spacing of $\Delta x = \frac{1}{n_x}$ and $\Delta r = \frac{1}{n_r}$, respectively. The physical tube length is named l_z and the physical pipe wall thickness is $l_r = r_1 - r_0$. In the normalized coordinate system, the pipe length is L=1 and the normalized wall thickness is $r_1^{'} - r_0^{'} = 1$. The governing equation (4.1) is put in a non-dimensional form, by defining the following dimensionless quantities:

$$z^* = \frac{z}{l_z}, \quad r^* = \frac{r - r_0}{l_r}, \quad t^* = \frac{t}{t_0}, \quad k_w^* = \frac{k}{k_0}, \quad T^* = \frac{T - T_0}{\Delta T} \tag{4.2}$$

where

$$\Delta T = T_1 - T_0, \quad t_0 = \frac{{l_r}^2}{\alpha}, \text{ and } \quad \alpha = \frac{k_0}{\rho_w \cdot C_{pw}} \tag{4.3}$$

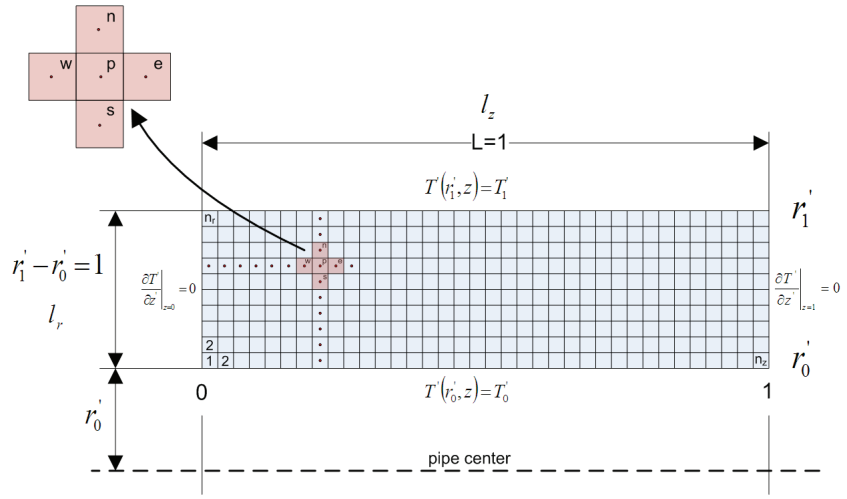

Figure 4.7.: Solution domain of the wall by use of a rectangular cartesian grid.

The thermal diffusivity is represented by α. L is the length/height of the pipeline and t_0 is a characteristic time constant due to the wall properties. The thermal conductivity is normalized according to a basic thermal conductivity referring to the internal surface conditions of the pipe. Inserting the dimensionless quantities into equation (4.1) leads to equation (4.4), where β=l_r/l_z. The subscript w refers to the conductivity in the pipe wall.

$$\frac{1}{r^*}\frac{\partial}{\partial r}\left(k_w^* r^* \frac{\partial T^*}{\partial r^*}\right)+\beta^2\frac{\partial}{\partial z^*}\left(k_w^*\frac{\partial T^*}{\partial z^*}\right)=\frac{\partial T^*}{\partial t^*} \tag{4.4}$$

4.2.3. Numerical solution of the Poisson equation

There are several numerical methods for solving the mathematical problem of (4.4). It seems obvious to use a finite volume approach to solve equation (4.1). The Finite volume principle is easy to implement for this simple geometry, and the method is numerically stable with, e.g, a second-order accuracy.

We want to bring (4.1) to a discrete differential form given as (J.1) in Appendix J, which can be solved fully implicit by the sparse technique described in Appendix J. The discretization is performed on a flexible grid in the radial direction for n_r *control volumes* (CV). The five discrete coefficients given in equation (J.1) (named a_n, a_s, a_p, a_e and a_w) are available for the *two-dimensional* (2D) equation given by equation (4.4). The coefficient is determined by the revaluation of the discretised terms of equation (4.1) and subsequent isolation of the coefficients of the primary dependent variable (this case T) for the five CV volumes, marked by

red in figure (4.7), which are involved in the discretization of the equation. The coefficients are given by:

$$
\begin{aligned}
a_n &= \begin{cases} \frac{2\cdot\Delta z}{r_n - r_p}\left(1+\frac{r_n-r_p}{4r_p}\right) & \text{for } i=1 \\ \frac{\Delta z}{r_n - r_p}\left(1+\frac{r_n-r_p}{2r_p}\right) & \text{for } n_r \geq i > 1 \end{cases} \\
a_s &= \begin{cases} \frac{2\cdot\Delta z}{r_p - r_s}\left(1+\frac{r_p-r_s}{4r_p}\right) & \text{for } i=n_r \\ \frac{\Delta z}{r_p - r_s}\left(1+\frac{r_p-r_s}{2r_p}\right) & \text{for } n_r > i \geq 1 \end{cases} \\
a_e &= \beta\frac{\Delta r}{\Delta z} \\
a_w &= a_e \\
a_0 &= \frac{\Delta r\cdot\Delta z}{\Delta t} \\
a_p &= -\left(a_w + a_e + a_s + a_n\right) - a_0 \\
&\text{and} \\
b_p &= T^{n-1}\cdot a_0
\end{aligned}
\tag{4.5}
$$

where a_n, a_s, a_e, a_w and a_p are referring to time step n, and the right side of the discrete equation (4.6), represented by the coefficient b_p, is referring to the previous time step n-1.

$$
a_n\Phi_n + a_s\Phi_s + a_p\Phi_p + a_e\Phi_e + a_w\Phi_w = b_p \tag{4.6}
$$

Equation (4.6) is solved by the implicit solver, described in Appendix (J). The independent variable r is discretised as:

$$
\begin{aligned}
r_n &= r_{i+1} \\
r_p &= r_i \qquad \text{for } i = 0, n_r+1 \\
r_s &= r_{i-1}
\end{aligned}
\tag{4.7}
$$

and

$$
\Delta r = \begin{cases} \frac{r_n - r_s}{2} \text{ for } n_r > i > 1 \\ r_n - r_p \text{ for } i = 1 \\ r_p - r_s \text{ for } i = n_r \end{cases} \tag{4.8}
$$

For an equidistant radial grid ($\Delta r = (r_1 - r_0)/n_r$), the expressions of a_n and a_s can be simplified to:

$$a_n = \frac{\Delta z}{\Delta r}\left(1 + \frac{\Delta z}{2r_p}\right) \tag{4.9}$$

and

$$a_s = \frac{\Delta z}{\Delta r}\left(1 - \frac{\Delta z}{2r_p}\right) \tag{4.10}$$

Note that the CVs are of half width at the boundaries, according to equation (4.5) and figure (4.7).

4.2.4. Thermal boundary conditions

The boundary conditions at the outer edge will typically be a Neumann condition in the form of a radiation flux condition. For model verification a Dirichlet boundary condition has been used, in the form of a temperature fixation. This would also make an impact at the pipe inner wall, where water / steam will dictate a temperature condition. Along the tube ends (z = 0 and z = 1), we have two Neumann conditions, with a typical zero gradient of the temperature field. Below is a brief describtion how the boundary conditions for the four peripheral surfaces according to equation (4.1) are implemented.

North boundary:
The Neumann condition is implemented as a sequential operation where we first adjust A_p 1): A_p=A_p+A_n, next the right side of 4.1 will be 2): $b_p = b_p - A_n * Q_n * \Delta r$ and finally 3): A_n=0. The Dirichlet temperature condition along the northern boundary is given as 1): A_p=A_p-A_n, 2): $b_p = b_p - 2 \cdot T_n$ and 3): A_n=0.

South boundary:
The Dirichlet temperature condition along the southern boundary is given as 1): A_p=A_p-A_s, 2): $b_p = b_p - 2 \cdot T_s$ and 3): A_s=0.

East boundary:
The Neumann flux boundary condition is implemented as 1): A_p=A_p+A_e, 2): $b_p = b_p - A_n \cdot Q_e \cdot \Delta r \cdot T_e$, where Q_e=0 (symmetry condition) and 3): A_e=0.

West boundary:
The West boundary condition is similar to the East condition 1): A_p=A_p+A_w, 2): $b_p = b_p - A_n \cdot Q_w \cdot \Delta r \cdot T_w$, where Q_w=0 (symmetry condition) and 3): A_w=0.

4.2.5. Stretching the FV grid

In order to model the very thin heat-conducting layer (fouling) at the tube inner side, for example caused by magnetite deposits, we can benefit from using a stretch of the grid, and not an equidistant grid, so that we can limit the number of calculation cells. The radial grid can be stretched so that the grid solution is intensified where one assumes the largest gradients in the solution field or if one wants to model anisotropic materials which could include a thin oxide layer on the pipe inner side with lower thermal conductivity. Therefore we introduce a stretch function for the refinement of the grid, close to the boundaries, to resolve a thin fouling layer. The stretch function uses a standard equidistant and normalized coordinate system as input and returns a normalized stretched grid. The

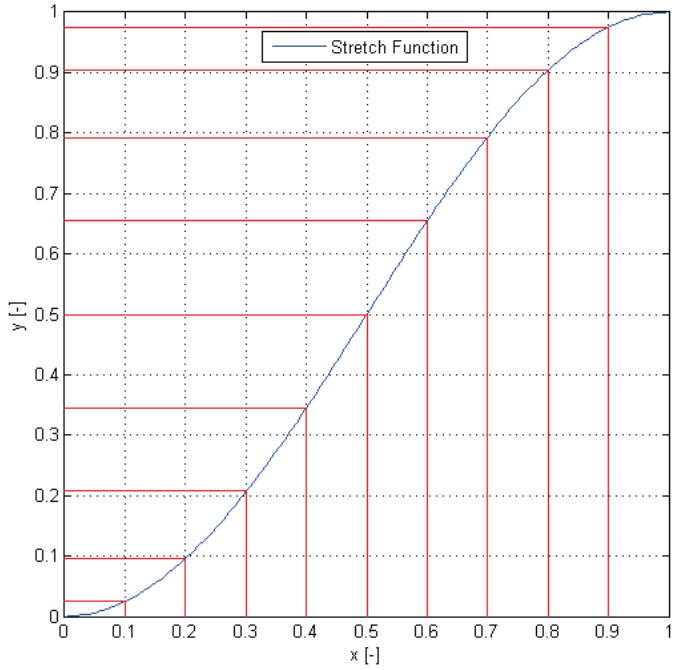

Figure 4.8.: Illustration of a stretch function.

stretching functions below fulfill the following conditions: *y(0)=0, y(1)=1* and the function must be monotonically increasing with $\frac{\partial y}{\partial r} > 0$. The function is able to stretch the grid along the north and south boundary, depending on the number of stretch functions used. We use a second-order stretch function, which ensures a C^1 continuity in the gradient field of T, as described in Appendix (G). The numerical solution of the normalized Poisson equation (4.4) is based on a finite volume approach and is verified against an analytic solution, which is established

by the use of the following four boundary conditions: two Dirichlet boundaries, $T(r_0) = T_0 = 0 and T(r_1) = T_1 = 1$ and two Neumann boundaries at the pipe ends, $\frac{\partial T}{\partial x}|_{z=0}$ =0 and $\frac{\partial T}{\partial x}|_{z=1} = 0$. The solution is compared with an analytical one-dimensional solution, see equation (4.14), and illustrated in figure (4.9). Additionally the simulation is performed with stretching of the grid along the north boundary in figure (4.10) and the south boundary in figure (4.11). Note that

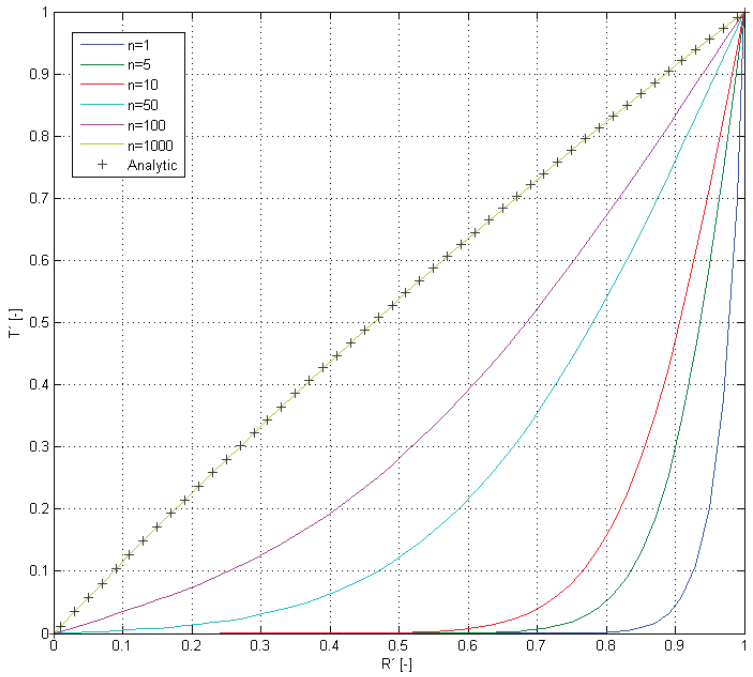

Figure 4.9.: Comparison of the numerical solution of equation (4.4) with (4.14).

the level of detail by stretching of the south boundary, is poor in areas with large gradients. This is experienced as a discontinuity in the calculated temperature distribution; see figure (4.11) along the north boundary. The thermal conductivity, **k**, is often treated as a constant, though this is not always true. While the thermal conductivity of a material generally varies with temperature, the variation can be small over a significant range of temperatures for some common materials. Fouling layers may consist of magnetite, oxide or iron particle deposition, having a thermal conductivity less than one decay of what we see in steel.
In anisotropic materials, the thermal conductivity typically varies with orientation; in this case, k is represented by a second-order tensor. In non-uniform materials, **k** varies with spatial location. Additionally the formation of a dense layer of magnetite has a markedly restrictive impact on the heat transfer rate;

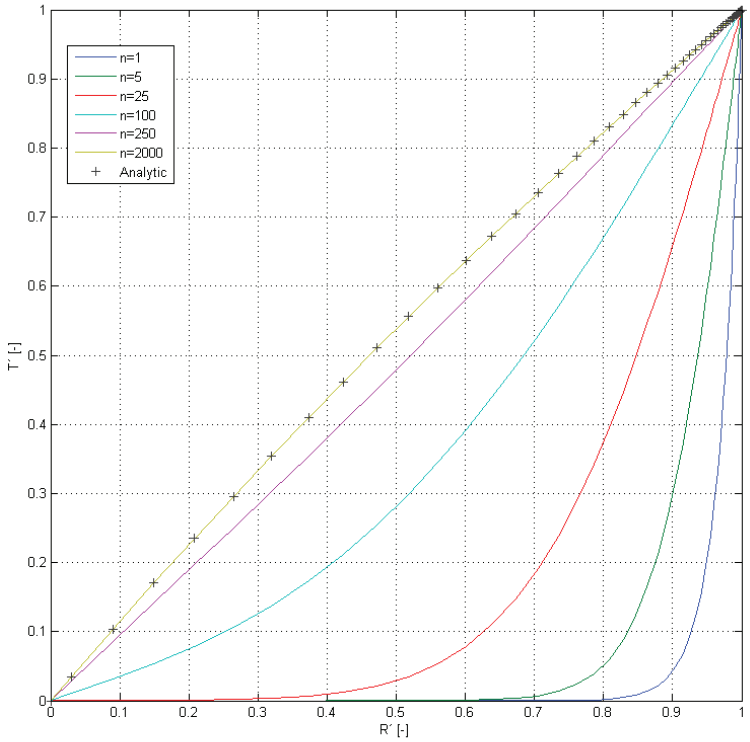

Figure 4.10.: Comparison of the numerical solution of equation (4.4) with (4.14) with a stretched North grid. n is the number of time steps.

therefore, with this stretching of the differential grid, we can define a layer which exactly match the thickness of both the topotactic and the epitaxy layer of the porous structures of magnetite, which have heat conductivity of 2.3 [W/mK] and 0.7 [W/mK], respectively. This phenomenon is described in the next section (4.3).

For many simple applications, Fourier's law is used in its one-dimensional form. In the r-direction:

$$\begin{aligned} q_z &= -k_w A \frac{\partial T}{\partial r} \\ &= -k_w 2\pi r L \frac{\partial T}{\partial r} \end{aligned} \tag{4.11}$$

The analytical solution is able to visualize the steady state radial temperature profile, based on the above boundary conditions. Additionally the rate of energy,

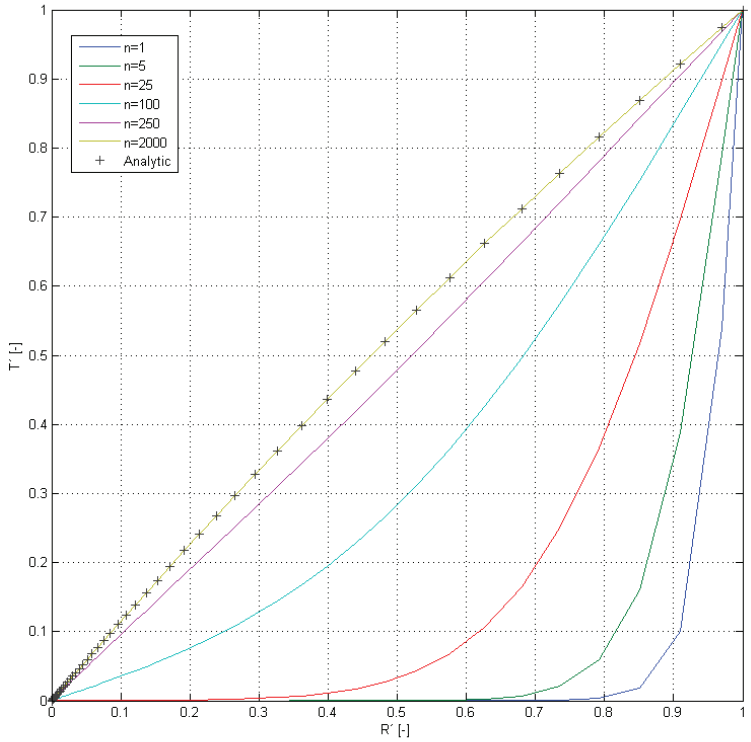

Figure 4.11.: Comparison of the numerical solution of equation (4.4) with (4.14) with a stretched South grid. n is the number of time steps.

which is conducted across any cylindrical surface in the solid, can be expressed as a function of the radius. For the one-dimensional heat conduction problem we can express the heat conduction as:

$$T(r) = C_1 \ln(r) + C_2. \tag{4.12}$$

To obtain the coefficients, C_1 and C_2, we introduce the following Dirichlet boundary conditions, where r is the pipe radius with suffix (i=inner) and (o=outer):

$$T(r_i) = T_i \wedge T(r_o) = T_o \tag{4.13}$$

and T_i and T_o refer to the specific radial position on the pipe wall (z). Solving for C_1 and C_2 and substituting back into the general solution, we obtain

$$T(r)_z = \frac{T_i - T_o}{\ln(\frac{r_i}{r_o})} \ln(\frac{r}{r_o}) + T_o. \tag{4.14}$$

By eliminating both the axial gradients in equation (4.4) and the dynamic terms, we can express an analytical solution for the problem, which is illustrated in the figures (4.9), (4.10) and (4.11) as the steady state solution marked by +.
From this result it is evident, for conduction in hollow cylinders like pipes, that the heat transfer rate is of the form

$$q_r = \frac{2\pi L k_w (T_i - T_o)}{\ln(\frac{r_i}{r_o})} \ [w]. \tag{4.15}$$

Note that the temperature distribution associated with radial conduction through a cylinder is logarithmic and not linear, as it is for a plane wall under the same thermal conditions. The temperature distribution in the pipe wall may change radically because of fouling on the outward and the inner pipe wall, due to changing values of thermal conductivity in the respective zones of fouling. Let us assume that we have a simple one-dimensional pipe model, with only axial heat transfer terms, and no spatial resolution of the radial dimension. In that case the wall temperature distribution represent an average temperature. In some cases, for example, if we need to determine the heat transfer through the pipe wall to the flowing fluid, it is useful to know the surface temperatures of the pipe inner wall. Let the average temperature for a slice element of the pipe be $\bar{T}_z$ and let $T(r)_z$ represent the radial temperature distribution by equation (4.14); hence the averaged wall temperature T_w can be estimated by:

$$\begin{aligned} T_w &= \frac{1}{A_c} \int_{r_i}^{r_o} 2\pi r \cdot T(r) dr \qquad (4.16) \\ &= \frac{2\pi}{A_c} \left[a_0 \left[x^2 \ln(x)/2 - x^2/4 \right]_{r_i}^{r_o} - a_0 \ln(r_o) \left[x^2/2 \right]_{r_i}^{r_o} \right] + T_o \cdot \left[x^2/2 \right]_{r_0}^{r_1} \\ &= a_1 \cdot T_i + (1 - a_1) \cdot T_o \end{aligned}$$

where a_1 is given by

$$a_1 = \frac{r_i^2}{r_i^2 - r_o^2} - \frac{1}{2ln(r_i/r_o)} \tag{4.17}$$

The inner wall temperature can be determined by use of equation (4.15), where S is the heated perimeter, and we find

$$T_i = \bar{T}_z + (1 + a) \left[\frac{q_z S \ln(\frac{r_i}{r_o})}{2\pi k_w} \right] \tag{4.18}$$

Thermal resistance (conduction) for n layers of isotropic material is defined from [25] as:

$$R_{cond} = \sum_{i=0}^{i=n} R_i = \frac{T_o - T_i}{q_z} = \frac{L}{k_w A} \tag{4.19}$$

The overall heat transfer coefficient U is defined as:

$$q_z = U_z A \Delta T_z \tag{4.20}$$

Where U_z and A as well as ΔT can refer to specific layers (i) in the radial pipe material

$$A_i = 2\pi r_i L. \tag{4.21}$$

For a composite wall in radial pipes, with n layers, the following equation (4.22) expresses an overall thermal resistance.

$$U_o A_o = U_i A_i = (\Sigma_{i=1}^{n} R_i)^{-1} \tag{4.22}$$

and

$$q = U_i\, A_i\, \Delta T, \;\; \Delta T = T_i - T_o \tag{4.23}$$

If we have a pipe wall consisting of three layers, meaning we have four surface temperatures, which are formulated in equations (4.24) and (4.25), then the different layers are referring to internal fouling given by layer A, the pipe material by layer B and the external fouling by layer C. The overall heat transfer coefficient

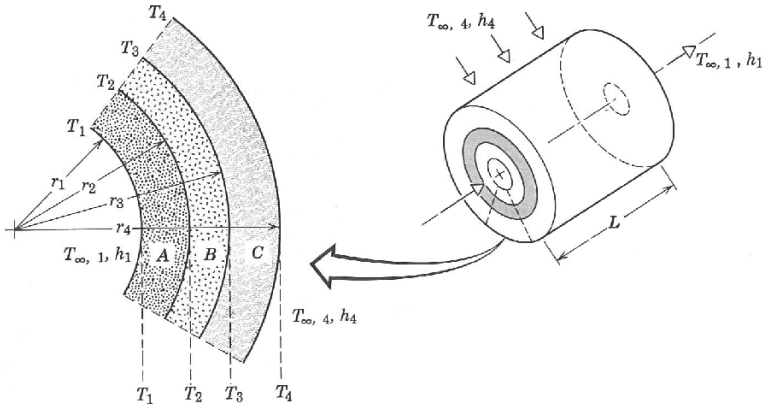

Figure 4.12.: Temperature distribution for a composite cylindrical wall, from [25].

is given as:

$$q = \frac{T_{\infty,i} - T_{\infty,o}}{R_{tot}} = U_i A_i (T_{\infty,i} - T_{\infty,o}) \tag{4.24}$$

where $T_{\infty,i}$ and $T_{\infty,o}$ are the temperatures outside the internal and the external thermal boundary, and r_1=r_i and r_4=r_o.

$$U_i = \frac{1}{\frac{1}{h_i} + \frac{r_1}{k_A}\ln(\frac{r_2}{r_1}) + \frac{r_1}{k_B}\ln(\frac{r_3}{r_2}) + \frac{r_1}{k_C}\ln(\frac{r_4}{r_3}) + \frac{r_1}{r_4 h_o}} \tag{4.25}$$

4.2.6. Time constant of the pipe wall

In the time domain, the usual choice to explore the time response is through the step response to a step input, or the impulse response to a Heaviside step function input. In the frequency domain (for example, looking at the Fourier transform of the step response, or using an input that is a simple sinusoidal function of time) the time constant also determines the bandwidth of a first-order time-invariant system, that is, the frequency at which the output signal power drops to half the value it has at low frequencies.

The dynamic response of the pipe wall is illustrated in figure (4.13) for a model with, e.g, 10 radial layers, where the time series of equidistant radial locations is named (r_1 to r_{10}) with r_1 closest to the inner diameter; the radial layers show the dynamic response in temperature, caused by a Heaviside step response function of unity applied on the outer tube surface. The corresponding time constants for the discrete radial locations are listed in table (4.2), where r=1 refers to the near inner layer and r=10 is the near outer layer, where T_∞ expresses the

Table 4.2.: Time constants for radial positions in the pipe wall, pipe data from equation (C.16).

Radial location (%)	$T_\infty[-]$	$T_\tau[-]$	$\tau[s]$
$r = 1$ (9)	0.10350	0.06542	8.47876
$r = 2$ (19)	0.21482	0.13579	8.24383
$r = 3$ (29)	0.32248	0.20385	7.82915
$r = 4$ (39)	0.42678	0.26978	7.22038
$r = 5$ (49)	0.52781	0.33364	6.39058
$r = 6$ (59)	0.62587	0.39563	5.31215
$r = 7$ (69)	0.72111	0.45583	3.96971
$r = 8$ (79)	0.81367	0.51434	2.42451
$r = 9$ (89)	0.90371	0.57125	0.91064
$r = 10$ (99)	0.99137	0.62667	0.00435

steady state temperature and T_τ the temperature according to the decay condition $(1 - e^{-1})$, and τ is the time constant for the individual wall layer. Note that

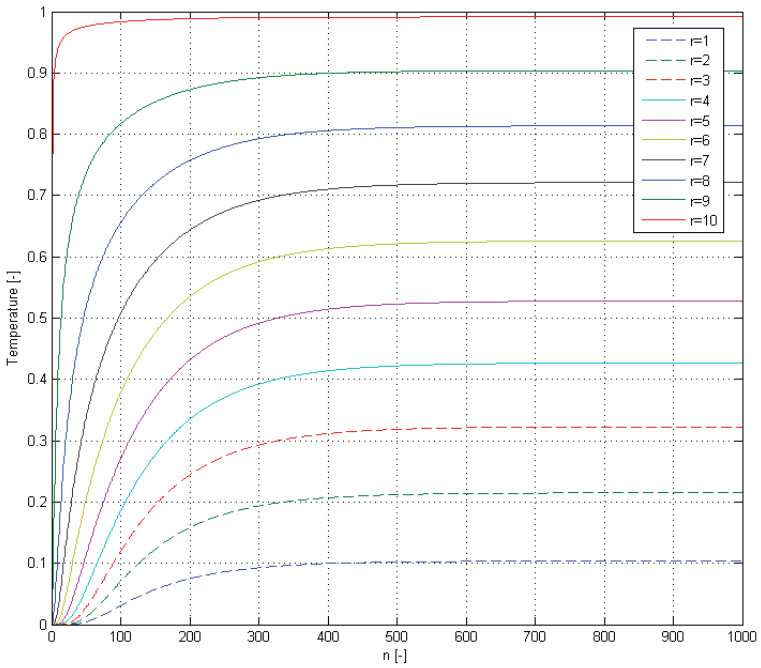

Figure 4.13.: Time series of the thermal response due to a pure Heaviside temperature jump applied to the outer tube surface.

$T_\tau = (1 - e^{-1}) \cdot T_\infty$. The dimensionless time conversion constant is t_0=7.065 [s], given by (4.2) and t_{max}=2.826 $\cdot 10^{-3}$. Note that the time series (r=10) closest to the outer wall appears as a first-order function, and the following time series have a higher order, indicated by the zero slope in the beginning of the simulation, which recalls a time delay of the heat front from the outer layers. From table (4.2) we can see that the time constant for the material near the outer and heated boundary is approximately three decades smaller than the bulk material at the inner side. This means that the temperature fluctuations are more violent in the current tube outer surface, than what is experienced on its inner surface. This is a very important message for dynamic simulations of heat pipes in panel walls, meaning that fatigue can be initiated in the pipe layer that occurs closest to the fluctuating boundary condition; it can typically be a temperature front in the furnace or a shock wave in the evaporator tubes. In the evaporator, there is a tendency for precipitation of porous magnetite at the inner side of the evaporator tube, particularly in the areas which are under direct influence of the high heat flux rate from the burner zones . This precipitation originates from iron compounds in the feed water, which are dissolved in the feed water system of the power plant.

The very largest particles of iron, can partially be removed by filters, even the smallest particles usually cannot be efficiently removed. This magnetite acts as an insulating layer, despite its modest thickness of a few hundred micron meters. This means that the material temperature in the evaporator tube wall now rises considerably and becomes more susceptible to fatigue fracture, which can start as small micro cracks in the infinitesimal material elements, positioned immediately below the magnetite layer. From there, the cracks can under favourable conditions, grow out into the surrounding material and ultimately cause a tube failure. Magnetite layer can be removed by an acid treatment of the evaporator tubes. The first acid treatment at SKV3 was carried out in 2011 after 13 years of operation.

4.3. Tube lifetime evaluation

The lifetime of heated tubes (evaporators and super-heaters) is limited, as the tubes degrade on a continuous basis due to the fireside corrosion, creep, fatigue and steam side oxidation. Evaporator stability is strongly related to temperature conditions in the tube material and must therefore be linked to the life time concept. The following contributions to lifetime degradation of heat pipes are described more thoroughly in [26] and [27]. Appendix D provides a more detailed description of the lift-time evaluation of DONG Energy plants. All degradation processes are highly temperature-dependent and is most dominant in super-heaters, as the temperature is greatest here, but one should not exclude the degradation process in evaporators, as it may appear in thick-walled components. In the context of the dynamic operation of power plants, the life-cycle concept of evaporator tubes and superheaters is essential. The fluctuations, for example, in a fluid flow can affect nucleation on the inner side of the evaporator tube and thus affect the lifetime negatively.

DONG Energy is experiencing the greatest problems with degradation in junction boxes or in the fins in-between each evaporator tube in the panel walls, which may be prone to fracture, caused by the cyclic loads. Steam side oxidation is responsible for a gradually increasing temperature over time, due to the growth of an oxide layer, with very low heat conductivity. This can be reduced by acidification of the tubes.

4.3.1. Corrosion

Fireside corrosion of a heat pipe exposed to combustion gas is caused by oxidation, molten salt corrosion or direct attack of corrosive gasses in the flue gas. For ordinary coal combustion, corrosion is usually caused by oxidation and molten

sulphate. When the temperature of the sulphate mix reaches the melting point, the corrosion rate increases significantly; however, if the metal wall temperature is kept above the dew point, the corrosion will decrease to a level where corrosion is solely oxidation, although oxidation at this high temperature level still is considerable. The calculation of the corrosion, however, uses a constant erosions rate, which of course influences the accuracy of the calculations.

4.3.2. Creep

Creep is also a material degradation process, highly dependent on temperature and stress, where the material destabilizes and the strength decreases with increased time, resulting in permanent plastic deformation. Creep data are available for all normal steels up to 10^5 hours service time or more, at temperatures relevant to boiler applications. The 10^5 hours creep rupture strength reduced with a safety factor, forms the basis in the algorithms used for designing, e.g, super-heater tubes. On the microscopic level, creep itself is known as so-called creep cavities along grain boundaries, illustrated in figure (4.14).

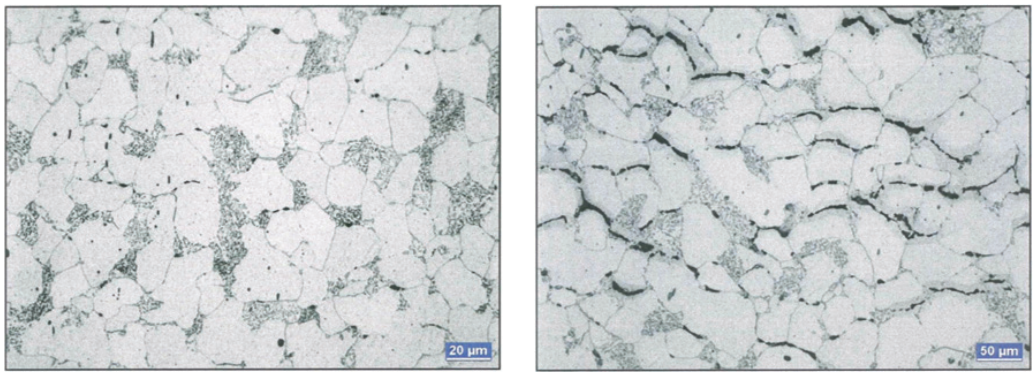

Figure 4.14.: Creep Cavities along grain boundaries, Left: Starting cavitation and Right: Coherent cavities - micro cracks. From internal DONG Energy report.

4.3.3. Oxidation

Steam oxidation turns the surface layer of the steel into oxides. The oxygen needed for oxidation and oxide growth is supplied from the oxygen contained in the steam and dissociation of the steam, thus resulting in the formation of oxygen ions diffusing through the oxide film inside the heat pipe to the steel. At the surface of the steel, metallic iron oxidizes forming iron ions (Fe^{2+}, Fe^{3+}). Part of these iron ions react with the oxygen ions in the situ (Fe_3O_4) and the remaining Fe^{2+} diffuses out through the oxide film. In the course of this process, Fe^{2+} is partly converted into Fe^{3+} and iron oxides are formed in a reaction with the

inwardly diffusion oxygen ions. Figure (4.15) illustrates an example from AVV1, wherein a pipe cross-section is examined under the microscope and in which we clearly can see both an oxide layer (Topotactic layer) and iron deposits in the form of porous structures (Epitaxy layer). The iron is dissolved in the water phase, and as the fluid enters the two-phase zone along the tube, the iron is deposited as magnetite on the walls. The formation of a dense layer of magnetite has a

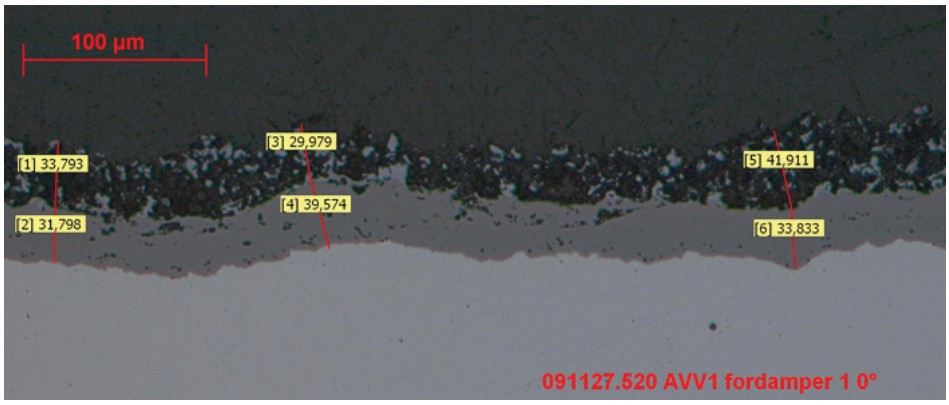

Figure 4.15.: Microscopic analysis of surface structures in an AVV1 evaporator tubes, internal analysis from [28]. The numbers in brackets refer to the thickness of the oxide layer. The light grey colour is the pipe wall.

markedly restrictive impact on the diffusion which impedes further oxidation, and therefore the oxidation rate often approaches a parabolic growth law. If the alloy contains either chromium or silicon, Cr will form either a spinel layer with iron or a pure Cr-oxide film, or for silicon a purely silicon oxide film on the metal surface, due to [26]. The homogeneous pure oxide films constitute very effective barriers against further oxidation, thus resulting in a lower oxidation constant or oxide growth law, which is cubic rather than parabolic. Small fluctuations in the content of Cr and Si may cause large changes to the oxidation constant and will often explain the relatively large scatter attached to the determination of oxide constants; see [29]. Pure Cr-oxides are formed in austenitic steels when the Cr-content exceeds approximately 22 %, but they are also formed in 18 % Cr steels with small grain size. Such films are particularly efficient in preventing further corrosion; the growth of the oxide film will follow the growth law of a higher order rather than that of a parabolic one; see [30]. The thermal conductivity of the oxide layer divided into a topotactic and an epitaxy layer of magnetite, with heat conductivity of 2.3 [W/mK] and 0.7 [W/mK], respectively, and which on average is given by λ_{oxide}= 1.1 [W/mK] and thus constitutes only a small percentage of the metal thermal conductivity λ_{metal}=15.0-20.0 [W/mK] @ 400 [^oC]. The magnetite thickness after 10^5 hours is typically 100-150 [μm].

4.3.4. Summary

Lifetime issues in critical components is forever in focus, and new methods can help to highlight new developments, which may affect the lifetime. A better insight into the operating conditions of the power plant as well as a better understanding of designing future components with the right materials and the right dimensions, will improve the operation flexibility of a plant. In the evaporator panel walls, the lifetime is typically limited by external corrosion and oxide formation immediately for the two-phase region. Instability problems associated with rapid start-up from cold conditions can cause both heavy pressure and temperature oscillations, which can affect the inner layer of the pipe wall and thus initiate the first germs of crack formation. This is closely linked to an understanding of the thermal-hydraulic flow conditions occurring in the heat pipes as well as a detailed description of the temperature gradients that occur in pipe material, initiated by the heat flux arising from the burning of fuel in the furnace. The fins welded to the evaporator tubes to form a gas-tight construction are also prone to breakage, initiated as a result of large temperature differences between the individual heat pipes, which can be related to a mal-distribution problem, likely related to dynamic conditions. This phenomenon will be studied in the next chapter.

5. Steady state flow stability

This chapter is an attemptat presenting the physical mechanisms of the most common flow instabilities. Among these phenomena, the ones with the possibility of producing oscillations are chosen and then analysed. Two-phase flows are prone to various types of instabilities. These can be divided into two general classes: static and dynamic instability.

5.1. Introduction

The phenomenon of thermally induced two-phase flow instability is of great interest in the design and operation of steam generators, boiling water reactors and re-boilers. Oscillations of flow rate and system pressure are undesirable, as they can cause mechanical vibrations and system control problems, and in extreme circumstances, can disturb the heat transfer characteristics so that the heat transfer surface may burn-out. In a recirculating plant, where burn-out must be avoided, flow oscillations could lead to transient burn-out. Under certain circumstances, large flow oscillations can lead to tube failures due to increases in wall temperatures. Another cause of failure would be due to thermal fatigue, resulting from continual cycling of the wall temperature; the thermal stresses set up in the panel wall of a USC boiler, can cause mechanical breakdown, leading to more serious accidents, such as release of hot steam into the boiler building risking considerable human damage and injury as well as large economic losses on the boiler and generation of electricity and district heating. Flow stability is of particular importance in water-cooled and steam generators. The safe operating regime of a two-phase heat exchanger can be determined by the instability threshold values of such system parameters as flow rate, pressure, wall temperatures, and exit mixture quality. The designer's job is to predict the threshold of flow instability so that one can design around it, in order to avoid the unwanted instabilities. This chapter provides a brief description of the most common steady state two-phase flow instabilities, with the attempt to discern which among these reveal characteristics agreeing with the problem in the power plant boiler. Therefore, it is important to define which of the following kinds of instabilities could actually generate oscillations in the evaporator. A 'steady flow' is one in which the system parameters are functions of the space variables only. A flow is said to be 'stable' when its new operating conditions tend toward the initial conditions asymptotically, when momentarily perturbed. Practically, steady two-phase flow operating conditions undergo fluctuations due to perturbations introduced through the boundary of the system (like changes

in inlet pressure, inlet enthalpy, mass flow or power input) or due to turbulence, nucleation or flow pattern transition, which are inevitable characteristics of two-phase flow. These fluctuations represent a small-scale disturbance. In certain domains of flow, however, the fluctuations can trigger large-scale disturbances, which are periodic in nature. Perturbations may grow and a new operating steady state takes over. There have been several extensive reviews of instabilities in two-phase flow systems, notably by [31], [32], [33], [34], [35], [36], [37] and [38]. There are many types of two-phase flow instabilities as shown in table (5.1), and the research activities have been so extensive that a complete account of them becomes infeasible. Another study [39] presents the research on two-phase flow in universities and colleges in Japan.

Type	Mechanism	Characteristics
Ledinegg instability	Internal pressure characteristics steeper than external characteristics in a negative slope region	Flow undergoes sudden, large amplitude excursion to a new stable operating condition
Boiling crisis	Ineffective removal of heat from heated surface	Wall temperature excursion and flow oscillation
Flow pattern transition instability	Bubbly flow has less void but higher pressure-drop than annular flow	Cyclic flow pattern transition and flow rate variations
Bumping Geysering Chugging	Periodic adjustment of metastable condition, usually due to lack of nucleation sites	Periodic process of super-heat and violent evaporation with possible expulsion and refilling

Table 5.1.: Classification of boiling two-phase steady state flow stabilities [31].

5.2. Two-phase momentum model

This section outlines the basic theory for pressure loss in heated pipes. The theory is mainly applied to smoothed pipes without internal rifles, but IRBTs are also briefly described in terms of both the friction and heat transfer. The current models that have been implemented, are only valid for water-steam flows. In

cases involving other systems, the modelling approach should be extended. The two-phase flow of a vapour-liquid mixture in a channel with heat supply, causes a variable density flow in a one-dimensional flow concept. If the pressure drop along the channel is relatively small compared with the absolute pressure, the flow is practically incompressible. This means that the density of each phase is practically constant. The change in bulk flow density is thus due to the phase change caused by boiling along the heated pipe. During the process of phase change, i.e., void increases, the phase and velocity distribution are changed and so is the momentum of the flow. Hence the pressure drop of a vertical two-phase flow consists of three components, frictional loss, momentum change and elevation pressure drop, arising from the effect of the gravitational force field. Based on the homogeneous momentum balance equation (8.86) for a heat pipe, we can derive empirical pressure loss relations with reference to the momentum change, gravity and friction. For convenience we choose to write the homogeneous momentum equation, from [40]:

$$\frac{\partial}{\partial t}(GA)+\frac{\partial}{\partial z}\left(\frac{G^2A}{\rho'}\right)=-A\frac{\partial \bar{p}}{\partial z}-F_wA-\bar{\rho}gA\cos(\theta). \tag{5.1}$$

If we assume a steady state condition and define the mass flux G and the cross-section area A as constant values in space, hence the steady state momentum balance for a heat pipe can be expressed as

$$\begin{aligned}\frac{\partial \bar{p}}{\partial z}&=-G^2\frac{\partial}{\partial z}\left(\frac{1}{\rho'}\right)-F_w-\bar{\rho}g\cos(\theta)\\&=\left(\frac{\partial \bar{p}}{\partial z}\right)_a+\left(\frac{\partial \bar{p}}{\partial z}\right)_f+\left(\frac{\partial \bar{p}}{\partial z}\right)_g\end{aligned} \tag{5.2}$$

The steady state total pressure drop in two-phase flows is a sum of three contributions: an acceleration pressure drop, Δp_A, a pressure drop due to friction, Δp_f and a hydrostatic pressure drop due to elevation change, Δp_G:

$$\Delta p_{tf}=\Delta p_A+\Delta p_f+\Delta p_G. \tag{5.3}$$

The individual contributions to the total pressure loss are briefly described in Appendix E.

5.3. Modelling framework

The focus area of the model framework is to establish a realistic model setup that ful-fill the measurement campaigns listed in table (3.2). The model is calibrated at part load (sample 4), because it operates in the two-phase flow

regime at that load. The model is verified in the other samples (1-3). The evaporator geometry of SKV3 is taken from supplier drawings, and the associated measurement campaigns are taken from the plant control system, where up to 6000 measurement points per second are recorded. The selected data, with a high accuracy, is used to determine the boundary conditions for the simulation scenarios.

5.4. Flow stability in panel walls

This chapter presents a study of flow mal-distribution in two parallel heated pipes, which is a model of a small part of the panel walls in a steam power plant boiler. The study is based on measurement campaigns conducted on Skærkækværket Unit 3; see table (3.1). The purpose of this study is to generate an increased basic understanding of the involved physical phenomena, and knowledge of the maldistribution issues in evaporator tubes, exposed at very high heat flux loads. The study is performed with and without sub-cooled inlet fluid.

Two-phase heat exchangers pose unique challenges as they are prone to various flow boiling instabilities; see [31], such as the Ledinegg flow excursion, parallel-channel flow mal-distribution, pressure-drop and density-wave flow oscillations. The Ledinegg instability arises when the flow boiling system operates in the two-phase negative-slope region of the demand pressure curve, where the demand pressure drop decreases with increasing mass flow rate; see [41] and [42]. Slight changes in the supply pressure drop will trigger a sudden flow excursion to either a sub-cooled or a superheated operating condition. Pressure-drop oscillations could occur when there exists large upstream compressibility of the flow boiling system, pressure-drop oscillations [43], [31]. This mal-distribution instability could cause large uncontrolled wall temperature differences. Different flow conditions were experimentally demonstrated and found to be heavily dependent on the prior state of the channels. Even for conventional-scale two-phase heat exchangers, flow mal-distribution also has dramatic negative consequences on thermal and mechanical performance, according to [44] and [45]. Attributed to local flow instabilities and mal-distribution, the critical heat flux condition could be prematurely initiated before the advantage of phase change is realized [46]. Local channel dry-out would severely compromise heat transfer performance and could lead to severe safety problems.

To investigate the mal-distribution of cooling water in the panel wall, we develop a numerical model, which consists of two parallel pipes. The model is based on a steady state lump model, described in section (5.2), where the heat transfer and pressure loss models are based on conventional theory for steam

power engineering, which are outlined in Appendix (E). The solution algorithm for solving the flow distribution in two parallel pipes is strongly un-linear and is solved by use of a conjugated gradient method with a constrained line search algorithm; see [20] and [22].

5.5. Mal-distribution - literature review

Here we focus on steam power engineering in the Benson boilers running part load, below Benson minimum. The usual geometries (panel walls as heat pipes) use a parallel channel configuration, in order to accommodate a large heat-transfer area in a limited space. This allows the building of large capacity equipment within a reasonable size, but it also leads to problems related to flow maldistribution. In many scenarios the flow distribution deviates from the design conditions, which is usually a homogeneous flow setup. The possible causes include poor header design or off-specification operating conditions, and channel blockage or size reduction due to differential thermal expansion or fouling. A comprehensive review on causes of mal-distribution can be found in [45].

Single-phase maldistribution has been widely studied, both in terms of a header design perspective [47], [48] and its effect on thermal performance [49] and [50]. A reduction in heat duty (defined as the total heat transferred) is found in all cases as a consequence of mal-distribution. For two-phase applications, research has been focused on the flow distribution in manifolds, both experimentally [51] and by numerical modelling [52] and [53]. The thermal performance analysis was limited to the effect of mal-distribution on the single-phase streams, such as in condensers and evaporators; see [54], [55], [56], [57] and [58]. As in the single-phase case, a deterioration of performance is predicted in most situations, but there is some experimental evidence of an increase in thermal performance on air-heated evaporators like [56] and [57]. Another interesting study is the mal-distribution in fin and tube evaporators [59], where the focus is on the evaporator efficiency and COP of a refrigeration circuit.

5.5.1. Model theory

In general, lots of geometries can be considered for steam power boilers, which can include two or more streams (Shah and Sekulic, 2003). In particular, this work studies a two-stream heat pipe panel wall model, sketched in figure (5.1). The scope of this work is limited to practical situations that fit the following simplifying assumptions:

- No internal rifled boiler tubes are analysed.
- A steady-state analysis is performed.

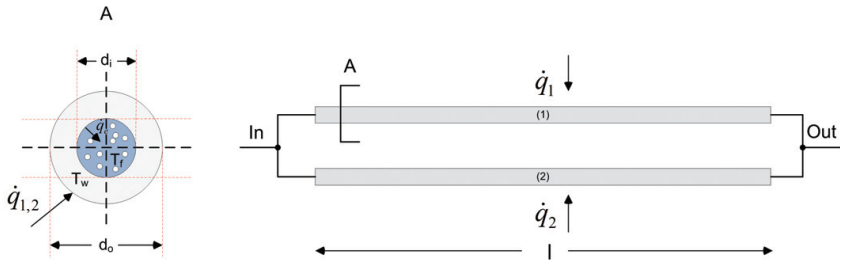

Figure 5.1.: Sketch of parallel heat pipe flow model (SKV3 boiler tubes).

- All working fluids are based on IAPWS97.
- Axial conduction in-between the heat pipes and to the surroundings is negligibl small.
- Mixing is not considered. This means that the parallel channels do not exchange mass and momentum.
- An elemental geometry can be identified where hot and cold streams exchange energy, and interaction with other channels is negligible.

The general modelling for the evolution of the streams is based on one-dimensional mass, momentum and energy balances for each channel, named, channel 1 and 2 as illustrated in figure (5.1). However, with the above considerations, the mass-balance equation gives a trivial result that is a constant flow rate in each channel. Then, the problem is governed by equations (5.1) via (5.2) for each channel, which represents the momentum balance for both tube-side fluids. The model is based on a steady state calculation of two parallel pipes, where the flow distribution is unknown and is a function of the supplied heat distribution. The load cases are listed in table (5.2). We define a *heat distribution factor* as

$$d_q \equiv \frac{\dot{q}_1}{\dot{q}_2} \tag{5.4}$$

where $\dot{q}_1$ and $\dot{q}_2$ denote the heat absorbed in pipe 1 and pipe 2, respectively. The heat flux is assumed constant along the axial direction of the pipe. The total pressure drop caused by gravity, friction and acceleration will force a hydraulic balance, given by the uniform pressure drop over the two pipes is described in

detail in Appendix (E). Hence we can formulate a set of equations leading to the non-linear equation below.

$$\text{Solve: } \begin{cases} m = m_1 + m_2, & \text{Continuity} \\ 0 = \Delta P(m_1, \dot{q_1}) - \Delta P(m_2, \dot{q_2}), & \text{Momentum} \\ \dot{q} = \dot{q_1} + \dot{q_2}, & \text{Energy} \end{cases} \tag{5.5}$$

where $\dot{q}_1$=$\alpha\dot{q}$, $\dot{q}_2$=$(1-\alpha)\dot{q}$ and α is a linear distribution factor of energy, hence $d_q = \frac{\alpha}{1-\alpha}$. The dimensionless mass flow is defined according to a reference mass flow for a reference simulation (design case) with $d_q \equiv 1$; see figures (5.8) and (5.9). Hence the dimensional *flow distribution factor* is defined as the relationship between $\dot{m}_1$ and $\dot{m}_2$.

$$d_m \equiv \frac{\dot{m}_1}{\dot{m}_2} \tag{5.6}$$

and the corresponding dimensionless *pressure loss factor* (d_p) is defined relative to the actual pressure loss (ΔP) versus the design pressure loss $\Delta P_{design}(d_p = 1)$:

$$d_{p-total} \equiv \frac{\Delta P_{total}}{\Delta P_{design}} \tag{5.7}$$

$$d_{p-viscos} \equiv \frac{\Delta P_{viscos}}{\Delta P_{design}} \tag{5.8}$$

The problem, given by equation (5.5) is solved by a conjugated gradient method, where realistic start guesses are needed for the model as well as a realistic definition interval for each parameter. The solver is a Newton-based solver using a Jacobian matrix with a constrained line search algorithm; see [20] and [22].

5.5.2. Simulation scenarios

The flow distribution in two parallel identical evaporator tubes depends on several factors. We will now examine primarily two factors, firstly, how the inlet pressure effects the sensitivity of the flow distribution (mal-distribution) in two heat pipes when the heat distribution factor varies (5.4) and secondly, how the degree of sub-cooling of the inlet fluid affects the mal-distribution by varying d_q.

Mal-distribution - saturated inlet condition

This analysis of flow mal-distribution is based on two different flow rates listed in tables (5.2) to (5.5), with saturated water at the inlet boundary. Measurements of enthalpy are used directly as the upstream boundary condition for pressure levels above the critical pressure. The tube geometry corresponds to what we have on the SKV3 boiler. This saturated inlet condition is particularly critical in connection with the flow distribution through the junction boxes to the evaporator tubes in a power plant, because saturated fluid is difficult to distribute to the panel walls, while the fluid can easily change mode from containing a bit of steam to being slightly sub-cooled. This affects the specific volume of the fluid so that the pressure loss in the evaporator string may cause non-uniform flow rates through the evaporator strings. The mal-distribution analysis below does not include modelling of the assembly boxes, but is only based on the assumption of two similar parallel evaporator tubes with a perfect junction box. The two-phase modelling approach will be based on Friedel, because Jirous deviates from the measurements in table (3.2) for low pressure; see tables (5.2) to (5.5) and Appendix E for further modelling details. As we can see from tables (5.2)

Simulation nr.	P_{in}	h_{in}	P_{out}	h_{out}	$\dot{q}$	ΔP_f	ΔP_g	ΔP_a	ΔP
	$[bar]$	$[kJ/kg]$	[bar]	$[kJ/kg]$	[MW]	[bar]	[bar]	[bar]	[bar]
1	50.00	1154.64	32.10	2803.00	824.18	16.673	0.457	0.770	17.900
2	100.00	1408.10	91.50	2740.77	666.33	7.603	0.658	0.235	8.496
3	150.00	1610.20	144.33	2626.40	508.10	4.703	0.847	0.117	5.666
4	200.00	1827.21	195.96	2435.60	304.19	2.943	1.044	0.052	4.039

Table 5.2.: Design cases for various pressure levels at m=1.0 kg/s (Friedel).

Simulation nr.	P_{in}	h_{in}	P_{out}	h_{out}	$\dot{q}$	ΔP_f	ΔP_g	ΔP_a	ΔP
	$[bar]$	$[kJ/kg]$	[bar]	$[kJ/kg]$	[MW]	[bar]	[bar]	[bar]	[bar]
1	50.00	1154.64	22.23	2800.28	822.83	26.229	0.417	1.117	27.763
2	100.00	1408.10	90.66	2741.85	666.87	8.458	0.647	0.238	9.343
3	150.00	1610.20	144.54	2625.84	507.82	4.498	0.845	0.117	5.459
4	200.00	1827.21	196.25	2434.02	303.41	2.664	1.035	0.052	3.751

Table 5.3.: Design cases for various pressure levels at m=1.0 kg/s (Jirous).

Simulation nr.	P_{in}	h_{in}	P_{out}	h_{out}	$\dot{q}$	ΔP_f	ΔP_g	ΔP_a	ΔP
	$[bar]$	$[kJ/kg]$	[bar]	$[kJ/kg]$	[MW]	[bar]	[bar]	[bar]	[bar]
1	50.00	1154.64	43.77	2798.74	411.03	5.648	0.440	0.139	6.228
2	100.00	1408.10	96.99	2730.92	330.71	2.290	0.659	0.054	3.004
3	150.00	1610.20	147.87	2616.70	251.63	1.247	0.855	0.028	2.130
4	200.00	1827.21	198.20	2423.03	148.96	0.743	1.048	0.012	1.803

Table 5.4.: Design cases for various pressure levels at m=0.5 kg/s (Friedel).

Simulation nr.	P_{in}	h_{in}	P_{out}	h_{out}	$\dot{q}$	ΔP_f	ΔP_g	ΔP_a	ΔP
	$[bar]$	$[kJ/kg]$	[bar]	$[kJ/kg]$	[MW]	[bar]	[bar]	[bar]	[bar]
1	50.00	1154.64	44.92	2798.00	410.84	4.417	0.533	0.135	5.085
2	100.00	1408.10	97.00	2730.90	330.70	2.226	0.716	0.054	2.997
3	150.00	1610.20	147.69	2617.20	251.75	1.393	0.890	0.028	2.310
4	200.00	1827.21	198.05	2423.89	149.17	0.864	1.072	0.012	1.948

Table 5.5.: Design cases for various pressure levels at m=0.5 kg/s (Jirous).

and (5.3) for a mass flow of 1.0 [kg/s] and (5.4) and (5.5) for a mass flow of 0.5 [kg/s] we have a significant difference in the friction pressure loss, and Jirous will overestimate for lower pressure (50 [bar]). Figures (5.2) to (5.5) illustrate the mal-distribution curves for scenarios 1-4, which are based on data from table (3.2). In the figures we have scaled the flow distribution factor (d_m) and the pressure distribution factor ($d_{p-total}$) for total pressure, given by equation (5.7) on the left ordinate axis and the viscous pressure distribution factor ($d_{p-viscous}$) to the right; see equation (5.8). In general we can see that d_m increases for decreasing d_q. This tendency is more clear for higher saturation pressure (operational pressure), which increases the risk of asymmetric flow in the evaporator tubes. For operational pressure above the critical point (220,64 [bar]) we see a monotone increased curve of total pressure loss for decreasing d_q, while we observe the opposite tendency for an operational pressure below the critical pressure with a monotone decreasing total pressure loss for decreasing d_q. If we focus on the relative viscous pressure loss alone, we can see a general dependency of the operating pressure, where the viscous pressure loss is decreasing for decreasing d_q.

Mal-distribution - sub-cooled inlet conditions

This scenario includes the state of the inlet conditions for the upstream boundary changed in equation (5.5), so that various levels of sub-cooling are achieved, for example, 20% of sub-cooling is defined as an inlet enthalpy that consists of the saturated water subtracted by 20% of the latent heat, given at the same saturation pressure. Otherwise we have unchanged conditions for flow and heat absorption, due to tables (5.2) to (5.5). The results of the simulations are illustrated in figures (5.6) to (5.13). One of the most interesting observations is that a high degree of sub-cooling results in the largest difference in the outlet enthalpy from pipe 1 and 2; see figure (5.10) to (5.13). Notice that the outlet enthalpy is constrained to a maximum of 3900 [kJ/kg], due to the formulation of IAPWS97, which gives the basis for the thermodynamic properties in our simulations. On the other hand we can see, that for fixed exit enthalpy on the pipe 1 or 2, we generally can accept a larger obliquity in the heat flux for decreasing sub-cooling. One example is that a fluid without sub cooling (saturated water) can handle a d_q=0.5, while a fluid with 25 % of sub cooling with the same outlet enthalpy, only can handle a

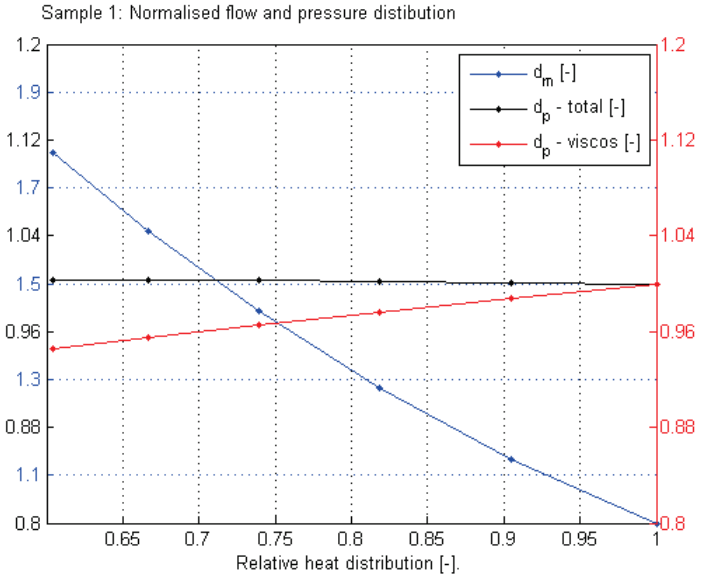

Figure 5.2.: Sample 1: Flow and pressure distribution.

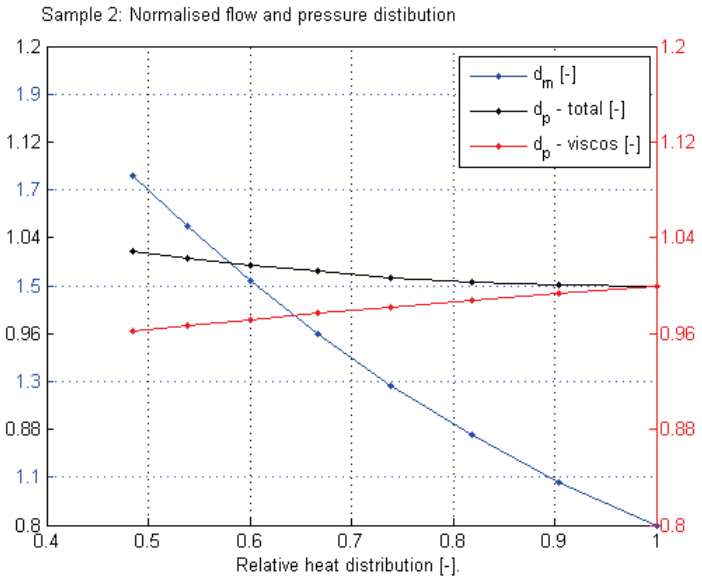

Figure 5.3.: Sample 2: Flow and pressure distribution.

d_q=0.68; see figure (5.12). In other words, a higher degree of sub-cooling leads to a greater temperature difference in the tubes, for a given d_q. This tendency is reduced for higher operating pressure. If we take a look at modern once-through Benson boilers, like SKV3, we observe a much lower obliquity in the heat flux, which is verified by CFD simulations; see figure (4.5). The simulations give

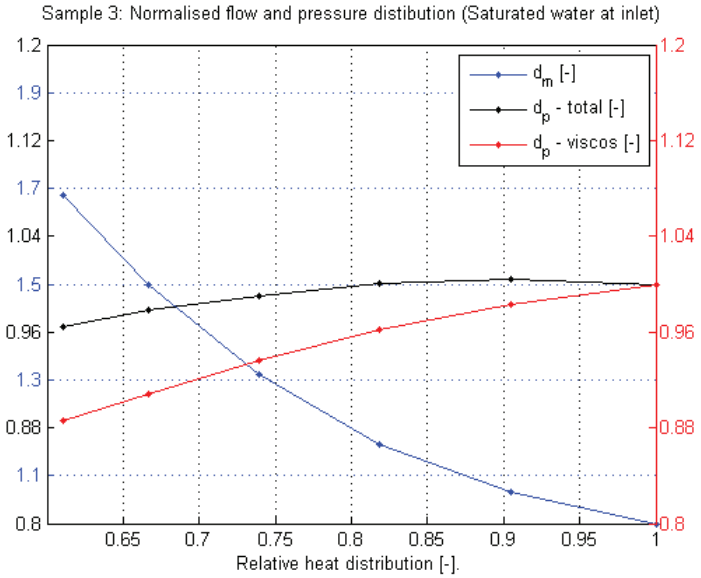

Figure 5.4.: Sample 3: Flow and pressure distribution.

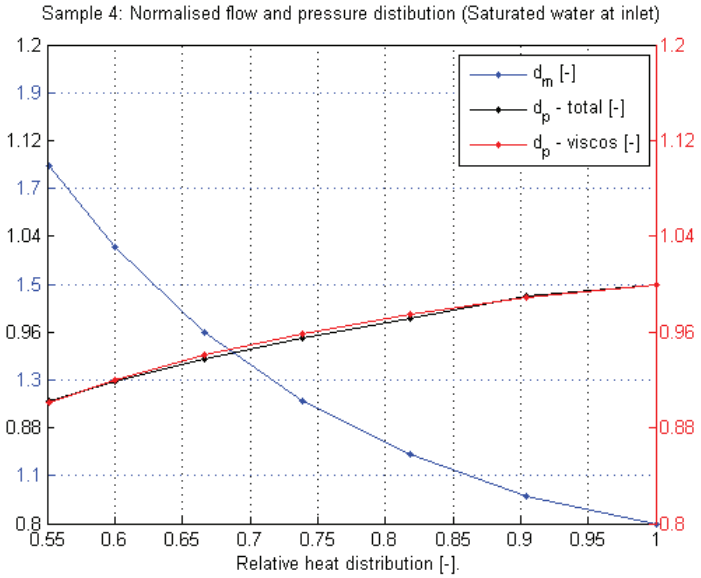

Figure 5.5.: Sample 4: Flow and pressure distribution.

the largest heat flux gradients in the bottom of the furnace: $\frac{\partial \dot{q}}{\partial z} \approx 20$ [kW/m^3]. On the other hand we have in mind the thermal diffusivity and low thermal conductivity in the pipe material, leading to very large temperature gradients, due to the discussions in section (8.5). But the heat flux gradients initiated by the

combustion processes, will not be able to induce a relative heat distribution factor less than approximately 0.85, based on the largest gradients in the bottom of the boiler as illustrated in figure (4.5). A panel wall geometry based on 38 [mm] pipes with 20 [mm] fins and 28 heat pipes (15 degree inclination) connected to one junction box gives:

$$\begin{aligned} d_q &\approx \frac{200[kW/m^2] - 20[kW/m^3] \cdot \sin(15^o) \cdot 6.0[m]}{200[kW/m^2]} \\ &\approx 0.85[-]. \end{aligned} \tag{5.9}$$

It is interesting to see how the relative pressure loss varies as a function of d_q for different operational pressure levels; see figures (5.6) and (5.7). For an operational pressure of 150 [bar], we see a change in circumstances, where the pressure drop has a minimum. This is caused by a combination of the applied boundary conditions (q, m_1 and m_2) as well as the working pressure. An operating pressure of 200 [bar] or more, causes a change in the relationship between the ratio of the relative pressure drop and d_q, which now gives a monotonically increasing relationship. Conversely, we see a monotonic decreasing relationship between the relative pressure drop and d_q at the operating pressure of only 50 and 100 [bar]; see figure (5.7). The relative mass flow on the ordinate axis in figure (5.8) and (5.9) is defined as the difference between the design mass flow and the actual flow and the figures illustrate how the mass flow varies according to d_q. We can immediately see that the greatest impact on the flow distribution is at low operation pressures, while at 200 [bar], we hardly see any significant difference compared to the design condition. This means that a high operational pressure has a stabilizing effect on the flow distribution according to figures (5.8) and (5.9).

Appendix (H) shows how the mass flow affects the flow friction pressure loss for the different operating pressure, and it is obvious that the frictional pressure loss is highly dependent on the mass flow through the tubes. This is illustrated in figures (H.1) to (H.12). The following conditions are generally observed for decreasing d_q: we see an increasing relative friction pressure in pipe 1 for decreasing mass flow (m). For increased operating pressure, we record higher relative friction loss due to an increase in specific volume. It is also seen that the relative mass flow out of the pipe 1 decreases for increasing m, while the relative enthalpy of pipe 1 increases for increasing m.

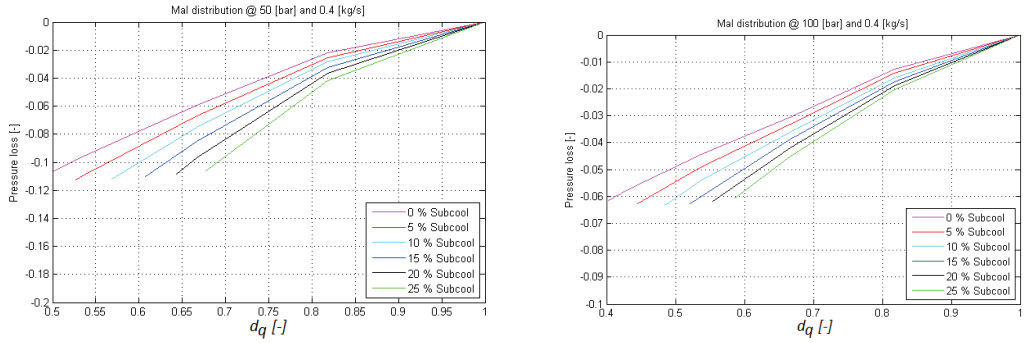

Figure 5.6.: Mal-distribution in panel wall - relative pressure loss with varying sub-cooling.

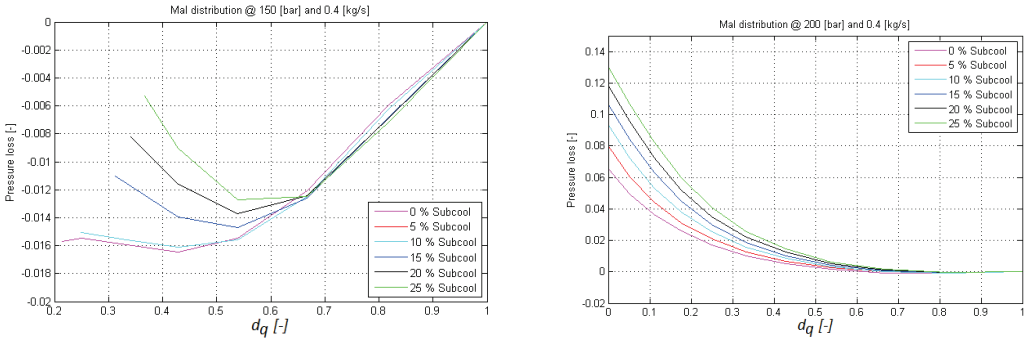

Figure 5.7.: Mal-distribution in panel wall - relative pressure loss with varying sub-cooling.

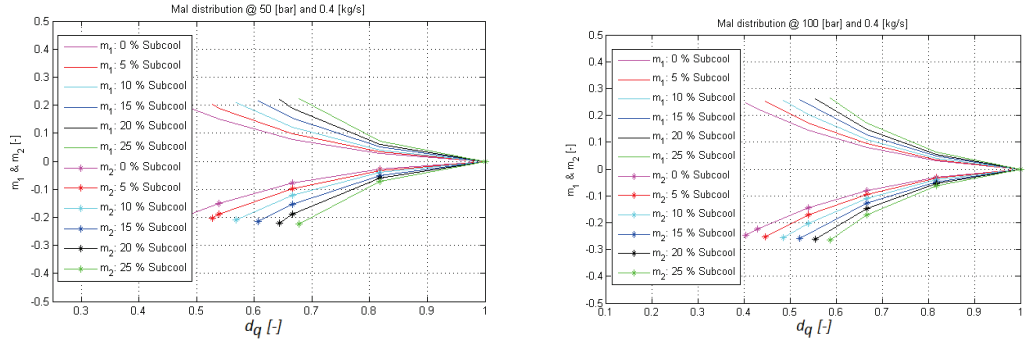

Figure 5.8.: Mal-distribution in panel wall - relative mass flow with varying sub-cooling.

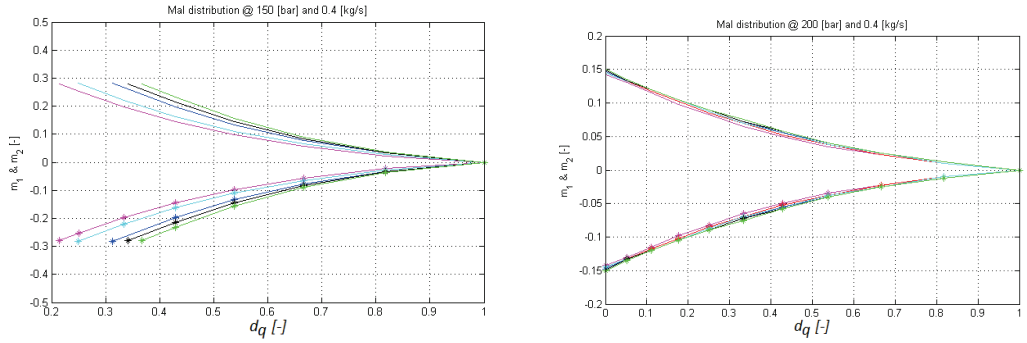

Figure 5.9.: Mal-distribution in panel wall - relative mass flow with varying sub-cooling. Legend similar to figure (5.8).

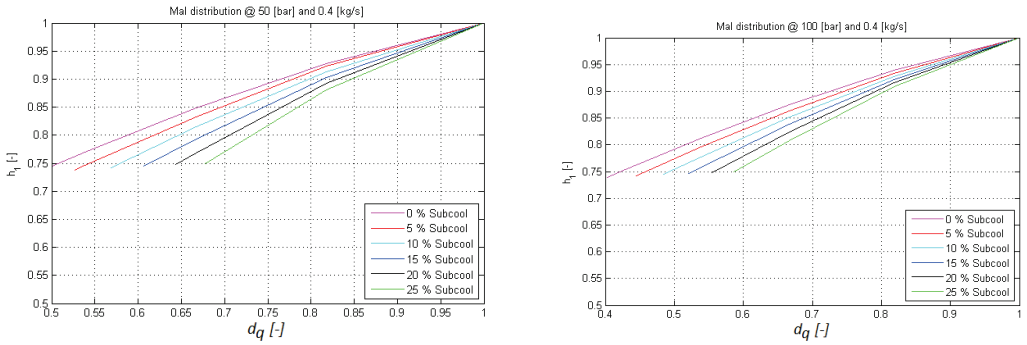

Figure 5.10.: Mal-distribution in panel wall - relative enthalpy outlet from pipe 1 with varying sub-cooling.

The general results of this work are that the pressure loss increases over the two parallel tubes for increasing sub-cooling with a pressure higher than 150 [bar]; otherwise we see a decrease in pressure loss. There is a larger flow mal-distribution for larger sub-cooling of the inlet fluid, and the heat pipe that receives most heat, has the lowest mass flow. This is supported by the fact that the pipe wall achieves a critical high temperature faster for using less sub-cooling. This trend decreases with increasing operating pressure.

5.5.3. Discussion

One of the main conclusions of this study in mal-distribution analyses, is that the distribution problem primarily is affected by the operating pressure in the pipe.

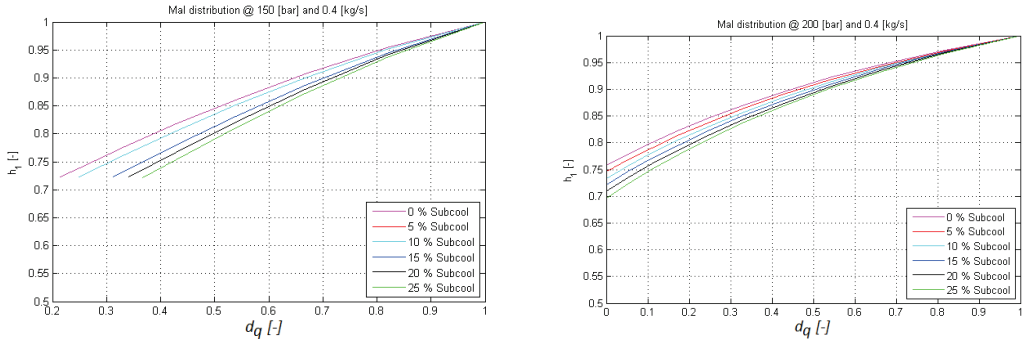

Figure 5.11.: Mal-distribution in panel wall - relative enthalpy outlet from pipe 1 with varying sub-cooling.

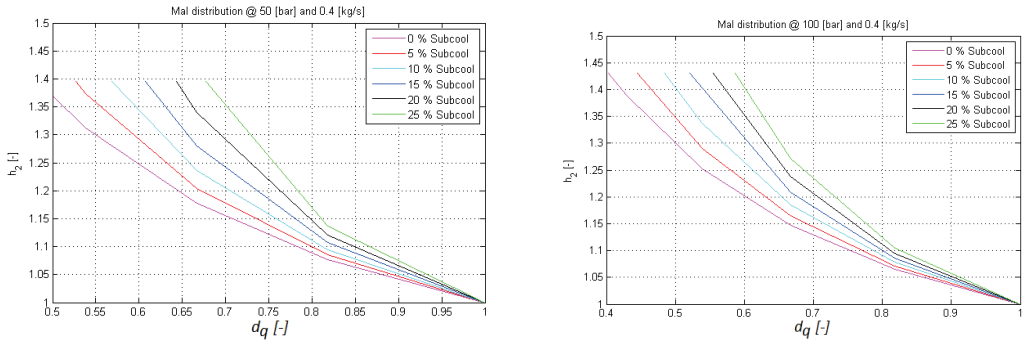

Figure 5.12.: Mal-distribution in panel wall - relative enthalpy outlet from pipe 2 with varying sub-cooling.

The lower the operating pressure is, the greater the difference between the mass flow in the two parallel pipes. In addition, the inlet mass flux to the system is also a parameter, which affects the bias of the flow distribution. The larger the inlet flow to the two pipes, the greater is the distribution of flow in both tubes. The pressure drop, which is the driving factor in the distribution problem, ensures that there will always be the same total pressure drop over the two pipe elements. Friction pressure loss is an essential factor in this game, but the geodetic height also plays a role in that context, so that it will reduce the influence of the friction pressure drop, especially in situations where the geodetic height difference is mainly composed of liquid and not vapour. An early superheat of the fluid in the heat pipe, eliminates the influence of the geodetic pressure difference, which leads to a higher mass flow through the actual pipe element.

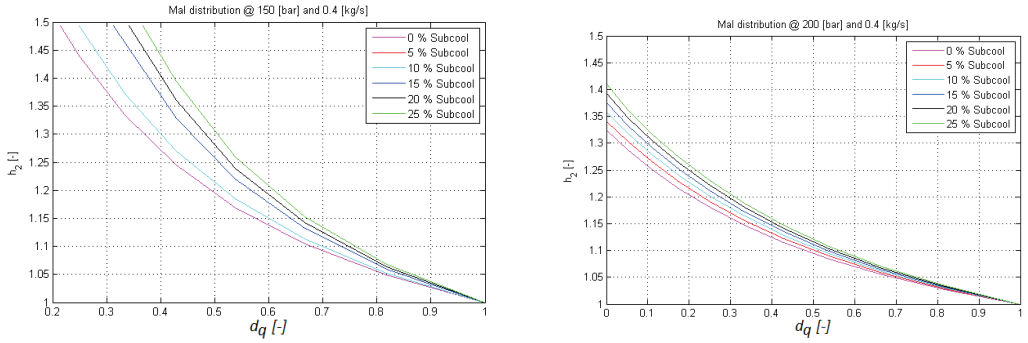

Figure 5.13.: Mal-distribution in panel wall - relative enthalpy outlet from pipe 2 with varying sub-cooling.

At the Danish Avedøreværket Unit 2 (AVV2) there were attempts to lower the evaporator pressure, from the original initial pressure of 90 [bar] (design load pressure) to 56 [bar], which is equivalent to 20% boiler load. The main challenge was to avoid hot steam to the turbines as well as a hot flue gas screen, due to the low mass flow rate through the boiler. The pressure drop through the boiler is high, because of the higher specific volume of the steam, at a relatively low evaporator pressure. Other challenges such as a high feed water temperature may worsen the distribution problem for the individual heat tubes in the panel wall, a smaller sub-cooling improves the maldistribution challenge of the low evaporator pressure, as illustrated in figure (5.8).

5.5.4. Summary

In general we see significant differences in the downstream conditions of the fluid for the selected scenarios. In certain critical situations, we can have high superheated steam in one piece of the pipe, while there is two-phase flow in the second pipe, with a low steam quality. This may have important implications for the lifetime of the heat pipe, as the material temperature follows the fluid temperature. Fortunately, the panel walls are constructed in a way that there may be heat transfer between the pipe sections, but this heat transfer is primarily based on conduction, with high temperature gradients to follow. Conduction between the pipe sections is not included in this analysis, but time constants and thermal diffusivity has been analysed in section (3), and indicates that the conduction is restricted by the relative low heat transfer coefficient for alloys at high temperature, which results in a high temperature gradient in the material and in that way allows high temperature in the material caused by mal-distribution. A higher degree of sub-cooling of the inlet flow, causes a greater enthalpy difference in the outlet of the tubes, which can only increase the load on the boiler tubes.

Low load operation of a Benson boiler, which continues to produce superheated steam, is not at risk of poor mal-distribution; here it is more likely a matter of ensuring a good heat transfer in stratified flow, due to the low mass flux, where the vapour phase causes a poor cooling of the pipe wall.

5.6. Ledinegg stability

Two-phase flow systems can induce a number of instability and oscillation phenomena. For a fixed set of boundaries, there are often multiple solutions for a steady state operation of a boiling two-phase flow system, some of which are unstable. Small perturbations can cause a system that has multiple solutions for a given boundary condition to move from one set of operation conditions to an entirely different set or oscillate back and forth among two or more unstable operation conditions. The two-phase flow stability is of great concern for steam boiler reactors, both on power plants as well as on smaller boiler and heat exchangers, and this phenomenon has been studied extensively and summarized in [40]. There are several other static instability modes, e.g, flow maldistribution instabilities, which can occur in systems where multiple parallel heated pipes are connected at both ends to common inlet and outlet plenums, and a pressure loss - mass flow view (ΔP, $\dot{m}$) includes a negative-sloped portion. Other examples include flow regime transitions, chugging and geysering.

Practical examples of static flow instabilities have been reported by eg., Margetts, [60], such as flow instability failures in several feed water economizers during some years of operation. Boiler feed water is typically preheated in a large number of parallel channels, by recovering heat from an ammonia plant (primary flow gases). Calculations suggested that the severely overheated tube had the highest heat load and was operating at the minimum in the pressure-drop - flow-rate curve, which was essentially flat and set by the remaining parallel unheated tubes in the bank. The problem was solved by eliminating one-third of the unheated tubes to increase the driving pressure drop of the heated tubes. In another case, Margetts [60], points out the failures observed in an economizer tube after some years of operation with considerably lower gas temperatures. It was speculated that the channel had experienced some flow excursion, and ultimately failed due to accelerated corrosion in the dry region. The solution to this problem was to install throttling restrictions at the inlet to each tube.

In this section a simple homogeneous steady state two-phase flow model is developed for the purpose of capturing flow oscillations caused by flow excursion also, referred to as Ledinegg instabilities [61], with water/steam as flowing media. The static instabilities represent discontinuities with respect to the steady-state operation of a system, and these can be analysed based on the system's steady

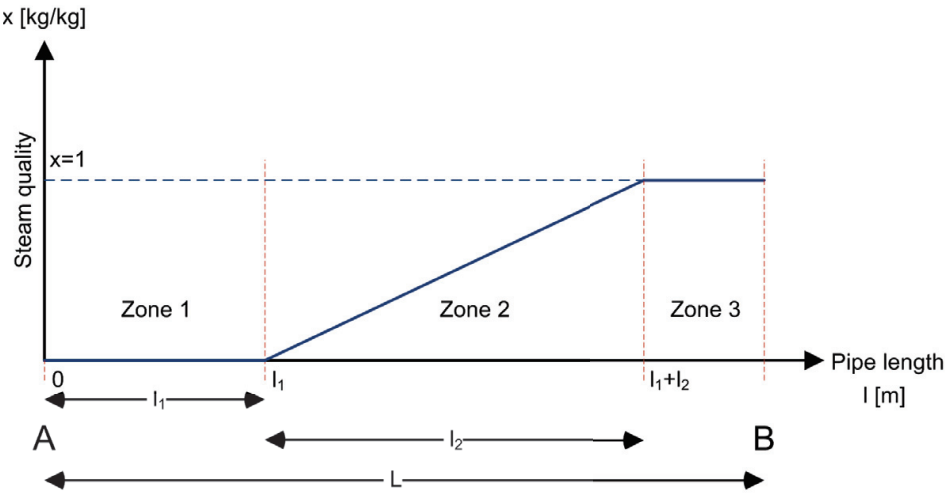

Figure 5.14.: Steam quality as function of pipe length.

state conservation equations. The model here is based on a prediction of the friction pressure loss in heat pipes. If the pipe is horizontally orientated, the gravitational pressure drop is ignored; otherwise we include the gravitational pressure drop for vertical heat pipes. Let us consider the system shown in figure (5.14), where sub-cooled liquid is pumped from a reservoir A and flows through the heated channel before entering reservoir B. Let us focus on a single heat pipe element with a total length of L, with a gravitational pressure loss, where the distribution of vapour along the heated pipe in the boiling zone is linearly distributed, caused by a constant heat flux $\dot{q}$. We consider a heated channel alone and assume that the inlet conditions are constant in time. The total pressure drop for the channel can be calculated by integrating the steady state one-dimensional mixture momentum conservation equation, by using an appropriated correlation for the slip ration and assuming thermodynamic equilibrium between the liquid and the vapour.

The pipe element for this stability analysis is divided into three zones, a sub-cooled zone from 0 to l_1, where the flow is single-phase. The second zone is established from l_1 to $l_1 + l_2$, where we have a two-phase boiling zone, and after this point the fluid is superheated in zone 3. Let us assume that l_1 and l_2 are fixed heating zones, and let the effect $\dot{q}$ [W/m] be the effect per length supplied to the tube, then the effect delivered in zone 1 is: $\dot{Q}_1 = \dot{q}l_1$ and $\dot{Q}_2 = \dot{q}l_2$, where $\dot{q}$ is constant along the pipe length L. If we assume stationary conditions, with a fluid

flow given by $\dot{m}$ and inlet enthalpy of h_{in}, hence we have two energy balances for the pipe element:

$$\begin{aligned} \dot{Q}_1 &= \dot{m}(h_l - h_{in}) \\ \dot{Q}_2 &= \dot{m}(h_g - h_l) \end{aligned} \tag{5.10}$$

where h_l is the saturation enthalpy for liquid (x=0) and h_g is the saturation enthalpy for steam (x=1), where x is the steam quality. Note that x is the steam quality defined in equation (8.77). The latent heat is given by $h_{lg} = h_g - h_l$. We have complete boiling, if the pipe length L $> l_1$+l_2, which can be reformulated into a critical mass flow (m_c) for which complete boiling occurs due to the specified heat flux. Hence

$$\dot{m}_c \geq \frac{\dot{q}L}{h_g - h_l} \tag{5.11}$$

which will exactly ensure saturated steam downstream the heat pipe. The corresponding pressure loss consists of contributions from the friction and gravity, and can simply be estimated by the expression below.

$$\begin{aligned} \Delta P &= \Delta P_f + \Delta P_g \\ &= \frac{f}{2} \cdot \overline{\rho u^2} + \bar{\rho} g L \\ &= \frac{f}{2A_c^2} \cdot \overline{\frac{\dot{m}^2}{\rho}} + \bar{\rho} g L \\ &\approx \frac{f}{2A_c^2} \cdot \frac{\overline{\dot{m}}^2}{\bar{\rho}} + \bar{\rho} g L \end{aligned} \tag{5.12}$$

$$\tag{5.13}$$

where $\bar{u}$ is the mean fluid velocity,$\bar{\rho}$ is the mean density and $\bar{v} = 1/\bar{\rho}$ is the mean specific volume. The contribution of the acceleration pressure drop is not included in this analysis and is not believed to cause significant changes in the outcome. We can now calculate the friction pressure drop and gravitational pressure drop for three cases:

- Complete boiling
- Partial boiling
- No boiling

5.6.1. Complete boiling

For the case of complete boiling, we can calculate the mean specific volume for the pipe length L $> l_1$+l_2, based on the density variation illustrated in

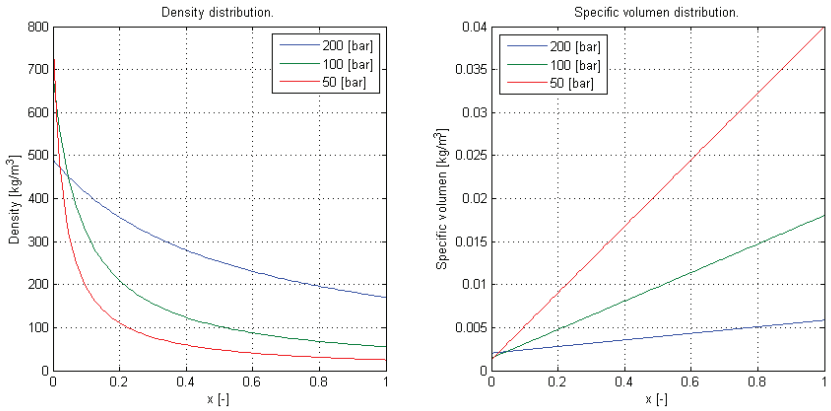

Figure 5.15.: Density and specific volume as a function of steam quality.

figure (5.15), where we assume a linear expression of $v(\varepsilon)$ due to equation (5.14):

$$v(\varepsilon) = \frac{\varepsilon}{l_2} v_g + \frac{1-\varepsilon}{l_2} v_l \quad \varepsilon \in [0, l_2] \tag{5.14}$$

Hence

$$\begin{aligned} \bar{v} &= \frac{1}{L}\left(\int_0^{l_1} v_l d\varepsilon + \int_0^{l_2}\left(\frac{\varepsilon}{l_2} v_g + \frac{l_2-\varepsilon}{l_2} v_l\right) d\varepsilon + \int_{l_1+l_2}^{L} v_l d\varepsilon\right) \\ &= \frac{l_1}{L}\frac{1}{\rho_l} + \frac{l_2}{2L}\left(\frac{1}{\rho_g} + \frac{1}{\rho_l}\right) + \frac{L-l_1-l_2}{L}\frac{1}{\rho_g} \end{aligned} \tag{5.15}$$

by setting

$$\frac{l_1}{L} = \frac{h_l - h_{in}}{h_g - h_{in}} \frac{m}{m_c} = a_1 z \tag{5.16}$$

$$\frac{l_2}{L} = \frac{h_g - h_l}{h_g - h_{in}} \frac{m}{m_c} = a_2 z \tag{5.17}$$

and with z=m/m_c and $a_3 = \rho_l/\rho_g$ we find:

$$\frac{\rho_l}{\bar{\rho}} = (1-z)a_3 + a_1 z + \frac{a_2}{2}(a_3+1)z \tag{5.18}$$

In order to determine the contribution from the gravitational pressure drop, we also provide the mean density which is by

$$\begin{aligned}\bar{\rho} &= \frac{1}{L}\int_0^{l_1}\rho_l d\varepsilon + \frac{1}{L}\int_0^{l_2}\rho(\varepsilon)d\varepsilon + \frac{1}{L}\int_{l_1+l_2}^{L}\rho_g d\varepsilon \\ &= a_1 z\rho_l + (1-z)\rho_g + \frac{1}{L}\int_0^{l_2}\rho(\varepsilon)d\varepsilon\end{aligned} \tag{5.19}$$

where

$$\rho(\varepsilon) = \frac{l_2}{(v_g - v_l)\varepsilon + l_2 v_l} \quad \varepsilon \in [0, l_2].$$

Hence we find the expression for the mean density for the complete boiling case

$$\begin{aligned}\bar{\rho} &= a_1 z\rho_l + (1-z)\rho_g + \frac{l_1}{L}\int_0^{l_2}\frac{d\varepsilon}{(v_g - v_l)\varepsilon + l_2 v_l} \\ &= a_1 z\rho_l + (1-z)\rho_g + \frac{a_2 z\rho_l}{a_3 - 1}\ln\left(\frac{\rho_l}{\rho_g}\right) \\ &= \rho_l\left(a_1 z + \frac{1-z}{a_3} + a_2 z\frac{\ln(a_3)}{a_3 - 1}\right)\end{aligned} \tag{5.20}$$

5.6.2. Partial boiling

In this situation, we have a mixture of liquid and steam (gas) at the outlet of the heat pipe, given by α_m, which can be formulated as L=l_1+$l_2 > l_1$. This may be explained by the fact that the flow velocity has just been increased so much that there is now no longer completely boiling and hence saturated steam downstream of the heat pipe. Now we have:

$$\begin{aligned}\bar{v} &= \frac{1}{L}\left(\int_0^{l_1} v_l d\varepsilon + \int_0^{l_2}\left(v_l + \alpha_m\varepsilon\frac{v_g - v_l}{l_2}\right)d\varepsilon\right) \\ &= \frac{l_1}{L}\frac{1}{\rho_l} + \frac{l_2}{2L}\left(\frac{1}{\rho_l}\left(2 + \alpha_m\frac{\rho_l - \rho_g}{\rho_g}\right)\right)\end{aligned} \tag{5.21}$$

where α_m can be reformulated as

$$\begin{aligned}(h_g - h_l)\alpha_m\dot{m} &= \dot{q}l_2 \\ &= \dot{q}(L - l_1) \\ &= m_c(h_g - h_{in}) - \dot{m}(h_l - h_{in})\end{aligned} \tag{5.22}$$

Hence we find

$$\alpha_m = \frac{1}{z}\frac{h_g - h_{in}}{h_g - h_l} - \frac{h_l - h_{in}}{h_g - h_l} = \frac{1}{1-a_1}\left(\frac{1}{z} - a_1\right) \tag{5.23}$$

and

$$\frac{l_2}{L} = z\frac{h_g - h_l}{h_g - h_{in}}\alpha_m = 1 - z\frac{h_l - h_{in}}{h_g - h_{in}} \tag{5.24}$$

Inserting (5.24) in (5.22) we find

$$\frac{\rho_l}{\bar{\rho}} = za_1 + \frac{1}{2}(1 - a_1 z)\left(2 + \frac{h_g - h_{in} - z(h_l - h_{in})}{z(h_g - h_l)}\frac{\rho_l - \rho_g}{\rho_g}\right) \tag{5.25}$$

Completely analogously to the calculation of the specific volume for complete boiling, we find here for the mean density

$$\begin{aligned}
\bar{\rho} &= \frac{1}{L}\int_0^{l_1} \rho_l d\varepsilon + \frac{1}{L}\int_0^{l_2} \rho(\varepsilon) d\varepsilon \\
&= \rho_l \frac{l_2}{L} + \frac{1}{L}\int_0^{l_2} \frac{l_2 d\varepsilon}{\alpha_m(\nu_g - \nu_l)\varepsilon + l_2 \nu_l} \\
&= \rho_l a_1 z + \frac{\alpha_m \rho_l}{a_3 - 1}\ln\left(\alpha_m \frac{1 - a_3}{a_3} + 1\right) \\
&= \rho_l \left(a_1 z + \frac{\alpha_m}{a_3 - 1}\ln\left(\alpha_m \frac{1 - a_3}{a_3} + 1\right)\right)
\end{aligned} \tag{5.26}$$

5.6.3. No boiling

In this situation such a high volume of fluid is sent through the heat pipe, that there is no boiling in the pipe section; hence we get

$$\frac{\bar{\rho}_l}{\rho} = \frac{\rho_l}{\rho_l} = 1. \tag{5.27}$$

Now the different cases can be summarized in the following expression for the friction pressure loss

$$\Delta P_f = \frac{f m_c^2}{2A_c^2 \rho_l}\begin{cases} a_3 z^2 + z^3\left(a_1 + \frac{a_2}{2}(a_3 + 1)\right) & \text{for } 0 \le z < 1 \\ z^2\left(a_1 z + \frac{1}{2}(1 - a_1 z)\left(2 + \frac{1 - a_1 z}{a_2 z}(a_3 - 1)\right)\right) & \text{for } 1 \le z < \frac{1}{a_1} \\ z^2 & \text{for } z \ge \frac{1}{a_1} \end{cases} \tag{5.28}$$

and for the gravitational pressure drop

$$\Delta P_g = \rho_l g L \begin{cases} a_1 z + \frac{1-z}{a_3} + a_2 z \frac{\ln(a_3)}{a_3 - 1} & \text{for } 0 \leq z < 1 \\ a_1 z + \frac{\alpha_m}{a_3 - 1} \ln\left(\alpha_m \frac{1-a_3}{a_3} + 1\right) & \text{for } 1 \leq z < \frac{1}{a_1} \\ 1 & \text{for } z \geq \frac{1}{a_1} \end{cases} \tag{5.29}$$

A simulation scenario is setup for both the friction pressure drop and gravitational pressure drop and a combination thereof, based on the data in table (5.6), and the

Sample nr.	p_{sat}	h_l	h_g	h_{in}	$\dot{q}$	ρ_l	ρ_g
Case	$[bar]$	$[kJ/kg]$	$[kJ/kg]$	$[kJ/kg]$	[kW/m]	$[kg/m^3]$	$[kg/m^3]$
1	1.00	417.504	2674.95	191.8	3724.8	958.632	0.596344
2	5.00	640.085	2748.11	429.3	3478.2	915.290	2.66805
3	10.00	762.515	2777.11	561.1	3324.1	887.129	5.14504
4	25.00	961.907	2801.93	777.9	3036.0	835.119	12.508
5	50.00	1154.64	2794.21	990.7	2705.3	777.369	25.3512
6	100.00	1408.06	2725.49	1276.3	2173.8	688.424	55.4631
7	200.00	1827.21	2412.35	1768.7	965.5	490.188	170.497

Table 5.6.: Raw data for stability plot. (Mass flow @ 1.5 [kg/s])

simulation results are performed for the seven cases as illustrated in figures (5.16) to (5.18), where the inlet enthalpy h_{in} is sub-cooled equivalent to 10 percent of the latent heat. The geometric data for the pressure loss calculations are based on data from SKV3, with f=0.03 [-] and $\dot{m}$=1.5 [kg/s]. When the total pressure drop for such a heat pipe is plotted as a function of the specific mass flux, often an S-shaped curve is obtained. The curve is sometimes referred to as the demand curve, because the pressure drop ΔP_f is needed for the flow to be established. Since the thermal load is constant in time and space, by reducing the mass flow rate (z), the equilibrium quality at the outlet increases. With very high mass flow rates, the fluid remains in a sub-cooled liquid state, and ΔP_f decreases with decreasing z. Deviation from the single-phase liquid ΔP_f curve starts at the *onset of nucleate boiling* (ONB) point. With the initiation of boiling, further reduction in z leads to an increase in flow quality at the exit and growth in the length of the heat pipe where boiling is under-way. The local minimum on demand curve is referred to as the *onset of flow instability* (OFI). Beyond the OFI point, further reduction in z can lead to an increase in ΔP_f, for low-pressure systems. The trend of the demand curve is changed for very low z values, where the flow quality is large everywhere in the heated channel, and ΔP_f monotonically decreases as z is reduced. Under certain conditions, it is possible to induce a horizontal

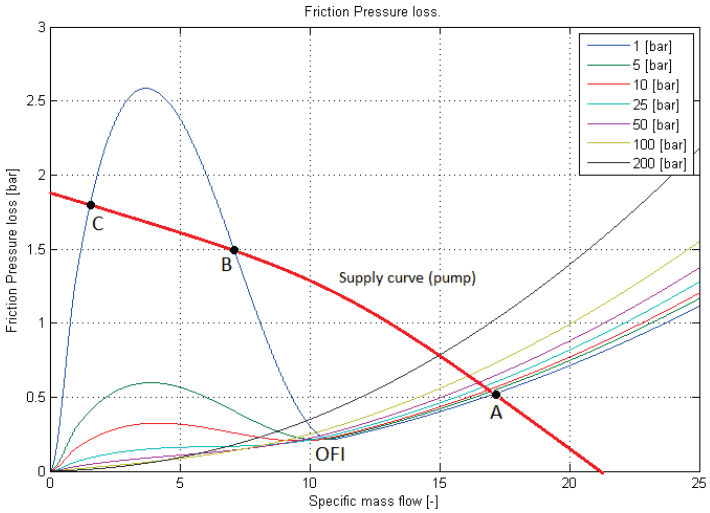

Figure 5.16.: Friction pressure loss for water in heat pipe (sub-cooling = 10 % of latent heat).

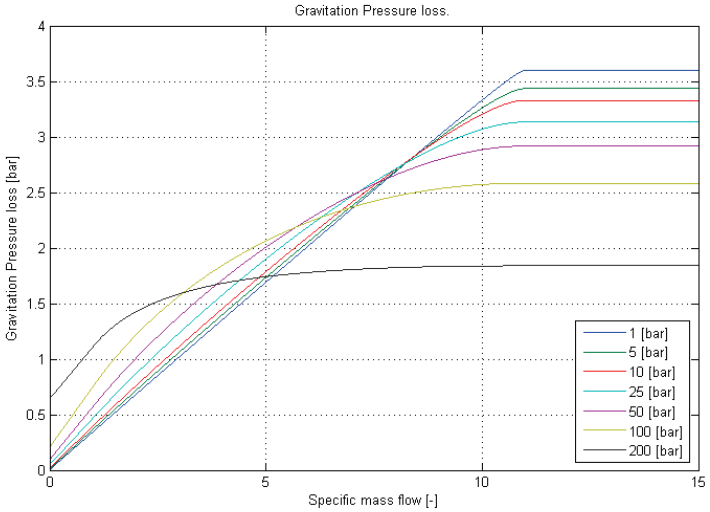

Figure 5.17.: Gravitational pressure loss for water in heat pipe (sub-cooling = 10 % of latent heat).

or negative slope of the curves illustrated in figure (5.16). These facts can be

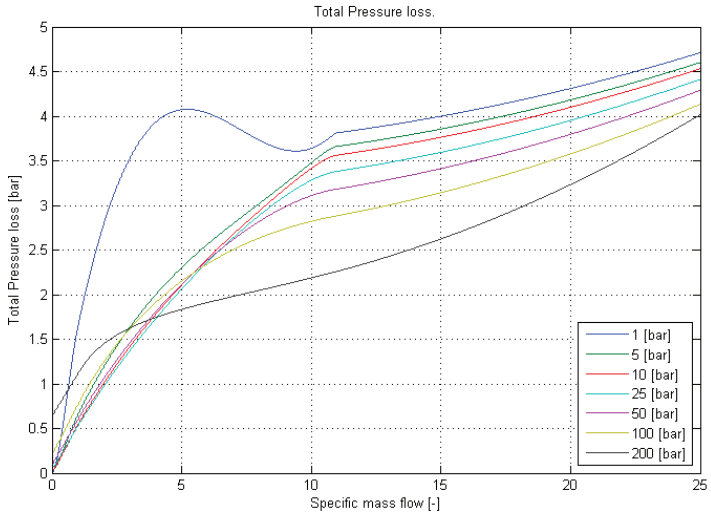

Figure 5.18.: Total pressure loss for water in heat pipe (sub-cooling = 10 % of latent heat).

analysed by differentiating (5.28) with respect to $z = m/m_c$ and setting it equal to zero. From this we find:

$$\frac{\partial \Delta P_f}{\partial z} = \frac{f m_c^2}{2A_c^2 \rho_l} \begin{cases} 2a_3 z + 3z^2 \left(a_1 + \frac{a_2}{2}(a_3+1)\right) & \text{for } 0 \le z < 1 \\ \frac{a_3-1}{2a_2}\left(\left[3a_1^2\right] z^2 + 4\left[\frac{1-a_1 a_3}{a_3-1}\right] z + 1\right) & \text{for } 1 \le z < \frac{1}{a_1} \\ 2z & \text{for } z \ge \frac{1}{a_1} \end{cases}$$

It is obvious that there is no local maximum or minimum of $0 \le z < 1$, while in the range of $1 \le z < 1/a_1$ there is a solution for

$$z_s = \frac{-b \pm \sqrt{b^2 - 4ac}}{2a} \tag{5.30}$$

where

$$a = 3a_1 \tag{5.31}$$

$$b = 2\frac{1 - a_1 a_3}{a_3 - 1}$$

$$c = 1 \tag{5.32}$$

The solution of (5.30) is strongly dependent on the saturation pressure, expressed indirectly through a_3, which states the ration between saturated liquid and saturated steam. Note that a_1, a_2 and a_3 are always positive; hence it is interesting to look at the second derivative, which is negative in the range of: $1 \leq z < 1/a_1$ for a_1+$a_2 > a_1 a_2$, which is similar to $a_1 < 1/a_2$. The condition for having two local extrema is: $b^2 - 4ac > 0$, which is similar to

$$a_3 > a_{3_c} = 1 + \frac{a_2}{a_1}(4 + 2\sqrt{3}) = 1 + \frac{h_g - h_l}{h_l - h_{in}}(4 + 2\sqrt{3}). \tag{5.33}$$

A sub-cooling of the inlet water of 10 % of the latent heat gives a_1=1/11 and a_2=10/11, which results in a_{3_c}=75.64 matching a saturation pressure of 22.25 [bar], consistent with the observations in figure (5.16), where we have no local extrema for a saturation pressure above the 25 [bar] legend in figure (5.16). Another interesting observation is, that if there is no sub-cool region present, i.e, h_{in}=h_l, this implies that with a_1 = 0 and a_2 = 1, which will give a strictly increasing pressure loss without any extrema. The solution to the inequality (5.33) shows that the density ration (a_3) fulfils the conditions for pressure oscillations in a heat pipe, for a value above a certain threshold size (a_{3_c}). On the other hand, if we increase the ration of sub-cooling from the present 10 % to a higher value, we will reduce the ratio a_2/a_1, which affects the threshold value of a_{3_c} downward and the saturation pressure in an upward direction. The corresponding derivative for the gravitational pressure drop is given by

$$\frac{\partial \Delta P_g}{\partial z} = \rho_l g L \begin{cases} a_1 - \frac{1}{a_3} + \frac{a_2 \ln(a_3)}{a_3 - 1} & \text{for } 0 \leq z < 1 \\ a_1 - \frac{1}{(1-a_1)(a_3-1)z^2}\left(\ln\left(\frac{1-a_3}{a_3}\alpha_m + 1\right) - \frac{z}{\alpha_m + a_3}\right) & \text{for } 1 \leq z < \frac{1}{a_1} \\ 0 & \text{for } z \geq \frac{1}{a_1} \end{cases}$$

Here we can see that the slope of ΔP_g is zero for z=$1/a_1$ and the graph (5.17) is monotonically increasing in the whole definition interval of $0 \leq z < \frac{1}{a_1}$. By summing the gravitational pressure drop and the friction pressure loss, we get an expression for the entire pressure loss in a vertical heat pipe, which is illustrated in figure (5.18), and can see that the local extrema for the low-pressure curves have been moved to a more favourable position for the vertical setup, compared to the pure horizontal setup.

$$\frac{\partial \Delta P}{\partial z} = \frac{f m_c^2}{2 A_c^2 \rho_l} \frac{\partial \Delta P_f}{\partial z} + \rho_l g L \frac{\partial \Delta P_g}{\partial z} = 0 \tag{5.34}$$

The local extrema for the entire pressure loss can be determined by differentiating the sum of the two pressure loss equations (5.28) and (5.29). This leads to

equation (5.34), solved numerically, by use of EES, which is illustrated in figure (5.19), for the entire interval of definition: $1 < z \leq 1/a_1$. On the left ordinate axis we list z=m/m_c and on the corresponding right side ordinate, we have the saturation pressure as a function of a_3. We can also see that the solution converges to a dual solution for a_3=1068, which corresponds to a saturation pressure of 1.55 [bar], under the given boundary conditions (pipe geometry, friction factor and elevation height). This double solution expresses a threshold value for the Ledinegg stability. There is no S-shaped curve above that threshold value according to the legends in figure (5.18), where the 5 [bar] pressure legend curve, expresses a monotonic increasing function for increasing z.

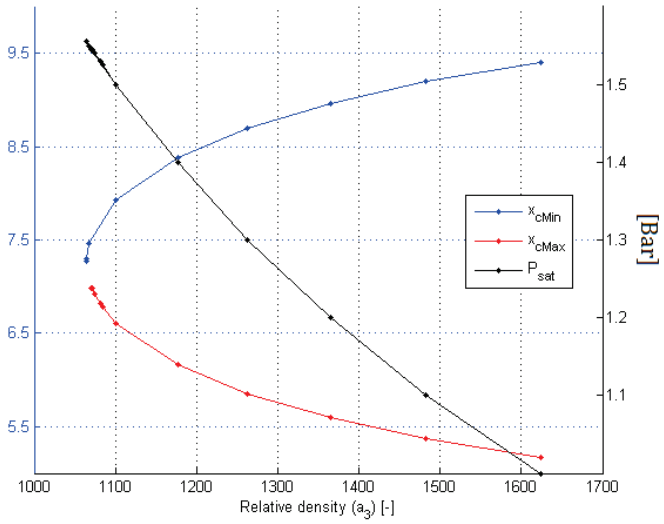

Figure 5.19.: Local minimum and maximum curves for varying density in a vertical heat pipe (sub-cooling = 10 % of latent heat).

5.6.4. Discussion

The simulation results are performed for pure water/steam properties and are based on IAPWS 97. The simulation results are very clear; for high values of the density ration $a_3 > a_{3c}$ pressure oscillations can occur in horizontal heat pipes. For water steam we can recommend a pressure level above 22.25 [bar] to avoid this Ledinegg stability phenomenon. A higher proportion of sub-cooling of the inlet flow will increase the likelihood of oscillations in horizontal pipe flows. A vertical heat pipe is more stable than a horizontal boiler with respect to the Ledinegg instability. The results are illustrated in figure (5.18), clarifing situation where the saturation pressure corresponding to the "1 bar" legend represents an S-shaped curve with both a local maximum and a local minimum in the range

of $1 < z < 1/a_1$, while at the "5 bar" legend, we only observe a monotonically increasing curve. For the corresponding horizontal plot, see (5.17) where we observe an S-shaped curve for the "1 bar", "5 bar" and "10 bar" legend.

The S-shaped pipe characteristic curve indicates that for a range of z, multiple solutions are possible. Steady state operation requires that the supply and demand values are to be the same, implying that only A, B and C in figure (5.16) are solutions. Points A and C are stable, because a perturbation in z at these points causes an imbalance between the demand values of figure (5.16) and the supply by a pump, that tends to bring the system back to its original steady state. Point B is unstable, because when the system operates at B, with a small perturbation in z, the system moves all the way to a stable and steady condition A, whereas a small negative perturbation in z leads all the way to the steady state condition C. By this simple analysis it can be shown that the system is stable if

$$\frac{\partial \Delta P_p}{\partial z} < \frac{\partial \Delta P_d}{\partial z} \tag{5.35}$$

where ΔP_p and ΔP_d represent the pump supply and the pipe demand difference values, respectively. Modifications to the system that make the slope of the demand curve more negative will destabilize the system, and modifications that lead to an opposite result stabilize. It can also be shown that increasing the pipe pressure drop is destabilizes, whereas increasing the pipe inlet pressure is stabilizing. These phenomena are often seen on the large Benson boilers, where the inlet manifold consists of small individual devices, for balancing the flow distribution to the panel walls in to the boiler. Sub-cooling implies the risk of Ledinegg flow instability. With no sub-cooling, we notice strictly monotone increasing pressure loss without any extrema.

5.6.5. Summary

The power plant of SKV3 has a technical minimum pressure of 80 bar, which means that there is no risk of Ledinegg instability in a large industrial power plant evaporator, shaped as parallel heat pipes. We have also seen that a vertical heat pipe results in a strong suppression of the Ledinegg instability phenomenon, so that only small low-pressure evaporators (pre-heaters, low-pressure marine boilers, etc.) may have a risk of instability caused by the Ledinegg phenomenon. The degree of sub-cooling is also a decisive factor in the formation of a density jump in this analysis and is a potentiating factor for the formation of Ledinegg instability, because no sub cool-region implies that with $a_1 = 0$ and $a_2 = 1$, which gives a strictly increasing pressure loss curve without any extrema.

6. Equation of states

We begin this next section by first detailing the equation of state for the most common water steam equations. These relatively simple mathematical expressions will be used in later chapters in the modelling of two-layer flow models, because here we divide the solution domain into two separate phases, one liquid and a gas phase, so it makes sense to use simple expressions for EOS. Later we will look at some ways both to reduce the computational work for calculating the EOS and to ensure continuity between the various state areas in the EOS. Detailed CFD methods are extremely computationally intensive and requires calling the EOS for each computational cell for each time step. In physics and thermodynamics, an equation of state (EOS) is a relation between state variables. More specifically, an equation of state is a thermodynamic equation describing the state of matter under a given set of physical conditions. It is a constitutive equation which provides a mathematical relationship between two or more state functions associated with the matter, such as, its temperature, pressure, volume, or internal energy. Equations of state are useful in describing the properties of fluids, mixtures of fluids and solids, and are necessary in connection with the implementation of computational fluid flow algorithms. Therefore, for EOS, there are both requirements for high computational accuracy (without discontinuities) and demands for low execution time.

6.1. Equation of states for water and steam

Instead of using external libraries, such as IAPWS 97, we cannot explicitly compute time derivatives, when differentiating property functions during use of the chain rule of differentiation. A simple solution to this problem is to provide derivative functions for each external function that is differentiated. In the following sections, all partial derivatives required to compute the time derivatives of density are derived for $\rho(p,h)$.

$$\frac{\partial \rho}{\partial t} = \left(\frac{\partial \rho}{\partial p}\right)_h \frac{dp}{dt} + \left(\frac{\partial \rho}{\partial h}\right)_p \frac{dh}{dt} \tag{6.1}$$

In order to compute the two partial derivatives in (6.1), a case differentiation between a one-phase and a two-phase state is required and will be outlined in the following sub-sections. The resulting partial derivatives of specific volume

can be transformed into partial derivatives of density using the following simple relation

$$\frac{\partial v}{\partial \rho} = -\frac{1}{\rho^2} \tag{6.2}$$

The difficulty with modelling a two-phase homogeneous approach is to specify an *equation of state* (EOS) that covers all possible fluid stages: a pure liquid, a two-phase mixture and a pure gas. Different EOS are used in pure phases and in the mixture. In the present work, we propose a stiffened liquid and gas EOS for the pure liquid and gas phases and a mixture formulation for the two-phase EOS.

Compressibility

Compressibility is a measure of the relative volume change of a fluid or solid as a response to a pressure (or mean stress) change. The compressibility depends strongly on whether the process is adiabatic or isothermal. Accordingly isothermal compressibility is defined as follows, taken from [18]:

$$\beta_T = -\frac{1}{V}\left(\frac{\partial V}{\partial P}\right)_T \tag{6.3}$$

where V is volume, p is pressure and the subscript T indicates that the partial differential is to be taken at constant temperature. Adiabatic compressibility is defined:

$$\beta_S = -\frac{1}{V}\left(\frac{\partial V}{\partial P}\right)_S \tag{6.4}$$

where S is entropy. The term "compressibility" is also used in thermodynamics to describe the deviance in the thermodynamic properties of a real gas from those expected from an ideal gas. The compressibility factor is defined as

$$Z = \frac{pV^*}{RT} \tag{6.5}$$

where P is the pressure of the gas, T is its temperature in Kelvin, and V^* is its molar volume. In the case of an ideal gas, the compressibility factor Z is equal to unity, and the familiar ideal gas law is recovered. The deviation from ideal gas behaviour tends to become particularly significant (or, equivalently, the compressibility factor stays far from unity) near the critical point, or in the case of high pressure or low temperature. In these cases, a generalized compressibility chart or an alternative equation of state better suited to the problem must be utilized to produce accurate results.

6.1.1. Water

When considering water under very high pressures (typical applications are underwater nuclear explosions, and sonic shocks) the stiffened equation of state [62] and eg. [63] is often used:

$$p = \rho(\gamma^0 - 1)e - \gamma p^0 \tag{6.6}$$

where e=C_vT is the internal energy per unit mass, γ^0 is an empirically determined constant and p^0 is another constant reference pressure, determined empirically. For an operating pressure of approximately 100 [bar], we can conclude that the stiffened EOS is normally inadequate for our analysis and serves only to apply to very high pressures. The associated speed of sound (in water) c, defined as $c^2 = \left(\frac{\partial P}{\partial \rho}\right)_S$, is given by:

$$c^2 = \gamma^0(p + p^0)/\rho = (\gamma - 1)C_p T, \tag{6.7}$$

where T is measured in Kelvin and C_p in $[J/kg^oC]$. This equation mispredicts the pressure estimation close to the saturation lines, but few simple alternatives are available for severely nonisentropic processes.

Density and change in temperature

Compressibility is related to the density of a fluid or substance, and in many practical situations can be approximated with a simple linear relation, z = 1+β(t-t_0). If we wish to describe the compressibility of the water at an operating pressure of 90 [bar], we make the following simple assumptions. When temperature is changed, the density of a fluid can be expressed by a linear interpolation expanded from a typical initial point as

$$\rho(t)_p = \frac{\rho_0}{1 + \beta(t - t_0)} \tag{6.8}$$

where $\rho(t)_p$ is the final density [kg/m^3] for fixed pressure p, ρ_0 is the initial density [kg/m^3], β is the volumetric temperature expansion coefficient $[m^3/m^3\ ^oC]$, t is the final temperature and t_0 is the initial temperature, both measured in [^{o}C]. Typical examples of the volumetric temperature coefficient β are:

- Water : β=3.07485·10^{-3} $[m^3/m^3\ ^oC]$ for p $\approx$ 90 [bar].
- Ethyl alcohol : β=0.0011 $[m^3/m^3\ ^oC]$ at atmospheric pressure [25].

Note that the volumetric temperature coefficients vary strongly with temperature.

Density and change in pressure

When the pressure is changed, the density of a fluid can be expressed by a linear compressibility coefficient, z = 1 - $\frac{(p_1-p_0)}{E}$, which leads to the linear expression below:

$$\rho(p)_t = \frac{\rho_0}{1-\frac{(p-p_0)}{E}} \tag{6.9}$$

where E is bulk modulus fluid elasticity given in [N/m^2], $\rho(p)_t$ is the final density [kg/m^3] for fixed temperature t, ρ_0 is the initial density [kg/m^3], p_1 is the final pressure and p_0 is the initial pressure, both measured in [N/m^2]. The Bulk Modulus Fluid Elasticity for some common fluids are:

- Water : E=2.7077 $\cdot 10^8$ [N/m2] for p $\approx$ 90 [bar].
- Ethyl alcohol : E=1.06 $\cdot 10^9$ [N/m^2] at atmospheric pressure [25].
- Oil : E=1.5$\cdot 10^9$ (N/m^2) at atmospheric pressure [25].

Density of a fluid changing both temperature and pressure

The density of a fluid when changing both temperature and pressure can be expressed by combining (6.8) and (6.9):

$$\rho(p,t) = \frac{\rho_0}{(1+\beta(t-t_0))(1-\frac{p-p_0}{E})} \tag{6.10}$$

6.1.2. Steam

In [62] there are explicit equations of state analysed and validated for steam, the Beattie-Bridgeman and Van der Waals state equations. In figure (6.1) a T-S plot is illustrated, which is divided into seven regions, of which regions CT1-CT3 is of our interest for analysing boiler stability in part load (90 [bar]). The region CT3 is based on the Van der Waals II state equation, which is found to provide good results close to the saturation line for medium pressure levels (90 [bar]). The Van der Waals state equation is based on a modification of the ideal gas law and approximates the behaviour of real fluids, taking into account the non-zero size of molecules and the attraction between them. It is given by

$$p = \frac{RT}{v-b} - \frac{a}{v^2} \tag{6.11}$$

where P is the absolute pressure measured in [kPa], $v = \rho^{-1}$ is the specific volume in [m^3/kg] and R = 461.522 [J/kgK]. The calibration coefficients are given in table (6.1). The Van der Waals equation provides good results, save for the region close to the saturation curve. A closer look at the T-S chart for steam will reveal that, in this region, the curvature of pressure and density changes

rapidly and is therefore difficult to model. The Bettie-Bridgemann equation consisting of fourth-order terms of density, turn out to be inferior when compared with the Van der Waals equation for the close to saturation region; see [62]. The theory behind the Beattie-Brigemann equation is further described in [64]. The Beattie-Bridgemann equation may be written in the form

$$p = RT\rho + \left(RTB - A - \frac{Rc}{T^2}\right)\rho^2 + \left(Aa - RTBb - \frac{RBc}{T^2}\right)\rho^3 + \frac{RBbc}{T^2}\rho^4 \tag{6.12}$$

The equation is seen to be quite accurate and in general, provides an accuracy which is better than that of Van der Waals; see [62]. For densities up to 80 % of the critical density ρ_c = 322 [kg/m^3], equation (6.12) provides an error less than 1 %, for the three properties (ρ,P and T), according to [62]. The coefficients are listed in table (6.1).

Table 6.1.: Constants for Bettie-Bridgemann and Van der Waals equations.

Coefficients.	**Van der Waals I**	**Van der Waals II**	**Bettie-Bridgemann I**	**Bettie-Bridgemann II**
A	–	–	0.915824	1.848857
B	–	–	0.001652	0.002725
a	6.624162	2.926529	0.005345	0.000792
b	0.016728	0.004059	0.005130	0.000273
c	–	–	8.52348$E5$	4.215885$E4$

6.1.3. Two-Phase region

This following sectionis develops the empirical relationships that approximately describe the essential thermodynamic properties used in the numerical solution of the thermal-hydraulic equations related to two-phase flow. On the basis of the stiffened gas EOS for each pure phase (liquid and gas), an expression for the pressure and temperature can be deduced from the thermal and mechanical equilibrium assumption. The equations for the partial derivatives for the two-phase state can be derived using a homogeneous model to describe the fluid flow

$$v = v_l + \frac{h - h_l}{h_g - h_l}(v_g - v_l) \tag{6.13}$$

where the coefficient to $(v_g - v_l)$ at the right side of equation (6.13) describes the steam quality x_e of the two-phase flow

$$x_e = \frac{h - h_l}{h_g - h_l} \tag{6.14}$$

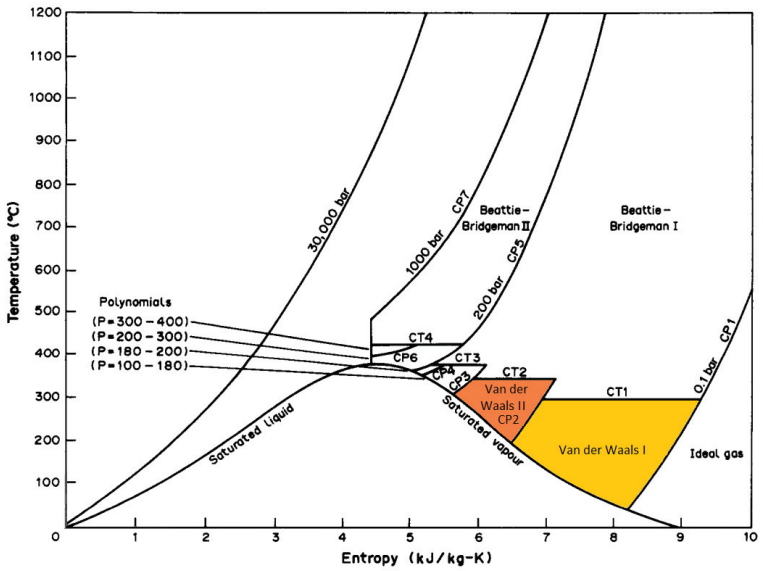

Figure 6.1.: T-S plot divided into regions of state equations [62].

Hence we can determine the following differentiation

$$\left(\frac{\partial v}{\partial h}\right)_p = \frac{v_g - v_l}{h_g - h_l} \tag{6.15}$$

and the belonging partial derivative of specific volume with respect to pressure for constant enthalpy can be written from [23] as:

$$\left(\frac{\partial v}{\partial p}\right)_h = \frac{v_l}{dp} + \frac{x}{dp}(v_g - v_l) + x_e\left(\frac{v_g}{dp} - \frac{v_l}{dp}\right) \tag{6.16}$$

where

$$\frac{\partial x}{\partial p} = \frac{-\frac{dh_l}{dp}(h_g - h_l) - (h - h_l)\left(\frac{dh_g}{dp} - \frac{dh_l}{dp}\right)}{(h_g - h_l)^2} \tag{6.17}$$

with

$$\frac{dh_l}{dp} = v_l(1 - \beta_l T) + C_{p,l}\frac{dT}{dp} \tag{6.18}$$

$$\frac{dh_g}{dp} = v_g(1 - \beta_g T) + C_{p,g}\frac{dT}{dp} \tag{6.19}$$

Hence the derivatives of the density at the phase boundaries can be expressed as

$$\frac{dv_l}{dp} = \beta_l v_l \frac{dT}{dp} - \kappa_l v_l \tag{6.20}$$

$$\frac{dv_g}{dp} = \beta_g v_g \frac{dT}{dp} - \kappa_g v_g \tag{6.21}$$

and the derivative of the temperature in (6.18) to (6.21) can be derived from the classical Clausius Clapeyron relation; see [23]. Note that β is the isobaric coefficient of expansion, κ is the isothermal compressibility and c_p is the specific heat capacity at constant pressure, which can be derived by Bridgemanns thermodynamic equations, see [40], and can be determined from medium properties as:

$$\beta = -\frac{1}{\rho}\left(\frac{\partial \rho}{\partial T}\right)_p, \kappa = \frac{1}{\rho}\left(\frac{\partial \rho}{\partial p}\right)_T \text{ and } c_p = \left(\frac{\partial e}{\partial T}\right)_p + p\left(\frac{\partial v}{\partial T}\right)_p \tag{6.22}$$

where e is the internal energy. Further partial derivatives are listed in Appendix K.

7. Interpolation in the steam table

In engineering practice, where real (specific) time performance, monitoring and optimisation of power plants are performed in real time (according to actual measurements of time), it is often necessary to obtain very accurate but simple relationships between water and steam properties with a minimum of computational time. Also detailed CFD methods are extremely computationally intensive and require calling the EOS for each computational cell for each time step. It is therefore important to map a way that is reasonably scalable and can deliver a good result with a limited inaccuracy. This section contains a number of compact numerical interpolation schemes for fast calculation of the thermodynamic properties developed, based on the IAPWS-97 (International Association for the Properties of Water and Steam); see [65]. These methods are based on linear, bilinear and second-order interpolation elements. We intend to resolve the saturation line by using triangular elements in the vicinity of the saturation line. This ensures the improvement of the resolution of the saturation line. Different interpolation schemes have been tested in order to identify (the optimum form/the most favourable form) with consideration of the desired accuracy and table lookup speed. The accuracy and computing speed of the interpolation schemes have been compared to those widely used in the IAPWS-97 standard, which is the reference application in this work. The fastest averaged lookup speed was found to be 1/33 of the reference calculation, referring to the pure bilinear scheme. The accuracy varies, depending on the area of interest, order of the element and the resolution of the interpolation grid. The computing time is dependent on the region of the area, but the greatest accuracy is achieved in the superheated region, where we have the smoothest function values, making it possible to use a simple and fast look-up function. The following work has been published in [15] and is included in Appendix O.

7.1. Introduction

Brereton [66] is motivated by Callandar's enthalpy function for dry steam. It is based on the observation that over a given pressure range, density at constant enthalpy is a nearly linear function of pressure within the tolerance of the skeleton steam tables. This is illustrated by the red curve in figure (7.1). Simple algebraic equations can thus provide dry-steam density within 0.05 % accuracy over a range of 50 to 200 [bar] and from saturation temperature to 690 [^oC]. Reference [67] describes the necessity of fast water/steam calculations for dynamic simulations

of boiler tubes. Here, Siemens uses look-up tables, where a large set of interpolation values of state variables has been stored for each necessary property function together with its first order partial derivative. Thus for an arbitrary argument input, the corresponding property function can be determined rapidly with the help of the next surrounding interpolation value. In most cases the interpolation

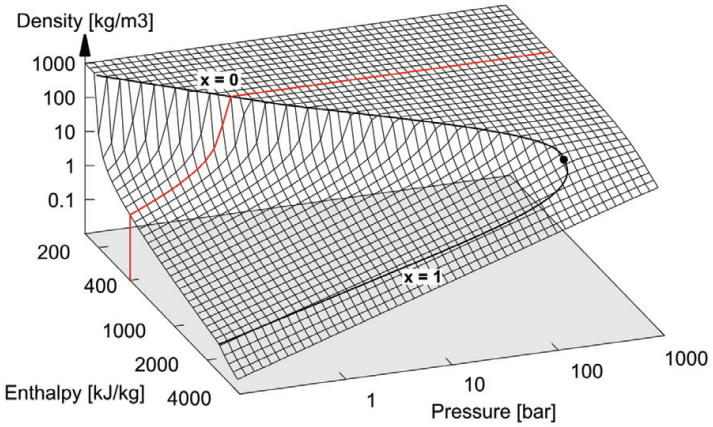

Figure 7.1.: Density as a function of Pressure and Enthalpy, [68].

is processed linearly, which is the easiest alternative. Several other authors have written about methods for improving the calculation speed of determining the thermodynamic properties of water and steam, including [69], where a package for the computation of water and steam properties has been developed. This package combines several aims: fast calculation, a good level of accuracy, consistency and high accuracy of the saturated liquid and gas states, generally resulting in a compromise where the advantage of sophisticated cubic interpolation and the optimum node/grid selection are partly reduced by the computational effort required to meet the severe restrictions of smooth derivatives and high accuracy at the saturation line. The package does not lead to a high speed general purpose package, but to a highly sophisticated package with many special features. In [70] there is a reconstruction of the property fluids for refrigerants in the REFPROP database [71]. This method is related to the method we describe below. We introduce an effort to decrease the computation time significantly by developing an advanced interpolation scheme for the steam properties without compromising the accuracy of the overall results. The presented method is based on the IAPWS 97 formulation and thus retains the accuracy of the recent formulation of steam properties. The method is based on the Finite Element Method [72]. We investigate which types of interpolation elements (linear, bilinear and iso-parametric) are best suited for the steam property calculations.

7.1.1. Motivation for the interpolation approach

One of the main advantages of using an interpolation scheme of the IAPWS-97, is fast calculation of the properties with high accuracy for the complete definition area. Using a low-order interpolation element allows for an unambiguous reverse calculation of the dependent parameter as a function of the two independent parameters. By using higher-order interpolation elements, both the interpolation and reverse calculations are based on iteration, extending the lookup time, however, increasing the accuracy. In the design and operation of fossil-fired power plants, accurate on-line (real-time) thermo hydraulic simulations are necessary. The advantage of using an interpolation scheme for calculating the thermodynamic properties, rather than a direct computation of IAPWS-97, is the possibility of providing very short calculation times without significant loss of accuracy. If the higher accuracy of the water and steam tables (IAPWS-97) is a requirement, e.g., in optimization problems, one may use interpolated correlations in the initial iterations and correct these to high accuracy by the accurate expressions in the last iterations. Another advantage of using interpolation is that it is possible to avoid discontinuities in the water and steam properties. These are illustrated by figure (7.1), in which it is obvious that the slope of the density as a function of pressure and enthalpy, or vice versa, is discontinuous at the saturation line. It is important to avoid numerically induced spikes or shocks in dynamic simulations of thermo-hydraulic flow systems. This may be done by avoiding discontinuities in-between regions in the IAPWS-97 formulation. We can solve this problem by the interpolation in the water/steam properties. It may be noted that discontinuities will not be observed physically in a finite volume as a phase change will not take place in the full volume at the same instant. For this reason a smothering of the discontinuity is not necessarily only a numerical detail of the method. Additionally the stability of a numerical method including derivatives, e.g., a Newton method, can be improved and may converge more easily, with fever iterations. The Jacobian matrix consists of smooth derivatives. Typically a solver for a steam power cycle will include derivatives of the thermodynamic properties.

7.1.2. Steam table regions

An algorithm has been developed to interpolate (approximate) one (or more) properties of water and steam as a function of two others. In this case we focus on the density as a function of the enthalpy and pressure of water and steam in the operation range of 0.1 to 4000 [kJ/kg] and 0.1 to 800 [bar], respectively. Next we outline the theory of the interpolation scheme, supplied with the basic algorithm, discretised nodes and corresponding elements for each region. The interpolation grid is divided into five regions, as shown in figure (7.2). Regions R_1, R_4 and R_5 consist only of uniform squared elements with four nodes, placed

in a rectangular Cartesian grid. Regions R_2 and R_3 consist of both squared and triangular elements. The five regions are defined based on the need to determine the density of a fluid, which is a challenging task, especially for water / steam at low pressure levels. We can easily change the number and location of the regions in order to accommodate other thermodynamic properties. The triangular elements are used in areas, where we need to resolve the saturation line. These triangular elements are linear or iso-parametric elements, with one side covering the saturation line. This ensures an accurate resolution of the saturation line, which cannot be handled by a rectangular bi-linear element, without increasing the number of elements. With the assumption that the interpolation table is dedicated

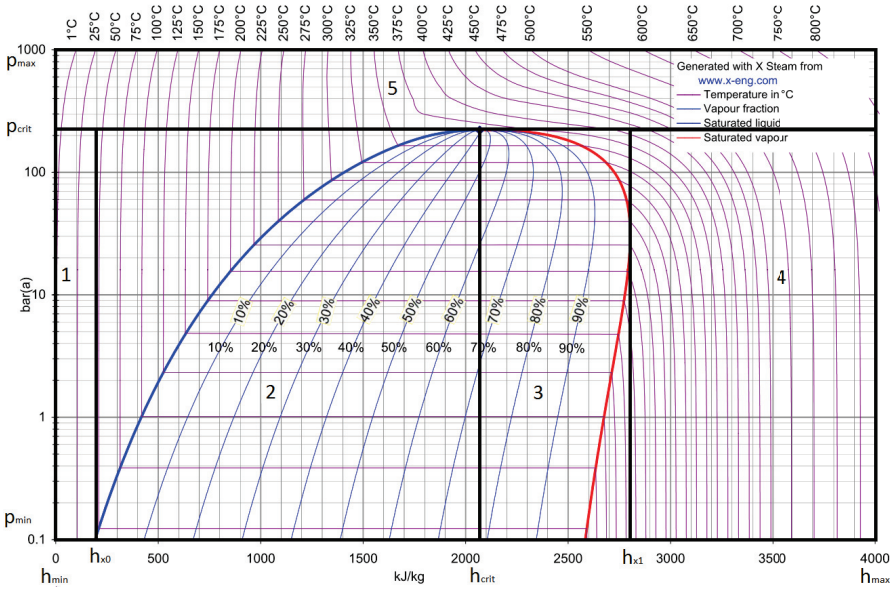

Figure 7.2.: Five Regions in the Pressure and Enthalpy diagram of water/steam, from www.x-eng.com.

to the interpolation of a water and steam model like IAPWS-97, we define two independent parameters p (pressure) and h (enthalpy) measured in [bar] and [kJ/kg], respectively, and covering five regions, with x=h and y=p. The definition area for each of the five regions is given in table (7.1), where the threshold values are given by: h_{crit}=2084.26 [kJ/kg], p_{crit}=220.19 [Bar], h_{x0}=191.81 [kJ/kg] and h_{x1}=2803.28 [kJ/kg], due to figure (7.2). A simple and fast algorithm for finding the correct region is shown in figure (7.3).

7.1.3. Creation of mesh

The creation of a compact grid has been implemented as a generic algorithm, and is specifically adapted to regions R_2 and R_3 in the two-phase region, by

Table 7.1.: Definition areas of each Region in the general interpolation scheme.

Region	$x_{min}[kJ/kg]$	$x_{max}[kJ/kg]$	$y_{min}[Bar]$	$y_{max}[Bar]$
1	0.10	191.81	0.1	220.19
2	191.81	2084.26	0.1	220.19
3	2084.26	2803.28	0.1	220.19
4	2803.28	4000.00	0.1	220.19
5	0.10	4000.00	220.19	800.00

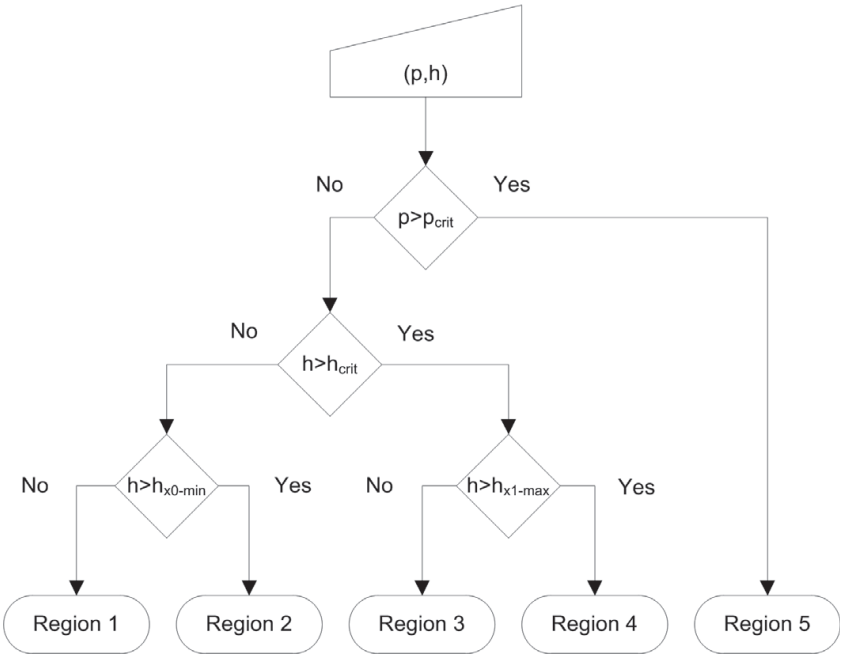

Figure 7.3.: Flow chart diagram for finding a region.

establishing a series of pressure lines or isobars (N_p). These are fundamental for the construction of the elements. The specific place where a rectangular element crosses a saturation line, is where a linear triangular element is established in order to preserve the function value along the saturation line. Figure (7.5) illustrates how the element structure is established between two pressure levels. A book-keeping system generally savies a pointer to the very first element in each row, except for the pure Cartesian bilinear grid, where we use a simple integer truncation to find the nearest grid points around the calculated point $P(x,y)$; see equation (7.9) below.

In regions R_2 and R_3, where the two-phase region of the fluid is described, we

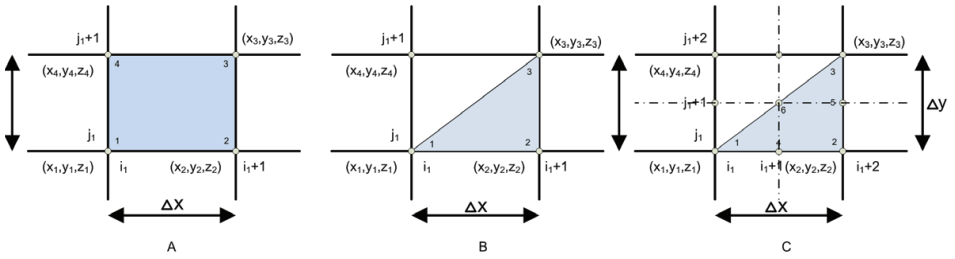

Figure 7.4.: Grids for bilinear (A), linear (B) interpolation and second-order (C) interpolation.

consider the saturation curve. Hence the element resolution in the x-direction is no longer equidistant in the vicinity of the saturation line, because the size of the element depends on the slope of the saturation curve ($\frac{\partial \rho}{\partial h}$), which leads to the above-mentioned book-keeping system. The very first element in each row is saved, for later speeding up the table lookup procedure, which is illustrated in figure (7.5). An algorithm is developed to obtain a fast and flexible way to establish a mesh and to search it. It works in the following way for 3, 4 and 6 node-element systems, but is similar for higher-order elements.

Algorithm:

1) Choose the pressure levels (not necessarily equidistant).
2) Calculate the definition area in h: h_{min} and h_{max}.
3) Establish a loop from j = 1 to N_p.
4) Calculate the saturation lines h_{sat}^{max} and h_{sat}^{min} for $p(j)$, $p(j+1)$ and possibly $p(j+2)$.
5) Start a main loop holding the pressure level given by $p(j)$ and $p(j+1)$ and $p(j+2)$.
6) Store pointer to the very first element in the main loop.
7) Initialise the two very first local nodes (n_1 and n_4) at h_{min}.
8) Start an inside loop with h=h+Δh.
9) Evaluate which element is restricting the size of h and update it on the basis of h and the type of element (3, 4 or 6 node); see figure (7.5).
10) Update local nodes n_2 and n_3.
11) Evaluate if h $> h_{max}$. If true, update the new node n_1 and n_4 and jump to 4) else set $n_1 = n_2$ and $n_4 = n_3$ and continue.

The above algorithm is generic for all regions, except for the evaluation step 9), which is unique for the three types of regions: the two-phase regions R_2,

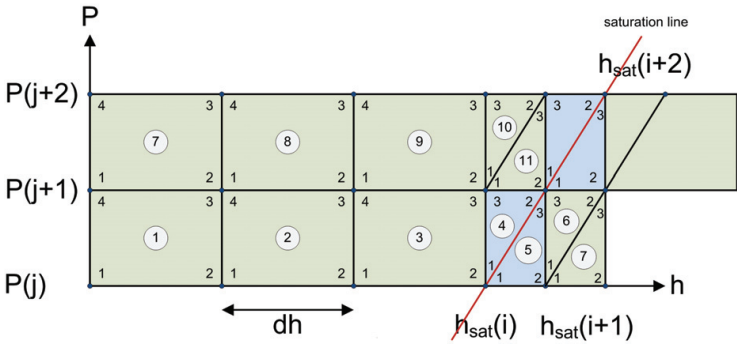

Figure 7.5.: Elements in region 2 or 3 with local nodes (two-phase region with saturation line).

R_3, the single-phase, sub-critical regions R_1, R_4 and the super-critical region R_5. For region R_2 we have to take into consideration that the very first element is a triangular element, because the marching loop is going from low to high pressure. In R_3 we have the opposite situation, with a triangular element at the very last element. Both R_2 and R_3 are a triangular element and placed at both sides of the saturation line, to ensure optimal resolution of the saturation line. The look-up system is based on look-up arrays for each element row at fixed pressure, which stores the very first element each row. Regions R_1, R_4 and R_5 are based on a solely equidistant grid structure, based on bilinear interpolation of four-node square elements. This look-up system is determined to be fast and simple.

7.1.4. Order of Interpolation scheme

Conceptually, the simplest element form of a two-dimensional kind is a rectangle, with sides parallel to the x and y axes in a Cartesian coordinate system. Let us assume that the function value $z(x,y)$ is expressed in a polynomial form in x and y. To ensure inter-element continuity of z along the top and bottom sides, the variation must be linear. In general, we seek element expansions which possess the highest order of a complete polynomial for a minimum of degrees of freedom. In this context it is useful to recall the Pascal triangle [72] from which the number of terms occurring in a polynomial in two variables, x, y, can be readily determined. We use Pascal's triangle which is a triangular array of

the binomial coefficients in a triangle, and determines the coefficients arising in binomial expansions.

$$(x+y)^n = \sum_{k=0}^{n} \left(\begin{array}{c} n \\ k \end{array} \right) x^{n-k} y^k \tag{7.1}$$

$$= a_0 x^n + a_1 x^{n-1} y + a_2 x^{n-2} y^2 + \ldots + a_{n-1} x y^{n-1} + a_n y^n, \tag{7.2}$$

for any non-negative integer n and any integer k between 0 and n. Notice the coefficients are the numbers in row n of Pascal's triangle. In general, when a binomial like x + y is raised to a positive integer power n, the coefficients a_i in this expansion are precisely the numbers on row n of Pascal's triangle. A first-order bilinear shape function can then be expressed as:

$$z(x,y) = a_0 + a_1 x + a_2 y + a_3 xy \tag{7.3}$$

matching four nodes in a square bilinear element. The interpolated function should not use the term of x^2 or y^2, but $x \cdot y$, which is the bilinear form of x and y. The corresponding second-order shape function is given as:

$$z(x,y) = a_0 + a_1 x + a_2 y + a_3 xy + a_4 x^2 + a_5 y^2 \tag{7.4}$$

which is associated with a six-node triangular element.

7.1.5. Lookup table

In a Cartesian equidistant grid system, with the grid spacing of Δx and Δy, it is very fast to calculate the neighbouring grid points in an element. Typically we use a simple expression to find the nearest grid points, involved in the bilinear interpolation, given by (7.8) to (7.9):

$$(x_1, y_1) = (\Delta x \cdot i_1, \Delta y \cdot j_1) \tag{7.5}$$

$$(x_2, y_2) = (\Delta x \cdot (i_1 + 1), \Delta y \cdot j_1) \tag{7.6}$$

$$(x_3, y_3) = (\Delta x \cdot (i_1 + 1), \Delta y \cdot (j_1 + 1)) \tag{7.7}$$

$$(x_4, y_4) = (\Delta x \cdot i_1, \Delta y \cdot (j_1 + 1)) \tag{7.8}$$

where the indices i_1, j_1 are given as

$$(i_1, j_1) = \left(\left| \frac{x - x_{min}}{\Delta x} \right|, \left| \frac{y - y_{min}}{\Delta y} \right| \right) \tag{7.9}$$

For a non- equidistant grid, we use a look-up vector to find the very first and the last element in a row of elements, defined by the pressure level. A

marching loop tests whether the spot point is in an element limited by two nodes.

7.2. Interpolation elements

This section outlines three types of interpolation elements, which can be used in combination with each other, and the theory follows in subsequent sections.

7.2.1. Linear interpolation elements

In the context of a triangle, we introduce the so-called barycentric coordinates, which are also known as area coordinates, because the coordinates of a point P with respect to triangle ABC are proportional to the (signed) areas of PBC, PCA and PAB; see figure (7.6). Barycentric coordinates are extremely useful in

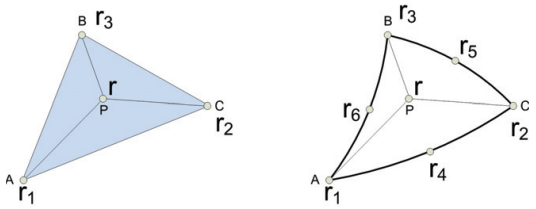

Figure 7.6.: Triangular elements T (3 and 6 nodes) for region 2 or 3 (in the vicinity of the saturation line).

engineering applications involving triangular subdomains. These make analytic integrals often easier to evaluate, and Gaussian quadrature tables are often presented in terms of area coordinates. First let us consider a triangle T defined by three vertices(nodes) r_1 , r_2 and r_3. Any point $\mathbf{r}$ located on this triangle may then be written as a weighted sum of these three vertices, i.e.,

$$\mathbf{r} = \xi_1 \cdot \mathbf{r}_1 + \xi_2 \cdot \mathbf{r}_2 + \xi_3 \cdot \mathbf{r}_3 \tag{7.10}$$

$$\xi_1 + \xi_2 + \xi_3 = 1 \tag{7.11}$$

where

$$\mathbf{r}_1 = (x_1, y_1, z_1), \quad \mathbf{r}_2 = (x_2, y_2, z_2) \quad \textit{and} \quad \mathbf{r}_3 = (x_3, y_3, z_3) \tag{7.12}$$

Inserting $\xi_3 = 1 - \xi_1 - \xi_2$ in (7.10) gives a plane, stretched by two vectors $\mathbf{r}_{12}$ and $\mathbf{r}_{13}$ and the corresponding normal vector is defined by: $\mathbf{n}=\mathbf{r}_{12} \times \mathbf{r}_{13}$. This plane can be expressed by the matrix $\mathbf{T}$:

$$\mathbf{T} = \begin{pmatrix} x_{13} & x_{23} \\ y_{13} & y_{23} \end{pmatrix}$$

and the corresponding area of the triangular element is

$$A = \frac{1}{2} det(\mathbf{T}) \tag{7.13}$$

where $x_{ij}=x_i - x_j$ and $y_{ij}=y_i - y_j$.

Hence the barycentric coordinates can be formulated as

$$\mathbf{T} \cdot \overline{\xi} = \mathbf{r} - \mathbf{r}_3 \tag{7.14}$$

which gives

$$\begin{aligned} \overline{\xi} &= \mathbf{T}^{-1} \cdot (\mathbf{r} - \mathbf{r}_3) \\ &= \frac{1}{det(\mathbf{T})} \begin{pmatrix} y_{23} & -x_{23} \\ -y_{13} & x_{13} \end{pmatrix} \cdot (\mathbf{r} - \mathbf{r}_3) \\ &= \frac{1}{(x_{13} \cdot y_{23} - x_{23} \cdot y_{13})} \begin{pmatrix} y_{23} & -x_{23} \\ -y_{13} & x_{13} \end{pmatrix} \cdot (\mathbf{r} - \mathbf{r}_3) \end{aligned} \tag{7.15}$$

or

$$\begin{aligned} \xi_1 &= \frac{y_{23} \cdot (x - x_3) - x_{23} \cdot (y - y_3)}{(x_{13} \cdot y_{23} - x_{23} \cdot y_{13})} \\ \xi_2 &= \frac{y_{13} \cdot (x - x_3) + x_{13} \cdot (y - y_3)}{(x_{13} \cdot y_{23} - x_{23} \cdot y_{13})} \\ \xi_3 &= 1 - \xi_1 - \xi_2 \end{aligned} \tag{7.16}$$

Since barycentric coordinates are a linear transformation of Cartesian coordinates, it turns out that they vary linearly along the edges and over the area of the triangle. If a point lies in the interior of the triangle T, all of the Barycentric coordinates lie in the open interval (0,1), which can be summarized in the following statements: a point $\mathbf{r}$ lies inside the triangle T if and only if $0 \leq \xi_i \leq 1 \; \forall \; i \; \in [1,2,3]$, then the point $\mathbf{r}$ lies in the triangle or on its edge. Now, we interpolate the value

of z given by (x,y) in T as: $\mathbf{n} = \mathbf{r}_{12} \times \mathbf{r}_{13}$ and $\mathbf{n} \cdot (\mathbf{r} - \mathbf{r}_1) = 0$ which is similar to

$$n_1 \cdot (x - x_1) + n_2 \cdot (y - y_1) + n_3 \cdot (z - z_3) = 0 \tag{7.17}$$

where $\mathbf{n}$ is the normal vector to the triangle ABC:

$$\begin{aligned} \mathbf{n} &= \begin{pmatrix} n_1 \\ n_2 \\ n_3 \end{pmatrix} \\ &= \begin{pmatrix} y_{21} \cdot z_{31} - z_{21} \cdot y_{31} \\ z_{21} \cdot x_{31} - x_{21} \cdot z_{31} \\ x_{21} \cdot y_{31} - y_{21} \cdot x_{31} \end{pmatrix} \end{aligned} \tag{7.18}$$

Hence

$$z(x,y) = z_1 - \frac{1}{n_3} \cdot [(x - x_1) \cdot n_1 + (y - y_1) \cdot n_2] \tag{7.19}$$

$$y(x,z) = y_1 - \frac{1}{n_2} \cdot [(x - x_1) \cdot n_1 + (z - z_1) \cdot n_3] \tag{7.20}$$

$$x(y,z) = x_1 - \frac{1}{n_1} \cdot [(y - y_1) \cdot n_2 + (z - z_1) \cdot n_3] \tag{7.21}$$

If one of the barycentric coordinates is zero, this means that $\mathbf{r}$ lies on a line segment defining T, and $\mathbf{r}$ is placed in the opposite direction of the barycentric coordinate, ie. if ξ_1 equals null, then $\mathbf{r}$ lies on the segment BC or on the line given by the vector: $\mathbf{r}_{23} = \mathbf{r}_3 - \mathbf{r}_2$. Correspondingly, if one of the barycentric coordinates is less than 0, this means that $\mathbf{r}$ is not inside the triangle T, but is positioned outside T in the opposite direction to the $\xi_i < 0$. This technique is useful if we want to traverse from one element to the neighbouring element.

7.2.2. Bilinear interpolation elements

The key idea behind the bilinear interpolation is to perform linear interpolation first in one direction, and then again in the other direction. It is an extension of the linear interpolation for interpolating functions of two variables (e.g., x and y) on a regular grid [72]. Although each step is linear in the sampled values and in the position, the interpolation as a whole is not linear but rather quadratic in the sample location. Nevertheless, one can make an inverse calculation of the dependent parameter z by use of bilinear interpolation, so the function $z(x,y)$ can be expressed explicitly as $y(x,z)$ or $x(y,z)$. Having a Cartesian rectangular coordinate system in which the four equidistant vertices(nodes), are given by:

$\mathbf{r}_1 = (x_1, y_1)$, $\mathbf{r}_2 = (x_2, y_2)$, $\mathbf{r}_3 = (x_3, y_3)$, and $\mathbf{r}_4 = (x_4, y_4)$, where z is known for all nodes, then the interpolation formula simplifies to

$$z(x,y) = [1-x, x] \begin{pmatrix} z_1 & z_4 \\ z_2 & z_3 \end{pmatrix} \cdot \begin{bmatrix} 1-y \\ y \end{bmatrix} \tag{7.22}$$

$$z(x,y) = \frac{z_1}{\Delta x \Delta y} \cdot (x_2 - x) \cdot (y_2 - y) + \frac{z_2}{\Delta x \Delta y} \cdot (x - x_1) \cdot (y_2 - y) \tag{7.23}$$

$$+ \frac{z_4}{\Delta x \Delta y} \cdot (x_2 - x) \cdot (y - y_2) + \frac{z_3}{\Delta x \Delta y} \cdot (x - x_1) \cdot (y - y_2) \tag{7.24}$$

$$= a_1 + a_2 \cdot x + a_3 \cdot y + a_4 \cdot x \cdot y \tag{7.25}$$

where

$$a_1 = \frac{1}{\Delta x \Delta y} \cdot [x_2 y_2 z_1 - x_1 y_2 z_2 - x_2 y_1 z_4 + x_1 y_2 z_3]$$
$$a_2 = \frac{1}{\Delta x \Delta y} \cdot [-y_2 z_1 + y_2 z_2 + y_1 z_4 - y_1 z_3]$$
$$a_3 = \frac{1}{\Delta x \Delta y} \cdot [-x_2 z_1 + x_1 z_2 + x_2 z_4 - x_1 z_3]$$
$$a_4 = \frac{1}{\Delta x \Delta y} \cdot [z_1 - z_2 - z_4 + z_3]$$

and $\Delta x = x_2 - x_1$ and $\Delta y = y_4 - y_1$. Alternatively we can calculate x(y,z) and y(x,z) implicitly as:

$$x(y,z) = \frac{-1}{a_2 + a_4 \cdot y} \cdot [z - a_1 + a_3 \cdot y] \tag{7.26}$$

and

$$y(x,z) = \frac{-1}{a_3 + a_4 \cdot x} \cdot [z - a_1 + a_2 \cdot x] \tag{7.27}$$

Iso-parametric triangles

If the triangle has variable metric, as in the curved-sided six-node triangle geometries shown in Figure (7.6), the foregoing formulas need adjustment because

the element of area Ω becomes a function of position. It can be shown that the differential area element is given by

$$\begin{aligned} d\Omega &= \mathbf{J} d\xi_1 d\xi_2 d\xi_3 \\ &= \frac{1}{2} \det \begin{bmatrix} 1 & 1 & 1 \\ \sum_{i=1}^{n} x_i \frac{\partial N_i}{\partial \xi_1} & \sum_{i=1}^{n} x_i \frac{\partial N_i}{\partial \xi_2} & \sum_{i=1}^{n} x_i \frac{\partial N_i}{\partial \xi_3} \\ \sum_{i=1}^{n} y_i \frac{\partial N_i}{\partial \xi_1} & \sum_{i=1}^{n} y_i \frac{\partial N_i}{\partial \xi_2} & \sum_{i=1}^{n} y_i \frac{\partial N_i}{\partial \xi_3} \end{bmatrix} \end{aligned} \tag{7.28}$$

where ξ_i, $i \in$[1,2,3] are normalized coordinates and the shape function N_i is given by equation (7.30). Above, $\mathbf{J}$ is the Jacobian determinant. The following theory is based on the considerations described in reference [72]. Consider the more general case of an iso-parametric element with n nodes and shape functions N_i. The element geometry is defined by the corner coordinates x_i, y_i, with $i \in$ [1...6]. Corners are numbered 1, 2, 3 in counter-clockwise direction. Side nodes are numbered 4, 5, 6, opposite to corners 3, 1, 2, respectively as illustrated in figure (7.6). The triangular normalised coordinates are as above denoted by ξ_1, ξ_2 and ξ_3, which satisfy ξ_1+ξ_2+ξ_3 = 1. The quadratic displacement field $u_x(\xi_1, \xi_2, \xi_3), u_y(\xi_1, \xi_2, \xi_3)$ is defined by the 12-node displacements u_{x_i}, u_{y_i} , $i \in$[1...6], as per the iso-parametric quadratic interpolation formula in [72], page 165. That formula is repeated here for convenience:

$$\begin{bmatrix} 1 \\ x \\ y \\ u_x \\ u_y \end{bmatrix} = \begin{bmatrix} 1 & 1 & 1 & 1 & 1 & 1 \\ x_1 & x_2 & x_3 & x_4 & x_5 & x_6 \\ y_1 & y_2 & y_3 & y_4 & y_5 & y_6 \\ u_{x1} & u_{x2} & u_{x3} & u_{x4} & u_{x5} & u_{x6} \\ u_{y1} & u_{y2} & u_{y3} & u_{y4} & u_{y5} & u_{y6} \end{bmatrix} \mathbf{N} \tag{7.29}$$

where the shape function $\mathbf{N}$ and the belonging gradients in ξ_i are given as:

$$\mathbf{N} = \begin{bmatrix} \xi_1(2\xi_1 - 1) \\ \xi_2(2\xi_2 - 1) \\ \xi_3(2\xi_3 - 1) \\ 4\xi_1\xi_2 \\ 4\xi_2\xi_3 \\ 4\xi_3\xi_1 \end{bmatrix} \tag{7.30}$$

$$\frac{\partial N_i}{\partial \xi_1} = \begin{bmatrix} 4\xi_1 - 1 \\ 0 \\ 0 \\ 4\xi_2 \\ 0 \\ 4\xi_3 \end{bmatrix}, \quad \frac{\partial N_i}{\partial \xi_2} = \begin{bmatrix} 0 \\ 4\xi_2 - 1 \\ 0 \\ 4\xi_1 \\ 4\xi_3 \\ 0 \end{bmatrix}, \quad \frac{\partial N_i}{\partial \xi_3} = \begin{bmatrix} 0 \\ 0 \\ 4\xi_3 - 1 \\ 0 \\ 4\xi_2 \\ 4\xi_1 \end{bmatrix} \tag{7.31}$$

If the metric is simply defined by the three corners, as in figure (7.6), the geometry shape functions are linear as in equation (7.16): $N_1 = \xi_1$, $N_2 = \xi_2$ and $N_3 = \xi_3$. Then the foregoing determinant reduces to that of equation (7.13), and $\mathbf{J} = \frac{1}{2}\mathrm{A}$ everywhere. But for general (curved) geometries $\mathbf{J} = \mathbf{J}(\xi_1, \xi_2, \xi_3)$, and the triangle area A cannot be factored out of the integration rules according to [72]. Instead we use the above gradients in a simple iteration procedure to estimate the barycentric coordinates for a specific point $P(x, y)$. The bulk of the shape function logic is concerned with the computation of the partial derivatives of the shape functions (7.31) with respect to x and y at any point in the element. For this purpose, we consider a generic scalar function $w(\xi_1, \xi_2, \xi_3)$ that is quadratically interpolated over the triangle by

$$w = w_1 N_1 + w_2 N_2 + w_3 N_3 + w_4 N_4 + w_5 N_5 + w_6 N_6 \tag{7.32}$$

where w may stand for 1, x , y, u_x or u_y , which are interpolated in the isoparametric representation in (7.29), or other element-varying quantities, such as fluid density, temperature, etc. Determining partial derivatives of w in (7.32) with respect to x and y and applying the chain rule twice yields

$$\begin{aligned} \frac{\partial w}{\partial x} &= \sum_{i=1}^{n} w_i \frac{\partial N_i}{\partial x} = \sum_{i=1}^{n} w_i \left(\frac{\partial N_i}{\partial \xi_1}\frac{\partial \xi_1}{\partial x} + \frac{\partial N_i}{\partial \xi_2}\frac{\partial \xi_2}{\partial x} + \frac{\partial N_i}{\partial \xi_3}\frac{\partial \xi_3}{\partial x} \right) \\ \frac{\partial w}{\partial y} &= \sum_{i=1}^{n} w_i \frac{\partial N_i}{\partial y} = \sum_{i=1}^{n} w_i \left(\frac{\partial N_i}{\partial \xi_1}\frac{\partial \xi_1}{\partial y} + \frac{\partial N_i}{\partial \xi_2}\frac{\partial \xi_2}{\partial y} + \frac{\partial N_i}{\partial \xi_3}\frac{\partial \xi_3}{\partial y} \right) \end{aligned} \tag{7.33}$$

where all sums are understood to run over $i = 1,...6$. In matrix form:

$$\begin{bmatrix} \frac{\partial w}{\partial x} \\ \frac{\partial w}{\partial y} \end{bmatrix} = \begin{bmatrix} \frac{\partial \xi_1}{\partial x} & \frac{\partial \xi_2}{\partial x} & \frac{\partial \xi_3}{\partial x} \\ \frac{\partial \xi_1}{\partial y} & \frac{\partial \xi_2}{\partial y} & \frac{\partial \xi_3}{\partial y} \end{bmatrix} \cdot \begin{bmatrix} \sum w_i \frac{\partial N_i}{\partial \xi_1} \\ \sum w_i \frac{\partial N_i}{\partial \xi_2} \\ \sum w_i \frac{\partial N_i}{\partial \xi_3} \end{bmatrix} \tag{7.34}$$

Transposing both sides of (7.34) while exchanging sides yields

$$\left[\begin{array}{ccc} \sum w_i \frac{\partial N_i}{\partial \xi_1} & \sum w_i \frac{\partial N_i}{\partial \xi_2} & \sum w_i \frac{\partial N_i}{\partial \xi_3} \end{array}\right] \cdot \left[\begin{array}{cc} \frac{\partial \xi_1}{\partial x} & \frac{\partial \xi_1}{\partial y} \\ \frac{\partial \xi_2}{\partial x} & \frac{\partial \xi_2}{\partial y} \\ \frac{\partial \xi_3}{\partial x} & \frac{\partial \xi_3}{\partial y} \end{array}\right] = \left[\begin{array}{cc} \frac{\partial w}{\partial x} & \frac{\partial w}{\partial y} \end{array}\right] \tag{7.35}$$

Now make $w \equiv (1, x, y)^T$ and stack the results row-wise:

$$\left[\begin{array}{ccc} \sum \frac{\partial N_i}{\partial \xi_1} & \sum \frac{\partial N_i}{\partial \xi_2} & \sum \frac{\partial N_i}{\partial \xi_3} \\ \sum x_i \frac{\partial N_i}{\partial \xi_1} & \sum x_i \frac{\partial N_i}{\partial \xi_2} & \sum x_i \frac{\partial N_i}{\partial \xi_3} \\ \sum y_i \frac{\partial N_i}{\partial \xi_1} & \sum y_i \frac{\partial N_i}{\partial \xi_2} & \sum y_i \frac{\partial N_i}{\partial \xi_3} \end{array}\right] \cdot \left[\begin{array}{cc} \frac{\partial \xi_1}{\partial x} & \frac{\partial \xi_1}{\partial y} \\ \frac{\partial \xi_2}{\partial x} & \frac{\partial \xi_2}{\partial y} \\ \frac{\partial \xi_3}{\partial x} & \frac{\partial \xi_3}{\partial y} \end{array}\right] = \left[\begin{array}{cc} \frac{\partial 1}{\partial x} & \frac{\partial 1}{\partial y} \\ \frac{\partial x}{\partial x} & \frac{\partial x}{\partial y} \\ \frac{\partial y}{\partial x} & \frac{\partial y}{\partial y} \end{array}\right] \tag{7.36}$$

It is obvious that $\frac{\partial x}{\partial x} = \frac{\partial y}{\partial y} = 1$ and $\frac{\partial 1}{\partial x} = \frac{\partial 1}{\partial y} = \frac{\partial x}{\partial y} = \frac{\partial y}{\partial x} = 0$ because x and y are independent coordinates. It is shown in [72] that, if $\sum N_i = 1$, the entries of the first row of the coefficient matrix are equal to a constant of unity, because the first equation in (7.37) is homogeneous. These entries can be scaled to unity because the first row of the right-hand side is null. Consequently we arrive at a system of linear equations of order 3, with two right-hand sides:

$$\mathbf{J} \cdot \mathbf{P} = \left[\begin{array}{ccc} 1 & 1 & 1 \\ J_{x1} & J_{x2} & J_{x3} \\ J_{y1} & J_{y2} & J_{y3} \end{array}\right] \cdot \left[\begin{array}{cc} \frac{\partial \xi_1}{\partial x} & \frac{\partial \xi_1}{\partial y} \\ \frac{\partial \xi_2}{\partial x} & \frac{\partial \xi_2}{\partial y} \\ \frac{\partial \xi_3}{\partial x} & \frac{\partial \xi_3}{\partial y} \end{array}\right] = \left[\begin{array}{cc} 0 & 0 \\ 1 & 0 \\ 0 & 1 \end{array}\right] \tag{7.37}$$

where $\mathbf{J}$ is called the Jacobian matrix and its determinant is scaled by one-half of the Jacobian: $\mathrm{A} = \frac{1}{2}\det(\mathbf{J})$, as used in the expression of the area of an element in (7.13). Additionally the sub-Jacobians in (7.37) are given by

$$\begin{aligned} J_{x1} &= \sum x_i \frac{\partial N_i}{\partial \xi_1}, \quad J_{x2} = \sum x_i \frac{\partial N_i}{\partial \xi_2}, \quad J_{x3} = \sum x_i \frac{\partial N_i}{\partial \xi_3} \\ J_{y1} &= \sum y_i \frac{\partial N_i}{\partial \xi_1}, \quad J_{y2} = \sum y_i \frac{\partial N_i}{\partial \xi_2}, \quad J_{y3} = \sum y_i \frac{\partial N_i}{\partial \xi_3} \end{aligned} \tag{7.38}$$

Solving system (7.37) gives

$$\begin{bmatrix} \frac{\partial \xi_1}{\partial x} & \frac{\partial \xi_1}{\partial y} \\ \frac{\partial \xi_2}{\partial x} & \frac{\partial \xi_2}{\partial y} \\ \frac{\partial \xi_3}{\partial x} & \frac{\partial \xi_3}{\partial y} \end{bmatrix} = \frac{1}{2A} \begin{bmatrix} J_{y23} & J_{x32} \\ J_{y31} & J_{x13} \\ J_{y12} & J_{x21} \end{bmatrix} = \mathbf{P} \tag{7.39}$$

with J_{xji}=J_{xj}-J_{xi}, J_{yji}=J_{yj}-J_{yi} and A=$\frac{1}{2}$($J_{x21}J_{y31}$-$J_{y12}J_{x13}$) $\neq 0$. Substituting this into (7.33), the partial derivatives of the shape functions are

$$\begin{bmatrix} \frac{\partial N_i}{\partial x} \\ \frac{\partial N_i}{\partial y} \end{bmatrix} = \mathbf{P}^T \begin{bmatrix} \frac{\partial N_i}{\partial \xi_1} & \frac{\partial N_i}{\partial \xi_2} & \frac{\partial N_i}{\partial \xi_3} \end{bmatrix}^T \tag{7.40}$$

where **P** is the 3x2 matrix of triangular coordinates defined in (7.39). To determine the barycentric coordinates for an iso-parametric element with $n = 6$ nodes, we have two residual functions for a given point $P(x,y)$, which can be incorporated into an external iterative loop, combined with an iterative backtrack loop of ξ_i:

$$R_x = \sum_{i=1}^{6} N_i x_i - x, \text{ and } R_y = \sum_{i=1}^{6} N_i y_i - y. \tag{7.41}$$

The iterative backtracking loop of ξ_i can be determined by the knowledge of the contributions of $\frac{\partial \xi_i}{\partial x}$ and $\frac{\partial \xi_i}{\partial y}$;

$$\begin{aligned} \xi_i^{n+1} &= \xi_i^n + \frac{\partial \xi_i}{\partial x} R_x + \frac{\partial \xi_i}{\partial y} R_y \\ &= \xi_i^n + \frac{J_{y23} R_x + J_{x32} R_y}{det(J)}, \quad i \in [1,2] \end{aligned} \tag{7.42}$$

hence we have

$$\Delta\xi_1 = \frac{J_{y23} R_x + J_{x32} R_y}{det(J)} \text{ and } \Delta\xi_2 = \frac{J_{y31} R_x + J_{x13} R_y}{det(J)} \tag{7.43}$$

7.2.3. Stretching of grid

By introducing a stretching of the pressure grid, we can ensure improvements in data representation, especially in areas where there are large gradients in the density. Therefore, we defined a simple stretching function, based on the theory outlined in Appendix G, which contributes to a moderate stretch of the pressure

grid in the vicinity of the saturation line, until the desired data representation is obtained. Figure (7.7) illustrates how the stretching works. Here the stretching of the network has greatest impact at both ends at x = 0 and x = 1. A simple

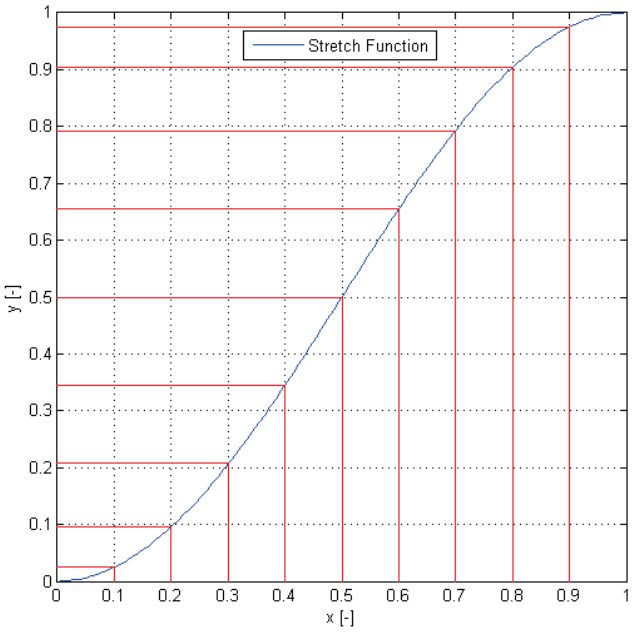

Figure 7.7.: Monotone increasing stretch function allowing dense grid at boundaries.

monotone increasing stretch function is given by (7.44):

$$y = \sin^2(\frac{\pi x}{2}), \quad (x,y) \in [0,...1] \tag{7.44}$$

and the reverse function is trivia,l given by

$$x = \frac{2}{\pi}\sin^{-1}(\sqrt{y}), \quad (x,y) \in [0,...1] \tag{7.45}$$

7.3. Timing the application

The timing of the simulations is very important because it provides the basis for evaluation of the interpolation elements in terms of time-consumption versus effectiveness. One of the performance indicators is the application timing; others can be related to the outcome of the application in terms of numerical results. The program timings are executed when other users are not active. The timing results can be affected by one or more CPU-intensive processes also running

while doing the timings, and the application has to be executed under the same conditions each time in order to provide the most accurate results, especially when comparing execution times of a previous version of the same program. If possible, the same system (processor model, amount of memory, version of the operating system, and so on) has to be used each time. For programs running less than a few seconds, it is important to run several timings to ensure safeguard against results. Overhead functions like loading libraries might influence short timings considerably. If the program displays a lot of text, redirection of the output from the program should be considered, which changes the times reported because of reduced screen I/O. Timings that show a large amount of system time may indicate a lot of time spent doing I/O, which might be worth investigating. For programs that run for less than a few seconds, it is important to run several timings to ensure that the results are not misleading. Overhead functions like loading shared libraries might influence short timings considerably. The elapsed, real, or 'wall clock' time, will be greater than the total charged actual CPU time. Charged actual CPU time, is shown for both the system and the user execution. The total actual CPU time is the sum of the actual user CPU time and the actual system CPU time. The computer used is a Lenovo portable PC (T520) with Intel(R) Core (TM) i5-2520M CPU @2.5 GHz 2 Core(s) with four logical processors, installed memory (RAM) is 8 GB - 64-bit operation system, Windows 7 Enterprise and service pack 1 Build 7601. Both the test application and the IAPWS-97 water steam table are implemented in C++ / FORTRAN 90, under Visual studio 2008, Professional Edition. The applications are compiled with an optimiser in order to achieve maximum speed.

7.4. Simulation results

Here follow comparisons of three different setups of interpolations. The first setup is based on a case using two main regions, R_6 which covers regions R_1 to R_4, and R_5 using a pure bilinear four node element. The second case is based on five regions using bilinear elements, supplied with a linear triangular element in the vicinity of the saturation line. Finally, there is a setup is using the five regions by applying an iso-parametric triangular element (six-node). The simulations are identified by a number (N_s). Meshes based on different element sizes in the five regions have been created for the individual simulations. The number of elements in each case are listed in table: table (7.3) for the two-region case, table (7.4) for the five-region case with bilinear elements and table (7.5) for the five-region case with triangular elements. The total number of nodes and elements are listed in the last column. We have a linear relationship between the total amount of nodes/elements versus the number of isobars used, N_p, because the step length in enthalpy, h, is approximately fixed and independent of N_p.

The results in terms of accuracy and simulation times for the three cases are presented in tables (I.1), (I.2) and (I.3). For comparison, reference simulations have been performed by running the pure IAPWS-97 water/steam application for pressure $p \in$ (1,10, 50, 100, 220, 300 and 700) [bar]. Corresponding time records are carried out by executing 8 million calculations, varying enthalpy linearly from 0.1 [kJ/kg] up to 4000 [kJ/kg]. The IAPWS 97 is implemented in the same environment as the comparable interpolation scheme. Time-consumption is listed in table (7.2). The averaged simulation time is 1.2248 [μs]. The interpolations are performed by stretching isobars in the bottom and top of each region, according to equation (7.44). We notice that it is relatively more time-consuming (5-6

$p[Bar]$	1	10	50	100	220	300	700
$t_{ref}[\mu s]$	0.8775	0.8229	0.7391	0.6923	0.3843	0.7937	0.8054

Table 7.2.: Time-consumption of executing IAPWS-97.

times) to perform the interpolation for an isobar passing in the vicinity of the critical pressure (p_{crit}). Grid structure for the three interpolation setups is plotted in the table (7.3-7.4), where both the number of nodes and elements are plotted as a function of the number of isobaric lines (N_p) in each region. We can see a proportionality between N_p and the number of elements for the bilinear elements and an approximate proportionality for the triangular node in R_2 and R_3. For

N_p	Items	R_6	R_5	$\sum_{i=1}^{5} R_i$
10	Elements:	3600	3600	7200
	Nodes:	4010	3609	7619
25	Elements:	9600	9600	18200
	Nodes:	10025	9624	19649
50	Elements:	19600	19600	39600
	Nodes:	20050	19649	39699
100	Elements:	39600	39600	79600
	Nodes:	40100	39699	79799
200	Elements:	79600	79600	159200
	Nodes:	80200	79799	159999

Table 7.3.: Number of nodes and elements in region (R_6=$\sum_{i=1}^{4} R_i$) and R_5 for four-node elements.

each simulation setup we perform a traversal with constant pressure and varying enthalpy from 0.5 [kJ/kg] to 3999.5 [kJ/kg] with a step of 0.5 [kJ/kg]). The isobar lines are: (1, 10, 50, 100, 220, 300 and 700 [bar]). The maximum, minimum

N_p	Items	R_1	R_2	R_3	R_4	R_5	$\sum_{i=1}^{5} R_i$
10	Elements:	180	1537	435	1278	3600	7030
	Nodes:	206	2280	525	1420	4009	8440
25	Elements:	600	219	210	2880	9600	19219
	Nodes:	650	4417	1194	3408	10024	21785
50	Elements:	2450	9217	2448	6958	19600	40673
	Nodes:	2512	12907	2557	7100	20049	45125
100	Elements:	9900	18817	9898	14058	39600	92273
	Nodes:	10100	26173	10122	14200	40099	100694
200	Elements:	39800	39957	39798	39800	79600	238955
	Nodes:	40040	55416	40235	40000	80199	255890

Table 7.4.: Number of nodes and elements in region 1-5) for three and four-node bilinear elements.

N_p	Items	R_1	R_2	R_3	R_4	R_5	$\sum_{i=1}^{5} R_i$
10	Elements:	360	3074	1142	2160	7200	13936
	Nodes:	920	8437	3068	5520	18418	36363
25	Elements:	1800	8834	3358	6730	9600	13362
	Nodes:	3074	23956	8913	14520	19200	14131
50	Elements:	4900	18434	7048	11760	39200	81342
	Nodes:	12300	49824	18647	29520	98498	208789
100	Elements:	19800	37634	19892	23760	79200	180286
	Nodes:	49799	101540	52557	59520	198598	462014
200	Elements:	79600	79914	79794	79600	159200	478108
	Nodes:	199201	215443	210667	199199	398798	1223308

Table 7.5.: Number of nodes and elements in region 1-5) for six-node elements.

and mean relative error, given by (7.46) are illustrated, as well as the standard deviation, which is a good indicator of how often significant differences in the interpolation occur compared to reference data. Finally, we notice the simulation time for a traversal of h, corresponding to the time records, carried out for the IAPWS-97 reference calculations (t_{Ref}), which is executed for 8 million steps, varying linearly from 0.1 [kJ/kg] up to 4000 [kJ/kg], in order to evaluate the impact of using different types of elements.

$$\varepsilon = \frac{\Phi_{Intp} - \Phi_{ref}}{\Phi_{ref}} \cdot 100\% \tag{7.46}$$

7.4.1. Bilinear four-node element

The first simulation setup includes a series of calculations based on the four-node bilinear element with varying mesh fineness, for different pressure levels (isobars). The calculations are listed in Table I.1. Figures (7.9) and (7.10) illustrate results for density interpolations based on sustained p and varying enthalpy from 0.5 [kJ/kg] up to 3999.5 [kJ/kg] with a step length of 0.5 [kJ/kg], for different N_p. In addition, the accuracy of each interpolation is illustrated in figure (7.8). In general the maximum error is located in the vicinity of the saturation line for saturated water and is very high, even for N_p=200. Herethere are very large negative steep gradients $\frac{\partial \rho}{\partial h} << 0$, especially for low pressure (p $<$ 10 [bar]), which are very difficult to resolve in a bilinear scheme. By using a bi-linear interpolation scheme, one avoids phenomena such as over and under-shooting the interpolated value; this is only true for higher-order polynomial elements. In general we see a stable and fast interpolation scheme, with a standard deviation below 1E-3 for p $>$ 50 [Bar] for all N_p, but we should be aware that if the steep gradients should dissolve, we need many more elements without affecting the lookup time, only the timing of the initial mesh creation. The averaged interpolation time for one point is 0.115 [μs] which is 10.65 times faster than IAPSW-97, and for the isobars in the vicinity of the critical pressure, we find an even higher performance, up to 33.4 times faster.

7.4.2. Bilinear four-node combined with triangular three-node elements

The next simulation setup is similar to the first, except for the use of triangular linear elements in the vicinity of the saturation line. The purpose of using triangular elements is to achieve a better resolution of the saturation curve, even if the triangular element is linear. The calculations are listed in Table I.2. In figures (7.12) and (7.13) the results for density interpolations are illustrated, based on sustained p and varying enthalpy from 0.5 [kJ/kg] up to 3999.5 [kJ/kg] with a

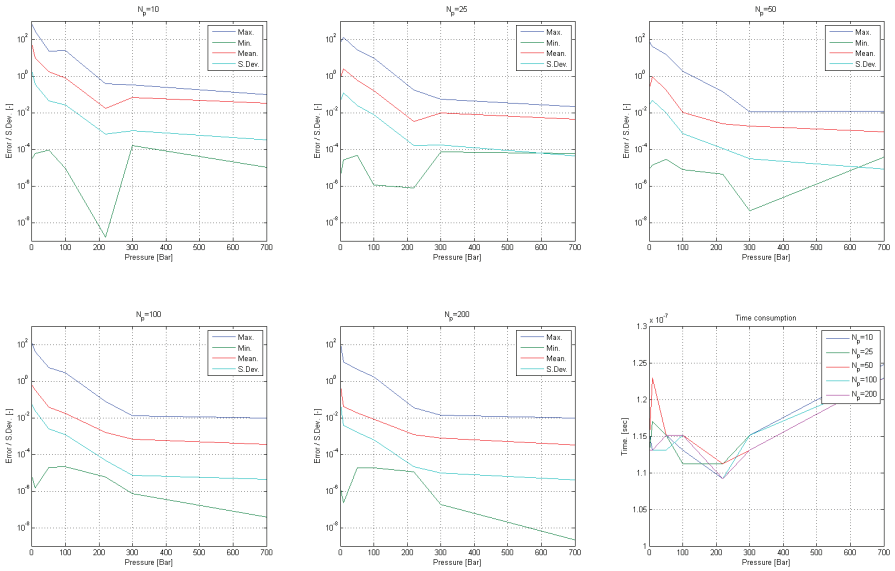

Figure 7.8.: Relative errors and standard deviation for different resolution of the pure bi-linear grid (N_s).

step length of 0.5 [kJ/kg], for different N_p. In addition, the accuracy of each interpolation is illustrated in figure (7.11). In general the maximum error also here is located in the vicinity of the saturation line for saturated water and is very high, even for N_p=200. We can see a minor improvement in the standard deviation of ρ, for p below the critical pressure, compared to the case without triangular elements. Again the density trough for low pressure is still very difficult to resolve by linear triangular elements. By using the linear interpolation scheme, we again avoid the over and under-shoot of the interpolated value. In general we see a stable and fast interpolation scheme, with a standard deviation below 1E-3 for all p $>$ 100 [bar] and $N_p > 25$. The averaged interpolation time for one point is 0.1899 [μs] for the two-phase region and 0.1180 [μs] for the superheated region (R_5) which is 7.3 and 6.7 times faster, respectively, than the reference IAPWS-97. We have an increased time-consumption since we use a lookup table, containing the start and end elements of each row of elements, involving a possible risk in running through a large table before the correct item is found for interpolation. In the pure bilinear interpolation, we can use the form described in equation (7.9).

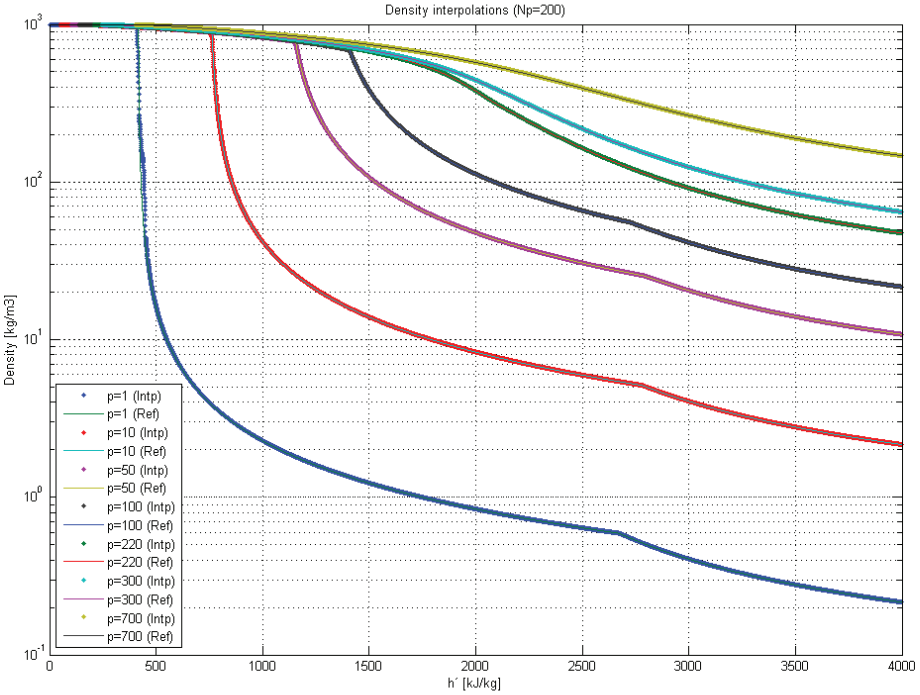

Figure 7.9.: Density as a function of Enthalpy for fixed pressure of 1.0 [Bar]. N_p varies from 10, 100 and 200.

7.4.3. Triangular six-node elements

The last simulation setup uses iso-parametric triangular elements for all regions. Here we operate with five regions as in the previous setup. The purpose of using triangular iso-parametric elements is to achieve a better resolution of the saturation curve as well as increasing the accuracy all over the domain, even if the triangular element is only of second-order. The calculations are listed in table I.3. Figures (7.15) and (7.16) illustrate the results for density interpolation based on constant pressure and varying enthalpy from 0.5 [kJ/kg] up to 3999.5 [kJ/kg] with a step length of 0.5 [kJ/kg] for different N_p. Additionally, the accuracy of each interpolation is illustrated in figure (7.14). In general the maximum error is still considerable, up to 400 %, and also here is located in the vicinity of the saturation line for saturated water, even for N_p=200. However, it is significantly lower than observed in the previously shown results. We find a significant improvement in the standard deviation for pressures below the critical pressure, compared to the case without triangular elements. Again the density trough for low pressure is still very difficult to resolve, even by an iso-parametric triangular element. A

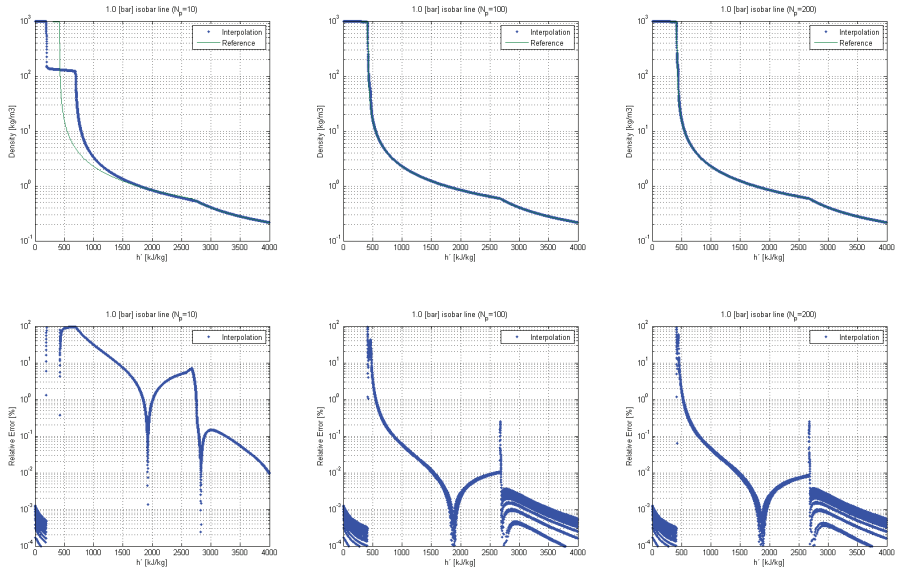

Figure 7.10.: Density as a function of Enthalpy for isobars varies from 1.0 to 700 [Bar]. N_p=200.

second-order element is not necessarily monotonically increasing or decreasing, indicating we have a risk, that the interpolation can be influenced by a numerical over-shoot or under-shoot. We see this clearly for $N_p = 10$ and, more surprisingly, also for $N_p = 200$. In the latter event we observe a sharp jump in function values inside the element nodes, for example, $\rho_1 = 989$, $\rho_2 = 0.32$, $\rho_3 = 903$, $\rho_4 = 1.30$, $\rho_5 = 10.9$ and $\rho_6 = 974$. The interpolated value is $\rho_{Intp} = 0.18$, while the IAPWS-97 gives 8.19. All ρ values are measured in [kg/m^3]. Here we experience a huge relative error as a result of the inability of the second-order elements to dissolve the very large gradients, that we experience at the density trough for low pressure. The averaged interpolation time for the entire domain is 5.6925 [ms] which is 4.6 times slower than the original IAPSW-97 implementation. The increased time-consumption is first of all due to the need to calculate the barycentric coordinates according to the algorithms (7.41) to (7.43) for each point $P(x, y)$. Secondly, it is due to the lookup table we use, which contains start and end elements of each row of elements, due to a non-equidistantly mesh in enthalpy, h.

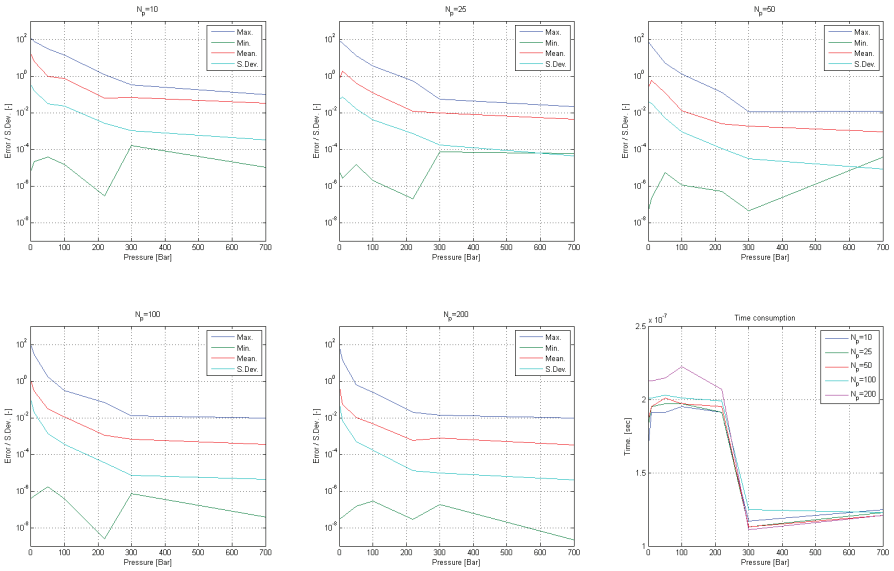

Figure 7.11.: Relative errors and standard deviation for different resolution of the Bi-linear grid with triangular elements in the vicinity of the saturation line (N_s).

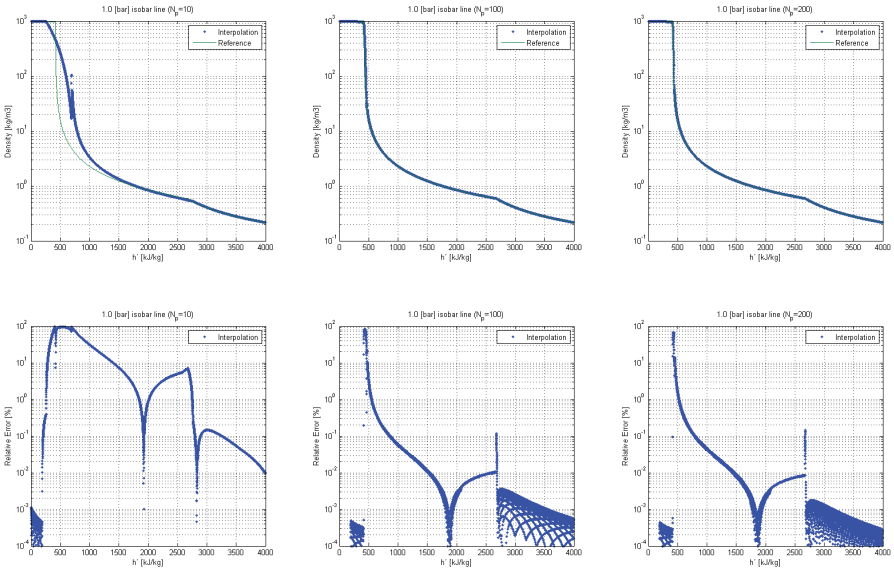

Figure 7.12.: Density as a function of Enthalpy for a fixed pressure of 1.0 [Bar]. N_p varies from 10, 100 and 200.

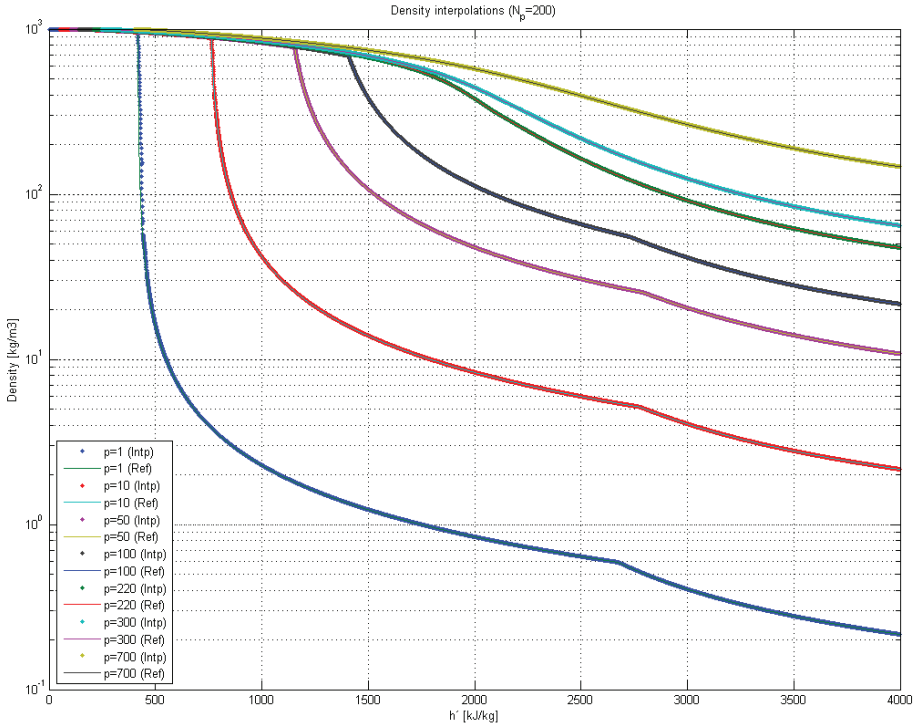

Figure 7.13.: Density as a function of Enthalpy for isobars varying from 1.0 to 700 [Bar]. N_p=200.

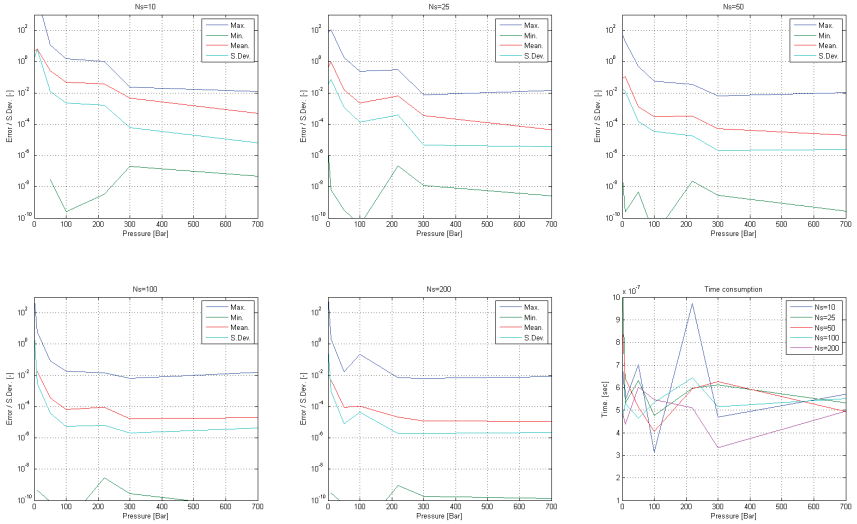

Figure 7.14.: Relative errors and standard deviation for different resolution of the second-order iso-parametric elements.

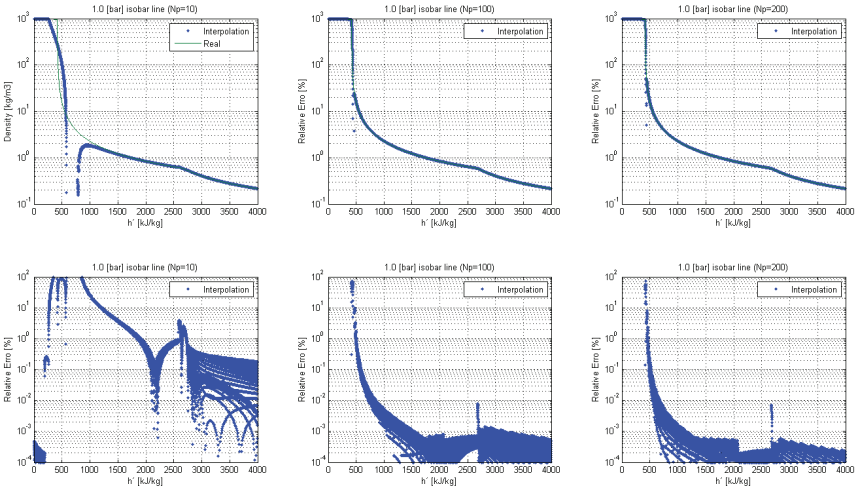

Figure 7.15.: Iso-parametric elements: Density as function of Enthalpy for fixed pressure of 1.0 [bar]. N_p varies from 10, 100 and 200.

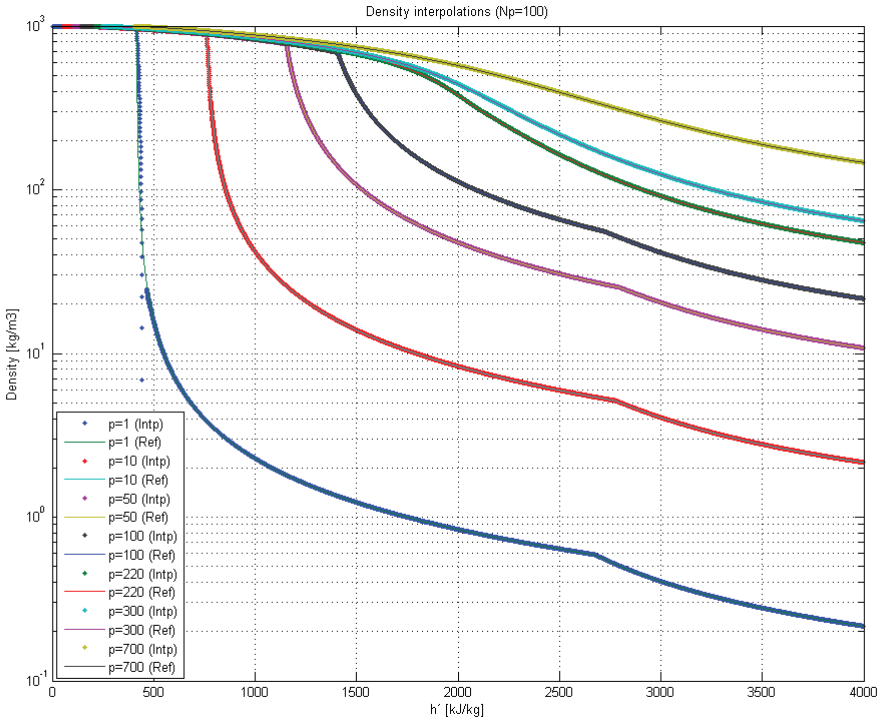

Figure 7.16.: Iso-parametric elements: Density as a function of Enthalpy for isobars varying from 1.0 to 700 [bar]. N_p=200.

7.5. Discussion

The benefits in using the iso-parametric elements are minimal in this case, since they are time-consuming and not able to resolve the density trough at low pressures. Yet for some reasons we recommend using such elements in the scope of smoothing the thermodynamic properties, calculated in individual regions in the IAPWS-97 Industrial Standard. We observed also the possibility of inaccurate interpolation along the saturation curve for water at low pressure levels. One example was N_p=200, $p = 1$ [bar] and $h = 578.75$ [kJ/kg]. In this iso-parametric element there are large differences in the function values of the nodes, ranging from 989.83 $[kg/m^3]$ down to 0.32 $[kg/m^3]$ by an exponential decrease in density, meaning a second-order element is not sufficient to dissolve the functional sequence of the element. If we use regions R_2 and R_3 with a higher minimum pressure ($p_{\min}$), the iso-parametric element gives very high accuracy and reproduces the results with a maximum relative error below 0.5 % (N_s=87) and a standard deviation less than 10^{-3} for $N_p > 50$. A general comment is also that it is not recommended to use a network based on only N_p = 10 isobaric lines; this causes an excessive interpolation inaccuracy. Conversely, we see that a network with N_P = 200 or more, provides relatively large networks, especially the iso-parametric element. The initial network generation takes several minutes to establish for N_p = 200 and greatest 1223308 nodes and 478108 iso-parametric elements, according to table (7.5). We have chosen to interpolate the density, because this thermodynamic property contains very sharp gradients, especially for low pressure, which in this way uncovers an absolute worst case with respect to interpolation. Other state properties would yield significantly better results, such as heat capacity, entropy and temperature. When modelling a dynamic two-phase flow process, one can ask questions about what happens to the density along the saturation line. Under normal circumstances, it is a well-known numerical trick to smooth the crossing from the sub-cooled liquid to the two-phase mixture, thereby blurring the steep gradient. If one then uses an interpolation scheme with a suitably large number of pressure lines, one is assured of a high degree of accuracy in the interpolated state variables, which does not only have to contain one value. In practice all necessary thermodynamic properties can be saved in each node in the interpolation table. A simple way to enhance the iso-parametric interpolation, is by modifying the surface function which is included in the interpolation element. If we introduce a contribution, which replaces the quadratic part with a reciprocal part of the variable, we get a better resolution of the density trough, as we see in the vicinity of the saturation curve for water. However this solution will give less desirable results for other quantities that behave square with respect to variations in pressure or enthalpy. The challenge with this method is that the interpolation

table is bulky. An example of N_p = 200 isobar lines and with 17 items stored in each node, provides a binary file of approximately 50 MB.

7.6. Summary

The high-lights in this section presents the result of investigations of three different methods of using interpolation schemes, based on the finite element methodology to represent thermodynamic state variables of water/steam as an alternative to using the complete formulation defined by IAPWS-97. The results show there is significantly reduced computation time, but also that there are challenges to using the suggested approach. One is that we find low accuracy of the results in parts of the calculation range, and two is that even higher time-consumption may occur selection of the elements.

We recommend bilinear schemes for interpolating the water/steam table of IAPWS-97. For pure bilinear interpolation we recommend at least N_p=200 or higher, since no look up table is required in this case. Modern computers do not restrict the amount of data storage significantly, so in practice we do not have to take memory into consideration. The improvements in introducing the triangular elements are too insignificant to justify the more intensive implementation of such scheme; however, the results are more accurate and we can reduce some memory demands. However, in the two-phase region, we need a look up table, which can be time-consuming for large grid arrangements. The iso-parametric triangular elements cannot be recommended for the entire domain and especially, if the argument is to save CPU costs. Alternatively the iso-parametric elements can with advantage be used when calculating the first-order derivative of the thermodynamic properties; thereby we ensure continuity in the first-order derivative. If the iso-parametric elements should be used near the density trough, a more dedicated shape function should be implemented. In such case, we can reduce the number of elements drastically and the computer costs, too. However, the barycentric coordinates will be costly to compute. It will be a challenge to find approval to use the iso-parametric elements. Hitherto when we decided to use the interpolation technique, we had to define the definition area of the problem of interest and thereby the size and number of regions in the interpolation model.

8. Dynamic modelling of thermo- hydraulic systems

This chapter has developed various models to describe the thermal-hydraulic conditions in a two-phase flow. The models vary widely in complexity and have both strengths and weaknesses. The most complex models allow a more detailed description of flow regimes, depending on the distribution of different sub-layers in the model as well as the orientation of the heat pipe (horizontal or vertical). A homogeneous model provides a more simplified description of the flow regimes, but achieves a faster execution time. We start by looking at a two-layer model, which forms the basis for description of the physics of the evaporation process. With this background a homogeneous model is derived, which subsequently is used to analyse load scenario studies in connection with the case study of SKV3. This chapter concludes with brief a four-layer model, which is detailed in Appendix (M).

8.1. Non-thermal equilibrium situations

A two-phase flow model for predominantly one-dimensional flow can be adapted to different flow regime patterns (vertical as well as horizontal stratification) and to pipes with or without rifling. The model uses a non-equilibrium approach and consists of two continuity equations, two momentum equations and two energy equations. This section starts with a brief review of various boiling and flashing mechanisms in two-phase flow, clearly revealing that thermal equilibrium is only a limiting case: when the processes take place at very slow rates or if there is extremely fine subdivision of the phases, so that there is an extremely large interfacial area where the heat exchanges can take place. It is only under such load conditions, that one can model two-phase flow systems assuming thermal equilibrium. For simplicity the derivation will follow from a symmetric stratified flow pattern in the figures; however, this does not limit the generality to other flow patterns.

Some degree of thermal non-equilibrium arises in practically all situation and specially in dynamic situations; thermal non-equilibrium must always be present so that heat and mass transfer can take place. Thermodynamic equilibrium does exist between a liquid and its vapour separated by a flat interface, e.g., water and steam in a closed vessel. In the classical case of stationary vapour / bubble in a large amount of liquid, the vapour and liquid temperatures are equal. However,

due to the effect of surface tension, see equation (E.66), even in this equilibrium situation, the system temperature must be slightly above the saturation temperature corresponding to the pressure of the liquid. It is only in the case of the flat interface, that both phases can be exactly at saturation.

In the equally classical case of nucleate boiling (NB) there must be a certain superheat of the liquid near the wall for the bubble to nucleate and grow. In the case of strong temperature gradients near the wall, one can have sub-cooled nucleate boiling (SNB) where bubbles nucleate, grow and even detach from the wall and survive for a while in the bulk of sub-cooled liquid.
In annular flow (forced convection) there is a temperature gradient in the liquid film on the wall, since the liquid layer immediately adjacent to the wall is at the wall temperature, while the interface is near saturation. This temperature gradient drives a heat flux to the interface where evaporation takes place. In a dispersed flow film boiling regime, a two-stage heat transfer phenomenon exists, from the wall to the vapour and from the vapour to the liquid droplets, where temperature gradients are the driving mechanisms for these heat exchange processes. The vapour gets superheated from the hot wall, while there is still water in the form of droplets in the flow channel, [73].

In the case of a rotating flow field, the rotation gravity will separate the heavy liquid droplets from the lighter steam, which results in a more homogeneous film layer at the wall. In this liquid film layer, the temperature gradient drives a heat flux to the interface where evaporation takes place. Turbulence will cause entrainment of new liquid droplets, which will interact mechanically and thermally with the steam in the pipe core.

Thermal non-equilibrium is present in flashing load situations, i.e., when changes in a pipe system (evaporator) results in super heating of the liquid and thereby produce vapour. An example of the absence of thermal equilibrium is a rapid de-pressurization of a liquid system. In this case the pressure may drop well below the saturation pressure that corresponds to the temperature of the liquid. The causes of this pressure under-shoot is clear; it takes time for bubbles to nucleate and grow by drawing heat from the surrounding fluid, consequently there is a departure from equilibrium, i.e., the liquid tends to remain at the original temperature, whereas the vapour that is being generated is close to saturation. Similarly, a sub-cooled discharge through a break or an orifice may expose fluid particles to a rapid change in pressure. If the outside pressure is below the saturation pressure corresponding to the temperature of the liquid, then the fluid flashes in a process similar to that of a rapid de-pressurization and there may be similar departure from equilibrium. Flashing is of importance for critical flows

that affect the safety of various processes in steam power engineering (steam power boilers).

8.2. Two-layer model

A general two-layer model is developed for predominantly one-dimensional flows in a vertical pipe element with internal rifles. In bubbly flows or liquid suspensions, the number of interfaces between the phases is too large to track, and it is widely accepted that average flow characteristics are sufficient to describe the relevant macroscopic dynamics. Averaging the equations, for example across the channel in Figure (8.1), yields models in which at every point in space, all fluid components co-exist with certain volume fractions. Such multi-phase models are inherently non-conservative due to momentum and energy exchange terms between the phases. They require closure relations which are not available from first physical principles, and even when motivated by physical considerations they yield controversial results. Pressure differences may develop between the phases, but they are not sustainable and tend to equilibrate. Yet assuming a single (equilibrium) pressure leads to ill-posedness due to loss of time-hyperbolicity of the governing equations; see [73] and [74]. This ill-posedness is not only an intriguing outcome, but also a major obstacle in the design of numerical methods. Hyperbolicity is also lost in two-pressure models if one of the phases is assumed incompressible. Now the one-dimensional flow is assumed compressible and a time-averaging of the velocity fluctuations is considered similar to the known averaging of turbulent fluctuations from single-phase fluid dynamics [40]. The model we outline here follows the principles outlined in [75]. It applies both to multi-fluid flows and to multi-phase flows. The model is hyperbolic. It tends to the Euler equations in each pure fluid zone. When summing mass, momentum, and energy equations of the two phases, we get back the Euler equations for the mixture. Our system of partial differential equations cannot be written in conservative form. This drawback usually leads to theoretical and practical difficulties in defining the weak solutions of the problem and in computing them. The model resolves stratified flow transport of fluid between the layers, caused by condensation or evaporation. The stratification can be vertically or horizontally orientated and enhanced by a swirl initiated by the IRBT or by the acceleration due to gravity. The rate of the interfacial mass transport processes caused by evaporation is named Γ, defined here as the rate of phase change per unit mixture volume and is positive for evaporation. The formulation includes separate sets of mass conservation, momentum and energy equations for each phase, which are represented by the belonging volume fractions of the total fluid; see figure (8.1).

8.2.1. Conservation laws

In a two-fluid model, the field equations are expressed in six conservation equations consisting of mass, momentum and energy equations for each phase. For notational convenience, we assume a gas phase and a liquid phase, and denote the respective flow variables by the subscript $()_k$, k$\in$ {l,g}. Since these field equations are obtained from an appropriate averaging of local instantaneous balance equations, the phasic interaction term appears in each of the averaged balance equations. These terms represent the mass, momentum and energy transfer through the interface between the two phases. These terms determine the

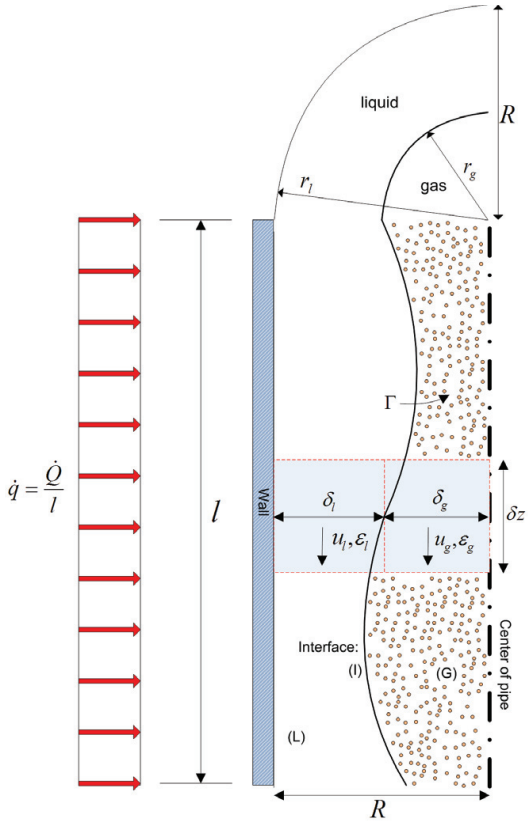

Figure 8.1.: Illustration of the two control volumes in the two-phase fluid. The fluid is flowing in a cylindrical channel with uniform radius R.

rate of phase changes and the degree of mechanical and thermal non-equilibrium between the phases; thus they are essential closure relations for the model system. A pipe channel is considered as a uniform channel with constant cross-section area (A) and no internal heat production. The model resolves stratified flow transport of fluid between the layers, caused by condensation or evaporation. The

field equations take the form as formulated in [40], [76] and [74], where we here describe the source/sink terms in more detail:

Conservation of mass

$$\frac{\partial\left(\varepsilon_g \rho_g A\right)}{\partial t} + \frac{\partial\left(\varepsilon_g \rho_g u_g A\right)}{\partial z} = \Gamma_g A \tag{8.1}$$

$$\frac{\partial\left(\varepsilon_l \rho_l A\right)}{\partial t} + \frac{\partial\left(\varepsilon_l \rho_l u_l A\right)}{\partial z} = \Gamma_l A \tag{8.2}$$

Here are the independent variables t and z represents the time in [s] and z is the spatial coordinate referring to the flow direction of the fluid given in [m]. The rate of the interfacial mass transport processes caused by evaporation is named Γ_k, defined here as the rate of phase change per unit mixture volume and is positive for evaporation ($\Gamma_g > 0$), for the k'th $(k \in \{g,l\})$ phase. In the equations, ε_k stands for the phase volume fraction, and ρ_k and u_k are the density and velocity for the k'th $(k \in \{g,l\})$ phase, respectively. For an isotherm model, the rate of phase change (Γ_k) would be zero. The volume fraction of total liquid can be described as the sum of a continuous liquid phase (ε_l) and a continuous gas phase (ε_g):

$$\varepsilon_l + \varepsilon_g = 1 \tag{8.3}$$

and the rate of phase change can be expressed by

$$\Gamma_l + \Gamma_g = 0. \tag{8.4}$$

The interface zone related to a cylindrical core layer (with the perimeter named

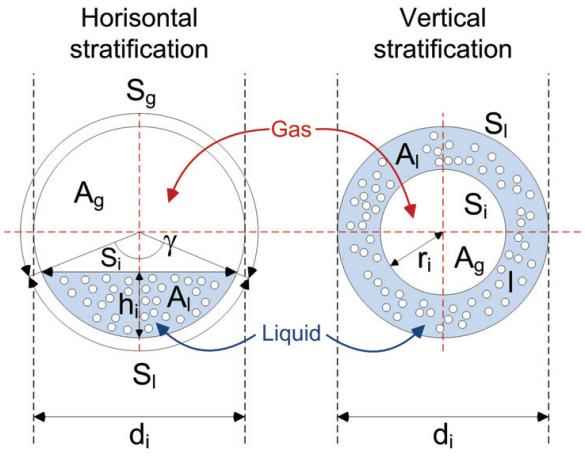

Figure 8.2.: Pipe cross-section.

S_i) separates the flow into two phases, named Gas (g) and Liquid (l). The interface zone is assumed radial and symmetric along the pipe centre axis (**k**), given by (8.18), where the perimeter for a vertical stratification is defined as:

$$S_i = 2\pi r_i \tag{8.5}$$

where

$$r_i = R\sqrt{\varepsilon_g} \tag{8.6}$$

For a horizontal stratification, we have the following relations:

$$\varepsilon_l = \begin{cases} \frac{S_l}{\pi d_i} - \frac{S_i}{\pi d_i} + \frac{2S_i h_i}{\pi d_i^2} & \text{for } h_i \leq d_i/2 \\ \\ 1 - \frac{S_g}{\pi d_i} + \frac{2S_i h_i}{\pi d_i^2} - \frac{S_i}{\pi d_i} & \text{for } h_i > d_i/2 \end{cases} \tag{8.7}$$

where d_i is the pipe inner diameter, h_i the height of the liquid column, S_l and S_g are the perimeter of the liquid and gas phases respectively; see figure (8.2). For h_i=$d_i/2$ we find: S_i=d_i, S_l=S_g=$d_i/2$, which leads to: ε_l=0.5.

Conservation of momentum

The formulations of the momentum equations are derived on the basis of Newton's 2^{nd} law to each layer control volume. The momentum transfer terms have to balance the forces acting on the fluid layers. The momentum balance is set up for each field (gas and liquid phase). The interfacial velocity is given as u_i and is acting parallel to the pipe main axis. The interfacial force along the interface I is represented by F_i per unit mixture volume. Interfacial drag and friction both contributes to this force. The forces are orientated positively in the direction of the pipe z-axis. The wall friction force is represented by $F_{w,k}$ for the fluids belonging to the wall measured per unit mixture volume. The parameter F_{vm} is the virtual mass force and occurs only when one of the phases accelerates with respect to the other phase. The virtual force is one of the key factors to make the Jacobian matrix in the non-homogeneous governing equations hyperbolic. F_{vm} results from the fact that the motion of the discontinuous phase results in the acceleration of the continuous phase as well. $F_{g,k}$ is the forces holding the gravitational forces due to gravity, and for practical reasons, we have

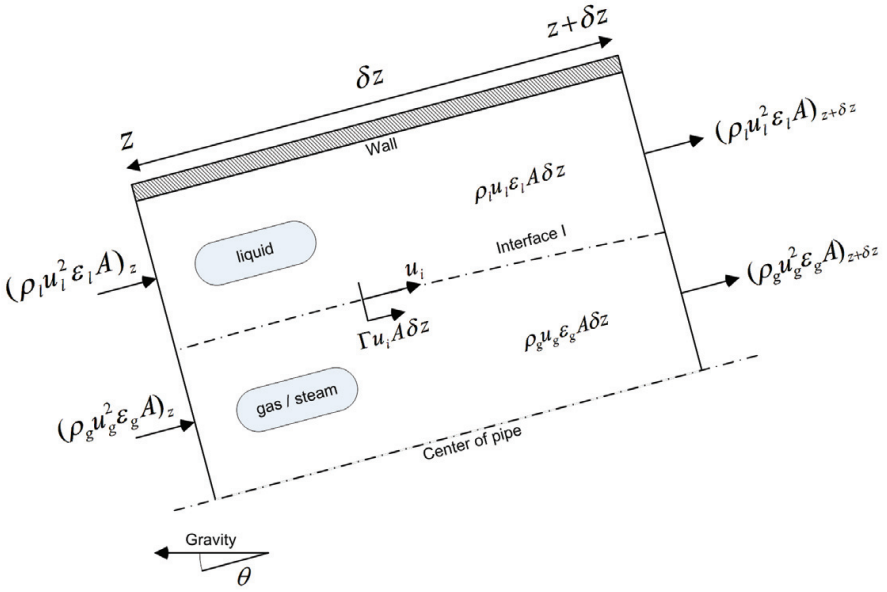

Figure 8.3.: Momentum transfer terms for the two fields on a slice of a pipe-element.

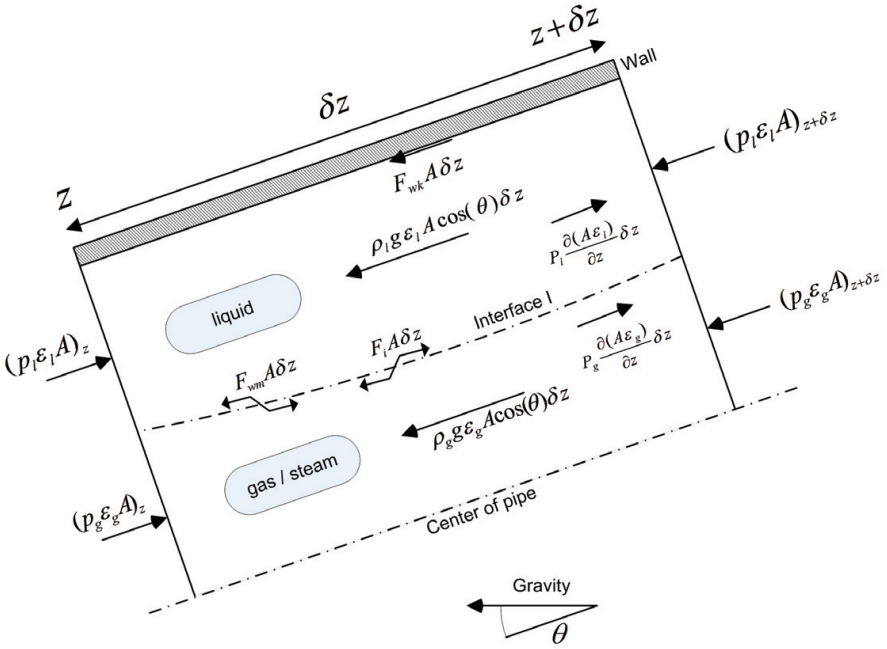

Figure 8.4.: Forces acting on the two fields on a slice of a pipe-element.

collected both the gravitational and the virtual force, under a single force named $F_{c,k}$=$F_{g,k}$+F_{vm}.

$$\frac{\partial\left(\varepsilon_g\rho_g u_g\right)}{\partial t}+\frac{\partial\left(\varepsilon_g\rho_g u_g^2+\varepsilon_g P_g\right)}{\partial z}=P_i\frac{\partial\varepsilon_g}{\partial z}+\Gamma_g u_i+F_{d,g}+F_{c,g}+F_{s,g} \tag{8.8}$$

$$\frac{\partial\left(\varepsilon_l\rho_l u_l\right)}{\partial t}+\frac{\partial\left(\varepsilon_l\rho_l u_l^2+\varepsilon_l P_l\right)}{\partial z}=P_i\frac{\partial\varepsilon_l}{\partial z}+\Gamma_l u_i+F_{d,l}+F_{c,l}+F_{s,l} \tag{8.9}$$

where the drag force for each layer can be handled as a velocity relaxation process detailed as:

$$F_{d,g} = F_{w,g} + F_i \tag{8.10}$$
$$= F_{w,g} + \lambda(u_l - u_g)$$
$$F_{d,l} = F_{w,l} - F_i \tag{8.11}$$
$$= F_{w,l} - \lambda(u_l - u_g)$$

where λ is related to the interfacial shear, described by equation (8.36). On the *right-hand side* (RHS) of the momentum equations (8.8) and (8.9) we have as the very first term, the interfacial pressure force acting along the interface layer; the second term denotes the momentum contribution, caused by the phase change in the fluid; next we have a drag force covering both the wall shear stresses per unit volume for the k'th fluid, represented as $F_{w,k}$ and the rate of momentum gained by interfacial drag along the interface (I) per unit volume, given by F_i. The second last term $F_{c,k}$ consists of two contributions, the gravitational force acting on the fluid: $F_{g,k}$ and the virtual mass term (F_{vm}) denoting the momentum contribution, due to the acceleration of one phase, with respect to the other phase. The very last term is the momentum gained by the shear stresses (viscos forces) in the two-layer momentum equations given by $F_{s,k}$, under the assumption that the fluid is Newtonian. The contribution from the shear stress could be $F_{s,k}$=$\frac{\partial \tau_{f,k}}{\partial z}$, where $\tau_{f,k}$ represents the shear stress generated in a gradient field of the fluid velocity. In principle, we excluded the contribution from the shear stresses in the two-layer momentum equations due to the assumption of a non-linear relation between the shear stress and the shear rate (non-Newtonian). This shear stress may in some situations be modelled as a second-order diffusion term (artificial diffusion), in the form of a mixing length theory, which can be added to the momentum equation for more dissipation, when it is required due to the singularity in the first derivative of the fluid density, near the saturation line. The pressure is given by P_k and the interfacial pressure is given by: $P_i = \varepsilon_g P_g + \varepsilon_l P_l$. A simple and widely used choice for the interfacial velocity is u_i=$(u_g + u_l)/2$ given by [76], but a mass based and more accurate estimate is given by [74] as:

$$u_i = \frac{\sum_k \varepsilon_k \rho_k u_k}{\sum_k \varepsilon_k \rho_k} \tag{8.12}$$

The first term on the *left-hand side* (LHS) of the momentum equations (8.8) and (8.9) is the dynamic rate of creation of momentum; the second term is responsible for the axial convection of momentum.

Conservation of energy

To derive the energy conservation equations for the flow fields, one should apply the first law of thermodynamics to the liquid and gas layer control volumes. A control volume composed of an infinitesimal segment of the flow channel is depicted in figure (8.5), where T_l and T_g are the bulk liquid and the gas temperature; T_i is the temperature at the interface layer, surrounding the cylindrical core of the gas phase (vertical stratification), with the perimeter S_i measured as the inside circle with radius r_i; see figure (8.2). The mass transfer caused by phase changes is represented along the interface by Γ_g and Γ_l, as illustrated in figure (8.5), and Γ_g and Γ_l are positive for evaporation and condensation, respectively. It is assumed that no heat generation occurs within the control volume and that heat diffusion is negligible in the convection dominated flow of forced evaporation (or condensation). Other parameters are as follows: q''_{il} and q''_{ig} are the heat fluxes between liquid and gas phases at the interphase I, measured in watts per meter squared. The heat fluxes are controlled by the temperature difference in-between the two layers.

The total enthalpy of flow region k is defined as the sum of the intrinsic enthalpy, the potential energy, the axial kinetic energy (axial velocity) and the rotation energy caused by the swirl (generated by the internal rifles in the boiler tube). The last one is more or less negligible compared to the intrinsic enthalpy. In the derivation the total specific energy e_{tk} and the specific convected energy e_k, we define in the terms below:

$$e_{tk} = \widetilde{h}_k + \frac{u_k^2}{2} - gz\cos(\theta) + r_{ck}a_{ck} \tag{8.13}$$

and

$$e_k = h_k + \frac{u_k^2}{2} - gz\cos(\theta) + r_{ck}a_{ck} \tag{8.14}$$

where $\widetilde{h}_k$ is the specific internal energy and h_k is the specific enthalpy, related by (8.15).

$$\widetilde{h}_k = h_k - p_k/\rho_k \tag{8.15}$$

The inclusion of $gz\cos(\theta)$ in the definition of e_{tk} and e_k is generality. Often we deal with the difference of total energy along the interface $e_{ti} - e_i$, whereby the $gz\cos(\theta)$ term cancels out in mixture models. The area based centre radius r_{ck}, is given by equations (8.30) and (8.31) for the gas and liquid layers, respectively. The heat flow across the wall is defined as positive for $T_w > T_l$ or $T_w > T_g$. Additionally, the heat transfer across the interface is defined as positive according to the illustration in figure (8.5) and is positive as long as the driving temperature across the interface is going from high to low temperature. The mass transfer

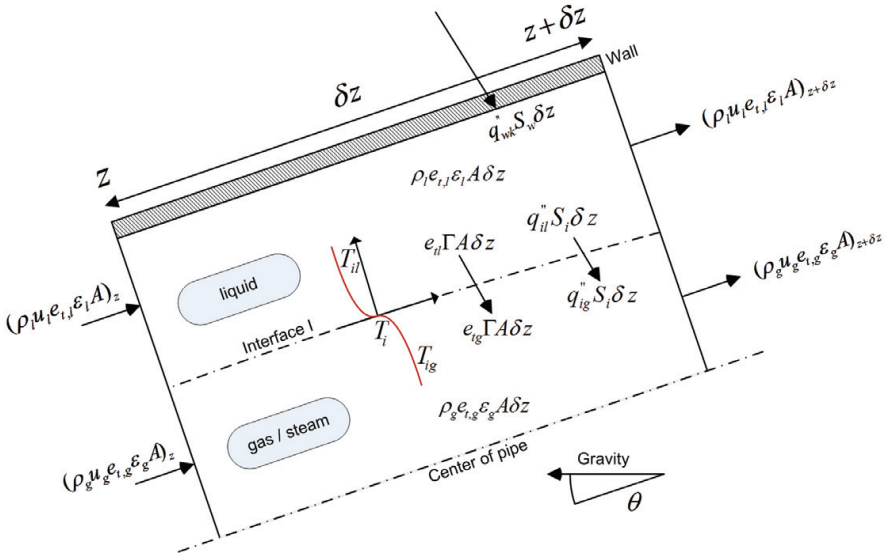

Figure 8.5.: Energy transfer and heat flow on a slice of a pipe-element.

across the interface due to evaporation or condensation is represented by Γ_k. The work terms are illustrated in figure (8.6), where in particular the pressure forces from the neighbour layer should be highlighted. The interfacial drag (friction force) as well as the virtual mass force along the interface, performs work along the interface cross-section. The outflow of energy is defined as positive.

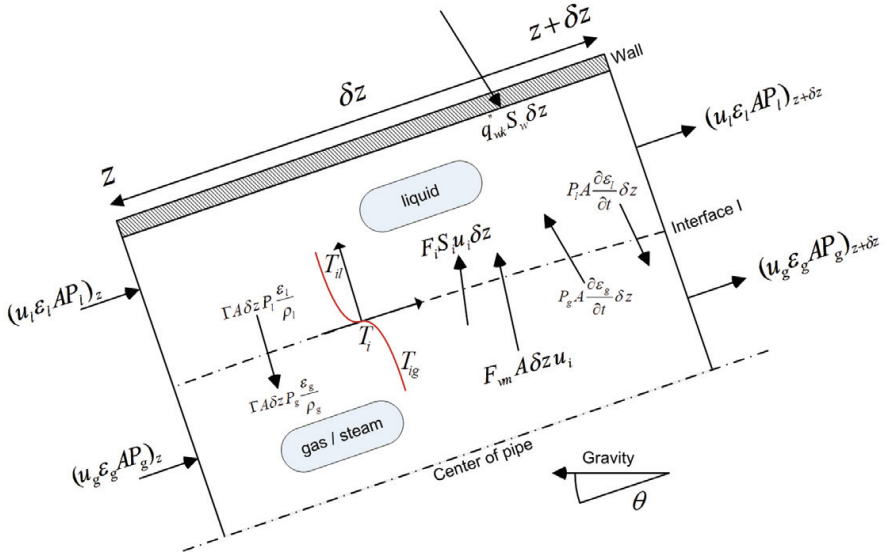

Figure 8.6.: Work terms on a slice of a pipe-element.

Reference [75] provides an expression for the energy balance in differential form. The two-phase energy conservation equations are expressed in Watt per volume as:

$$\frac{\partial(\varepsilon_g \rho_g E_g)}{\partial t} + \frac{\partial(\varepsilon_g \rho_g E_g u_g)}{\partial z} = P_i u_i \frac{\partial \varepsilon_g}{\partial z} + \Gamma_g E_i + F_{d,g} u_i + F_{c,g} u_i + Q_{w,g} + Q_i \tag{8.16}$$

$$\frac{\partial(\varepsilon_l \rho_l E_l)}{\partial t} + \frac{\partial(\varepsilon_l \rho_l E_l u_l)}{\partial z} = -P_i u_i \frac{\partial \varepsilon_g}{\partial z} + \Gamma_l E_i + F_{d,l} u_i + F_{c,l} u_i + Q_{w,l} - Q_i \tag{8.17}$$

The total energy is given as: E_k=e_k+1/2u_k^2 and the internal energy e_k for the k'th fluid is given by (8.13) and (8.15). The dynamic transport term is described by the first part on the LHS in (8.16) and (8.17), and it expresses the rate of increase in the total energy per measured unit of volume. The second term is the axial transport of the total energy. The formulation includes various interfacial terms, such as, mass transfer Γ_g, drag force F_d and convective heat exchange Q_i, which are usually given by empirical constitutive relations, depending on the process under study: evaporation, condensation, combustion, etc. On the RHS in (8.16) and (8.17) the first term expresses the work done by the pressure forces at the interface, and the second term is the energy transport due to mass transfer caused by evaporation, condensation or combustion. The third term accounts for the work done by the drag forces at the wall. The fourth term represents both the work done by both the gravity and the work done by the virtual mass force along the interface due to the acceleration of one phase with respect to the other phase. The fifth term represents the rate of heat flux across the wall and is defined as positive for $T_w > T_l$ or $T_w > T_g$. The sixth and last term is the heat flow across the interface and is positive for $T_l > T_g$ due to simple conduction in-between the two layers.

8.2.2. Screw path in rifled pipe

A Cartesian coordinate system is defined by the three unit vectors:

$$\mathbf{i} = (1,0,0),\ \mathbf{j} = (0,1,0),\ \mathbf{k} = (0,0,1) \tag{8.18}$$

where **i** and **j** are two vectors placed in the cross-section plane of the pipe, and **k** is the cross product of **i** and **j** and is parallel to the axial flow direction of the pipe. The form of the IRBT can be described as a regular circular pipe with an inside hydraulic radius R and additional material inside. The inside material forms a number of fins or ribs (N_f) along the pipe wall; see figure (2.4). The fins follow a

circular helix with the angle γ to the unfold left screw plane, illustrated in figure (8.7), where the first coordinate axis represents the axial direction of the pipe (z), which is parallel to the unit vector **k**, and the second coordinate axis is the periphery of the pipe, measured in radians. Note that l_p is the projected period length of the screw path, orientated in the **k** direction. Hence,

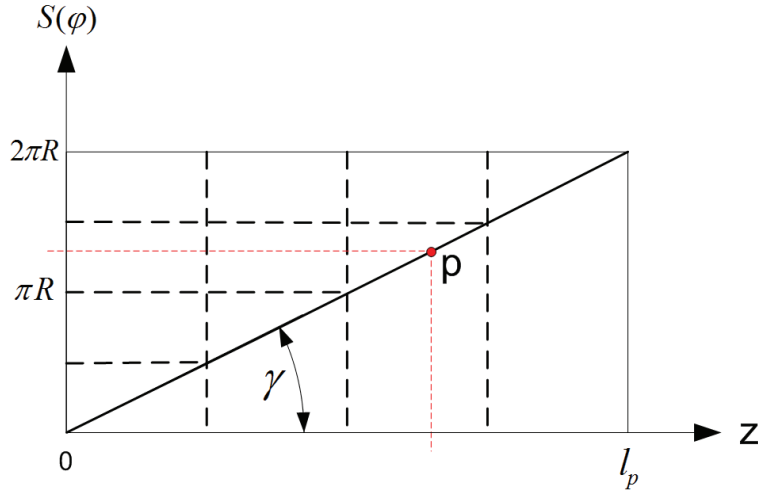

Figure 8.7.: Unfold left screw boiler tube. Linear relationship between perimeter (S) and l_p.

$$\tan(\gamma) = \frac{2\pi R}{l_p} \tag{8.19}$$

A point $\vec{P}$ positioned along the helix can be expressed by the hydraulic radius R and the angle of rotation φ; see equation (8.20). The angle of rotation φ can be expressed by equation (8.21), where ω is the frequency of rotation and γ is determined by the rifle geometry. In the special case where $\gamma = 0$ (situation without rifles), there is no coupling between the perimeter S and the helix position $\vec{P}$.

$$\vec{P}(\varphi) = R \begin{pmatrix} \cos(\varphi) \\ \sin(\varphi) \\ \frac{\varphi}{\tan(\gamma)} \end{pmatrix} \tag{8.20}$$

where

$$\varphi = \omega t \tag{8.21}$$

Hence, the corresponding velocity is given by differentiation of equation (8.20) with respect to time:

$$\vec{U} = \frac{\partial \vec{P}}{\partial t} = R\omega \begin{pmatrix} -\sin(\omega t) \\ \cos(\omega t) \\ \frac{1}{\tan(\gamma)} \end{pmatrix} \tag{8.22}$$

and the absolute velocity is given as

$$\begin{aligned} u_p = \left|\vec{U}\right| &= R\omega\sqrt{\frac{1}{\tan^2(\gamma)} + 1} \\ &= \frac{R\omega}{\sin(\gamma)} \end{aligned} \tag{8.23}$$

Assume a particle moving with a speed (u_c) along the centreline of the pipe, representing the mean fluid velocity, without any slip condition along the wall boundary (uniform velocity distribution). Hence, u_c must be equal to the **k** velocity component of $\vec{U}$, which gives

$$u_c = \frac{R\omega}{\tan(\gamma)} \tag{8.24}$$

In IRBTs the flow field is affected by a swirl, which leads to a higher wall friction. The changes in the wall friction in relation to a pipe without rifles, can approximately be expressed by the relationship between absolute velocities of u_p and u_c defined by Π and named: *Slip Correction Factor*, due to internal rifles.

$$\Pi = \frac{u_p}{u_c} = \frac{1}{\cos(\gamma)}, \text{ valid for } \pi/2 > \gamma > 0 \tag{8.25}$$

Boiler pipes without rifles ($\gamma = 0$) gives $\Pi = 1$, which means that the slip velocity is unchanged. Equation (8.25) does not take into account the effect of dissipation of the swirl, caused by a too high fin angle (γ). The ultimate situation is where γ is close to $\pi/2$ (perpendicular to the axial direction **k**) so that the pipe cross-sectional area will be reduced relatively to the fin height versus pipe radius and even the friction coefficient will increase vigorously. When the flow is rotating, caused by the internal rifles, the interfacial pressure jump can be estimated on the basis of the pressure reduction caused by the rotating flow. The slip velocity is adjusted according to the increased wall shear stress initiated by the screw path

along the internal rifles in the channel. The radial velocity in a rotating flow can be expressed by:

$$\frac{\partial P}{\partial r} = \frac{\rho V_r^2}{r} \tag{8.26}$$

where V_r is the radial velocity, indirectly given by equation (8.24) and is assumed to be proportional to ω; see figure (8.8). The radial distance is measured from the centre axis of the pipe (**k**). The distribution of V_r may be estimated. Two boundary conditions may exist: $V_r(0) = 0$ and $V_r(R) = R\omega$, which is inside the boundary layer indicated in figure (8.8). Hence we require a flow distribution given by:

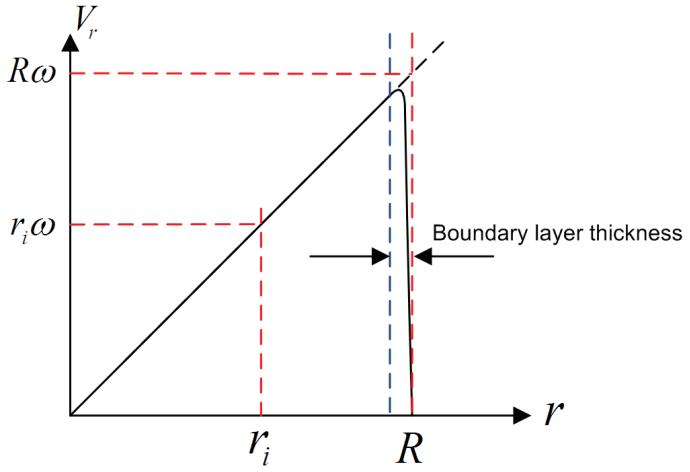

Figure 8.8.: Radial velocity as function of the pipe radius.

$$V_r(r) = \omega r,\ r \in [0, R[\tag{8.27}$$

By integrating equation (8.27) above the two layers and substituting r_i with equation (8.6) we obtain the relationships below:

$$\begin{aligned}\Delta P = P_g - P_l &= \int_0^R \frac{\rho V_r^2}{r} dr = \int_0^{r_i} \frac{\rho_g V_r^2}{r} dr + \int_{r_i}^R \frac{\rho_l V_r^2}{r} dr \\ &= \omega^2\left(\frac{1}{2}\rho_g r_i^2 + \frac{1}{2}\rho_l R^2 - \frac{1}{2}\rho_l r_i^2\right) = \frac{1}{2}\omega^2\left(r_i^2(\rho_g - \rho_l) + R^2\rho_l\right)\end{aligned} \tag{8.28}$$

The swirl generates a centrifugal acceleration given as: $a_{ck} = \frac{1}{2}\omega^2 r_{ck}\Theta$ where $k \in \{g, l\}$. The coefficient Θ is a function of the fin geometry in the IRBT as well as the helix angel γ, stated in equation (8.19). A qualified guess of Θ is estimated to 0.75, which is equivalent to the statement that only 75 % of the theoretically

possible rotational kinetic energy is converted to rotational forces in the form of a resultant acceleration. The rotation speed is correlated to ω. The area based centre radius, r_{ck}, is calculated in analogy to the momentum of inertia for mechanical objects surrounded by two cylinders (r_i and r_j) where

$$r_{ck} = \sqrt{\frac{r_i^2 + r_j^2}{2}} \tag{8.29}$$

For the two phases, r_{ck} is expressed by equations (8.30) and (8.31).

$$r_{cg} = \sqrt{\frac{r_i^2 + 0^2}{2}} = R\sqrt{\varepsilon_g/2} \tag{8.30}$$

$$r_{cl} = \sqrt{\frac{R^2 + r_i^2}{2}} = R\sqrt{\frac{1+\varepsilon_g}{2}} = R\sqrt{1-\varepsilon_l/2} \tag{8.31}$$

8.2.3. Constitutive relations

The wall friction force acting on the fluid element is $F_{w,k}$, and is the force acting on the fluid in contact with the wall by the length scale a_w, i.e., $F_{w,l}$ for the liquid layer and $F_{w,g}$ for the gas phase. Note that the forces are weighted by $1/a_w$, which denotes the length scale of the heated wall surface area per unit volume (a_w=$\frac{S_w}{A}$). In a similar manner, a_i has the physical meaning of the interfacial area per unit volume (a_i=$\frac{S_i}{A}$). The wall friction force is given by (8.32):

$$F_{w,k} = \frac{\tau_{w,k}}{a_w} \tag{8.32}$$

where $\tau_{w,k}$ is the wall shear stress, and subscript k denotes the phase in contact with the wall (k=l or g). The wall shear stress is typically expressed as:

$$\tau_{wk} = \frac{1}{2} f_{wk} \rho_k |u_k| u_k, \; k = l \vee g \tag{8.33}$$

where the f_{wk} denotes the wall friction factor, which can be determined by, i.e., the Colebrook and White formulation:

$$f_w : \begin{cases} \frac{1}{\sqrt{f_w}} = -2\log_{10}\left(\frac{k}{3.7\,d_i} + \frac{2.51}{Re\,\sqrt{f_w}}\right) & \text{for } Re > 4000 \\ f_w = \frac{64}{Re} & \text{for } Re \leq 2000 \end{cases} \tag{8.34}$$

where k is the pipe inner roughness thickness, measured in meters and the Reynolds number, *Re*, is given by (A.14). In the two-phase region the friction factor is adjusted according to a two-phase multiplier, formulated by [77]. In that case f_w is based on fluid properties for saturated liquid. The shear stress between the wall and the phase k is described by τ_{wk}, where the subscript k denotes the phase in contact with the wall, i.e., u_g for the gas and u_l for the liquid. The term F_i represents the interface force per unit mixture volume and is positive for $u_g > u_l$. The parameter F_{vm} is the virtual mass force and occurs only when one of the phases accelerates with respect to the other phase. The motion of the discontinuous phase results in the acceleration of the continuous phase as well. A simple and widely used expression for one-dimensional separated flow is given by [78] and is:

$$F_{vm} = -C_{vm} \cdot \left(\frac{\partial u_g}{\partial t} + u_g \frac{\partial u_g}{\partial z} - \frac{\partial u_l}{\partial t} - u_l \frac{\partial u_l}{\partial z} \right) \tag{8.35}$$

where $C_{vm} = C \cdot \varepsilon_g \cdot \varepsilon_l \cdot \bar{\rho}$ and C≈1. In terms of magnitude F_{vm} is significant only if the gas phase is dispersed. The exact form of the virtual mass force term is only known from theory for some simple and idealized conditions; see [79]. Similarly the interfacial shear stress in-between the phases can be formulated as:

$$\tau_i = \frac{1}{2} f_i \rho_i \left| u_g - u_l \right| (u_g - u_l) \tag{8.36}$$

where $\rho_i = \rho_g \cdot \varepsilon_g + \rho_l \cdot \varepsilon_l$ expresses the density of the mixing fluid at the interface (I). Correspondingly the friction factor ($f_i = f_g \cdot \varepsilon_g + f_l \cdot \varepsilon_l$) is given as an averaged value of the respective friction factors of pure liquid and gas. Terms related to the interfacial drag force F_i are responsible for a velocity relaxation process, which is expressed in equation (8.41). The interfacial drag force may be written in the same form as the pressure relaxation term: a relaxation coefficient multiplied by the velocity difference, $F_i = \lambda (u_l - u_g)$, where λ is a positive parameter or function with a finite value.

8.2.4. Jump conditions

The interfacial heat flux and the mass exchange rate Γ_g across the interface section covered by the perimeter S_i are linked through the following jump condition at the interface, where any contribution from kinetic energies was ignored ($e_k \approx h_k$):

$$\Gamma_g \cdot (h_{ig} - h_{il}) = a_i \left(q''_{ig} - q''_{il} \right) \tag{8.37}$$

where h_{ig} and h_{il} are the saturated enthalpies of the liquid and steam layers at the interface cross-section line. The thermal jump appears when the fluid is

entering the two-phase region in the water/steam table, see [80]. The following assumptions are made: the thermal-hydraulic conditions along the interface are saturated fluids; hence we have a simple relationship between mass transfer and latent heat of evaporation h_{lg} at the interface formulated by:

$$\Gamma_g \cdot h_{lg} = a_i \cdot \left(q''_{ig} - q''_{il} \right) \tag{8.38}$$

If we consider a control volume enclosing the interface and having an infinitesimal thickness, equation (8.38) constitutes an energy balance of this control volume. In the presence of superheated steam and sub-cooled liquid, there will be no heat transfer initiated by convective transport of evaporated fluid by Γ_g. Instead there will be an intense heat transfer created by the temperature gradient in-between the two layers. Here q''_{ig} and q''_{il} will be responsible for the heat transfer from the sub-cooled liquid to the interface, where a fraction of the heat flux penetrates the liquid and is used to heat up the gas. The remaining fraction produces saturated steam at the interface.

8.3. Two-layer model setup

With the above model setup we have ten unknowns and only six conservation equations for mass, momentum and total energy, given by (8.1) to (8.17). Furthermore we need two equations of state (EOS) - one for each phase, detailed in Chapter 6, and the equation for the sum of the volume fractions is given by equation (8.4). To close the system of equations, we need one more equation. Here we have two options. The first opportunity is to model the pressure difference between the two phases, by means of empirical models for the surface tension, described in section (8.3.5) and further detailed in [73], or by a model of the pressure difference in-between the two phases in relation to the pressure drop between the two phases initiated as a result of IRBT. An alternative way is to formulate an additional transport equation for void fraction, which is done in [75], [74] and [63]. The void fraction is convected by a speed equaling the interfacial speed of the fluid, and the source term is described by a relaxation process, giving the possibility of handling singularities by shock phenomena (Riemann surface).

8.3.1. Two-layer model with relaxation

We start our model description with focus on the six conservation equations, given by equations (8.1), (8.2), (8.8), (8.9), (8.16) and (8.17), supplemented by a transport equation for void fraction, as proposed by [75], [74] and [63] . The seventh transport equation is formulated as transport of ε_g with a convective

velocity given by the interface rate u_i and a relaxation term as a production term. The transport equation for the void fraction (ε_g) is given by:

$$\frac{\partial \varepsilon_g}{\partial t} + u_i \frac{\partial \varepsilon_g}{\partial z} = -\mu(P_l - P_g). \tag{8.39}$$

Here μ is a pressure relaxation parameter, with $\mu \to \infty$ to instantaneous relaxation. The resulting system can be summarized in a compact vector notation in the form of a *system of balance laws* (SBL), given by:

$$\frac{\partial \Phi(z,t)}{\partial t} + \frac{\partial f(\Phi(z,t))}{\partial z} = S(\frac{\partial \Phi}{\partial z}, \Phi(z,t)), \;\; \Phi \in R^n, n = 7, \;\; t \geq 0 \wedge \;\; z \in \Omega. \tag{8.40}$$

where the system may be written in a conservative form

$$\frac{\partial \Phi(z,t)}{\partial t} + \frac{\partial f(\Phi(z,t))}{\partial z} = S_{ex} + S_r + S_c, \;\; \Phi \in R^n, n = 7, \;\; t \geq 0 \wedge \;\; z \in \Omega \tag{8.41}$$

Here the source terms are dependent on $\frac{\partial \Phi}{\partial z}$ and $\Phi(z,t)$. The SBL can also be written in a non-conservative form

$$\frac{\partial \Phi(z,t)}{\partial t} + \mathbf{J} \frac{\partial \Phi(z,t)}{\partial z} = S_r + S_c, \;\; \Phi \in R^n, n = 7, \;\; t \geq 0 \wedge \;\; z \in \Omega \wedge \;\; z \in \Omega \tag{8.42}$$

where S_{ex} in equation (8.40) denotes the exchange terms between the phases, S_r the source terms describing relaxation of velocity and pressure, and S_c denotes the gravitational and virtual forces. In our work, we neglect the virtual mass force, or else it could be included in S_{ex}. The vector function f denotes the conservative flux terms, while $\mathbf{J}(\frac{\partial \Phi}{\partial z}, \Phi(z,t))$ includes the Jacobian terms, $\frac{\partial f}{\partial \Phi}$, like (8.46). The independent variable Φ and the corresponding flux vector are now given as:

$$\Phi = \begin{pmatrix} \varepsilon_g \\ \varepsilon_g \rho_g \\ \varepsilon_g \rho_g u_g \\ \varepsilon_g \rho_g E_g \\ \varepsilon_l \rho_l \\ \varepsilon_l \rho_l u_l \\ \varepsilon_l \rho_l E_l \end{pmatrix}, \;\; f(\Phi) = \begin{pmatrix} u_i \varepsilon_g \\ \varepsilon_g \rho_g u_g \\ \varepsilon_g \rho_g u_g^2 + \varepsilon_g p_g \\ \varepsilon_g u_g (\rho_g E_g + p_g) \\ \varepsilon_l \rho_l u_l \\ \varepsilon_l \rho_l u_l^2 + \varepsilon_l p_l \\ \varepsilon_l u_l (\rho_l E_l + p_l) \end{pmatrix}$$

The source vector can be divided into three parts describing relaxation, the gravitational effects and the non-conservative exchange terms, given by:

$$S_{ex}(\Phi) = \begin{pmatrix} \varepsilon_g \frac{\partial u_i}{\partial z} \\ 0 \\ p_i \frac{\partial \varepsilon_g}{\partial z} \\ p_i u_i \frac{\partial \varepsilon_g}{\partial z} \\ 0 \\ p_i \frac{\partial \varepsilon_l}{\partial z} \\ p_i u_i \frac{\partial \varepsilon_l}{\partial z} \end{pmatrix}, \quad S_r(\Phi) = \begin{pmatrix} -\mu(p_l - p_g) \\ 0 \\ F_{d,g} \\ u_i F_{d,g} \\ 0 \\ F_{d,l} \\ u_i F_{d,l} \end{pmatrix}$$

and

$$S_c(\Phi) = \begin{pmatrix} 0 \\ \Gamma_g \\ \Gamma_g u_i + F_{c,g} + F_{s,g} \\ \Gamma_g E_g + u_i F_{c,g} + Q_i \\ \Gamma_l \\ \Gamma_l u_i + F_{c,l} + F_{s,l} \\ \Gamma_l E_g + u_i F_{c,l} - Q_i \end{pmatrix}$$

where E_k represents the total energy: E_k=e_k+1/2u_k^2. Note that equation (8.39) is rewritten due to the chain rule for differentiation.

8.3.2. Void fraction

The main problem in solving equation (8.41) is that the sound velocity is very high in pure liquid regions, typically in the range of 950-1550 [m/s]; hence, the corresponding eigenvalues belonging to (8.41) become large. Consequently, the corresponding matrix **J** in (8.42) must be chosen with large diagonal elements, which in turn introduce a strong dissipative structure. This leads to a strong 'smearing out' effect of the volume fraction contact discontinuities and, by that, the scheme becomes unsuitable for simulations of typical two-phase mass transport processes. The contact discontinuities will be discussed in detail in section 8.3.4. Hence gradients of ε_g become difficult to compute accurately if $\varepsilon_g \in [0, 1]$, and errors that are introduced may destabilize the computation. Therefore we introduce a transformation of ε_g in order to stabilize the computation based on [81] and define the variable

$$\beta \equiv \ln(\frac{\varepsilon_g}{\varepsilon_l}), \quad \text{or} \quad \varepsilon_g = \frac{e^\beta}{1+e^\beta}. \tag{8.43}$$

Hence the corresponding partial derivative of β with respect to ε_g is

$$\frac{\partial \varepsilon_g}{\partial \beta} = \varepsilon_g \cdot \varepsilon_l. \tag{8.44}$$

Now ε_g is guaranteed to be in the range of $\varepsilon_g \in]0, 1[$ and is not subject to negative values even if there are oscillations in β. The Hamilton-Jacobi equation for β is the same as the equation for ε_g, namely, $\beta_t + H(\beta_x) = 0$ with the Hamiltonian $H(\Phi) = u_i \Phi$.

8.3.3. Stability analysis of the two-layer model

The last thing to do when developing a model of two-phase flow is to analyse the model for stability. The two-fluid approach contains non-conservative terms (i.e. $P_i \frac{\partial \varepsilon}{\partial z}$), which do not necessarily remain hyperbolic in all situations, meaning that the initial value problem may be 'ill-posed' for a large class of initial conditions. In this work, the system is composed of seven partial differential equations: one transport equation for the volume fraction, two for the mass of each fluid, two for the momentum of each fluid and two for the energy of each fluid. Several definitions of the interfacial velocity and of the interfacial pressure have been proposed in different references mentioned above [75], [74] and [63]. Here we adopt an original approach, based on the analysis of the one-dimensional Riemann problem and on the definition of discontinuous solutions in order to deal with non-conservative products and to ensure the maximum principle for the volume fraction, as presented in [75] . We restrict ourselves to the one-dimensional framework. The following mathematical analysis is done without any source terms (Γ_k, F_d and Q_i). Rewriting the equations due to the primitive variables (dependent variables), given by $W = (\varepsilon_g, \rho_g, u_g, P_g, \rho_l, u_l, P_l)^T$, where

$$\frac{\partial W}{\partial t} + \mathbf{J}_w \frac{\partial W}{\partial z} = 0 \tag{8.45}$$

the corresponding Jacobian matrix $\mathbf{J}_w$ is given by [75] as:

$$\mathbf{J}_w = \begin{pmatrix} u_i & 0 & 0 & 0 & 0 & 0 & 0 \\ \frac{\rho_g}{\varepsilon_g}(u_i - u_g) & u_g & \rho_g & 0 & 0 & 0 & 0 \\ \frac{P_g - P_i}{\varepsilon_g \rho_g} & 0 & u_g & \frac{1}{\rho_g} & 0 & 0 & 0 \\ \frac{\rho_g c_{gi}^2}{\varepsilon_g}(u_i - u_g) & 0 & \rho_g c_g^2 & u_g & 0 & 0 & 0 \\ \frac{\rho_l}{\varepsilon_l}(u_i - u_l) & 0 & 0 & 0 & u_l & \rho_l & 0 \\ \frac{P_l - P_i}{\varepsilon_l \rho_l} & 0 & 0 & 0 & 0 & u_l & \frac{1}{\rho_l} \\ \frac{\rho_l c_{li}^2}{\varepsilon_l}(u_i - u_l) & 0 & 0 & 0 & 0 & \rho_l c_l^2 & u_l \end{pmatrix} \tag{8.46}$$

where

$$c_k^2 = \frac{\frac{P_k}{\rho_k^2} - \frac{\partial e_k}{\partial \rho_k}|_{P_k}}{\frac{\partial e_k}{\partial P_k}|_{\rho_k}} \tag{8.47}$$

and

$$c_{ki}^2 = \frac{\frac{P_i}{\rho_k^2} - \frac{\partial e_k}{\partial \rho_k}|_{P_k}}{\frac{\partial e_k}{\partial P_k}|_{\rho_k}} \tag{8.48}$$

represents the sound of speed of phase k and the sound of speed of the interface, respectively. The eigenvalues of $\mathbf{J}_w$ are precisely the solutions λ_i, i $\in$ (1,..,m) to the equation: det($\mathbf{J}_w$-$\Lambda\cdot$ $\mathbf{I}$) = 0, where Λ is a diagonal matrix holding λ_i. According to [75] the eigenvalues are given as

$$\bar{\lambda} = \begin{pmatrix} u_i \\ u_g \\ u_g + c_g \\ u_g - c_g \\ u_l \\ u_l + c_l \\ u_l - c_l \end{pmatrix}$$

Thanks to this result, the eigenvalues are all real values meaning the hyperbolic SBL, given by (8.40), is stable for $t \geq 0 \wedge\ z \in \Omega$. The approximation of the convective terms and source terms is cast into a two-step solution algorithm, using a splitting method as described in [63], [74] and [75]. The convective part is computed using Finite Volume schemes (Finite difference in 1D) adapted to the non-conservative frame. One method, based on the fifth-order WENO scheme, is tested and used here. Concerning the relaxation terms (drag force and pressure relaxation), we propose an approximation in agreement with the properties satisfied by smooth solutions. Several numerical tests are performed to compare the robustness and the accuracy of both the splitting method (when computing shock tube test cases) and the *moving contact discontinuity* problem.

8.3.4. Relaxation terms

Here we deduce a proposal for solving the seven coupled partial differential equations (8.41), assuming that the six fluid transport equations have a hyperbolic nature, as prescribed in section 8.3.3. The solver algorithm is based on a very little dissipative solver (fifth-order WENO) coupled with a split-step algorithm, based on a pressure and velocity relaxation principle, which draws the transport

interface seen in the two-phase flow. The method is used in particular in [63], [74] and [75]. Except under certain specialized conditions of homogeneous flow, interacting two-phase media typically involve non-equilibrium processes. Differences in velocity, pressure and temperature promote transfer of momentum, energy and mass between the phases. With each process is associated a rate, which determines the length of time scale for equilibration of the process. If the rate is rapid the process is in equilibrium over much of the flow, except perhaps in certain thin regions, the relaxation zones. Equilibrium with respect to even one of the processes renders the mathematical model simpler, because the corresponding relaxation zone can then be treated as a surface of discontinuity, across which the equilibrating quantity jumps. This relaxation principle is well described in the literature; see [63], [74] and [75].
Across thin zones it reduces to at most a lower-order set of ordinary differential equations which must be integrated, i.e., the structure resolved, in order to relate the state behind to the state ahead. Unlike a conservative system, the jump conditions are now very much a function of the internal physics of the discontinuity. They cannot be determined a priori, and therefore impose a greater burden on the designer of computational schemes, if one wishes to capture the thin structures without resolving them. The EOS should be integrated into this process. Source terms act only locally in equation (8.40), and can therefore not increase the characteristic speeds of information, determined by the eigenvalues of the governing system; this should hold also in the stiff limit ε -> 0 according to equation (9.70). In the present section, we outline the procedure for handling the relaxation processes we are interested in. For two-phase flows, a general relaxation model was proposed by Baer and Nunziato [82]. Several authors ([63], [83], [84], [85] and [86]) have used relaxation systems to construct numerical schemes for various two-phase flow models, based on ideas originally suggested by Jin and Xin [87]. The compressible two-pressure, two-velocity flow model is time-hyperbolic at all flow regimes according to [63], but allows for the phases to be out of thermodynamic equilibrium. Restoring equilibrium between the phases via relaxation processes further introduces interphase exchange terms, for example, exchange terms due to velocity non-equilibrium (frictional drag) or due to pressure non-equilibrium. In addition, the formulation of a transport equation for the void fraction is included. Here the transport of the front (Riemann problem) is based on the advection of the corresponding interface layer (u_i). When the velocity and pressure related source/sink terms (S_r) involve finite rate law, meaning the values of μ and λ are not infinite, the integration can be performed by an appropriated time integrator. The distinction appears when the so called relaxation terms for u and p are infinite, which happens over a Riemann front. The relaxation terms, expressed by μ and λ, are particularly important since they allow solution of the boundaries at the interfaces in-between two layers. This

step is of paramount importance for the solution of (8.41).

We use a method based on [63] where a decomposition of the system (8.41) is done in two parts and allows us to apply advanced numerical techniques (WENO) as described in the next section and which are successfully applied to single-phase flows (or compressible Euler equations). The time integration may be performed by a split-step algorithm. Let us briefly outline the main steps of the method. Being given the state variables at time $t^n, \varepsilon_k^n, \rho_k^n, u_k^n$ and E_k^n, we proceed as follows.

1. (Hydro-dynamical step) First we perform the time integration of the thermo-hydraulic systems using the usual approximate Riemann solver and then we include the source terms, S_{ex} and S_c, in equation (8.41).

2. Here the time integration accounts for the relaxation effects, given by S_r, in order to restore the equality of the pressures between the two phases.

In principle we are solving the ODE given by equations (8.51) with the two source terms, S_{ex} and S_c, and (8.59) with the source term S_r.

Let Φ_j^n denote the numerical approximation to the cell average of the vector of unknowns $\Phi(x,t_n)$ in control volume j at time step n. With Φ_j^n as an initial value, the solution at the next time step, Φ_j^{n+1} , can be found as follows:

1. Find Φ_j^* as the solution of the hyperbolic part of (8.41) at t_{n+1} with the source terms, S_{ex} and S_c.

2. Find Φ_j^{n+1} as the solution of the relaxation system (8.51) at t_{n+1} with Φ_j^* as the initial value.

For step 1, a so-called WENO scheme will be employed, and it is detailed in section 9.5. For step 2, a numerical solver for ordinary differential equations will be used for finite-rate relaxation. For infinite/instantaneous relaxation, it is more efficient to employ the procedure detailed in the next two subsections. Specific values for the pressure-relaxation parameter, μ, are most often unknown. However, the assumption of equal phasic pressures is widespread, and can be accounted for by setting μ to a large value. It is then more efficient to solve the problem directly than to solve the system (8.42) of partial differential equations. After the hyperbolic step, the volume fraction is modified so as to render the two phasic pressures equal, keeping $\varepsilon_k\rho_k$ and $\varepsilon_k\rho_k u_k$ constant. Munkejord, [88] solved a second-degree equation for the volume fraction. In this study, however, it was found to be a more robust approach to solve a second-order equation for the pressure instead.

Pressure relaxation

A wave propagation in a two-phase fluid is in a non-equilibrium pressure state ($p_g \neq p_l$), and a pressure relaxation process will develop so that the pressure will tend toward equilibrium, ($p_g = p_l$). Locally, after wave propagation, the pressure relaxation process undergoes a volume variation, given by (8.49), where the energy interphase exchange term ε_i is included to act as an interfacial source term, or pressure-relaxation term in the current jargon:

$$\frac{\partial \varepsilon_g}{\partial t} = \mu(p_l - p_g) \tag{8.49}$$

where μ is a positive pressure-relaxation parameter, named the dynamic compaction viscosity [$Pa^{-1}s^{-1}$]. This volume variation induces energy variations due to the interfacial pressure work, given by [63]:

$$\begin{aligned} \frac{\partial \varepsilon_g \rho_g E_g}{\partial t} &= \mu p_i(p_l - p_g) \\ \frac{\partial \varepsilon_l \rho_l E_l}{\partial t} &= -\mu p_i(p_l - p_g) \end{aligned} \tag{8.50}$$

The relaxation terms may become large. Therefore, the equation system (8.41) is split in two, and solved using a fractional-step technique. The hyperbolic part of the system is (8.41) with $\lambda \equiv 0$ and $\mu \to \infty$. The remainder is the relaxation part:

$$\begin{aligned} &\frac{\partial}{\partial t}(\varepsilon_g) = -\varepsilon_i, \quad \frac{\partial}{\partial t}(\varepsilon_g \rho_g) = 0, \\ &\text{and} \\ &\frac{\partial}{\partial t}(\alpha_l \rho_l) = 0, \quad \frac{\partial}{\partial t}(\varepsilon_g E_g) = p_i \varepsilon_i. \end{aligned} \tag{8.51}$$

The equation is derived by looking at the continuity and energy equation in (8.51). Thus we obtain

$$\frac{\partial}{\partial t}\left(\varepsilon_g \rho_g u_g^2\right) = 0 \tag{8.52}$$

and hence

$$\frac{\partial}{\partial t}(\varepsilon_g \rho_g e_g) = -p_i \frac{\partial}{\partial t}(\varepsilon_g) \tag{8.53}$$

which can be integrated to give an expression for the equilibrium pressure p, where $p_i \approx (p + p_i^*)/2$. In a similar way we can formulate an expression for the liquid phase. Having two expressions like (8.53) and the assumption of an infinitely fast pressure relaxation (μ=∞) implies that the final pressure is common

to both phases: p=p_g=p_l; hence we find a positive solution for p by solving equation (8.54) by an iterative procedure:

$$\varepsilon_g \rho_g e_g(\rho_g, p) + \varepsilon_l \rho_l e_l(\rho_l, p) = \varepsilon_g^o \rho_g^o e_g^o + \varepsilon_l^o \rho_l^o e_l^o \tag{8.54}$$

where the internal energy is a function of density and pressure. If we assume a simple EOS, such as the stiffness equation given by equation (6.6), we can get the relaxation pressure analytically by inserting the expression for $\rho_k e_k$ in equation (8.53). Hence we get the two equations below, which by eliminating the pressure p and using ε_g=$1-\varepsilon_l$

$$\varepsilon_g \frac{p+\gamma_g p_{\infty,g}}{\gamma_g - 1} = \varepsilon_g^o \rho_g^o e_g^o - \bar{p}_i(\varepsilon_g - \varepsilon_g^o) \tag{8.55}$$

$$\varepsilon_l \frac{p+\gamma_l p_{\infty,l}}{\gamma_l - 1} = \varepsilon_l^o \rho_l^o e_l^o + \bar{p}_i(\varepsilon_g - \varepsilon_g^o) \tag{8.56}$$

yields a quadratic equation in ε_g and the solution that satisfies $\varepsilon_g \in [0,1]$ is the one which gives us the relaxation pressure. The solution to ε_g is given as:

$$\varepsilon_g = \frac{-a_1 + \sqrt{a_1^2 - 4a_0 a_2}}{2a_0}, \tag{8.57}$$

where

$$\begin{aligned}
a_0 &= (\gamma_g - \gamma_l)\bar{p}_i + \gamma_g P_{g,\infty} - \gamma_l P_{l,\infty} \\
a_1 &= -\bar{p}_i \varepsilon_g^o (\gamma_g - \gamma_l) - \bar{p}_i(\gamma_g - 1) - (\gamma_g - 1)\varepsilon_g^o \rho_g^o e_g^o \\
&\quad - (\gamma_l - 1)\varepsilon_l^o \rho_l^o e_l^o + \gamma_l P_{l,\infty} - \gamma_g P_{g,\infty} \\
a_2 &= (\gamma_g - 1)(\varepsilon_g^o \rho_g^o e_g^o + \bar{p}_i \varepsilon_g^o)
\end{aligned}$$

The coefficient a_0 will always be positive for $\gamma_g > \gamma_l$, $a_1 < 0$ for $\gamma_g > 1$ and $\gamma_l > 1$ and finally $a_2 > 0$ for $\gamma_g > 1$.

Velocity relaxation

In this subsection, the momentum-source term τ_i is included to act as an interfacial drag term, or velocity-relaxation term in the current jargon:

$$\tau_i = \lambda(u_l - u_g) \tag{8.58}$$

where λ is a velocity-relaxation parameter. The instantaneous velocity-relaxation procedure can also be applied after the hyperbolic step, or after the instantaneous pressure-relaxation step, if applicable.

$$\frac{\partial}{\partial t}(\varepsilon_g) = 0, \quad \frac{\partial}{\partial t}(\varepsilon_g \rho_g) = 0, \quad \frac{\partial}{\partial t}(\varepsilon_g \rho_g u_g) = \tau_i,$$
and
$$\frac{\partial}{\partial t}(\varepsilon_g E_g) = u_i \tau_i, \quad \frac{\partial}{\partial t}(\varepsilon_l \rho_l) = 0, \quad \frac{\partial}{\partial t}(\varepsilon_l \rho_l u_l) = -\tau_i, \quad \frac{\partial}{\partial t}(\varepsilon_l E_l) = -u_i \tau_i. \tag{8.59}$$

It is immediately clear from equation (8.59) that $\varepsilon_k \rho_k$=Const, k $\in$ {g,l}. Combining the mass and momentum equations of equation (8.59) for each layer yields the two ODEs

$$\begin{aligned} \frac{\partial u_g}{\partial t} &= \frac{\tau_i}{\varepsilon_g \rho_g}, \\ \frac{\partial u_l}{\partial t} &= -\frac{\tau_i}{\varepsilon_l \rho_l} \end{aligned} \tag{8.60}$$

Subtracting the two differential equations in (8.60) from each other and integrating then yields the result

$$u_i - u_g = (u_l^* - u_g^*) \exp\left(-\lambda \left[\frac{1}{\varepsilon_g \rho_g} - \frac{1}{\varepsilon_l \rho_l}\right] t\right) \tag{8.61}$$

where the superscript * represents the solution after the thermo-hydraulic time step. It is clear that when λ tends to infinity for a finite time increment t, u_g tends to u_l for λ being positive. Adding the two contributions in equation (8.60) results in

$$\varepsilon_g \rho_g \frac{\partial u_g}{\partial t}) + \varepsilon_l \rho_l \frac{\partial u_l}{\partial t} = 0. \tag{8.62}$$

which can be integrated to

$$\varepsilon_g \rho_g (u_g - u_{g,0}) + \varepsilon_l \rho_l (u_l - u_{l,0}) = 0 \tag{8.63}$$

If the velocity relaxation is infinitely fast, the common velocity can be expressed by the relaxed (mixture) velocity

$$u = u_g = u_l = \frac{\varepsilon_g \rho_g u_g^* + \varepsilon_l \rho_l u_l^*}{\varepsilon_g \rho_g + \varepsilon_l \rho_l} \tag{8.64}$$

where the superscript * denotes the initial value supplied to the velocity-relaxation procedure. This is the mass-weighted velocity or the interface velocity u_i.

Evaluation of relaxation schemes

The evaluation of the two-phase schemes is rather complex. We have selected one problem, that shows the challenge in modelling void waves, using a very minimally dissipative fifth-order WENO scheme for solving the PDEs. The initial data are listed below:

$$\begin{aligned} u_g &= u_l = 1.0, & p_g &= p_l = 1.0, \\ \gamma_g &= 1.4, & \gamma_l &= 1.2, \\ (\rho_g)_L &= 2.0, & (\rho_g)_R &= 1.0, \\ (\rho_l)_L &= 1.0, & (\rho_l)_R &= 2.0, \\ (\varepsilon_g)_L &= 0.1, & (\varepsilon_g)_R &= 0.9. \end{aligned} \tag{8.65}$$

The data corresponds to a void wave which is also a contact surface in each phase. The wave separates the two phases that are in mechanical equilibrium. The model uses an EOS based on a simple stiffness equation, given by (6.6). The results are illustrated in figure (8.9), which confirms that the mechanical equilibrium between the phases is preserved for a moment, with pressures and velocities remaining uniform. By adding diffusion (0.01 $[m^2/s]$) to the momentum equations, we

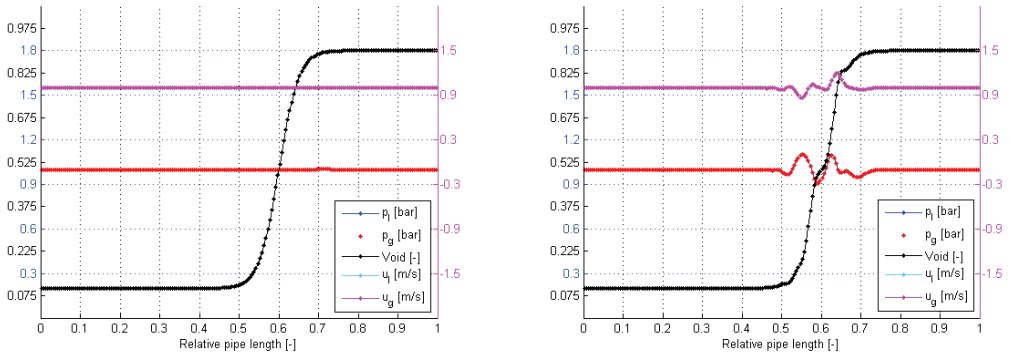

Figure 8.9.: Solutions of propagation of a void wave, with (left) and without (right) diffusion, after 2 [s] of simulation.

introduce a more smooth solution, which after many time steps preserves the uniform pressure and velocity profiles.

Summary

In this chapter we have formulated fundamental two-phase flow models, based on a two-layer model that can be used for both horizontally and vertically oriented evaporator tubes. The initial model consists of two separate fluid layers, which describe the gas or the liquid phase in a two-phase flow. The models are based on a traditional transport equation, where the source terms ensure the communication between the two phases. Related studies show how the two-layer model can be solved with respect to shock phenomena, and we outline a velocity and pressure relaxation model. We performe a simple test case to illustrate the relaxations principle, and we see for higher-order schemes, which are very little dissipative, that minor fluctuations appear around the front, after a few thousand time steps. By applying artificial diffusion, we achieve a uniform profile of pressure and speed. It is recommended to use a more diffusive scheme, when the seven-equation model has to be solved, or at least add artificial diffusion to the very little dissipative WENO scheme. The literature outlines several different eigenvalue analyses [89], [90] and [91] of two-layer fluid flow problems, and one is particularly worth mentioning, because the analysis can be transformed into a set of dependent variables, similar to the dependent variables in equation (8.42). This allows us to estimate both the stability conditions and the transport rates linked to the model setup.

8.3.5. Surface tension

This section shows the formulation of a two-layer flow model, where the pressure difference between the two phases is related to the surface tension of the fluid. We perform an eigenvalue analysis in this context, showing a relationship between the two sets of primitive variables, which provides a coupling between the formulation released in section (8.42) and the system in (8.69), and hereby demonstrates that the system of equations in (8.42) has a hyperbolic nature. In situations without rotating currents and with a moderate inclination of the evaporator tube, we will see a horizontal stratification of the flow pattern where the surface tension between the two phases has an impact on the pressure distribution between the two phases. It is well known that the mathematical property of the governing equations is improved by introducing physical terms in the governing equations. Reference [89], for example, adds the surface tension equation to the governing equations, and Travis [90] took account of the viscous stresses in the momentum equations. The analysis revealed that to ensure real eigenvalues of the governing transport equations, the interfacial pressure had to be lower than the bulk pressure by an amount proportional to the square of the relative velocity. According to [75] there are two problems in particular for which the two-phase flow models are ill-conditioned:

- Relaxation phenomena behind a shock and pressure wave in two-phase mixtures.
- Interface conditions between pure fluids or mixtures.

Saurel [75] proposes separate ways to solve these problems. The first model describes the pressure between the two phases as:

$$
\begin{aligned}
&1)\ p_g - p_l = 0 \ \text{ if the fluids are perfect, leading to ill-posedness.}\\
&\qquad \text{due to loss of hyperbolicity}\\
&2)\ p_g + \frac{2\sigma}{R} - p_l = 0 \ \text{ if the surface tension effects are considered.}\\
&3)\ p_g + \tilde{p}(\varepsilon_g) - p_l = 0 \ \text{ if the mixture is composed of powder or gas}\\
&\qquad \text{A fourth option could be to utilize the knowledge of an internal}\\
&\qquad \text{rotating flow:}\\
&4)\ p_g - p_l = \omega R(\frac{\sqrt{\varepsilon_g}}{\rho_g} + \frac{1-\sqrt{\varepsilon_g}}{\rho_l}), \text{according to IRBT, equation(8.28).}
\end{aligned}
\tag{8.66}
$$

In this approach outlined by [92] , we consider both phases as compressible, where the pressures p_k are given by the appropriate equation of states, $p_k = p_k(e_k, \rho_k)$, and as proposed by Chung [73] and co-workers, the interfacial pressure jump terms are introduced based on the surface tension in the two-fluid momentum equations, where the system of equations manifests real eigenvalues in all the bubbly, slug, and annular flow regimes, when the interfacial pressure jump terms are expressed as a product of effective bulk moduli and the gradient of interfacial area density. I refer to Chung [73] for further details, but will for the sake of clarity mention the definition of surface thickness of a bubble, known as β

$$\beta \equiv \frac{2\sigma}{R_i}\frac{1}{L_g + L_l} = \frac{\delta}{2R_i} \tag{8.67}$$

where R_i, R_g and R_l are defined in figure (8.10) and equation (8.68). The phasic bulk moduli are given as: $L_g = \rho_g C_g^2$ and $L_l = \rho_l C_l^2$. We now assume a finite interfacial thickness δ between the two radii R_g and R_l.

$$p_g - p_l = \frac{2\delta}{R_g + \delta/2}\left(\frac{\sigma}{\delta}\right) \quad = \frac{2\delta}{R_l - \delta/2}\left(\frac{\sigma}{\delta}\right) \tag{8.68}$$

The surface tension σ is introduced in equation (E.65), and R is the averaged bubble radius. By introducing the definition $X_k \equiv (\frac{\partial \rho_k}{\partial p_k})_{u_k}$, $Y_k \equiv (\frac{\partial \rho_k}{\partial u_k})_{p_k}$ we

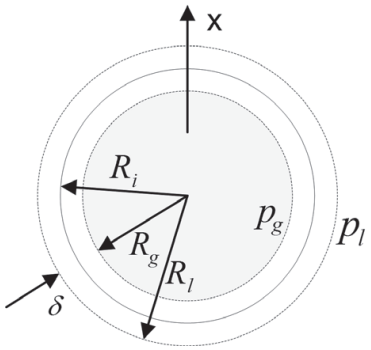

Figure 8.10.: Hypothetical sphere with an infinitesimal thickness δ.

get the identity $\frac{\partial p_g}{\partial x}=\frac{\partial p_l}{\partial x}$ which is derived from equation (8.68) for the equilibrium state of the bubble. Hence we can write the governing equations from [73]:

$$\mathbf{A}\frac{\partial \mathbf{U}}{\partial t}+\mathbf{B}\frac{\partial \mathbf{U}}{\partial z}=\mathbf{C}. \tag{8.69}$$

We define a set of independent variables given by $\mathbf{U}=[\varepsilon_g, p_g, u_g, u_l, E_g, E_l]^T$ and the left-hand side is simplified by $\mathbf{C}=[\phi_{c,g}, \phi_{c,l}, \phi_{m,g}, \phi_{m,l}, \phi_{e,g}, \phi_{e,l}]^T$, where the subscripts c, m and e stand for continuity, momentum and energy respectively. The belonging matrices are given as:

$$\mathbf{A}=\begin{pmatrix} \rho_g & \varepsilon_g X_g & 0 & 0 & \varepsilon_g Y_g & 0 \\ -\rho_l & \varepsilon_l X_l & 0 & 0 & 0 & \varepsilon_l Y_l \\ 0 & 0 & \varepsilon_g \rho_g & 0 & 0 & 0 \\ 0 & 0 & 0 & \varepsilon_l \rho_l & 0 & 0 \\ p_g & 0 & 0 & 0 & \varepsilon_g \rho_g & 0 \\ -p_l & 0 & 0 & 0 & 0 & \varepsilon_l \rho_l \end{pmatrix} \tag{8.70}$$

and

$$\mathbf{B}=\begin{pmatrix} \rho_g u_g & \varepsilon_g u_g X_g & \varepsilon_g \rho_g & 0 & \varepsilon_g Y_g u_g & 0 \\ -\rho_l u_l & \varepsilon_l u_l X_l & 0 & \varepsilon_l \rho_l & 0 & \varepsilon_l u_l Y_l \\ \beta L_g & \varepsilon_g & \varepsilon_g \rho_g u_g & 0 & 0 & 0 \\ -\beta L_l & \varepsilon_l & 0 & \varepsilon_l \rho_l u_l & 0 & 0 \\ p_g u_g & 0 & \varepsilon_g p_g & 0 & \varepsilon_g \rho_g u_g & 0 \\ -p_l u_l & 0 & 0 & \varepsilon_l p_l & 0 & \varepsilon_l \rho_l u_l \end{pmatrix} \tag{8.71}$$

Equation (8.69) can be transformed into

$$\frac{\partial \mathbf{U}}{\partial t} + \mathbf{G}\frac{\partial \mathbf{U}}{\partial z} = \mathbf{E} \tag{8.72}$$

where $\mathbf{G}=\mathbf{A}^{-1}\cdot\mathbf{B}$ and $\mathbf{E}=\mathbf{A}^{-1}\cdot\mathbf{C}$, and hence the governing equations can be written as:

$$\frac{\partial \mathbf{V}}{\partial t} + \mathbf{H}\frac{\partial \mathbf{V}}{\partial z} = \mathbf{M} \tag{8.73}$$

where the conservation vector $\mathbf{V}$ is given as:

$$\mathbf{V} = [\varepsilon_g\rho_g, \varepsilon_l\rho_l, \varepsilon_g\rho_g u_g, \varepsilon_l\rho_l u_l, \varepsilon_g\rho_g E_g, \varepsilon_l\rho_l E_l]^T \tag{8.74}$$

which can be identified as a subset of what we see in equation (8.42). Thus we have a unique coupling between two transformations of transport equations for two-layer fluid models. The belonging matrices are given as: $\mathbf{H}=\mathbf{J}\cdot\mathbf{G}\cdot\mathbf{J}^{-1}$, $\mathbf{M}=\mathbf{J}\cdot\mathbf{E}$ and $\mathbf{J}=\frac{\partial \mathbf{V}}{\partial \mathbf{U}}$. The eigenvalues of matrix $\mathbf{G}$ in equation (8.72) are determined by a sixth-order polynomial equation obtained by

$$\mathrm{Det}(\mathbf{G} - \bar{\lambda}\mathbf{I}) = 0. \tag{8.75}$$

Here is assumed that the relative surface thickness β is constant equal to 1.0 which leads to a sixth-order polynomial equation, having different analytical solutions depending on the pressure jump terms, expressed as a product of the effective bulk moduli L_i, L_o and the gradient of the interfacial area density X_k and Y_k; these correspond to different types of flow regimes. For further informations about the assumptions, see [73]. The eigenvalues can be calculated for bubbly flow:

$$\bar{\lambda}_{Bubbly} = \begin{pmatrix} u_g \\ u_l \\ u_g + C_g \\ u_g - C_g \\ u_l + C_l\sqrt{\frac{\rho_g C_g^2}{\varepsilon_l C_g^2\rho_g + \varepsilon_g C_l^2\rho_l}} \\ u_l - C_l\sqrt{\frac{\rho_g C_g^2}{\varepsilon_l C_g^2\rho_g + \varepsilon_g C_l^2\rho_l}} \end{pmatrix}$$

Slug flow:

$$\bar{\lambda}_{Slug} = \begin{pmatrix} u_g \\ u_l \\ u_g + C_g \\ u_g - C_g \\ u_l + C_l \\ u_l - C_l \end{pmatrix}$$

Annular flow:

$$\bar{\lambda}_{Annular} = \begin{pmatrix} u_g \\ u_l \\ u_g + C_g \\ u_g - C_g \\ u_l + C_l \sqrt{\frac{\varepsilon_l \rho_g C_g^2}{\varepsilon_l C_g^2 \rho_g + \varepsilon_g C_l^2 \rho_l}} \\ u_l - C_l \sqrt{\frac{\varepsilon_l \rho_g C_g^2}{\varepsilon_l C_g^2 \rho_g + \varepsilon_g C_l^2 \rho_l}} \end{pmatrix}$$

The first two eigenvalues $(\lambda_{1,2})=(u_g, u_l)$ represent the convective velocity of the gas and liquid phases, respectively. Eigenvalue $(\lambda_{3,5})$ represents approximately the sonic speeds in the gas and the liquid phase. For bubbly and slug flows, the sonic speed can be obtained by the void fraction weighting, due to [73]:

$$C_t = \frac{\lambda_3 \lambda_5}{\varepsilon_l \lambda_3 + \varepsilon_g \lambda_5} \tag{8.76}$$

The speed of sound is illustrated in figure (8.11). A calculation of the sound of speed, based on IAPWS-97, gives for saturated liquid and vapour at 95 [bar]: C_g(x=0)=475 [m/s] and C_l(x=1)=868 [m/s], rendering the following relationship for the local velocity of sound in bubbly and slug flows, as illustrated in figure (8.11). For the Annular flow regime, the individual phasic sonic speeds have to be used. In [73] the computed total and phasic sonic speeds are compared with the experimental data produced by Henry et al. [93]. For the bubbly flow, the total sonic speed agrees reasonably well with the experimental data in the void fraction range $0 < \varepsilon_g < 0.2$. The increasing deviation in the range of $\varepsilon_g > 0.2$ is probably caused by transition of the flow regimes. Additionally they conclude that the sonic speed of the water-air slug flow is in good agreement between the computed and experimental data in the entire void fraction range $0 < \varepsilon_g < 1$. The sonic speed of the gas phase of the annular flow agrees well with the experimental data, [93]. For the liquid phase, unfortunately, experimental data do not exist. The computed result shows that sonic speed of the liquid phase is subject to a rapid initial decrease, for a very low void fraction range, due to the

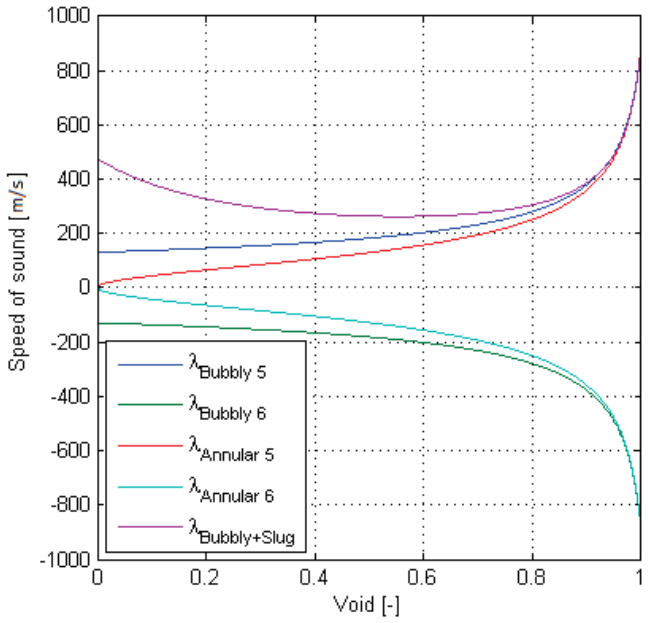

Figure 8.11.: Eigenvalues representing Bubbly and Annular flow regimes for water/steam @ 95 [bar].

effect of increasing elasticity at the interface. For further studies, we refer to [73] and [94].

8.3.6. Summary

In this section we developed a two-layer thermal-hydraulic flow model, which is able to predict the dynamic phenomena in evaporator tubes with stratified flow. The model requires a set of constitutive relations to close the system of equations, since it is sensitive to the flow regime and geometry (horizontal versus vertical). The model includes a relaxation approach to ensure surface discontinuity, across which the equilibrating quantity of velocity and pressure jumps. The model is assumed to be fully hyperbolic, with real eigenvalues, associated to the Jacobian matrix obtained by formulating the complete system of equations in a non-conservative form, where the interfacial pressure jump can be described by the surface tension model, for traditional smoothed tubes. For IRBTs we can in a similar way estimate the interfacial jump due to the centrifugal acceleration generated by the swirl. This will ensure real eigenvalues of the system. Additionally the analysis provides an estimate of the local speed of sound through the entire two-phase domain in a two-phase flow, simplified by an assumption of the pressure between the two phases.

8.4. Homogeneous model

Although the assumptions of thermodynamic equilibrium are often made in two-phase flow models, the phases rarely find themselves at thermal equilibrium. Moreover, the phases very often have different local as well as averaged velocities, which can be categorised as a departure from hydraulic equilibrium where $u_l \neq u_g$. Thus, the absence of hydraulic and thermal equilibrium is the rule rather than the exception in mult- phase flows. In this section we will develop a homogeneous dynamic flow model, based on the two-layer flow model derived in section (8.2). The homogeneous model is based on the assumption of both hydraulic and thermal equilibrium, and the consequences and aspects will be discussed in that context. The homogeneous model setup and the corresponding simulations results of a power plant evaporator are published in [17] and included in Appendix P.

8.4.1. Notations

The assumption of thermal equilibrium is very useful in the treatment of the governing equations for two-phase flow. For the case of boiling water and steam we assume that both phases are at the saturation temperature $T^s(p)$ corresponding to the local pressure p. Based on that assumption it is easy to calculate a local equilibrium quality x_e, which is a very useful, but not necessarily a real quantity, compared to the true flow quality based on the ration of the gas to total flow rates:

$$\begin{aligned} x &= \frac{\dot{m}_g}{\dot{m}_g + \dot{m}_l} \\ &= \frac{\rho_g u_g \varepsilon_g A}{\rho_g u_g \varepsilon_g A + \rho_l u_l \varepsilon_l A} \end{aligned} \tag{8.77}$$

The local equilibrium quality, x_e, can be calculated by (8.78) under the assumption that the saturation enthalpies correspond to the local pressure, h_l=$h_l^s(p)$ and h_g=$h_g^s(p)$, then we can calculate the local equilibrium quality, x_e, from:

$$x_e = \frac{h - h_l^s}{h_g^s - h_l^s} \tag{8.78}$$

The volume fraction of total liquid can be described as the sum of a continuous liquid phase (ε_l) and a continuous gas phase (ε_g):

$$\varepsilon_l + \varepsilon_g = 1. \tag{8.79}$$

For a pure two-layer fluid, the mixture density $\bar{\rho}$ and the mass flux G are defined as:

$$\bar{\rho} = \rho_g \cdot \varepsilon_g + \rho_l \cdot \varepsilon_l \tag{8.80}$$

and

$$\begin{aligned} G &= \frac{\dot{m}_g + \dot{m}_l}{A} \\ &= G(1-x) + Gx \\ &= \rho_l u_l \varepsilon_l + \rho_g u_g \varepsilon_g \end{aligned} \tag{8.81}$$

The slip ratio (S=$\frac{u_g}{u_l}$) between the two phases can be expressed by the void fractions and thereby lead to the following expression for the void fraction as a function of S:

$$\varepsilon_g = \left[1 + \frac{\rho_g}{\rho_f}\frac{1-x}{x}S\right]^{-1} \tag{8.82}$$

In homogeneous two-phase flow, there is no slip between the phases (S=1), which leads to the zero moment of density [40]:

$$\bar{\rho} = \left[\frac{x}{\rho_g^s} + \frac{1-x}{\rho_l^s}\right]^{-1} \tag{8.83}$$

8.4.2. Conservation of mass

The mass conservation equations are derived for a slice of a pipe element as illustrated in (8.1). The mass conservation equations for the total liquid and gas volume fractions are obtained by summing (8.1) and (8.2):

$$\frac{\partial}{\partial t}(\varepsilon_l \rho_l A) + \frac{\partial}{\partial t}(\varepsilon_g \rho_g A) + \frac{\partial}{\partial z}(\varepsilon_l \rho_l u_l A) + \frac{\partial}{\partial z}(\varepsilon_g \rho_g u_g A) = 0. \tag{8.84}$$

(8.84) can be recast as:

$$\frac{\partial}{\partial t}(\bar{\rho} A) + \frac{\partial}{\partial z}(GA) = 0 \tag{8.85}$$

where the mixture density $\bar{\rho}$=$\rho(\bar{p}, \bar{h})$ for a homogenius fluid. The interfacial mass transfer model assumes that total mass transfer is partitioned along the vapour/liquid interface (i). For a homogeneous model, the rate of phase change (Γ_k) in (8.1) and (8.2) would be summarized to zero.

8.4.3. Momentum equations

The mixture momentum equation can be obtained by adding (8.8) and (8.9). As expected, all the interfacial force terms cancel out, leaving:

$$\frac{\partial}{\partial t}(GA)+\frac{\partial}{\partial z}\left(\frac{G^2A}{\rho^{'}}\right)=-A\frac{\partial \bar{p}}{\partial z}-AF_w-AF_s-\bar{\rho}gA\cos\theta \tag{8.86}$$

where $\bar{\rho}$ is given by (8.80) and $\bar{p}=p_l\varepsilon_l+p_g\varepsilon_g$ and $\rho^{'}$ is named the momentum density [40] and is defined as

$$\rho^{'}=\left(\frac{(1-x)^2}{\rho_l\varepsilon_l}+\frac{x^2}{\rho_g\varepsilon_g}\right)^{-1} \tag{8.87}$$

For a homogeneous flow, one assumes u=u_g=u_l, which leads to $\bar{\rho}=\rho^{'}$. Hence we have:

$$\frac{\partial}{\partial t}(GA)+\frac{\partial}{\partial z}\left(\frac{G^2A}{\bar{\rho}}\right)=-A\frac{\partial \bar{p}}{\partial z}-S_w\tau_w-AF_s-\bar{\rho}gA\cos\theta \tag{8.88}$$

where τ_w is given by (2.1) and F_s via τ_f is a calibration term, due to axial shear stresses, modelled by the Van Driest mixing length theory, for example, which here is assumed proportional to a diffusion term.

$$\begin{aligned}\tau_f&=-\frac{\partial}{\partial z}\left(\rho\bar{u'v'}\right)\\&\approx -l^{\,2}\bar{\rho}\frac{\partial^2 u}{\partial z^2}\end{aligned} \tag{8.89}$$

The corresponding wall shear stress is dependent on whether inside ribs are used or not. For smooth pipes, the dimensionless coefficient, f_w, can be based on the Darcy friction factor, which can be found from a Moody diagram or more precisely from the Colebrook equation; see (E.18). For IRBTs the friction coefficients are multiplied by equation (2.2). In the two-phase region, the friction factor is adjusted according to a two-phase multiplier, formulated by Jirous, [77]. In that case f_w is based on fluid properties for saturated liquid. For the Jirous formulation, the two-phase multiplier is calculated by (E.42) and for Friedel we use (E.37). For vertical stratification we use equation (E.38). The size of the eddy viscosity is evaluated in section 8.6.

8.4.4. Energy equations

The mixture energy equation is obtained by adding (8.16) and (8.17), where conservation of energy across the interface requires that all the interfacial terms cancel out; hence

$$\begin{aligned}\frac{\partial}{\partial t}\left(\varepsilon_l\rho_l e_{tl}A+\varepsilon_g\rho_g e_{tg}A\right)+\frac{\partial}{\partial z}\left(\varepsilon_l\rho_l e_{tl}u_lA+\varepsilon_g\rho_g e_{tg}u_gA\right)\\ -\dot{q}_rS_w+\frac{\partial}{\partial z}\left(u_l\varepsilon_l p_lA+u_g\varepsilon_g p_gA\right)\\ +p_lA\frac{\partial\varepsilon_l}{\partial t}-p_gA\frac{\partial\varepsilon_g}{\partial t}=0.\end{aligned} \tag{8.90}$$

By using (8.13) and neglecting the last two terms due to gravity and rotational energy, we have

$$A\frac{\partial}{\partial t}\left(\bar{\rho}\bar{h}+\frac{1}{2\rho^{'}}G^2-\bar{p}\right)+\frac{\partial}{\partial z}\left(GhA+\frac{1}{2\rho^{''2}}G^3A\right)=S_w\dot{q}_r-GAgcos(\theta) \tag{8.91}$$

where $\bar{\rho}$ is an in-situ mixture density; $\bar{\rho}=\rho_l\varepsilon_l+\rho_g\varepsilon_g$, $\rho^{'}$ is given by (8.87), $\bar{P}=P_l\varepsilon_l+P_g\varepsilon_g$, and $\rho^{''}$ is named the second-order momentum density [40] and is defined as

$$\rho^{''}=\left[\frac{(1-x)^3}{(\rho_l\varepsilon_l)^2}+\frac{x^3}{(\rho_g\varepsilon_g)^2}\right]^{-1} \tag{8.92}$$

Notice that both h and $\bar{h}$ appear in (8.91), where h is the mixed-cup enthalpy, referring to a frozen flow field picture and results from equation (8.93), and $\bar{h}$ is the situ mixture enthalpy, due to [40]. The former can be developed from the thermodynamic equilibrium quality as shown by

$$\begin{aligned}\bar{\rho}\bar{h}&=\rho_l h_l\varepsilon_l+\rho_g h_g\varepsilon_g\\ \dot{m}\bar{h}&=\dot{m}_l h_l+\dot{m}_g h_g.\end{aligned} \tag{8.93}$$

When assuming thermodynamic equilibrium, one has $\bar{\rho}=\rho^{''}=\rho^{'}=\rho(\bar{p},\mathrm{h})$, which leads to

$$A\frac{\partial}{\partial t}\left(\bar{\rho}h+\frac{1}{2\bar{\rho}}G^2-\bar{p}\right)+\frac{\partial}{\partial z}\left(G\bar{h}A+\frac{1}{2\bar{\rho}^2}G^3A\right)=S_w\dot{q}_r-GAgcos(\theta). \tag{8.94}$$

8.4.5. Model setup

The homogeneous model consists of three conservation equations given by (8.85), (8.86) and (8.91), which can be reformulated in the three non-dependent variables ρ(density), $\dot{m}$(mass flow) and E(internal energy), where the dependant variables z $\in$ [0 ,..., l_z] and t $\in$ [0 ,..., ∞[. For $\dot{m}$ = $\bar{\rho}$uA we find:
Continuity equation:

$$\frac{\partial}{\partial t}\left(\bar{\rho}A\right)+\frac{\partial}{\partial z}\left(\dot{m}\right)=0 \tag{8.95}$$

Momentum equation:

$$\frac{1}{A}\frac{\partial}{\partial t}\left(\dot{m}\right)+\frac{1}{A}\frac{\partial}{\partial z}\left(\dot{m}u\right)=-\frac{\partial \bar{p}}{\partial z}-\bar{\rho}g\cos\left(\theta\right)-F_w \tag{8.96}$$

where $F_w=\frac{S_w}{A}\tau_w$, and τ_w is given by (2.1).
Energy equation:

$$\frac{\partial}{\partial t}\left(\bar{\rho}A\bar{h}+\frac{1}{2}\bar{\rho}Au^2-pA\right)+\frac{\partial}{\partial z}\left(\dot{m}\bar{h}+\dot{m}\frac{1}{2}u^2\right)=\dot{q}_rS_w-\dot{m}g\cos\left(\theta\right). \tag{8.97}$$

Then equation (8.97) can be reformulated by using the definition of the total specific convected energy: $\bar{e}=\bar{h}+1/2u^2+gz\cos\left(\theta\right)$, and by using the continuity equation to eliminate the gravitational terms on the left side, we find:

$$\frac{\partial}{\partial t}\left(A(\bar{\rho}\bar{e}-\bar{p})\right)+\frac{\partial}{\partial z}\left(\dot{m}\bar{e}\right)=\dot{q}_rS_w-\dot{m}g\cos\left(\theta\right) \tag{8.98}$$

where $\dot{q}_r$ represents the heat flux per unit surface area through the inner wall. Note that the swirl energy is neglected in the formulation of $\bar{e}$. The internal energy E is given as: E=$(\bar{\rho}\bar{e}-\bar{p})\cdot A$, which is measured in [J/m].
Hence we can summarize the *system of balance laws* (SBL) into a conservative and compact vector notation, given by:

$$\frac{\partial\Phi(z,t)}{\partial t}+\frac{\partial \mathrm{f}(\Phi(z,t))}{\partial z}=\mathrm{g}_s(\Phi(z,t))+\mathrm{g}_d\left(\frac{\partial\Phi}{\partial z},\Phi(z,t)\right), \tag{8.99}$$
$$\Phi\in R^m, m=3,\ \ t\geq 0\wedge\ \ z\in\Omega$$

where the dependent variable Φ and the flux vector f are given as

$$\Phi = \begin{pmatrix} \bar{\rho}A \\ \dot{m} \\ \bar{e} \end{pmatrix}, \quad \mathrm{f}(\Phi) = \begin{pmatrix} \dot{m} \\ \frac{\dot{m}^2}{\bar{\rho}A} + \bar{p}A \\ \frac{(\bar{e}+\bar{p}A)\dot{m}}{\bar{\rho}A} \end{pmatrix}$$

and the source and diffusion vector are given as:

$$\mathrm{g}_s(\Phi) = \begin{pmatrix} 0 \\ \bar{p}\frac{\partial A}{\partial z} - \bar{\rho}gA\cos\theta - \sqrt{\frac{\pi}{A}}f_w\frac{\dot{m}|\dot{m}|}{\bar{\rho}A} \\ S_w\dot{q}_e - \dot{m}g\cos(\theta) \end{pmatrix} \text{ and } \mathrm{g}_d(\Phi) = \begin{pmatrix} 0 \\ \frac{l^2 S_w}{\bar{\rho}A^3}\frac{\partial \dot{m}^2}{\partial z^2} \\ 0 \end{pmatrix}$$

The independent variable t represents the time in [s], and z is the spatial coordinate referring to the flow direction of the fluid given in [m]. The dependent variables are $\bar{\rho}$, $\dot{m}$ and e, meaning the fluid density, mass flow and total energy of the conserved fluid, respectively. The pressure can be determined iteratively by water steam tables: $p = \mathrm{p}(e, \bar{\rho})$. A is the tube cross-section area, measured in $[m^2]$. The source term g_s consists of both source/sink terms related to gravity- and wall friction forces. The diffusion term g_d includes a contribution from the mixing length eddy viscosity (l^2=0.01 $[m^2/s]$), working as a damping term in the vicinity of the saturation line of water. A recommended size of attenuation area is found to be $x \in [-0.02, 0.02]$. The internal energy e is given as: $e = (\rho\bar{E} - p)\cdot A$, which is measured in [J/m]. Here the fluid temperature T_f is a function of $\bar{\rho}$ and h. The constitutive relations due to the thermodynamic properties are based on IAPWS 97, and are interpolated in a bilinear scheme, described in [15] for minimising the computational work. Note that the gravity is reduced according to the heat pipe inclination ($\sin(11.4^o)$) on the SKV3 boiler.

8.4.6. Auxiliary relations

The Water / Steam library IAPWS 97 by [80] is used as a general equation of state, to derive the speed of sound and the thermodynamic properties of water and steam. In some relations we need a relationship for pressure as a function of density and enthalpy: p=p(ρ,$\bar{h}$). This can be done by a simple Newton Rapson solver, where we iterate on p by given h and ρ. To improve the computational speed it is recommended to use a bilinear interpolation; see [15], where we create a look-up table within approximately 160000 nodes, which ensures an accuracy below 4% as an absolute maximum, due to a smoothing of the interpolated properties in the vicinity of the saturation line. It is only in the vicinity of the saturation line of water, where we experience an significant error; otherwise the averaged relative error is 0.3%.

8.4.7. Boundary conditions

It is convenient to use physically measurable boundary conditions to force the model. Therefore, the following properties are used as boundary conditions: velocity (u), pressure (p) and enthalpy (h). This allows us to rewrite the boundary conditions given by (9.81) and (9.82) to those properties, which are described by Φ; see (9.71). The Dirichlet boundary conditions are given by (8.100), and the corresponding Neumann boundary conditions are obtained by applying the chain rule for differentiation of complex functions, and are given by (8.101).

$$\text{Dirichlet BC}: \begin{cases} \rho A. \\ \rho A u. \\ \rho A(h + \frac{u^2}{2} + gz\cos(\theta)) - pA. \end{cases} \tag{8.100}$$

where θ is the angle of the pipe inclination with respect to the horizontal.

$$\text{Neumann BC}: \begin{cases} A\frac{\partial \rho}{\partial z} + \rho\frac{\partial A}{\partial z}. \\ uA\frac{\partial \rho}{\partial z} + \rho u\frac{\partial A}{\partial z} + \rho A\frac{\partial u}{\partial z}. \\ \frac{\partial(\rho A)}{\partial z}\left[h + \frac{u^2}{2} + gz\cos(\theta)\right] + \rho A\left[\frac{\partial h}{\partial z} + u\frac{\partial u}{\partial z} + g\cos(\theta)\right] \\ -A\frac{\partial p}{\partial z} - p\frac{\partial A}{\partial z}. \end{cases} \tag{8.101}$$

8.4.8. Stability analysis

The *system of balance laws* (SBL) given by (8.99) with g_s=g_d=0 are reformulated into a non-conservation form, with flux Jacobians:

$$\bar{M}_t + \mathbf{J}(\bar{M}) \cdot \bar{M}_x = 0, \tag{8.102}$$

where $\bar{\mathbf{M}} = \mathbf{P}^{-1} \cdot \Phi$, and $\mathbf{P}$ is the eigenvector corresponding to the eigenvalues. The matrix $\mathbf{J}(\Phi)$ is diagonalizable, which means it can be decomposed into: $\mathbf{J}$=$\mathbf{P}$ $\cdot\Gamma\cdot \mathbf{P}^{-1}$, where

$$P = [r_1, r_2, r_3]^T = \begin{pmatrix} 1 & 1 & 1 \\ u-a & u & u+a \\ H-ua & 1/2u^2 & H+ua \end{pmatrix}$$

and

$$\Gamma = \begin{pmatrix} \gamma_1 & 0 & 0 \\ 0 & \gamma_2 & 0 \\ 0 & 0 & \gamma_3 \end{pmatrix}$$

Here $r_1 = [1, u-a, H-ua]^T$, $r_2 = [1, u, \frac{1}{2}u^2]^T$, $r_3 = [1, u+a, H+ua]^T$ are the right eigenvectors of the matrix **J** corresponding to the eigenvalues $\gamma_1 = u - a$, $\gamma_2 = u$ and $\gamma_3 = u + a$. The total enthalpy H is given by: $H = \frac{E+p}{\rho}$. The eigenvalues are always real values meaning that the *SBL* are hyperbolic and stable.

8.5. Dynamic pipe wall model

The heat transfer processes from a combustion process (radiation and convection) to the water and steam curcuit in a power plant, use the pipe wall as the transfer median, to transport the energy from the furnace to the cooling media, in this case water / steam flowing in the panel wall.

8.5.1. 1D - pipe wall model

The solution of problems involving heat conduction in solids can, in principle, be reduced to the solution of a single differential equation, the heat conduction equation. As an alternative, we could use equation (4.4) to describe the spatial temperature resolution of the pipe material. The single-layer equation can be derived by making a thermal energy balance on a differential volume element in the solid. A volume element for the case of conduction only in the z-direction is illustrated in figure (8.12). The balance equation for the volume element is:

$$\begin{aligned} \text{(rate of accumulation of energy)} &= \text{(rate of energy in)} \\ &\quad - \text{(rate of energy out)} \\ &\quad + \text{(net rate of energy generation)} \end{aligned} \tag{8.103}$$

The generation term is set to zero, but could be an electric current or the decay of a radioactive material. The rate at which thermal energy enters the volume element across the face at z is given by the product of the heat flux and the uniform cross-sectional area, $\dot{q}_z|_z A_c$, where $A_c = \pi(d_o^2 - d_i^2)/4$. Similarly, the rate at which thermal energy leaves the element across the face at z + Δz is $\dot{q}_z|_{z+\Delta z} A_c$. For a homogeneous heat source/sink of strength $\dot{q}_r$ per unit area, the net rate of generation is $\dot{q}_r$ S Δz, where S is the pipe perimeter of impact. Finally, the rate of accumulation is given by the time derivative of the thermal energy content

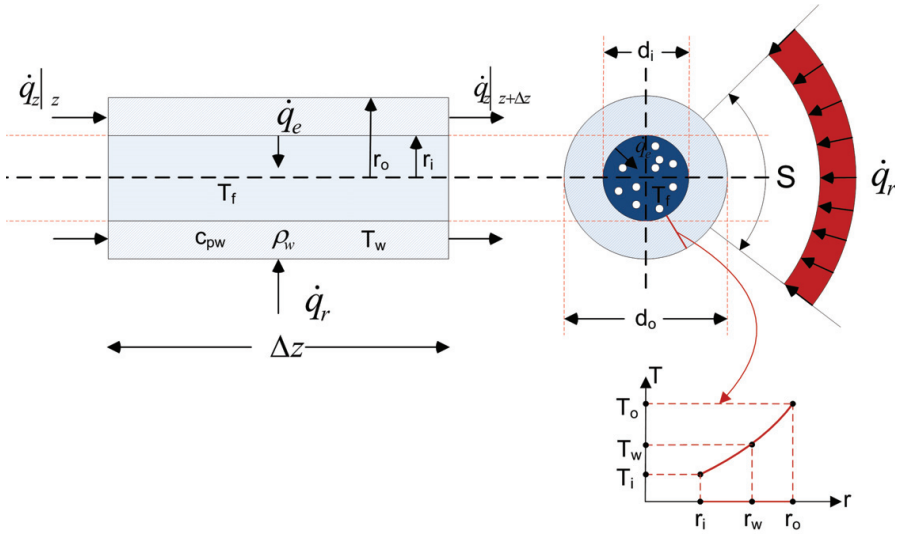

Figure 8.12.: Energy transfer and heat flow terms on a slice of a pipe wall element.

of the volume element, which is $C_{pw}\rho_w(T - T_{ref})A_c$, where T_{ref} is an arbitrary reference temperature. Thus, the balance equation becomes:

$$\Delta z\, \rho_w\, C_{pw} A_c \frac{\partial T_w}{\partial t} = (\dot{q}_z|_z - \dot{q}_z|_{z+\Delta z})A_c + \dot{q}_r S \Delta z - \dot{q}_e d_i \pi \Delta z \tag{8.104}$$

where C_{pw} and ρ_w are the heat capacity and the density of the pipe wall, given by equation (8.107). By dividing (8.104) by Δz and letting $\Delta z \to 0$, we get a first-order PDE describing the energy balance in the pipe element as a function of t and z.

$$\rho_w\, C_{pw} A_c \frac{\partial T_w}{\partial t} = -A_c \frac{\partial \dot{q}}{\partial z} + \dot{q}_r S - \dot{q}_e d_i \pi \tag{8.105}$$

The heat flux $\dot{q}$ per unit area can be expressed via the Fourier formula: $\dot{q} = -k_w \frac{\partial T_w}{\partial z}$, where k_w is the thermal conductivity measured in [w/mK]. For isotropic materials, we use the thermal diffusivity given by equation (4.2): $\alpha = \frac{k_w}{\rho_w C_{pw}}$ in $[m^2/s]$, which in a sense is a measure of thermal inertia and expresses how fast heat diffuses through a piece of solid. For a typical panel wall, the thermal dif-

fusivity is approximately $1.98 \cdot 10^{-6}$ [m^2/s] at 200°C; see [95]. Hence the energy balance for the isotropic pipe wall can be described by:

$$\frac{\partial T_w}{\partial t} = \alpha \frac{\partial^2 T_w}{\partial z^2} + \frac{\dot{q}_r}{\rho_w C_{pw}} \frac{S}{A_c} - \frac{\dot{q}_e}{\rho_w C_{pw}} \frac{d_i \pi}{A_c}, \qquad z \in [0, l_z] \wedge t \geq 0 \tag{8.106}$$

where $\dot{q}_r$ is the radiation from the furnace and $\dot{q}_e$ is the convective heat transfer between the flowing fluid in the pipe and the pipe wall inner surface, $\dot{q}_e$=$h(T_w - T_f)$. The convective heat transfer coefficient is named h, and the driving temperature difference is given by the temperature difference between the wall mean temperature (T_w), outlined in equation (4.16), and the mixture fluid temperature (T_f). For isotropic materials, we have expressions of C_{pw}, k_w and ρ_w as a function of temperature in Kelvin from [95] and [96]:

$$\begin{aligned} C_{pw} &= 6.683 + 0.04906 \cdot T + 80.74 \cdot \ln(T) \text{ [J/kgK]} \\ k_w &= 9.705 + 0.00176 \cdot T - 1.60 \cdot 10^{-6} \cdot T^2 \text{ [w/mK]} \\ \rho_w &= 7850 \text{ [kg/}m^3\text{]} \text{ at } 20°C \text{ for 13CrMo44} \end{aligned} \tag{8.107}$$

The wall density is assumed constant in temperature T. A simple, fast and robust model of the heat transfer in film boiling is given by [97]. The heat transfer coefficient h_{fb} is given by equation (E.61). The single-phase laminar heat transfer coefficient is calculated from equation (E.63). The total heat transfer coefficient is given by (8.108), and consists of two contributions: one from the convective heat transfer boundary layer associated to the flowing fluid inside the heat pipe and one that relates to conduction through the pipe wall material:

$$h = \frac{1}{\frac{1}{h_c} + \frac{r_i}{k_w} \cdot \ln(r_w / r_i)} \tag{8.108}$$

where h_c expresses the heat transfer coefficient due to the thermal boundary on the inner side of the pipe wall and r_w is defined by $T_w = T(r_w)_z$. h_c is smoothed in-between h_s and h_{fb} depending of the dryness (x) of the fluid.

$$h_c = \begin{cases} h_s & \text{for } x > 1 \vee x < 0 \\ \\ h_{fb} & \text{for } 0 \geq x \leq 1 \end{cases} \tag{8.109}$$

Additionally, h_c is adjusted on the basis of a smoothing between laminar and turbulent single-phase flow as well as for two-phase flow. The smoothing function

is described in Appendix G and is of second-order due to table (G.1) for n=2. The associated slopes are determined numerically. Since we use the calculated average wall tube temperature as the driver in the calculation of the total heat transport to the fluid, we must know r_w. Due to the knowledge of radial conduction in the pipe, we use a simple analytical wall temperature profile for estimating the inner wall temperature, expressed by the averaged wall temperature (T_w), based on the heat transfer through the isotropic pipe wall to the flowing fluid given by equation (4.16). Let $T(r)_z$ represent the radial temperature distribution in the pipe wall by equation (4.14), which can be rewritten as

$$T(r)_z = a_0 \ln(\frac{r}{r_o}) + T_o \tag{8.110}$$

where $a_0 = \frac{T_i - T_o}{\ln(\frac{r_i}{r_o})}$ and r is the pipe radius with suffix (i=inner) and (o=outer). Hence, for small values of the thermal diffusivity, the averaged wall temperature can reasonably be estimated by equation (4.16). Hence the entire heat transfer can be estimated for the temperature range in-between the wall mean temperature (T_w) and the fluid mixture temperature (T_f), which is assumed homogeneous and well mixed with a temperature boundary layer represented by h_c. The one dimensional pipe wall model only consists of the axial heat transfer term, and has no spatial resolution in the radial dimension.
The inner wall temperature (T_i) can be determined by use of the equation for pure conduction through the pipe:

$$\dot{q}_r S = \frac{2\pi k_w}{\ln(r_o/r_i)}(T_o - T_i) = \frac{2\pi k_w}{\ln(r_w/r_i)}(T_w - T_i) \ \ [w/m]. \tag{8.111}$$

Hence we find T_i by insertion (4.14) in (8.111):

$$T_i = T_w - \frac{q_r S \ln(\frac{r_o}{r_i})(1 - a_1)}{2\pi k_w} \tag{8.112}$$

where a_1 is given by equation (4.17). Hence r_w in (8.108) can be determined from (4.14) and (8.112) and we find

$$\begin{aligned} h &= \frac{1}{\frac{1}{h_c} + \frac{r_i(a_1 - 1)}{k_w} \cdot \ln(r_i/r_o)} \\ &= \frac{1}{\frac{1}{h_c} + \frac{r_i}{k_w} \cdot \ln(r_w/r_i)} \end{aligned} \tag{8.113}$$

Note that the heat flux is positive for $T_i > T_f$. Using the model parameters for the

panel wall of SKV3 (from table (10.2)), we find a_1=0.423 and the temperature fall above the pipe wall is: T_o-T_i=27.9 [^oC], which gives a temperature gradient in the pipe wall of dT/dr= 3930 [$^oC/m$] for a heat flux of $\dot{q}_e$=100 [kW/m^2]. The heat conduction in the material is the most significant barrier for an effective cooling of the tube wall.

8.5.2. Summary

There are two types of models for the description of the temperature distribution in the tube material, which is the component that will transmit the heat from the combustion chamber to the water / steam circuit of a power plant. Therefore, it is essential that the material is properly illuminated with respect to both the temperature distribution throughout the material as well as an estimate of the temperature gradients, caused by the fluctuating external boundary conditions. The two-dimensional tube model predicts the time constants for a specific material used on the SKV3 power plant outlined in section 4.2 . We can see that the time constant of an infinitesimal material element, which is subjected to a temperature fluctuation, is many decades less than for a similar infinitesimal material element, that is furthest from the fluctuating boundary condition. This material can react more quickly to the temperature boundary condition; therefore the phenomenon of fatigue may be a potential risk, as the infinitesimal material element can initiate small fatigue cracks that can propagate to the rest of the unaffected material. This phenomenon may be enhanced in certain circumstances, for example, if there occurs fouling on the inside of the tube, so that the tube temperature offset rises, due to the poor thermal conductivity of the fouling layer. Hence a fluctuating two-phase flow (slugs of superheated steam or temperature slugs of sub-cooled water) may initiate local temperature fluctuations at a higher temperature level, as in the surrounding pipe material and thereby potentially initiate a fatigue fracture. This phenomenon is more likely in a superheater, where the temperature level is significantly higher; this also implies to the selection of which dedicated type of material can sustain the very high pressures and high temperature levels, up to 600 [^oC]. The one-dimensional tube model is intended to form a link in the axial direction of the tube, so that the temperature variations are able to diffuse in the axial direction of the pipe, due to the thermal diffusivity. This achieves a more accurate description of the material temperature, which indirectly determines how much energy is transformed from the boiler room to the flowing medium in the pipe.

8.6. Turbulent stresses due to two-phase flow in general

In connection with the solution of the homogeneous two phase flow model, problems arise when trying to calculate the flow, moving from a stage of sub-cooled liquid to a stage of two-phase flow in a heat pipe. In this process, the

density has a trough with a very steep gradient, at the entrance to the two-phase region. There is a discontinuity in the first derivative of the density, at the entrance to the two-phase region, which affects the flow equations significantly and causes the generation of a pressure correction, due to momentum conservation. There are two options to dampen this oscillation: firstly, the introduction of a moderate smoothing of phase boundaries in EOS, so that there is C^1 continuity in density over the entire definition area. A second option is locally to inject turbulence or a kind of artificial diffusion to the momentum equation, in order to dampen pressure oscillations, without providing production and/or dissipation of kinetic energy to the flow, as is known from other turbulence models. The advantage of this is, that we can control the flow oscillations and address them locally, to manage the pressure fluctuations, generated due to the phase shift. This strong negative gradient in density increases with decreasing pressure. Here we formulate some general ideas about using a mixing length theory in the modelling of turbulent two-phase flow, in order to scale the magnitude of the eddy diffusion viscosity. Furthermore, we setup a model for the contribution of eddy viscosity derived from the principles of internal rifled boiler tubes (IRBT).

8.6.1. Shear distribution in various flow patterns

The difficulties of using a one-dimensional homogeneous flow model in describing a two-phase flow, where only the axial dimension is stated, are that the effect of various phase and velocity distributions cannot be separated, and that no effect of local bubble slip velocity can be considered. In an attempt to improve the general description of two-phase flows, basic analytical and experimental studies have been conducted during the last decades, for phase, velocity and shear distribution for various flow patterns; see Kinney et al. [98], Gill et al. [99] and [100], where measurements show that the logarithmic law for an isotherm two-phase flow follows the mixing length theory with a mixing length scale less than observed for a single-phase fluid. In the one-dimensional equation of motion, it is not possible to model radial components, but we take a look at the formulated two-dimensional theory from [101]. The procedure is fully analogous to what we know from the "Reynolds Averaging", which refers to the process of averaging the velocity components. This variable can be decomposed into a fluctuating part, and an average part in the following way:

$$\begin{aligned} \bar{u} &\equiv \frac{1}{\Delta t}\int_{\Delta t} u(t)dt, \\ u' &\equiv u(t) - \bar{u} \end{aligned} \tag{8.114}$$

where Δt is a long enough time to average out the fluctuations in the velocity u. This simplification to the full Navier-Stokes equations is related to the well known

"Reynolds stresses" due to the effect of turbulence on the mean flow and related to the "eddy viscosity". These terms are generally much larger than the normal viscous friction terms. Here we additionally have a contribution from the effect of various phases. In this work the mixing length theory serves as a calibration tool, which acts locally in the global solution domain, without any assumptions of the radial distribution of the flow properties. The mixing length theory assumes cells of fluid of varying sizes constantly moving in random directions relative to the mean flow. At the surface of a body, molecules transfer momentum to the surface as they collide, resulting in a tangential, shear force. When molecules hit the surface of a body, they bounce around among the surface molecules and finally leave with a tangential velocity which is, on average, that of the surface itself. Thus, the average tangential velocity near the surface of a body is zero with respect to the body. This is the so-called no-slip condition. This layer of slow-moving fluid near the body surface is called the boundary layer, and the viscosity of the fluid causes a distribution of tangential velocity above the surface. As the tangential momentum of the fluid molecules is transferred to the surface, a shear stress is produced.

On the basis of the classical Van Driest modification of Prandtl's single-phase mixing length theory, we have an expression for the homogeneous mixing length theory, where

$$\nu_t = l^2 \left| \frac{\partial u}{\partial z} \right| \tag{8.115}$$

The mixing length is not obvious. It is usually established through measurements of turbulent shear stresses and velocity gradient. To complete this model, Prandtl assumed l=κz, where κ=0.41 is the Von Karman constant, noting that very near the wall only small eddies were possible, with larger eddies being possible with increasing distance from the wall. Many things may be questioned in this model: first of all, the two-phase flow does not behave like a Newtonian fluid under isothermal conditions, but there is no experiments pointing to the opposite at very high pressure at non-isotherm conditions, such as present in Benson boilers. Additionally turbulent motion is not small compared to the transverse scales of the flows, so $u^{'} \neq l\frac{\partial u}{\partial r}$ and is in fact related to the velocity at finite distances, making the entire idea of having universal partial differential equations suspect. Therefore, we use a simple scalar quantity as a calibration parameter, related to the eddy viscosity ν_t, which in turn can be related to the diffusion term in our transport model. Therefore, we scale the strength of the eddy diffusivity on the basis of a Boussinesq consideration, which is done by [102] and will be outlined in the next section.

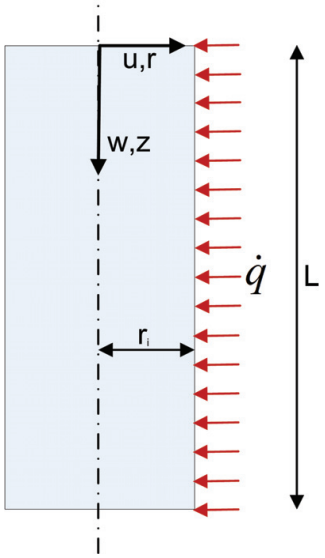

Figure 8.13.: Geometry of a circular heat pipe.

8.6.2. Large eddy phenomena in thermo-convective rotating flows

A rotary flow may, in addition to separating a flow comprised of heavy and light fluid particles, also cause a mixing of the fluid as a result of intensive vortex formation. This section is based on work involving buoyancy effects caused by natural convection, described by a vorticity-streamfunction formulation of the Boussinesq equations. This gives an opportunity to create a coupling between the radial velocity components in a flow and the production of eddy viscosity.

Turbulence in thermal-hydraulic flows is formulated by [102], wherein a vorticity formulation is applied to the Boussinesq approximation. This implies a description of the order of the vorticity-induced eddy viscosity in the Boussinesq approximation, which leads us to an estimate of the order of eddy viscosity in a homogeneous one-dimensional flow model. Consider a vertical cylinder (heat pipe) of radius r_i and length L, as shown in figure (8.13). Thus, due to buoyancy effects, the fluid motion is originally categorised as natural convection, where the motion is related to viscous forces. If the heat pipe is provided with internal rifles, so that the flow is brought into a rotation, the flow can be characterized as a forced convection phenomenon, where the Reynolds number is high-turbulent. Such rotational flow in this context can be advantageously formulated for small fluid velocities as a Boussinesq approximation. Consider a fluid with a coefficient of thermal expansion α and density ρ such that

$$\rho(T) = \rho_0 \left(1 - \alpha(T - T_0)\right), \tag{8.116}$$

where T is the fluid temperature and ρ_0 is the density when T=T_0. Hence the governing flow equations for the velocity vector $\mathbf{V}$ and temperature T can be written as

$$\frac{\partial \mathbf{V}}{\partial t} + \omega \times \mathbf{V} = \nabla \cdot \left(\frac{1}{2}|\mathbf{V}|^2 + g \cdot z + p \right) - \alpha g(T - T_0) + \nu \nabla^2 \mathbf{V}, \tag{8.117}$$

$$\frac{\partial T}{\partial t} + \nabla \cdot (T\mathbf{V}) = k\nabla^2 T, \tag{8.118}$$

$$\nabla \cdot \mathbf{V} = 0. \tag{8.119}$$

The pressure term in (8.117) can be eliminated by introducing a streamfunction ψ to satisfy the continuity equation and applying the curl operator on the pressure term. This results in the vorticity-streamfunction formulation of the Boussinesq equations,which in a non-dimensionalized and symmetric form, for $t_0 = {r_i}^2/\nu$, $V_0 = \nu/R$ and $\Delta T_0 = T_1 - T_0$, see (A.18) are written as:

$$\frac{\partial w}{\partial t} + \frac{\partial uw}{\partial z} = Gr\frac{\partial T}{\partial r} + \frac{\partial}{\partial t}\left(\frac{1}{r}\frac{\partial rw}{\partial r} \right) + \frac{\partial^2 w}{\partial z^2}, \tag{8.120}$$

$$\frac{\partial T}{\partial t} + \frac{\partial uT}{\partial r} + \frac{\partial wT}{\partial z} + \frac{uT}{r} = \frac{1}{Pr}\left(\frac{1}{r}\frac{\partial}{\partial r}\left(r\frac{\partial T}{\partial r} \right) + \frac{\partial^2 T}{\partial z^2} \right), \tag{8.121}$$

$$\frac{\partial}{\partial r}\left(\frac{1}{r}\frac{\partial \psi}{\partial r} \right) + \frac{\partial}{\partial r}\left(\frac{1}{r}\frac{\partial \psi}{\partial z} \right) = w, \tag{8.122}$$

$$u = \frac{1}{r}\frac{\partial \psi}{\partial z}, \tag{8.123}$$

$$w = -\frac{1}{r}\frac{\partial \psi}{\partial r}, \tag{8.124}$$

where the polar coordinates (r,z) are defined as shown in figure (8.13); (u,w) denote the velocity components in the (r,z) directions, respectively, *Gr* is the Grasshof number and *Pr* the Prandtel number as a result of the non-dimensionalizing procedure. *Gr* and *Pr* are defined in (A.8) and (A.11), respectively.

The Rayleigh number is defined in (A.13) as the product of the Grashof number and the Prandtl number; hence the Rayleigh number itself may also be viewed as the ratio of buoyancy and viscosity forces times the ratio of momentum and thermal diffusivities and can be deduced from the relation:

$$Ra = Gr \cdot Pr \cdot \lambda^3, \tag{8.125}$$

where λ=L/r_i is the aspect ratio, where z $\in$ [0,λ] and r $\in$ [0,1]. At high Rayleigh numbers the flow becomes turbulent, which means it becomes dominated by eddy-structures of varying size. The calculations may be carried out by utilizing Large Eddy Simulations (LES), which is a technique where only the large-scale motions are computed, whereas the smallest turbulent eddies are modelled by a Sub-Grid scale model. This is accomplished by applying a spatial filter on the governing equations and decomposing the variables in a filtered part and a fluctuating part: f= $\bar{f}$+$f^{'}$, where $\bar{f}$ denotes the filtered part and $f^{'}$ the fluctuating part. Applying the filters on the vorticity-streamfunction formulation of the Boussinesq equations (8.124), we obtain from [102]:

$$\frac{\partial \bar{w}}{\partial t}+\frac{\partial \bar{u}\bar{w}}{\partial z}+\frac{\partial \bar{w}\bar{w}}{\partial z}=Gr\frac{\partial \bar{T}}{\partial r}+\frac{\partial}{\partial t}\left(\frac{1}{r}\frac{\partial r\bar{w}}{\partial r}\right)+\frac{\partial^2 \bar{w}}{\partial z^2}+\Omega, \quad (8.126)$$

$$\frac{\partial \bar{T}}{\partial t}+\frac{\partial \bar{u}\bar{T}}{\partial r}+\frac{\partial \bar{w}\bar{T}}{\partial z}+\frac{\bar{u}\bar{T}}{r}=\frac{1}{Pr}\left(\frac{1}{r}\frac{\partial}{\partial r}\left(r\frac{\partial \bar{T}}{\partial r}\right)+\frac{\partial^2 \bar{T}}{\partial z^2}\right)+\Theta, \quad (8.127)$$

$$\frac{\partial}{\partial r}\left(\frac{1}{r}\frac{\partial \bar{\psi}}{\partial r}\right)+\frac{\partial}{\partial r}\left(\frac{1}{r}\frac{\partial \bar{\psi}}{\partial z}\right)=\bar{w}, \quad (8.128)$$

$$\bar{u}=\frac{1}{r}\frac{\partial \bar{\psi}}{\partial z}, \quad (8.129)$$

$$\bar{w}=-\frac{1}{r}\frac{\partial \bar{\psi}}{\partial r}, \quad (8.130)$$

where

$$\Omega=\frac{\partial}{\partial r}\left(\overline{uw}-\bar{u}\bar{w}\right)+\frac{\partial}{\partial z}\left(\overline{uw}-\bar{u}\bar{w}\right), \quad (8.131)$$

$$\Theta=\frac{\partial}{\partial r}\left(\overline{uT}-\bar{u}\bar{T}\right)+\frac{\partial}{\partial z}\left(\overline{wT}-\bar{w}\bar{T}\right)+\frac{\overline{uT}-\bar{u}\bar{T}}{r}. \quad (8.132)$$

Except for the terms Ω and Θ, which have to be modelled, we see that the filtered equations take the exactly same form as the original ones. From [102] we use the same eddy-viscosity hypothesis to determine an estimate of the eddy-viscosity formulated as a function of $\bar{w}$

$$\nu_t=(C\Delta)^3\sqrt{\left(\frac{\partial \bar{w}}{\partial r}\right)^2+\left(\frac{\partial \bar{w}}{\partial z}\right)^2} \quad (8.133)$$

where C=0.2 and Δ=$\sqrt{\Delta r\Delta z}$ is the filter width. For a one-dimensional approach, the spatial resolution in the radial direction is limited to a cell width equal to the pipe inner diameter d_i. If we assume that the radial velocity profile can be

expressed by (8.27), which is illustrated in figure (8.8), we can substitute the radial velocity component in (8.133), which leads to the expression below for the eddy viscosity in a homogeneous two-phase flow in IRBT.

$$\nu_t = (C\sqrt{d_i \Delta z})^3 \omega \tag{8.134}$$

where ω is the angle of rotation, forced by the internal rifles, which is given by equation (8.24) and can be expressed as: ω=tan$(\gamma) \cdot u_c / r_i$. The magnitude of the eddy viscosity can be set in perspective, by looking at a practical example of an evaporator tube with a length of 193.5 [m] and an inner diameter of 25.4 [mm], resolved in 400 elements and with sub-cooled water at 95 [bar], flowing with a mean centre inlet velocity (u_c) of 1 [m/s]; hence the magnitude of the eddy viscosity is approximately given by:

$$\nu_t = \frac{(C \Delta z d_i)^3 \tan(\gamma) u_c}{8\nu} \approx 0.01[m^2/\text{s}]. \tag{8.135}$$

Note that tan (γ) = 1 means the angle of fin is 45 ^{o}. The kinematic viscosity of sub-cooled water at 95 [bar] is: ν=1.2$\cdot$ 10^{-7} [m^2/s].

8.6.3. Summary

This section has shown the turbulence models in relation to two-phase flows and currents in rotation, under the influence of a heat flux. The model assigns the order of the turbulence level in a turbulent (rotating) flow of sub-cooled fluid, affected by a heat flux. Phase changes affect the flow to such an extent, that we must turn to more detailed models to get a more qualified knowledge about the level of turbulence under different flow regimes, but we have chosen to use this averaged estimate as the best practice in the vicinity of the saturation region of liquid and use it only locally in the solution domain as a filter to dampen unwanted oscillations as a result of a discontinuity in the first-order derivative of the averaged fluid density. This leads to a diffusion term that can be active for x_e $\in [-x_0, x_0]$, where x_0 is an infinitesimal amount of steam quality in the vicinity of saturated liquid, based on the enthalpy basis.

8.7. Four-field model

In order to model a two-phase flow, based on a flow regime consideration, we have established a model inspired by Bonizzi and Banerjee [103]. Originally they describe the two-phase flow on the basis of an isothermal process, i.e., using only continuity and momentum conservations, and in addition, using a series of constitutive relations for describing the transport between the four layers, which appear in the model. By adding four energy transport equations to the

model, we have a golden opportunity to study how the flow regimes are built and destroyed, under the influence of a heat flux in a boiler. The models are not implemented in the WENO solver, developed in section (9.5) and included in the thesis, because it can form the conceptual framework and inspiration for further work on the two-phase currents in power plant boilers. The model description is found in Appendix (M). The four-field model is based on the premise

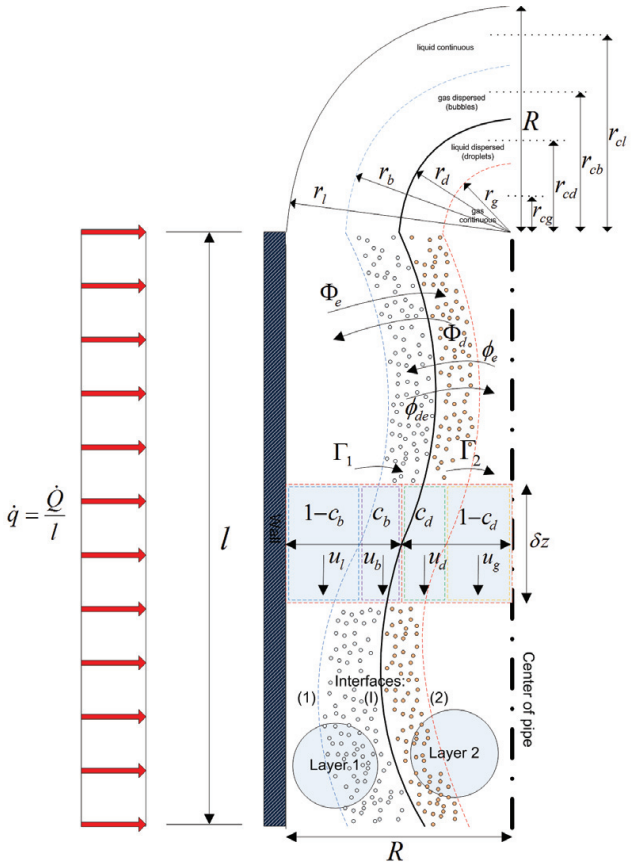

Figure 8.14.: Illustration of the four different control volumes in the two-phase fluid. The fluid is flowing in a cylindrical channel with uniform radius R.

that in terms of predominantly one-dimensional flows, much of the important behaviour can be captured by considering continuous and dispersed liquid and gas phases (water/steam) i.e., four fields. For example, slug flow may be thought of as a continuous gas phase, containing a few droplets, each with the liquid phase intermittently interspersed and containing entrained gas bubbles. Bubbly flow, following this line of thought, would then consist of a continuous liquid phase containing gas bubbles with a negligible continuous gas layer (containing droplets). Furthermore, an annular flow would consist of a continuous gas phase

containing liquid droplets and a continuous liquid phase including gas bubbles. Obviously, within this one-dimensional context, the distinction between stratified flows and annular flows would be difficult to capture as a consequence of the one-dimensional formula. The four-field model is dedicated for both horizontal stratified as well as vertical boiler tubes with internal rifles (IRBT).

It is therefore essential to note that there are many two-phase flow problems that require a multi-dimensional formula for their elucidation, e.g., the influence of varying fin geometry on the heat transfer and pressure loss in the IRBT. Having said this, there is a wide range of applications of interest that could yield to useful resolutions by implementing a one-dimensional approach, particularly for relatively slow transients in flow.

This approach implicitly propagates interfacial area, but the area is divided into a continuous component and a dispersed component, associated with the bubbles and droplets in the liquid and the gas phase, respectively. The rates of the transport processes that occur at the continuous and dispersed components are different, and the approach captures this naturally. The formula includes separate sets of conservation, momentum and energy equations for each field, and the fields are represented by the belonging volume fractions of the total fluid; see figure (8.14). For non-isotherm flow, 12 conservation equations are required for the four fields: four continuity equations, four momentum equations and four energy equations. Additionally, three relations for the radial pressure distribution are needed to close the numerical problem, if we should continue the approach of ensuring full parabolicity, by specifying the driving pressure difference in-between the different layers, instead of looking at the relaxation processes in-between the four layers, as seen in the two-layer approach.

8.8. Summary

This chapter has developed three models, with primary focus on the homogeneous and two-layer model. The models are tuned so that each of them is aligned relative to the number of degrees of freedom (DOFs) and number of transport equations and additional constitutive relations. Stability tests in the form of an eigenvalue analysis are also carried out, showing that the transport equations are hyperbolic and are suitable for solution by using the properly selected time integrator. The two-layer model offers a high degree of complexity in the selection of constitutive relations, and the two most prominent models involve an imperial model of the pressure difference between the two flowing media or the introduction of a transport equation for void fraction. A third option is to solve the system of equations using a Roe method [88], where the Jacobian contains

elements including the virtual mass force, which also ensures that the Jacobian has real eigenvalues and hyperbolic nature, or else a flux-based WENO approach is recommended, like [63].

Finally, we have formulated a four-field model that can serve as the basis for further work. The challenge here is to find appropriate constitutive relations, especially for heat transfer between the individual phases in the model. One must expect a high degree of complexity in connection with the solution of the system, since one must ensure that also here the system of equations is of hyperbolic nature, i.e., real eigenvalues. One must also make some assumptions for the pressure and velocity relaxation between the four layers, in the case of a Riemann problem.

9. Solving hyperbolic transport equation

The starting point for this chapter is the challenge of developing a robust numerical solver, to handle the very strong thermal-hydraulic transients, that can occur in a power plant evaporator. Many numerical challenges are brought into play. Choices of solution strategy including type of grid (staggered/non-staggered/nested), solution method (explicit/implicit), time integration method, initial conditions, and boundary conditions are just a few of the many challenges that, the developer is confronted with in the construction of a numerical solver. Therefore it is valuable to explain the entire process and clarify the most necessary components to be included in the implementation of a dynamic solver. An additional challenge is to find a numerical scheme, that can handle steep gradients without numerical diffusion and over-shooting and under-shooting in the solution domain. In this section, we are concerned with solving numerically one-dimensional hyperbolic *system of balance laws* (SBL), given by:

$$\frac{\partial \Phi(z,t)}{\partial t} + \frac{\partial f(\Phi(z,t))}{\partial z} = s(\frac{\partial \Phi}{\partial z}, \Phi(z,t)), \;\; t \geq 0 \wedge \;\; z \in \Omega. \tag{9.1}$$

The homogeneous system associated with equation (8.99) and the two layer model given by equation (8.41) are both hyperbolic *systems of balance laws* (SBL). Both the SBL and SCL (*systems of closure laws*) systems are subject to the initial condition:

$$\Phi(z,0) = \Phi_0(z) \tag{9.2}$$

and the following boundary conditions given by:
Dirichlet boundaries:

$$\begin{aligned} \Phi(z=0,t) &= \Phi_A(t), \\ \Phi(z=l_z,t) &= \Phi_B(t) \end{aligned} \tag{9.3}$$

and Neumann boundaries:

$$\begin{aligned} \frac{\partial \Phi(z=0,t)}{\partial z} &= \frac{\partial \Phi_A(t)}{\partial z}, \\ \frac{\partial \Phi(z=l_z,t)}{\partial z} &= \frac{\partial \Phi_B(t)}{\partial z} \end{aligned} \tag{9.4}$$

The above boundary conditions can be given by a combination of each type of boundaries, and are only specified if there are ingoing flow conditions at the

boundaries. Here Φ is the unknown m-dimensional vector function, f(Φ) the flux vector and s(Φ) a continuous source vector function on the right-hand side (RHS); with z as the single spatial coordinate and t the temporal coordinate, Ω is partitioned in n_z non-overlapping cells: $\Omega = \cup_{i=1}^{n_z} I_i \in [0, l_z]$, where l_z is a physically length scale in the spatial direction. From the original equations as given in equation (9.1), the equations are written in a non-conservative form as:

$$\frac{\partial \Phi(z,t)}{\partial t} + \mathbf{J}\frac{\partial \Phi(z,t)}{\partial z} = S\left(\frac{\partial \Phi}{\partial z}, \Phi(z,t)\right), \quad t \geq 0 \wedge z \in \Omega \tag{9.5}$$

where $\mathbf{J}$ is called the flux Jacobian, which is a diagnosable matrix equal to:

$$\mathbf{J} = \mathbf{P} \cdot \Lambda \cdot \mathbf{P}^{-1} = \begin{pmatrix} \frac{\partial f_1(z,t)}{\partial \Phi_1} & \frac{\partial f_1(z,t)}{\partial \Phi_2} & \cdots & \frac{\partial f_1(z,t)}{\partial \Phi_m} \\ \frac{\partial f_2(z,t)}{\partial \Phi_1} & \frac{\partial f_2(z,t)}{\partial \Phi_2} & \cdots & \frac{\partial f_2(z,t)}{\partial \Phi_m} \\ \cdots & \cdots & \cdots & \cdots \\ \frac{\partial f_m(z,t)}{\partial \Phi_1} & \frac{\partial f_m(z,t)}{\partial \Phi_2} & \cdots & \frac{\partial f_m(z,t)}{\partial \Phi_m} \end{pmatrix}$$

and

$$\mathbf{P} = [r_1, r_2, ..., r_m]. \tag{9.7}$$

Here r_1, r_2,..., r_m are the eigenvectors of the flux Jacobian $\mathbf{J}$ corresponding to the eigenvalues λ_1, λ_1, ..., λ_m given by Λ:

$$\Lambda = \begin{pmatrix} \lambda_1 & 0 & ... & 0 \\ 0 & \lambda_2 & ... & 0 \\ ... & ... & ... & ... \\ 0 & 0 & ... & \lambda_m \end{pmatrix}$$

The eigenvalues of $\mathbf{J}$ are precisely the solutions λ_i, i$\in$(1,...,m) to the equation:

$$\det(\mathbf{J} - \Lambda \cdot \mathbf{I}) = 0. \tag{9.8}$$

If the matrix has real entries, the coefficients of the characteristic polynomial are all real. However, the roots are not necessarily real. If the eigenvalues are all real, the equation system is hyperbolic and its solutions are stable against small disturbances.
In general, the real part of the eigenvalues can have both a positive and a negative sign, and a simple one-sided differencing scheme will be appropriate only if the real parts of all eigenvalues have the same sign. The general system will, however, have some eigenvalues with a positive real part, and one side will be upwind for

them, while the others have a negative sign on the real part and consequently the upwind side will be opposite for them. A typical way to resolve this problem is to split such a system into one with a positive real part of the eigenvalues and one with a negative real part, and to treat them separately. These are the flux vector splitting methods, also called the Boltzmann approach, discussed in [104]. Another reasonable method could be to use a numerical scheme, which is independent of the sign of the convective flux as well as the sign of the system eigenvalues. Schemes, whose support does not depend on the sign of the characteristic speeds, are called centred schemes. One of the simplest and most approximate methods considered is the Lax-Friedrichs flux, which originally was developed in the context of finite-difference methods and later applied to the finite-volume context. Here the flux is estimated as:

$$f_{LF}(\Phi^+,\Phi^-) = \frac{1}{2}(f(\Phi^+)+f(\Phi^-)) - \frac{\lambda_{max}}{2}(\Phi^+ - \Phi^-), \tag{9.9}$$

where the signal speed λ_{max}=$\Delta x/\Delta t$. This means the speed of a wave is assumed to be such that it reaches the cell boundaries exactly within a time step Δt. For uniform grids, each wave of the global problem therefore has the same speed. This is of course a truth with modifications; thus Rusanov developed a monotone flux [105], where the signal speed is replaced by $\lambda_{max} = \max((|v|+c)^+,(|v|+c)^-)$, where c is the local speed of sound. This leads to a slightly improved accuracy of the method. Another important contributor for the estimation of fluxes is the so-called HLLE Monotone Flux method, which was developed by Harten, Lax and van Leer [106]. The monotone flux simplifies the approximate Riemann problem even further. It neglects the contact surfaces, as described in section (8.3.4), and consequently assumes that between a shock wave and the corresponding expansion wave, only a single homogeneous state is present. For hyperbolic systems of two equations this is correct, but for the Euler equations addressed herein this is a rough approximation. Even if the resolution of contact surfaces is poor, this monotone flux is still a robust and efficient one, whose accuracy is, on the global level, often sufficient. An advantage of this flux is, that it can be applied easily to different thermodynamic property models. The scheme is implemented as an a-priori estimation for the fastest signal speeds, and its monotone flux is defined as:

$$f_{HLLE}(\Phi^+,\Phi^-) = \frac{c_r^+ f(\Phi_l) - c_r^- f(\Phi_r)}{c_r^+ - c_l^-} + \frac{c_r^+ c_l^-}{c_r^+ - c_l^-}(\Phi_r - \Phi_l), \tag{9.10}$$

Here, the signal speeds are c_r^+=$\max(0, u_r + c_r, \bar{u} + \bar{c})$ and c_l^-=$\min(0, u_l - c_l, \bar{u} - \bar{c})$, respectively. In these equations, the Roe average velocity $\bar{u}$ and the Roe average

speed of sound $\bar{c}$ have been used; see [88].

After introducing some monotone numerical fluxes, methods to obtain higher-order approximations of the solution to (9.1) will be considered.
Godunov's theorem [107] provides the theoretical foundation to the statement, that linear second-order schemes are more accurate in smooth regions of a problem solution to (9.1) than first-order schemes. There are near strong gradients and shocks; however, these methods produce spurious oscillations, and monotone methods do not exhibit such spurious oscillations. In the case of linear schemes, their limited first-order accuracy is disadvantageous however. One option to eliminate or reduce spurious oscillations for higher-order methods is to introduce artificial viscosity. This can be tuned such that it is large enough to suppress oscillations in the neighbourhood of discontinuities and then it is small elsewhere to maintain accuracy; see (8.6). A disadvantage of this approach is that the quantity of artificial viscosity is problem-dependent and therefore requires fine-tuning by the user. This approach is not followed here, but is discussed later where the case studies of evaporator simulations are described. Instead a less empirical approach to introduce viscosity is adopted, in order to circumvent the limitations formulated by Godunov's theorem; schemes with variable coefficients, i.e., nonlinear schemes, are considered. Such schemes can adapt themselves to the local nature of the solution. Harten [108] defined High-Resolution Methods as numerical methods with the following properties:

- The solution is free of spurious oscillations.
- Second or higher-order of accuracy in smooth parts of the solution.
- The resolution of discontinuities in the solution is high, depending on the size of the stencil.

A class of methods fulfilling these properties is that of Total Variation Diminishing methods, described by [108]. See this reference for a definition of the total variation. For brevity, only the case of a smooth function Φ(t), for which the total variation is

$$TV(\Phi) = \int_{\infty}^{\infty} \left| \frac{\partial \Phi(z)}{\partial z} \right| dz \tag{9.11}$$

and the case of a mesh function $\Phi^n = \{\Phi_i^n\}$ are mentioned. For the latter, the total variation is defined as

$$TV(\Phi^n) = \sum_{i=-\infty}^{\infty} \left| \Phi_{i+1}^n - \Phi_i^n \right| \tag{9.12}$$

Fundamental properties of the exact solution of the conservation law (9.1) such as no creation of new local extrema lead to the conclusion that the total variation

TV(Φ(t)) is a decreasing function of time; see [106]. Consequently, Total Variation Diminishing methods mimic a property of the exact solution. For a general scalar conservation law, Harten [109] provided a theorem on a sufficient condition for a particular class of nonlinear schemes with two coefficients to be Total Variation Diminishing (TVD). These conditions are essentially four inequalities on these two coefficients. As the coefficients may in general be data-dependent, Harten's theorem provides a tool for the construction of nonlinear schemes that circumvent Godunov's theorem stated above. Harten [109] also presented a class of explicit second-order accurate finite difference schemes for the computation of weak solutions of hyperbolic conservation laws; these were obtained by applying a non-oscillatory first-order accurate scheme to an appropriately modified flux function. The so-derived second-order accurate schemes achieve second-order resolution while preserving the robustness of the original non-oscillatory first order accurate scheme. Hence the classic TVD approach can be formulated as an adaptive switch between the characteristics of a monotone first-order numerical flux f^{LO} and those of a higher-order constant coefficient flux f^{HI} which is to make the following assumption by [110].

$$f^{TVD} = f^{LO} + \varphi(f^{HI} - f^{LO}) \tag{9.13}$$

Here, φ is a flux limiter function that implements the adaptive algorithm, which will be described later in section 9.3.

9.1. Numerical grid

With the exception of the Finite Element Method, there are usually two kinds of grid arrangements used to solve fluid flow problems: staggered grids and non-staggered grids. For the non-staggered grids, flux variables and scalar variables (such as fluid properties) are stored in the same locations, while for the staggered grids, flux components and scalar variables are stored at different locations, with shifted half control volume in each coordinate direction. Staggered grids are popular because of their ability to prevent checker board pressure in the flow solution, caused by odd-even decoupling between the pressure and velocity. However, the implementation of the staggered grid method is tedious, since the multi-dimensional momentum equations are discretized at different control volumes shifted in different directions from the main control volume. The programming difficulties increase when one deals with curvilinear or unstructured grids. As a result, nearly all codes written on curvilinear or unstructured grids use non-staggered grid arrangements for the solution of fluid flow problems. On the other hand non-staggered grids are prone to produce a false pressure field, a checker-board pressure, if special precautions are not taken. For this reason, in the early 1980 and earlier, non-staggered was rarely used for incompressible

flow. However, in nearly three decades the non-staggered grid (or collocated grid) has been used more widely, after the introduction of a momentum interpolation method to eliminate the checker board pressure problem. For hyperbolic systems of partial differential equations, the non-staggered grid is commonly used and does not introduce the above checker board pressure problem. A staggered / non-staggered grid is depicted in figure (9.1). The disadvantage of using staggered grids is that different variables are stored at different places, and this makes it more difficult to handle different control volumes for different variables and to keep track of the metrics. The developed non-staggered grid is suitable for the

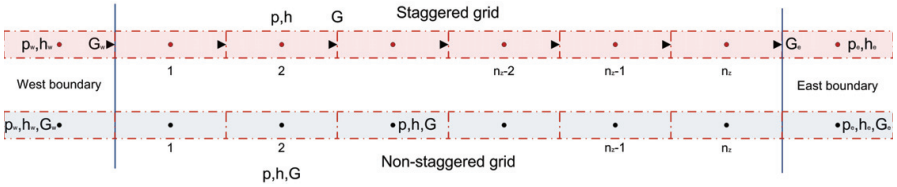

Figure 9.1.: Staggered grid in one dimension.

modelling of transport of mass, momentum and energy.

9.2. Second-order schemes

In the following the Godunov method for solving hyperbolic SCL will be outlined. The basic scheme of Godunov uses piecewise constant approximations for each cell, and results in a first-order upwind discretisation of the above problem with cell centres indexed as j. A semi-discrete scheme can be defined for the following SCL as follows,

$$\frac{\partial \Phi(z,t)}{\partial t} + \frac{1}{\Delta z}\left[f(\Phi(z_{j+1},t)) - f(\Phi(z_j,t))\right] = 0, \;\; t \geq 0, \;\; z \in \Omega \qquad (9.14)$$

where the continuous source vector function s(Φ) initially is set to zero. This basic scheme is not able to handle shocks or sharp discontinuities as they tend to become smeared. An example of this effect is shown in figure (9.2), which illustrates a 1D advective equation with a step wave propagating to the right. The simulation is carried out with a mesh of 100 cells and uses a second order (Crank-Nicolson) method for the time integration. A monotone numerical flux is defined using a function f:

$$f_{i+1/2} = f^*(\Phi^-_{i+1/2}, \Phi^+_{i+1/2}). \qquad (9.15)$$

Here, $\Phi^-_{i+1/2}$ is in general an approximation of the vector of conserved variables at $x_{i+1/2}$ in the left limit, and $\Phi^+_{i+1/2}$ in the right limit. If f satisfies

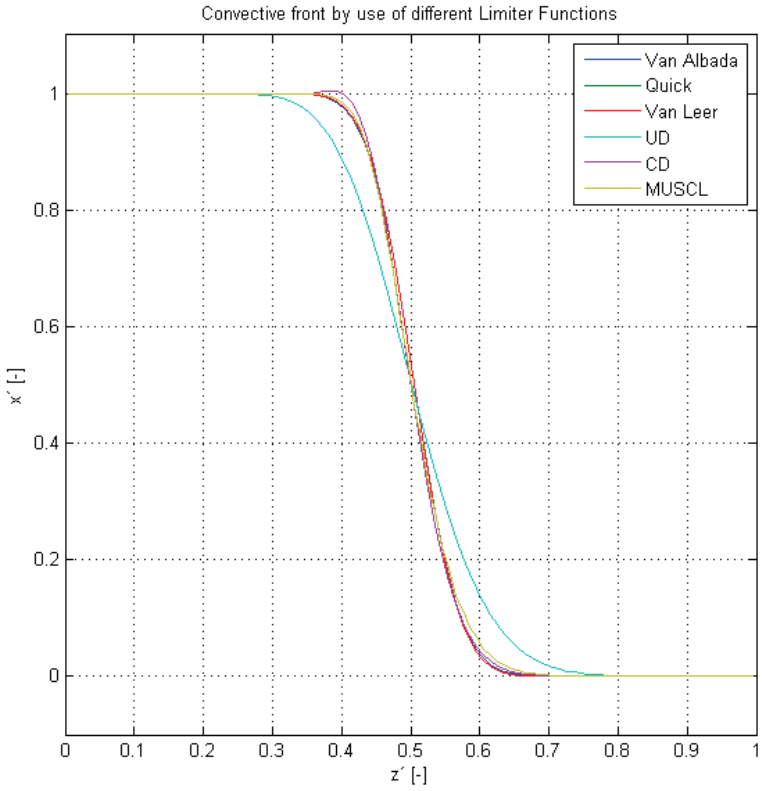

Figure 9.2.: Comparison of different TVD schemes + CD + UD- schemes.

the following conditions then (x) is a monotone flux according to reference [111]:

- f^*(a, b) is Lipschitz continuous in both arguments (strong form of uniform continuity for functions).
- f^*(a, b) is a non-decreasing function in (a) and a non-increasing function in (b).
- f^*(a, b) is consistent with the physical flux f, i.e.,f^* (a, a) = f^*(a).

Each monotone flux can be used without reconstruction with the approximation $\Phi^-_{i+1/2} \approx \Phi_i$ and $\Phi^+_{i+1/2} \approx \Phi_{i+1}$. The results are first-order schemes. Alternatively, any more sophisticated approach may be used to reconstruct $\Phi^\pm_{i+1/2}$. Monotone fluxes are classified as either upwind methods or central methods. Upwind methods are discretized equations on a mesh according to the direction of propagation of the convective information on that mesh. Central methods do not make a distinction based on the direction of the propagation of the convective

information. Within the upwind methods, both Godunov-type methods and flux vector splitting methods are presented based on [104]. To provide higher resolution of discontinuities, Godunov's scheme can be extended to use piecewise linear approximations of each cell, resulting in a central difference scheme that is second-order accurate in space. The piecewise linear approximations are obtained from

$$\Phi(z,t) = \Phi(z_j,t) + \frac{z - z_j}{z_{j+1} - z_j}\left(\Phi(z_{j+1},t) - \Phi(z_j,t)\right), \;\; z \in [z_j, z_{j+1}]. \quad (9.16)$$

Thus, evaluating fluxes at the cell edges, we get the following semi-discrete scheme

$$\frac{\partial \Phi(z,t)}{\partial t} + \frac{1}{\Delta z}\left[f(\Phi(z_{j+1/2},t)) - f(\Phi(z_{j-1/2},t))\right] = 0, \;\; t \geq 0, \;\; z \in \Omega \quad (9.17)$$

where $f(\Phi(z_{j+1/2},t))$ and $f(\Phi(z_{j-1/2},t)$ are the piecewise approximate values of cell edge variables, i.e.,

$$\Phi(z_{j+1/2},t) = \frac{1}{2}\left(\Phi(z_j,t) + \Phi(z_{j+1},t)\right) \quad (9.18)$$

$$\Phi(z_{j-1/2},t) = \frac{1}{2}\left(\Phi(z_{j-1},t) + \Phi(z_j,t)\right) \quad (9.19)$$

Although the above second-order scheme provides greater accuracy for smooth solutions, it is not a total variation diminishing (TVD) scheme and introduces spurious oscillations into the solution where discontinuities or shocks are present. An example of this effect is shown in figure (9.3), which illustrates a 1D advective equation , with a step wave propagating to the right. This loss of accuracy is to be expected due to Godunov's theorem, which says that linear numerical schemes for solving partial differential equations (PDEs), having the property of not generating new extrema (monotone scheme), can be at most first-order accurate. The simulation was carried out with a mesh of 100 cells and used a second-order (Crank-Nicolson) method of time integration. TVD-based numerical schemes extend the idea of using a linear piecewise approximation to each cell by using slope limited left and right extrapolated states. This results in the following high resolution, TVD discretisation scheme,

$$\frac{\partial \Phi(z_j,t)}{\partial t} + \frac{1}{\Delta z}\left[f(\Phi^*_{z_{j+1/2}}) - f(\Phi^*_{z_{j-1/2}})\right] = 0, \;\; t \geq 0, \;\; z \in \Omega. \quad (9.20)$$

The numerical fluxes $f(\Phi^*_{z_{j\pm1/2}})$ correspond to a nonlinear combination of first and second-order approximations to the continuous flux function. The symbols

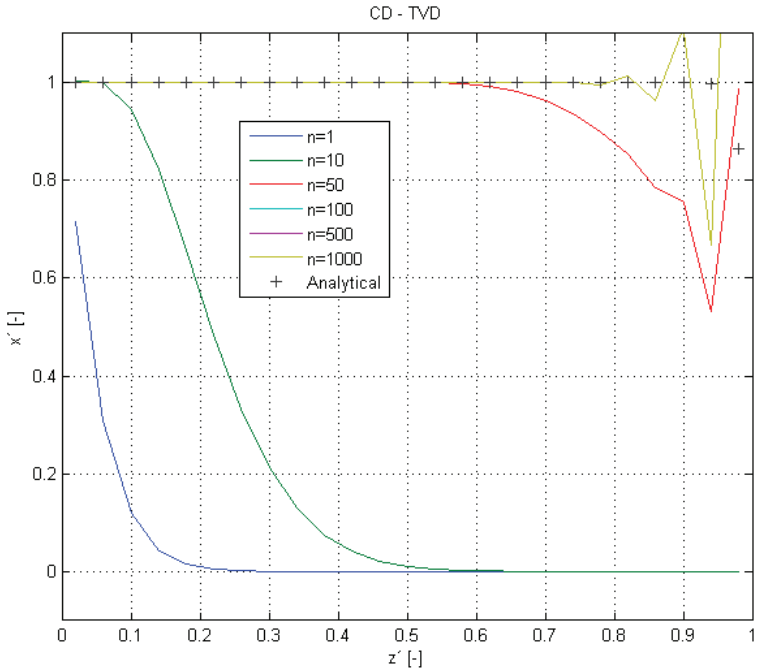

Figure 9.3.: Simulation with a high cell Peclet number initiating wiggles in the CD simulation. n is the timestep number.

$\Phi^*_{z_{j\pm1/2}}$ represent scheme-dependent functions (of the limited extrapolated cell edge variables), and are written shortly as $\Phi^*_{j\pm1/2}$, i.e.,

$$\Phi^*_{j\pm1/2} = \Phi^*(\Phi^-_{j\pm1/2}, \Phi^+_{j\pm1/2}) \tag{9.21}$$

where

$$\begin{aligned} \Phi^-_{j+1/2} &= \Phi_j + \frac{1}{2}\varphi(r_i)(\Phi_{j+1} - \Phi_j), \\ \Phi^+_{j+1/2} &= \Phi_{j+1} - \frac{1}{2}\varphi(r_{i+1})(\Phi_{j+2} - \Phi_{j+1}), \end{aligned} \tag{9.22}$$

and

$$\begin{aligned} \Phi^-_{j-1/2} &= \Phi_{j-1} + \frac{1}{2}\varphi(r_{i-1})(\Phi_j - \Phi_{j-1}), \\ \Phi^+_{j-1/2} &= \Phi_j - \frac{1}{2}\varphi(r_i)(\Phi_{j+1} - \Phi_j), \end{aligned} \tag{9.23}$$

where r is the argument to the limiter function $\varphi(r)$ and represents the ration of the successive gradients on the solution mesh, i.e.,

$$r_j = \frac{\Phi_j - \Phi_{j-1}}{\Phi_{j+1} - \Phi_j} \tag{9.24}$$

The Limiter function limits the slope of the piecewise approximations to ensure the solution is TVD, thereby avoiding the spurious oscillations that would otherwise occur around discontinuities or shocks.

9.3. Flux limiter

Flux limiters are used in high resolution schemes; these are numerical schemes used to solve problems in science and engineering, particularly fluid dynamics, described by partial differential equations (PDEs). They are used in high resolution schemes to avoid the spurious oscillations (wiggles) that would otherwise occur with high-order spatial discretisation schemes due to shocks, discontinuities or sharp changes in the solution domain. The use of flux limiters, together with an appropriate high resolution scheme, makes the solutions be total variation diminishing (TVD). Flux limiters are also referred to as slope limiters, because both have the same mathematical form, and both have the effect of limiting the solution gradient near shocks or discontinuities. In general, the term flux limiter is used when the limiter acts on system fluxes, and slope limiter is used when the limiter acts on system states. The main idea behind the construction of flux limiter schemes is to limit the spatial derivatives to realistic values; for scientific and engineering problems this usually means physically realisable values. They are used in high resolution schemes for solving problems described by PDEs and only come into operation when sharp wave fronts are present. For smoothly changing waves, the flux limiters do not operate and the spatial derivatives can be represented by higher-order approximations without introducing non-real oscillations. The limiter function is constrained to be greater than or equal to zero, i.e., r $\geq$ 0. Therefore, when the limiter is equal to zero (sharp gradient, opposite slopes or zero gradient), the flux is represented by a low resolution scheme. Similarly, when the limiter is equal to 1 (smooth solution), it is represented by a high resolution scheme. The various limiters have differing switching characteristics and are selected according to the particular problem and solution scheme; see equation (9.13). No particular limiter has been found to work well for all problems, and a particular choice is usually made on a trial and error basis. Thus, the accuracy of a TVD discretization degrades to first-order at local extrema, but tends to second-order over smooth parts of the domain. The algorithm is straight-forward to implement. Once a suitable scheme for $f^*_{j+1/2}$ has been chosen, such as the Kurganov and Tadmor scheme [112], the solution can

proceed using standard numerical integration techniques as presented by Gottlieb in [113]. Different flux limiter functions $\varphi(r)$ are listed in the following table (9.1), taken from [114]. It is easy to see that the *upwind differencing* (UD) scheme

Table 9.1.: Some of the most popular limiter functions, source: [114].

Name	**Limit function**	**Source**
Van Leer	$\frac{r+\|r\|}{1+r}$	Van Leer (1974)
Van Albadar	$\frac{r+r^2}{1+r^2}$	Van Albada et al. (1982)
Min-Mod	$\Phi(r) = \begin{cases} \min(r,1) & \text{if } r > 0 \\ 0 & \text{if } r \leq 0 \end{cases}$	Roe (1985)
SUPERBEE	$\max(0, \min(2r,1), \min(r,2))$	Roe (1985)
Sweby	$\max(0, \min(\beta r,1), \min(r,\beta))$	Sweby (1988)
QUICK	$\max(0, \min(2r,(3+r)/4,2)$	Leonard (1988)
UMIST	$\max(0, \min(2r,(1+3r)/4,(3+r)/4,2)$	Lien and Leschziner (1993)

($\Phi_{j+1/2} = \Phi_j$) for $f_{j+1/2} > 0$ leads to a Limiter Function $\varphi(r)$=0 and the *central differencing* (CD) scheme ($\Phi_{j+1/2} = (\Phi_j + \Phi_{j+1})/2$) leads to $\varphi(r)$=1. All the above limiters indicated as being symmetric, exhibit the following symmetry property,

$$\frac{\varphi(r)}{r} = \varphi(\frac{1}{r}). \tag{9.25}$$

This is a desirable property as it ensures that the limiting actions for forward and backward gradients operate in the same way. According to [114], the admissible limiter regions for second-order TVD schemes are illustrated in figure (9.4). Unless indicated to the contrary, the above limiter functions are second-order TVD. This means that they are designed such that they pass through a certain region of the solution, known as the TVD region, in order to guarantee stability of the scheme. Second-order, TVD limiters satisfy at least the following criteria:

$$\begin{aligned} \varphi(1) &= 1, \\ r \leq \varphi(r) &\leq 2r, \quad \text{for} \quad 0 \leq r \leq 1, \\ 1 \leq \varphi(r) &\leq r, \text{for} \quad 1 \leq r \leq 2, \\ 1 \leq \varphi(r) &\leq 2, \text{for} \quad r > 2, \end{aligned} \tag{9.26}$$

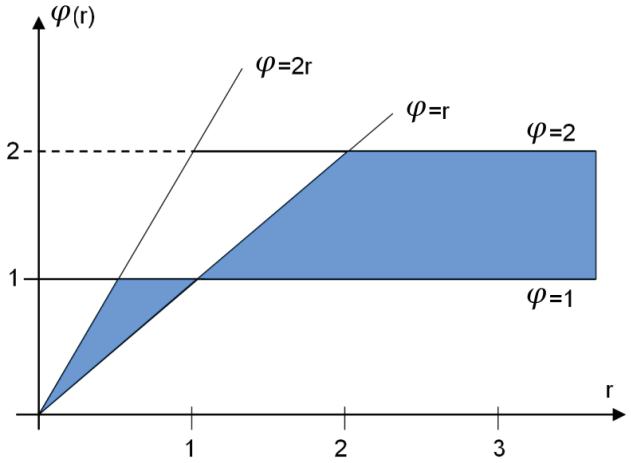

Figure 9.4.: Admissible limiter region for second-order TVD schemes.

Figure (9.2) shows a comparison between the Limiter functions shown in table (9.1). Simulations give different slopes of the pure convective front, initiated by a Heaviside step function on the upstream boundary. For comparison, the UD and CD schemes are shown in the same figure (9.2). The CD scheme gives minor overshoots as is evident in the same figure. It can be seen that TVD solutions show far less false diffusion than the UD scheme and are almost as close to the exact solution as the QUICK scheme. Moreover, they do not show any non-physical overshoots and undershoots. The four TVD solutions are quite close to each other, which is also a recurring feature in more broadly based performance comparisons in the literature, [110], [115] and [108]. In figure (9.5) we can see how sensitive the moving front is on the choice of limiter function. Again the simulations are without diffusion. The CD-scheme initiates oscillations, with an intensive over-shoot, or exceeds its steady-state value, while the other Limiter functions, classified as TVD, only affect the shape of the front, without introducing over and under-shoots of the front.

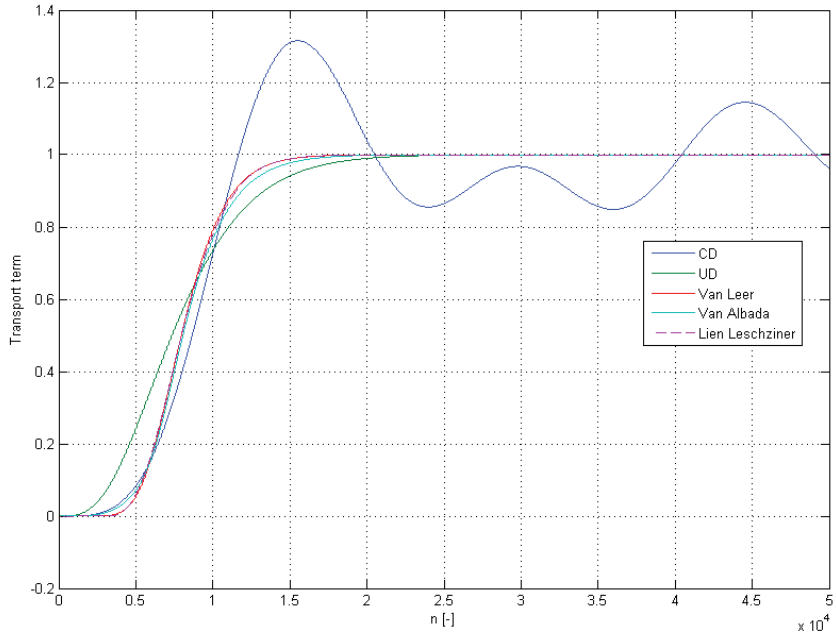

Figure 9.5.: Comparison of different TVD schemes for n_z=5.

9.4. Higher-order schemes

Significant efforts are made to remove the numerical oscillations created by higher-order numerical schemes of hyperbolic conservation laws near discontinuities, e.g., [116]. A successful numerical method should resolve discontinuities with correct positions, sharp non-oscillatory profiles and retain high order accuracy in smooth parts. A prominent class of such methods is **w**eighted **e**ssentially **n**on-**o**scillatory (WENO) schemes; see, e.g., [117] and [118]. The WENO scheme is suitable for solving convection dominated partial differential equations, containing potential discontinuities in the solution; see [119]. Examples of such problems are the Euler or Navier-Stokes equations in computational fluid dynamics. WENO is an extension of the **e**ssentially **n**on-**o**scillatory (ENO) scheme, introduced by [120]. The essential idea in the WENO methodology is to make a linear combination of lower-order reconstructions to obtain a higher-order approximation. The combination coefficients, also called linear weights or ideal weights, are obtained from the local geometry of the mesh and the order of accuracy. When the grid is uniform or smoothly varying, the linear weights remain positive. This section contains a brief introduction to some of the fundamental concepts and an overview of the primary challenges in solving hyperbolic partial differential equations.

The definition of hyperbolicity only concerns equation (9.5) above; it means that the Jacobian matrix **J** has real eigenvalues and a set of associated eigenvectors forming a basis of $\Re^m$, where m is the dimension of vector Φ. Consider the uniform non-staggered spatial grid, depicted in figure (9.6), where the cell I_j=$\left[z_{j-1/2}, z_{j+1/2}\right]$ has a cell width Δz, and let Δt be the time step. We denote the

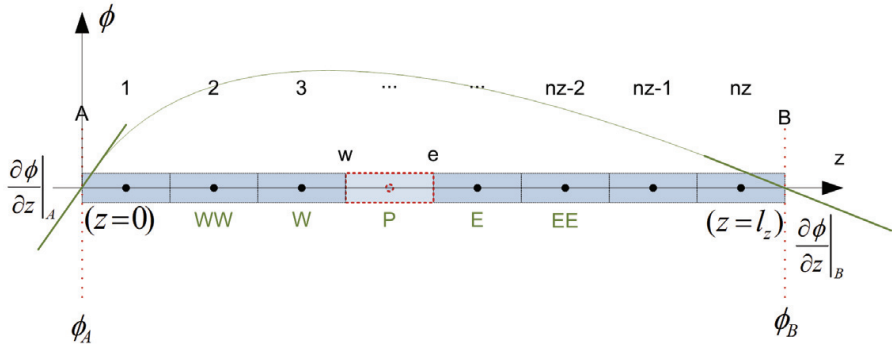

Figure 9.6.: Boundary conditions in pipe model.

spatial grid points by z_j=jΔz, t^n=nΔt and $\Phi_j^n = \Phi(z_j, t^n)$. Since the solution of (9.1) with the belonging initial conditions, given by (9.2) and the two types of boundary conditions, given by (9.3) and (9.4), can develop discontinuities even for smooth initial data, the quantities that will be used on the discrete level, are cell averages. The numerical approximation of the cell averages in the cell I_j is denoted by $\bar{\Phi}_j^n$:

$$\bar{\Phi}_j^n = \frac{1}{\Delta z}\int_{I_j} \Phi(z, t^n)dz. \tag{9.27}$$

The starting point for the construction of Godunov-type schemes for conservation laws is the equivalent integral formulation of the system (9.1) with s(Φ(z,t)) initially assigned zero. Assuming that the cell averages at time t_n , $\bar{\Phi}_j^n$ are known, our goal is to compute the cell averages at the next time step t^{n+1} as:

$$\begin{aligned}\bar{\Phi}(z, t+\Delta t) = \bar{\Phi}(z,t) - \frac{1}{\Delta z}[&\int_{r=t}^{t+\Delta t} f(\Phi(z+\frac{\Delta z}{2}, \tau))d\tau \\ &- \int_{r=t}^{t+\Delta t} f(\Phi(z-\frac{\Delta z}{2}, \tau))d\tau]\end{aligned} \tag{9.28}$$

9.5. Polynomial reconstruction

In this sub-section, we review Godunov-type central schemes in one spatial dimension. We recall the construction of the non-staggered central scheme for

conservation laws. We denote the sliding averages of Φ(z,t) over the interval (z-Δz/2, z+Δz/2). At time level t = t^n we consider (9.28) with the piecewise polynomial initial condition, given by (9.29),

$$\tilde{\Phi}(z,t^n) = p_j^n(z), \quad z_{j-1/2} < z < z_{j+1/2}, \quad \text{for} j \in [1,n_z]. \tag{9.29}$$

First, from $\bar{\Phi}_j^n$ we reconstruct the point values of the function $\bar{\Phi}(z,t^n)$ via a suitable nonlinear piecewise polynomial interpolation $p_j(z,t)$ taking into account conservation, accuracy and non-oscillatory requirements, for each cell I_j. At each cell interface $z_{j+1/2}$ the reconstruction produces two different values of the function $\Phi(z)$, namely, the left and the right extrapolated value at a certain time t^n:

$$\Phi_{j+1/2}^L = p_j(z_{j+1/2}), \quad \Phi_{j+1/2}^R = p_{j+1}(z_{j+1/2}), \tag{9.30}$$

obtained from the cell averages $\bar{\Phi}_j^n \equiv \bar{\Phi}(z_j,t^n)$, computed at the previous time step. This piecewise polynomial reconstruction should be conservative, accurate to order r, and non-oscillatory. Then the piecewise polynomial $\tilde{\Phi}(z,t^n)$ is evolved exactly according to (9.28), and the solution at time t=t^{n+1} is obtained in terms of its sliding averages, $\bar{\Phi}(z,t^{n+1})$.

The governing equations introduced in equation (9.1) were derived from the integral relations based on the assumption of smoothness of the variables, which is not fulfilled for the applications considered in this section. In order to include weak solutions of (9.1), an integral form of the equations is used. Therefore, the equation is integrated over the interval I_j to obtain

$$\frac{d\bar{\Phi}(z_j,t)}{dt} = s(\bar{\Phi}(z_j,t)) - \frac{1}{\Delta z}\left(f(\bar{\Phi}(z_{j+1/2},t)) - f(\bar{\Phi}(z_{j-1/2},t))\right) \tag{9.31}$$

where $f(\bar{\Phi}(z_{j+1/2},t))$ is the numerical flux at $z_{j+1/2}$ and time t. This numerical flux function at the cell boundaries is defined as a monotone function of left and right extrapolated values as described in equation (9.30).

$$f(\bar{\Phi}(z_{j+1/2},t)) = f(\Phi_{j+1/2}^L, \Phi_{j+1/2}^R) \tag{9.32}$$

In the next sub-sections, we will present the WENO reconstructions as mentioned in [116], which supply the required piecewise polynomial $p_j^n(z)$. Fifth-order WENO reconstruction of the point values uses a five-point stencil, S_5 which is sub-divided into three sub-stencils, $\{S_1;S_2;S_3\}$ as shown in figure (9.7). Initially we select an optimal polynomial of degree r=4, denoted $\tilde{\Phi}_{opt}$, on the central stencil $S_5 = \{I_{i-2},I_{i-1},I_i,I_{i+1},I_{i+2}\}$. Hence the optimal polynomial can be expressed

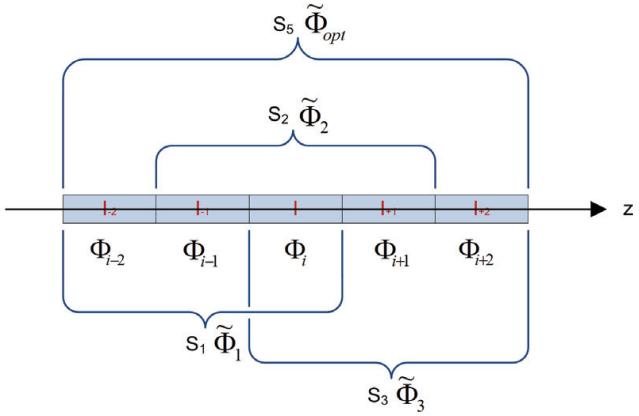

Figure 9.7.: Discrete stencils for the Central WENO procedure.

as:

$$\tilde{\Phi}_{opt} \equiv \sum_{j=1}^{5} a_{j-1}(z-z_i)^{j-1} \tag{9.33}$$

Additionally we have from [116] an uniquely defined relation for $\tilde{\Phi}_{opt}$:

$$\bar{\Phi}_{i+k} = \frac{1}{\Delta z}\int_{I_{i+k}} \tilde{\Phi}(z)_{opt}dz, \quad k \in \{-2,-1,0,1,2\}\,. \tag{9.34}$$

Thus, we are able to establish a linear system for the undetermined coefficients, $\{a_i\}$. This system can be re-written for a uniform Cartesian grid as:

$$\mathbf{U} = \mathbf{C} \times \mathbf{A} \tag{9.35}$$

with the following notations: $\mathbf{U} \equiv \left[\bar{\Phi}_{i-2}, \bar{\Phi}_{i-1}, \bar{\Phi}_i, \bar{\Phi}_{i+1}, \bar{\Phi}_{i+2},\right]^t$, $\mathbf{A} \equiv [a_j]^t_{j\in 0,\ldots,4}$ and $\mathbf{C}$ is given by (9.36) according to [116]:

$$\mathbf{C} \equiv \begin{cases} c_{1,j} = \frac{(-1)^j}{j\Delta z}\left[(\frac{3\Delta z}{2})^j - (\frac{5\Delta z}{2})^j\right], \\ c_{2,j} = \frac{(-1)^j}{j\Delta z}\left[(\frac{\Delta z}{2})^j - (\frac{3\Delta z}{2})^j\right], \\ c_{3,j} = \frac{\Delta z^{j-1}}{j(2)^j}\left[1+(-1)^{j+1}\right] \qquad \text{for } j \in \{1\ldots5\}, \\ c_{4,j} = \frac{(-1)^j}{j\Delta z}\left[(\frac{3\Delta z}{2})^j - (\frac{\Delta z}{2})^j\right], \\ c_{5,j} = \frac{(-1)^j}{j\Delta z}\left[(\frac{5\Delta z}{2})^j - (\frac{3\Delta z}{2})^j\right]. \end{cases} \tag{9.36}$$

For solving the Riemann's problem, arising at each interface, we only need the approximations to the values of $\Phi(z)$ at the cell boundaries. These values are calculated according to the relation:

$$\Phi^{+}_{i+1/2} = \left({}^{t}\mathbf{D} \times \mathbf{C}^{-1}\right) \times \mathbf{U} \equiv \sum_{j=1}^{5} \tilde{a}_{j-1} \bar{\Phi}_{i+j-3} \tag{9.37}$$

with the following definition: $\mathbf{D} \equiv \left[(\frac{\Delta z}{2})^{j-1}\right]_{j=1,\ldots,5}$. The constants $\tilde{a}_j$ depend on the cell sizes, Δz, but not on the function Φ itself. For the calculations of $\Phi^{-}_{i+1/2}$, the constants $\tilde{a}_j$ are simply calculated by modifying the form of the vector: $\mathbf{D} \equiv \left[(-1)^{j+1}(\frac{\Delta z}{2})^{j-1}\right]_{j=1,\ldots,5}$. When the grid is uniform, the expressions for the polynomial coefficients, $\tilde{a}_j$, do not depend on the points of discretization. In such a case, these expressions can be explicitly formulated to determine fully $\tilde{\Phi}_{opt}(z)$ and, later, the smoothness indicators, by solving equation (9.35) with respect to $\mathbf{A}$:

$$\mathbf{A}_{S_5} = \begin{cases} a_0 = \frac{1067}{960}\bar{\Phi}_i - \frac{29}{480}\left(\bar{\Phi}_{i+1} + \bar{\Phi}_{i-1}\right) + \frac{3}{640}\left(\bar{\Phi}_{i+2} + \bar{\Phi}_{i-2}\right), \\ a_1 = \frac{1}{48\Delta z}\left[34\left(\bar{\Phi}_{i+1} - \bar{\Phi}_{i-1}\right) + 5\left(\bar{\Phi}_{i-2} - \bar{\Phi}_{i+2}\right)\right], \\ a_2 = \frac{-1}{16\Delta z^2}\left[\bar{\Phi}_{i-2} + 22\bar{\Phi}_i + \bar{\Phi}_{i+2} - 12\left(\bar{\Phi}_{i+1} + \bar{\Phi}_{i-1}\right)\right], \\ a_3 = \frac{-1}{12\Delta z^3}\left[2\left(\bar{\Phi}_{i+1} - \bar{\Phi}_{i-1}\right) + \left(\bar{\Phi}_{i-2} - \bar{\Phi}_{i+2}\right)\right], \\ a_4 = \frac{1}{24\Delta z^4}\left[\bar{\Phi}_{i-2} + 6\bar{\Phi}_i + \bar{\Phi}_{i+2} - 4\left(\bar{\Phi}_{i+1} + \bar{\Phi}_{i-1}\right)\right]. \end{cases} \tag{9.38}$$

Finally, the calculated point-values at the cell boundary z = $z_{i+1/2}$ are such that

$$\Phi_{i+1/2} \equiv \tilde{\Phi}_{opt}(z_{i+1/2}) = \Phi(z_{i+1/2}) + O(\Delta z^5). \tag{9.39}$$

To derive an essentially non-oscillatory reconstruction, we need to define three supplementary polynomials ($\tilde{\Phi}_1, \tilde{\Phi}_2, \tilde{\Phi}_3$), approximating $\Phi(z)$ with a lower accuracy on I_i. Thus, we define the polynomial of second-order accuracy, $\tilde{\Phi}_1(z)$, on the reduced stencil S_1: (I_{i-2}, I_{i-1}, I_i), $\tilde{\Phi}_2(z)$ is defined on the stencil S_2: (I_{i-1}, I_i, I_{i+1}), whereas $\tilde{\Phi}_3(z)$ is defined on the stencil S_3: (I_i, I_{i+1}, I_{i+2}); see figure (9.7). Now, we have to invert a 3×3 linear system similar to (9.35) for the unknown coefficients $\{a_j\}, j \in \{0,\ldots,2\}, j \in \{1,\ldots,3\}$ and $j \in \{2,\ldots,4\}$, defining $\tilde{\Phi}_1, \tilde{\Phi}_2, \tilde{\Phi}_3$,

respectively. Once again, the constants determining the interpolation are precomputed and stored before solving the PDEs. When the grid is uniform, the values of the coefficients for $\tilde{\Phi}_1, \tilde{\Phi}_2$ and $\tilde{\Phi}_3$ can be explicitly formulated.
For $\tilde{\Phi}_1$ defined on S_1, we have:

$$\mathbf{A}_{S_1} = \begin{cases} a_0 = \frac{23}{24}\bar{\Phi}_i + \frac{1}{12}\left(\bar{\Phi}_{i-1} - \bar{\Phi}_{i-2}\right), \\ a_1 = \frac{1}{2\Delta z}\left(3\bar{\Phi}_i - 4\bar{\Phi}_{i-1} + \bar{\Phi}_{i-2}\right), \\ a_2 = \frac{1}{2\Delta z^2}\left(\bar{\Phi}_i - 2\bar{\Phi}_{i-1} + \bar{\Phi}_{i-2}\right). \end{cases} \tag{9.40}$$

For $\tilde{\Phi}_2$ defined on S_2, we have:

$$\mathbf{A}_{S_2} = \begin{cases} a_0 = \frac{13}{12}\bar{\Phi}_i - \frac{1}{24}\left(\bar{\Phi}_{i-1} + \bar{\Phi}_{i+1}\right), \\ a_1 = \frac{1}{2\Delta z}\left(\bar{\Phi}_{i+1} - \bar{\Phi}_{i-1}\right), \\ a_2 = \frac{1}{2\Delta z^2}\left(\bar{\Phi}_{i+1} - 2\bar{\Phi}_i + \bar{\Phi}_{i-1}\right). \end{cases} \tag{9.41}$$

The last $\tilde{\Phi}_3$ is defined on S_3, which gives:

$$\mathbf{A}_{S_3} = \begin{cases} a_0 = \frac{23}{24}\bar{\Phi}_i + \frac{1}{12}\left(\bar{\Phi}_{i+1} - \frac{1}{2}\bar{\Phi}_{i+2}\right), \\ a_1 = \frac{-1}{2\Delta z}\left(3\bar{\Phi}_i - 4\bar{\Phi}_{i+1} + \bar{\Phi}_{i+2}\right), \\ a_2 = \frac{1}{2\Delta z^2}\left(\bar{\Phi}_i - 2\bar{\Phi}_{i+1} + \bar{\Phi}_{i+2}\right). \end{cases} \tag{9.42}$$

The coefficient a_0 in (9.42) is not identical with what is stated in [116].

9.6. WENO Reconstruction

If the discrete stencil defining $\tilde{\Phi}_{opt}(z)$ contains a discontinuity or large gradients, spurious oscillations can appear in the numerical solution. To avoid such a problem, we construct a WENO procedure that smoothly adapts the stencil in the neighbourhood of a singularity. Defining the non-oscillatory re-

construction on cell I_i by $\tilde{\Phi}^i(z)$, we want the following properties to be verified:

$$\tilde{\Phi}^i(z) = \begin{cases} \tilde{\Phi}_1(z) \text{ if the solution is not smooth and the stencil } S_1 \\ \text{is in the smooth regions,} \\ \\ \tilde{\Phi}_2(z) \text{ if the solution is not smooth and the stencil } S_2 \\ \text{is in the smooth regions,} \\ \\ \tilde{\Phi}_3(z) \text{ if the solution is not smooth and the stencil } S_3 \\ \text{is in the smooth regions,} \\ \\ \tilde{\Phi}_{opt}(z) \text{ if the stencil } S_5 \text{ is in the smooth regions.} \end{cases} \tag{9.43}$$

To implement a specific solution technique, we extended the principle of the central WENO interpolation defined in [121]. First, we construct an ENO interpolant as a convex combination of polynomials, based on different discrete stencils. Specifically, we define in the discrete cell I_i:

$$\tilde{\Phi}^i(z) \equiv \sum_j w_j \times \tilde{\Phi}_j(z), \quad \sum_j w_j = 1 \quad \text{for} \quad w_j \geq 0, \quad j \in \{1,..,4\}, \tag{9.44}$$

and $\tilde{\Phi}_1$, $\tilde{\Phi}_2$ and $\tilde{\Phi}_3$ are the previously defined polynomials. $\tilde{\Phi}_4$ is the second-order polynomial, defined on the central stencil S_5 and is calculated so that the convex combination in (9.44), will be fifth-order accurate in smooth regions. Therefore, it must verify:

$$\tilde{\Phi}_{opt}(z) = \sum_j C_j \times \tilde{\Phi}_j(z) \ \ \forall z \in I_i, \ \ \sum_j C_j = 1 \ \ \text{for} \ \ C_j \geq 0, \ \ \ j \in \{1,..,4\}. \tag{9.45}$$

The constants C_j represent ideal weights for (9.44) and we make the choice as in [116]:

$$C_1 = C_3 = 1/8, C_2 = 1/4 \text{ and } C_4 = 1/2. \tag{9.46}$$

Then the central polynomial, $\tilde{\Phi}_4(z)$, can be calculated from (9.45):

$$\tilde{\Phi}_4(z) = \frac{1}{C_4}\left[\tilde{\Phi}_{opt}(z) - C_1\tilde{\Phi}_1(z) - C_2\tilde{\Phi}_2(z) - C_3\tilde{\Phi}_3(z)\right] \ \ \forall z \in I_i. \tag{9.47}$$

which after inserting, (9.38), (9.40), (9.41), (9.42) in (9.47), gives:

$$\mathbf{A}_{S_5}: \begin{cases} \bar{\Phi}^{+}_{j+1/2} = -\frac{1}{60}\bar{\Phi}_{i-2} - \frac{7}{120}\bar{\Phi}_{i-1} + \frac{73}{120}\bar{\Phi}_{i} + \frac{21}{40}\bar{\Phi}_{i+1} + \frac{-7}{120}\bar{\Phi}_{i+2} & , \\ \bar{\Phi}^{-}_{j-1/2} = -\frac{7}{120}\bar{\Phi}_{i-2} + \frac{21}{40}\bar{\Phi}_{i-1} + \frac{73}{120}\bar{\Phi}_{i} - \frac{7}{120}\bar{\Phi}_{i+1} - \frac{1}{60}\bar{\Phi}_{i+2} & . \end{cases} \tag{9.48}$$

Note that, although the stencil defining $\tilde{\Phi}_4(z)$ is the five-point stencil S_5, this polynomial is only a second-order approximation of $\Phi(z)$. Note that the role of $\tilde{\Phi}_4(z)$ is only to recover high-order accuracy in smooth regions. The fifth-order WENO reconstruction is then being defined in the discrete cell I_j by:

$$\Phi_{j+1/2} = p_j(x_{j+1/2}) = \sum_{k=1}^{4} w_k \cdot \tilde{\Phi}^{+^{(k)}}_{j+1/2}, \tag{9.49}$$

$$\Phi_{j-1/2} = p_j(x_{j-1/2}) = \sum_{k=1}^{4} w_k \cdot \tilde{\Phi}^{-^{(k)}}_{j-1/2}, \quad \sum_{k=1}^{4} w_k = 1, \tag{9.50}$$

where the reconstruction polynomials now can be determined at the face values of I_j, which for j+1/2 we find:

$$\begin{aligned} \tilde{\Phi}^{+^{(1)}}_{j+1/2} &= \frac{1}{6}\left[2\bar{\Phi}_{j-2} - 7\bar{\Phi}_{j-1} + 11\bar{\Phi}_{j}\right] \\ \tilde{\Phi}^{+^{(2)}}_{j+1/2} &= \frac{1}{6}\left[-\bar{\Phi}_{j-1} + 5\bar{\Phi}_{j} + 2\bar{\Phi}_{j+1}\right] \\ \tilde{\Phi}^{+^{(3)}}_{j+1/2} &= \frac{1}{6}\left[2\bar{\Phi}_{j} + 5\bar{\Phi}_{j+1} - \bar{\Phi}_{j+2}\right] \\ \tilde{\Phi}^{+^{(4)}}_{j+1/2} &= \frac{1}{120}\left[-2\bar{\Phi}_{j-2} - 7\bar{\Phi}_{j-1} + 73\bar{\Phi}_{j} + 63\bar{\Phi}_{j+1} - 7\bar{\Phi}_{j+2}\right] \end{aligned} \tag{9.51}$$

and for j-1/2 we find:

$$\begin{aligned} \tilde{\Phi}^{-^{(1)}}_{j-1/2} &= \frac{1}{6}\left[-\bar{\Phi}_{j-2} + 5\bar{\Phi}_{j-1} + 2\bar{\Phi}_{j}\right] \\ \tilde{\Phi}^{-^{(2)}}_{j-1/2} &= \frac{1}{6}\left[2\bar{\Phi}_{j-1} + 5\bar{\Phi}_{j} - \bar{\Phi}_{j+1}\right] \\ \tilde{\Phi}^{-^{(3)}}_{j-1/2} &= \frac{1}{6}\left[11\bar{\Phi}_{j} - 7\bar{\Phi}_{j+1} + 2\bar{\Phi}_{j+2}\right] \\ \tilde{\Phi}^{-^{(4)}}_{j-1/2} &= \frac{1}{120}\left[-7\bar{\Phi}_{j-2} + 63\bar{\Phi}_{j-1} + 73\bar{\Phi}_{j} - 7\bar{\Phi}_{j+1} - 2\bar{\Phi}_{j+2}\right] \end{aligned} \tag{9.52}$$

To complete the reconstruction of $\tilde{\Phi}^{(i)}(z)$, we only need to compute the non-oscillatory weights, w_j. To define these weights, we follow the reasoning of [122]. To achieve the optimal interpolation, (9.45), in smooth regions, the weights w_j must smoothly converge to the ideal weights C_j as Δz approaches zero. In an opposite way, in regions with discontinuity, the weights should effectively remove the contribution of stencils, containing the discontinuity, according to properties in (9.43). To this end, combining (9.44) and (9.45) gives:

$$\tilde{\Phi}^{(i)}(z) = \tilde{\Phi}_{opt}(z) + \sum_{j\in\{1,..,4\}} (w_j - C_j) \times \tilde{\Phi}_j(z) \;\; \forall z \in I_i. \tag{9.53}$$

Since $\tilde{\Phi}_j$=$\Phi_j(z)$+$O(\Delta z^3)$, j $\in \{1,2,3,4\}$, wherever the solution is smooth and (9.53) can be re-written as

$$\tilde{\Phi}^{(i)}(z) = \tilde{\Phi}_{opt}(z) + \sum_{j\in\{1,..,4\}} (w_j - C_j) \times (\Phi_j(z) + O(\Delta z^3)) \;\; \forall z \in I_i. \tag{9.54}$$

Therefore, the second term of (9.54) must be at least a $O(\Delta z^5)$ quantity for $\Phi(z)$ to be approximated at fifth-order by $\tilde{\Phi}^i(z)$ in regions of smoothness. Then the necessary and sufficient conditions are:

$$\begin{cases} \left(\sum_{j\in\{1,..,4\}} w_j - 1\right) \times \Phi(z) = O(\Delta z^5), \\ \\ \sum_{j\in\{1,..,4\}} (w_j - C_j) = O(\Delta z^2). \end{cases} \tag{9.55}$$

It is sufficient to require

$$\begin{cases} \sum_{j\in\{1,..,4\}} w_j - 1 \leq O(\Delta z^5), \\ \\ (w_j - C_j) \leq O(\Delta z^2), w_j \geq 0 \;\; \forall j \in \{1,2,3,4\}. \end{cases} \tag{9.56}$$

Up to this point, the development of the fifth-order WENO scheme has been general. To determine fully the *central WENO* (CWENO) scheme, we need now to specify the non-oscillatory weights.

9.7. Non-oscillatory weights

For the one-dimensional context, the WENO procedure has been defined on a five-point uniform stencil and designed to be fifth-order accurate in regions of smoothness. To this end, we define a finite-volume discretisation in which we consider the cell averages of the variable as the discrete unknowns. The reconstruction of point-values is then ensured by unique fifth-order polynomials.

Below we adapt this procedure for the non-linear weights to maintain the theoretical convergence properties of the optimum reconstruction, whatever problem is considered.

First of all, we calculate the general indicators of smoothness, defined in [121]:

$$IS_j^i = \frac{1}{\Phi_{max}^2} \sum_{k=0}^{2} \Delta z^{2k-1} \times \int_{I_i} \left(\frac{d^k \tilde{\Phi}_j}{dz^k} \right)^2 dz, \quad j \in \{1,2,3,4\}, \tag{9.57}$$

where Φ_{max} is calculated over the whole calculation domain Ω: Φ_{max}=$max|\Phi|_{z\in\Omega}$ and k describes the number of equations. These indicators describe the smoothness of the solution over the cell I_i, according to the particular stencil, selected to define $\tilde{\Phi}_j(z)$ on that cell. In regions of smoothness, $IS_j^i << 1$, whereas $IS_j^i = O(\Delta z)$ in cells with strong gradients or discontinuities. Specifically, (9.57) can be explicated for $\tilde{\Phi}_1$, $\tilde{\Phi}_2$ and $\tilde{\Phi}_3$ on a non-uniform mesh:

$$IS_j^i = a_1^2 \Delta z^2 + \frac{13}{3} a_2^2 \Delta z^4 + O(\Delta z^6), \quad j \in \{1,2,3\}. \tag{9.58}$$

The general form of IS_4^i is given by [116]:

$$IS_4^i = a_1^2 \Delta z^2 + \left[\frac{13}{3} a_2^2 + \frac{1}{2} a_1 a_3 \right] \Delta z^4 + O(\Delta z^6). \tag{9.59}$$

For each quadratic polynomial $\tilde{\Phi}_j(z), j \in \{1,2,3\}$, the polynomial coefficients $\{a_p\}$ are being calculated by numerically inverting (9.35). The coefficients for $\tilde{\Phi}_4(z)$ have then been deduced from formula (9.47). When the mesh is uniform, the coefficients $\{a_p\}$ have explicitly been given by formulae (9.38), (9.40), (9.41) and (9.42). The polynomial coefficients for $\tilde{\Phi}_j(z)$ have then been determined.

To calculate the weights, we review another technique to improve the classical smoothness indicators to obtain weights that satisfy the sufficient conditions for optimal order of accuracy. It is well known from [116] that the original WENO is fifth-order accurate for smooth parts of the solution domain except near sharp fronts and shocks. This idea is taken from [123] and uses the whole five-point stencil S_5 to define a new smoothness indicator of higher-order than the classical smoothness indicator IS_i. For estimating the weights w_k, k $\in \{1,2,3,4\}$, we proceed as follows: Define

$$IS_k^* = \frac{IS_k + \varepsilon}{IS_k + \varepsilon + \tau_5} \tag{9.60}$$

where IS_k, k $\in \{1,2,3\}$ are given by (9.58), IS_4 given by (9.59) and τ_5=$|IS_1 - IS_3|$ due to [124] and [123]. The constant ε is a small number. In some articles $\varepsilon \approx$ from $1 \cdot 10^{-2}$ to $1 \cdot 10^{-6}$; see [121]. Here we use much smaller values of ε for the schemes in order to force this parameter to play only its original role of disallowing vanishing denominators at the weight definitions. The weights w_k are defined as:

$$w_k = \frac{\alpha_k^*}{\sum_{l=1}^{4} \alpha_l^*}, \quad \alpha_k^* = \frac{C_k}{IS_k^*}, \ \ k \in \{1,2,3,4\} \tag{9.61}$$

where C_k is given by (9.46). To determine the order of approximation of the new weights w_k^* with respect to the ideal weights, we firstly study the smooth case and take ε=0. From (9.58) to (9.59) and the properties of τ_5 we obtain

$$\left(1 + \frac{\tau_5}{IS_k}\right) = 1 + O(\Delta z^3), \ \ k \in \{1,2,3,4\}, \tag{9.62}$$

therefore

$$w_k = C_k + O(\Delta z^3), \ \ k \in \{1,2,3,4\}. \tag{9.63}$$

Thus the weights in equation (9.63) satisfy the sufficient condition, providing the fifth-order accuracy to the CWENO at smooth regions. Another advantage is that this implementation according to our experience, reduces the computational CPU cost with more than 20 %, compared to the more time-consuming implementation given by [116].

9.8. Flux Splitting

In this section we review the derivation of the central-upwind flux presented in [125]. We consider the one-dimensional system (9.1) of m strictly hyperbolic conservation laws. We start with a piecewise polynomial reconstruction $p_j(z)$ with possible discontinuities at the interface points $z_{j+1/2}$. These discontinuities propagate with the right- and the left-sided local speeds, which can be estimated by

$$c_{j+1/2}^{+} = \max\left\{\lambda_N\left(\frac{\partial f(\Phi_{j+1/2}^{-})}{\partial \Phi}\right), \lambda_N\left(\frac{\partial f(\Phi_{j+1/2}^{+})}{\partial \Phi}\right), 0\right\}, \tag{9.64}$$

$$c_{j+1/2}^{-} = \min\left\{\lambda_1\left(\frac{\partial f(\Phi_{j+1/2}^{-})}{\partial \Phi}\right), \lambda_1\left(\frac{\partial f(\Phi_{j+1/2}^{+})}{\partial \Phi}\right), 0\right\},$$

with $\lambda_1 < ... \ \lambda_N$ being the eigenvalues of the Jacobian given by $\mathbf{J}$=$\frac{\partial f(\Phi(z,t))}{\partial \Phi}$. Here, $\Phi_{j+1/2}^{+}$=$p_{j+1}(z_{j+1/2})$, and $\Phi_{j+1/2}^{-}$=$p_j(z_{j+1/2})$ are the corresponding right and

left values of the piecewise polynomial interpolant $\{p_j(z)\}$ at the cell interface z=$z_{j+1/2}$, due to equation (9.33). An exact evolution of the reconstruction is followed by an intermediate piecewise polynomial reconstructions and finally projected back onto the original cells, providing the cell average at the next time step Φ_j^{n+1}. Further details can be found in [125]. The semi-discrete central-upwind scheme presented in [125] can be written as:

$$\frac{d\Phi_j(t)}{dt} = -\frac{1}{\Delta z}\left[F_{j+1/2} - F_{j-1/2}\right] = L_j(\Phi). \tag{9.65}$$

where the numerical flux is given by the HLLE monotone flux method (9.10):

$$\begin{aligned} F_{j+1/2} = & \frac{c^+_{j+1/2} f(\Phi^-_{j+1/2}) - c^-_{j+1/2} f(\Phi^+_{j+1/2})}{c^+_{j+1/2} - c^-_{j+1/2}} \\ & + \frac{c^+_{j+1/2} c^-_{j+1/2}}{c^+_{j+1/2} - c^-_{j+1/2}} \left[\Phi^+_{j+1/2} - \Phi^-_{j+1/2}\right]. \end{aligned} \tag{9.66}$$

Notice that the accuracy of this scheme is being determined by the accuracy of the reconstruction and the ODE solver (time integration). In this section the numerical solutions of (9.65) have advanced in time by means of the third-order TVD Runge-Kutta method, described by [126] (see next section). When the grid is uniform, the computations are simplified by using (9.38), (9.40), (9.41) and (9.42) for the polynomial coefficients. Then, the calculation of $\tilde{\Phi}^+_{i+1/2}$,$\tilde{\Phi}^-_{i+1/2}$ produces the following simplified result:

$$\begin{aligned} \tilde{\Phi}^+_{i+1/2} = & \left(-\frac{7}{120}w_4 - \frac{1}{6}w_1\right)\bar{\Phi}_{i-2} + \left(\frac{1}{3}w_2 + \frac{5}{6}w_1 + \frac{21}{40}w_4\right)\bar{\Phi}_{i-1} \\ & + \left(\frac{5}{6}w_2 + \frac{1}{3}w_1 + \frac{11}{6}w_3 + \frac{73}{120}w_4\right)\bar{\Phi}_i + \left(-\frac{1}{6}w_2 - \frac{7}{6}w_3 - \frac{7}{120}w_4\right)\bar{\Phi}_{i+1} \\ & + \left(\frac{1}{3}w_3 - \frac{1}{60}w_4\right)\bar{\Phi}_{i+2} \end{aligned} \tag{9.67}$$

$$\begin{aligned} \tilde{\Phi}^-_{i+1/2} = & \left(-\frac{1}{60}w_4 + \frac{1}{3}w_1\right)\bar{\Phi}_{i-2} + \left(-\frac{1}{6}w_2 - \frac{7}{6}w_1 - \frac{7}{120}w_4\right)\bar{\Phi}_{i-1} \\ & + \left(\frac{5}{6}w_2 + \frac{1}{3}w_3 + \frac{11}{6}w_1 + \frac{73}{120}w_4\right)\bar{\Phi}_i + \left(\frac{1}{3}w_2 - \frac{5}{6}w_3 + \frac{21}{40}w_4\right)\bar{\Phi}_{i+1} \\ & + \left(-\frac{1}{6}w_3 - \frac{7}{120}w_4\right)\bar{\Phi}_{i+2} \end{aligned}$$

The weights w_j, j$\in \{1,2,3,4\}$ are given by (9.61).

9.9. Source Term

Let us consider the general SCL given by (9.1) and restrict our analysis to the source term of the form: $s(\Phi,t)$ as a continuous source vector function $\neq$ zero. By integrating system (9.1) over a finite space-time control volume $I_i,\Delta t$, one obtains a finite volume formulation for the system of balance laws, which usually takes the form

$$\Phi(z,t)_j^{n+1} = \Phi(z,t)_j^n - \frac{\Delta t}{\Delta z}\left(f_{j+1/2} - f_{j-1/2}\right) + \Delta t \cdot s(z,t)_j,\ \ t \geq 0,\ \ z \in \Omega, \quad (9.68)$$

The integration of (9.1) in space and time gives rise to a temporal integral of the flux across the element boundaries $f_{j+1/2}$ and to a space-time integral s_j of the source term inside I_j. In practice, one must replace the integrals of the flux and the source in (9.68) by some suitable approximations, meaning we need to choose a concrete numerical scheme. For SCL, only a numerical flux must be chosen. In this case, the classical properties required are consistency, stability and accuracy. For SBL also a numerical source must be chosen. Here, not only the three classical properties are required, but some additional properties are needed for the global numerical scheme: it should be well-balanced, i.e., able to preserve steady states numerically. It should also be robust on coarse grids, if the source term is stiff. A coarse grid is a grid whose size does not take into account the source term, i.e., the characteristic space and time steps are based on the associated homogeneous SCL only. Finally, the scheme should be asymptotically consistent or in other words asymptotic-preserving, if the source term is stiff. This means according to [127] that the scheme should give the correct asymptotic behaviour even if the source term is insufficiently resolved. We now restrict our analysis to source terms of the form $s(\Phi,z)$. Compared with SCL, the presence of a source term generally has consequences on the behaviour of SBL solutions. First of all, SBL may have non-trivial steady solutions, with $\tilde{\Phi}(z)$ given in the following system:

$$\frac{\partial f(\tilde{\Phi}(z,t))}{\partial z} = s(\tilde{\Phi}(z,t)),\ \ t \geq 0,\ \ z \in \Omega. \quad (9.69)$$

Additionally, SBL may tend towards reduced systems as we will explain now. At least two processes are involved in SBL: a conservative process associated to the homogeneous part of (9.1) (with s=0) a characteristic speed u_f , and a dissipative/productive process, associated to the source term s, with a characteristic speed

u_g. If the time derivative is scaled according to the speed u_f, the dimensionless form of a SBL system reads as:

$$\frac{\partial \Phi(z,t)}{\partial t} + \frac{\partial f(\Phi(z,t))}{\partial z} = \frac{1}{\varepsilon} s(\Phi(z,t)), \;\; t \geq 0, \;\; z \in \Omega, \tag{9.70}$$

where all the variables in (9.70) are dimensionless and where $\varepsilon \equiv \frac{u_f}{u_g}$ is the ratio between characteristic speeds. A very small ratio $\varepsilon << 1$ means that the dissipative/productive process is too fast, compared to a conservative process, needing to be fully observed. Such a source term is called a *stiff* source term. In mathematics, a stiff equation is a differential equation where certain numerical methods for solving the equation are numerically unstable, unless the step size is extremely small. It has proven difficult to formulate a precise definition of stiffness; however, the main idea is to include some terms of rapid variation into the equation, leading to rapid variation in the solution. The presence of a stiff source term may lead the original system towards an asymptotic reduced system, see [128], which might turn out to have a different mathematical nature than the original one.

9.10. Convection-Diffusion equations

By introducing a diffusion part we change the nature of the mathematical problem to a time-parabolic problem. The reason for including this part is, for example, in a homogeneous thermo-hydraulic evaporator model, we get a sharp change in fluid density, in the moment a fluid enters the two-phase region; this discontinuity in the derivative of the density initiates violent pressure waves in the solution, which can be attenuated by local artificial diffusion in the region, where this phenomenon occurs. Let us again consider the general SBL, given by, e.g., equation (9.1), where the source term s is replaced by a dissipative flux:

$$\frac{\partial \Phi(z,t)}{\partial t} + \frac{\partial f(\Phi(z,t))}{\partial z} = \frac{\partial}{\partial z}\left(g(\Phi(z,t), \frac{\partial \Phi}{\partial z}) \right), \;\; t \geq 0, \;\; z \in \Omega. \tag{9.71}$$

The gradient of g is formulated on the compressed form: $g(\Phi, \frac{\partial \Phi}{\partial z})_z$ as a nonlinear function $\neq$ zero. This term can degenerate (9.71) to a strongly parabolic equation, admitting non-smooth solutions. To solve it numerically is a highly challenging problem. Our fifth-order semi-discrete scheme, (9.65)-(9.66), can be applied to (9.1) in a straightforward manner, since we can treat the hyperbolic and

the parabolic part simultaneously. This results in the following conservative scheme:

$$\frac{d\Phi_j(t)}{dt} = -\frac{1}{\Delta z}\left[F_{j+1/2} - F_{j-1/2}\right] + G_j(\Phi, t). \tag{9.72}$$

Here $F_{j+1/2}$ is our numerical convection flux, given by equation (9.66) and G_j is a high-order approximation to the diffusion flux term. Similar to the case of the second-order semi-discrete scheme of [129], operator splitting is not necessary for the diffusion term. By using a fourth-order central differencing scheme, outlined by [130], we can apply our fifth-order semi-discrete scheme, given by (9.65) and (9.66), to the parabolic equation (9.1), where g is a function of ϕ and its derivative in space. The diffusion term can be expressed by a high-order approximation:

$$\begin{aligned} G_j(t) = &\frac{1}{12\Delta z}\left[-G(\Phi_{j+2}, (\Phi_z)_{j+2}) + 8 \cdot G(\Phi_{j+1}, (\Phi_z)_{j+1})\right] \\ &- \frac{1}{12\Delta z}\left[8 \cdot G(\Phi_{j-1}, (\Phi_z)_{j-1}) + G(\Phi_{j-2}, (\Phi_z)_{j-2})\right] \end{aligned} \tag{9.73}$$

where

$$(\Phi_z)_{j+2} = \frac{1}{12\Delta z}\left[25\Phi_{j+2} - 48\Phi_{j+1} + 36\Phi_j - 16\Phi_{j-1} + 3\Phi_{j-2}\right] \tag{9.74}$$

$$(\Phi_z)_{j+1} = \frac{1}{12\Delta z}\left[3\Phi_{j+2} + 10\Phi_{j+1} - 18\Phi_j + 6\Phi_{j-1} - \Phi_{j-2}\right] \tag{9.75}$$

$$(\Phi_z)_{j-1} = \frac{1}{12\Delta z}\left[\Phi_{j+2} - 6\Phi_{j+1} + 18\Phi_j - 10\Phi_{j-1} - 3\Phi_{j-2}\right] \text{ and} \tag{9.76}$$

$$(\Phi_z)_{j-2} = \frac{1}{12\Delta z}\left[-3\Phi_{j+2} + 16\Phi_{j+1} - 36\Phi_j + 48\Phi_{j-1} - 25\Phi_{j-2}\right] \tag{9.77}$$

and Φ_j are the point-values of the reconstructed polynomials (9.34).

9.11. Boundary conditions for non-staggered grid

This black box solver is as a starting point hyperbolic, but we apply quite generally upstream and downstream boundary conditions in this setup, depending on the nature of the system of equations. If we select a globally dominant diffusion part (parabolic system), we need two boundary conditions; while in hyperbolic

systems, we typically only need one boundary condition for a scalar equation. Now consider a hyperbolic system, like (9.1) on a bounded interval a≤x≤b. This is called the *Initial Boundary Value Problem*, or IBVP for short, since it is time-dependent, for which we need both initial data and boundary data. For a system of m equations we need a total of m boundary conditions. Typically some conditions must be prescribed at the left boundary (z=A) and sometimes at the right boundary (z=B). The number of conditions, required at the two boundaries, depends on the number of eigenvalues of the Jacobian **J** that are positive and negative, respectively, and whether the information enters or exits the boundaries.

So far, we have only described methods for updating cell averages $\bar{\Phi}_j$ assuming that we have neighbouring cell values $\bar{\Phi}^n_{j-1}$ and $\bar{\Phi}^n_{j+1}$ and perhaps values further away as needed in order to compute the cell fluxes $F^n_{j+1/2}$ and $F^n_{j-1/2}$. In practice we must always compute on some finite set of grid cells, covering a bounded domain. In the first and last cells we will not have the required neighbouring information. Instead we must have some set of physical boundary conditions that must be used in updating these cell values. By extending the computational domain to include a few additional cells on either end of the solution domain, called ghost cells, the values of the ghost cells are somehow set at the beginning of each time step, depending on the boundary condition. Figure (9.8) illustrates a grid with three ghost cells at each boundary. These values provide the neighbouring cell values needed in updating the cells near the physical domain. The updating formula is then exactly the same in all cells, and there is no need to develop a specific flux limiter method in order to work with the boundary instead of the initial data. Suppose the mathematical problem is on the physical domain

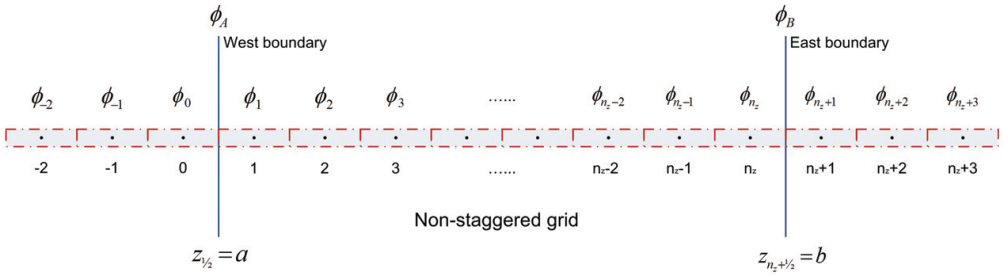

Figure 9.8.: The computational grid [a,b] is extended to a set of ghost points for specifying boundary conditions.

[a,b], which is sub-divided into cells I_1,I_2,...,I_{n_z} with $z_{1/2}$=a and $z_{n_z+1/2}$=b, so that Δz= (b-a)/n_z. If we use a method where $F^n_{j-1/2}$ depends only on Φ^n_{j-1} and Φ^n_j, then we need only one ghost point on either end. The ghost cell I_0=[a-Δz,a] allows us to calculate the flux $\Phi^n_{1/2}$ at the left boundary A, while the ghost cell

I_{n_z+1}=[b,b+Δz] is used to calculate the flux $\Phi^n_{n_z+1/2}$ at the right boundary B. With a flux limiter method or a fifth-order WENO approach of the type described above, we will generally need two ghost cells at each boundary, since a jump in Φ^n_0-Φ^n_{-1} will be needed in limiting the flux correction in $F^n_{1/2}$. For a method with an even higher-order of accuracy, additional ghost points would be needed. Consider again the WENO scheme, where the maximal fifth-order polynomial reconstruction requires a five-point stencil S_5, involving the nodes of I_{j-2}, I_{j-1}, I_j, I_{j+1} and I_{j+2}, for each computational cell in the space of j=1 to n_z. In the following we focus on the non-staggered grid for developing a method to predict the values of Φ on the boundaries, whether we are talking about Dirichlet or Neumann boundaries. If we look at the very first computational cell along the

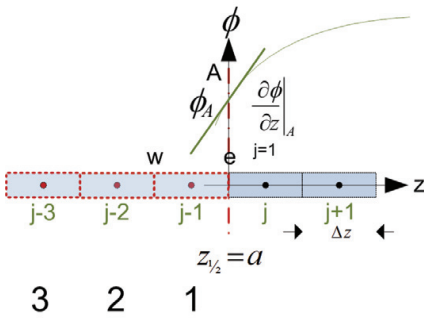

Figure 9.9.: Boundary conditions at the West boundary (up-stream). The ghost points are marked with a red dot.

West boundary, we need to be able to predict the values of Φ, for the five-point stencil, beginning with the I_{j-2},I_{j-1} and I_j node, which is outside the solution domain (for j=0) (three ghost points); see figure (9.6). The idea behind the ghost point approach is to express the value of the solution at control points outside the computational domain in terms of the values inside the domain plus the specified boundary condition. This allows the boundary condition to be imposed by a simple modification of the internal coefficients, using the coefficients of the fictitious external point. This can result in a weak imposition of the boundary condition, where the boundary flux might not exactly agree with the boundary condition. The three ghost points are here successively calculated by a third-order Taylor expansion around the boundary A, involving I_{-2}, I_{-1} and I_0, and can be used to predict the connection between the I_j cell, marked by red in figure (9.6), and the boundary condition, given by Φ_A, where Δz is the size of the CVs (uniform grid spacing). A straightforward procedure for deriving general finite difference approximations is obtained by means of the following Taylor series expansion (polynomial interpolation) procedure:

1. Choose a point z_0 and a set of r points on the grid in the vicinity of z_0 which

will be used to approximate the function and it's derivatives $f_0^{(m)}$, m = 0, 1,..., r-1. We call this collection of grid points the finite difference stencil. The point z_0 may be one of the stencil points, but this is not required.

2. Write the r-term Taylor series expansion of f(z), about the point z=z_0, and evaluate the result at each point on the stencil to get a system of r equations.

3. Invert this system of equations to find the coefficients of the corresponding r-point finite difference schemes for the function $f_0 \equiv f_0^{(0)}$ itself, plus its first r-1 derivatives $f_o^{(m)}$, m = 1, 2,..., r-1.

Recall now that the Taylor series expansion of the function f(z) about the point z=z_0 is given by

$$f(z) = \sum_{m=0}^{\infty} \frac{(z-z_0)^m}{m!} f_0^{(m)}. \tag{9.78}$$

By establishing a Taylor expansion around the boundary A (or B), we can express a relationship between the ghost points outside the solution domain and the grid points inside the domain:

$$\begin{aligned}
\Phi_0 &= \Phi_A - \frac{1}{2}\Delta z \Phi_A^{(1)} + \frac{1}{8}\Delta z^2 \Phi_A^{(2)} + ... \\
\Phi_{-1} &= \Phi_A - \frac{3}{2}\Delta z \Phi_A^{(1)} + \frac{9}{8}\Delta z^2 \Phi_A^{(2)} + ... \\
\Phi_{-2} &= \Phi_A - \frac{5}{2}\Delta z \Phi_A^{(1)} + \frac{25}{8}\Delta z^2 \Phi_A^{(2)} + ...
\end{aligned} \tag{9.79}$$

Hence the boundaries are:
Dirichlet BC at A:

$$\begin{aligned}
\Phi_{-2} &= 32\Phi_A - 50\Phi_1 + 25\Phi_2 - 6\Phi_3 \\
\Phi_{-1} &= \frac{64}{5}\Phi_A - 18\Phi_1 + 8\Phi_2 - \frac{9}{5}\Phi_3 \\
\Phi_0 &= \frac{16}{5}\Phi_A - 3\Phi_1 + \Phi_2 - \frac{1}{5}\Phi_3
\end{aligned} \tag{9.80}$$

Neumann at A:

$$\begin{aligned}
\Phi_{-2} &= \frac{1}{23}\left[-240\Delta z\frac{\partial\Phi}{\partial z}\|_A - 250\Phi_1 + 375\Phi_2 - 102\Phi_3\right] \\
\Phi_{-1} &= \frac{1}{23}\left[96\Delta z\frac{\partial\Phi}{\partial z}\|_A - 54\Phi_1 + 104\Phi_2 - 27\Phi_3\right] \\
\Phi_0 &= -\frac{1}{23}\left[24\Delta z\frac{\partial\Phi}{\partial z}\|_A - 21\Phi_1 - 3\Phi_2 + \Phi_3\right]
\end{aligned} \tag{9.81}$$

Similar we find for the downstream boundary B:
Dirichlet BD at B:

$$\begin{aligned}
\Phi_{n_z+3} &= 32\Phi_B - 50\Phi_{n_z} + 25\Phi_{n_z-1} - 6\Phi_{n_z-2} \\
\Phi_{n_z+2} &= \frac{64}{5}\Phi_B - 18\Phi_{n_z} + 8\Phi_{n_z-1} - \frac{9}{5}\Phi_{n_z-2} \\
\Phi_{n_z+1} &= \frac{16}{5}\Phi_B - 3\Phi_{n_z} + \Phi_{n_z-1} - \frac{1}{5}\Phi_{n_z-2}
\end{aligned} \tag{9.82}$$

Neumann BC at B:

$$\begin{aligned}
\Phi_{n_z+3} &= \frac{1}{23}\left[-240\Delta z\frac{\partial\Phi}{\partial z}\|_B - 250\Phi_{n_z} + 375\Phi_{n_z-1} - 102\Phi_{n_z-2}\right] \\
\Phi_{n_z+2} &= \frac{1}{23}\left[96\Delta z\frac{\partial\Phi}{\partial z}\|_B - 54\Phi_{n_z} + 104\Phi_{n_z-1} - 27\Phi_{n_z-2}\right] \\
\Phi_{n_z+1} &= -\frac{1}{23}\left[24\Delta z\frac{\partial\Phi}{\partial z}\|_B - 21\Phi_{n_z} - 3\Phi_{n_z-1} + \Phi_{n_z-2}\right]
\end{aligned} \tag{9.83}$$

9.12. Time discretization

Strong Stability Preserving (SSP) time discretization methods were developed to address the need for nonlinear stability properties in the time discretization, as well as the spatial discretization, of hyperbolic PDEs. The research in the field of SSP methods centres around the search for high order SSP methods where the CFL time step restriction leads to a large as possible time step. These methods include the case where there are more stages than required for the order, in order to maximize the CFL coefficient. This section presents the numerical setup which constitutes the framework for a dynamic model of an evaporator, which is a cumbersome calculation process, as the equation of state (EOS) is based on an industry standard (IAPWS-97) for the sake of precise expression. With a formulation given in a conservative form (flux-based), we must iterate the pressure as a function of density and enthalpy, which is very time-consuming.

In principle we should use a time integrator of the same order as the WENO reconstruction, such as an SSP RK(5,5) solver, see [113], but experience shows that these higher-order integrators are much more time-consuming than e.g., a third-order TVD time integrator used in both [116] and [131]. The semi-discrete (9.65) is a system of time-dependent ODEs, which can be solved by any stable ODE solver, retaining the spatial accuracy of the scheme. Here we use the TVD Runge-Kutta method presented by [126] which can be categorized as an (SSP-RK(3,3)):

$$\frac{d\Phi}{dt} = L(\Phi), \tag{9.84}$$

where $L(\Phi)$ is an approximation to the derivative $-\frac{\partial f(\Phi)}{\partial z} + s(\frac{\partial \Phi}{\partial z}, \Phi, z, t)$ in the differential equation given by (9.1). The optimal third-order TVD Runge-Kutta method (SSP-RK(3,3)) is given by

$$\begin{aligned}
\Phi_j^{(1)} &= \Phi_j^n + \Delta t L(\Phi_j^n), \\
\Phi_j^{(2)} &= \frac{3}{4}\Phi_j^n + \frac{1}{4}\Phi_j^{(1)} + \frac{1}{4}\Delta t L(\Phi_j^{(1)}), \\
\Phi_j^{n+1} &= \frac{1}{3}\Phi_j^n + \frac{2}{3}\Phi_j^{(2)} + \frac{2}{3}\Delta t L(\Phi_j^{(2)}), \quad \text{for } j \in [1, n_z].
\end{aligned} \tag{9.85}$$

As an alternative, we could use a (SSP-RK(5,4)), which is a fourth-order method consisting of five stages and is given by

$$\begin{aligned}
\Phi_j^{(1)} &= \Phi_j^n + 0.391752226571890\Delta t L(\Phi_j^n), \\
\Phi_j^{(2)} &= 0.444370493651235\Phi_j^n + 0.555629506348765\Phi_j^{(1)} \\
&\quad + 0.368410593050371\Delta t L(\Phi_j^{(1)}), \\
\Phi_j^{(3)} &= 0.620101851488403\Phi_j^n + 0.379898148511597\Phi_j^{(2)} \\
&\quad + 0.251891774271694\Delta t L(\Phi_j^{(2)}), \\
\Phi_j^{(4)} &= 0.178079954393132\Phi_j^n + 0.821920045606868\Phi_j^{(3)} \\
&\quad + 0.544974750228521\Delta t L(\Phi_j^{(3)}), \\
\Phi_j^{n+1} &= 0.517231671970585\Phi_j^{(2)} + 0.096059710526147\Phi_j^{(3)} \\
&\quad + 0.063692468666290\Delta t L(\Phi_j^{(3)}) + 0.386708617503269\Phi_j^{(4)} \\
&\quad + 0.226007483236906\Delta t L(\Phi_j^{(4)}), \quad \text{for } j \in [1, n_z].
\end{aligned} \tag{9.86}$$

In [126], one can see that even a very nice second-order TVD spatial discretization may give an oscillatory result, depending on whether the time discretization is by

a non-TVD, but, linearly stable, Runge-Kutta method. Thus it would always be safer to use TVD Runge-Kutta methods for hyperbolic problems. The stability condition for the above schemes is

$$CFL = \max\left(u_j^n \frac{\Delta t}{\Delta z}\right) \leq 1, \tag{9.87}$$

where CFL stands for the *Courant-Friedrichs-Lewy* condition and u_j^n is the maximum propagation speed in cell I_j at time level n.

9.13. Implementation

The implementation of the WENO approach is illustrated in figure (9.10), where the time integration loop is shown. Step 1 is the model, with the model specifications and allocation of array structures, and Step 2 is initialization of the time integration loop. Step 3 is evaluation of the time step due to the CFL number specified. Step 4 is coverage of the entire Runge Kutta time integration, which is divided into three parts, due to the third-order TVD integrator. The upstream and downstream boundaries are updated in the Boundary module. They can be constant or varying in time. In general there are three possibilities of specifying boundary conditions: Dirichlet, Neumann or non-condition. In the method of *Indicators* we calculate the four indicators IS_i, i$\in$[1..4]. The *Reconstruction* module deals with the weight functions as well as calculates the corresponding reconstructed polynomials. In the module named *Fluxes*, the flux vector is estimated including both contributions from the source/sink term and diffusion term. In Step 5 the calculation info is estimated and stored in files. The time loop runs until the time t exceeds the end of the simulation time t_{end}.

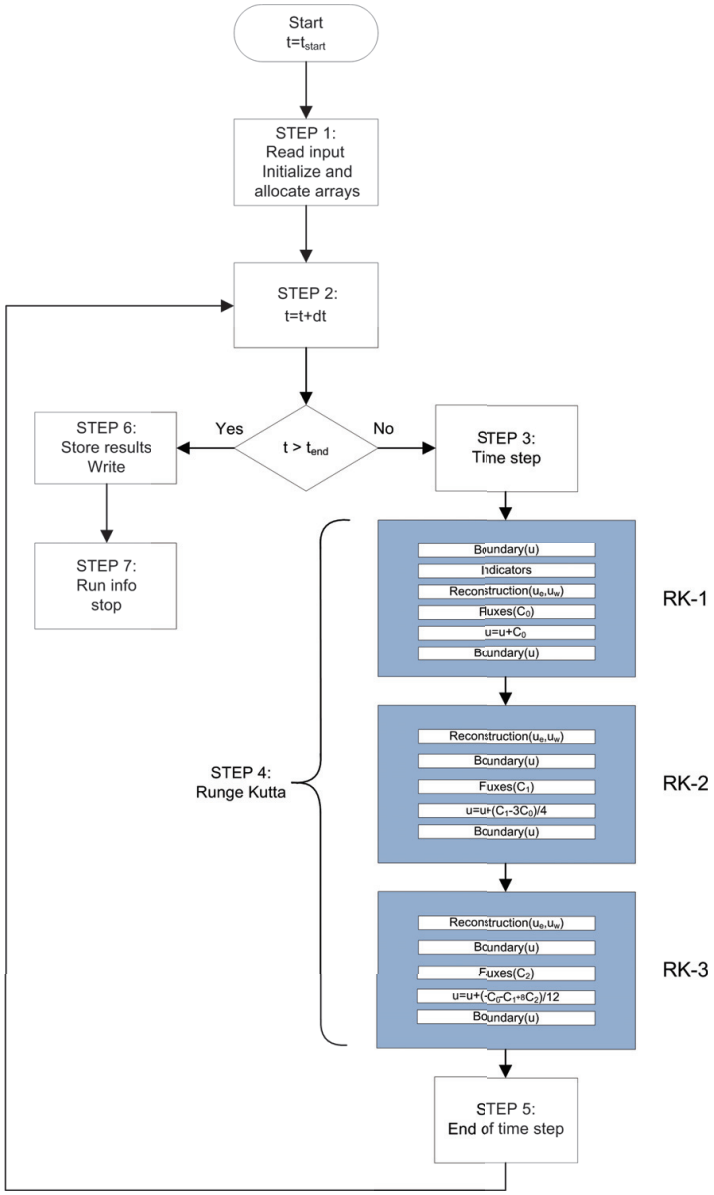

Figure 9.10.: Flow diagram for the WENO time integration loop based on a SSP-RK(3,3).

9.14. Numerical validation of hyperbolic solvers

In this section we compare numerical results of both a scalar and a system of hyperbolic equations and compare the results with analytical results, from the literature as well as other published results, in order to test whether the method is implemented correctly. The scalar models will focus on solving the inviscid Burger equation, which is a standard test example in the literature for

solving hyperbolic equations. Finally the well-known Sod problem is solved by a system of Euler equations and is evaluated according to numerical results in literature.

9.14.1. Consistency

A consistency test is made by solving (9.88) numerically and compare the solution with an analytical solution given by (9.89) for varying grid spacing.

$$\frac{\partial \Phi}{\partial t} + \frac{\partial f(\Phi)}{\partial z} = \frac{\partial}{\partial z}\left(\Gamma \frac{\partial \Phi}{\partial z}\right), \ t \geq 0 \ \wedge \ z \in \Omega \tag{9.88}$$

where $\Omega \in [0, 1]$. The governing equation (9.88) is forced by an *Initial Boundary Value Problem* given by two Dirichlet boundary conditions: $\Phi_A = 1$ for z=0 and $\Phi_B = 0$ for z=1 and an initial field of Φ(z,t=0)=0. The number of computational cells varies from:n_z = 10 to 320. The convective velocity is constant u=1.0 [m/s] (f(Φ) $= u \cdot \Phi$); the length l_z=1 [m] and the density $\rho = 1$ $[kg/m^3]$ are constant. The diffusion coefficient is Γ=0.2 $[kg/m \cdot s]$ in g(Φ) $= \frac{\partial}{\partial z}\left(\Gamma \cdot \frac{\partial \Phi}{\partial z}\right)$.

The steady state simulation results are compared with a corresponding analytical solution, given by:

$$\frac{\Phi - \Phi_A}{\Phi_B - \Phi_A} = \frac{\exp(\rho \cdot u \cdot x/\Gamma) - 1}{\exp(\rho \cdot u \cdot l_z/\Gamma) - 1}, \ t \geq 0 \ \wedge \ z \in \Omega. \tag{9.89}$$

The numerical solution to (9.88) is illustrated in figure (9.11), where different solution profiles are shown over time, and the steady state solution is the basis of the consistency test by recalculation of the numerical model for varying grid spacing. The results are shown in figure (9.12) and are compared with simpler numerical schemes such as Van Leer and a Central Difference scheme.

Numerical tests show, with no surprise, varying accuracy, depending on the numerical solution strategy used. The classical Van Leer TVD scheme and a Central Difference scheme (CD) provide a familiar second and first-order accuracy, respectively, while the central WENO scheme, with a reduced fourth-order diffusion term, gives a close to fourth-order accuracy (WENO4) for the steady state solution. In [116] and [123] the central WENO scheme without a diffusion term has a fifth-order accuracy.

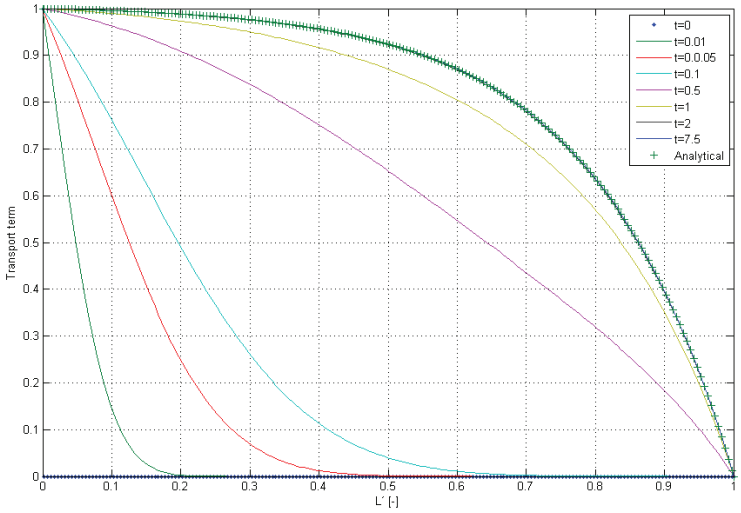

Figure 9.11.: Numerical and analytical solutions to (9.88).

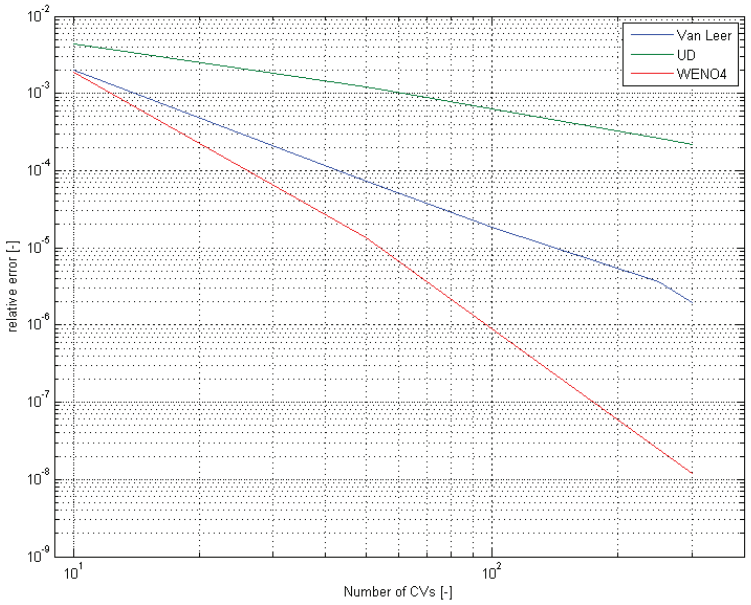

Figure 9.12.: Consistency.

9.14.2. Burgers equation

In this example we simulate the pre- and post-shock solution to the inviscid Burgers equation given by

$$\frac{\partial \Phi}{\partial t} + \frac{\partial}{\partial z}\left(\frac{1}{2}\Phi^2\right) = 0, \;\; t \geq 0 \;\wedge\; z \in \Omega \tag{9.90}$$

and the corresponding initial condition is given by Φ(x,0)=sin$(\pi x/l_z)$. Ω is partitioned in n_z non-overlapping cells: $\Omega = \cup_{i=1}^{n_z} I_i \in [0, l_z]$, where l_z is a physical length scale in the spatial direction. The simulation results are based on the fifth-order central WENO formulation, and the outcome is illustrated in (9.13) and is similar to what is observed in [118] and [129].

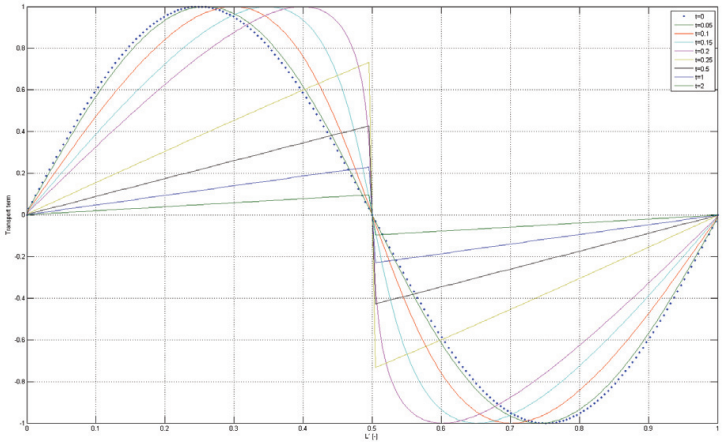

Figure 9.13.: Burgers equation with N=200 and l_z=1.

The results indicate that the solution is perfectly symmetric and a planar disturbance propagates outward at the characteristic speed for the artificial medium, as expected. We can see a shock formation centred at z=0.5.

9.14.3. Euler equation

We extend the fifth-order WENO scheme to obtain the solution of Euler's equations of gas dynamics:

$$\frac{\partial \Phi}{\partial t} + \frac{\partial f(\Phi)}{\partial z} = 0, \;\; t \geq 0 \;\wedge\; z \in \Omega \tag{9.91}$$

where

$$\Phi = \begin{pmatrix} \rho \\ \rho \cdot u \\ E \end{pmatrix}$$

and the flux vector is given as:

$$F(\Phi) = \begin{pmatrix} \rho \cdot u \\ \rho \cdot u^2 + p \\ u \cdot (E + p) \end{pmatrix}$$

Here ρ, u, p and E are the fluid density, velocity, pressure and total energy of the conserved fluid, respectively. The ideal gas law (polytrophic gas) is used as the equation of state, to derive the speed of sound c, given as: c=$\sqrt{\frac{\gamma p}{\rho}}$. The ration of the specific heats is: $\gamma = \frac{c_p}{c_v} = 1.4$ and the pressure p=$(\gamma - 1)(E - \frac{1}{2}\rho u^2)$.

The linearized Euler equations are obtained by linearization of the Euler equations in non-conservation form, as in (9.5), with flux Jacobians:

$$\frac{\partial \mathbf{M}}{\partial t} + \mathbf{J} \cdot \frac{\partial \mathbf{M}}{\partial z} = 0, \;\; t \geq 0 \;\wedge\; z \in \Omega. \tag{9.92}$$

An eigenvalue analysis, as given in section (8.4.8), leads to the following eigenvectors: $r_1 = [1, u - c, H - uc]^T$, $r_2 = [1, u, \frac{1}{2}u^2]^T$, $r_3 = [1, u + c, H + uc]^T$ corresponding to the eigenvalues $\gamma_1 = u - c$, $\gamma_2 = u$ and $\gamma_3 = u + c$. We solve the Sod problem up to t=0.01 [s] for a spatial length of l_z=20 [m], with the following initial conditions:

$$\Phi(x,0) = \begin{cases} (1, 0, 2.5 \cdot 10^5)^T & 0 \leq x < \frac{l_z}{2} \\ (0.125, 0, 0.25 \cdot 10^5)^T & \frac{l_z}{2} \leq x \leq l_z. \end{cases} \tag{9.93}$$

The simulation results are based on CFL=0.90, and the density, pressure and velocity distributions are illustrated in (9.14), (9.15) and (9.16), respectively.
The figure (9.14) represents five regions (R_1, R_2, R_3, R_4 and R_5) in the spatial space of z $\in$ [0,1], which have different densities. Region $R_1 \in$ [0,0.3[, $R_2 \in$ [0.3,0.5[, $R_3 \in$ [0.5,0.63[, $R_4 \in$ [0.63,0.78[and $R_5 \in$ [0.78,1]. Two regions R_1 and R_5 are in constant state equaling the initial state, and both fluids are initially in rest. R_2 represents a rarefaction wave moving to the left. Although the density and pressure are continuous in this region, some of the derivatives of the fluid quantities may not be continuous. The front in-between region R_3 and R_4 represents the so-called contact discontinuity, where the pressure and

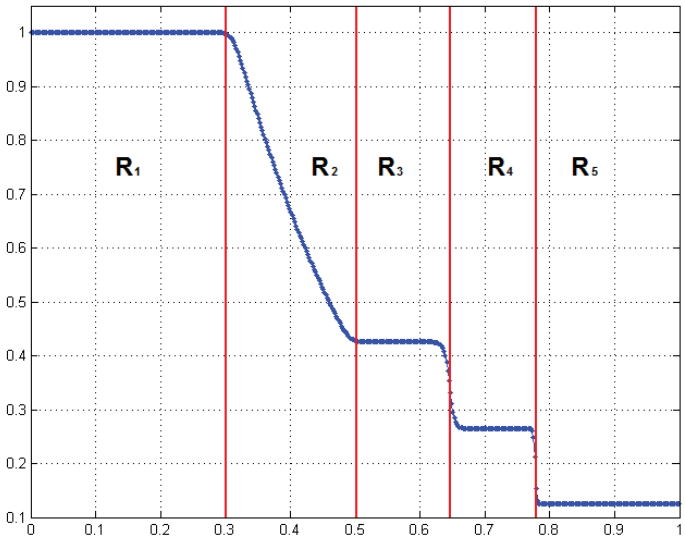

Figure 9.14.: Sod problem with N=500 - Density [kg/m^3] distribution at t=0.01 [s].

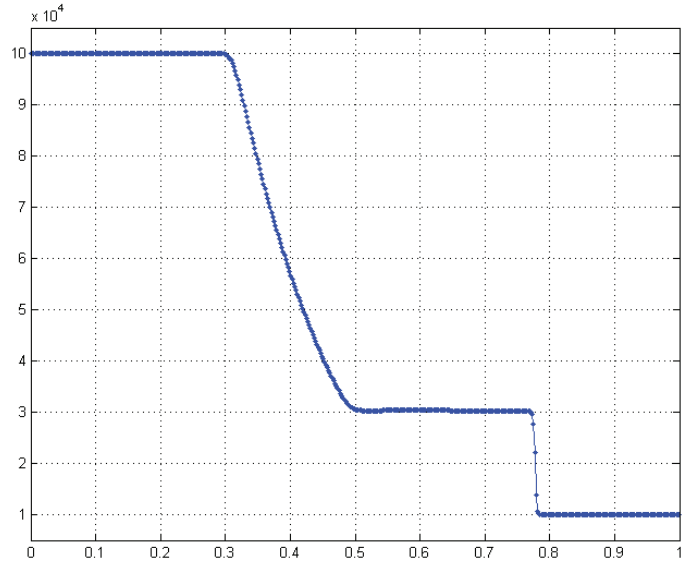

Figure 9.15.: Sod problem with N=500 - Pressure [Pa] distribution at t=0.01 [s].

the specific energy are not a continuous function. The front in-between regions R_4 and R_5 represents the location of the shock wave moving to the right with

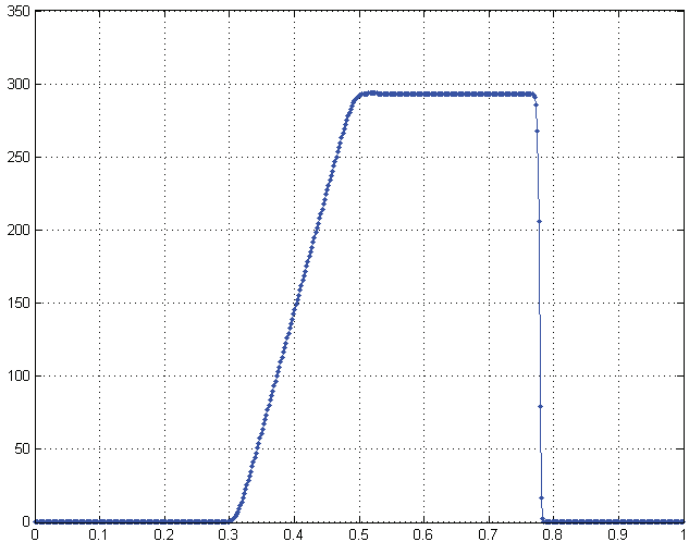

Figure 9.16.: Sod problem with N=500 - Velocity [m/s] distribution at t=0.01 [s].

the sound of speed. Assuming the same gas in the two chambers, the ration of the specific heats are identical: $\gamma = \gamma_1 = \gamma_5$; hence, the two local speeds of sound can be determined and inserted in formula (9.94), taken from [132], page 225, the shock strength to $p_4/p_5 = 3.031$, which fits with the results in figure (9.15).

$$\frac{p_1}{p_5} = \frac{p_4}{p_5}\left[1 - \frac{(\gamma-1)(a_5/a_1)(p_4/p_5-1)}{\sqrt{2\gamma}\sqrt{2\gamma+(\gamma+1)(p_4/p_5)}}\right]^{\frac{-2\gamma}{\gamma-1}} \tag{9.94}$$

Across a shock all of the quantities (ρ, m, e and p) will in general be discontinuous. The simulation results show oscillation free properties. The corners at the endpoints of the rarefaction are almost perfectly sharp, and the constant states of R_1 and R_5 are well defined matching the initial state. In general the distribution of the density, pressure and velocity fit very well with similar cases in the literature; see [129]. The timing results are improved with up to 20% by use of the modified weight functions given by [131] compared to the traditional squared weight factors from [116].

9.15. Conclusions

We have developed a robust numerical tool that is highly flexible in terms of configuration, so that the application can handle source / sink terms, diffusion terms and initial fields as line data. In addition two types of boundary conditions can be specified, one Neumann and Dirichlet condition on both upstream and downstream boundaries. The convective term of the solver has the WENO of fifth-order accuracy, which is shown by several authors; see e.g. [123] and [116]. The diffusion term is only dissolved to fourth-order accuracy, and with respect to the time integrator, we here have several options; but for our purposes, we find the third-order TVD Runge Kutta integrator to be appropriate. The Central WENO schemes are designed for problems with piecewise smooth solutions containing discontinuities. The Central WENO scheme has been quite successful in the above applications, especially for solving the Burgers equation containing both shocks and complicated smooth solution structures. The conclusion is that both the scalar and the vector-based versions of the solver are non-oscillatory in the sense of satisfying the total-variation diminishing property in the one-dimensional space.

10. Dynamic flow stability

In this chapter the dynamic analysis will be based on a method for solving the thermo-hydraulic transport equations based on a shock capturing scheme, taking into consideration density-waves as well as pressure-drop oscillations, not only during start-up of power plant boilers, but also during operational situations involving abrupt events, such as high-pressure preheater shut-down or a different firing setup, or various heat flux profiles in the furnace.

An in depth review of historical approaches to both static and dynamic flow stability in two-phase systems is described by [31]. Some pioneering work has been carried out in two-phase flow dynamics using the tools of non-linear dynamical systems. Archard et al. [133] performed Hopf bifurcation analysis on non-linear density-wave oscillations in boiling channels, which is a local bifurcation analysis of a dynamical system, where a fixed point loses stability, as a pair of complex conjugate eigenvalues of a linearisation around the fixed point crosses the imaginary axis of the complex plane. Rizwanuddin and Doming ([134], [135]) conduct non-linear numerical simulations of density-wave oscillations. Ozawa et al. [136] have used the so-called Lyapunov stability theory to determine the stability of a parallel-channel system against pressure-drop type oscillations. The method is based on the assumptions regarding the modifications necessary in non-linear systems to the linear theory of stability, based on linearizing near a point of equilibrium. Zhang et al. [137] developed an explicit criterion for density-wave instability by using the same Lyapunov theory. Padki et al. [138] analysed the pressure-drop type and Ledinegg instabilities by the Hopf bifurcation method.

10.1. Introduction

In general, modelling two-phase phenomena starts with a formulation of the conservation equations. The homogeneous thermo-hydraulic model (9.1) is solved by the set of four conservation equations, written for the conservation of mass, momentum and energy for the fluid, given by equation (8.99), and one energy conservation equation for the wall (8.106). Boundary and initial conditions are then defined for a particular problem under consideration. At each step of the formulation and solution, various physical assumptions and approximations need be made, which have to be justified by the measurement campaigns described in section (5.3).

A two-phase flow is said to be subject to a dynamic instability, when there is sufficient interaction and delayed feedback between the inertia of flow and compressibility of the two-phase mixture. The dynamic instabilities can be characterized as in table (10.1). We will mainly focus on density-wave and pressure-drop oscillations and force the thermo-hydraulic model with boundary conditions that will ful-fill this setup. Thermal oscillations will affect the life of the evaporator tubes. In this section we set up and solve a homogeneous

Type	Mechanism	Characteristics
Acoustic oscillations	Resonance of pressure waves	High frequencies (10-100 Hz) related to time required for pressure wave propagation in System
Density-wave oscillations	Delay and feedback effects in relationship between flow rate, density, and pressure-drop	Frequencies related to transit time as a continuity wave
Pressure-drop oscillations	Dynamic interaction between channel and compressible volume	Very low frequency periodic process
Thermal oscillations	Interaction of variable heat transfer coefficient with flow dynamics	High magnitude temperature oscillations in the solid due to transitions between different boiling regimes
Boiling water reactor instability	Interaction of void reactivity coupling with flow dynamics and heat transfer	Strong only for small fuel time constant and under low pressure
Parallel channel instability	Interaction among parallel channels	Various modes of flow redistribution or U-tube manometer oscillations

Table 10.1.: Classification of boiling two-phase dynamic flow stabilities [31].

thermal-hydraulic model for an evaporator tube, given by $\Omega \in [0, l_z]$, where l_z is the tube length. The flow model is calibrated against measured data from the full-

scale (400 [MW_{el}]) evaporator at Skærbækværket Unit 3 (SKV3) in Fredericia (Denmark), given by sample 4 in table (3.1).

10.2. Model setup

The developed homogeneous model, described in Chapter (8) is solved using the numerical tools described in Chapter (9), i.e., a fifth-order WENO scheme, with corresponding diffusion and source term. The method is outlined in section (9.5) and consists of 400 computational points with a CFL number of 0.8. A third-order TVD time integrator is used, for reasons of ensuring a high numerical stability as well as minimizing the time-consumption in the calculations. The numerical scheme is tested for consistency and stability with respect to both a scalar model and a system of hyperbolic equations and both have been successfully compared to analytical results, from the literature as well as other published results. This work is outlined in section 9.5 and published in [15]. Three Dirichlet boundary conditions are applied for the hydraulic case and two Neumann boundaries are applied for the thermal pipe wall model, given as zero gradients in the wall temperature at each pipe end (no heat loss).

The intention is to model an evaporator, that can induce pressure and density oscillations initiated by the compressibility, arising as a result of a phase shift in the lower part of the evaporator. Therefore, we apply a constant downstream Dirichlet pressure boundary condition that corresponds to a stiff system downstream the evaporator tube, meaning without any pressure absorption effects from compressibility in the downstream turbine system. A good analogy for this is a geyser, with a constant surface pressure and an intense heat absorption in the bottom region, whereby an oscillating pressure wave is initiated due to the compressibility and density reduction of the fluid, caused by intense heat from the underground. Additionally we force the model with both a constant enthalpy and mass flux located on the upstream boundary, supplied by a heat flux profile along the entire heat pipe.

The model is gently started (soft start) in two steps: at t=0 [s] the pure hydraulic model is gently started over 4 seconds, without heat flux. After ten seconds of simulation, the heat flux is built-up during four seconds to 100 [kW/m^2], in accordance with the operating observations obtained at SKV3. This is done to avoid heavy shock waves moving forward and back in the entire solution domain. The computational results are stored as line series for an equidistant time step and as time series at two stations, located at z_A=$\frac{l_z}{8}$ and z_B=$\frac{7l_z}{8}$, named stations A and B, respectively, where l_z is the total tube length.

The dynamic start-up process for a constant linear heat flux profile can be seen in figures (10.1) and (10.2),

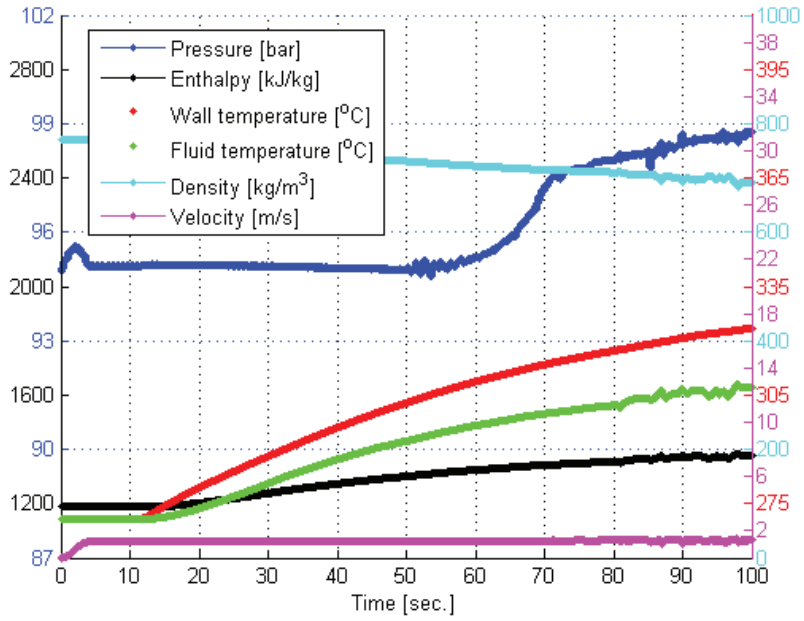

Figure 10.1.: Soft start response of SKV3 evaporator model @ station A.

where the density is given in $[kg/m^3]$, pressure in [bar], temperature in $[^oC]$, enthalpy in [kJ/kg] and mixture velocity in [m/s]. Note that the temperature curves for the fluid and the pipe wall both refer to the same temperature scale corresponding to the red fluid temperature scale on the right-hand side of the graph. This fact is applied in the whole chapter. If the soft start period is reduced to only one second, heavy-pressure oscillations occur; see figure (10.3). The soft start model is based on a third-order theory outlined in Appendix (G) and in [139], which gives a C^2 continuous sequence, which means zero gradients of the first derivative at both ends of the soft start period. Now we can summarize the *system of balance laws* (SBL) for the evaporator model into a compact vector notation, given by (8.99) and (8.106):

$$\frac{\partial \Phi(z,t)}{\partial t} + \frac{\partial \mathrm{f}(\Phi(z,t))}{\partial z} = \mathrm{g}_s(\Phi(z,t)) + \mathrm{g}_d\left(\frac{\partial \Phi}{\partial z}, \Phi(z,t)\right), \qquad (10.1)$$
$$\Phi \in R^m, m = 4, \quad t \geq 0 \wedge \quad z \in \Omega$$

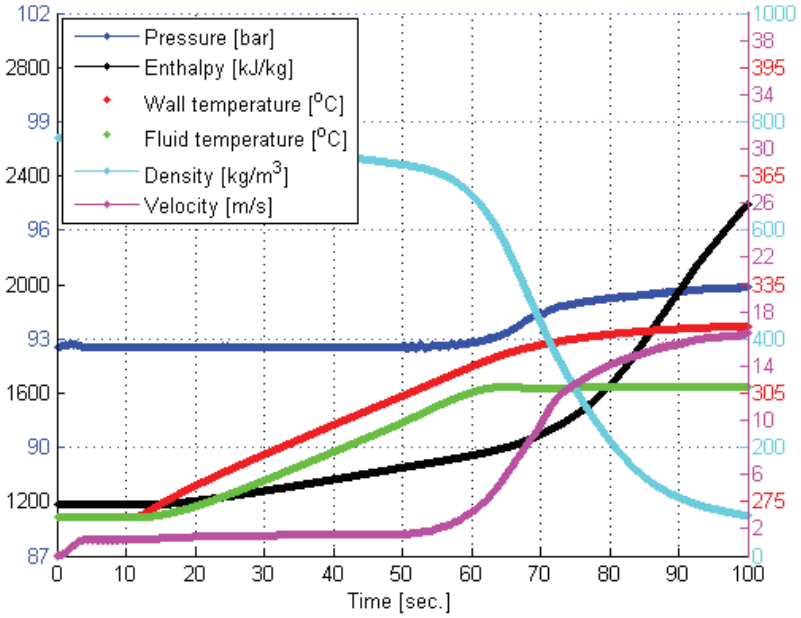

Figure 10.2.: Soft start response of SKV3 evaporator model @ station B.

where the dependent variable Φ and the flux vector f are given as

$$\Phi = \begin{pmatrix} \bar{\rho}A \\ \dot{m} \\ \bar{e} \\ T_w \end{pmatrix}, \quad \mathrm{f}(\Phi) = \begin{pmatrix} \dot{m} \\ \frac{\dot{m}^2}{\bar{\rho}A} + \bar{p}A \\ \frac{(\bar{e}+\bar{p}A)\dot{m}}{\bar{\rho}A} \\ 0 \end{pmatrix}$$

and the source and diffusion vector are given as:

$$\mathrm{g}_s(\Phi) = \begin{pmatrix} 0 \\ \bar{p}\frac{\partial A}{\partial z} - \bar{\rho}gA\cos\theta - \sqrt{\frac{\pi}{A}}f_w\frac{\dot{m}|\dot{m}|}{\bar{\rho}A} \\ S_w\dot{q}_e - \dot{m}g\cos(\theta) \\ \frac{\dot{q}_r}{\rho_w C_{pw}}\frac{S_w}{A} - \frac{\dot{q}_e}{\rho_w C_{pw}}\frac{d_i\pi}{A} \end{pmatrix} \quad \text{and} \quad \mathrm{g}_d(\Phi) = \begin{pmatrix} 0 \\ \frac{l^2 S_w}{\bar{\rho}A^3}\frac{\partial \dot{m}^2}{\partial z^2} \\ 0 \\ \alpha\frac{\partial^2 T_w}{\partial z^2} \end{pmatrix}$$

Here the fluid temperature T_f is a function of $\bar{\rho}$ and h. The constitutive relations due to the thermodynamic properties are based on IAPWS 97, and are interpolated in a bilinear scheme, described in Chapter 7, for improving the computational speed of the model; see [14]. Other constitutive relations for the pipe wall properties are given by (8.107). The model data are listed below in table (10.2). Note that the gravity is reduced according to the heat pipe inclination ($\sin(11.4^o)$).

For isotropic materials, we have expressions of C_{pw}, k_w and ρ_w as a function of temperature in Kelvin from [95] and [96]. For isotropic materials, we use the thermal diffusivity given by equation: $\alpha = \frac{k_w}{\rho_w C_{pw}}$ in $[m^2/s]$, which in a sense is a measure of thermal inertia and expresses how fast heat diffuses through a piece of solid. For a typical panel wall, the thermal diffusivity is approximately $1.98 \cdot 10^{-6}$ $[m^2/\mathrm{s}]$ at $200°C$.

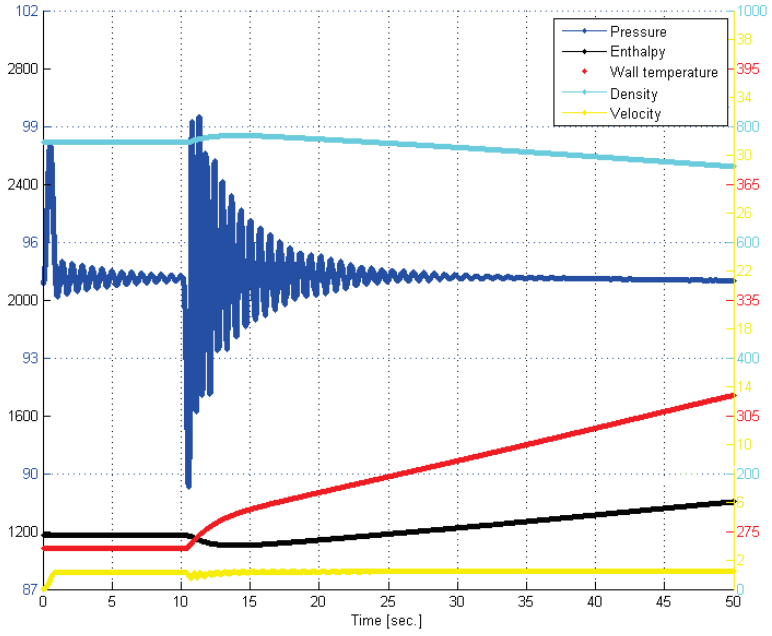

Figure 10.3.: Time series for short dynamic soft start start-up process @ station A.

Table 10.2.: Geometrical and numerical specifications for SKV3 heat pipe.

Parameter	Value	Unit	Parameter	Value	Unit
Gravity (g) - projected	1.9399	[m/s^2]	Spatial start position	0.000	[m]
Spatial end position (L)	193.499	[m]	Inner diameter of pipe (d_i)	23.8	[mm]
Outer diameter of pipe (d_o)	38.0	[mm]	Heat conductivity in wall (k_w)	20.278	[w/mK]
Wall density (ρ_w)	7850.0	[kg/m^3]	Specific heat capacity of pipe wall (Cp_w)	527.21	[J/kg/K]
Heat flux ($\dot{q}_e$)	100.0	[kW/m^2]	Wall roughness (λ)	1.0E-6	[m]
Initial Enthalpy - left side	1187.6988	[kJ/kg]	Initial Enthalpy - right side	1187.6988	[kJ/kg]
Initial Pressure - left side	92.3762	[Bar]	Initial Pressure - right side	92.3762	[Bar]
Initial Velocity - left side	0.0	[m/s]	Initial Velocity - right side	0.0	[m/s]
Pressure BC (Dirichlet - right side)	92.3762	[Bar]	Enthalpy BC (Dirichlet - left side)	1187.6988	[kJ/kg]
Velocity BC (Dirichlet - left side)	1.1711	[m/s]	Simulation time	400.0	[s]
Output frequency	0.1	[s]	CFL number	0.80	[-]
Number of computational grids (N_p)	400	[-]	Slip Correction Factor	1.0	[-]

10.3. Model calibration

The hydraulic model is calibrated in relation to the static operating data, which are available from SKV3; see table (3.2). As a starting point, we focus on a model that works in part load, i.e., where we simulate the entire two-phase process in the evaporator, including sub-cooling and superheating. We aimed as a basis for the calibration simulation a heat flux value of approximately 83.8 [kW/m^2], according to the average flux received by the evaporator in sample 4. The only calibration parameter we are dealing with, is the wall friction, which is determined by a hydraulically smooth industrial boiler tube (The surface roughness is negligible.) The tube length is estimated to be a total of 193.5 m. including various bends and junction boxes. We calculate the upstream pressure in the steady state condition to approximately 97.5 [bar]$\pm$0.2 [bar], which approximately corresponds to the measured upstream pressure in sample 4, 96.87 [bar], - a deviation of approximately 0.5 [bar] for hydraulic smooth pipes. Note that the calculated pressure drop is very sensitive to the specified velocity boundary condition. There appears, however, minor pressure oscillations on the upstream boundary, initiated by a phase shift in the vicinity of the transition area to the two-phase region. The artificial diffusion is estimated in section (8.6) to 0.01 [m^2/s] and is active for $x_e \in$ [-0.01,0.01]. Basically, the downstream condition should also reflect the measured static outlet enthalpy of 2764.38 [kJ/kg] and a corresponding steady state mass flow, even before the requirement of static energy balance is ful-filled. Here we are only slightly below the average measured static values, corresponding to an enthalpy of 2701 [kJ/kg] and a mass flux of 0.3807 [kg/s] at the very first computational cell versus 0.3816 [kg/s] at the very last computational cell. Based on the above considerations, we can

conclude that the model meet our observations in table (3.2) (sample 4), although the model is not at completely steady state. We can see from figure (10.5) that,

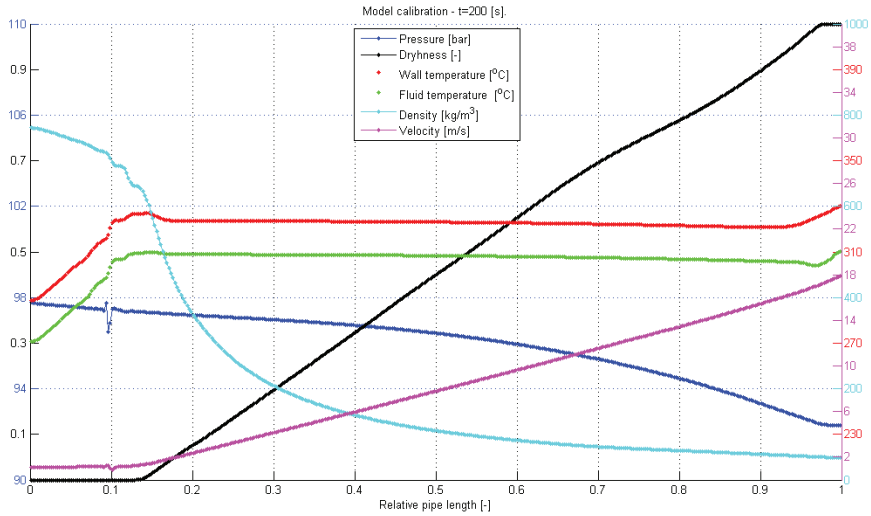

Figure 10.4.: Line series of heat pipe calibration, t=200[s].

e.g., the pressure signal contains oscillations, and the corresponding frequency components are difficult to identify. The signal can be analysed using FFT to find the frequency components of a signal in the time domain. We use the Matlab FFT package for analysing the power spectral density of the pressure signal. From figure (10.5) we see the entire time series of the pressure located in station B. In figure (10.6) is a close-up of the pressure time series measured from 150 [s] to 155 [s] of simulation, wherein the offset is adjusted, as the integral of the whole time series is zero. This period represents a typical pressure response and therefore contains one more dominant frequency, thus it is possible to identify a higher-order spectrum. A FFT spectral density analysis is carried out on a subset of the time series in station B. The result is shown in figure (10.7). We can see that the pressure fluctuations primarily consists of a class of waves with frequencies of $f^{'} \approx 0.25 \cdot$n [Hz] and with decreasing intensity, where n is a positive integer. This very low frequency periodic process according to table (10.1) can be classified as pressure-drop oscillations due to the dynamic interaction between channel and compressible specific volume in the fluid. The maximum wave-length is given by the length of the tube, l_z=193.5 [m] and the corresponding phase velocity $u_f = \lambda \cdot f^{'} \cdot \text{n} = l_z \cdot 0.25 \cdot \text{n} = 48.4 \cdot \text{n}$ [m/s]. From figure (10.4) we can see that the pressure waves are initiated only 10% upstream the tube which corresponds to a standing wave with a phase velocity of 484·n [m/s]. It is interesting to see that the phase velocity can be identified within the orders of magnitude of the estimated

speed of sound in a two-phase flow (250 m/s to 868 m/s @ 95 bar), based on the eigenvalue analysis of the two-layer fluid model in equation (8.41). The speed of sound is illustrated in figure (8.11).

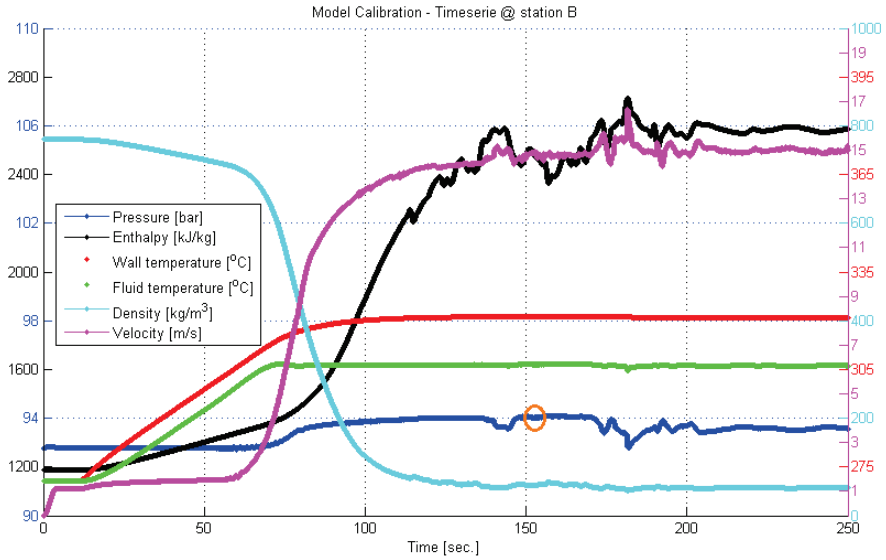

Figure 10.5.: Time series of heat tube calibration, station B.

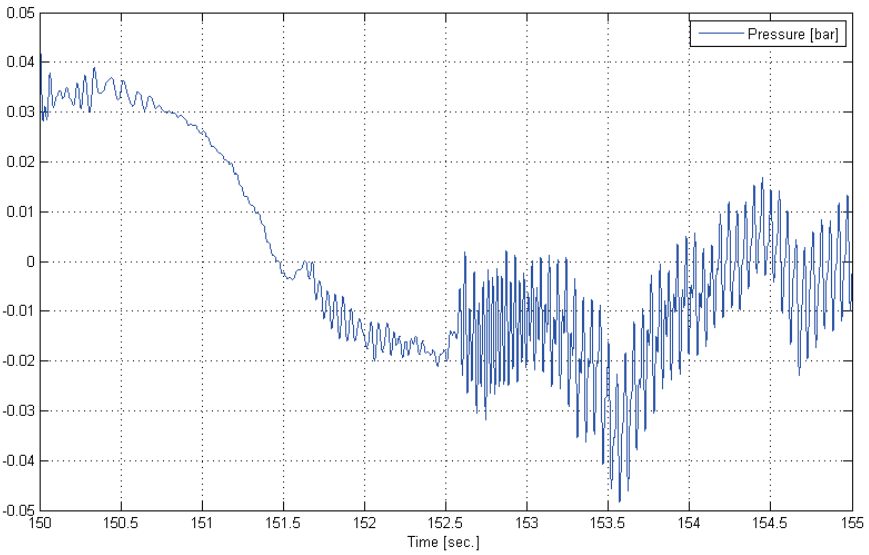

Figure 10.6.: Time sequence used for the FFT analyses at station B.

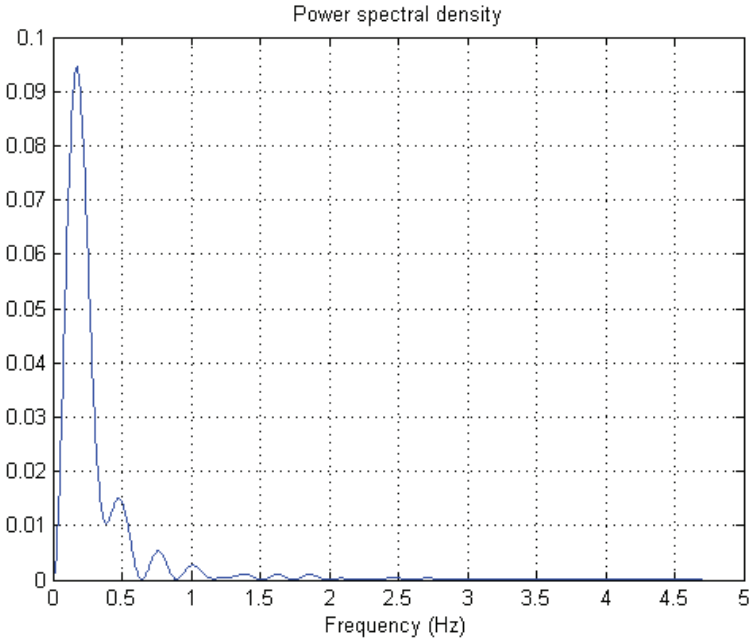

Figure 10.7.: FFT analysis based on time series in figure (10.6).

10.4. Heat Flux profiles

Here follow calculations for investigating how different heat flux profiles affect the dynamics of an evaporator during a start-up period. CFD studies in Chapter (4) show that the heat flux distribution has an approximately parabolic profile at full load - and in part load, we expect an even larger parabolic distribution of heat flux. Therefore, it is interesting to examine how the flux distribution in a boiler effects the start-up process in a power plant evaporator. Operational experience from SKV3 indicates major start-up problems, which is attempted to be reduced by firing with the top burner floor. We will investigate this in the following, where we examine the dynamic response from the evaporator by four different heat flux profiles. We use a moderate flux distribution coefficient, corresponding to a maximum redistribution of the heat flux of 10% ($\Delta q = 0.1$), meaning that the heat flux profile along the tube is altered a maximum of 10 %.

10.4.1. Constant heat flux profile

A constant heat flux profile indicates a constant heat flux on the panel wall, which results in a corresponding effective cooling of the pipe wall and can be used as a reference calculation for the study of different flux profiles. This scenario is of academic interest and reveals a more gentle impact of the evaporator. A constant heat flux profile in the evaporator string is illustrated in figure (10.8).

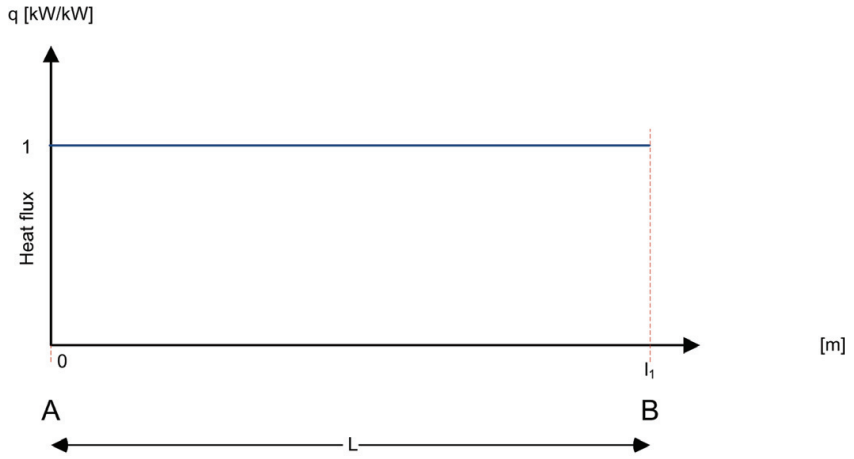

Figure 10.8.: Constant heat flux to boiler.

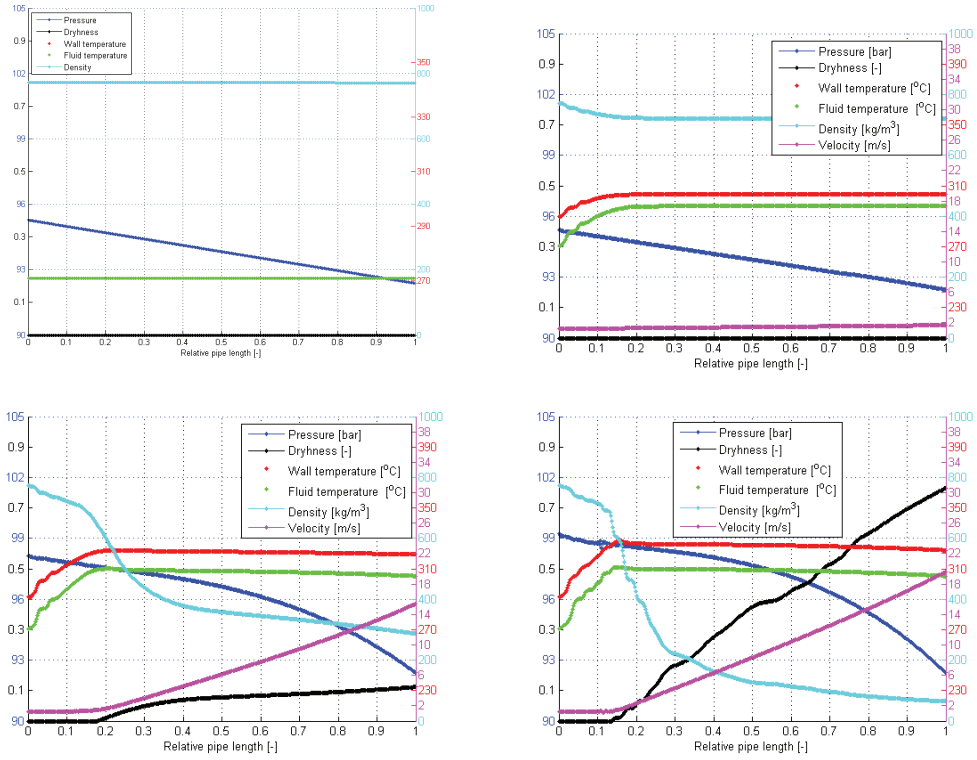

Figure 10.9.: Initial conditions and the solution of SKV3 evaporator model after 50, 75 and 100 seconds.

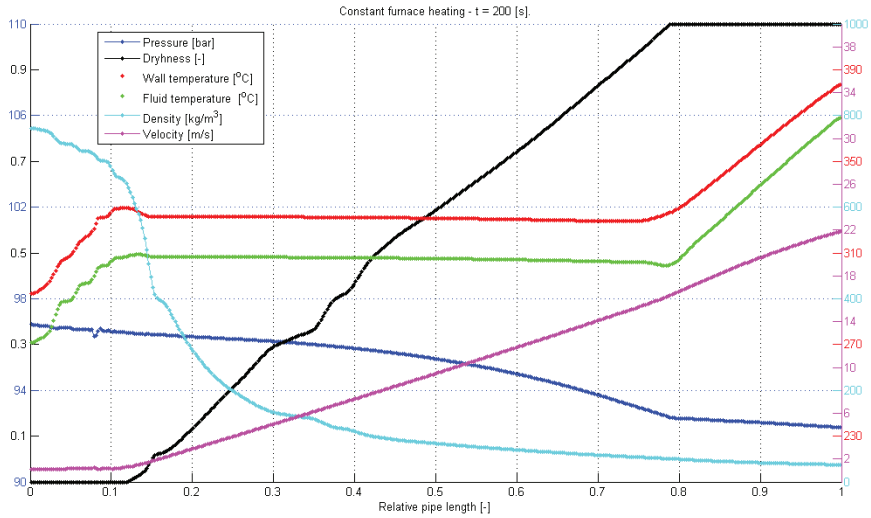

Figure 10.10.: Constant heat flux to boiler, after 200 [s].

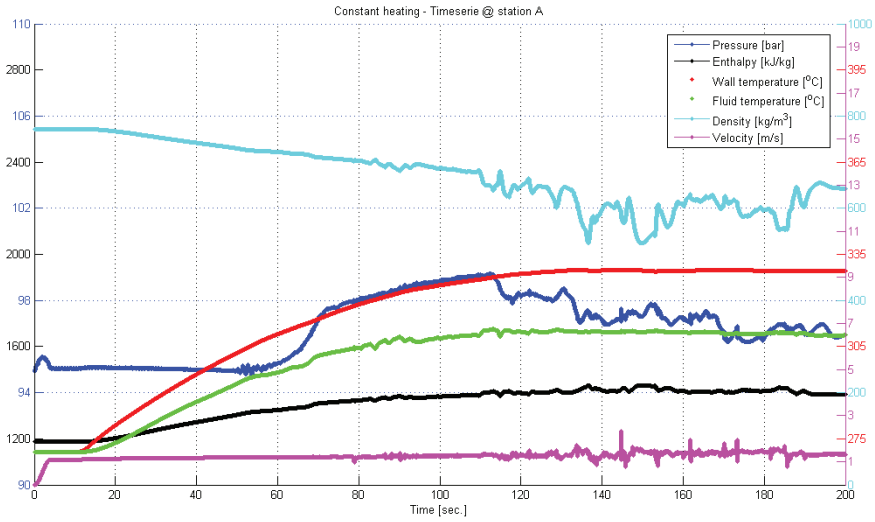

Figure 10.11.: Time series of constant heat flux on SKV3 evaporator model at location A.

The numerical model is configured according to table (10.2), and the heat flux is specified to 100 [kW/m^2]. Figure (10.9) illustrates the output results for each 25 seconds of simulation, referring to the solution of both the homogeneous flow equations as well as the wall tube model. A close to static solution is obtained after approximately 400 seconds, and is depicted in figure (10.13), although a

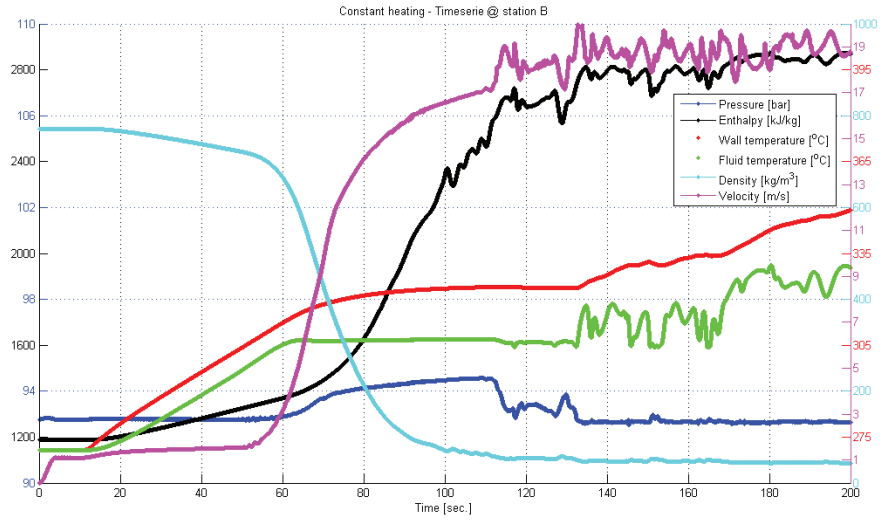

Figure 10.12.: Time series of constant heat flux of SKV3 evaporator model at location B.

static solution is a truth with modifications. Small perturbations in pressure and density are constantly induced, because the model is successively fed with the pressure oscillations created from the transition zone of the sub-cooled to the two-phase fluid, where the very large density gradients occur. These oscillations are controlled by artificial diffusion due to the local turbulence model in the area of transition from single to two-phase flow as well as a smoothing of the EOS. The results show how the state of the fluid gradually moves from the inlet condition, in the form of sub-cooled water, to the two-phase zone, in which the boiling is starting, and finally reaches the super-heating zone, where the dry steam is superheated to about 385 ^oC. The pressure drop is fixed downstream in the form of a Dirichlet boundary condition, corresponding to measured pressure levels from (SKV3). The pressure distribution along the evaporator reflects different pressure loss models, the pressure gradient of single and two-phase regions, respectively. The two-phase region makes use of the two-phase multiplier outlined in (E.42), which multiplies the pressure gradient with up to 16 times relative to the pressure gradient for saturated water. The inlet velocity is specified as an upstream Dirichlet boundary condition, and is soft started by use of the before-mentioned smooth function, having a soft start period of four seconds. This ensures a smooth hydraulic flow condition of the cold evaporator. After wards, the heating is built up smoothly, applied by the same smoothing technique, so that undesirable thermal shock phenomena are avoided. The super-heated steam leaves the downstream boundary at a steady state flow condition with a

speed of approximately 24 [m/s]. Pressure oscillations occur as a result of large upstream fluid compressibility in the flow boiling system; see ([43], [31]). These pressure oscillations appear in the form of pressure fluctuations, arising from the singularity we experience in the gradient field of the fluid density, when saturation is approached and can be generated in the form of a standing wave in front of the boiling zone of the fluid. This phenomenon is also present in horizontal evaporators. The dryness line in figure (10.13) expresses the mass based percentage of the steam flowing in the evaporator tube; not surprisingly, this process is linearly varying and corresponds to a constant heat flux along the tube. By reducing the number of computational cells to, e.g., 50 elements,

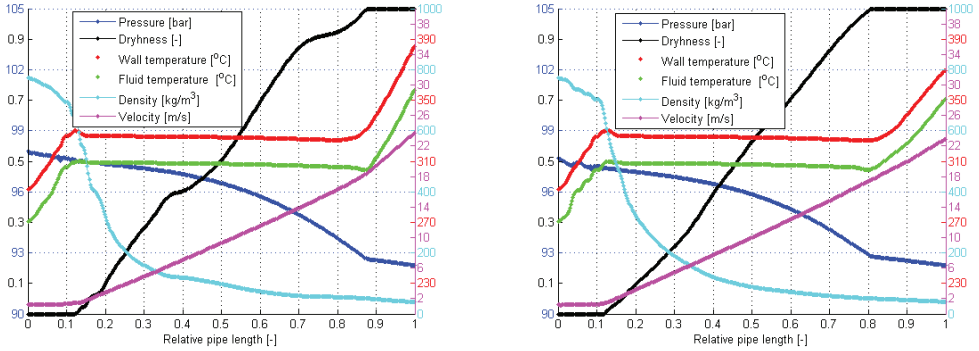

Figure 10.13.: Solutions of SKV3 evaporator model after (L) 210 [s] and (R) 400 [s].

without adjusting the artificial diffusion, one would observe a more intensive standing wave at the entrance of the two-phase region, due to intensive heating of the differential cell in the vicinity of the boiling zone, where we have an intensive negative slope in the density as a function of the enthalpy; hence the density change becomes so violent that a pressure wave is established to ensure momentum balance.

10.4.2. Linear heat flux profile with bottom firing

Operating experience from the SKV3 says that there are inconveniences in the evaporator during start-up when firing low, i.e., when the lower burner roofs are in action during start-up. This enables us to model, by assuming a stylistic heat flux profile, and implement a dynamic thermal hydraulic calculation based on the homogeneous flow model. The profile is illustrated in figure (10.14), with $\Delta q = 0.1$. Physically this can lead to massive slug formations (pressure and density). We have eyewitness reports from operational staff at SKV3 about how the high-pressure steam line from the evaporator during start-up has moved up to

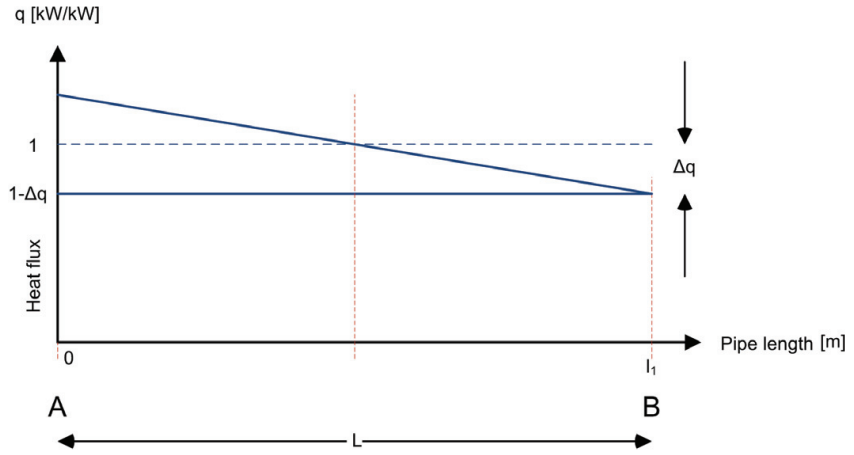

Figure 10.14.: Bottom firing in boiler - linear heat flux to boiler with Δ q=0.1.

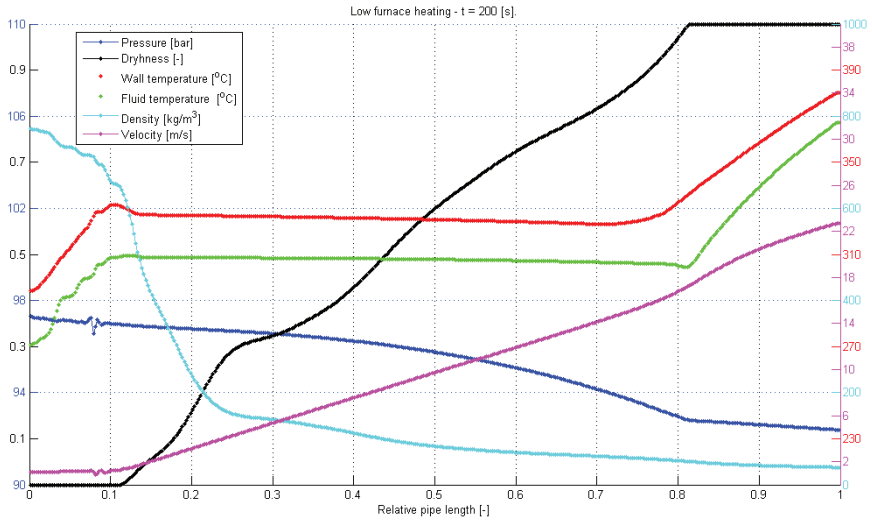

Figure 10.15.: Bottom firing in SKV3 boiler, after 200 [s].

1/2 meter and in this context has destroyed the insulation around the HP-pipe line and also damaged the associated thermocouples. It is violent forces that are at play, when provoked slugs in the form of density waves or pressure surges act in the steam pipes. Figure (10.15) shows a dryness profile, which differs from the corresponding simulation with a constant heat flux profile. The difference reflects that the bottom firing case has not yet reached a steady-state condition, and thus is slower to settle into a stable plateau. This emphasizes that the two time series, as illustrated in figures (10.16 and 10.17), after 110 [s] from the start of simulation, show considerable density fluctuations in station A and both

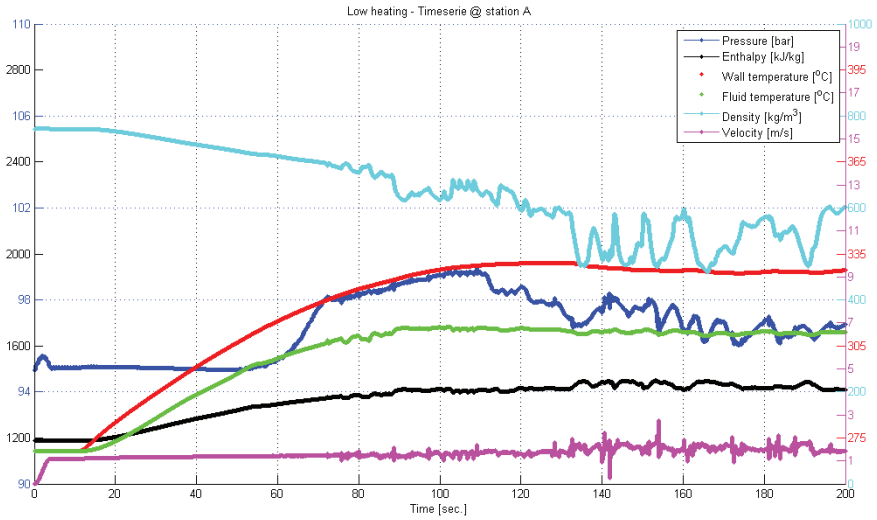

Figure 10.16.: Time series of bottom firing in SKV3 evaporator model at station A.

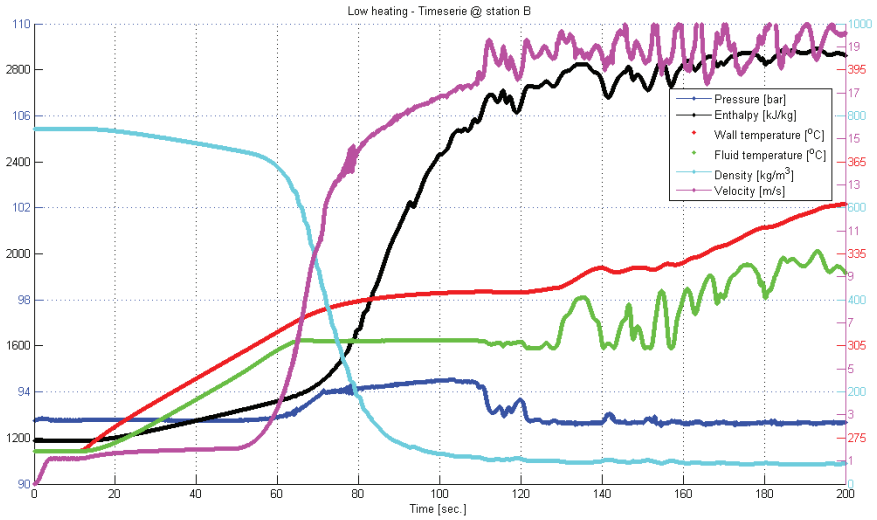

Figure 10.17.: Time series of bottom firing in SKV3 evaporator model at station B.

a strong temperature and a velocity fluctuation in station B. The temperature fluctuations in station B are damped towards the end of the simulation and become stable around 330 [^oC]. Note that both the tube wall temperature and the fluid temperature refer to the same temperature scale on the right axis of figures (10.16 and 10.17). Especially temperature fluctuations may be critical with respect to the fatigue of pipe material in general, especially when we draw

attention to the material structures on the inner surface of the tube, which are extremely sensitive to temperature fluctuations, due to the short time constant shown in table (4.2).This is compensated to some extent by the thermal diffusion, which smooths the temperature distribution in the pipe wall, here illustrated as an averaged wall temperature. This phenomenon may be an early-stage cracking, particularly in the super-heaters, in which the steam temperature is considerably higher.

10.4.3. Linear heat flux profile with top firing

Operating experience from the SKV3 in particular indicates a greater stability in the evaporator, when the firing is intensified in the top of the boiler. We attempt to model this using a linear heating profile, with the highest heat flux at the top of the boiler. The profile is illustrated in figure (10.18) and the boiler specifications are similar to the previous setup, except for the reverse heat flux slope with Δ q=0.1. Figure (10.19) shows an instant picture of the thermodynamic properties

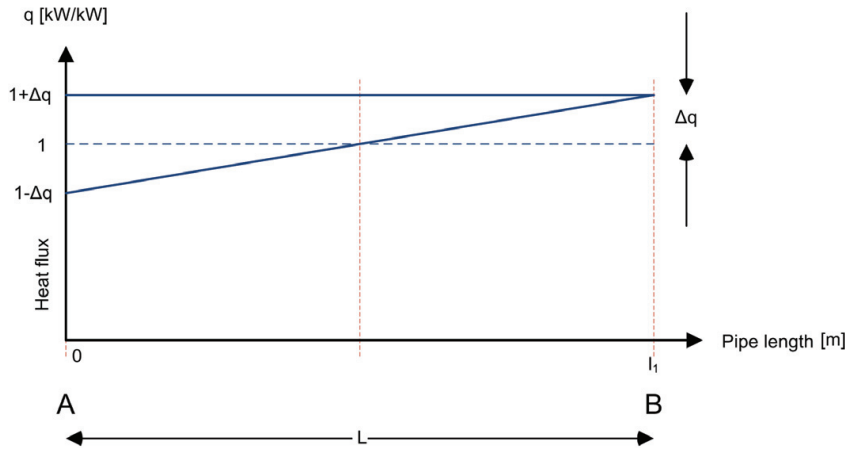

Figure 10.18.: Top firing in boiler with linear heat flux to boiler.

of the fluid in the pipe after 200 [s] of real time from the start of the boiler. It is noteworthy that the steam quality is progressing nearly linearly through the evaporator, but has not yet reached a steady state condition. The outlet temperature of the steam is slightly higher than the scenario with low firing. Similarly, we can see a significant difference in both the pressure and the velocity profile compared to the situation with low combustion in the boiler room. The inlet pressure is here approximately 1.5 bar lower, and the steam outlet velocity is only 21 [m/s] compared to 23 [m/s] for the scenario with low firing. Also in this scenario one can see violent fluid temperature fluctuations downstream at station B.

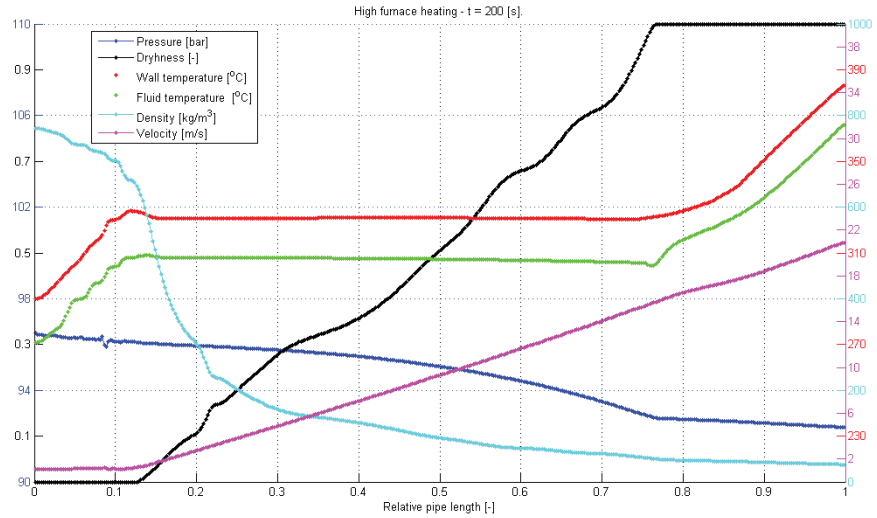

Figure 10.19.: Top firing in SKV3 boiler, after 200 [s].

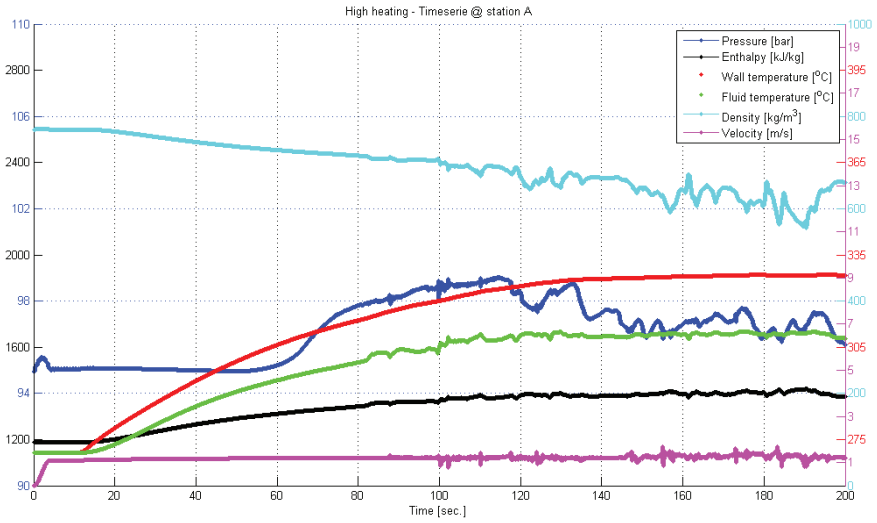

Figure 10.20.: Time series of top firing in SKV3 evaporator model at station A.

10.4.4. Parabolic heat flux profile with (parabolic firing)

In accordance with the CFD studies carried out in Chapter (4), we can correlate the flux distribution according to a parabolic profile, so that the flux intensity is greatest around the centre point of the burner zone, which for SKV3 consists of the four burner floors. It should be noted that the maximum value of the flux intensity, is somewhat above the centre point of the burner system. A parabolic

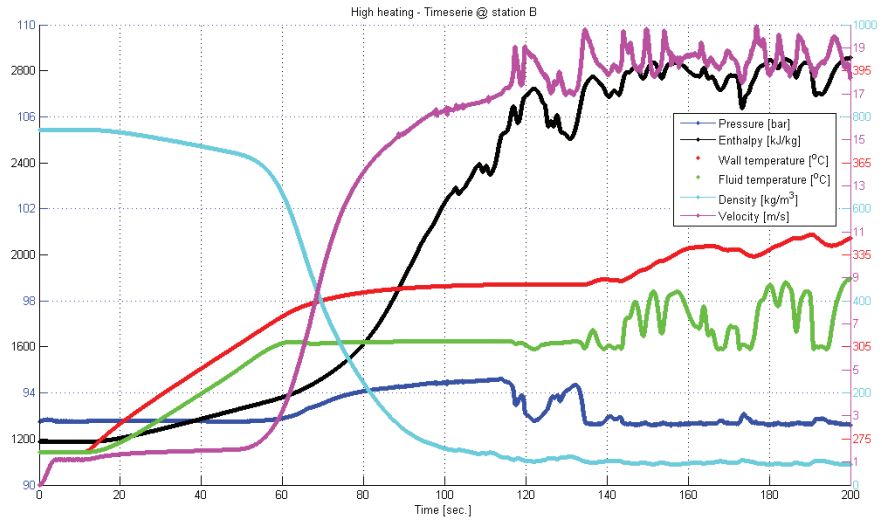

Figure 10.21.: Time series of top firing in SKV3 evaporator model at station B.

heat flux profile in an evaporator string is illustrated in figure (10.22) as a relative flux distribution profile and can be idealised as a second-order symmetrical profile,

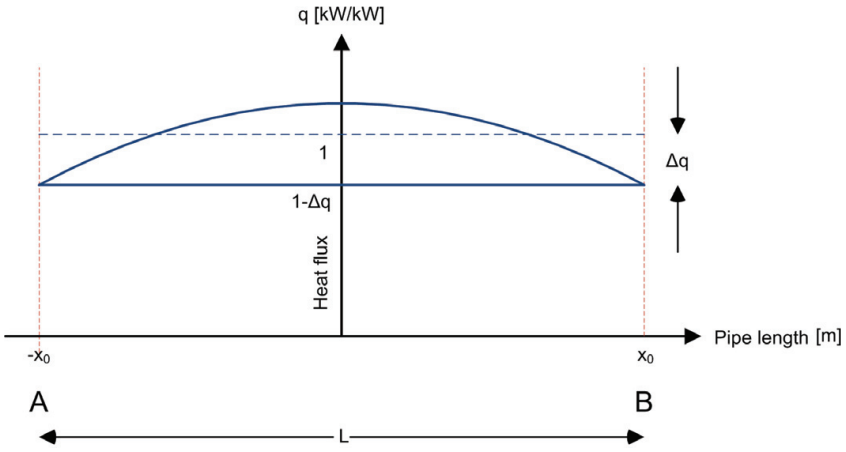

Figure 10.22.: Normal firing in boiler with weak parabolic heat flux to boiler.

given by

$$q^*(x) = a \cdot (x + x_0)(x - x_0) + b, \quad b = 1 - \Delta q. \tag{10.2}$$

A simple requirement for the distribution function is that the integral of the distribution function over the entire interval of definition must be of unity, so that we do not add more energy than expected for the evaporator tube. We

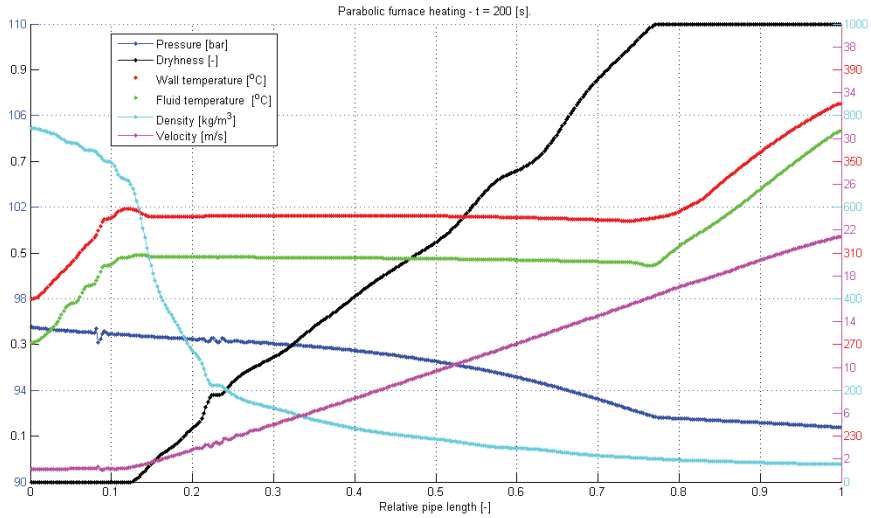

Figure 10.23.: Parabolic firing in SKV3 boiler, after 200 [s].

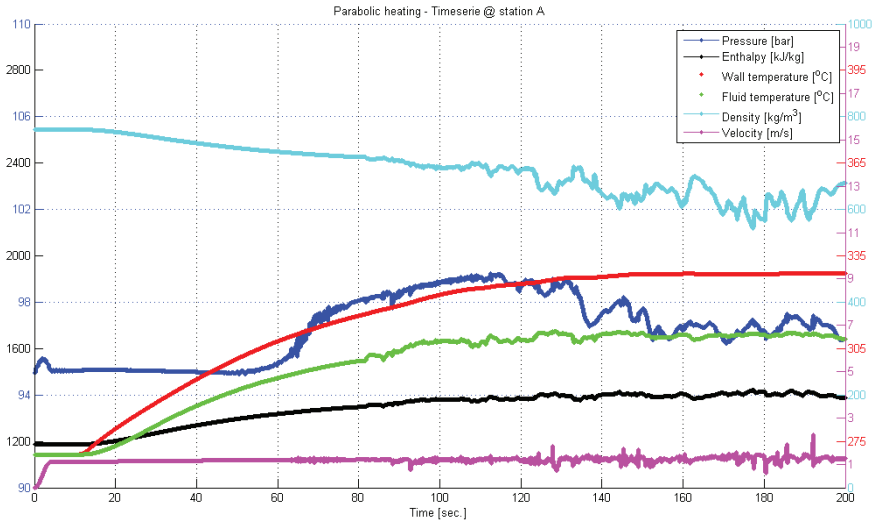

Figure 10.24.: Time series of parabolic firing in SKV3 evaporator model at station A.

can thus ensure that the distribution function has the desired functionality by requiring:

$$\begin{aligned}\int_{-x_0}^{x_0} q^*(x)dx &= 2x_0 \cdot 1 \\ &= \int_{-x_0}^{x_0} (a\cdot(x+x_0)(x-x_0)+b)dx \\ &= -\frac{4a}{3}x_0^3 + 2bx_0\end{aligned} \tag{10.3}$$

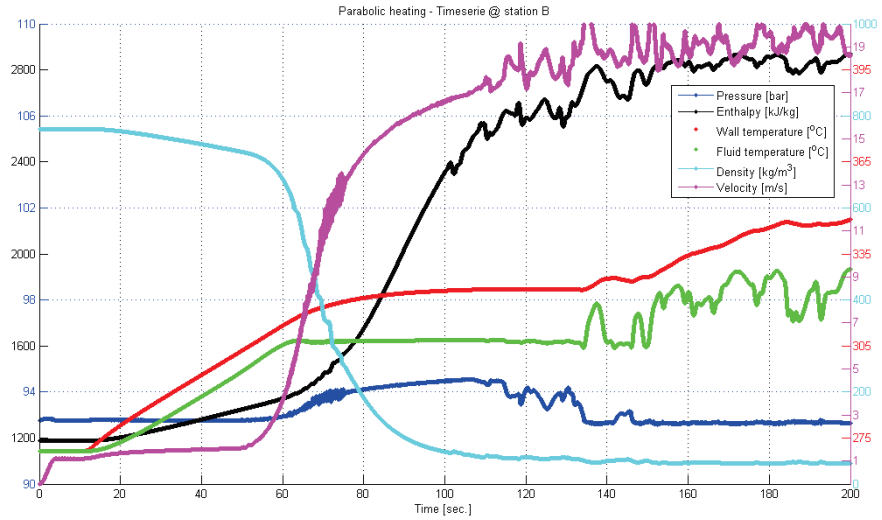

Figure 10.25.: Time series of parabolic firing in SKV3 evaporator model at station B.

Hence the coefficient can be estimated to

$$a = -\frac{\Delta q}{x_0^2} \tag{10.4}$$

and for x_0=1, the equation (10.2) can be formulated as

$$q^*(x) = \frac{3\Delta q}{2} \cdot (1 - x^{*2}) + 1 - \Delta q, \quad x^* \in [-1, +1] \tag{10.5}$$

wherein x^* is a dimensionless position in the evaporator. We can see that the maximum flux occurs at $x^* = 0$, corresponding to $q^* = 1 + \Delta q\,/2$. Similarly, the minimum flux attached to the top and the bottom of the evaporator for x^*=$\pm x_0$, respectively. Here we find $q^*(\pm x_0)$ = 1-Δq. We can again observe an almost linear relationship between steam quality and pipe length, corresponding to a distinct stable heat absorption. The outlet temperature of the evaporator is the lowest of all scenarios, and the inlet pressure corresponds to the scenario with constant heat flux. This reflects that the models are not in dynamic equilibrium, since all scenarios receive the same effect.

10.5. Comparison of the flux profiles

The start-up process with different heat flux profiles causes different dynamic pressure responses. As shown in the figure (10.26) for station A, one observes different pressure build-ups, where we clearly can see that the low combustion

causes a faster and steeper pressure build-up than the other profiles, so that the top firing causes the smallest pressure build-up. Immediately thereafter, the response of the more or less homogeneous pressure build-up, is replaced by a more oscillating process, where the moving average gradually decreases over time. All four scenarios have an oscillating response; however, there is a trend to bottom firing have a more moderate exit amplitude. In station B we almost see identical pressure structures, but with varying timing. The bottom firing scenario flattens out soon and settles at a stable level, while the top firing scenario flattens out later and also attempts a second pressure build-up, but quickly falls back to the final level of the downstream pressure. When we look at the time series of enthalpy in station A, there is no significant difference observable among the four scenarios. Downstream station B, a time delay occurs of the enthalpy front, and not surprisingly, we see the fastest enthalpy front for low firing, while high firing has the slowest front; see (10.27). After 80 [s] of simulation we see a gradually

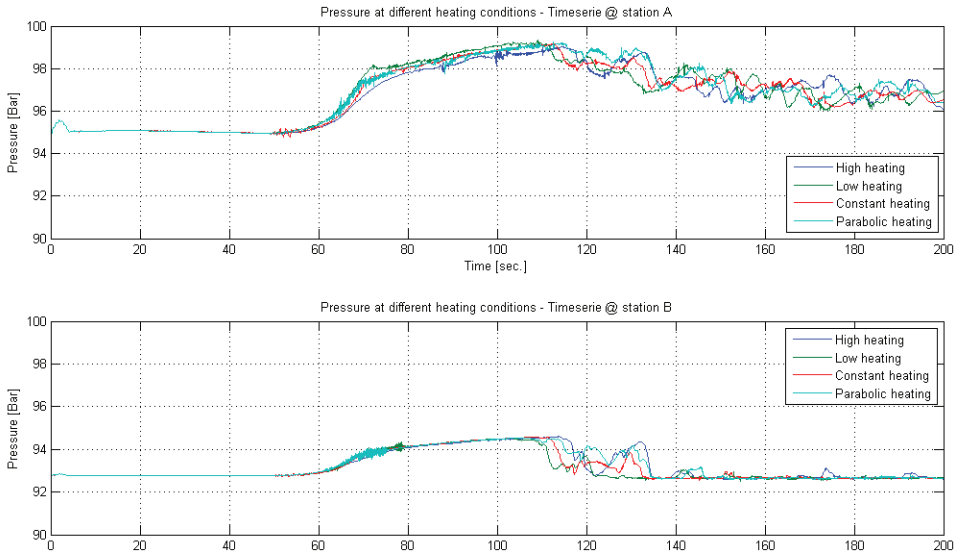

Figure 10.26.: Comparison of the firing profiles on the SKV3 evaporator with respect to fluid pressure.

more oscillating density-wave in station A, see figure (10.28), which dominates the rest of the simulation period. In station B we see a significantly higher density for the bottom firing scenario, but with a lower degree of oscillation compared to the other scenarios. Here we find surprisingly the greatest density oscillations in the top firing scenario. The fluid temperature is illustrated in figure (10.30). In station A there is a steeper increase in fluid temperature for the low firing

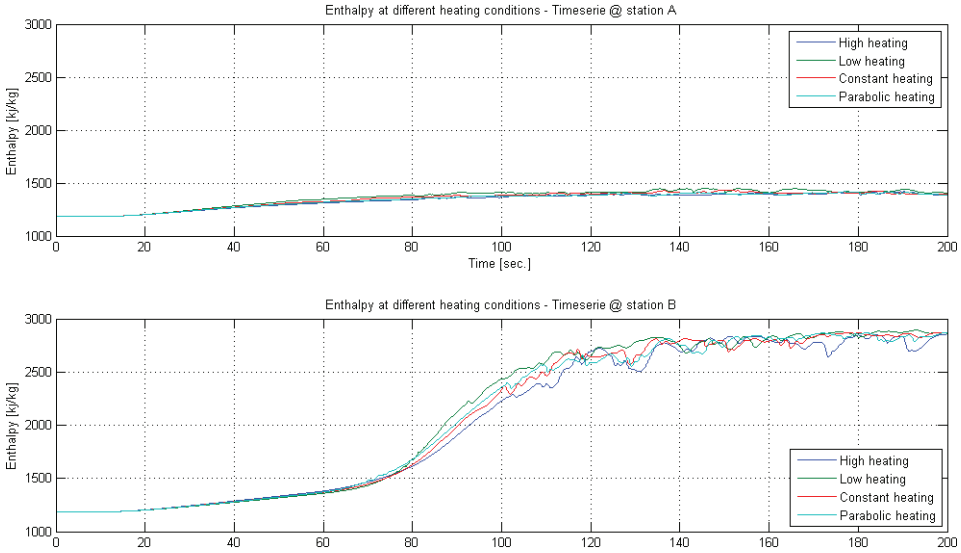

Figure 10.27.: Comparison of the firing profiles on the SKV3 evaporator with respect to fluid enthalpy.

scenario, which ends on the same level as for the other scenarios, due to the entrance to the two-phase region (almost identical saturation pressure). In station B, we conversely see the largest temperature gradient before the two-phase region for top firing, and again, the temperature ends at the same level, as entering the two-phase region. In the superheated region, we again see drastic temperature fluctuations, surprisingly most notably for the high-fired scenarios. The observed momentary temperature fluctuations are above 20 degrees, for the top-firing scenario. The associated material temperature is dampened much, compared to the fluid temperature, and here we see the highest material temperature in the bottom firing scenario, with a difference of approximately 10 [^{o}C] compared to the top firing scenario. The material temperatures are illustrated in figure (10.29). At station A, we can see a significantly higher material temperature (+3 [^{o}C]) for the bottom-firing scenario, compared to the other scenarios.

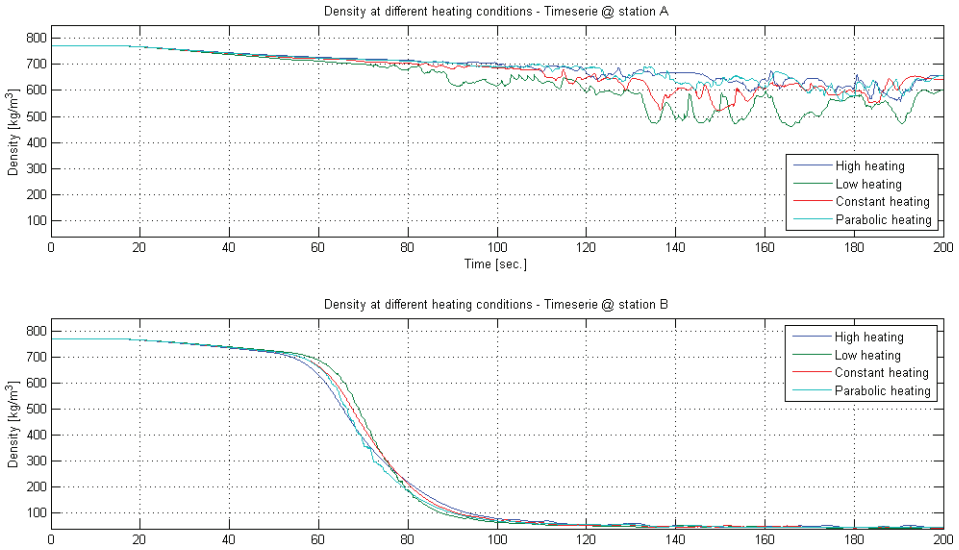

Figure 10.28.: Comparison of the firing profiles on the SKV3 evaporator with respect to fluid density.

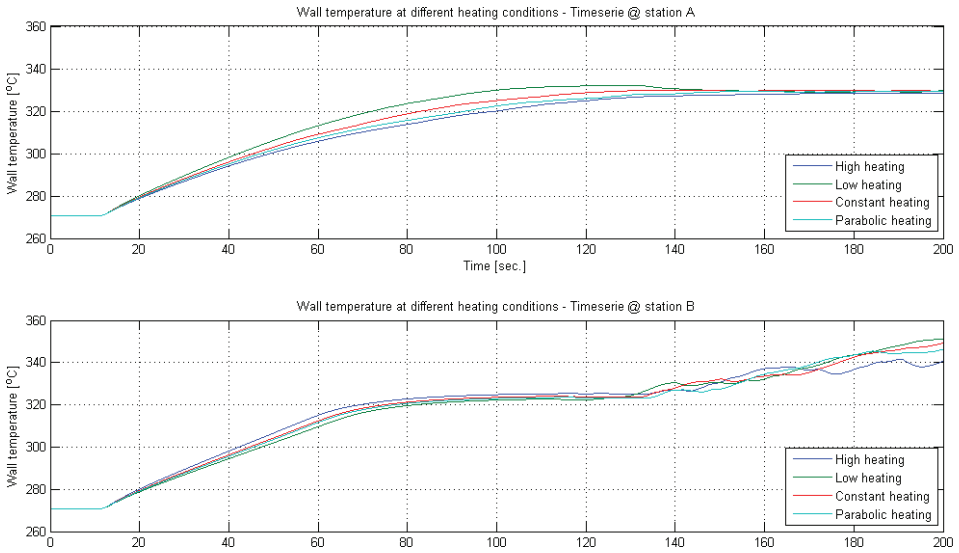

Figure 10.29.: Comparison of the firing profiles on the SKV3 evaporator with respect to wall temperature.

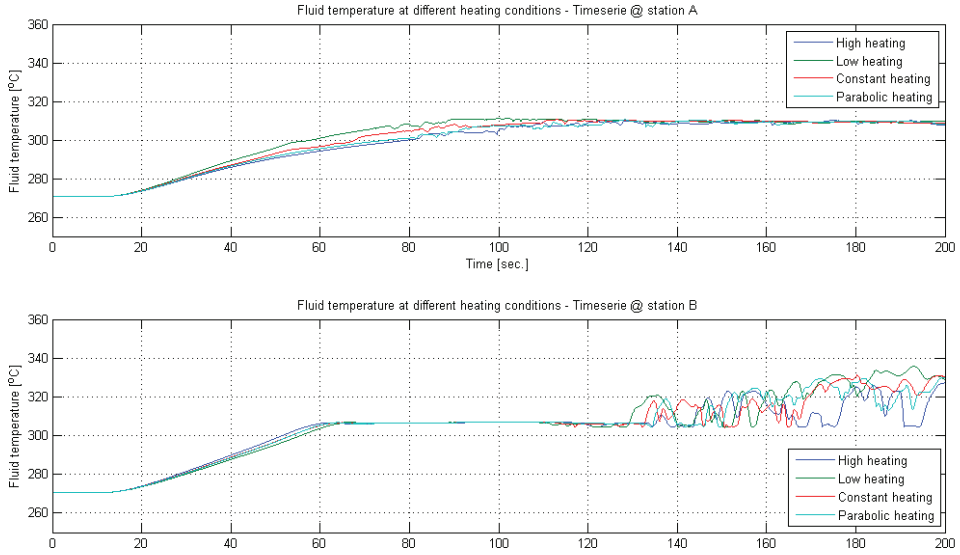

Figure 10.30.: Comparison of the firing profiles on the SKV3 evaporator with respect to fluid temperature.

10.6. Preheater failure

A high-pressure preheater improves the electrical efficiency of a power plant, by re-using a part of the steam from the HP turbine outlet, so that the feed water temperature is raised towards the economiser (ECO). With a preheater failure, we will experience an immediately decreasing feed water temperature toward the ECO and evaporator. We use again the homogeneous dynamic evaporator model to analyse what happens when a HP-preheater shuts down over four seconds. Time series from the simulation is illustrated in figures (10.31 and 10.32). The green vertical line indicates the time of shut-down of the preheater. By smoothly changing the feed water temperature on the SKV3 model on the upstream Dirichlet boundary from 1187 [kJ/kg] to 750 [kJ/kg] during 4 [s], the temperature jumps from 270.7 $[^oC]$ to 220 $[^oC]$. The model responds promptly, and by observing the time series located upstream and downstream to the evaporator (stations A and B), we can see a response as a function of time. Not surprisingly, we see a response in the upstream station, which is very similar to the upstream boundary condition, whereas in the downstream station B, we experience a peak in the steam temperature, despite, that we are feeding the system with lower temperature. This is due to the compressibility in the evaporator, so that the fluid now takes up less space in the upstream section. The residence time of the downstream fluid becomes longer, for a short while, which finaly results in a higher superheating

of the fluid. After a certain period, this superheated fluid is advected out of the downstream boundary and we now see a reduced superheating. In general,

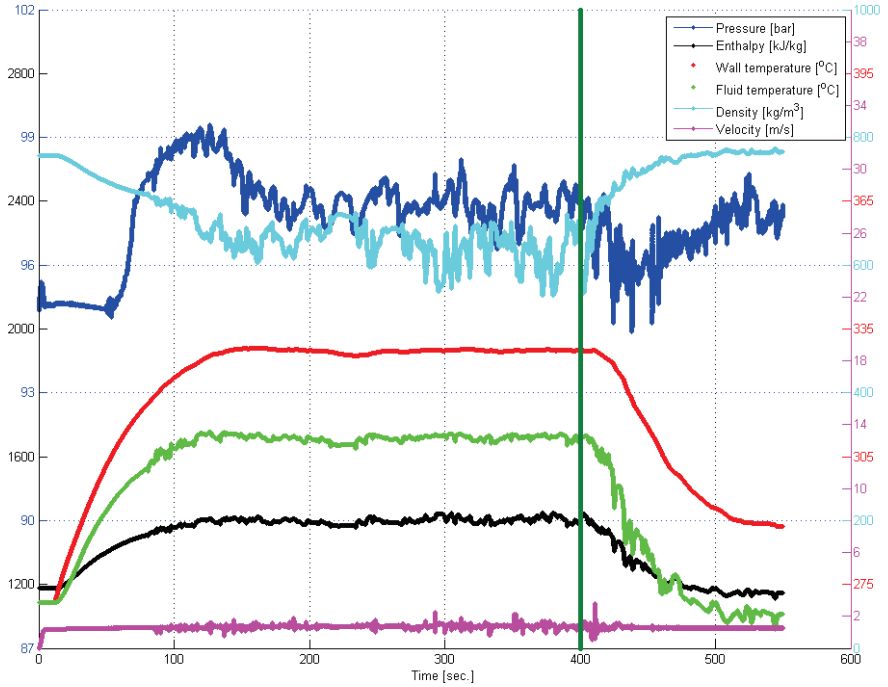

Figure 10.31.: Preheater failure after 400 [s]. Left and right figures represent the time series at station A.

temperature (enthalpy) deviations from a set point in the separator are regulated by a fast control loop that adjusts both the firing and the feed water flow rate. This enthalpy control cannot compensate for what happens in each evaporator tube; the enthalpy control can only reduce the deviations from a set point that occurs in the separator, by using a feed forward control loop. The large temperature decrease at the evaporator inlet, which occurs after a high-pressure preheater trip, cannot be out-balanced by the control. This is hazardous to the evaporator in the long term.

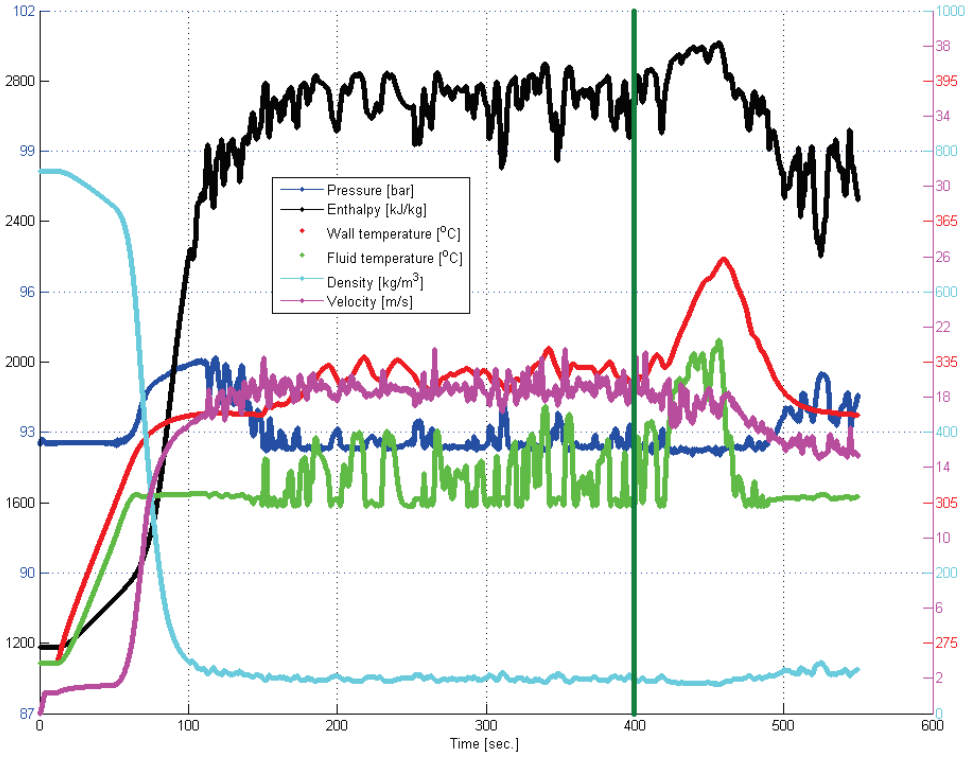

Figure 10.32.: Preheater failure after 400 [s]. Left and right figures represent the time series at station B.

10.7. Internal rifled boiler tubes

One parameter that determines the heat transfer rate on the inside of the pipe is the fluid velocity near the inner pipe wall (shear velocity). If the friction velocity can be increased without increasing the net mass flux through the boiler, the heat transfer rate can be increased. With that technology in mind, it is possible to build a more compact boiler. Internal rifled boiler tubes (IRBT) are an attempt to speed up the fluid velocity at the tube wall and achieve the vertical tubes of a boiler construction. The mass flux through the IRBT is usually in the range of 1000 [kg/m^2s] at base load and is less than the half of the mass flux in traditional Benson boiler panel walls, with a moderate pipe inclination.
In addition to the increase in heat transfer, the IRBTs are characterised by an excellent performance concerning two phase-flow. The swirl is very effective for separation of liquid from gas. The centrifugal force will increase the rate of light fluid to the centre of the pipe and force the heavy fluid components to

near the wall. This will improve the cooling of the pipe, and thereby increase the heat transfer and decrease the wall temperature of the pipe. Additionally the IRBTs have the following advantages: the rifles will enlarge the surface of convective heat transfer moderately, thereby increasing the turbulent intensity in the boundary layer and increasing the relative velocity between the wall and the core fluid by rotational flow.
The advantages of the IRBT have a price. The pressure loss is higher than in traditional boiler tubes, but this can be used in a constructive way. When super-critical boilers operate at part load, stability problems can occur. The problem is usually solved by inserting individual pressure losses at each pipe inlet section. Thus the increased pressure loss in the IRBT can be utilized to replace the traditional built-in pressure loss devices, and thereby not increase the pumping power.

10.7.1. Modified boiler geometry

Retrofitting the SKV3 boiler to a system equipped by Siemens type RR5 internal rifled boiler tubes (IRBT), will normally lead to a complete redesign of both the furnace- and the evaporator system. But in this fictive case we use the same heat transfer area, despite the fact, that the IRBTs considerably improve the heat transfer in the boiling zone. In this new setup, the length of the boiler tubes is reduced from 193.5 [m] to 38.25 [m] according to the height of the evaporator section of the furnace, and the number of parallel tubes is increased from the original 4 x 56 to 4 x 270 parallel tubes. We have consciously chosen to use a very low mass flux (corresponding to approximately 10% load), also named "micro load", specifically to analyse the effects of the wall temperature distribution. It should be emphasized that this simulation scenario is a fictional setup and is rather a calculation example of what can happen in evaporator tubes, if near-zero flow momentarily occurs.
The vertical IRBT leads to a decrease in the mass flux, which is illustrated in (10.33) for instant pictures of 50, 100, 150 and 200 [s] of simulation. The wall temperature varies in time and reaches a peak, while the flow locally approaches zero, caused by local pressure oscillations initiated by the compressibility at the entrance of the two-phase region. The poor cooling caused by near-zero flow can have disastrous consequences for the pipe material and may ultimately lead to a meltdown of the evaporator tube. In practice, this is avoided by increasing the circulation through the evaporator. The pressure drop through the evaporator tube is unrealistically low and ultimately trips the firing, due to the very low mass flux (105 [kg/m^2s]). Normally, the mass flux of IRBT is approximately 1000-1200 [kg/m^2s] at base load and typically limited to 250 [kg/m^2s] at the Benson minimum load for vertical tubes; see [4] p. 518. In figures (10.34) and (10.35) are listed the time series of the thermo-hydraulic data at two stations

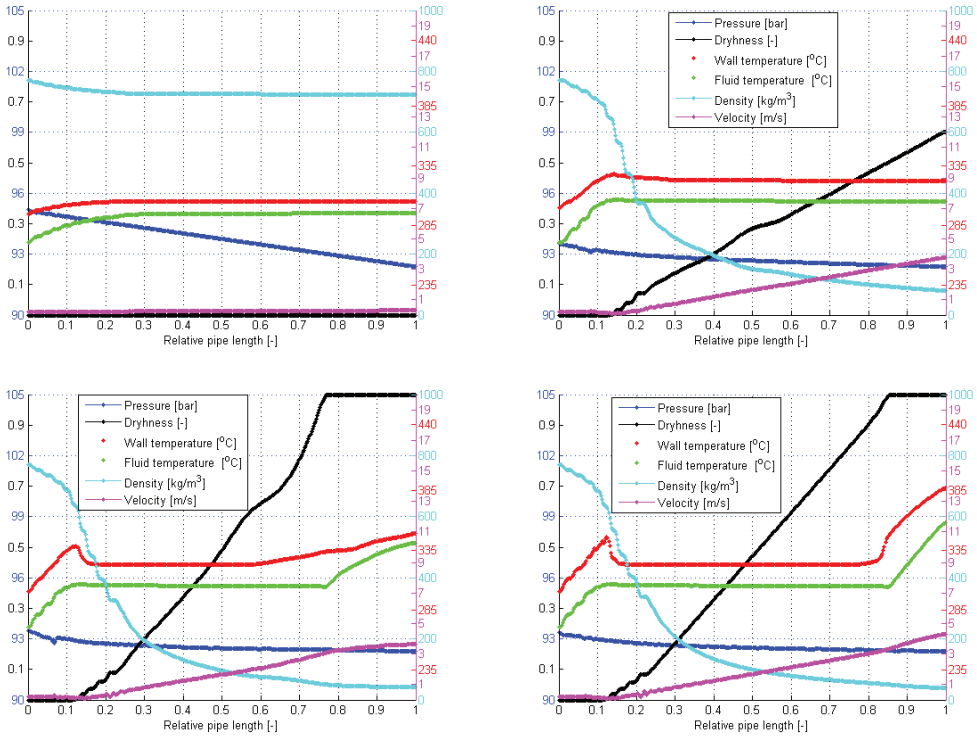

Figure 10.33.: Solution of Modified SKV3 vertical evaporator model with SLMF after (LT):50, (RT):100, (LB):150 and (RB):200 [s] (Micro load).

located at A and B, A(z=$\frac{1}{8}l_z$) and B(z=$\frac{7}{8}l_z$). The thermo-hydraulic conditions at station A are situated in the sub-cooled region, while station B conditions are in the super-heated region. Both stations are affected by the compressibility effect, initiated at the entrance to the boiling zone. Pressure waves approach upstream and downstream due to the eigenvalues of the hyperbolic governing equations (λ_1=c, λ_2=u+c and λ_3=u-c) where λ_i, i=1,3 are the eigenvalues, and c is the local speed of sound for the two-phase mixture and u is the convective velocity of the fluid. In the downstream station B, we can also see minor slugs of enthalpy for t=90 [s], which also refer to the compressibility phenomena. Another setup is made for 100% load (super-critical), where the mass flux is set to 1000 [kg/m^2s] and the heat flux is changed to a linear profile of 500 [kW/m^2], so that full superheating is achieved downstream the evaporator. The exit pressure of the evaporator is at baseload approximately 280 [bar]. The other geometric data are unchanged and thus equal to the first simulation with IRBT; see table (10.2). The result of a calculation is represented after 200 [s] as a line series in figure (10.36) and the corresponding time series at station B is illustrated in figure (10.36).

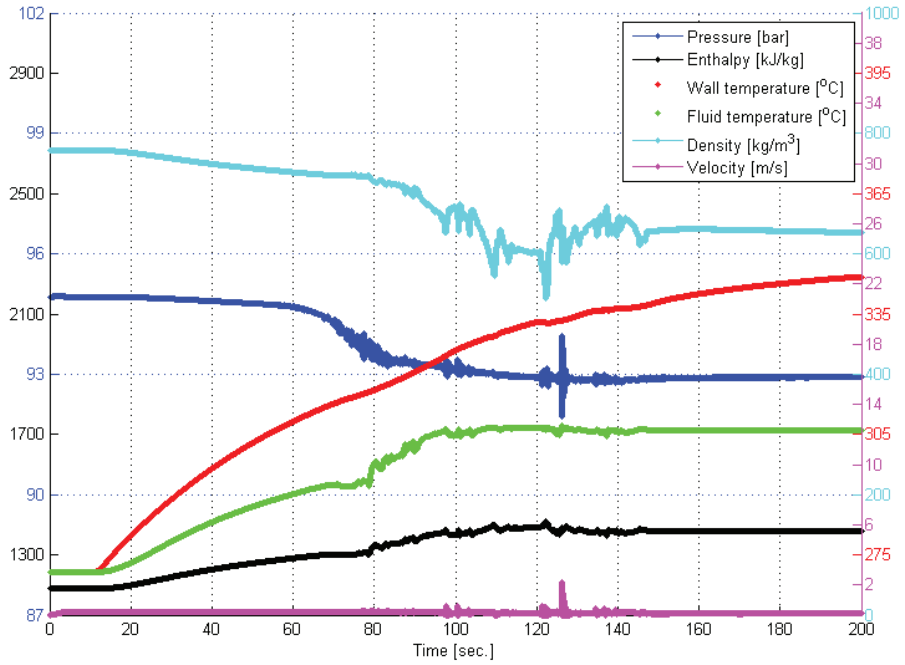

Figure 10.34.: Modified SKV3 vertical evaporator model with IRBT at station A.

Initially there is a relatively large geodetic pressure drop, which gradually fades out as the fluid starts to boil, and the density of the fluid becomes smaller. As evaporation occurs, it increases the fluid velocity to approximately 8 [m/s] at the exit boundary. There is a conversion of a geodetic pressure to a friction pressure drop. Despite the corrected pressure loss calculations with the RR5 rifle tube, we see a relatively moderate pressure drop, but junction boxes will increase the pressure drop, while ensuring a minor imbalance in the outlet temperature of the vertical evaporator. Another noteworthy relation is the increased temperature difference between the fluid and the tube, which leads to an increased risk of cracking in the boiler fins.
A similar calculation of pressure loss for an evaporator tube without internal rifling gives an absolute pressure drop of 1.5581 [bar], while there is a pressure drop of 1.6470 [bar] for IRBT. This provides an increased pressure drop of only 8890 [Pa], which can be attached to the friction pressure loss alone, as the geodetic pressure drop is identical in the two situations, as departure conditions are basically the same (h_{out}=2862.08 [kJ/kg] and u_{out}=8.17 [m/s]) and thus the

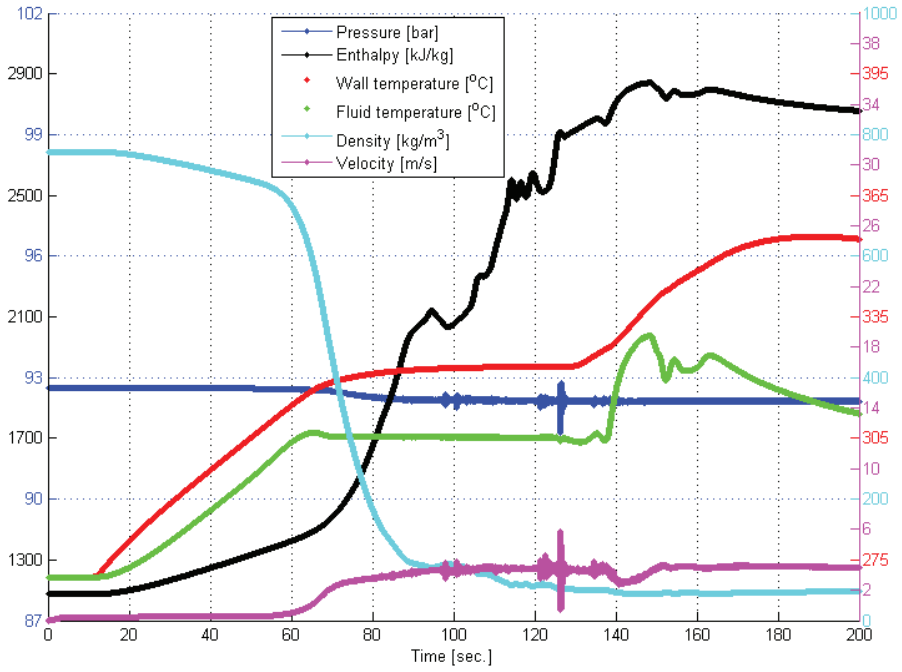

Figure 10.35.: Modified SKV3 vertical evaporator model with IRBT at station B.

geodetic pressure drop. This corresponds to the *Slip Correction Factor* (Π), given by (8.25), due two internal rifles:

$$\begin{aligned}\Delta P &= \Delta P_{IRBT} - \Delta P_{Smooth} \\ &= 8890[Pa] \\ &= \sum_{i=1}^{N} f_w \rho_i \frac{u_c \Pi |u_c \Pi|}{2} - \sum_{i=1}^{N} f_w \rho_i \frac{u_c |u_c|}{2} \\ &= (\Pi^2 - 1)\Delta P_{Smooth} = (\Pi^2 - 1)1.5581 \cdot 10^5 [Pa]\end{aligned} \tag{10.6}$$

Hence $\Pi = \frac{1}{cos(\gamma)}$ according to equation (8.25) and γ=13.4^o, which is far from the typical angle for IRBT, where the rib angle to cross-section is between 47^o to 60^o according to Griem [7]. We can thus conclude that the pressure loss in IRBT cannot be estimated by a simple adjustment of the hydraulic pressure loss due to the *Slip Correction Factor* (Π), but is subject to more complex accounting rules, as found in [10], [11] and [13]. This is evidence of the complexity of the flow processes, both for single-phase flow but especially for two-phase flows.

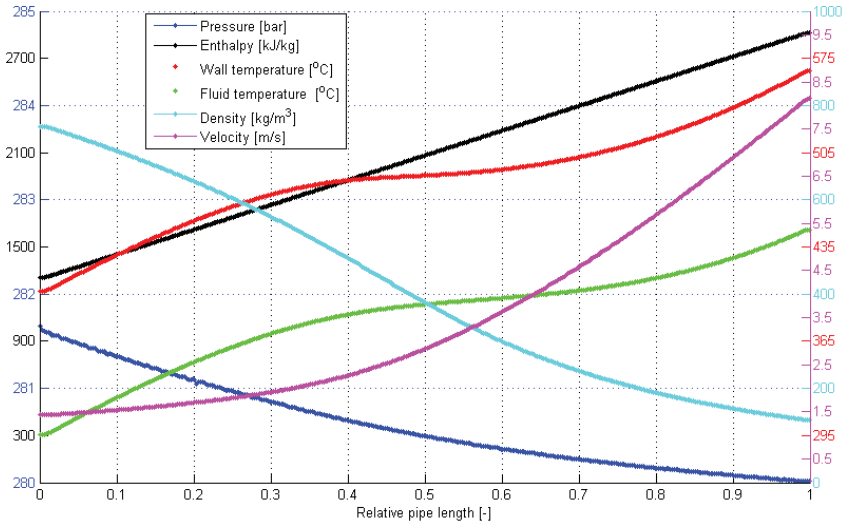

Figure 10.36.: Vertical IRBT at base load. Line profile after 200 [s].

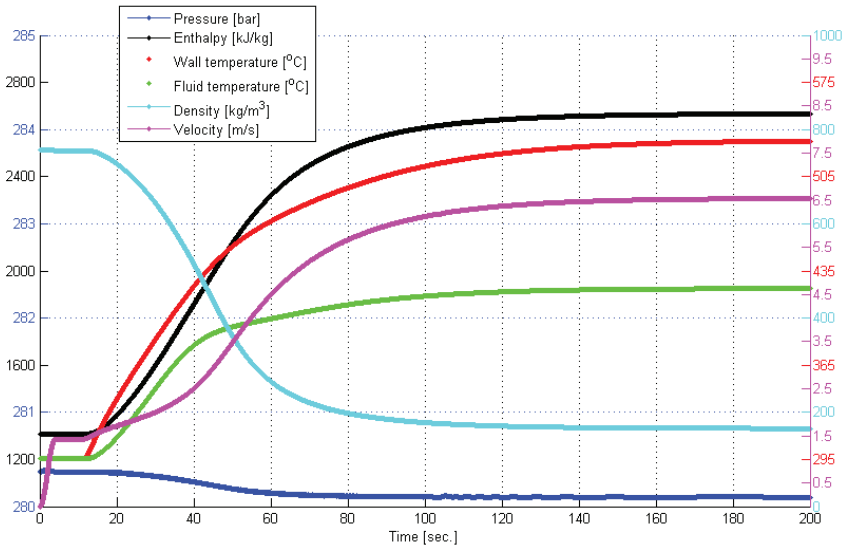

Figure 10.37.: Vertical IRBT at base load. Time series at station B.

10.8. Low-pressure evaporators

During the last decade, Danish utilities (Vattenfall AB and DONG Energy A/S) have invested much effort in the optimisation of thermal power plants in order to outbalance the fluctuations imposed by wind and sun. One could argue that we could phase out the existing thermal plants and switch to open pass gas turbines

to solve the problem, but this is a rather expensive solution because we have a fleet of quite new super-critical power plants that still have a significant life time. Simultaneously, the power stations are committed to supply district heating to a large customer base. This means that there is a strong link between the production of district heating and electricity, which can result in a significant overproduction of electricity, when the weather is cold and windy. This can be accomplished by, for example, reducing the outlet pressure of the SKV3 evaporator, while bypassing the VHP turbine, so that the pressure of the evaporator is aligned with the HP turbine. Bypassing the VHP tubine at low load corresponds to an evaporator pressure decrease from approximately 90 [bar] to 46 [bar] at the evaporator outlet. This leads to less power output without compromising the district heating production, but the unit efficiency deteriorates, without affecting the C_v value, given by equation (3.1), which is a static expression for pricing the district heating.

In this section, we examine how a power plant evaporator (SKV3) with smooth pipes behaves, when the boiler outlet pressure is reduced considerably below the normal circulation pressure for Benson boilers. Four simulations with different firing profiles are performed, so that the sensitivity to uneven heating can be assessed. Note that the applied input enthalpy (boundary condition) is unchanged relative to the previous calculations. This results in minimal sub-cooling, though sub-cooling still exists. In practice this can lead to mal-distribution problems, as discussed in section (5.5).

10.8.1. Heat flux profiles

Here we carry out calculations with the aim of investigating how different heat flux profiles affect the dynamics of a low-pressure configuration of the SKV3 evaporator during a dynamic start-up period of 200 [s]. There are four different profiles to be examined: a constant heat flux on the panel wall as illustrated by figure (10.10), a linear profile representing situations with bottom firing of the boiler as illustrated in figure (10.14), a parabolic heat flux profile in the evaporator string as illustrated in figure (10.22) and finally a linear profile representing situations with top firing of the boiler as illustrated in figure (10.19).

Constant heat flux profile

A constant heat flux profile is used as a reference calculation for the study of different flux profiles. This scenario is also of academic interest and involves a more gentle impact of the evaporator. The outcome of the linear heat flux simulation shows a very stable evaporator, illustrated in figure (10.38), with a very high pressure drop (15.7 [bar]) and an outlet steam velocity of 48 [m/s], which is very high. The steam quality profile is perfectly linear along the pipe, indicating a constant and stable heat uptake. The corresponding time series at

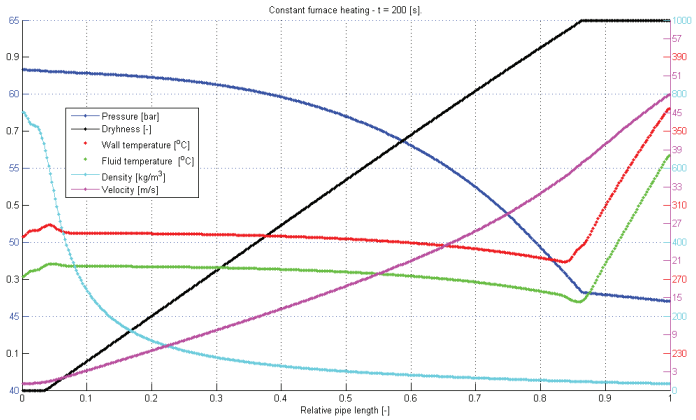

Figure 10.38.: Constant heat flux to boiler, after 200 [s].

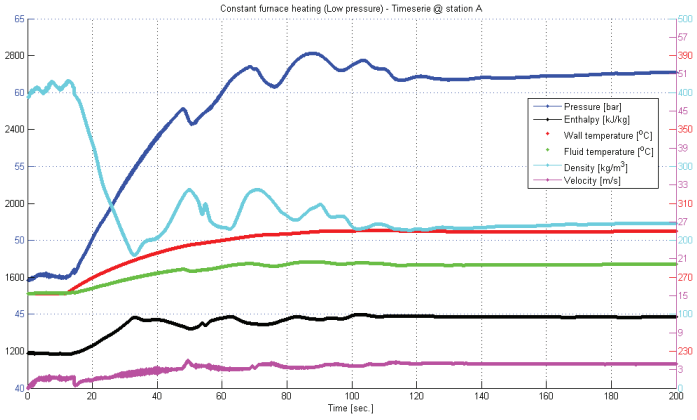

Figure 10.39.: Time series of constant heat flux at the SKV3 evaporator model at station A.

station A and B are illustrated in figures (10.39) and (10.40). There occur violent pressure oscillations in connection with the start-up of the model, and the model is first stabilized after approximately 140 [s]. The pressure oscillations achieve a size of up to 5.5 [bar] and thus may be critical in the supply of steam for each evaporator tube (mal-distribution). These oscillations occur in combination with enthalpy fluctuations and affect the flow velocity, which momentarily may rise 10 [m/s] within a period of less than one second. We can thus conclude that the start-up period in a low-pressure evaporator is a violent dynamical phenomenon for the first approximately 140 [s] of simulation.

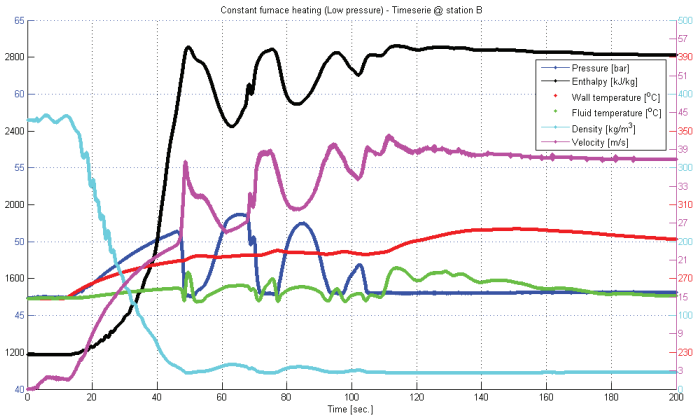

Figure 10.40.: Time series of constant heat flux at the SKV3 evaporator model at station B.

Linear heat flux profile with bottom firing

Experience from earlier simulations has shown that bottom firing leads to higher dynamic instability in the evaporator, and is no exception in this situation with reduced evaporator pressure. After 200 [s] we see a steady state picture of the axial profile of the thermo-hydraulic properties; see figure (10.41). As shown in figure (10.43), the system reaches a steady state condition after more than 160 [s] from the start, whereas the scenario with linear heat flux uses 140 [s] to reach steady state. At the upstream station we see the same tendencies, but with less oscillations; see figure (10.42). The dynamic transients are also more violent here, where the fluid velocity fluctuates dramatically (up to 15 [m/s] in less than one second). The pressure fluctuates violently, too, but falls quickly into a plateau after only 100 [s] after start-up. The fluid velocity and enthalpy oscillations are dampened gradually, until a steady state situation is reached after 160 [s] from the start. This indicates that at a lower evaporator pressure, there is a greater compressibility in the evaporator, with a steeper negative gradient in the density, while entering the two-phase region. Operating experience from the SKV3 reveals that there are evaporator instabilities during start-up when firing low, i.e., when the lower burner rows are in action during start-up. This tendency is strengthened when the evaporator pressure is reduced.

Linear heat flux profile with top firing

Operating experience from the SKV3 in particular indicates a greater stability in the evaporator, when the firing is intensified in the top of the boiler. We attempt to model this using a linear heating profile, with the highest heat flux at the top of the furnace, as shown in figure (10.19). The lower operation pressure leads to a

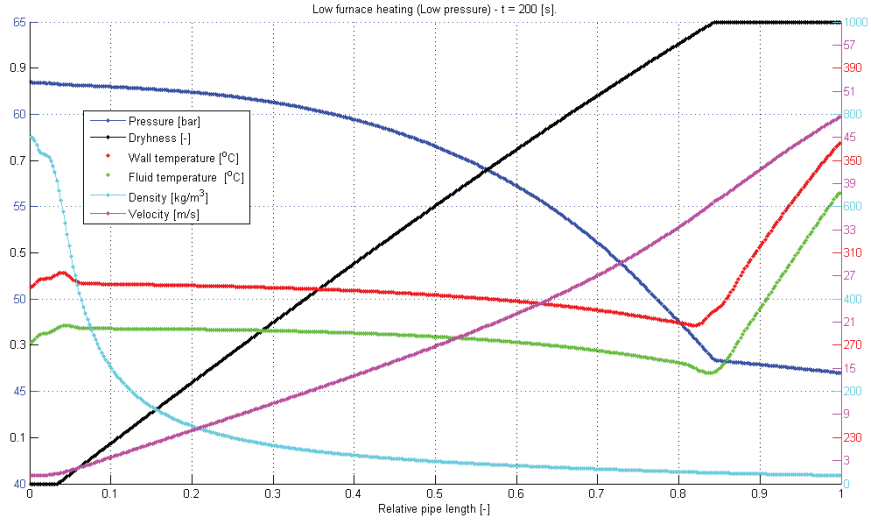

Figure 10.41.: Bottom heating in the SKV3 boiler after 200 [s].

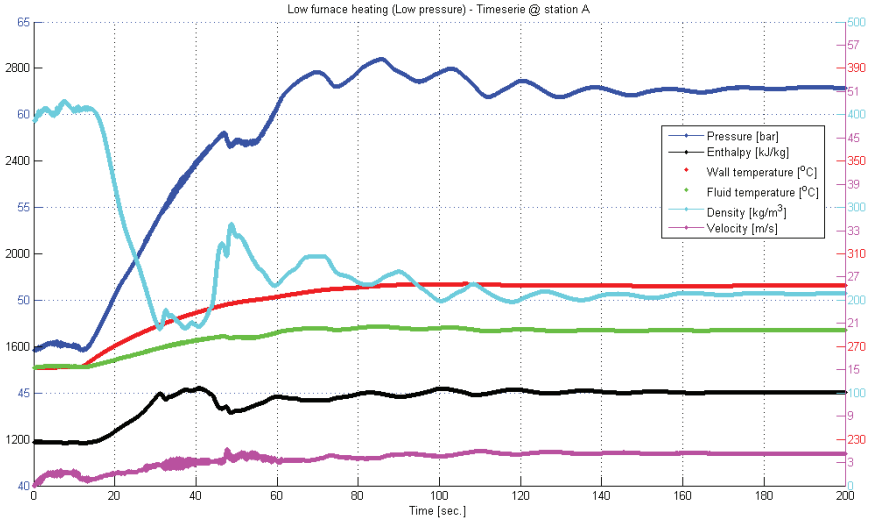

Figure 10.42.: Time series of bottom heating in the SKV3 evaporator model at station A.

high degree of stability after 200 [s].

Figure (10.44) shows how the thermodynamic properties of the fluid change along the pipe, for the top firing scenario. It is worth noting that the enthalpy increases linearly with the length of the tube, with no enthalpy slugs at all, which indicates a high level of stability in the production of the superheated steam.

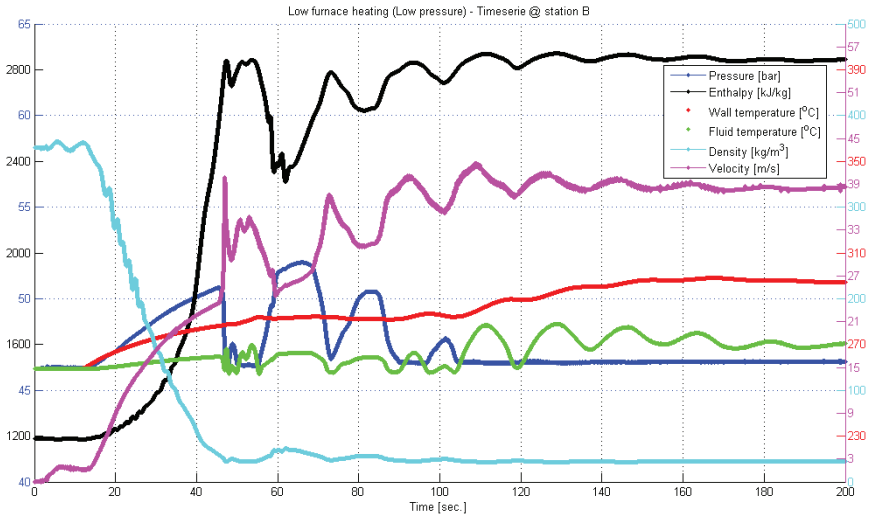

Figure 10.43.: Time series of bottom heating in the SKV3 evaporator model at station B.

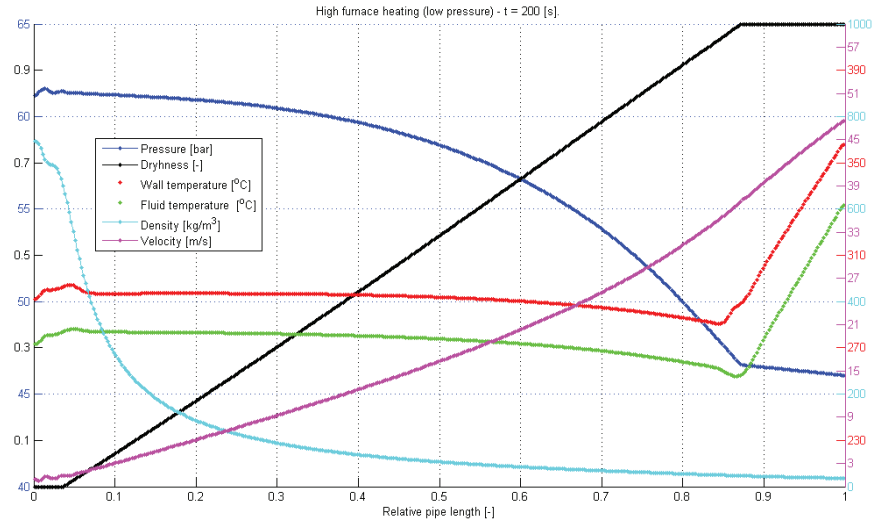

Figure 10.44.: Top heating in the SKV3 boiler after 200 [s].

Similarly, we can see a significant difference in both the pressure and the velocity profile compared to the situation with low combustion in the furnace. The pressure is here approximately 0.5 [bar] lower and the steam outlet velocity is here similar, 47 [m/s] against 48 [m/s] in the first scenario. The time series in stations A and B (figures 10.48 and 10.49) show an unstable start-up process of the evaporator, with stable conditions after 140 [s] from the start. This means that top firing

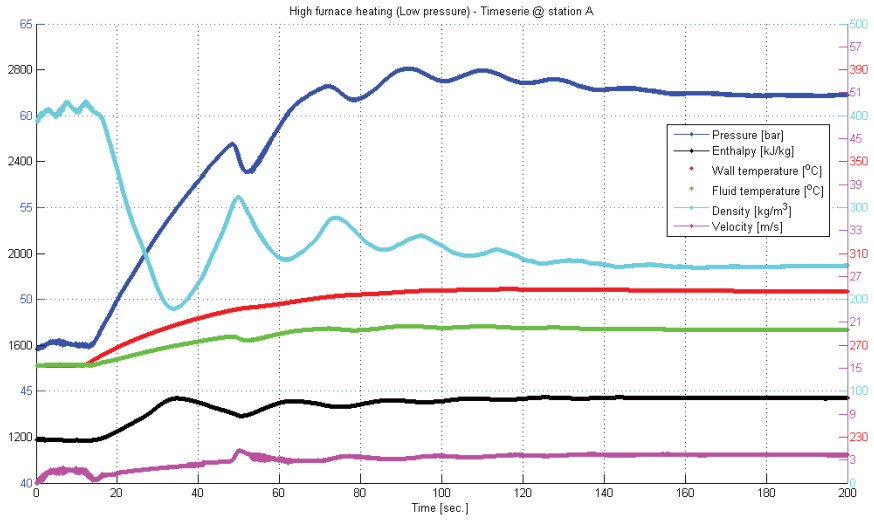

Figure 10.45.: Time series of top heating in the SKV3 evaporator model at station A.

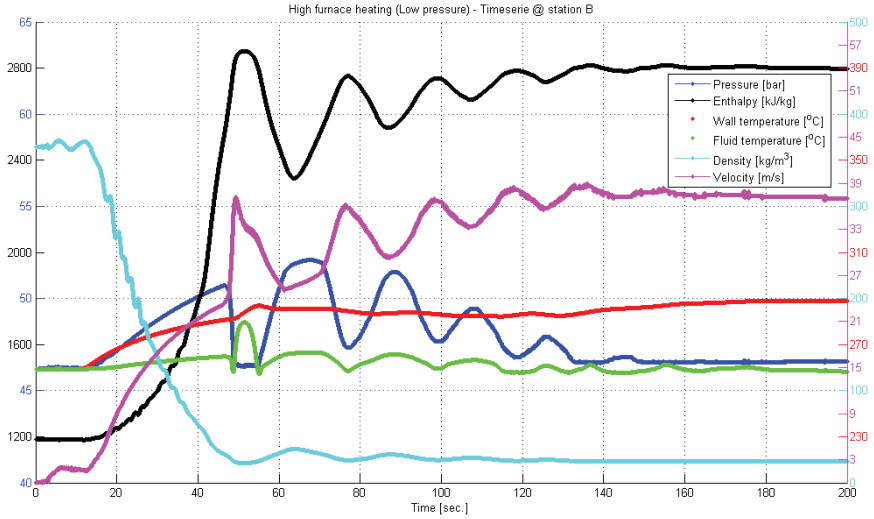

Figure 10.46.: Time series of top heating in the SKV3 evaporator model at station B.

appears more stable compared to bottom heating, which coincides with the results we found for the evaporation process at 90 bar pressure.

Parabolic heat flux profile with parabolic firing

In accordance with the CFD studies carried out in Chapter (4), we can correlate the flux distribution according to a parabolic profile so that the flux intensity

is greatest around the centre point of the burner zone, consisting of the four burner floors for SKV3. It should be noted that the maximum value of the flux intensity, is somewhat above the centre point of the burner system. We see

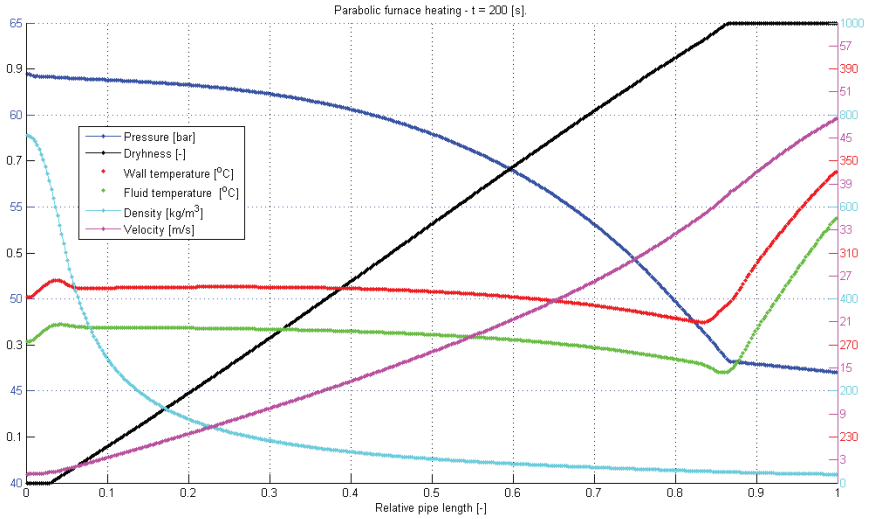

Figure 10.47.: Parabolic heating in SKV3 boiler after 200 [s].

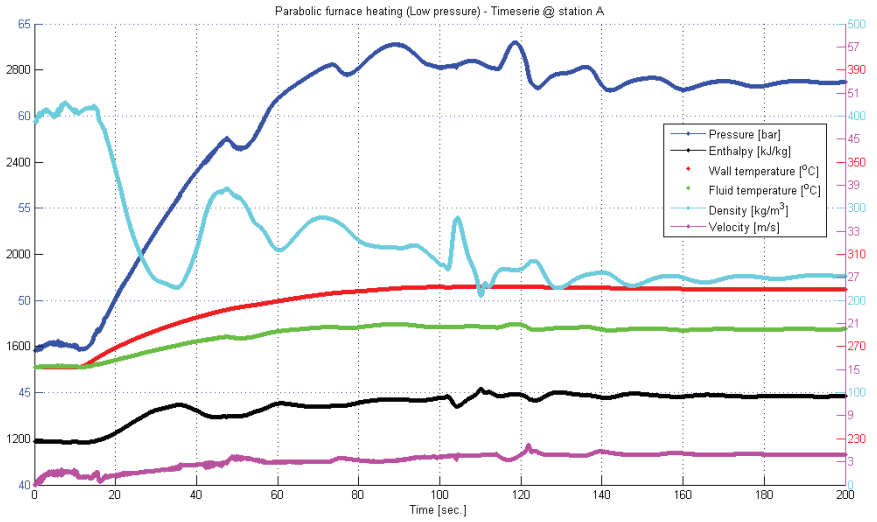

Figure 10.48.: Time series of parabolic heating in SKV3 evaporator model at location A.

a couple of pressure/enthalpy slugs in figure (10.49) and after approximately

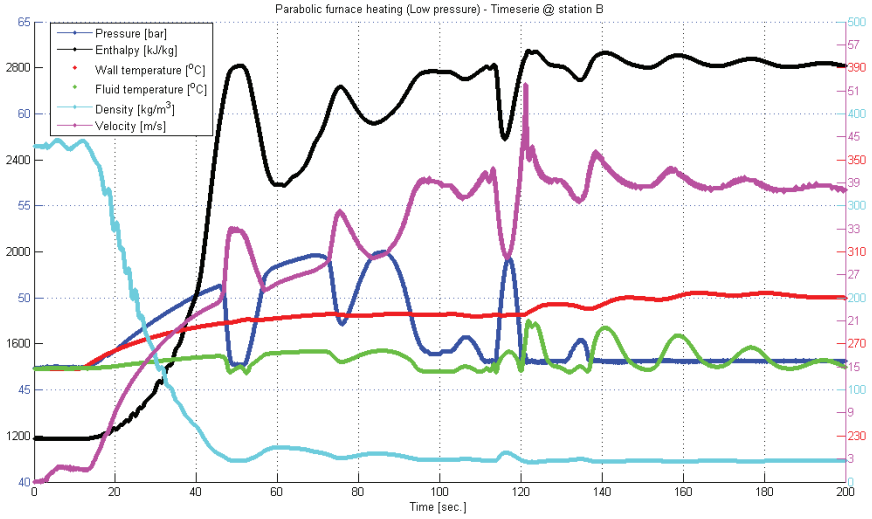

Figure 10.49.: Time series of parabolic heating in SKV3 evaporator model at location B.

117 [s] simulation, the pressure rises rapidly. The fluid is here in a saturated condition in which the saturation temperature increases only slightly as function of the pressure rise. Subsequently, the pressure drops back to the original level, and the temperature follows back down to the original level as well, until the enthalpy suddenly rises rapidly above the level from before. Here we experience a kind of flashing, where the fluid is changing state from saturated steam to superheated steam, with significant temperature increases to follow (+15 [^oC]). In this context, the fluid velocity increases violently, locally up to 20 [m / s] within seconds. These slugs die gradually as time passes, and the flow stabilizes in a static situation after about 200 [s] of simulation.

10.8.2. Comparison of the flux profiles

In general, we can see that reduced sub-cooling provides a more smooth solution over time, without the strong pressure oscillations initiated from the two-phase transition point. This is despite that the density jump is even more pronounced at lower pressure. But the degree of sub-cooling and thus the lower compressibility of water than steam is enough to change this. The start-up process with different heat flux profiles causes different pressure distribution. In figure (10.50) for station A, one can observe a different pressure build-up, in terms of both time and place. The greatest pressure wave build-up in the evaporator occurs in the bottom firing scenario, and this occurs earlier compared to the other runs. The lowest pressure build-up occurs ultimately at top firing and arrives later. At station B, there is no significant difference in the pressure observations. At station B, we

can also see that the enthalpy fluctuations occur earlier and more frequently at the bottom firing than the other scenarios; see (10.51). There are very significant

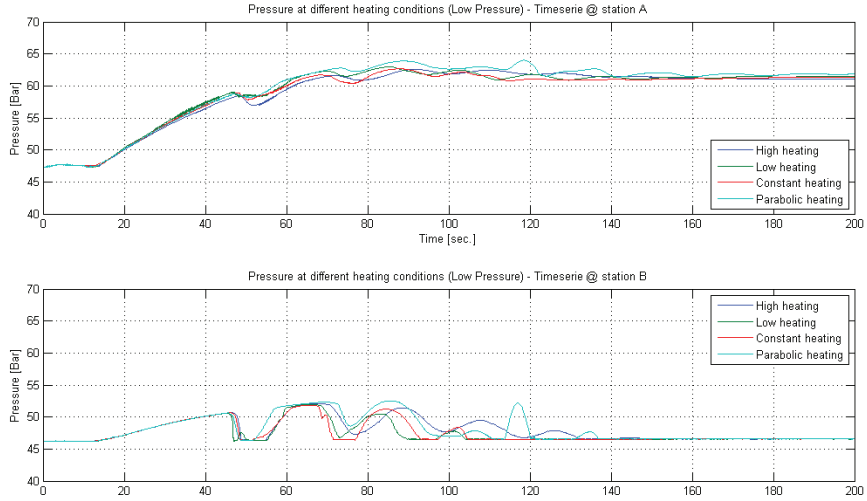

Figure 10.50.: Comparison of the firing profiles on the SKV3 evaporator with respect to fluid pressure.

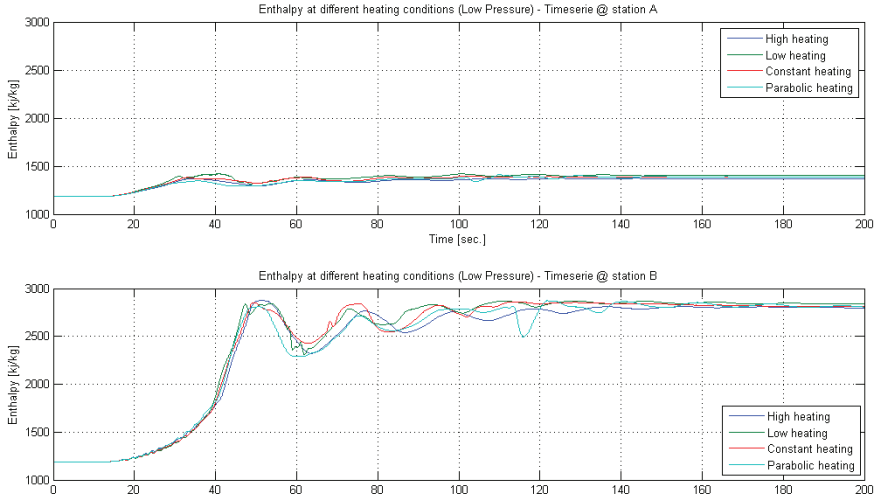

Figure 10.51.: Comparison of the firing profiles on the SKV3 evaporator with respect to fluid enthalpy.

differences in density for the bottom firing at station A. Here there is a lower

density level created, significantly, earlier in the simulation, supplied with a clear pulsation, but without exceeding the density level of the other three flux configurations. The same trend is reflected in the fluid temperature, which is illustrated in figure (10.54). Here we also assume a higher value for the bottom firing, supplied with early pulsations to follow. This phenomenon can affect the delicate metal structures of the tubing, which are susceptible to fatigue fractures. The material temperature is illustrated in figure (10.53), here shown as an average

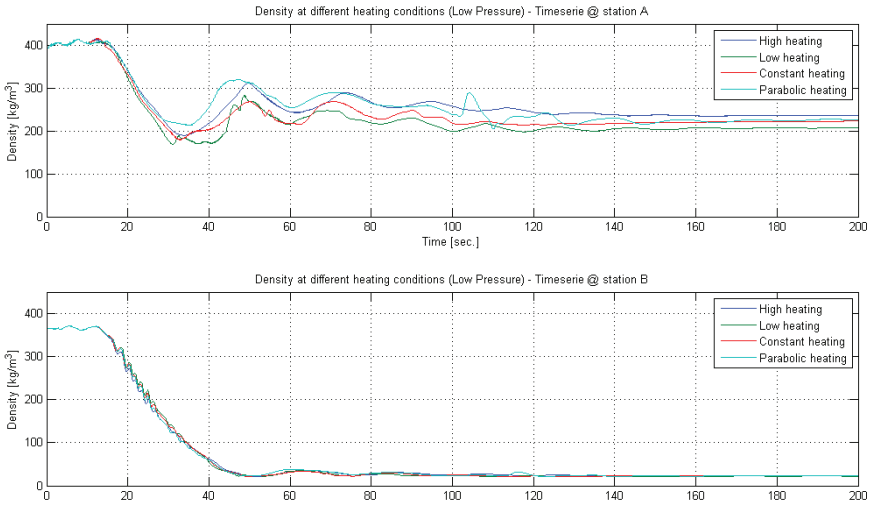

Figure 10.52.: Comparison of the firing profiles on the SKV3 evaporator with respect to fluid density.

temperature of the tube wall. At station A, we can see a significantly higher material temperature (+3 [^{o}C]) for the bottom-firing scenario, compared to the other scenarios. At station B, this is not applicable before we pass the two-phase region and move into the superheat region.

10.8.3. Comparison of high versus low-pressure evaporator

The evaporator at AVV2 is almost identical to that of SKV3. DONG Energy - Thermal Power has carried out experiments with reduced evaporator pressure at AVV2, where outlet pressure was reduced from 90 [bar] to 56 [bar] and minimum flow was 86 [kg/s]. This did not cause any major drama, even though the boiler manufacturer has assigned a minimum pressure of 90 [bar]. When we compare the two simulations carried out at 90 [bar] and 56 [bar], respectively, we notice that the high-pressure case has higher sub-cooling of the fluid (inlet enthalpy common for both cases). The homogeneous model considers the sub-cooled liquid as almost incompressible, which leads to rapid pressure oscillations in

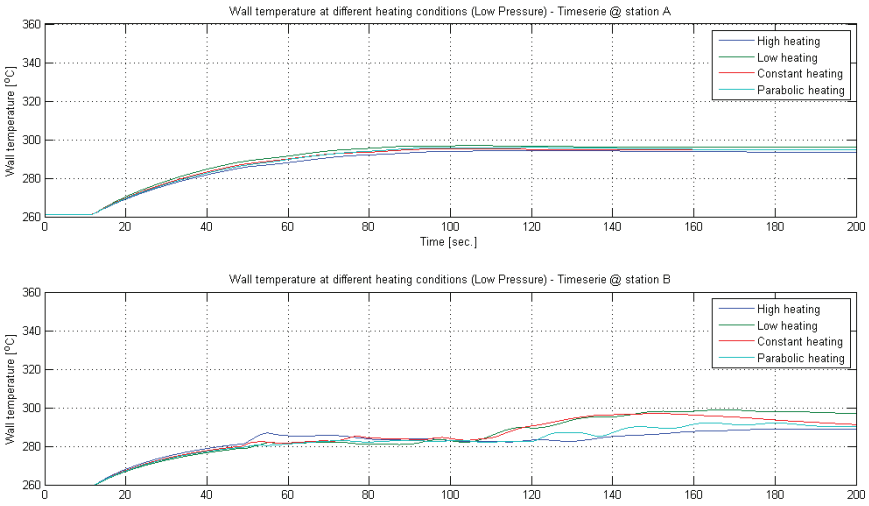

Figure 10.53.: Comparison of the firing profiles on the SKV3 evaporator with respect to wall temperature.

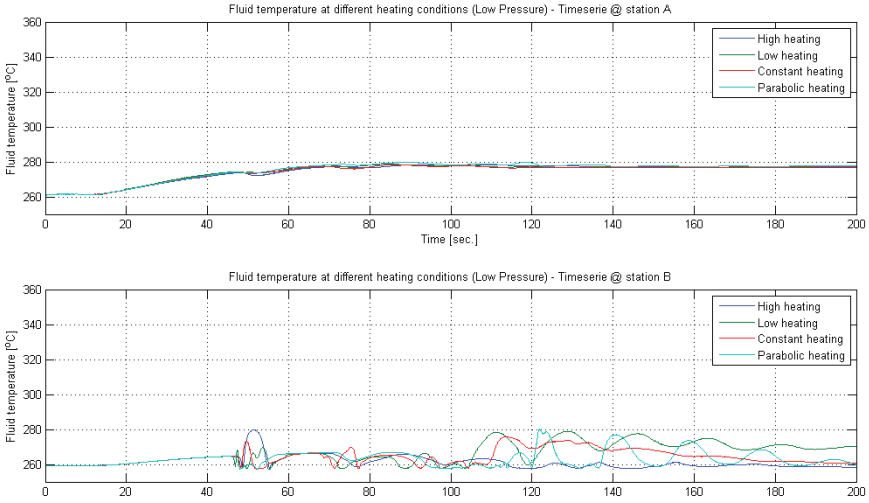

Figure 10.54.: Comparison of the firing profiles on SKV3 evaporator with respect to fluid temperature at stations A and B.

the sub-cooled sector of the evaporator, and when the fluid is transferred to the two-phase region, the density dramatically decreases with pressure oscillations to follow. In the case of low-pressure evaporation, we have a moderate sub-cooling of the fluid, but conversely an even more withdrawn reduction of density, when

passing the two-phase region. This initiates violent pressure oscillations, which die out after approximately 100 [s]; see figure (10.56). It is worth noting that shortly after the start of firing, a peak occurs in the mass flux. The peak is highest for high-pressure evaporation with approximately 4250 [kg/m^2s] after approximately 72 [s], while the low-pressure evaporation peaks earlier after only 25 [s] with a maximum mass flux of 2900 [kg/m^2s]; see figure (10.57). One can observe more violent pressure and enthalpy fluctuations for low-pressure evaporation; see figures (10.55) and (10.56). Pressure oscillations are more common downstream of the evaporator; while at upstream station A, more quiet pressure conditions appear, which apparently do not affect the mal-distribution to the panel walls.

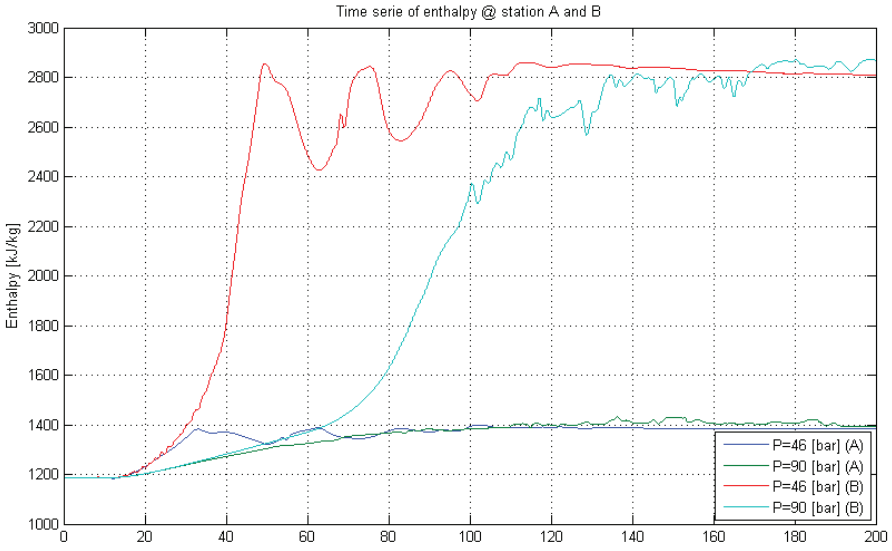

Figure 10.55.: Comparison of enthalpy at different evaporation pressure at station A and B.

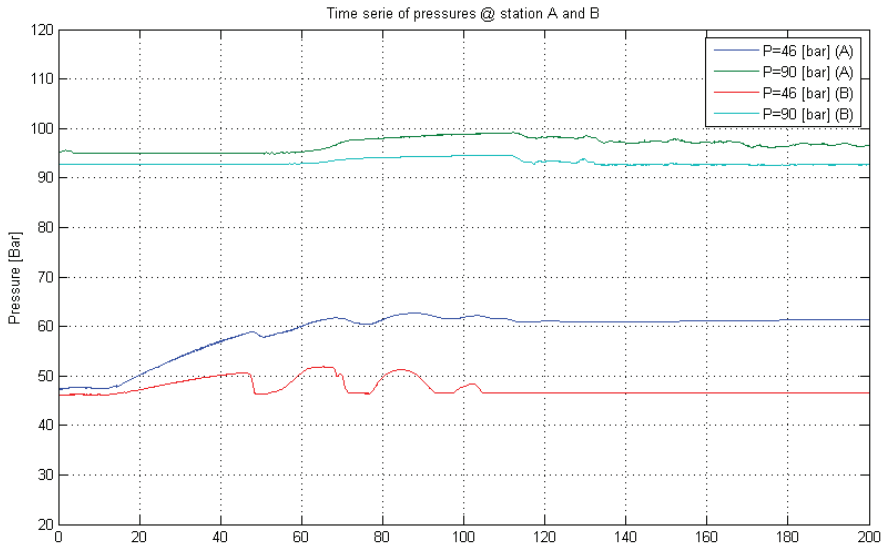

Figure 10.56.: Comparison of pressure level at different evaporation pressure at station A and B.

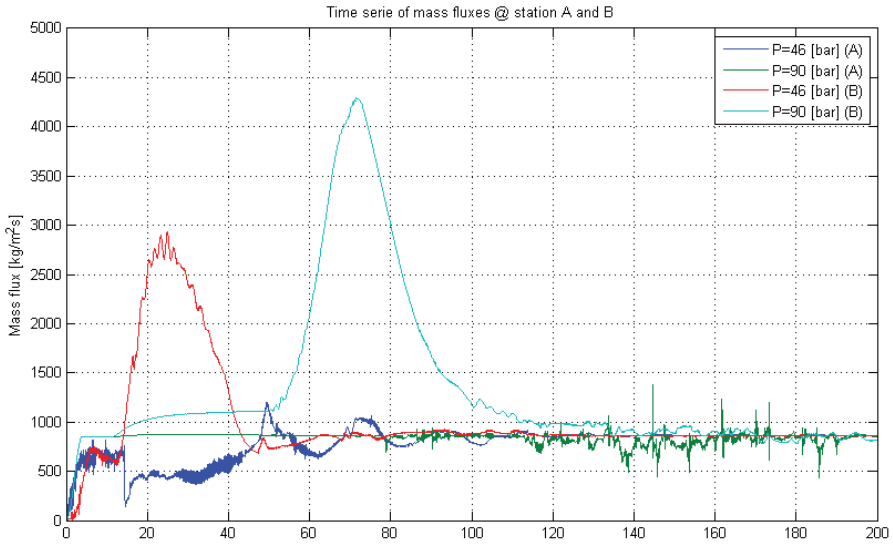

Figure 10.57.: Comparison of mass flux at different evaporation pressure at station A and B.

10.9. Summary

In this chapter, we use the fifth-order WENO solver to simulate the dynamic response of evaporator tubes corresponding to SKV3. Initially we describe the calibration process for the evaporator model, based on measurements from a steady state load case from SKV3 (sample 4) in section (3.4). The application is usable for various purposes, and initially we analyse four different heat flux distributions on the evaporator tube. We can observe several interesting dynamic phenomena that can be related to the classifications of dynamic stability outlined in table (10.1). Focusing on density-wave oscillations, we can see that bottom firing clearly reinforces the occurrence of density-waves, especially in the upstream section of the pipe (station A), where we can notice significant oscillations. There is a coupling between the density and the fluid velocity through the continuity equation. At certain periods, the fluid velocity is very low (read near-zero flow) and this can cause a significant temperature rise in the inner layer of the tube material. This again can increase the thermal load on the pipe wall, but we cannot trace any radial wall temperature increase in the simulation, because of the small time constants and because we are calculating an averaged tube wall temperature. The inner heat transfer will be weakened considerably when the flow rate approaches zero.

Another phenomenon which can be observed, is that the fluid temperature downstream is generally higher for the bottom firing scenario and there are temperature fluctuations of moderate strength. Furthermore, the development of a pressure front occurs quickly in the bottom firing scenario, which gradually weakens, when the flow approaches a static state condition. During the transient period before steady state conditions are achieved, pressure oscillations occur, which also make up a category of the dynamic phenomena listed in table (10.1). The remarkable thing is that the top firing scenario leads to surprising violent thermal fluctuations in fluid temperature, something that cannot be measured under operation of a plant. Conversely, we see that the top firing gives a more stable evaporator, in the sense that the evaporator has a lower degree of fluctuations in pressure and fluid velocity in the sub-cooled region, leading to a more safe operation of the evaporator during start-up. The applied load gradients are large, compared to the maximum allowable gradients on SKV3; see figure (3.2). Further more, the restrictions compared to reduced lifetime of thick-walled components, like junction boxes or valves, are not taken into account in this analysis.

In addition, we take a look at the SKV3 evaporator hypothetically equipped with internal rifles (IRBT) and analyse how it would behave at very low flux. The conclusion is that very low flow rates lead to poor convective heat transfer in the

sub-cooled region, while the two-phase region gives a more stable cooling of the tube wall.

An adjacent scenario occurs with IRBT at base load (100% load), where the mass flux is significantly higher (1000 [kg/m^2s]) and here we see how an initial hydrostatic pressure of dense fluid is converted to a stable pressure loss of moving super heated fluid, after which the pressure loss stabilizes at 1.65 [bar]; see figure (10.36). The pressure is above the critical pressure, leading to a continuous description of the density throughout the entire simulation process which also leads to a smooth pressure build-up through the evaporator. It should be emphasized that the SKV3 boiler with IRBT is a hypothetical example; usually the number of parallel tubes in the evaporator is adjusted to match the recommended mass flux at 100% load and the pressure drop reflects the price of how far down one wants to place Benson minimum load.

Lastly we touch upon a situation which is related to the major challenges that the introduction of renewable energy imposes in the form of sun and wind. With the close bond between district heating and electricity production, characterized by a so-called back-pressure plant, it is tempting to convert a traditional power plant with the ability to bypass the VHP and HP turbines and thus reduce both the electricity production and the evaporator pressure. We see from the calculations that we obviously have a moderate pressure drop in the evaporator, starting from a stable operation wherein the geodetic pressure drop is dominant, until we reach a steady state condition with a lower friction dominated pressure loss. It is interesting to note the presence of temperature slugs in the homogeneous evaporator model and that the model is able to establish the sometimes sharp gradients in the solution. This demonstrates that there really exist violent slugs at low operating pressures, but the oscillations die out after a relatively short time (160 [s]); see, e.g., figure (10.44).

We have now developed a tool that can be used in further studies of the evaporator stability, and we must of course ensure compliance with the evaporator design rules, especially rules related to the flow distribution to panel walls via junction boxes. Here significant sub-cooling is usually used in order to ensure a satisfactory distribution of a single-phase fluid to the evaporator wall.

11. Discussion

The purpose of this thesis is to clarify the challenges that the thermal power plant industry in Denmark are facing, with an energy market dominated by renewable energy. These issues are related to the load dynamics of the steam generator in a power plant boiler. This knowledge is rooted in mathematical methods for identification of operational flexibility in power plant evaporators. In this thesis numerical models are developed to study static as well as dynamic stability, in relation to load gradients in steam power plant evaporators, but also longer-term issues, such as material creep and fatigue of tubes, fins and thick-walled components are described. The study gives an increased understanding of the main phenomena that lead to static stability, i.e., Ledinegg instability and flow mal-distribution initiated by non-uniform heat uptake in panel walls. A robust numerical tool based on the WENO approach is developed in this project. The tool is designed for dynamic problems with piecewise smooth solutions containing discontinuities. The Central WENO scheme has been quite successful in the investigation of start-up phenomena and load gradients containing complicated non-smooth solution structures in power plant boilers. The thesis gives several examples of sensitivity analyses on different heat flux distributions, both in normal part load (25-35 % load), but also in extreme low-pressure operation (12 % load). This discussion is primarily based on the five main Chapters, namely, 5, 7, 8, 9 and 10, with brief comments on each section and a more thorough assessment linked to the thesis.

11.1. Steady state flow stability

In the measurement campaigns carried out for Skærbækværket Unit 3 (SKV3), we can observe large temperature differences in the pipe wall on sample 3 in section 3.4, which reflects an operating situation where the plant is in a transition from recirculation mode to once-through mode. Here temperature differences are recorded of up to approximately $\pm\ 35^{o}$ in adjacent tubes in the panel walls, which indicate the presence of superheated steam in some of the tubes and sub-cooled liquid in others. This is a dynamic phenomenon and cannot be characterized as a Ledinegg phenomenon, but could be a flow distribution problem which is initiated by a changing operation condition, where the recirculation operation ceases with increased load. In our calculation of mal-distribution of two parallel tubes we see, in certain critical situations, highly superheated steam in one piece of the heat tube, while there is two-phase flow with low steam quality in the second tube. This may have important implications for the lifetime of the heat tubes, as the

material temperature mainly follows the fluid temperature. Fortunately, the panel walls are constructed in such a way, that there may be heat transfer between the pipe sections (fins), but this heat transfer is primarily based on conduction, with high temperature gradients to follow. Conduction between the pipe sections is not included in the modelling work, but time constants and thermal diffusivity have been analysed in section (4.2). This indicates that the conduction is restricted by a relatively low heat transfer coefficient for alloys at high temperatures, which may result in a high temperature gradient in the tube material and in that way cause high temperature in the material. At low load operation of Benson boilers, where we still have full super-heating of the outlet steam, the risk of burnout caused by mal-distribution is minimal. Here we shall be more concerned about the poor cooling of the panel wall, caused by stratified flow in the boiler tubes, where the vapour phase causes a poor cooling of the pipe wall. It is highly essential to ensure a certain degree of sub-cooling at the inlet to the junction boxes of the evaporator, so that a single-phase fluid is distributed to the respective evaporator tubes. This can be characterized as external conditions relative to both the Ledinegg and mal-distribution analyses in contrast to the findings in the analysis of mal-distribution where we found that less sub-cooling gives less mal-distribution; these trends weaken for increased operating pressure.

For water/steam flow in a tube, we can see that the time constant of the internal wall subjected to an interior temperature fluctuation is many decades smaller than that of the exterior pipe wall. This inner tube wall material can react more quickly to varying temperature conditions; therefore, phenomena such as fatigue may be a potential risk, as the material element can initiate small cracks that can propagate to the rest of the material. This phenomenon is strongly dependent on the type of material and may be more pronounced under certain circumstances, for example, if substantial fouling occurs on the inner side of the heat tube (oxide layers or Fe^{+} deposits), so that the temperature rises due to the poor thermal conductivity of the fouling layer. Hence a fluctuating two-phase flow (i.e., slugs of superheated steam or sub-cooled water) may initiate temperature fluctuations at a higher offset in the surrounding pipe material, and thereby initiate small micro fractures in the fins connecting the heat tubes in a panel wall. Especially tensile stresses caused by the abrupt cooling are critical to the steel. This phenomenon is much more common in super-heater tubes, where the temperature level is significantly higher. This also implies the selection of a dedicated type of material that can sustain the high pressure and temperature levels, up to 325 [bar] and 600 [^{o}C], respectively.

11.2. Equation of state

The equation of state (EOS) for water / steam is an important part of a thermo-hydraulic calculation process and is probably one of the biggest time-consumers in CFD simulations. Numerous articles have been published on the subject, and many EOS are simple with limited accuracy, e.g., the Van der Waals state equation; see equation (6.11). The advantage of using an interpolation scheme for calculating the thermodynamic properties, rather than a direct computation of, e.g., IAPWS-97, is the possibility to provide very short calculation times without significant loss of accuracy. It is highly desirable, in connection with the implementation of EOS, to maintain continuity of the thermodynamic properties throughout the operating range, which is one of the basic features we look into. Hence it is possible to avoid discontinuities in the water and steam properties in-between five different sub-areas in, e.g., IAPWS-97. It is obvious that the slope of the density as a function of pressure and enthalpy, or vice versa, is discontinuous at the saturation line, and this introduces pressure waves in the solution of the momentum equations. Therefore, it is important to describe these phase transitions as continuous functions, to verify the strength of the pressure oscillations that the discontinuity in density gradient causes. We have chosen a moderate smoothing, based on a second-order theory outlined in Appendix (G), to eliminate the problem with discontinuity of the derivative in density around the saturation lines. For testing different interpolation schemes, we do not use smoothing at all, which results in significant deviations between actual and interpolated values in the vicinity of the saturation lines. If we need to focus on reduction of simulation time, the choice of interpolation model falls on a simple bilinear interpolation scheme with a minimum of 160,000 nodes, which covers the domain; $h \in [0,3900]$ [kJ/kg] and $p \in [0.1, 800]$ [bar]. This table occupies only a small amount of space in the memory of a computer. The computational cost is decreased by a maximum factor of 33, but approximately a factor of 11 in average. The suggested improvement of the interpolation table using linear triangular elements instead of bilinear elements along the saturation curves is not found to give the desired increase in accuracy, in relation to the significant increase in computational costs. The benefits of using the iso-parametric triangular elements are too insignificant to justify the more intensive implementation of such scheme, but the results are a bit more accurate, and we can reduce memory demands, by reducing the number of elements. However, in the two-phase region, we need a look up table which can be time-consuming for large grid arrangements. Hence the iso-parametric triangular elements cannot be recommended for the two-phase domain, especially since the argument is to reduce computational costs and since a second-order iso-parametric element may cause over-shoots and under-shoots in the interpolated solution. If the iso-parametric elements are used near the density

trough, a more dedicated shape function should be implemented. In such case, we can reduce the number of elements drastically and the computational costs, too. However, the barycentric coordinates will be costly to compute. It will be a challenge to find motivation to use the iso-parametric elements. Another factor that one should be aware of, is to restrict the definition area of the interpolation table, as there are very significant time-savings obtainable here, both in terms of grid generation, but also for table lookup.

11.3. Dynamic modelling of thermo-hydraulic systems

Interaction between fluid mechanical conditions in the boiler tube and the stress conditions that occur in the corresponding wall, is critical for the control of a power plant boiler. There are many factors that can affect the stress conditions in the tube wall, and therefore one must take into account early in the design phase of mathematical modelling, what kind of parameters the model should be able to respond to, like heat flux profiles on the outer side of the tube as well as, e.g., pressure and temperature slugs inside or at the upstream or downstream boundaries. Of course there are a number of limitations that for practical reasons we have to deal with, for example, the level of detail in the fluid mechanical flow equations, which are only dissolved in one dimension. The use of a full two-layer (or four-field) two-phase flow model, causes a more than doubling of computation time, which already is very long, because the pressure is calculated by an iterative process, as a function of the enthalpy and density, for each time step and computational cell. This iterative process is significantly improved, by the introduction of bilinear interpolation of the EOS. A one-dimensional tube wall model is intended to form a link in the axial direction of the tube, so that the temperature variations are able to diffuse, due to the thermal diffusivity of the material in the axial direction. This achieves a more accurate description of the material temperature, which indirectly determines how much energy is transformed from the boiler room to the flowing medium in the pipe. The radial temperature distribution for the 1D model is based on a logarithmic profile for isotropic materials.

Based on the two-layer thermo-hydraulic model, a homogeneous evaporator model is derived, which presumes both thermodynamic and hydraulic equilibrium, implying that the fluid is described by a common enthalpy and transport speed. In this context, the one-dimensional pipe wall model is used to ensure the transport of energy from the furnace to the water / steam circuit. The homogeneous thermo-hydraulic model provides us with some numerical challenges, in the sense that there occurs a singularity in the first derivative of the fluid density, around the saturation lines in the EOS. This means that there are strong pressure waves induced to compensate for sudden sharp negative gradients. Two activities

have been applied to control this pressure oscillation. The first approach concerns a local smoothing of the density around saturation curves, which is implemented in the EOS. The next approach is to impose artificial diffusion, whose strength is estimated from a Boussinesq equation, outlined in section (8.6), modelled as heat transfer in a rotating fluid in a pipe. In that way the thermo hydraulic flow can be controlled, and we are able to calibrate the model in relation to measured data from SKV3. Unfortunately, we have only limited measurements at inlet and outlet of the evaporator, which only allow us to calibrate the wall friction coefficients, but do not allow us to calibrate the artificial diffusion, either in strength or extent.

Finally, we have developed a theoretical platform for analysing the transport equations of a full four-field thermo-hydraulic model, in order to estimate the flow regimes and thus allocate the correct constitutive pressure and heat transition models, for describing the dissipative parts of the governing transport equations. The challenge here will be to control the interfacial source / sink terms, which link the different layers together. The model considers the continuous and dispersed liquid and gas phases (water/steam) as four fields, meaning two continuous gas and liquid phases, and a continuous liquid phase containing gas bubbles, and finally a continuous gas layer containing fluid droplets. It will be an obvious area for research to obtain a complete understanding of the mechanisms which exist in this four-field model and charting a flow regime map, which can be compared with experiments from the literature. This requires a numerical solution of 12 coupled partial differential equations, which can be solved, for example, by means of a WENO scheme. The homogeneous model take typically five hours for a simulation of a single period of 200 [s]. Here an iteration tolerance of $1.0 \cdot 10^{-12}$ is used.

11.4. Solving hyperbolic transport equations

A thorough analysis and classification of the mathematical problem we are looking into, is decisive for the mathematical / numerical method that we apply for solving the governing equations. In general, the two-phase flow transport equations can be classified as time hyperbolic problems, by an eigenvalue analysis. The introduction to this work begins with a general presentation of second-order methods for solving hyperbolic PDEs and the TVD concept is presented. From here we take a look at the latest higher-order methods for solving hyperbolic PDEs and we draw up a comprehensive toolbox of methods for solving a wide range of PDEs, where we include both a diffusion term and a source/sink term, basically for meeting the requirements from the governing equations of two-phase flow. In that extent the governing equations are classified as a temporal and local time parabolic problem, though the diffusion term only works in a very limited area of

our total solution area, so the principles of hyperbolic models remain in focus globally. The Central WENO schemes are designed for problems with piecewise smooth solutions containing discontinuities and have been quite successful in solving some common test cases, as the Burgers equation containing both shocks and complicated smooth solution structures, and solving the Sod test of Euler's equations.

11.5. Dynamic flow stability

In this thesis we would like to demonstrate the ability to simulate the dynamic conditions in a homogeneous two-phase flow in a power plant evaporator and thus complement the recent years, research efforts at DONG Energy - Thermal Power, in areas such as material creep and fatigue (FEM calculations), furnace load (CFD calculations) and more intelligent furnace control in the feed water, fuel and combustion control systems, restricted by an intelligent distributed control system (DCS). On that basis we can contribute with new knowledge about the flow stability and dynamic effects in power plants, caused by both internal and external physical conditions, resulting in improved power plant flexibility. We have implemented and tested the fifth-order WENO solver and used it to simulate the dynamic response of evaporator tubes corresponding to SKV3, on the basis of a calibrated model, based on measurements from SKV3 (sample 4) in section 3.4.

The developed dynamic model is applicable for very different thermo-hydraulic problems, and we analyse initially four different heat flux distributions on the evaporator tube during the start-up phase, where we observe different dynamic pressure responses. The results that are presented in section (10.4) are not as clear as expected, but we can observe that start-up of the boiler, from zero flow to full combustion in part load [100 kW/m^2], can lead to slightly different dynamic response from the boiler, when changing firing profile at constant heat uptake. We see a higher degree of density fluctuations upstream the boiler, when low firing is applied, while top firing causes more heat-related fluctuations downstream the evaporator (temperature and enthalpy). The applied load gradients are larger than those we see in the real world; see figure (3.2). Also the restrictions with respect to reduced lifetime of thick-walled components, like junction boxes or valves, are not taken into account in this analysis.

We attempt to simulate a high pressure pre-heater failure on SKV3. This causes an immediate decreasing feed water temperature of approximately 50 [^oC] toward the ECO and evaporator. Not surprisingly, the simulations show a response in the upstream section of the evaporator, which is similar to the upstream boundary

condition; whereas in the downstream section of the tube, we experience a short term increase in the steam temperature (seen up to maximum 22 ^oC, in figure (10.32)), despite, that we are feeding the system with less energy. This increase in the evaporator outlet temperature occurs, because the evaporator tubes are now filled with water instead of steam, i.e., the tubes must be 'refilled' before the downstream steam is pushed out, now at a higher temperature due to the residence time of the downstream fluid becoming longer.

In addition, we look at the SKV3 evaporator hypothetically equipped with vertical internal rifles (IRBT) and analyse how they behave at very low flux (micro load) conditions. We have found that very low mass flow rates lead to bad convective heat transfer in the transition zone between the sub-cooled liquid and the two-phase region, due to near-zero wall flow; while in the two-phase region, we notice a more stable cooling of the tube wall. An additional computation is carried out at base load (100% load) for the IRBT, with supercritical operation pressure. Here the mass flux is adjusted to the design requirement of approximately 1000-1200 [kg/m^2s] of fluid through the tube. The simulation results show how an initial hydrostatic pressure of dense fluid is converted to a stable pressure loss of moving super-heated fluid, after which the pressure stabilizes at a plateau of 1.65 [bar]; see figure (10.36). We do not see any apparent stability problems due to density gradients, since we are operating with super-critical steam data. Normally this operating situation is the design requirements for maximum steam production at base load of a Benson boiler. To ensure high operational flexibility of the Benson boiler, the minimum load should be taken into consideration. At minimum load a mass flux flow rate of approximately 200 [kg/m^2s] is normally recommended for IRBT. It is thus this minimum flow that limits how far down in part load the plant must operate, before it turns into circulation mode. The price of a high flexibility is hence the pressure drop at base load operation.

Last, we touch upon a situation related to the major challenges that the traditional thermal power plants are facing, in connection with the introduction of renewable energy (sun and wind). With the close bond between district heating and electricity production, which is characterized by a so-called back-pressure plant, it is tempting to reduce the live steam pressure and bypass the high-pressure turbines and thus reduce both electricity production and the evaporator pressure. We see from the calculations that we obviously have a significant pressure drop in the evaporator. The low-pressure evaporator simulation, with an exit pressure of 46 [bar] compared to a normal pressure of 90 [bar], shows a stable response, which after 180 [s] is in a steady state condition; see figures (10.47) to (10.49). The pressure loss is approximately 18 [bar]. It is interesting to see that the homogeneous model takes into account the load gradients of pressure and enthalpy, which

can initiate the mentioned thermal slugs. It is also interesting to note the presence of thermo slugs in the homogeneous evaporator model. The model is able to resolve the sometimes steep gradients in the tubes, which demonstrates that violent slugs really exist at low operating pressures - even in a homogeneous model.

We have in this project developed a numerical tool that can be used in further studies of evaporator stability. We must of course ensure compliance with the many design rules used in the design of evaporators, especially rules related to flow distribution in panel walls via junction boxes. Here usually significant sub-cooling (20 ^oC) is required, in order to ensure a satisfactory distribution of a single-phase fluid to the evaporator wall. For low-pressure operation we can clearly conclude that the bottom firing scenario gives thermal-hydraulic conditions expressing a high degree of instability, compared to the three other scenarios. This despite we only have redistributed approximately 10% of the heat. This start-up phenomenon can in popular terms be compared to a geyser, where we have a compressible fluid in the bottom of the boiler tube and a nearly incompressible (cold) fluid to the top. This is of great concern for boiler manufacturers and requires focus on the size of the water/steam separator.

12. Conclusion

This conclusion summarizes the main findings from Chapter 5, 7, 8, 9 and 10. These chapters represent the five main subjects of the investigation, together with the last chapter of analysis and discussion contained in this thesis.

12.1. Steady state flow stability

One of the main conclusions of this mal-distribution analysis study outlined in Chapter (5), is that the flow distribution problem is primarily affected by the operating pressure in the heat tube. The lower the operating pressure, the greater the difference between the mass flow in two parallel heat tubes, for a certain deviation in heat uptake. In addition, the inlet mass flux to the heat tube system is also a parameter, which affects the bias of the mal-distribution. The larger the inlet flow to the two pipes, the greater is the mal-distribution in the heat tubes. This can be correlated to the pressure drop, which is the driving factor in the distribution problem, since there must always be the same total pressure drop over the two heat tube elements. Friction pressure loss is an essential factor in this process. But the geodetic height also plays a role in that context, as it will reduce the influence of the friction pressure drop, especially in situations where the geodetic height mainly consists of liquid and not vapour. An early superheat of the fluid in the heat tube, significantly reduces the influence of the geodetic pressure difference, due to the higher specific volume (lower density). This again leads to a higher mass flow through the actual heat tube element. A higher degree of sub cooling of the inlet flow, causes a larger enthalpy difference at the outlet of the heat tubes, which in turn increases the load on the boiler tubes. Accordingly, we see that the pressure loss increases over the two parallel tubes for increasing sub-cooling at pressure levels near the critical pressure. At pressure levels below 150 [bar] the opposite phenomenon occurs. Increasing sub-cooling of the inlet fluid results in a larger flow mal-distribution, and the heat tube that receives highest heat input, has the lowest mass flow, meaning we have a pipe system with negative flow characteristics. We can reversely conclude that the pipe wall is more prone to a high critical temperature, when using higher sub-cooling at evaporator inlet. This trend decreases with increasing operating pressure. The degree of sub-cooling is also a decisive factor in the formation of density jumps in the Ledinegg instability analysis. It is a potentiating factor for the formation of Ledinegg instability, because no sub-cool region gives a strictly increasing pressure loss curve without any extrema. The simulations of SKV3, which have a minimum pressure of 90 [bar], show no risk of Ledinegg

instability. We have also seen that vertically arranged evaporator tubes result in a strong suppression of the Ledinegg instability phenomenon. In fact only small low-pressure evaporators (pre-heaters, low-pressure marine boilers, etc.) may have a risk of instability caused by the Ledinegg phenomenon (boiler operating less than 22.25 [bar]).

12.2. Equation of state

A bilinear interpolation scheme has been developed in Chapter (7), characterized by a very fast look up record and fairly good precision, except in the region near the saturation line, in which there is discontinuity in the first derivative of the density with respect to the enthalpy. This uncertainty has no practical negative impact, since this discontinuity is blurred by the use of a smoothing function. In that way the interpolation tool provides a continuous and differentiable solution over the entire solution domain. The bilinear element is compared to both a linear triangular element, and an iso-parametric element. Both are not of advantage in this context, since the iso-parametric element has a long computation time, due to its higher order, and the triangle element in combination with the bilinear scheme leads to a more complicated look up function, and is therefore more expensive to calculate.

12.3. Dynamic modelling of thermo-hydraulic systems

In this thesis we developed the theoretical basis for a two-layer thermo-hydraulic flow model and its constitutive relations, referring to both traditional plain heated pipes as well as IRBT, which depend on flow regime and geometry (horizontally versus vertically orientated tubes). The model is described in Chapter (8) and includes a relaxation approach to support water/vapor surface discontinuity, across which the equilibrating quantity of velocity and pressure jumps. The model is assumed to be fully hyperbolic, with real eigenvalues, associated to the Jacobian obtained by formulating the entire system of equations in a non-conservative form. There are two types of models for the description of the temperature distribution in the tube material, which is responsible for the transmission of heat from the furnace to the water / steam circuit of a power plant. These tube wall models are related to the lifetime concept as described in section (4.3).

12.4. Solving hyperbolic transport equations

We have developed a robust numerical PDE solver that is highly flexible in terms of configuration. The theory is outlined in Chapter (9). The application can handle source / sink terms, diffusion terms and initial fields as line data. Two types of boundary conditions can be specified, one Neumann and Dirichlet condition on both upstream and downstream boundaries. The convective part of the

solver (fluxes) is based on a fifth-order hyperbolic WENO solver, supplied with a diffusion model of fourth-order accuracy. The diffusion model can be allocated to specific sites in the solution domain, in order to smoothen, e.g., pressure waves induced by a jump in density. Additionally it is possible to specify source/sink terms to the transport model. As time integrator, we can choose from a wide range of options, but depending on the complexity of the task and requirements of stability, we have chosen a third-order TVD time integrator, although a fourth-order SSP-RK is available. A third-order time integrator is significantly faster than the improved fourth-order five-stage SSP-RK algorithm. The conclusion is that both the scalar and the vector-based version of the WENO solver are non-oscillatory in the sense of satisfying the total-variation diminishing property in the one-dimensional space.

The higher-order WENO scheme is used to verify a test sample of propagation of void waves, in the context of a two-layer fluid model. A void wave separates two-phases that are in mechanical equilibrium. The simulation results confirm that the mechanical equilibrium between the phases is preserved, with pressure and velocity remaining uniform (Riemann problem). It turns out that the higher-order WENO scheme is only slightly dissipative in that, after a few thousand time steps, the solution begins to form small disturbances on both sides of the contact discontinuity, which can be attenuated away completely by introducing a moderate diffusion. The test example has been solved in the literature without diffusion, but with the use of a second-order Roe scheme that is more dissipative, devised by Phil Roe. The solution to this problem is to implement an iterative solution, where we use the EOS to estimate both pressure and velocity relaxations terms.

12.5. Dynamic flow stability

In Chapter (10) is modelled an evaporator string of SKV3, as a homogeneous 1D thermo-hydraulic model, solved by use of a WENO solver. We use bilinear interpolated values for the water / steam data, based on IAPWS-97. Thus, we can demonstrate that this application is able to handle complicated flow phenomena, which during a start-up, will initiate pressure waves that might affect the mal-distribution in the panel walls, and consequently affect the hydrodynamic stability of an evaporator. We have already seen through measurements, how the temperature distribution in panel walls can have high disparity, initiated by dynamic flow conditions, when the plant goes from circulation operation to Benson operation.

In this thesis we demonstrate the ability to simulate the dynamic conditions

in a power plant evaporator, based on a homogeneous two-phase flow model. This work thus complements the recent years, research efforts at DONG Energy - Thermal Power A/S, in areas such as material creep and fatigue (FEM calculations), furnace load (CFD calculations) and more intelligent furnace control of feed water, fuel and combustion control systems, restricted by an intelligent distributed control system (DCS). Thus this thesis contributes with new knowledge on stability and dynamic effects in power plant evaporators, caused by both internal and external physical conditions, such as sliding operation pressure, preheater trip, extreme low operational pressure and IRBT. We have implemented and tested the fifth-order WENO solver and used it to simulate the dynamic response of evaporator tubes in SKV3, on the basis of a calibrated model, based on measurements from SKV3 (sample 4 in section 3.4). The results can be summarized as:

- Low firing, i.e., firing with the lowest burner rows, in the furnace leads to more frequent density-waves upstream the evaporator at pressure below 95 [bar]. This can increase the flow mal-distribution.
- High firing leads to more frequent thermal oscillations downstream the boiler pipe at pressures below 95 [bar].
- Low firing at low operational pressure (46 [bar]) leads to strong and unambiguous flow stability, both density and pressure waves as well as thermal oscillations.
- We can with the homogeneous model identify simple flashing phenomena, enthalpy and pressure slugs, as a result of the non-oscillatory and total-variation diminishing approach.
- A preheater failure affects the evaporator downstream with a short temperature peak to follow. It causes thermal stresses in the evaporator tube. Furthermore, we see large enthalpy transients at the separator. They can however be reduced by a fast feed water pump control.
- IRBT may in principle be designed for operation at the Benson minimum, so that the desired operation flexibility is achieved. The consequence is unfortunately a high pressure drop at base load.

The homogeneous two-phase flow model is widely applicable, and it is easy to implement other liquid media than water, simply by updating the EOS look up table. This means that we can easily calculate an evaporator in a heat pump system. We have developed a homogeneous thermo-hydraulic model and solved it by use of a WENO solver, where we use interpolated values for the water / steam data based on IAPWS-97. Thus, we can demonstrate that this application

is able to handle complicated flow phenomena, which during an upstart will initiate pressure waves that might affect the mal-distribution in the panel walls, and consequently affect the stability of an evaporator. We have already through measurements seen examples of how the temperature distribution in panel walls can show great disparity, which is initiated by dynamic flow conditions, when running a plant from circulation to Benson operation.

The use of vertical internal rifled boiler tubes leads to a low mass flow boiler design, because the spiral ribs force the heavy fluid phase (water) to the tube wall, thus maintaining the water film up to a higher steam quality. The ribbed tubes postpone the dryout so it occurs at higher steam qualities. One of the major benefits for a vertical tube furnace design is the positive flow response characteristic for a low mass flux system. The tube flow response requires the water mass flow rate to increase with higher heat input to maintain system pressure loss. These characteristics of a once-through boiler furnace design are highly desirable. An advantage of the low mass flux system is also a reduction in pressure loss through the furnace, so the feed pump power is reduced and the cycle efficiency correspondingly increased. The boiler ramp rate is not improved significantly compared to smooth tubes. One of the biggest advantages of IRBT is the ability to operate far down in the load as a once-through boiler (typically 20 % load). There are obvious structural benefits of using SLMF technology, because the boiler is lighter and more compact with fewer welds and as such will require fewer construction hours to build. The relative pressure drop through an IRBT is significantly higher than for traditional design, but when the evaporator tubes hang vertically, the total pressure drop is typically lower than what we see in traditional Benson boilers. One of the major disadvantages is that the flow distribution through the vertical boiler tubes is very sensitive to the heat flux distribution in the boiler. This can result in varying heat flux through the panel walls, which can result in local instability in the flow field and lead to zero flow conditions and result in *DNB* or in the worst case a melting tube wall. To prevent this phenomenon, the boiler manufacturers have sometimes built in structural changes in the evaporator system, such that a mixing of the fluid from a certain part of the vertical evaporator is established before the fluid again is fed into the next section of vertical evaporator tubes. This is done to reduce the temperature disparity in the evaporator, thereby ensuring a more uniform flow through the evaporator. These enthalpy mixing boxes are expensive, and lead to an increase in pressure loss.

12.6. Recommendations for further work

Ther main recommendations for further work: Experimental validation, Model improvement, Range of simulation cases and Model setup improvement.

12.6.1. Experimental validation

The results presented in this thesis are based on both steady state and dynamic numerical studies of a power plant evaporator, and therefore the most obvious issue for further work lies in a validation of the experimental data. One possibility is to use experimental data from, e.g., Siemens large high-pressure test facility in Erlangen, see [3] and [9], to verify the dynamic model at different load conditions. However, material from the Siemens test rig is confidential and can not be published.

12.6.2. Model improvement

Another important numerical aspect is to implement the two-layer or the four-field models into the WENO scheme and reproduce some of the numerical results presented in this thesis. Unfortunately, many constitutive relations require a closer examination, especially in the four-field model, which requires empirical relations for heat transfer between the many interface layers. A multi-layer model allows us to investigate the impact of interfacial relations compared to the homogeneous model developed in this thesis and allows us to estimate flow regime maps. With respect to the internal rifled boiler tubes, it is of interest to build a two-layer model where the pressure differential, in order to ensure hyperbolic governing equations, can be described on the basis of the rotating flow, which causes just a pressure difference between the two-phases. This can replace the surface tension model in the two-layer model. Similar actions are carried out for the four-field model.

12.6.3. Range of simulation cases

Furthermore, it would be interesting to extend the range of simulation cases to include dynamic load changes from the Benson minimum load to, e.g.,100 % load, and build up a dynamic two-string model for investigations of mal-distribution. This would allow us to see the effects from pulsed heat flux from the burners. Another interesting scenario would be to examine the start-up conditions at an elevated operating pressure, which then is reduced slowly to the desired operating point, so that the risk of instability is reduced.

12.6.4. Model setup improvement

Another issue for further work would be to investigate the evaporator as part of a larger system, consisting of super-heater and turbine system. If the evaporator is part of a complex system, the downstream boundary conditions of the evaporator are not constant in time anymore. The different dynamic responses could thus be studied.

Bibliography

[1] Anonymous, Danmarks Energifremskrivning (2012), October 2012 Edition, no. 11, Energistyrelsen, ISBN: 978-87-7844-941-2, 2012.

[2] K. Trangbæk and B. Elmegaard, Modelling and Optimization of biomass-based Energy production, PSO project 4114 (Jan. 2008).

[3] H. Schmidt, W. Köhler and W. Kastner, "high-pressure test facility - 25 years of operation, framatome anp gmbh", VGB Power Tech (2001) 25–31.

[4] H. Effenberger, Dampferzeugung, ISBN 3-540-64175-o Springer-Verlage, Berlin, 2000.

[5] VDI, VDI-Wärmeatlas, 9th Edition, Springer, Berlin Heidelberg, 2002.

[6] J. Pan, Y. Dong, H. Yu, Q. Bi, H. Hua, F. Gao, Z. Yang, Mathematical modeling and thermo-hydraulic analysis of vertical water wall in an ultra supercritical boiler, Applied Thermal Engineering 29 (2009) 2500–2507.

[7] H. Griem, Untersuchung zur thermohydraulik innenberippter verdampferohre, PhD thesis, Technische Universität München, Lehrstuhl für Termische Kraftanlagen (1).

[8] Anonymous, Guarantee test results of steam turbine SVS3 - 98550369-KPG/TCM 99-6907 Confidential, KEMA, Arnhem, 25 January 1999, Arnhem, The Netherlands, 1999.

[9] J. Franke, Untersuchung der hydrodynamischen Stabilität, Von fachbereich Maschinenbau an der Technischen Hochschule Darmstadt zur Erlangung des Grades eines Doktor-Ingenieurs (Dr.-Ing.) genehmigte Dissertation vorgelegt von Dipl.-Phys. Joachim Franke aus Breslau. (1).

[10] J. Pan, D. Yang, Z. Dong, T. Zhu, Q. Bi, Experimental investigation on heat transfer characteristics of low mass flux rifled tube upward flow, International Journal of Heat and Mass Transfer 54 (2011) 2952–2961.

[11] Yang, D., Pan, J., Zhou, C., Zhu, X., Bi, Q. and Chen, T., Experimental investigation on heat transfer and frictional characteristics of vertical upward rifled tube in supercritical CFB boiler, Experimental Thermal and Fluid Science 35 (2011) 291–300.

[12] X. Zhu, Q. Bi, Q. Su, D. Yang, J. Wang, G. Wu, S. Yu, Self-compensating characteristic of steam-water mixture at low mass velocity in vertical upward parallel internally ribbed tubes, Applied Thermal Engineering 30 (2010) 2370–2377.

[13] X. Fan, S. Wu, Heat transfer and frictional characteristics of rifled tube in a 1000 MW supercritical lignite-fired boiler, School of Energy Science and Engineering, Harbin Institute of Technology, China 1 (2010) 1–5.

[14] Johansen, A. O., Elmegaard B. and Sørensen, J. N., Implementation and test of a fifth-order Central WENO scheme for solving hyperbolic balance laws, Applied Thermal Engineering (1) (2012) 1–25.

[15] Johansen, A. O. and Elmegaard B., Finite element method interpolation scheme for fast calculation of water/steam properties, Applied Thermal Engineering (1) (2013) 1–25.

[16] Johansen, A. O. and Elmegaard B., A homogeneous two-phase flow model of an evaporator with internally rifled tubes, SIMS 2012 (1) (2013) 1–21.

[17] Johansen, A. O. and Elmegaard B., Homogeneous two-phase flow model of a vertical steam evaporator implemented in a fifth-order Central WENO scheme for hyperbolic balance laws, Heat and Fluid Flow (1) (2013) 1–25.

[18] J. M. Smith, H. C. V. Ness, M. M. Abbott, Chemical Engineering Thermodynamics, 6th Edition, McGraw Hill, 2001.

[19] Philip J. Bell, Chao Hui Chen and Ian Torkington, First Posiflow Benson Boiler Completes Seven Years of Service, Doosan Babcock Energy Ltd, May 2010 | Power (May).

[20] A. O. Johansen, Simulation and optimisation of thermal power stations by use of turabs, Proceedings of the 17th International Conference on ECOS 3 (2004) 1267–1277.

[21] W. Press, S. Teukolsky, W. Vetterling, B. Flannery, Numerical Recipes in C. The Art of Scientific Computing, 2nd Edition, Cambridge, University Press, ISBN 0 521 43108 5, 1994.

[22] J. E. Dennis, R. B. Schnabel, Numerical Methods for Unconstrained Optimisation and Nonlinear Equations, Prentice Hall Series in Computational Mathematics, ISBN 0-13-627216-9, 1983.

[23] Baehr, Diederichsen, Berechnungsgleichungen für enthalpie und entropie der komponenten von luft und verbrennungsgasen, 2nd Edition, Vol. 1, BWK, ISBN 0 521 43108 5, 1988.

[24] G. VGB PowerTech Service, Guidelines - KKS-Identification System for Power Stations, 6th Edition, Verlag technisch-wissenschaftlicher Schriften, Postbox 10 39 32, D-45039 Essen, 2007.

[25] F. P. Incropera, D. P. Dewitt, Fundamentals of Heat Transfer, 1st Edition, John Wiley and Sons, Inc., 1981.

[26] N. Henriksen, O. H. Larsen and R. Blum, Lifetime evaluation of superheater tubes exposed to steam oxidation, high temperature corrosion and creep, Power Plant Chemical Technology - Conference Proceedings, International Conference Kolding, Denmark, 4-6 Sept. (1) (1996) 6.1–6.23.

[27] E. Metcalfe et al., New steels for advanced plant up to 620 ^{o}C., The society of Chemical Industry, London, UK, organised by NP (1).

[28] A. N. Hansson, AVV1: Fordamperpøver udtaget ved revision 2009, internal DONG Energy report, Doc. nr.: 696637 (Feb. 2009).

[29] W. Huijbregts, Bespreking van de in de literatuur vermelde oxidatiesnedheden van ferrietische Cr-stahle in overhitte stoom, KEMA 60064-SO 89-3036 (1).

[30] N. Otsuka, H. Fujikawa, Scaling of austenitic stainless steels and nickel base alloys in high-temperature steam at 973k, Corrosion 47 (4) (1991) 240–248.

[31] S. Kakac, B. Bon., A review of two-phase flow dynamic instabilities in tube boiling system, Int. J Heat Mass Transfer 51 (2008) 399–433.

[32] J.A. Boure, A.E. Bergles, L.S. Tong, Review of two-phase flow instability, Nucl. Eng. Des. 25 (1) (1973) 165–192.

[33] A.E. Bergles, F. Mayinger, T.N. Veziroglo (Eds.) and S. Kakac, Review of instabilities in two-phase systems, Hemisphere, Washington, D.C., Two-Phase Flows and Heat Transfer.

[34] A.E. Bergles, J.G. Collier, J.M. Delhaye, G.F. Hewitt and F. Mayinger, Instabilities in two-phase flow systems, Two-Phase and Heat Transfer in the Power and Process Industries, Hemisphere Publishing Corp., McGraw-Hill Book Company (13).

[35] G. Yadigaroglu, J.M. Dehaye, M. Giot and M.L. Riethmuller, Two-phase flow instabilities and propagation phenomena, Thermohydraulics of Two-phase Flow Systems for Industrial Design and Nuclear Engineering, Mc Graw-Hill, New York (1) (1981) 353–404.

[36] M. Ishii, Wave phenomena and two-phase flow instabilities, Handbook of Multiphase Systems, Hemisphere, Washington DC (1) (2008) 2.95–2.122.

[37] R. Lahey, An assessment of the literature related to LWR in sability mode, NUREG/CR1414.

[38] H.T. Liu, S. Kakac, An experimental investigation of thermal induced flow instabilities in a convective boiling upflow system, Wärme- und Stoffübertragung 26 (1) (1991) 364 – 376.

[39] K. Akagawa, A.E. Bergles and S. Ishigai, Recent Japanese researchers on two-phase flow instabilities.

[40] S. M. Ghiaasiaan, Two-Phase Flow, Boiling, and Condensation in Conventional and Miniature Systems, 1st Edition, Cambridge University Press, Georgia Institute of Technology, 2008.

[41] J. Xu, J. Zhou, Y. Gan, Static and dynamic flowinstability of a parallel microchannel heat sink at high heat fluxes, Energy Convers. Manag. 46 (2005) 313–334.

[42] T.J. Zhang, T. Tong and Y. Peles, et al., Ledinegg instability in microchannels, Heat Mass Transfer 52 (2009) 5661–5674.

[43] A.E. Bergles and J.H. Lienhard, et al., Boiling and evaporation in small diameter channels, Heat Transf. Eng. 24 (2003) 18–40.

[44] J. Kitto, J. Robertson, Effects of maldistribution of flow on heat transfer equipment performance, Heat Transfer Eng. 10 (1989) 18–25.

[45] A. Mueller, J. Chiou., Review of various types of flow maldistribution in heat exchangers., Heat Transfer Eng. 9(2) (1988) 36–50.

[46] A. Bergles, S. Kandlikar, On the nature of critical heat flux in microchannels, ASME J. Heat Transfer 127 (1) (2005) 101–107.

[47] M. Bassiouny, H. Martin, Flow distribution and pressure drop in plate heat exchangers. ii. z-type arrangement, Chemical Engineering Science 39 (4) (1984) 693–700.

[48] J. Wang, Pressure drop and flow distribution in parallel-channel configurations of fuel cells: U-type arrangement, International Journal of Hydrogen Energy 33 (21) (2008) 6339–6350.

[49] S. Lalot, P. Florent, S. Lang, A. Bergles, Flow maldistribution in heat exchangers, Applied Thermal Engineering 19 (8) (1999) 847–863.

[50] N. Srihari, B. Rao, B. Sunden, S. Das, Transient response of plate heat exchangers considering effect of flow maldistribution, International Journal of Heat and Mass Transfer 48 (15) (2005) 3231–3243.

[51] S. Vist, J. Pettersen, Two-phase flow distribution in compact heat exchanger manifolds, Experimental Thermal and Fluid Science. The International Symposium on Compact Heat Exchangers 28 (2-3) (2004) 209–215.

[52] M. Ahmad, G. Berthoud, P. Mercier, General characteristics of two-phase flow distribution in a compact heat exchanger, International Journal of Heat and Mass Transfer 1-2 (52) (2009) 442–450.

[53] Ablanque N., Oliet C., Rigola J., Pérez-Segarra C. and Oliva A., Two-phase flow distribution in multiple parallel tubes, International Journal of Thermal Sciences 6 (49) (2010) 909–921.

[54] Rabas T., The effect of tubeside maldistribution on the thermal performance of condensers used in multistage flash distillation plants, Desalination (55) (1985) 515–528.

[55] Bobbili P.R., Sunden B., Das S.K., Thermal analysis of plate condensers in presence of flow maldistribution, International Journal of Heat and Mass Transfer 25-26 (49) (2006) 4966–4977.

[56] Timoney D.J. and Foley P.J., Some effects of air flow maldistribution on performance of a compact evaporator with r134a, Heat Recovery Systems and CHP14 (5) (1994) 517–523.

[57] Aganda A.A., Coney J.E.R., Sheppard C.G.W., Airflow maldistribution and the performance of a packaged air conditioning unit evaporator, Applied Thermal Engineering 20 (6) (2000) 515–528.

[58] Chen N., Xu, L., Dong Feng H., Yang C.G., Performance investigation of a finned tube evaporator under the oblique frontal air velocity distribution, Applied Thermal Engineering 25 (1) (2005) 113–125.

[59] M. R. Kærn, Analysis of flow maldistribution in fin-and-tube evaporators, Ph.D. thesis, DTU Mechanical Engineering, DCAMM Special Report No.S132.

[60] R.J.Margetts, Excursive instability in feedwater coils, AIChE Paper prepared for presentation at 13th National Heat Transfer Conference, Denver, Colorado.

[61] M. Ledinegg, Instäbilitat der strömung bei natürlichen und zwangumlauf, Varme 61 (1938) 891–898.

[62] Muneer T. and Scott S.M., Density and Temperature explicit equations of state for steam, Energy Convers. Mgmt. 31 (4) (1990) 315–325.

[63] Smadar Karni, Eduard Kirr, Alexander Kurganov and Guergana Petrova, Compressible Two-phase flows by central and upwind schemes, ESAIM: Mathematical Modelling and Numerical Analysis 38 (3) (2004) 477–493.

[64] Muneer T., An equation of state for steam for system analysis, Energy Convers. Mgmt. 25 (3) (1984) 273–275.

[65] Anonymous, International Association for the Properties of Water and Steam, IAPWS Formulation 1997 for the Thermodynamic Properties of Ordinary Water Substance for General and Scientific Use, IAPWS Release, IAPWS Secretariat, 1997.

[66] D. H. Brereton, Approximate equations for the properties of dry steam from a generalization of callendar's equation, Int. J. heat and Fluid Flow, Glasgow College of Technology, UK (1).

[67] A. Butterlin, D. Schiesser, H. Steuer, Usage of water & steam properties in computational intensive dynamic simulations, Siemens Energy, Power Generation (47).

[68] G. Mühlthaler, Anwendung objektorientierter Simulationssprachen zur Modellierung von Kraftwerkskomponenten, PhD thesis, Technische Universitt Hamburg, 2000.

[69] W. Müller, Fast and accurate water and steam properties programs for two-phase flow calculations, Nuclear Engineering and Design 51149 (1994) 449–458.

[70] G. Xia, D. Li, C. L. Merkle, Consistent properties reconstruction on adaptive cartesian meshes for complex fluids computations, Journal of Computational Physics 225 (1) (2007) 1175 – 1197.

doi:10.1016/j.jcp.2007.01.034.
URL http://www.sciencedirect.com/science/article/pii/S0021999107000605

[71] E. W. Lemmon, M. L. Huber, NIST Standard Reference Database 23, NIST National Institute of Standards and Technology, 4th Edition.

[72] O. C. Zienkiewich, J. L. Taylor, The Finite Element Method, 4th Edition, Vol. 1, McGraw-Hill, London, 1989.

[73] Moon-Sun Chung, Keun-Shik Chang and Sung-Jae Lee, Numerical solution of hyperbolic two-fluid two-phase flow model with non-reflecting boundary conditions, Int. J. Engineering Science 40 (1) (2002) 789–803.

[74] Jun Zhou, Li Cai, Jian-Hu Feng and Wen-Xian Xie, Numerical simulation for two-phase flows using hybrid scheme, Applied Mathematics and Computation 186 (1) (2007) 980 – 991.

[75] Richard Saurel and Rémi Abgrall, A multiphase godunov method for compressible multifluid and multiphase flows, Journal of Computational Physics 150 (1) (1999) 425 – 467.

[76] Wallis, G. B., One-dimensional two-phase flow, 3rd Edition, McGraw-Hill, 1969.

[77] F. Jirous, Analytische methode der berechnung des naturumlaufes bei dampferzugern, VGB Heft 5 (1978) 366–372.

[78] T. Watanabe, M. Hirano, F. Tanabe, H. Kamo, The effect of virtual mass on the numerical stability and efficiency of system calculations, Nucl. Eng. Design, 120, 181-192. (1990) 181–192.

[79] G. Hewitt, J. Delhave, N. Zuber, Inertial coupling in two-phase flow: Macroscopic properties of suspension in an inviscid fluid, vol 5, chapter 4 Edition, In Multiphase Science and Technology, 1969.

[80] W. Wagner, H. J. Kretzschmar, International Steam Tables - Properties of Water and Steam Based on the Industrial Formulation IAPWS-IF97, 2nd Edition, Springer, Berlin Heidelberg, 2008.

[81] F. Coquel, K. E. Amine, E. Godlewski, B. Perthame, P. Rascle, A numerical method using upwind schemes for the resolution of two-phase flows, Journal of Computational Physics 1 (136) (1997) 272–288.

[82] M. Baer, J. Nunziato, A two-phase mixture theory for the deflagration-to-detonation transition (ddt) in reactive granular materials, Int. J. Multiphase Flow 1 (12) (1986) 861–889.

[83] F. C. M. Baudin, Q. H. Tran, A semi-implicit relaxation scheme for modeling two-phase flow in a pipeline, SIAM J. Sci. Comput. 1 (27) (2005) 914–936.

[84] M. Baudin, C. Berthon, F. Coquel, R. Masson, Q. Tran, A relaxation method for two-phase flow models with hydrodynamic closure law, Numer. Math. 1 (99) (2005) 411–440.

[85] F. Coquel, Q. Nguyen, M. Postel, Q.H.Tran, Entropy-satisfying relaxation method with large time-steps for euler IBVPs, Math. Comput. 1 (79) (2010) 1493–1533.

[86] S. Evje, K. Fjelde, Relaxation schemes for the calculation of two-phase flow in pipes, Modelling 36 1 (1) (2002) 535–567.

[87] S. Jin, Z. Xin, The relaxation schemes for systems of conservation laws in arbitrary space dimensions, Commun. Pure Appl. Math. 1 (48) (1995) 235–276.

[88] Svend Tollak Munkejord, Comparison of roe-type methods for solving the two-fluid model with and without pressure relaxation., Computers and Fluids (36) (2007) 1061–1080.

[89] J.D. Ramshaw and J.A. Trapp, Characteristics, stability, and short-wave length phenomena in two-phase flow equation systems, Nucl. Sci. Eng 66 (1) (1978) 93 – 102.

[90] J. R. Travis, F. H. Harlow, A. A. Amsden, Numerical calculation of two-phase flows, Nucl. Sci. Eng 61 (1) (1976) 1 – 10.

[91] J.H. Stuhmiller, The influence of interfacial pressure forces on the character of two-phase flow model equations, Int. J. Multiphase Flow 3 (1) (1977) 551–560.

[92] M. Blander, J. L. Katz, Bubble nucleation in liquids, AIChE J 21 (1) (1975) 833–848.

[93] R. Henry, M. Grolmes, K. Fauske, Pressure pulse propagation in two-phase one- and two-component mixtures, ANL-7792.

[94] M.-S. Chung, S.-B. Park, H.-K. Lee, Sound speed criterion for two-phase critical flow, agency for defense development, Chinhae, Kyungnam 645-600, South Korea, Journal of Sound and Vibration 276 (13) (2004) 13–26.

[95] P. D. Bentz, R. Prasad, Kuldeep, Thermal performance of fire resistive materials i. characterization with respect to thermal performance models, NIST, Building and Fire research Laboratory, Gaithersburg (MD 20899-8615).

[96] M. Rohrenwerke, Rohre aus warmfesten und hochwarmfesten Stahlen Werkstoffblatter, 1st Edition, MannesMann Rohrenwerke, 1988.

[97] F. Brandt, FDBR-FACHBUCHREIHE - wärmeübertragung in Dampferzeugern und Wärmeaustauschern, band 2 Edition, Vulkan-Verlag, Essen., 1985.

[98] G. R. Kinney, A. E. Abramson, J. L. Sloop, Internal-liquid-film cooling experiments with air-steam temperatures to 2000 ^{o}F in 2-inch and 4-inch Diameter Horizontal Tubes, NACA Report no. 1087 1 (1) (1952) 1.

[99] L. E. Gill, G. Hewitt, J. W. Hitchon, Sampling probe studies of the gas core in annular two-phase flow, part 1. the effect of length of phase and velocity distribution, Chem. Eng. Sci. 18 (1) (1963) 525–535.

[100] L. E. Gill, G. Hewitt, J. W. Hitchon, Sampling probe studies of the gas core in annular two-phase flow, part 2. studies of the effect of phase flow rates on phase and velocity distributions, U.K. Report AERE-R 3955 (1).

[101] Y. Sato, K. Sekoguchi, Liquid velocity distribution in two-phase bubble flow, Int. J. Multiphase Flow,79-95. (2).

[102] Sørensen J.N., Kristensen S.Aa. and Christensen L.K., Direct and large eddy simulations of thermo-convective flows, Lecture Notes in Computer Science, Department of Energy Engineering, Fluid Mechanics Section. Technical University of Denmark, DK-2800 Lyngby 1 (2) (2005) 631–640.

[103] M. Bonizzi, A. P., Banerjee, Flow regime independent, high resolution multi-field modelling of new-horizontal gas-liquid flows in pipelines, Int. J. Multiphase Flow (35) (2009) 34–46.

[104] E. F. Toro, Riemann Solvers and Numerical Methods for Fluid Dynamics: A Practical Introduction, 1st Edition, Vol. 1, Springer, London, 1997.

[105] Rusanov, V. V., Calculation of interaction of non-steady shock waves with obstacles, USSR Computational Mathematics and Mathematical Physics 1 (1) (1961) 267–279.

[106] A. Harten, P. D. Lax, On upstream differencing and godunov-type schemes for hyperbolic conservation law, SIAM Review 25 (1) (1983) 35–61.

[107] S. K. Godunov, A finite difference method for the computation of discontinuous solutions of the equations of fluid dynamics, Matematicheskii Sbornik 47 (1) (1959) 357 – 393.

[108] A. Harten, On a class of high resolution total-variation-stable finite-difference schemes, SIAM J. Numerical Anal. 1 (Vol 21.) (1983) 1–23.

[109] A. Harten, High resolution schemes for hyperbolic conservation laws, Journal Of Computational Physics 49 (1) (1983) 357 – 393.

[110] P. K. Sweby, High resolution schemes using flux limiters for hyperbolic conservation laws, SIAM J. Numer. Anal. Vol. 21 ,995-1011 (5) (1984) 995–1011.

[111] C.-W. Shu, Essentially non-oscillatory and weighted essentially non-oscillatory schemes for hyperbolic conservation laws, Advanced numerical approximation of nonlinear hyperbolic equations 1697 (1) (1998) 325 – 432.

[112] A. Kurganov, E. Tadmor, New high-resolution semi-discrete central schemes for hamilton-jacobi equations, J. Comput. Phys. (160) (2000) 720–742.

[113] Sigal Gottlieb, On high order strong stability preserving runge-kutta and multi step time discretizations, Journal of Scientific Computing 25 (1) (2004) 105–128.

[114] H. Versteeg, W. Malalasekera, An Introduction to COMPUTATIONAL FLUID DYNAMICS, The Finite Volume Method, 2nd Edition, Pearson, Prentice Hall, Harlow, England, 2007.

[115] F. S. Lien, M. A. Leschziner, Upstream monotonic interpolation for scalar transport with application to complex turbulent flows, Int. J. Numerical Methods Fluids (19) (1993) 527–548.

[116] G. Capdeville, A central WENO scheme for solving hyperbolic conservation laws on non-uniform meshes, J. Comp. Phys. 4 (227) (2008) 2977–3014.

[117] G. S. Jiang, C. W. Shu, Efficient implementation of weighted ENO schemes, J. Comput. Phys. (126) (1996) 202–228.

[118] J. Qiu, C. W. Shu, On the construction, comparison and local characteristic decomposition for high-order central weno schemes, J. Comput. Phys. (183) (2002) 187–209.

[119] Liu Y., Shu C. W. and Zhang M., High order finite difference weno schemes for nonlinear degenerate parabolic equations, SIAM Journal on Scientific Computing 33 (2) (2011) 939–965.

[120] A. Harten, B. Engquist, S. Osher, S. Chakravarthy, Uniformly high order essentially non-oscillatory schemes, III J. Comput. Phys. (71) (1987) 231–303.

[121] D. Levy, G. Pupo, G. Russo, Compact central WENO schemes for multidimensional conservation, SIAM J. Sci. Comput. (22) (2000) 656–672.

[122] C. W. Shu, Essential non-oscillatory and weighted essential non-oscillatory schemes for hyperbolic conservation laws, 1st Edition, Springer, Lecture Notes in Mathematics, 1997.

[123] M. Castro, B. Costa, W. S. Don, High order weighted essentially non-oscillatory WENO-Z schemes for hyperbolic conservation laws, Journal of Computational Physics (230) (2010) 1766–1792.

[124] R. Borges, C. B., W. Costa, S. Don, An improved weighted essentially non-oscillatory scheme for hyperbolic conservation laws, J. Comput. Phys. (227) (2008) 3191–3211.

[125] A. Kurganov, S. Noelle, G. Petrova, Semi-discrete central-upwind schemes for hyperbolic conservation laws and hamilton-jacobi equations, SIAM J. Sci. Comp. (23) (2001) 707–740.

[126] S. Gotlieb, C. Shu, Total variation diminishing runge-kutta schemes, Math. Comp., 73-85 (67) (1998) 73–85.

[127] Michael Dumbser, Cedric Enaux and Eleuterio F. Toro, Explicit Finite Volume Schemes of Arbitrary High Order of Accuracy for Hyperbolic Systems with Stiff Source Terms, Preprint submitted to Elsevier Science (2007) 1–45.

[128] G. Q. Chen, C. D. Levermore, T. Liu, Hyperbolic conservation laws with stiff relaxation terms and entropy, Communications on Pure and Applied Mathematics 6 (47) (1994) 787–830.

[129] A. Kurganov, E. Tadmor, New high-resolution central schemes for nonlinear conservation laws and convection-diffusion equations, J. Comput. Phys. (160) (2000) 241–282.

[130] A. Kurganov, D. Levy, A third-order semidiscrete central scheme for conservation laws and convection-diffusion equations, SIAM J. Sci. Comp. 4 (22) (2000) 1461–1488.

[131] Y. H. Zahran, An efficient WENO scheme for solving hyperbolic conservation laws, App. Math. and Comp. (212) (2009) 37–50.

[132] L. Bjørnø, Strømningslære, Polyteknisk Forlag, 1984.

[133] J.L. Achard and D. A Drew and R.T. Lahey, The analysis of non-linear density-wave oscil1ations in boiling channels, J. Fluid Mech. 155 (1) (1985) 213 – 232.

[134] Rizwan-Uddin, J.J. Doming, Numerical simulations and the nonlinear dynamics of two-phase flow in heated channels, AIChE Symp. Ser. 83 258 (1) (1987) 190 – 198.

[135] Rizwan-uddin, J. Doming, Chaotic attractor in a periodically forced two-phase flow system, J. Nucl. Sci. Eng. 100 (4) (1988) 393–404.

[136] M. Ozawa, K. Akagawa, T. Sakaguchi, Flow instabilities in parallel-channel flow systems of gas-liquid two-phase mixtures, Int. J. Multiphase Flow 15 (1) (1988) 639–657.

[137] Z. Zhang, Z. Gao, D. Wang, An explicit criterion for analyzing two phase flow density wave instability, in: X.J. Chen, T.N. Veziroglu, C. L.Tien (Eds.), Multiphase Flow and Heat Transfer, Hemisphere, , New York, NY (1).

[138] S. K. M.M. Padki, K. Palmer, T. Veziroglo, Bifurcation analysis of pressure-drop oscillations and the Ledinegg instability, Int. J. Heat Mass Transfer 35 (2) (1992) 525–532.

[139] C. C. Richter, Proposal of New Object-Oriented Equation-Based Model Libraries for Thermodynamic Systems, 1st Edition, Vol. 1, Von der Fakultät für Maschinenbau, der Technischen Universität Carolo-Wilhelmina zu Braunschweig, 2008.

[140] L. S. Tong, Boiling Heat Transfer and Two-Phase Flow, John Wiley and Sons, Inc. New York - London - Sidney, Atomic Power Division, Westinghouse Electric Corporation - Pittsburgh, Pennsylvania, 1965.

[141] W. M. Rohsenow, J. P. Hartnett, E. N. Ganic, Handbook of Heat Transfer, 2nd Edition, Vol. 1, McGraw-Hill Book Co., 1984.

[142] J. G. Collier, A. E. S. Kakac, Heat Exchangers Thermal-Hydraulic Fundamentals and Design, Vol. 1, Bergles and F. Mayinger, Hemisphere Publishing Corp., Washington, D. C., 1981.

[143] J. Collier, J. Thome, Convective Boiling and Condensation, 1st Edition, Oxford University Press, 1993.

[144] F. P. Incropera, F. P. D. Witt, Fundamentals of Heat and Mass Transfer, 3rd Edition, Wiley, New York, 1990.

[145] J. C. Chen, A correlation for boiling heat transfer to saturated fluids in convective flow, ASME Int. Eng. Chem. Process Design and Development 63-HT-34, 5 (1963) 322–329.

[146] J. R. Fair, What you need to design thermosyphon reboilers, Petroleum Refiner, 2nd Edition, Vol. 39, 1960.

[147] M. R. Glickstein, R. H. Whitesides, Forced convection nucleate and film boiling of several aliphatic hydrocarbons, ASME 9th. Nat. Heat Transfer Conf. Seattle 67 (1967) 67–HT–7.

[148] J. G. Collier, J. R. Thome, Convective Boiling and Condensation, 3rd Edition, Clarendon Press, Oxford, England, 1994.

[149] O. Barker, Simultaneous flow of oil and gas, Oil Gas J. (53) (1954) 185–195.

[150] A. Fluent, ANSYS Fluent® 12.0 Theory Guide, 1st Edition, ANSYS, Inc. Lebanon, 2009.

[151] F. Dryer, I. Glassman, High-temperature oxidation of co and ch4, Fourteenth Symposium (international) on Combustion 14 (1) (1973) 987–1003.

DTU Mechanical Engineering
Section of Thermal Energy
Technical University of Denmark

Nils Koppels Allé, Bld. 403
DK- 2800 Kgs. Lyngby
Denmark
Phone (+45) 4525 4131
Fax (+45) 4588 4325
www.mek.dtu.dk
ISBN: 978-87-7475-382-7

DCAMM
Danish Center for Applied Mathematics and Mechanics

Nils Koppels Allé, Bld. 404
DK-2800 Kgs. Lyngby
Denmark
Phone (+45) 4525 4250
Fax (+45) 4593 1475
www.dcamm.dk
ISSN: 0903-1685

Numerical study of evaporators in power plants for improved dynamic flexibility
Appendix A-Q

PhD Thesis

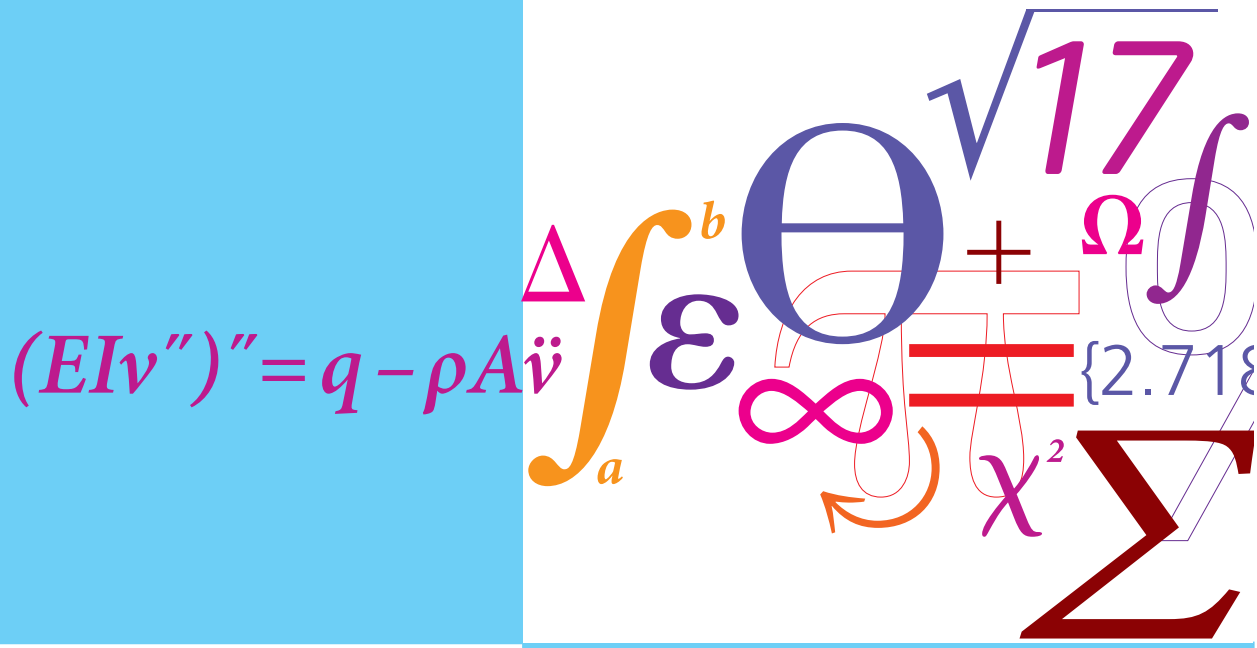

Axel Ohrt Johansen
DCAMM Special Report No. S165
March 2013

DTU Mechanical Engineering
Department of Mechanical Engineering

A. Dimensionless numbers

In this appendix, we deal with an initial definition of the various dimensionless numbers related to thermo-hydraulic two phase flow problems, used in this work.

A.1. Dimensional analysis

In mathematics and science, dimensional analysis is a tool to understand the properties of physical quantities independent of the units used to measure them, which makes sense when we deal with complex subjects such as two phase flow. Every physical quantity is some combination of mass, length, time, electric charge, and temperature, (denoted M, L, T, Q, and K, respectively). For example, speed, which may be measured in meters per second (m/s) and has the dimension LT^{-1}.

Dimensional analysis is routinely used to check the plausibility of derived equations and computations. It is also used to form reasonable hypotheses about complex physical situations that can be tested by experiment or by more developed theories of the phenomena, and to categorize types of physical quantities and units based on their relations to or dependence on other units, or their dimensions if any. All physical dimensions in this work are measured in SI system or a smaller variety of it.

The basic principle of dimensional analysis was known to the 19th-century French mathematician Joseph Fourier, who made important contributions based on the idea that physical laws like Newton's second law: F = m·a, should be independent of the units employed to measure the physical variables. This led to the conclusion that meaningful laws must be homogeneous equations in their various units of measurement, a result which was eventually formalized in the Buckingham π theorem. This theorem describes how every physically meaningful equation involving n variables can be equivalently rewritten as an equation of n - m dimensionless parameters, where m is the number of fundamental dimensions used. Furthermore, and most importantly, it provides a method for computing these dimensionless parameters from the given variables. The boiling mechanism in two-phase flow is so complicated, that a pure analytical expression for the heat transfer, derived from basic relations, has not yet been obtained. It is therefore convenient to employ dimensional analysis, which will give the qualitative descriptions various boiling mechanisms and facilitate the empirical correlation of boiling heat transfer data. The most commonly used non dimensional groups in

boiling heat transfer and two phase flow are summarized in the below paragraphs, taken from [140], [40] and from Wikipedia, the free encyclopaedia (Aug., 2010).

A.2. Constants in fluid mechanics and thermodynamics

The dimensionless constants that arise in the results obtained, come from a more detailed analysis of the underlying physics, and often arises from integrating some differential equation. Dimensional analysis itself has little to say about these constants, but it is useful to know that they very often have a magnitude of order unity. This observation can allow one to sometimes make 'back of the envelope' calculations about the phenomenon of interest, and therefore be able to more efficiently design experiments to measure it, or to judge whether it is important, etc. In fluid mechanics and thermodynamics, the dimension of any physical quantity can be expressed in terms of the fundamental dimensions (or base dimensions) M (mass in kilo), L (length in meter), T (time in seconds) and K (temperature in kelvin) - these form a 4-dimensional vector space. This is not the only possible choice, but it is the one most commonly used. For example, one might choose force, length and mass as the base dimensions, with associated dimensions F, L, M; this corresponds to a different basis, and one may convert between these representations by a change of basis. The choice of the base set of dimensions is, thus, partly a convention, resulting in increased utility and familiarity. It is, however, important to note that the choice of the set of dimensions cannot be chosen arbitrarily - it is not just a convention - because the dimensions must form a basis: they must span the space, and be linearly independent.

Brinkman Number

The Brinkman number (Br) is a dimensionless number related to heat conduction from a wall to a flowing viscous fluid, commonly used in polymer processing. There are several definitions; one is

$$Br = \frac{\mu u^2}{k(T_w - T_b)} \tag{A.1}$$

where μ is the fluid's dynamic viscosity, u is the fluid's velocity, k is the thermal conductivity of the fluid, T_b is the bulk fluid temperature and T_w is the wall temperature.

Boiling number

The Boiling number (Bo) is defined as the ration of vapour velocity away from the heating surface to flow parallel to the surface. The vapour velocity is evaluated on the basis of heat transfer q''_w by latent heat transport $h^s_{lg}\rho_g u_g$:

$$Bo = \frac{q''_w}{h^s_{lg}\rho_g u_g} \tag{A.2}$$

Buoyancy modulus

The Buoyancy Modulus (Bu) is defined as the ration of the difference in bubble density to liquid density.

$$Bu = \frac{\rho_l - \rho_g}{\rho_l} \tag{A.3}$$

Eckert number

The Eckert number (Ec) is a dimensionless number used in fluid dynamics. It expresses the relationship between a flow's kinetic energy and enthalpy, and is used to characterize dissipation. It is defined as

$$Ec = \frac{u^2}{c_p \Delta t} \tag{A.4}$$

where u is a characteristic velocity of the flow. c_p is the constant-pressure specific heat of the flow. Δt is a characteristic temperature difference of the flow.

Euler number

The Euler number (Eu) is a dimensionless number used in fluid flow calculations. It expresses the relationship between a local pressure drop Δp e.g. over a restriction and the kinetic energy per volume, and is used to characterize losses in the flow, where a perfect frictionless flow corresponds to an Euler number of 1. The Euler Number can be written in the form:

$$Eu = \frac{\Delta p}{\rho u^2} \tag{A.5}$$

where ρ is the density of the two phase mixture or of a single component of the mixture. The term Δp is the friction pressure drop of flow or the pressure difference across the boundary of a bubble and u is the fluid velocity.

Eötvös number

In fluid dynamics the Eötvös number (Eo) is a dimensionless number. Together with the Morton number it can be used to characterize the shape of bubbles or drops moving in a surrounding fluid. Eötvös number may be regarded as proportional to buoyancy force divided by surface tension force.

$$Eo = \frac{\Delta\rho g L^2}{\sigma} \tag{A.6}$$

where $\Delta\rho$ is the difference in density of the two phases, g the gravitational acceleration, L ia a characteristic length and σ is the surface tension belonging to the bubble surface.

Froude number

The Froude number is a dimensionless number defined as the ratio of a characteristic velocity to a gravitational wave velocity. It may equivalently be defined as the ratio of a body's inertia to gravitational forces. In fluid mechanics, the Froude number is used to determine the resistance of an object moving through water, and permits the comparison of objects of different sizes. The Froude number is defined as:

$$Fr = \frac{u}{c} \tag{A.7}$$

where u is a characteristic velocity , and c is a characteristic surface water wave propagation velocity (c=$\sqrt{g \cdot d}$), where g is the acceleration due to gravity and d is the characteristic depth of the liquid column. The Froude number is thus analogous to the Mach number.

Grashof number

The Grashof number (Gr) is a dimensionless number in fluid dynamics and heat transfer which approximates the ratio of the buoyancy to viscous force acting on a fluid. It frequently arises in the study of situations involving natural convection.

$$Gr = \frac{g\beta(T_s - T_\infty)L^3}{\nu^2} \tag{A.8}$$

where g is the acceleration due to Earth's gravity, β is the volumetric thermal expansion coefficient (equal to approximately 1/T, for ideal fluids, where T is absolute temperature), T_s is the surface temperature of the surrounding object, T_∞ is the bulk temperature, L is the length and ν kinematic viscosity.

Jakob number

The Jakob Number (Ja) is defined as the ration of the sensible heat carried by a two phase fluid to the latent heat of a bubble with the same volume:

$$Ja = \frac{c_p \rho_l (T_w - T_b)}{h^s_{fg} \rho_g} \tag{A.9}$$

which expresses the relative effectiveness of the liquid-vapour exchange in the two phase fluid. T_w and T_b is the temperature of the wall and bubble respectively. c_p and ρ_l expresses the specific heat capacity and the density of the bubble respectively, h^s_{fg} is the latent heat and ρ_g is the density of the gas phase (bubble).

Nusselt number

Heat transfer at a surface boundary within a fluid, can be correlated to the Nusselt number, which expresses the ratio of convective to conductive heat transfer across (normal to) the boundary. The conductive component is measured under the same conditions as the heat convection but with a (hypothetically) stagnant (or motionless) fluid. A Nusselt number close to unity, namely convection and conduction of similar magnitude, is characteristic of 'slug flow' or laminar flow. A larger Nusselt number corresponds to more active convection, with turbulent flow typically in the 100-1000 range. The Nusselt Number for bubbles (Nu_b) is defined as the ration of the boiling heat transfer rate to the conduction heat transfer through the liquid film:

$$Nu_b = \frac{\delta l q''}{k_l (T_w - T_b)} \tag{A.10}$$

The symbol δl is the thickness of the liquid film, which can be the same order of magnitude as a bubble diameter, or it may be chosen as some other dimensions, depending on the physical model visualized. The term k_l is the thermal heat conduction of the liquid and T_w and T_b is the temperature of the wall and bubble respectively.

Prandtl number

The Prandtl number of the liquid (Pr_l) is a dimensionless number approximating the ratio of momentum diffusivity (kinematic viscosity) and thermal diffusivity.

$$Pr_l = \frac{\nu}{\alpha} = \frac{c_p \mu}{k} \tag{A.11}$$

Note that whereas the Reynolds number and Grashof number are subscripted with a length scale variable, Prandtl number contains no such length scale in its definition and is dependent only on the fluid and the fluid state. As such, Prandtl number is often found in property tables alongside other properties such as viscosity and thermal conductivity.

Richardson number

The Richardson number (Ri) is the dimensionless number that expresses the ratio of potential to kinetic energy:

$$Ri = \frac{g \cdot L}{u^2} \tag{A.12}$$

where g is the acceleration due to gravity, L a representative vertical length scale, and u is a representative velocity. If the Richardson number is much less than unity, buoyancy is unimportant in the flow. If it is much greater than unity, buoyancy is dominant (in the sense that there is insufficient kinetic energy to homogenize the fluids). If the Richardson number is of order unity, then the flow is likely to be buoyancy-driven: the energy of the flow derives from the potential energy in the system originally.

Rayleigh number

The Rayleigh number for a fluid is a dimensionless number associated with buoyancy driven flow (also known as free convection or natural convection). When the Rayleigh number is below the critical value for that fluid, heat transfer is primarily in the form of conduction; when it exceeds the critical value, heat transfer is primarily in the form of convection. The Rayleigh number is defined as the product of the Grashof (Gr) number, which describes the relationship between buoyancy and viscosity within a fluid, and the Prandtl number (Pr), which describes the relationship between momentum diffusivity and thermal diffusivity. Hence the Rayleigh number itself may also be viewed as the ratio of buoyancy and viscosity forces times the ratio of momentum and thermal diffusivities. For free convection near a vertical wall, this number is

$$Ra_x = Gr_x Pr = \frac{g\beta}{\nu\alpha}(T_s - T_\infty)x^3 \tag{A.13}$$

where x is a characteristic length (in this case, the distance from the leading edge), Ra_x is the Rayleigh number at position x, Gr_x is the Grashof number at position x, Pr is the Prandtl number, g is the acceleration due to gravity, T_s is the surface temperature (temperature of the wall), T_∞ is the quiescent temperature (fluid temperature far from the surface of the object), ν is the kinematic viscosity, α is thermal diffusivity and β is the thermal expansion coefficient.

In the above, the fluid properties Pr, ν, α and β are evaluated at the film temperature, which is defined as $T_f = (T_s + T_\infty)/2$. For most engineering purposes, the Rayleigh number is large, somewhere around 10^6 to 10^8.

Reynolds number

In fluid mechanics, the Reynolds number (Re) is a dimensionless number that gives a measure of the ratio of inertial forces to viscous forces and consequently quantifies the relative importance of these two types of forces for given flow conditions. Reynolds numbers frequently arise when performing dimensional analysis of fluid dynamic problems, and are also used to characterize different flow regimes, such as laminar or turbulent flow: laminar flow occurs at low Reynolds numbers (Re < 2300), where viscous forces are dominant, and is characterized by smooth, constant fluid motion, while turbulent flow occurs at high Reynolds numbers and is dominated by inertial forces, which tend to produce chaotic eddies, vortices and other flow instabilities. In two phase flow the Reynolds number can be related to the bubble formation, (Re_b), which is a dimensionless number defined by the ration of the bubble inertial force to the liquid viscous force. This number indicates the intensity of the liquid agitation induced by bubble motion.

$$Re_l = \frac{\rho_g u_b d_b}{\mu_l} \tag{A.14}$$

where ρ_g is the density of the bubble, u_b is the speed of the bubble and d_b the diameter of the bubble. Finally we have μ_l as the dynamic viscosity of the surrounding liquid.

Sherwood number

The Sherwood number, (Sh) (also called the mass transfer Nusselt number) is a dimensionless number used in mass-transfer operation. It represents the ratio of convective to diffusive mass transport, and is defined as follows

$$Sh = \frac{u \cdot L}{\alpha} \tag{A.15}$$

where L is a characteristic length, α is mass diffusivity (m^2/s) and u is the mass transfer coefficient (m/s). It can also be further defined as a function of the Reynolds and Schmidt numbers. This is a very concrete way of demonstrating the analogies between different forms of transport phenomena.

Stanton number

The Stanton number, (St), is a dimensionless number that measures the ratio of heat transferred into a fluid to the thermal capacity of fluid. It is used to characterize heat transfer in forced convection flows.

$$St = \frac{h}{c_p \rho u} \tag{A.16}$$

where h is the convection heat transfer coefficient, ρ is the density of the fluid, c_p is the specific heat of the fluid and u is the velocity of the fluid. It can also be represented in terms of the fluid's Nusselt, Reynolds, and Prandtl numbers:

$$St = \frac{Nu}{Re \cdot Pr} \tag{A.17}$$

where Nu is the Nusselt number, Re is the Reynolds number and Pr is the Prandtl number. The Stanton number arises in the consideration of the geometric similarity of the momentum boundary layer and the thermal boundary layer, where it can be used to express a relationship between the shear force at the wall (due to viscous drag) and the total heat transfer at the wall (due to thermal diffusivity).

A.3. Dimensionless quantities

The governing equations for two-phase pipe flow with external heat flux, can be transformed into a dimensionless coordinate system by introducing a number dimensionless quantities. One of the advantages in using dimensionless quantities is, that it is easier to evaluate the stability conditions in the corresponding numerical solver. Another very important argument for working with dimensionless quantities is that it is easier to judge whether some coefficients in the governing equations are important or not and which parameter is important to change for evaluation of the sensitivity of the numerical model, according to the Buckingham π theorem. Finally it is useful to know the magnitude of some dimensionless numbers, which normally is visibly in the governing equations and thereby gives an idea of what kind of physical problem we are doing with and therefore be

able to more efficiently design simulation campaigns to fit real experiments. The below quantities are used in this work:

$$
\begin{aligned}
&\rho^* = \frac{\rho}{\rho_0}, \quad h^* = \frac{h}{u_0^2}, \quad p^* = \frac{p}{\rho_0 \cdot u_0^2} \\
&T^* = \frac{T}{T_0}, \quad t^*_{wall} = \frac{t}{t_0}, \quad \text{where } t_0 = \frac{l^2}{\alpha} \text{(based on thermal diffusivity)} \\
&\alpha = \frac{k}{\rho c_p}, \quad t^*_{fluid} = \frac{t}{t_0}, \quad \text{where } t_0 = \frac{d_i^2}{\nu} \text{(based on kinematic viscosity)} \\
&z^* = \frac{z}{l}, \quad u^* = \frac{u}{u_0}, \quad G^* = \frac{G}{G_0} \\
&G_0 = \rho_0 \cdot u_0, \quad A^* = \frac{A}{A_0}
\end{aligned}
\tag{A.18}
$$

Subscript 0 indicates a reference point, which may be an upstream boundary condition or a steady state condition to the mathematical problem.

B. Operating range of the thermal power plant SKV3

In this appendix are listed static cycle calculations of the thermal power plant SKV3. The calculations are based on the consolidated simulation tool Turabs 2, developed by DONG Energy - Thermal Power A/S. The simulations have the aim of identifying a complete operating range in terms of both heat production and net electricity production. The calculation results in a so-called PQ diagram, see figure (3.1). In table B.1 are listed abbreviations for the most relevant calculation data to the specific loading points. There are a total estimated 145 load points in two tables, see table B.2 and B.3.

Table B.1.: Abbreviations used in connection with the PQ load calculations.

Item	**Explanation**	**Unit**
Q_{dh}	District heat production	[Kj/s]
P_{net}	Nett electricity production	[Kw]
Node	Turabs calculation node	[-]
Quality	Quality of calculation, 0: Interpolation used, 1: Converged simulation	[-]
C_v	$\frac{P_{cond}-P_{actual}}{Q_{dh}}$	[-]
Q_{boil}	Gross fired boiler output	[Kj/s]
Q_{exp}	Heat consumption in gasexspander	[Kj/s]
Q_{brut}	Gross electricity production	[Kw]
P_{ef}	Internal consumption	[Kw]
m	High pressure steam flow	[Kg/s]
m_{qw}	Cooling water flow	[Kg/s]
P_{kon}	Condenser pressure	[Bar]
t_{HP}	Outlet temperature HT boiler	[°C]
t_{RH1}	Outlet temperature RH1 boiler	[°C]
Q_{RH1}	Injection flow in RH1	[kg/S]
Q_{RH2}	Outlet temperature RH2 boiler	[°C]
Q_{RH2}	Injection flow in RH2	[kg/s]
η_{ked}	Boiler efficiency	[-]
Mode=1	Normal operating all preheaters (PH) active	[-]
Mode=2	HPPH=50 LPPH=100, HPPH=High Pressure PreHeater	[%]
Mode=3	HPPH=0 LPPH=100, LPPH=Low Pressure PreHeater	[%]
Mode=4	HPPH=0 LPPH=50	[%]
Mode=5	HPPH=0 LPPH=0	[%]
Mode=6	HPPH=100 LPPH=50	[%]
Mode=7	HPPH=50 LPPH=50	[%]
Mode=8	HPPH=100 LPPH=0	[%]
Mode=9	HPPH=50 LPPH=0	[%]
m_{PH9}	Steam flow to HPPH9	[kg/s]
m_{PH10}	Steam flow to HPPH10	[kg/s]

N	Q_{dh}	P_{net}	Node	Quality	C_v	Q_{boil}	Q_{exp}	P_{brut}	P_{ef}	m_{qw}	m_{fw}	P_{kon}	t_{HP}	t_{RH1}	m_{RH1}	t_{RH2}	m_{RH2}	η_{ked}	Mode	m_{FV9}	m_{FV10}
1	0	431085	1	1	0.0409	953221	5200	456630	29016	269.6	13339	0.0228	582.00	580.00	7.37	580.00	4.04	0.9570	3	0	0
2	0	410190	2	1	0.0901	890691	5200	432057	25467	269.6	13087	0.0214	582.00	580.00	6.11	580.00	3.21	0.9565	2	8.5	14.4
3	0	391688	3	1	0.1269	836875	4861	410932	22610	269.6	12806	0.0202	582.00	580.00	5.02	580.00	2.50	0.9560	1	14.7	27.7
4	0	343426	4	1	0.1322	732622	3931	358383	17631	233.1	12216	0.0185	582.00	580.00	2.92	580.00	1.12	0.9554	1	13.0	22.7
5	0	294263	5	1	0.1380	628369	3000	305682	13369	197.2	11479	0.0170	582.00	580.00	1.15	580.00	0.20	0.9549	1	11.1	18.0
6	0	244008	6	1	0.1445	524115	2319	252401	9836	160.8	10611	0.0156	582.00	580.00	0.63	580.00	0	0.9542	1	9.0	13.7
7	0	192123	7	1	0.1928	419862	1638	198263	7046	127.5	9657	0.0143	582.00	572.43	0.10	554.89	0	0.9526	1	7.0	10.0
8	0	160269	8	1	0.2529	356730	1225	165422	5717	107.5	9016	0.0136	582.00	556.58	0	539.07	0	0.9515	1	5.7	7.9
9	0	126053	9	1	0.2954	293597	813	130508	4667	89.6	8390	0.0129	532.85	521.80	0	506.89	0	0.9491	1	4.6	6.2
10	0	93357	10	1	0.4073	230465	400	97400	3887	70.5	7666	0.0122	507.21	484.76	0	478.62	0	0.9453	1	3.4	4.5
11	0	63122	11	1	0.5391	167332	0	67043	3394	48.9	6768	0.0113	514.64	498.14	0	483.29	0	0.9335	1	2.2	2.8
12	71573	428158	12	1	0.0409	953221	5200	447716	23077	269.5	12860	0.0204	582.00	580.00	7.37	580.00	4.04	0.9570	3	0	0
13	143146	418827	13	1	0.0856	953221	5200	438189	22931	269.4	12149	0.0182	582.00	580.00	7.37	580.00	4.04	0.9570	3	0	0
14	214719	409268	14	1	0.1016	953221	5200	428413	22764	269.3	11214	0.0163	582.00	580.00	7.37	580.00	4.04	0.9570	3	0	0
15	286292	400127	15	1	0.1081	953221	5200	419051	22589	269.2	10038	0.0146	582.00	580.00	7.37	580.00	4.04	0.9570	3	0	0
16	316764	393911	16	1	0.1174	953221	5200	412734	22520	269.2	9487	0.0140	582.00	580.00	7.37	580.00	4.04	0.9570	3	0	0
17	347237	387593	17	1	0.1253	953221	5200	406321	22456	269.2	8910	0.0134	582.00	580.00	7.37	580.00	4.04	0.9570	3	0	0
18	377709	381146	18	1	0.1322	953221	5200	399782	22395	269.2	8288	0.0128	582.00	580.00	7.37	580.00	4.04	0.9570	3	0	0
19	408181	374651	19	1	0.1383	953221	5200	393201	22340	269.2	7632	0.0122	582.00	580.00	7.37	580.00	4.04	0.9570	3	0	0
20	438654	368059	20	1	0.1437	953221	5200	386561	22322	269.2	7038	0.0115	582.00	580.00	7.37	580.00	4.04	0.9570	3	0	0
21	469126	361424	21	1	0.1485	953221	5200	379869	22295	269.2	6698	0.0108	582.00	580.00	7.37	580.00	4.04	0.9570	3	0	0
22	499599	355467	22	1	0.1514	953221	5200	373872	22282	269.2	6524	0.0099	582.00	580.00	7.37	580.00	4.04	0.9570	3	0	0
23	530071	351243	23	1	0.1506	953221	5200	369630	22282	269.2	6528	0.0090	582.00	580.00	7.37	580.00	4.04	0.9570	3	0	0
24	530077	351267	24	1	0.1506	953221	5200	369629	22257	269.2	6243	0.0091	582.00	580.00	7.37	580.00	4.04	0.9570	3	0	0
25	530083	351290	25	1	0.1505	953221	5200	369628	22233	269.2	5957	0.0091	582.00	580.00	7.37	580.00	4.04	0.9570	3	0	0
26	62845	404526	26	1	0.0901	890691	5200	424046	23160	269.5	12560	0.0194	582.00	580.00	6.11	580.00	3.21	0.9565	2	8.5	14.4
27	125690	396282	27	1	0.1107	890691	5200	415603	23003	269.5	11857	0.0176	582.00	580.00	6.11	580.00	3.21	0.9565	2	8.5	14.4
28	188534	387872	28	1	0.1184	890691	5200	406982	22834	269.4	10981	0.0160	582.00	580.00	6.11	580.00	3.21	0.9565	2	8.5	14.4
29	251379	379769	29	1	0.1210	890691	5200	398668	22663	269.3	9921	0.0145	582.00	580.00	6.11	580.00	3.21	0.9565	2	8.5	14.4
30	281650	373632	30	1	0.1298	890691	5200	392425	22586	269.3	9366	0.0139	582.00	580.00	6.11	580.00	3.21	0.9565	2	8.5	14.4
31	311921	367372	31	1	0.1373	890691	5200	386062	22513	269.3	8781	0.0133	582.00	580.00	6.11	580.00	3.21	0.9565	2	8.5	14.4
32	342193	361008	32	1	0.1437	890691	5200	379601	22444	269.3	8158	0.0127	582.00	580.00	6.11	580.00	3.21	0.9565	2	8.5	14.4
33	372464	354608	33	1	0.1492	890691	5200	373109	22382	269.3	7502	0.0121	582.00	580.00	6.11	580.00	3.21	0.9565	2	8.5	14.4
34	402735	348212	34	1	0.1539	890691	5200	366649	22346	269.3	6812	0.0115	582.00	580.00	6.11	580.00	3.21	0.9565	2	8.5	14.4
35	433006	342085	35	1	0.1573	890691	5200	360434	22285	269.3	6090	0.0108	582.00	580.00	6.11	580.00	3.21	0.9565	2	8.5	14.4
36	463277	336380	36	1	0.1593	890691	5200	354674	22253	269.3	5719	0.0099	582.00	580.00	6.11	580.00	3.21	0.9565	2	8.5	14.4
37	493548	332378	37	1	0.1577	890691	5200	350631	22229	269.3	5444	0.0090	582.00	580.00	6.11	580.00	3.21	0.9565	2	8.5	14.4
38	55184	384687	38	1	0.1269	836875	4861	403752	22467	269.5	12264	0.0186	582.00	580.00	5.02	580.00	2.50	0.9560	1	14.8	27.7
39	110367	377399	39	1	0.1295	836875	4861	396271	22308	269.5	11588	0.0171	582.00	580.00	5.02	580.00	2.50	0.9560	1	14.8	27.7
40	165551	369985	40	1	0.1311	836875	4861	388657	22144	269.5	10780	0.0157	582.00	580.00	5.02	580.00	2.50	0.9560	1	14.8	27.7
41	220734	362795	41	1	0.1309	836875	4861	381269	21979	269.4	9829	0.0144	582.00	580.00	5.02	580.00	2.50	0.9560	1	14.8	27.7
42	250790	356738	42	1	0.1394	836875	4861	375101	21895	269.4	9272	0.0138	582.00	580.00	5.02	580.00	2.50	0.9560	1	14.8	27.7
43	280846	350543	43	1	0.1465	836875	4861	368798	21815	269.4	8684	0.0132	582.00	580.00	5.02	580.00	2.50	0.9560	1	14.8	27.7
44	310902	344270	44	1	0.1525	836875	4861	362423	21740	269.4	8062	0.0126	582.00	580.00	5.02	580.00	2.50	0.9560	1	14.8	27.7
45	340958	337960	45	1	0.1576	836875	4861	356016	21671	269.4	7406	0.0120	582.00	580.00	5.02	580.00	2.50	0.9560	1	14.8	27.7
46	371014	331661	46	1	0.1618	836875	4861	349646	21626	269.4	6719	0.0114	582.00	580.00	5.02	580.00	2.50	0.9560	1	14.8	27.7
47	401070	325668	47	1	0.1646	836875	4861	343560	21559	269.4	6000	0.0107	582.00	580.00	5.02	580.00	2.50	0.9560	1	14.8	27.7
48	431126	320424	48	1	0.1653	836875	4861	338237	21501	269.4	5250	0.0099	582.00	580.00	5.02	580.00	2.50	0.9560	1	14.8	27.7
49	461182	316552	49	1	0.1629	836875	4861	334360	21511	269.4	5957	0.0088	582.00	580.00	5.02	580.00	2.50	0.9560	1	14.8	27.7
50	470702	306808	50	1	0.1803	836875	4861	321361	18306	233.9	4956	0.0089	582.00	580.00	5.02	580.00	2.50	0.9560	3	0	0
51	56409	335967	51	1	0.1322	732622	3931	350734	17473	233.0	11516	0.0170	582.00	580.00	2.92	580.00	1.12	0.9554	1	13.0	22.7
52	112817	328300	52	1	0.1341	732622	3931	342870	17309	233.0	10679	0.0156	582.00	580.00	2.92	580.00	1.12	0.9554	1	13.0	22.7
53	169226	320684	53	1	0.1344	732622	3931	335061	17147	233.0	9699	0.0143	582.00	580.00	2.92	580.00	1.12	0.9554	1	13.1	22.7
54	198723	314767	54	1	0.1442	732622	3931	329041	17067	233.0	9141	0.0137	582.00	580.00	2.92	580.00	1.12	0.9554	1	13.1	22.7
55	228220	308742	55	1	0.1520	732622	3931	322917	16991	233.0	8557	0.0131	582.00	580.00	2.92	580.00	1.12	0.9554	1	13.1	22.7
56	257717	302647	56	1	0.1582	732622	3931	316728	16921	233.0	7943	0.0125	582.00	580.00	2.92	580.00	1.12	0.9554	1	13.1	22.7
57	287213	296513	57	1	0.1633	732622	3931	310506	16857	233.0	7298	0.0119	582.00	580.00	2.92	580.00	1.12	0.9554	1	13.1	22.7
58	316710	290391	58	1	0.1675	732622	3931	304321	16815	233.0	6622	0.0113	582.00	580.00	2.92	580.00	1.12	0.9554	1	13.1	22.7
59	346207	284582	59	1	0.1700	732622	3931	298428	16752	233.0	5917	0.0106	582.00	580.00	2.92	580.00	1.12	0.9554	1	13.1	22.7
60	375704	279576	60	1	0.1699	732622	3931	293351	16699	233.0	5181	0.0098	582.00	580.00	2.92	580.00	1.12	0.9554	1	13.1	22.7
61	405201	276037	61	1	0.1663	732622	3931	289815	16714	233.0	5957	0.0087	582.00	580.00	2.92	580.00	1.12	0.9554	1	13.1	22.7
62	409923	271415	62	1	0.1757	732622	3931	284062	15603	217.8	4419	0.0089	582.00	580.00	2.92	580.00	1.12	0.9554	2	6.8	10.6
63	470698	306789	63	1	0.1804	836875	4861	321362	18326	233.9	5457	0.0089	582.00	580.00	5.02	580.00	2.50	0.9560	3	0	0
64	470695	306771	64	1	0.1804	836875	4861	321364	18346	233.9	5957	0.0089	582.00	580.00	5.02	580.00	2.50	0.9560	3	0	0
65	58128	286239	65	1	0.1380	628369	3000	297465	13205	197.1	10615	0.0155	582.00	580.00	1.15	580.00	0.20	0.9549	1	11.1	18.0
66	116257	278113	66	1	0.1389	628369	3000	289149	13044	197.1	9603	0.0142	582.00	580.00	1.15	580.00	0.20	0.9549	1	11.1	18.1
67	145266	272345	67	1	0.1509	628369	3000	283286	12969	197.1	9052	0.0136	582.00	580.00	1.15	580.00	0.20	0.9549	1	11.1	18.1
68	174275	266460	68	1	0.1595	628369	3000	277310	12897	197.1	8469	0.0130	582.00	580.00	1.15	580.00	0.20	0.9549	1	11.1	18.1
69	203285	260525	69	1	0.1660	628369	3000	271290	12831	197.1	7866	0.0124	582.00	580.00	1.15	580.00	0.20	0.9549	1	11.1	18.1
70	232294	254545	70	1	0.1710	628369	3000	265230	12771	197.1	7232	0.0118	582.00	580.00	1.15	580.00	0.20	0.9549	1	11.1	18.1
71	261303	248569	71	1	0.1749	628369	3000	259197	12732	197.1	6569	0.0112	582.00	580.00	1.15	580.00	0.20	0.9549	1	11.1	18.1
72	290313	242920	72	1	0.1769	628369	3000	253471	12673	197.1	5878	0.0106	582.00	580.00	1.15	580.00	0.20	0.9549	1	11.1	18.1

Table B.2.: Simulations for PQ diagram - part 1.

N	Q_{dh}	P_{net}	Node	Quality	C_v	Q_{boil}	Q_{exp}	P_{brut}	P_{ef}	m_{qw}	m_{fw}	P_{kon}	t_{HP}	t_{RH1}	m_{RH1}	t_{RH2}	m_{RH2}	η_{ked}	Mode	m_{FV9}	m_{FV10}
73	319322	238037	73	1	0.1761	628369	3000	248523	12623	197.1	5159	0.0098	582.00	580.00	1.15	580.00	0.2	0.9549	1	11.1	18.1
74	348331	234590	74	1	0.1713	628369	3000	245086	12642	197.1	5957	0.0087	582.00	580.00	1.15	580.00	0.2	0.9549	1	11.1	18.1
75	352581	230484	75	1	0.1809	628369	3000	240167	11844	184.7	4414	0.0088	582.00	580.00	1.15	580.00	0.2	0.9549	2	5.7	8.4
76	356700	226578	76	1	0.1898	628369	3000	235512	11107	173.1	4414	0.0088	582.00	580.00	1.15	580.00	0.2	0.9549	3	0	0
77	356699	226550	77	1	0.1898	628369	3000	235513	11137	173.1	5186	0.0088	582.00	580.00	1.15	580.00	0.2	0.9549	3	0	0
78	356698	226521	78	1	0.1899	628369	3000	235515	11167	173.1	5957	0.0087	582.00	580.00	1.15	580.00	0.2	0.9549	3	0	0
79	61289	235150	79	1	0.1445	524115	2319	243353	9673	160.7	9555	0.0142	582.00	580.00	0.63	580.00	0	0.9542	1	9.0	13.7
80	90203	229443	80	1	0.1615	524115	2319	237557	9601	160.7	9007	0.0136	582.00	580.00	0.63	580.00	0	0.9542	1	9.0	13.7
81	119116	223620	81	1	0.1712	524115	2319	231649	9532	160.7	8428	0.013	582.00	580.00	0.63	580.00	0	0.9542	1	9.0	13.7
82	148030	217731	82	1	0.1775	524115	2319	225681	9469	160.7	7824	0.0124	582.00	580.00	0.63	580.00	0	0.9542	1	9.0	13.7
83	176944	211802	83	1	0.1820	524115	2319	219679	9411	160.7	7197	0.0118	582.00	580.00	0.63	580.00	0	0.9542	1	9.0	13.7
84	205858	205867	84	1	0.1853	524115	2319	213692	9375	160.7	6541	0.0112	582.00	580.00	0.63	580.00	0	0.9542	1	9.0	13.7
85	234772	200241	85	1	0.1864	524115	2319	207997	9320	160.7	5857	0.0105	582.00	580.00	0.63	580.00	0	0.9542	1	9.0	13.7
86	263686	195386	86	1	0.1844	524115	2319	203083	9272	160.7	5146	0.0098	582.00	580.00	0.63	580.00	0	0.9542	1	9.0	13.7
87	292600	191945	87	1	0.1779	524115	2319	199654	9294	160.7	5957	0.0087	582.00	580.00	0.63	580.00	0	0.9542	1	9.0	13.7
88	296213	188513	88	1	0.1873	524115	2319	195648	8728	151.1	4410	0.0088	582.00	580.00	0.63	580.00	0	0.9542	2	4.5	6.3
89	299608	185317	89	1	0.1959	524115	2319	191940	8225	142.2	4410	0.0088	582.00	580.00	0.63	580.00	0	0.9542	3	0	0
90	299607	185289	90	1	0.1960	524115	2319	191942	8255	142.2	5184	0.0088	582.00	580.00	0.63	580.00	0	0.9542	3	0	0
91	299606	185260	91	1	0.1961	524115	2319	191943	8285	142.2	5957	0.0087	582.00	580.00	0.63	580.00	0	0.9542	3	0	0
92	29645	186407	92	1	0.1928	419862	1638	192461	6974	127.5	9103	0.0137	582.00	572.43	0.10	554.89	0	0.9526	1	7.0	10.0
93	59290	180556	93	1	0.1951	419862	1638	186528	6905	127.5	8516	0.0131	582.00	572.43	0.10	554.89	0	0.9526	1	7.0	10.0
94	88935	174615	94	1	0.1969	419862	1638	180510	6841	127.5	7896	0.0125	582.00	572.43	0.10	554.89	0	0.9526	1	7.0	10.0
95	118580	168631	95	1	0.1981	419862	1638	174456	6784	127.5	7255	0.0119	582.00	572.43	0.10	554.89	0	0.9526	1	7.0	10.0
96	148225	162627	96	1	0.1990	419862	1638	168406	6749	127.5	6586	0.0113	582.00	572.43	0.10	554.89	0	0.9526	1	7.0	10.0
97	177870	156908	97	1	0.1980	419862	1638	162620	6693	127.5	5888	0.0106	582.00	572.43	0.10	554.89	0	0.9526	1	7.0	10.0
98	207515	151967	98	1	0.1935	419862	1638	157622	6647	127.5	5162	0.0098	582.00	572.43	0.10	554.89	0	0.9526	1	7.0	10.0
99	237160	148495	99	1	0.1840	419862	1638	154167	6669	127.5	5957	0.0087	582.00	572.43	0.10	554.89	0	0.9526	1	7.0	10.0
100	240083	145752	100	1	0.1931	419862	1638	151033	6285	120.3	4408	0.0088	582.00	572.43	0.10	554.89	0	0.9526	2	3.5	4.6
101	242770	143227	101	1	0.2014	419862	1638	148180	5962	113.7	4408	0.0088	582.00	572.43	0.10	554.89	0	0.9526	3	0	0
102	242769	143198	102	1	0.2015	419862	1638	148181	5992	113.7	5183	0.0087	582.00	572.43	0.10	554.89	0	0.9526	3	0	0
103	242768	143169	103	1	0.2017	419862	1638	148182	6022	113.7	5957	0.0087	582.00	572.43	0.10	554.89	0	0.9526	3	0	0
104	29645	152772	104	1	0.2529	356730	1225	157844	5651	107.5	8431	0.013	582.00	556.58	0	539.07	0	0.9515	1	5.7	7.9
105	58334	147063	105	1	0.2264	356730	1225	152066	5592	107.5	7832	0.0124	582.00	556.58	0	539.07	0	0.9515	1	5.7	7.9
106	87501	141200	106	1	0.2179	356730	1225	146137	5537	107.5	7198	0.0118	582.00	556.58	0	539.07	0	0.9515	1	5.7	7.9
107	127606	133167	107	1	0.2124	356730	1225	138037	5483	107.5	6288	0.011	582.00	556.58	0	539.07	0	0.9515	1	5.7	7.9
108	145836	129729	108	1	0.2094	356730	1225	134562	5452	107.5	5857	0.0105	582.00	556.58	0	539.07	0	0.9515	1	5.7	7.9
109	175003	124885	109	1	0.2022	356730	1225	129666	5408	107.5	5145	0.0097	582.00	556.58	0	539.07	0	0.9515	1	5.7	7.9
110	204170	121474	110	1	0.1900	356730	1225	126275	5432	107.5	5957	0.0087	582.00	556.58	0	539.07	0	0.9515	1	5.7	7.9
111	206611	119242	111	1	0.1986	356730	1225	123707	5100	101.7	4408	0.0088	582.00	556.58	0	539.07	0	0.9515	2	2.8	3.7
112	208831	117197	112	1	0.2063	356730	1225	121387	4828	96.5	4408	0.0088	582.00	556.58	0	539.07	0	0.9515	3	0	0
113	208830	117168	113	1	0.2064	356730	1225	121389	4859	96.5	5183	0.0087	582.00	556.58	0	539.07	0	0.9515	3	0	0
114	208828	117139	114	1	0.2065	356730	1225	121390	4889	96.5	5957	0.0087	582.00	556.58	0	539.07	0	0.9515	3	0	0
115	34658	115816	115	1	0.2954	293597	813	120188	4599	89.7	7674	0.0123	532.85	521.80	0	506.89	0	0.9491	1	4.6	6.2
116	57764	111233	116	1	0.2566	293597	813	115556	4557	89.7	7167	0.0118	532.85	521.80	0	506.89	0	0.9491	1	4.6	6.2
117	86646	105491	117	1	0.2373	293597	813	109775	4526	89.7	6519	0.0112	532.85	521.80	0	506.89	0	0.9491	1	4.6	6.2
118	115528	100039	118	1	0.2252	293597	813	104266	4476	89.7	5842	0.0105	532.85	521.80	0	506.89	0	0.9491	1	4.6	6.2
119	144410	95295	119	1	0.2130	293597	813	99474	4434	89.7	5139	0.0097	532.85	521.80	0	506.89	0	0.9491	1	4.6	6.2
120	173292	91971	120	1	0.1967	293597	813	96173	4460	89.7	5957	0.0087	532.85	521.80	0	506.89	0	0.9491	1	4.6	6.2
121	175194	90376	121	1	0.2036	293597	813	94208	4092	85.1	4410	0.0088	532.85	521.80	0	506.89	0	0.9491	2	2.2	2.9
122	176957	88896	122	1	0.2100	293597	813	92419	3785	80.9	4410	0.0088	532.85	521.80	0	506.89	0	0.9491	3	0	0
123	176956	88867	123	1	0.2101	293597	813	92420	3815	80.9	5184	0.0087	532.85	521.80	0	506.89	0	0.9491	3	0	0
124	176955	88838	124	1	0.2103	293597	813	92421	3845	80.9	5957	0.0087	532.85	521.80	0	506.89	0	0.9491	3	0	0
125	23392	83829	125	1	0.4073	230465	400	87822	3848	70.6	7180	0.0119	507.21	484.76	0	478.62	0	0.9453	1	3.4	4.4
126	46784	79273	126	1	0.3010	230465	400	83242	3828	70.6	6658	0.0113	507.21	484.76	0	478.62	0	0.9453	1	3.4	4.4
127	70176	74787	127	1	0.2646	230465	400	78710	3787	70.6	6124	0.0108	507.21	484.76	0	478.62	0	0.9453	1	3.4	4.4
128	93568	70700	128	1	0.2421	230465	400	74583	3751	70.6	5570	0.0102	507.21	484.76	0	478.62	0	0.9453	1	3.4	4.4
129	116961	67090	129	1	0.2246	230465	400	70939	3720	70.6	4999	0.0095	507.21	484.76	0	478.62	0	0.9453	1	3.4	4.4
130	140353	64578	130	1	0.2050	230465	400	68459	3754	70.6	5957	0.0087	507.21	484.76	0	478.62	0	0.9453	1	3.4	4.4
131	141832	63623	131	1	0.2096	230465	400	66996	3247	67.2	4412	0.0088	507.21	484.76	0	478.62	0	0.9453	2	1.6	2.1
132	143156	62764	132	1	0.2137	230465	400	65689	2800	64.2	4412	0.0088	507.21	484.76	0	478.62	0	0.9453	3	0	0
133	143155	62735	133	1	0.2139	230465	400	65690	2830	64.2	5185	0.0087	507.21	484.76	0	478.62	0	0.9453	3	0	0
134	143154	62706	134	1	0.2141	230465	400	65691	2860	64.2	5957	0.0087	507.21	484.76	0	478.62	0	0.9453	3	0	0
135	17222	53837	135	1	0.5391	167332	0	57724	3367	49.0	6425	0.0112	514.64	498.14	0	483.29	0	0.9335	1	2.1	2.7
136	34443	50626	136	1	0.3628	167332	0	54482	3339	49.0	6042	0.0108	514.64	498.14	0	483.29	0	0.9335	1	2.1	2.7
137	51665	47446	137	1	0.3034	167332	0	51276	3314	49.0	5649	0.0103	514.64	498.14	0	483.29	0	0.9335	1	2.1	2.7
138	68887	44473	138	1	0.2707	167332	0	48278	3291	49.0	5247	0.0099	514.64	498.14	0	483.29	0	0.9335	1	2.1	2.7
139	86108	41898	139	1	0.2465	167332	0	45682	3272	49.0	4835	0.0094	514.64	498.14	0	483.29	0	0.9335	1	2.1	2.7
140	103330	40120	140	1	0.2226	167332	0	43946	3315	49.0	5957	0.0087	514.64	498.14	0	483.29	0	0.9335	1	2.1	2.7
141	104298	39837	141	1	0.2232	167332	0	43006	2658	46.9	4415	0.0088	514.64	498.14	0	483.29	0	0.9335	2	1.0	1.3
142	105170	39589	142	1	0.2238	167332	0	42161	2061	45.0	4414	0.0088	514.64	498.14	0	483.29	0	0.9335	3	0	0
143	105169	39561	143	1	0.2240	167332	0	42162	2091	45.0	5186	0.0087	514.64	498.14	0	483.29	0	0.9335	3	0	0
144	105168	39532	144	1	0.2243	167332	0	42163	2121	45.0	5957	0.0087	514.64	498.14	0	483.29	0	0.9335	3	0	0

Table B.3.: Simulations for PQ diagram - part 2.

C. Fin cross sectional area in rifled pipe

In this appendix is outlined the net cross section area of an IRBT. The cross section of a fin is illustrated in figure (C.1). The number of fins are defined as N_f, were a single fin cross sectional area can defined by the below equations, referring to figure (C.1) (illustration A-C).
By inserting R_{tot} and h_f in the Pythagoras relation of figure (C.1) (illustration B), we have:

$$l_4^2 = (R_{tot} - h_f)^2 + 1/4b_f^2 \tag{C.1}$$

From figure (C.1) (illustration B) we can see that the maximum internal radius (R_{tot}) can be expressed by l_1 and l_4

$$R_{tot} = l_1 + l_4 \tag{C.2}$$

Additionally, we have the following relationship for determine l_5, see figure (C.1) B.

$$l_4^2 = l_5^2 + \left(\frac{l_2}{2}\right)^2 \tag{C.3}$$

From figure (C.1) (illustration C), the length l_2 can be expressed by the law of sines:

$$\frac{\sin(\beta)}{l_2} = \frac{\sin(\frac{\pi}{2} + \alpha_1)}{l_3} = \frac{\cos(\alpha_1 + \beta)}{l_1} \tag{C.4}$$

With $\cos(\alpha_1) = l_5/l_4$ and $\sin(\alpha_1) = l_2/(2 \cdot l_4)$ we find:

$$\frac{\sin(\beta)}{l_2} = \frac{\cos(\alpha_1)\cos(\beta) - \sin(\alpha_1)\sin(\beta)}{l_1} = \frac{l_1 \cdot l_2 \cdot l_5}{2 \cdot l_4} \tag{C.5}$$

The rifle cross sectional area (A_c) can now be calculated as:

$$\begin{aligned} A_c &= 2\left(\frac{\alpha}{2\pi} R_{tot}^2 \pi - (A_1 + A_2 + A_3)\right) \\ &= \alpha R_{tot}^2 - 2(A_1 + A_2 + A_3) \end{aligned} \tag{C.6}$$

C. Fin cross sectional area in rifled pipe

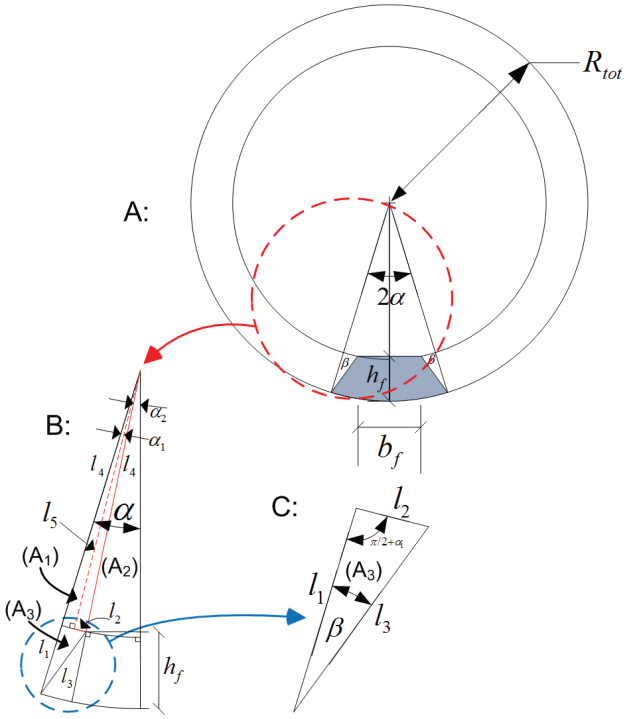

Figure C.1.: Sketch of the fin area in a rifled boiler tube.

where A_1 to A_3 are illustrated in figure (C.1):

$$A_1 = \frac{l_2 \cdot l_5}{4} \tag{C.7}$$

$$A_2 = \frac{b_f \cdot (R_{tot} - h_f)}{4} \tag{C.8}$$

$$\begin{aligned} A_3 &= \frac{l_1 l_3 \sin(\beta)}{2} \\ &= \frac{l_1 \cdot l_2 \cdot l_5}{2 \cdot l_4} \end{aligned} \tag{C.9}$$

The rifles are reducing the cross sectional area of the pipe with the below factor ζ

$$\begin{aligned}\zeta &= \frac{R_{tot}^2\pi - N_f A_c}{R_{tot}^2\pi} \\ &= 1 - \frac{N_f \alpha R_{tot}^2 - 2N_f(A_1 + A_2 + A_3)}{R_{tot}^2\pi} \\ &= 1 - N_f\frac{\alpha}{\pi} + 2N_f\frac{A_1 + A_2 + A_3}{R_{tot}^2\pi}\end{aligned} \tag{C.10}$$

and the hydraulic diameter R is:

$$R = R_{tot}\sqrt{\zeta} \tag{C.11}$$

The angel α is determined by adding two angles (α_1 and α_2), which is given by equation (C.12) and (C.13).

$$l_4\cos(\alpha_1) = l_5 \tag{C.12}$$

$$l_4\cos(\alpha_2) = R_{tot} - h_f \tag{C.13}$$

From C.1 we have:

$$\alpha = 2\alpha_1 + \alpha_2 \tag{C.14}$$

For a typical rifled boiler tube (RR5), we have the below data:

$$\begin{aligned}N_f &= 6 \\ R_{tot} &= 14mm \\ h_f &= 1mm \\ b_f &= 4mm \\ \beta &= 10^o = 0.174533 \\ l_p &= 100mm\end{aligned} \tag{C.15}$$

(C.16)

which gives a cross section reduction factor of ζ=0.8546 (by use of EES) and a corresponding hydraulic pipe diameter of R=12.94 mm.

D. Estimation of lifetime

A simple approach for calculation consumed lifetime in a heat tube is based on a stepwise calculation of the stresses in the material, which exceeds the rupture stress at the averaged service temperature of the material. The calculation is using time steps of typically 100-1000 hours and material stress is calculated according to equation (D.1), where r_i=$r_{i_{t=0}}$-c·t is the distance from the centre to tube inner surface, given in [m], r_o=$r_{o_{t=0}}$+x is the distance from the centre to tube surface, given in [m], where x is the material loss due to oxidation [m] and where $r_{i_{t=0}}$ and $r_{o_{t=0}}$ are the distances from the centre of the pipe to inner surface and outer surface respectively at time = 0, both given in [m]. The operational pressure p is given in [N/mm^2]:

$$\sigma_{material} = p\frac{r_i + r_o}{2(r_o - r_i)} \tag{D.1}$$

where the rupture time is given by equation (D.2). Here is A a constant and n is the Norton exponent

$$t_{rupture} = A \cdot \sigma^{-n} \ \text{[hours]} \tag{D.2}$$

The secondary creep rate ε' is given as

$$\varepsilon' = B\sigma^n \tag{D.3}$$

where B=C/A and

$$\varepsilon' \cdot t_{rupture} = C \tag{D.4}$$

The temperature dependant Norton constant n is derived from equation (D.5) and (D.6) as the slope of the Wler curve.

$$n = \frac{\ln(10^5) - \ln(10^4)}{\ln(\sigma_{rupture(10^5)}) - \ln(\sigma_{rupture(10^4)})} \tag{D.5}$$

$$A = 10^5 \cdot \sigma^n_{rupture(10^5)} \tag{D.6}$$

where $\sigma_{rupture(10^4)}$ and $\sigma_{rupture(10^5)}$ are the rupture stress at 10^4 and 10^5 [h] respectively, given in [N/mm^2]. After each time step (Δt_i), the accumulated consumed *lifttime fraction* (LTF) defined by equation (D.7) is calculated.

$$LTF = \sum_i \frac{\Delta t_i}{t_{rupture_i}} \tag{D.7}$$

and the corresponding life time t_{life} is defined as: $t_{life} = \sum_i \Delta t_i$ for LTF = 1. With time the temperature in the heat pipe will increase due to steam oxide formation, as the oxide film constitutes a significant resistance against heat transfer, which can be estimated by the detailed wall model, given by equation (4.4) or by the simple overall heat transfer coefficient (4.25). This process is self-supporting as higher material temperature lead to higher oxidation rate.

Apart from its impact on corrosion and creep, steam side oxidation may in itself constitute a problem. Thick magnetite films may exfoliate causing blocking of the heat pipes and valves resulting in reduced flow and elevated pressure drop. Furthermore, magnetite particles may cause erosion of the turbines. Typical data for a life cycle analysis is given in table (D.1), taken from [26]. We are referring

Table D.1.: Reference data for super heaters, taken from [26].

Reference data	**Unit**	**PF-USC**	**PFBC-USC**
Inside diameter, $(2r_{i_0})$	mm	22	22
Thickness, $(r_{o_0} - r_{i_0})$	mm	8	8
Material		347H FG	347H FG
Pressure, (p)	bar	295	295
Corrosion rate, (c)	$mm/10^5$	2	2
Steam temperature, (T_{steam})	^oC	590	590
heat transfer coeff. - steam side (α_i)	$kW/m^2 \cdot K$	5	5
Heat conductivity, metal (λ_{metal})	$W/m \cdot K$	24.9	24.9
Oxide conductivity (λ_{oxide})	$W/m \cdot K$	1.0	1.0
Heat flux, outer surface $(\dot{q})$	kW/m^2	$20-30$	$80-100$

to [26] for a detailed description of steam oxidation constants and thermal conductivity of the oxide film as function of temperature. There has been carried out a lifetime assessment, see [28], for two samples taken at Avedøreværket unit 1 (AVV1), at two different locations inside the boiler. The first sample 1 is taken at elevation 27.6 [m] and sample 3 is taken at elevation 21.6 [m]. Both samples are made on the west wall, approx. 3.5 [m] from the back wall. The operating time was 148000 hours, with inlet conditions: T_{steam} = 347 [^oC] and p = 292 [bar] and outlet conditions: T_{steam} = 406 ^oC] and p = 283 [bar]. Vapour quantity was 215 [kg/s] and heat flux at sample 1 was estimated to q_1 = is 108 [kW/m^2] and q_2 = was 292 [kW/m^2]. The lifetime simulations, based on the outlined theory in this chapter, is illustrated in figure (D.1). Assessing the lifetime of the sample 1 and 3 shows, that the lifetime is determined by the sample 3. An acidification

of the evaporator is expected to be carried out after180000 hours of operation (4.5 years) with 7000 hours of operation / year. By acidification is the oxide layer

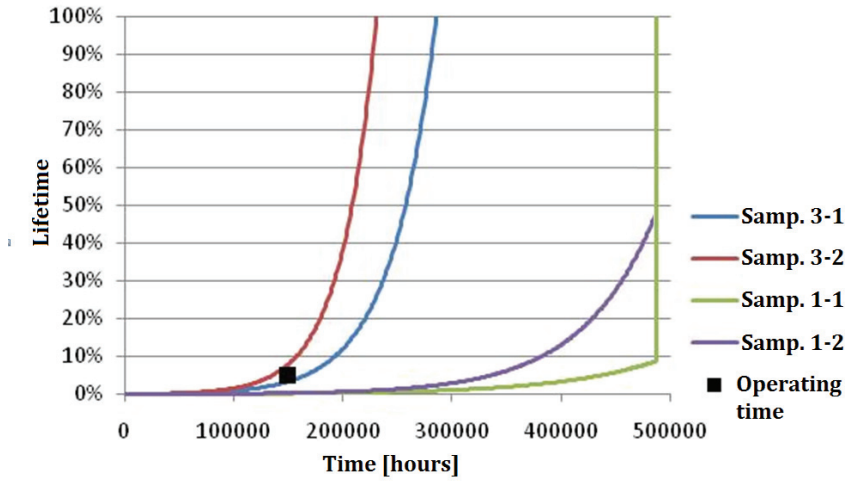

Figure D.1.: Input for lifetime calculations are oxidation, corrosion rate, creep data and operating data. Data from DONG Energy - confidential internal report, [28].

and iron deposits removed and the metal temperature is lowered to the starting point.

E. Pressure drop and heat transfer for internal two phase flows in pipes

In this appendix is derived the classical formula that reflects pressure drop and heat transfer for internal two phase flows in pipes.

E.1. Pressure loss in two phase flows in pipes

In the following, is the empirical relationships derived, which is used to calculate both the friction-, gravity- and acceleration pressure drop in the two phase flow.

E.1.1. Acceleration pressure loss

The acceleration pressure loss can be expressed as

$$\left(\frac{\partial \bar{p}}{\partial z}\right)_a = -G^2 \frac{\partial}{\partial z}\left(\frac{1}{\rho'}\right) \tag{E.1}$$

Note that ρ' is the momentum density defined by (E.4). Hence the momentum change or acceleration pressure drop ΔP_a is

$$\begin{aligned} \Delta P_a &= \int_0^L \left(\frac{\partial \bar{p}}{\partial z}\right)_a dz \\ &= \frac{\dot{m}^2}{A^2} \int_0^L \frac{\partial}{\partial z}\left(\frac{1}{\rho'}\right) \\ &= \frac{\dot{m}^2}{A^2}\left(\frac{1}{\rho'_{out}} - \frac{1}{\rho'_{in}}\right) \end{aligned} \tag{E.2}$$

The acceleration drop between two cross sections, 1 and 2, of a pipe is calculated from the change in mean density of the mixture:

$$\Delta p_A = \left(\frac{\dot{m}}{A}\right) \cdot \left(\frac{1}{\bar{\rho}_2} - \frac{1}{\bar{\rho}_1}\right) \tag{E.3}$$

where the mixture density is evaluated using the momentum density, [5]:

$$\rho' = \left(\frac{x^2}{\rho_g \varepsilon} + \frac{(1-x)^2}{\rho_l (1-\varepsilon)}\right)^{-1} \tag{E.4}$$

E.1.2. Gravitational pressure loss

The gravitational pressure drop can be estimated, if we know the distribution of the density along the pipe length axis

$$\begin{aligned}\Delta P_g &= \int_0^L \left(\frac{\partial \bar{p}}{\partial z}\right)_g dz \\ &= g\cos\theta\bar{\rho}_m \\ &= g\cos\theta\sum_{i=1}^{N}\frac{\bar{\rho}_i}{N}\end{aligned} \tag{E.5}$$

It assumes an expression for the mean density, that in a simple manner can be calculated as a mean value of the in- and outlet density, or the heat pipe element can be modelled is N sub-elements, so that we can take into account a non-uniform flux distribution. The change in hydrostatic pressure due to elevation change can also be calculated from:

$$\Delta p_G = (\rho_l \cdot (1-\varepsilon) + \rho_g \cdot \varepsilon)) \cdot g \cdot \Delta h \tag{E.6}$$

In [5], the volume fraction of vapour in the mixture is calculated from Rouhani:

$$\varepsilon = \left(\frac{C_0}{\bar{\varepsilon}} + \frac{\rho_g \cdot u_{gj}}{x \cdot \left(\frac{\dot{m}}{A}\right)}\right)^{-1} \tag{E.7}$$

Where

$$C_0 = 1 + 0.2 \cdot (1-x) \cdot \left(\frac{(g \cdot D)^{0.25} \cdot \rho_l^{0.25}}{\left(\frac{\dot{m}}{A}\right)}\right) \tag{E.8}$$

$$u_{gj} = 1.18 \cdot [g \cdot \sigma \cdot (\rho_l - \rho g)]^{0.25} \cdot \frac{(1-x)}{\sqrt{\rho_l}} \tag{E.9}$$

$$\bar{\varepsilon} = \frac{\rho_l \cdot x}{\rho_l \cdot x + (\rho_g \cdot (1-x))} \tag{E.10}$$

In the model of [77] the volume fraction of vapour, ε, is calculated as:

$$\varepsilon = \frac{x}{\frac{\rho_g}{\rho l}\sigma + x\left(1 - \frac{\rho_g}{\rho_l \sigma}\right)} \tag{E.11}$$

Where the slip parameter, σ, is evaluated from:

$$\sigma = 10^{0.031636+\left(0.07773+0.51306\cdot\log\frac{\rho_l}{\rho_g}\right)\cdot\log\frac{\rho_l}{\rho_g}} \text{ for 5 bara < p < 10 bara} \quad \text{(E.12)}$$

If the pressure p exceeds 190 [bar] we make an adjustment

$$\text{if p} > 190 : \sigma = \sigma - (\sigma - 1.0)\cdot(p - 190.0)/31.2 \quad \text{(E.13)}$$

where p is given in [bar].

E.1.3. Friction pressure loss

The friction pressure loss can in a similar manner be estimated as

$$\begin{aligned}\Delta P_f &= -F_w \\ &= -f_D \frac{G^2}{2 d_i \bar{\rho}_m}\end{aligned} \quad \text{(E.14)}$$

The heat pipe models pressure drop for a fluid flowing through a one-dimensional pipe of circular cross section. The theory is well established and may be found in ref. [5]. The frictional pressure loss is calculated by the general formula

$$\Delta P_f = \frac{1}{2}\rho v^2 \left(f\left(\mathrm{Re}, \varepsilon\right) \frac{L}{d_i} + \sum_k \eta_k \right) \quad \text{(E.15)}$$

where ρ is density (mkg), v is mean velocity (ms), L is length of the pipe (m), d_i is the inner diameter of the pipe (m), f is the Darcy-Weisbach loss factor (-) and η_k is the is the discrete loss factor of change no. k of the pipe structure like a bend or change of cross sectional area. Discrete loss factors may be found in ref. [5], DIN-norm, or equivalent. For non-circular pipes is the hydraulic diameter, d_h, defined as 4 times the ratio of the cross sectional area to the wetted periphery (S):

$$d_h = 4\frac{A}{S} \quad \text{(E.16)}$$

The basic assumptions of a homogeneous model are: 1) equal linear velocities of vapour and fluid, 2) thermodynamic equilibrium between the two phases, and 3) a suitably defined single-phase friction- and heat transfer factor is applicable to the two-phase flow. The homogeneous mixture model performs reasonable well, when the two phase flow pattern represents a well-mixed configuration like dispersed bubbly flow, but for flow patterns like slug flow and stratified flow, with flow regime transitions, empirical correlations remain the most widely applied method to estimate the friction pressure loss in a two phase flow. Most empirical

correlations use the concept of two-phase multipliers and are applied to all flow regimes. The concept is described many places in the literature, including [40]. In general it is based on the relationship

$$\left(\frac{\partial P}{\partial z}\right)_f = \frac{4}{d_i} f_w \bar{\rho} u^2 \tag{E.17}$$

The term f_w is the dimensionless coefficient based on the Darcy friction factor. It can be found from a Moody diagram or more precisely by solving the Colebrook equation:

$$f_w : \begin{cases} \frac{1}{\sqrt{f_w}} = -2\log_{10}\left(\frac{k}{3.7\ d_i} + \frac{2.51}{Re\ \sqrt{f_w}}\right) & \text{for } Re > 4000 \\ \\ f_w = \frac{64}{Re} & \text{for } Re \leq 2000 \end{cases} \tag{E.18}$$

where k is the pipe inner roughness thickness, measured in meter and the Reynolds number, Re is given by: Re=Gd_i/μ and G=$\bar{\rho} \cdot u$. In the two-phase region the friction factor is adjusted according to a two-phase multiplier, formulated by [77]. A more simple expression for turbulent flow is the Blasius' correlation for the Fanning friction factor

$$f = 0.079 \cdot Re^{-1/4} \tag{E.19}$$

Now we formulate the homogeneous two-phase friction pressure loss as

$$\left(\frac{\partial P}{\partial z}\right)_f = \frac{4}{d_i}\ f_{TP}\ \bar{\rho}_{TP}\ u^2 \tag{E.20}$$

where

$$f_{TP} = 0.079 \cdot Re_{TP}^{-1/4} \tag{E.21}$$

with

$$Re_{TP} = \frac{G d_i}{\mu_{TP}} \tag{E.22}$$

and

$$\rho_{TP} = \left(\frac{x}{\rho_g} + \frac{1-x}{\rho_l}\right)^{-1} \tag{E.23}$$

Hence an appropriate estimate for μ_{TP} is a simple correlation for the dynamic viscosity of a homogeneous gas-liquid two phase mixture

$$\mu_{TP} = \left(\frac{x}{\mu_g} + \frac{1-x}{\mu_l} \right)^{-1} \tag{E.24}$$

Inserting equation (E.21) and (E.23) in equation (E.20) we get a method to provide the friction pressure drop calculation

$$\left(-\frac{\partial P}{\partial z} \right)_f = \Phi^2 \cdot \left(-\frac{\partial P}{\partial z} \right)_{f,L} \tag{E.25}$$

The right hand side pressure gradient is single-phase flow based and correspond to a mixture of pure liquid. The parameter Φ^2 is the two phase multiplier. When we let the multiplier refer to pure liquid phase flow, we find

$$\left(-\frac{\partial P}{\partial z} \right)_{f,L} = -0.079 \cdot \left(\frac{G d_i}{\mu_L} \right)^{-1/4} \frac{4}{d_i} \frac{G^2}{\rho_L} \tag{E.26}$$

Hence Φ^2 is given as

$$\Phi^2 = \left[1 + x \frac{\mu_L - \mu_G}{\mu_G} \right]^{-1/4} \cdot \left[1 + x \frac{\rho_L - \rho_G}{\rho_G} \right] \tag{E.27}$$

Several empirical estimations of the loss factor f are available (see [40], [97], [141] and [142]. For dynamic studies, the Churchill-equation is favoured due to its explicit form and the smooth transition from laminar to turbulent flow regimes. This comes at a cost but possesses potential savings by fine tuning the implementation. The calculation is shown below.

$$f = 8 \left[\left(\frac{8}{\mathrm{Re}} \right)^{12} + \frac{1}{(B+C)^{1.5}} \right]^{\frac{1}{12}} \tag{E.28}$$

$$C = \left(\frac{37350}{\mathrm{Re}} \right)^{16} \tag{E.29}$$

$$B = \left(2.457 \ln \left(\frac{1}{A} \right) \right)^{16} \tag{E.30}$$

$$A = \left(\frac{7}{\mathrm{Re}} \right)^{0.9} + \frac{0.27k}{d_i} \tag{E.31}$$

$$\tag{E.32}$$

where

k is the absolute roughness (m)

Re is is the Reynold's number $(-)$

The Churchill equation is illustrated in figure (E.1). A transition zone can be advantageously implemented such that a monotonic decreasing function of C^1 is established, in order to prevent undesired pressure fluctuations in the model, The transition zone can be modelled as listed in table (G.1) with n=2. The loss

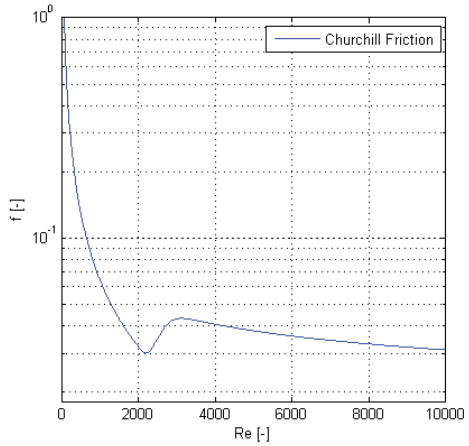

Figure E.1.: Churchill friction factor as function of Re.

factor f is formulated using the kinetic energy flow rate and thus the average axial velocity v. The mass flow rate to the pipe section relates to velocity by the simple relation

$$m = \rho A v = \rho \left(\frac{\pi}{4} d_h^2 \right) v \tag{E.33}$$

where d_h is the hydraulic diameter. Thus equation (E.15) may be rewritten as

$$\Delta p_f = \frac{8}{\pi} \frac{m}{\rho d_h^4} \left(f\left(\mathrm{Re}, \varepsilon\right) \frac{L}{d_h} + \sum_k \eta_k \right) \tag{E.34}$$

For gas-liquid two phase flows, the frictional pressure drop is evaluated based on the method proposed by Martinelli, where the frictional pressure drop for the mixture is a product of the frictional pressure drop for one phase, Δp_f, and a two-phase multiplier, ϕ:

$$\Delta p_{2p} = \Delta p_{f,i} \cdot \phi_i^2 \tag{E.35}$$

Where i indicates that the single phase pressure drop is evaluated on the liquid phase or the gas phase. In case there are minor losses from fittings, valves, bends etc., the total frictional pressure drop becomes:

$$\Delta p_{2p} = \left(\Delta p_{f,i} + 1.5 \cdot \eta \cdot \frac{1}{2} \frac{\dot{m}^2}{A^2 \cdot \rho_i} \right) \cdot \phi_i^2 \tag{E.36}$$

Where η is the minor loss coefficient for single phase flow, and $\dot{m}^2$ is the total mass flux squared. The model by Friedel (as referred in [143]), which appears to be the most accurate method available at this time, calculates the two phase multiplier for $\Delta p_{f,i}$ being liquid (i=l). For horizontal flow configuration we have:

$$\begin{aligned} \phi^2 \quad &= A + 3.24 \cdot x^{0.78} (1-x)^{0.224} \cdot \left(\frac{\rho_f}{\rho_g} \right)^{0.91} \\ &\cdot \left(\frac{\mu_g}{\mu_f} \right)^{0.19} \left(1 - \frac{\mu_g}{\mu_f} \right)^{0.7} \cdot Fr_{\text{hom}}^{-0.045} \cdot We_l^{-0.035} \end{aligned} \tag{E.37}$$

and for vertical, downward flow, Friedel's correlation gives

$$\begin{aligned} \phi^2 \quad &= A + 48.6 \cdot x^{0.8} (1-x)^{0.29} \cdot \left(\frac{\rho_f}{\rho_g} \right)^{0.90} \\ &\cdot \left(\frac{\mu_g}{\mu_f} \right)^{0.73} \left(1 - \frac{\mu_g}{\mu_f} \right)^{7.4} \cdot Fr_{\text{hom}}^{0.03} \cdot We_l^{-0.12} \end{aligned} \tag{E.38}$$

where A=$(1-x)^2 + x^2 \cdot \frac{f_g}{f_l} \cdot \frac{\rho_l}{\rho g}$. This model is only valid for $\frac{\mu_l}{\mu_g} > 1000$. The friction factor for gas (g) or liquid (l) only are:

$$f_j = 0.079 \cdot \text{Re}_j^{-0.25}, \quad \text{j} \in [g, l] \tag{E.39}$$

The Froude and Weber numbers are found from:

$$\bar{Fr} = \frac{\left(\frac{\dot{m}}{A} \right)^2}{g \cdot \bar{\rho}^2 D} \tag{E.40}$$

and

$$We_i = \frac{D \cdot \left(\frac{\dot{m}}{A} \right)^2}{\sigma \cdot \bar{\rho}} \tag{E.41}$$

The model is general for both IAPWS, IFC67 and IF97. The only minor difference is the critical temperature for the two steam tables. The model that is based on Jirous, [77] calculates the two phase multiplier as:

$$\phi^2 = 1 + B \cdot x \cdot \left(\frac{\rho_l}{\rho f} - 1 \right) \tag{E.42}$$

Where the coefficient B is:

$$B = 1.58 - 0.47 \frac{p}{p_c} - 0.11 \cdot \left(\frac{p}{p_c} \right)^2 \tag{E.43}$$

Note that the critical pressure (p_c) is 221.2 [bar] for water/steam. If x > 0.9 is carried out an adjustment of B:

$$\text{if x} > 0.9 : B = B - (B-1) \cdot (10 \cdot x - 9) \tag{E.44}$$

The void fraction α is given as

$$\alpha = x/(\sigma/\rho_{lg} + x \cdot (1.0 - \sigma/)\rho_{lg}) \tag{E.45}$$

where $\rho_{lg} = \rho_l/\rho_g$ and the surface tension is given by equation (E.66). The correlation of (E.42) is compared to the well-known and more computation intensive model of Friedel and is illustrated in figure (E.2).

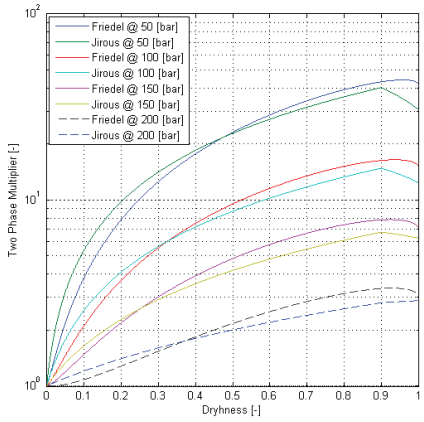

Figure E.2.: Comparison of two-phase-multipliers of Jirous and Friedel.

E.2. Heat transfer with phase change inside tubes

The vaporization inside tubes involves a number of different flow regimes, see figure (E.4), each of which requires a different evaluation of the heat transfer coefficient plus a local temperature difference, which in turn requires corresponding pressure drop calculations. Below is listed the various equations used for the design of vertical in tube vaporizers. Although horizontal in-tube vaporization is also used, the heat transfer equations and methods are the same, but the flow pattern now includes a stratified two-layer region. The major difference between horizontal and vertical in-tube vaporization is the definition of and the flow criteria used to define the limits of each regime. The appropriate heat transfer equation is then used for each regime.

E.2.1. Single phase liquid region.

In a circulating vaporizer the temperature of the liquid entering the tube is below the local boiling point due to the effect of the hydrostatic head on the saturation temperature. This temperature difference is called *Approach point* and is the difference between saturation temperature and feed water temperature entering the evaporator. This liquid zone extends to the point where the temperature has increased and the local pressure decreased, such that the local saturation point has been reached. Actually some further superheat is required to initiate nucleation. The liquid zone heat transfer coefficients are calculated from [144]:

$$\begin{aligned} Nu_c &= \frac{h_c d_i}{k_l} \\ &= 0.17 \left(\frac{d_i G}{\mu_l}\right)^{0.33} \left(\frac{\mu_l}{k_l}\right)^{0.43} \left(\frac{Pr_l}{Pr_w}\right)^{0.25} \left(\frac{d_i^3 \rho_l^2 g \beta \Delta T}{\mu_l^2}\right)^{0.1} \end{aligned} \tag{E.46}$$

for $L/d_i > 50$ and $\frac{d_i G}{\mu} < 2000$. For turbulent flow and $\frac{d_i G}{\mu} > 10{,}000$ use from [25]:

$$Nu_c = 0.023 {Re_l}^{0.8} {Pr_l}^{1/3} \tag{E.47}$$

where Re_l and Pr_l are given in A.14 and A.11 respectively and spline interpolate, with boundaries given by equation (G.20), between these two equations on a Re number basis for $2000 < Re < 10{,}000$ and their corresponding slopes.

E.2.2. Boiling region.

The boiling region can be further subdivided into a sub cooled boiling, saturated boiling, and two-phase boiling regions with predictive equations for each [141]

and [142]. Another approach taken by Chen [145] is to combine the saturated and two-phase regions into one, with an equation combining the convective and nucleate boiling mechanisms

$$h_b = Sh_{nb} + h_{cb} \tag{E.48}$$

where h_b is the boiling coefficient, h_{nb} is the nucleate boiling coefficient and h_{cb} is the convective coefficient, all measured in [W/m^2]. The coefficient S is named the Chen suppression factor after [145].
The convective coefficient is a function of the Martinelli two-phase flow parameter, X_{tt}, and the Chen correlation using this factor is

$$\begin{aligned} \frac{h_{cb}}{h_c} &= f(X_{tt}) \\ &= F_{ch} \end{aligned} \tag{E.49}$$

where

$$F_{ch} = 2.35\left[\frac{1}{X_{tt}} + 0.213\right]^{0.73} \tag{E.50}$$

and

$$X_{tt} = \frac{1-x}{x}\left(\frac{\rho_v}{\rho_l}\right)^{0.57}\left(\frac{\mu_l}{\mu_v}\right)^{0.11} \tag{E.51}$$

here x is the weight fraction of vapour measured in [kg/kg], ρ_j, μ_j, where (j∈[l,v]) is the density and dynamic viscosity for liquid and vapour respectively and h_c is the liquid phase heat transfer coefficient based on the amount of liquid present by equation (E.64). The nucleate boiling coefficient, h_{nb}, is determined as

$$h_{nb} = h_{nbl}F_m \tag{E.52}$$

where F_m is a correction applied for mixtures and h_{nbl} is the coefficient determined from the Nucleate Pool boiling model, given by

$$h_{nb} = A^* q^{0.7} F(P_r) \tag{E.53}$$

Note that A^* is a constant evaluated at a reference reduced pressure of $P_r = 0.0294$ and F(P_r) is a function of reduced pressure. The Chen suppression factor, S, is determined as follows:

$$S = \frac{1}{0.1 + 2.53 \cdot 10^{-6} Re^{1.17}} \tag{E.54}$$

where the two phase Reynolds number Re_{tp} is given as

$$Re_{tp} = Re_l F_{ch}^{1.17} \quad \text{and} \quad Re_l = \frac{d_i G}{\mu_l} \tag{E.55}$$

Hence equation (E.48) can be solved for h_b. The sub cooled boiling coefficient can be obtained by again using equation (E.48) but with S = ($\Delta T_b/\Delta T_0$) where ΔT_b is the temperature difference between the tube wall and the saturation temperature of the liquid at the given local pressure and ΔT_0 is the difference between the tube wall and sub cooled bulk temperature. Instead of the convective coefficient, h_{nbl}, the liquid coefficient (eqn. E.63 or E.64) is used. The nucleate coefficient, h_{nbl}, is obtained from the transformed equation (E.53) as

$$h_{nbl} = 5.43 \cdot 10^{-8} P_c^{2.3} \Delta T^{2.33} F(P)^{3.33} \tag{E.56}$$

and equation (E.57) changed to (E.52) where F_m is given by a mixture correction factor, used to modify the calculated coefficient of the volatile component h_{nbl}, determined from equation (E.57) so that the mixture coefficient is given by the product of h_{nbl} and F_m where

$$F_m = exp(-0.015 B_R) \tag{E.57}$$

where B_R is the boiling range, dew point-bubble point, with a lower limit of $0.1^o C$.

E.2.3. Mist flow.

In mist flow the small amount of remaining liquid is entrained as droplets and the tube wall is essentially dry. The heat transfer coefficient drops rapidly and approaches that of heat transfer to gas. In this regime sensible heat is transferred to the gas which in turn transfers some of the heat to the droplets until they are completely evaporated after which only sensible heat transfer to gas occurs. The main problem is the determination of the vapour temperature, hence, temperature difference. Two extreme conditions are: (1) no heat is transferred to the droplets hence the vapour temperature rises rapidly; and (2) heat is rapidly transferred to the droplets until they disappear and during this evaporation phase, the vapour is at saturation temperature. Condition (1) is approached at low pressures and

velocities and condition (2) at high pressure and velocities. The actual case is somewhere between (1) and (2). Some attempts to develop empirical and theory based equations are reported in [142] but the range of data seem too limited. We would recommend to use an equation like (E.64) based on gas properties and then make an engineering judgement guess of the fraction of the sensible heat transferred to the gas that is used up as latent heat for the evaporation of drops. The resulting effect on vapour temperature could be used to calculate an LMTD for the mist region and with the calculated gas coefficient used to determine the heat flux. The mist region can be determined from a Fair map [146] or from the simple equation derived from this map

$$G_{mm} = 21.07 X_{tt} \tag{E.58}$$

where G_{mm} is measured in SI units and expresses the maximum mass velocity before mist flow begins.

E.2.4. Film boiling.

This type of boiling should be avoided, if possible, due to control problems, possible fouling, and lack of data on pressure drop calculations. But if the temperature difference is high enough over the entire tube length, then the heat transfer coefficient can be calculated by the correlation given by [147]:

$$Nu = 0.106 Re^{0.64} Pr^{0.4} (\rho_b/\rho_v)^{0.5} \tag{E.59}$$

where the bulk average density on a no slip basis is

$$\rho_b = \frac{\rho_l}{x(\frac{\rho_l}{\rho_v} - 1) + 1} \tag{E.60}$$

Properties in equation (E.59) are based on the liquid. However, the main problem is to determine the mass velocity, G. In film boiling inside a tube, we have a core of liquid surrounded by an annular layer of gas, which is of very low viscosity. No data in the open literature exist for this case and, thus, determining the circulation rate is a real problem. An alternative estimate of the film coefficient could be made, based on pool boiling correlations. A simple, fast and robust model of the heat transfer is given by [97]. The heat transfer coefficient α is given by

$$\alpha = c_1 \dot{q}^{0.673} \quad [W/m^2K] \tag{E.61}$$

where the coefficient c_1 is given as

$$c_1 = \frac{0.06136}{\left[1 - \left(\frac{T_s}{378.64}\right)^{0.0025}\right]^{0.73}} \tag{E.62}$$

where T_s is the saturation temperature and is measured in $[^oC]$. The single phase laminar heat transfer coefficients is calculated from

$$\begin{aligned} Nu_s &= \frac{h_s d_i}{k_f} \\ &= 4.36 \end{aligned} \tag{E.63}$$

and is valid for $L/d_i > 50$ and $\frac{d_i G}{\mu} < 2000$. For turbulent single phase flow and $\frac{d_i G}{\mu} > 10{,}000$ we use the Dittus-Boelter equation:

$$\begin{aligned} Nu_s &= \frac{h_s d_i}{k_f} \\ &= 0.023 \left(Re_f\right)^{0.8} \left(Pr_f\right)^{1/3} \end{aligned} \tag{E.64}$$

where Re_f and Pr_f are given in A.14 and A.11 respectively.

E.3. Two-phase flow regimes in rod bundles

One of the major challenges in modelling two phase flows is to determine the structure of the flow, i.e. the geometry of the interfaces is not determined a priori, but is rather a part of the solution of the flow fields. In single-phase flow of fluid in a conduit, we know the geometry (shape of the conduit) and are left to determine the velocity distribution, pressure drop, etc. - either experientially or theoretically. In contrast, when there are two fluids flowing simultaneously in a conduit, one cannot tell a priori how the phases are going to distribute themselves, e.g., are the bubbles going to be distributed uniformly throughout the liquid, or are they going to coalesce and form slugs? Actually, the distribution of phases is part of the solution of the flow fields. Naturally, the radial distribution of the gas phase in a pipe determines other design parameters such as heat transfer, pressure drop, etc., and without knowing this distribution, one cannot calculate the others. Furthermore, the phases normally do not have the same velocity, since it is likely that the gas (steam) may flow at a higher axial velocity than the liquid. Therefore, it is obvious to consider the flow patterns or flow regimes.

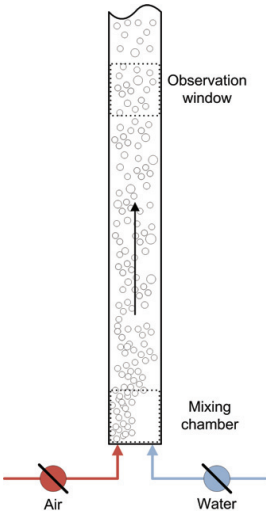

Figure E.3.: Flow regimes experiment in vertical pipes. From [148]

E.3.1. Flow patterns

In the following we describe the nature of two-phase flows in vertical pipes and discuss the various regimes. To better describe the flow patterns and the flow regime map, consider the following simple conceptual experiment. A transparent tube, orientated vertically, has a mixing chamber at the bottom and is connected, through valves and flow meters to supply of liquid (e.g. water) and gas (e.g. air), see figure (E.3). The two supply valves are opened somewhat and the flow pattern in the tube is observed. The setting of the valves is changed and another flow pattern may now be observed. Some of the common flow patterns are now described in the following.

Bubble flow

The gas is dispersed as discrete bubbles in the continuous liquid. The bubbles may have different shapes and sizes, but they are smaller than the pipe diameter. The bubbles flow regime can be subdivided into two sub-regimes - bubble flow in vertical positioned tubes at low liquid flow rates and dispersed bubble flow at high liquid flow rates. Liquids behave as if they are separated from their surroundings by an elastic skin that always under tension and has the tendency to contact. Intermolecular forces are the cause of this tendency. For the molecules inside the liquid bulk, forces from all directions cancel each other out and the molecules remain at near equilibrium. The interface between immiscible fluids can be modelled as an infinitely thin membrane that resists stretching and has a tendency to contact. Surface tension σ characterizes the interface's resistance to stretching. The surface tension is related to the Helmholtz and Gibbs free

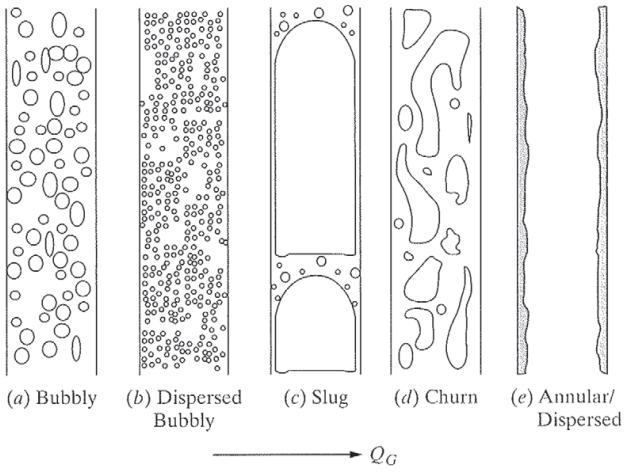

Figure E.4.: Major flow regimes in heated vertical pipes for increased heat uptake (Q_G). From [7]

energies, see [40], and when all the forces are balanced, the resulting equation is known as the Young - Laplace equation:

$$\Delta P = \sigma \left(\frac{1}{R_x} + \frac{1}{R_y} \right) \tag{E.65}$$

where

$$\sigma = 0.0238(1 - \frac{T}{T_{cr}})^{1.25} \left[1 - 0.639 \left(1 - \frac{T}{T_{cr}} \right) \right]. \tag{E.66}$$

here T is the temperature measured in Kelvin and σ is in [N/m] and T_{cr} is the critical temperature, also given in Kelvin. R_x and R_y are radii of curvature in each of the axes that are parallel to the surface and for a squared surface we have R=R_x=R_y. Finally ΔP is the pressure difference beneath and above the interphase given in equation (E.65) and is measured in [Pa].

Slug flow

When the steam quality increases, the bubbles coalesce and form larger bubbles, of a size similar to the pipe diameter. These are called Taylor bubbles and have a characteristic spherical cap nose and are somewhat abruptly terminated. The elongated gas bubbles are separated by liquid slugs, which may have smaller bubbles in it. The Taylor bubbles are separated from the wall by a film of liquid, which may flow downward, even though the net flow of the liquid is

upward. The size of the slug units, Taylor bubbles and liquid slugs may vary considerably.

Churn flow

When the velocity of the flow is increased (i.e., both valves are further opened), the slugs break down into a seemingly unstable regime. Liquid may be following up and down in an oscillatory fashion. This is a flow regime in between the slug flow and the annular flow, where liquid is displaced to the tube wall. In small diameter tubes the churn flow regime may not develop and the transition slug-annular may be a smooth one.

Annular flow

The bulk of the liquid flows on the wall, as a film and the gas is the continuous phase at the centre of the tube. Normally, there is some liquid entrained in the continuous gas in the form of small droplets, and there may be some gas in the liquid film in form of bubbles. In the liquid-gas interface (if gas velocity is high enough) there may be large amplitude waves, which break up. The break of the waves is the continuous source of the droplets in the gas core.

Wispy annular flow

When the liquid flow rate is increased, there is a considerable amount of liquid in the gas core due to entrainment. These liquid droplets then coalesce to form large lumps or wisps of liquid. This regime occurs at high mass velocities, and where the dimensionless superficial velocities are $U_G^* > 1$ and $U_L^* > 2{,}5$ to 3,0.

$$U_g^* = U_{sg}\rho_g^{1/2}(gD(\rho_l - \rho_g))^{-1/2} \tag{E.67}$$

and

$$U_l^* = U_{sl}\rho_l^{1/2}(gD(\rho_l - \rho_g))^{-1/2} \tag{E.68}$$

where ρ is the density g the acceleration due to gravity and D the pipe inner diameter. The subscripts l, g and s are referring to liquid, gas and superficial velocity respectively.

E.3.2. Flow pattern maps

The first person to recognise the importance of flow pattern as a starting point for the calculation of pressure drop, void fraction, heat and mass transfer was Barker, [149]. He published the earliest flow pattern map for horizontal flow. There were many attempts to generalize the flow pattern maps, but this is obviously very difficult to achieve, since there is a long list of relevant physical variables: the superficial velocities, the densities, viscosities, surface tension, pipe geometry (diameter, rifles, roughness, inclination), acceleration due to gravity and rotation

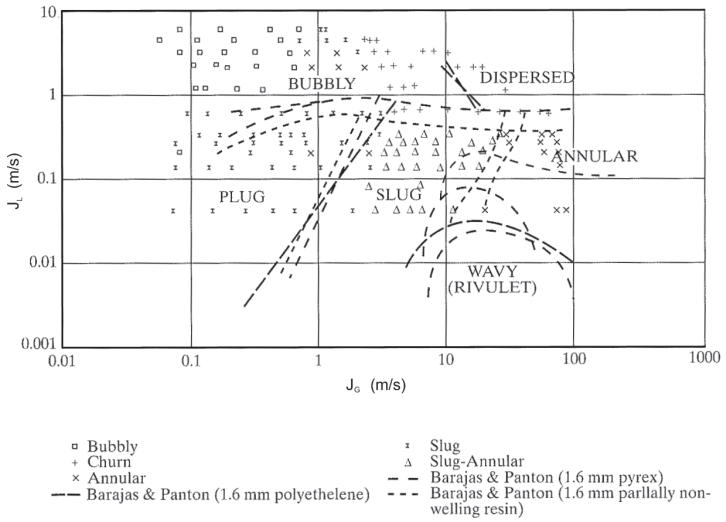

Figure E.5.: The effect of surface wettability on air-water flow regimes. Symbols represent data of Triplett et al. (1999a), and flow regime names are from Barajas and Panton (1993).

of the flow field. With these, one can have eight dimensionless groups. Some of the variables may be of less importance, but the number of dimensionless groups is still quite large.

Some maps are now being discussed and a simplified model is then shown, which attempts to generalize the maps and to predict the transitions from one regime to another. Yet, it should be emphasized that the flow regime maps are not general and should be extrapolated cautiously, since, for example, there is experimental evidence of substantial effect of pipe diameter, pressure, etc.

A popular map for horizontal flow is shown in figure (E.5). This map is based on air and water data in a relative small pipe and has the superficial velocities (J_G, J_L) as coordinates.

The boundaries in the flow regime map vary considerably for various researchers. Considerable efforts were spent to solve the problem, and many sets of coordinates have been proposed, e.g. momentum flux for the respectively phases, in addition to the more conventional coordinates U_{sg} vs U_{sl} (here U_s is the total superficial velocity and U is the true velocity of each phase). Flow boiling is considerably more complicated than pool boiling (boiling processes without an imposed forced flow, where fluid flow is caused by natural convection phenomena only), owing to the coupling between hydrodynamics and boiling heat transfer processes. A sequence of two-phase and boiling heat transfer regimes takes place along the heated channels during flow boiling, as a result of the increasing quality. The two-phase flow regimes in a boiling channel are therefore 'devel-

oping' everywhere and are morphologically different than their namesakes in adiabatic two-phase flows. In this context the preferred configuration for boiling channels is vertical up flow, where the buoyancy helps the mixture flow, and the slip velocity between the two phases that is caused by their density difference actually improves the heat transfer. In figure (E.6) the flow is illustrated in detail and heat transfer regimes in a uniformly heated vertical channel with upward flow that is subject to moderate heat flux, when the fluid at the inlet is sub cooled liquid. The wall and fluid temperatures are also schematically displayed in the figure. Near the inlet where the liquid sub cooling is too high to permit bubble nucleation, the flow regime is single-phase liquid, and the heat transfer regime is forced convection. Following the initiation of boiling, the sequence of flow regimes includes bubbly, slug, and annular, followed by dispersed droplet flow, and eventually a single-phase pure vapour flow field. Nucleate boiling is predominant in the bubbly and slug two-phase flow regimes and is followed by forced convective evaporation where the flow regime is predominantly annular. This is an extremely efficient heat transfer regime in which the heated wall is covered by a thin liquid film, which can be increased, if the flow pattern has a nature of axial rotation, as seen in rifled boiler tubes. The liquid film is cooled by evaporation at

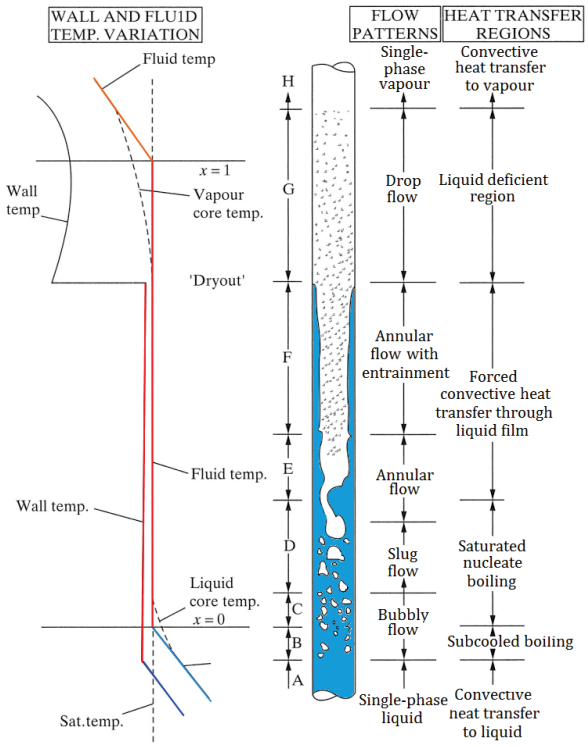

Figure E.6.: Two-phase flow and boiling regimes in a vertical pipe with a moderate wall heat flux. [148]

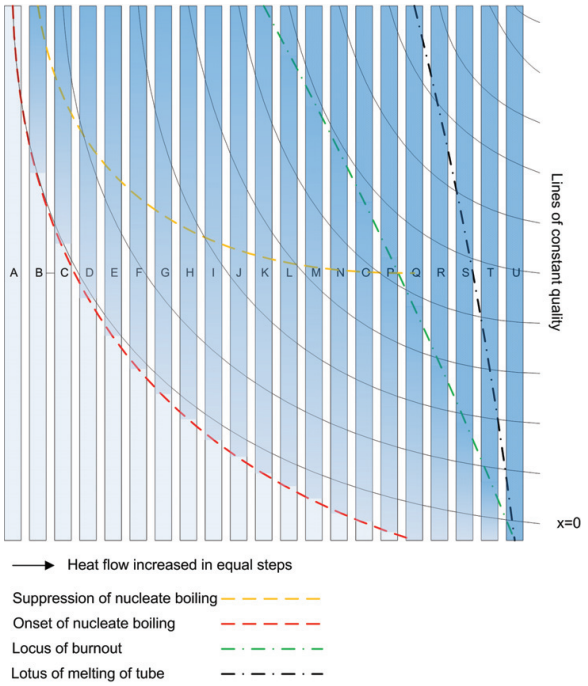

Figure E.7.: Evaporation in a vertical pipe with increased heat flux from left (A) to right (U).

its surface, making it unable to sustain a sufficiently large superheat for bubble nucleation. Droplet entrainment can occur when vapour flow rate is sufficiently high, leading to dispersed-droplet flow. Further downstream, the liquid film may eventually completely evaporate and lead to dry out. Substained macroscopic contact between the heated surface and liquid does not occur downstream from the dry out point, although sporadic deposition of droplets onto the surface may take place. Further downstream, the entrained droplets will eventually completely evaporate, and a pure vapour single-phase flow field develops. The heat transfer coefficient in the liquid-deficient region is much lower than in the nucleate boiling or forced convection evaporation regimes. As a result, the occurrence of dry out is accompanied with a large temperature rise for the heated surface. The dry out phenomenon is thus similar to the critical heat flux for pool boiling.

Having a liquid at constant velocity entering a tube, where the heat transfer in the tube is successive increased. The heat input is illustrated in steps A-U, as illustrated in figure (E.6). The total increment in heat flux is equal to the required heat, to ensure a saturation temperature at the end of the tube. As illustrated in figure (E.7), the flow pattern develops from single phase flow to through bubble flow, slug flow, churn flow and annular flow. The first generation of vapour takes

place by nucleation at the wall and the locus of the onset of nucleation is shown with red dash-dot line. If the heat flux is low (step B), then nucleation may be delayed beyond the point at which the thermodynamic quality x is zero. At high heat fluxes, nucleation occurs before the steam quality reach zero (x=0), which is named sub cooled boiling. As the flow velocity (and hence convective heat transfer) increases, nucleation may be suppressed and complete suppression is illustrated by the yellow dash-dot line. In the annular flow regime, liquid is lost from the film by evaporation and entrainment. When the liquid film flow rate at the end of the channel is reduced to zero (step L), the wall becomes dry ('dry out') or 'burnout'). At further increase of heat flux, the dry out points is propagated upstream, as shown by the green dash-dot line. For constant heat flux, the post-dry out region is hot and eventual the tube may melt, as illustrated by the **black dash-dot line**.

F. Measurements performed at the power plant SKV3

This appendix contains four sets of measurement data (sample 1-4) performed at the power plant SKV3 dated October 2011. Measurement data is recorded in the control system of the power plant and processed further into a InSql® database where data can be treated. Measurement data covers typical operating situations where the boiler is running in both Benson mode or circulation mode. It should be noted that the measurements of the panel wall temperatures is of low solution, while they are measured so that the control system only receives measurements when the temperature/pressure variation is greater than 1 [^oC] / 0.25 [bar].

F.1. Sample 1

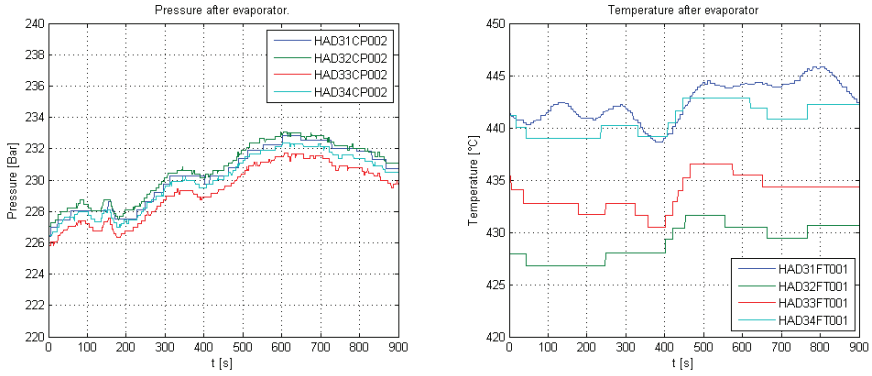

Figure F.1.: Pressure and temperature after boiler top section - sample 1.

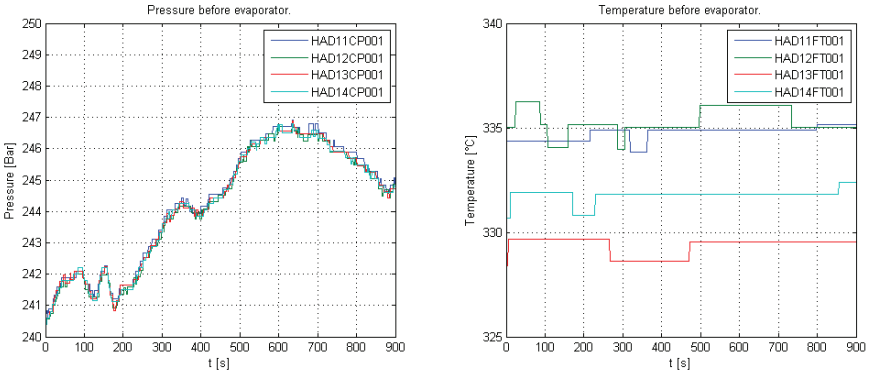

Figure F.2.: Pressure and temperature after ECO - sample 1.

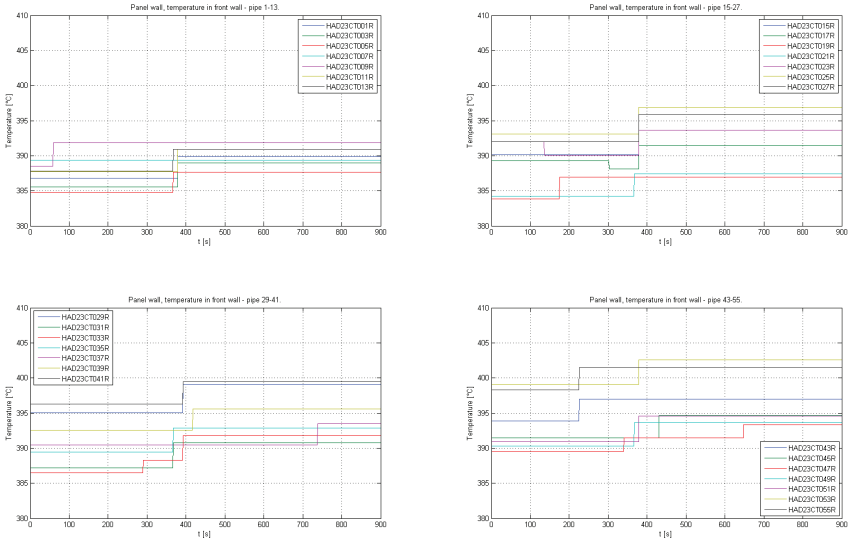

Figure F.3.: Wall temperature in boiler tubes on front wall - sample 1.

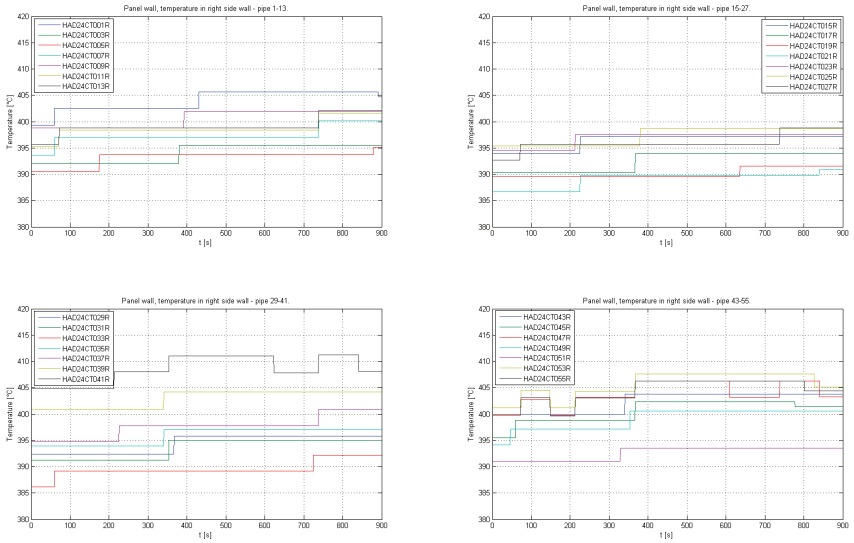

Figure F.4.: Wall temperature in boiler tubes on right side wall - sample 1.

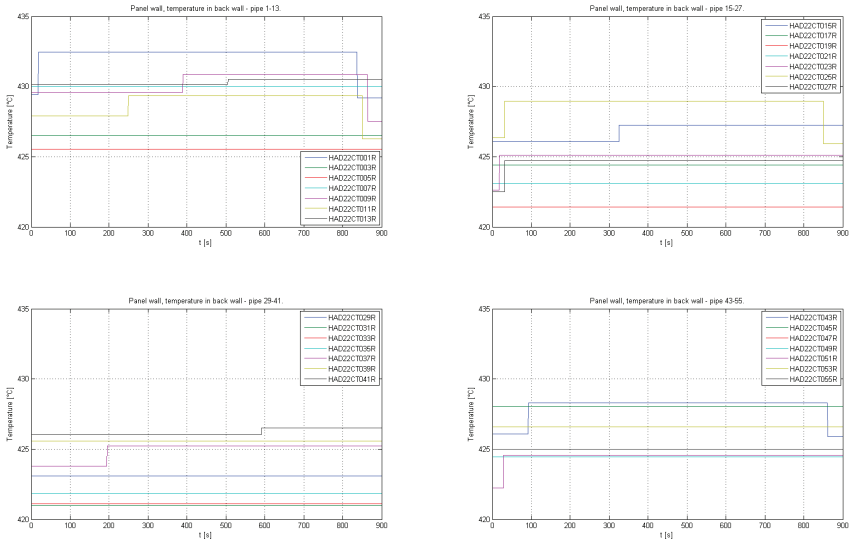

Figure F.5.: Wall temperature in boiler tubes on back wall - sample 1.

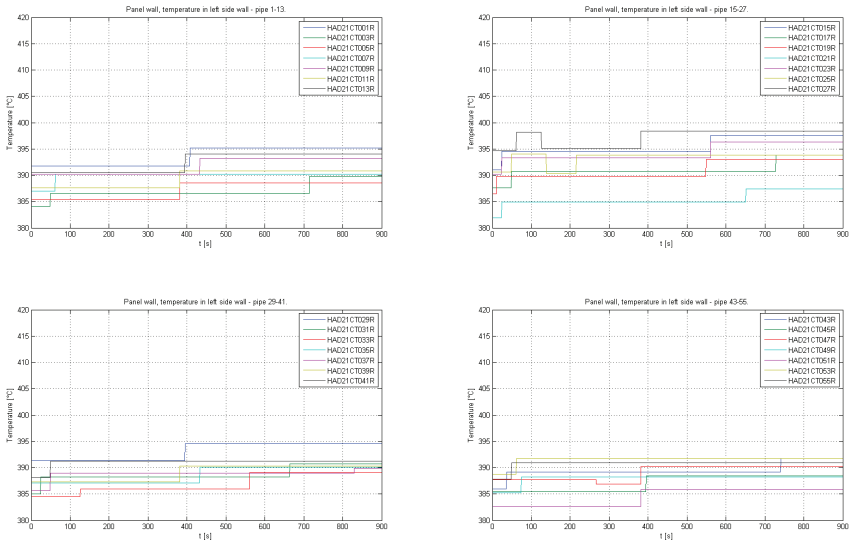

Figure F.6.: Wall temperature in boiler tubes on left side wall - sample 1.

F.2. Sample 2

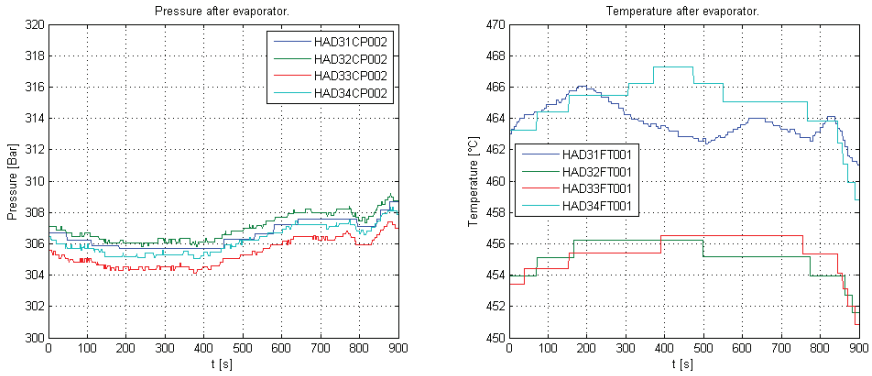

Figure F.7.: Pressure and temperature after boiler top section - sample 2.

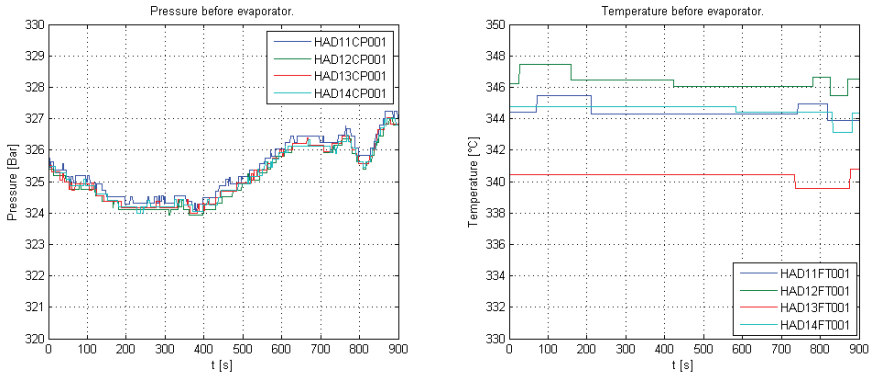

Figure F.8.: Pressure and temperature after ECO - sample 2.

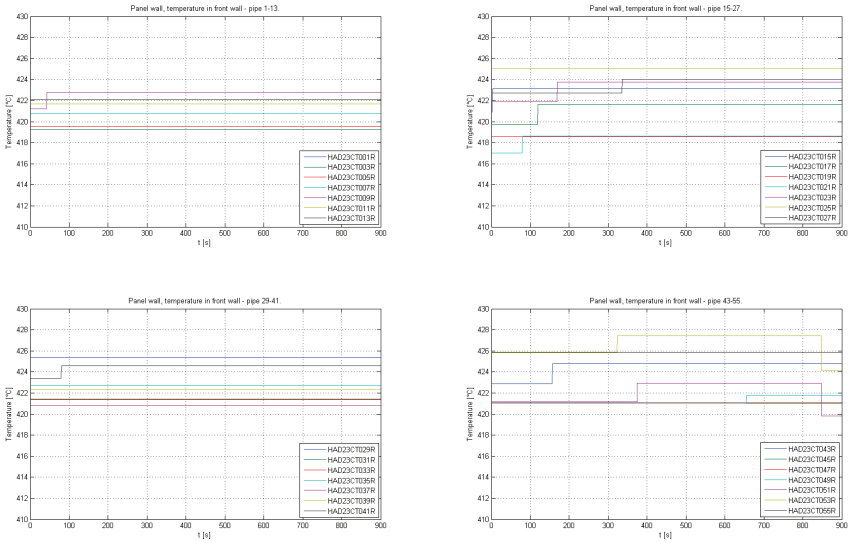

Figure F.9.: Wall temperature in boiler tubes on front wall - sample 2.

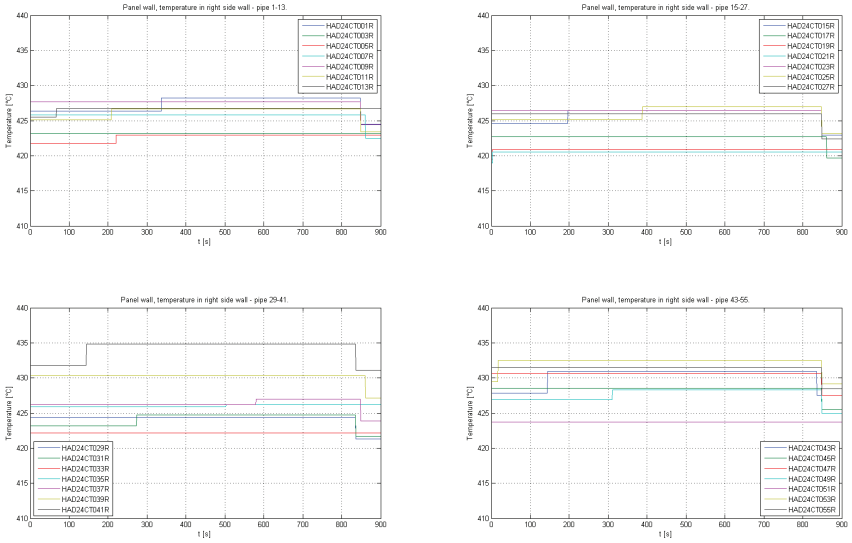

Figure F.10.: Wall temperature in boiler tubes on right side wall - sample 2.

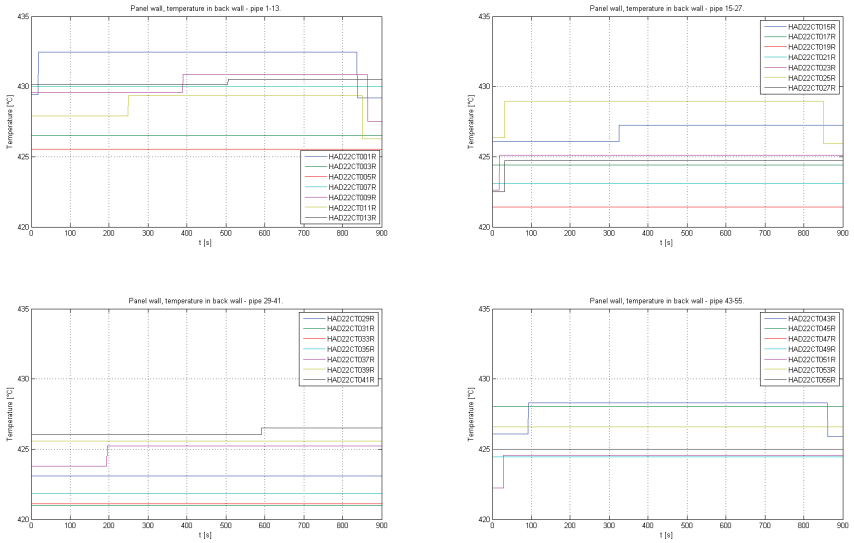

Figure F.11.: Wall temperature in boiler tubes on back wall - sample 2.

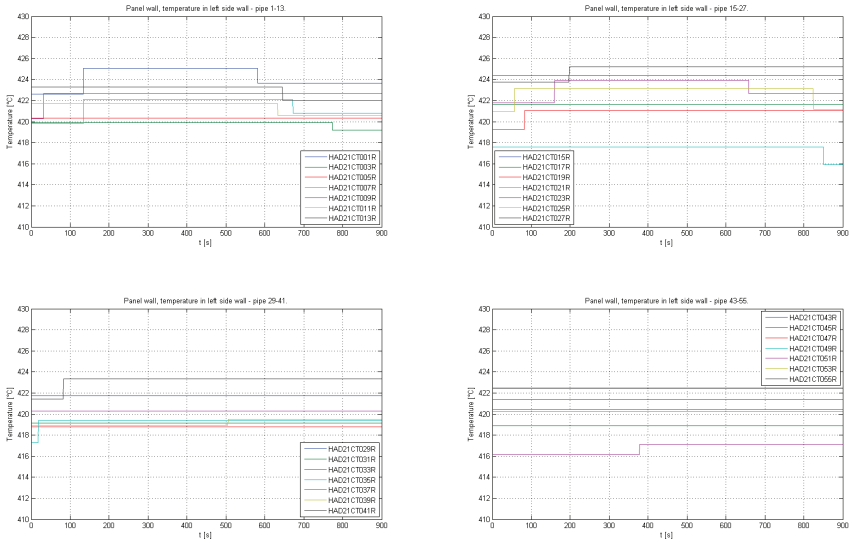

Figure F.12.: Wall temperature in boiler tubes on left side wall - sample 2.

F.3. Sample 3

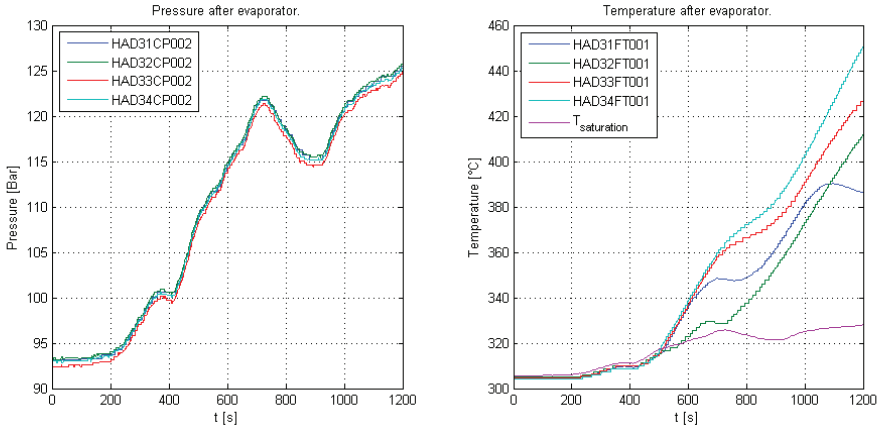

Figure F.13.: Pressure and temperature after boiler top section - sample 3.

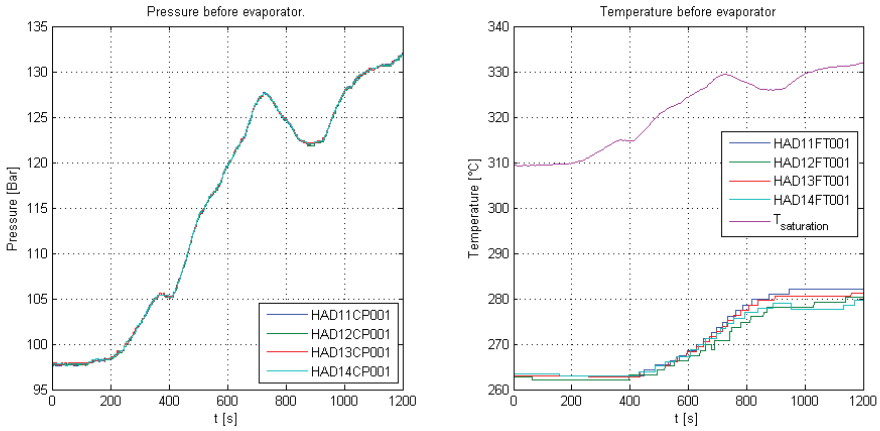

Figure F.14.: Pressure and temperature after ECO - sample 3.

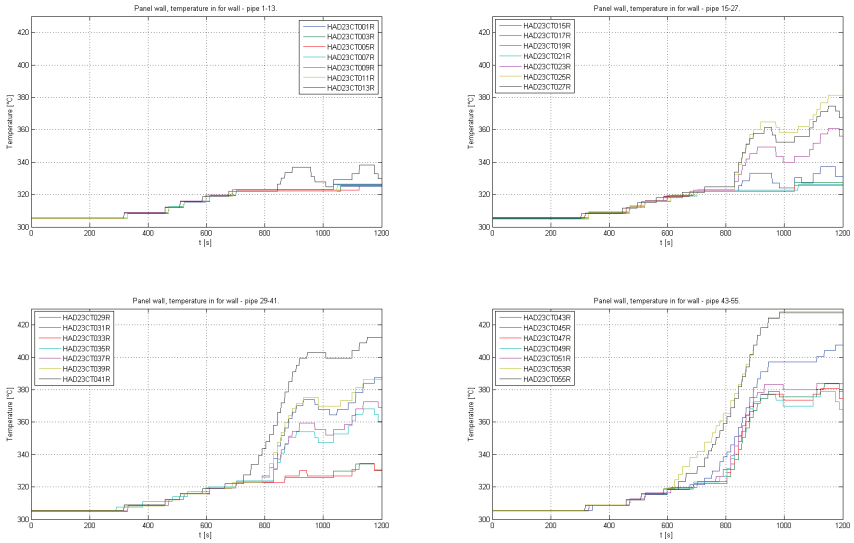

Figure F.15.: Wall temperature in boiler tubes on front wall - sample 3.

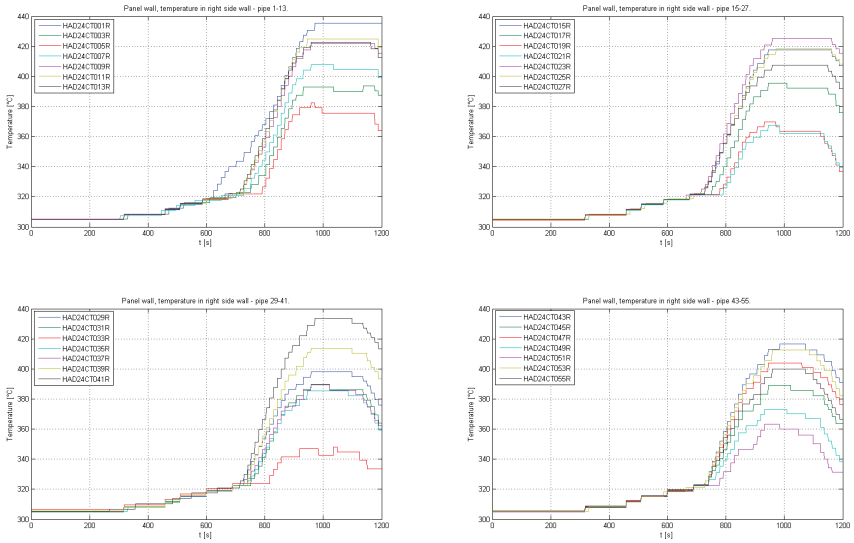

Figure F.16.: Wall temperature in boiler tubes on right side wall - sample 3.

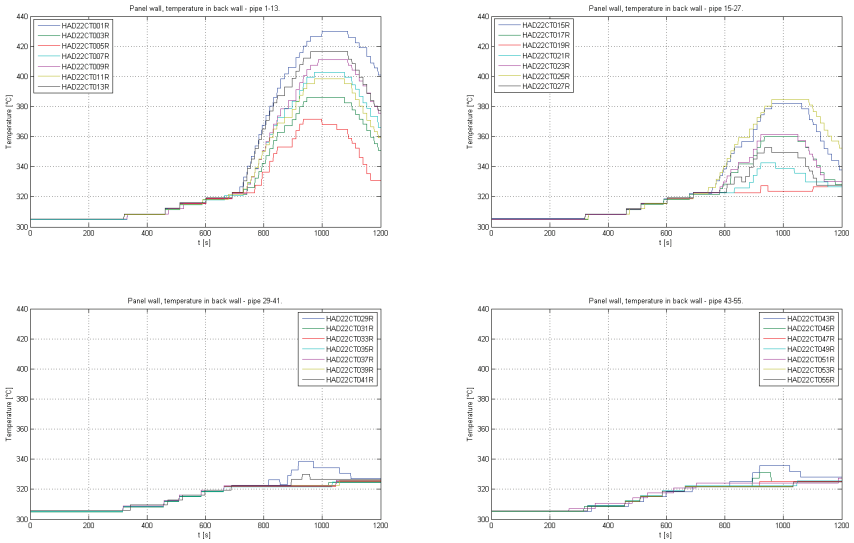

Figure F.17.: Wall temperature in boiler tubes on back wall - sample 3.

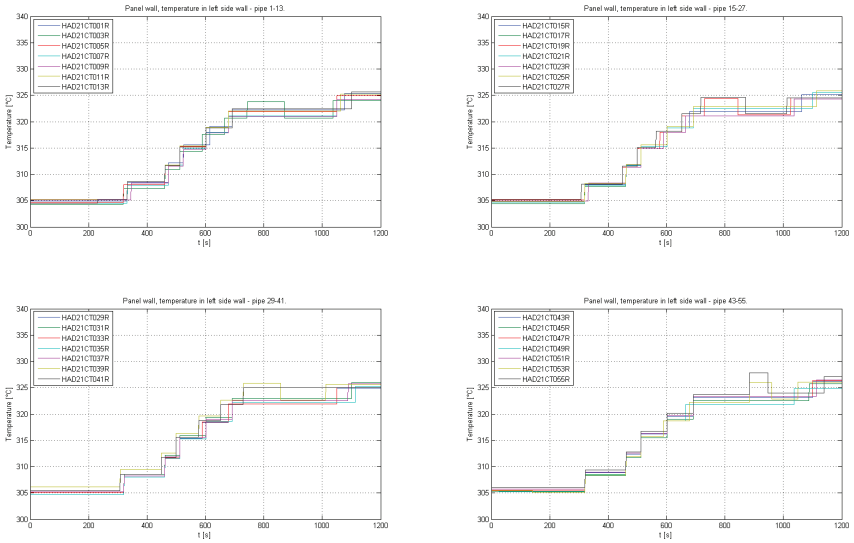

Figure F.18.: Wall temperature in boiler tubes on left side wall - sample 3.

F.4. Sample 4

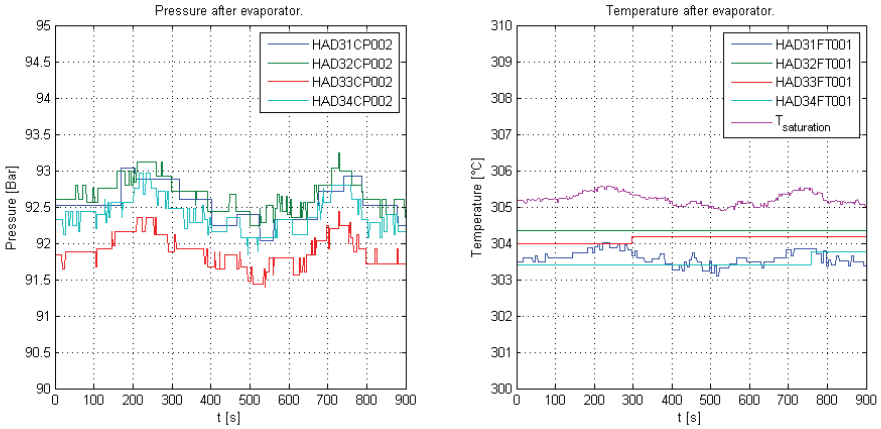

Figure F.19.: Pressure and temperature after boiler top section - sample 4.

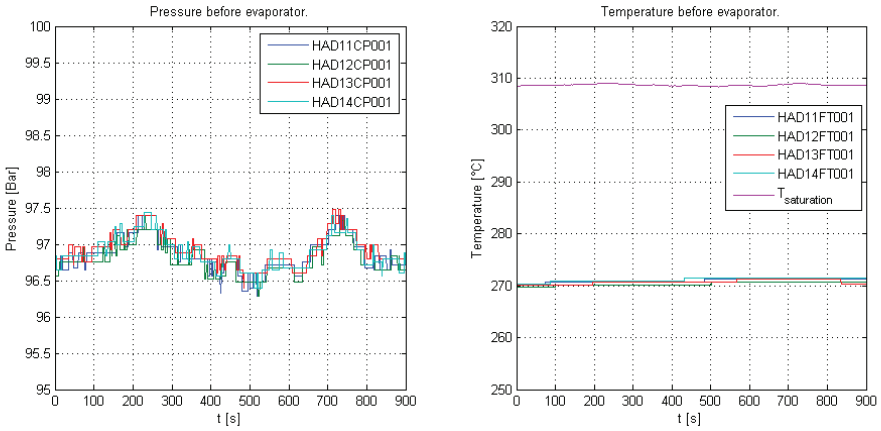

Figure F.20.: Pressure and temperature after ECO - sample 4.

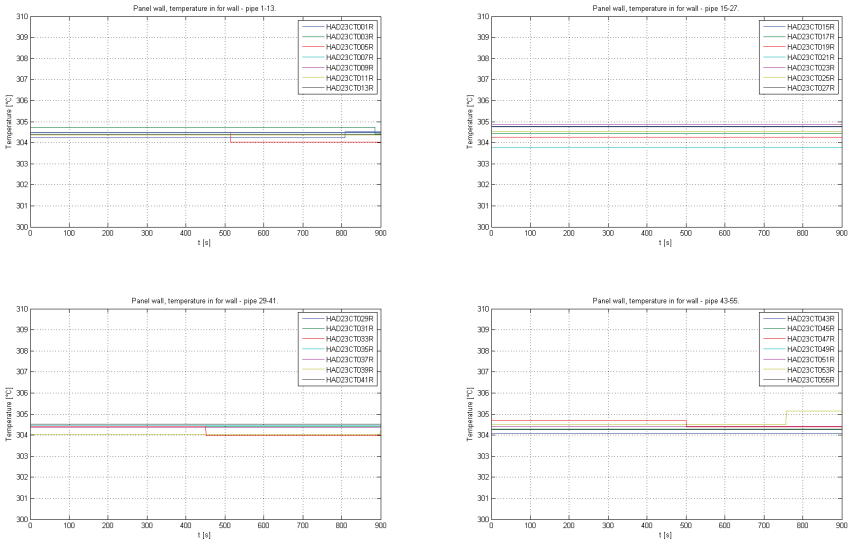

Figure F.21.: Wall temperature in boiler tubes on front wall - sample 4.

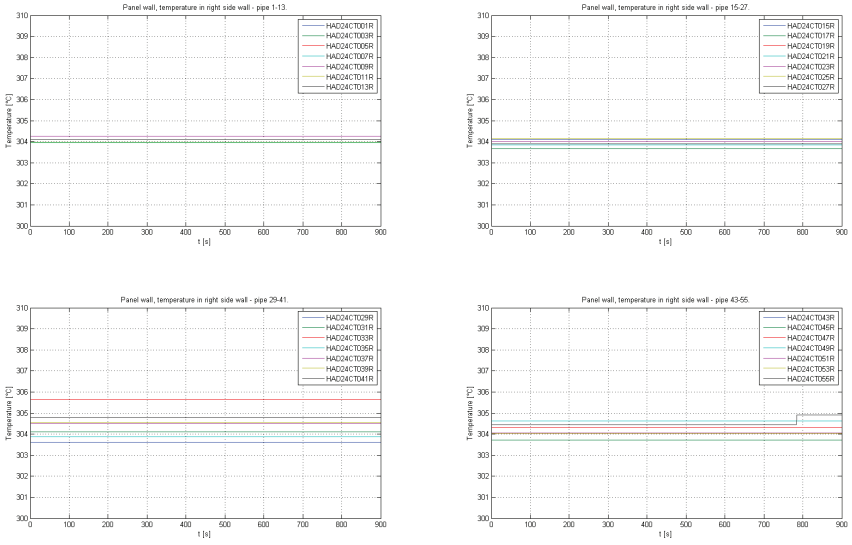

Figure F.22.: Wall temperature in boiler tubes on right side wall - sample 4.

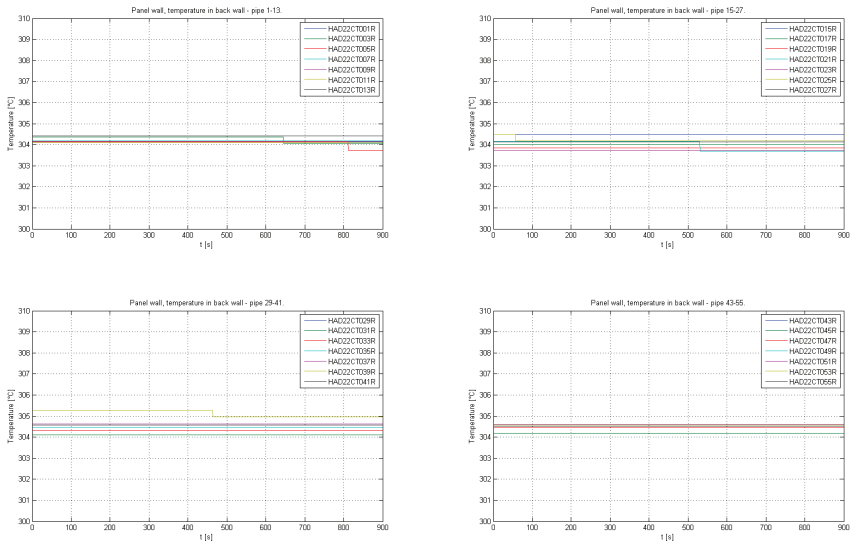

Figure F.23.: Wall temperature in boiler tubes on back wall - sample 4.

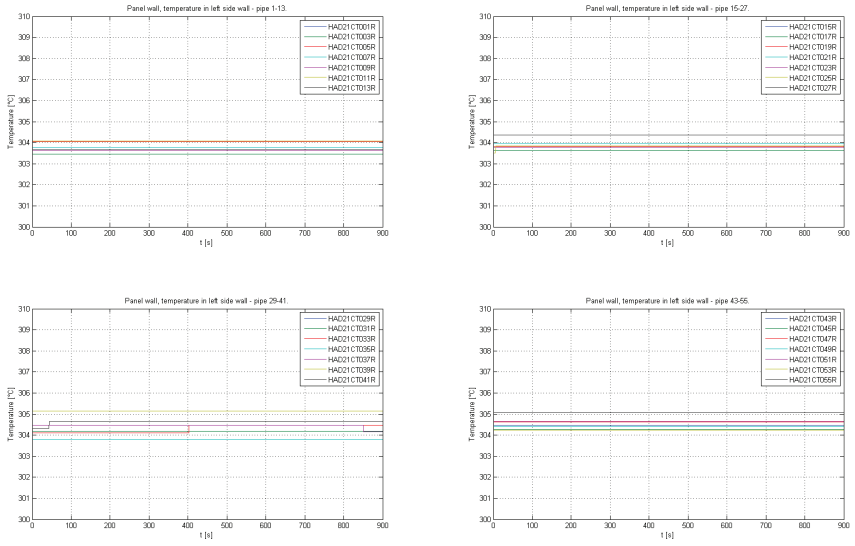

Figure F.24.: Wall temperature in boiler tubes on left side wall - sample 4.

G. Transition functions

Transition functions are required in many component models to switch smoothly and continuously between different functions. A good example are heat transfer and pressure drop correlations that are usually only valid within certain regions. The continuous transition between those regions is a typical problem in numerical simulations.

G.1. Smooth transition functions

Transition functions are provided to allow for a smooth transition between different functions with a variable number of smooth derivatives. These functions T(x) can be used in the following way to switch between the two functions $g_0(x)$ and $g_1(x)$, wherein T(x) is a normalized function and is provided with boundary conditions at x=x_0 and x=x_1, corresponding to the slope at each end of the range of definition.

$$G(x) = g_0(x) \cdot T(x) + g_1(x) \cdot (1 - T(x)), \quad x \in \Re \tag{G.1}$$

where

$$T(x) \equiv \begin{cases} 1 & \text{for } x < x_0, \\ t(x) & \text{for } x_0 \leq x \leq x_1, \\ 0 & \text{for } x > x_1. \end{cases} \tag{G.2}$$

In order that T(x) is smooth, the following restrictions apply for t(x)

$$\frac{dt(x)}{dx}|_{x=x_0} = 0 \text{ and } \frac{dt(x)}{dx}|_{x=x_1} = 0 \tag{G.3}$$

The simplest way to find a suitable function is according to [139] to look at the fundamental trigonometric function

$$\frac{dt(\varphi)}{d\varphi} = a\cos(\varphi) \tag{G.4}$$

where a is a scaling factor and φ the phase defined by

$$\varphi = \left(\frac{x - x_0}{\Delta x} - 1/2 \right) \pi, \quad \text{where } \Delta x = x_1 - x_0 \tag{G.5}$$

fulfils these restrictions. This yields the following function for t(φ).

$$t(\varphi) = a \sin(\varphi) + b \tag{G.6}$$

The two parameters a and b can be computed from equation (G.3). From equation (G.4) follows that the first derivative of the transition function T(x) defined as

$$\frac{dT(x)}{dx} \equiv \begin{cases} 0 & \text{for } x < x_0, \\ \frac{dt(x)}{dx} & \text{for } x_0 \leq x \leq x_1, \\ 0 & \text{for } x > x_1. \end{cases} \tag{G.7}$$

is not smooth at x = x_0 and x = x_1 . This discontinuity can have negative effects on the solution process because the WENO solver has to handle functions with discontinuous first derivatives. Equation (G.4) can be generalized to

$$\frac{dt(\varphi)}{d\varphi} = a \cos^n(\varphi) \tag{G.8}$$

where n is a positive integer yielding the following function for t(φ)

$$t(\varphi) = a \left(\frac{\cos^{n-1}(\varphi) \sin(\varphi)}{n} + \frac{n-1}{n} \int \cos^{n-2}(\varphi) d\varphi \right) + b \tag{G.9}$$

The two parameters a and b can again be computed from equation (G.3). The resulting function t(φ) is $(n-1)^{th}$ order continuous. In table (G.1) is shown the functions (t(φ)), its derivatives and values for a and b for n = 1, 2, 3, 4. In figure (G.1) is shown the function T(x) and its derivative dT(x)/dx respectively for n = 1, 2, 3, 4. For many heat transfer and pressure drop correlations, the functions g_0 and g_1 does not cover the same definitions area. Let us assume that $g_0 \in$]-∞,x_0] and $g_1 \in$ [x_1,+∞]. If we want to apply (G.2) directly for smoothing of g_0 and g_1, we can exploit the knowledge of the slope(s_0 and s_1) of g_0 and g_1 respectively, at x_0 and x_1 and thus extrapolate g_0 and g_1, so that a common definition area is achieved. The following two functions satisfy the conditions for linear extrapolation: $g_0'(x) = g_0(x_0) + s_0 \cdot (x - x_0)$ and $g_1'(x) =$

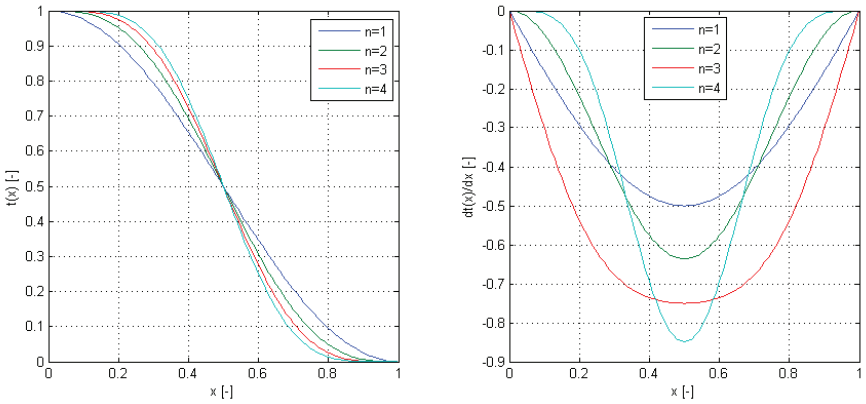

Figure G.1.: Function values and derivatives of smooth transition function for n=(1,2,3,4).

Table G.1.: Function t(φ) used in smooth functions T(x) for n=(1,2,3,4).

n	t(φ))	$\frac{dt(\varphi))}{d\varphi}$	a	b
1	$a\sin(\varphi)+b$	$a\cos(\varphi)$	-1/2	1/2
2	$\frac{a}{2}(\cos(\varphi)\sin(\varphi)+\varphi)+b$	$a\left(1-\sin^2(\varphi)\right)$	-2/π	1/2
3	$\frac{a}{3}\left(\cos^2(\varphi)\sin(\varphi)+2\sin(\varphi)\right)+b$	$\frac{a}{3}\left(\cos^2(\varphi)(2-\cos^2(\varphi))+2\cos(\varphi)\right)$	-3/4	1/2
4	$\frac{a}{8}\left(2\cos^3(\varphi)\sin(\varphi)+3\cos(\varphi)\sin(\varphi)+3\varphi\right)+b$	$\frac{a}{8}\left(2\cos^2(\varphi)(4\cos^2(\varphi)-3)+3(2\cos^2(\varphi)-1)+3\right)$	-8/3π	1/2

$g_1(x_1)-s_1(x_1-x_0)+s_1\cdot(x-x_0)$. Next, equation (G.2) can be used with $g_0^{'}(x)$ or $g_1^{'}(x)$. Hence G(x) can be formulated as

$$G(x)\equiv\begin{cases} g_0(x) & \text{for } x<x_0, \\ g_0^{'}(x)\cdot t(x)+g_1^{'}(x)\cdot(1-t(x)) & \text{for } x_0\le x\le x_1, \\ g_1(x) & \text{for } x>x_1. \end{cases} \tag{G.10}$$

G.2. Spline functions

A special class of functions is especially suitable as transition functions and here the choice falls on spline functions. A spline curve is a mathematical representation for which it is easy to build an interface that will allow a user to design and control the shape of complex curves and surfaces. The general approach is that the user enters a sequence of points, and a curve is constructed whose shape closely follows this sequence. The points are called control points.

A curve that actually passes through each control point is called an interpolating curve. The degree of a polynomial corresponds with the highest coefficient that is non-zero. The degree three polynomial - known as a cubic polynomial - is the one that is most typically chosen for constructing smooth curves in computer graphics. It is used because it is the lowest degree polynomial that can support an inflection, known from the beam theory of solid mechanics - so we can make interesting curves, and it is very well behaved numerically - that means that the curves will usually be smooth like a lower order polynomial (second order) and not jumpy like a noise signal. Spline functions can be advantageously composed in piecewise polynomial curves, so that the functional relationship can be parameterised to avoid unwanted oscillations and non-smooth shapes - polynomials with degree higher than three tend to be very sensitive to the positions of the control points and thus do not always make smooth shapes. Let us have n pieces of third order polynomials $t_i(x) \in \Re$ for x $\in [x_0, x_1]$.

$$t_i(x) = a_i + b_i \cdot x + c_i \cdot x^2 + d_i \cdot x^3, \quad \text{for } x \in [x_0, x_1] \ \wedge \ i \in [1, ..n] \tag{G.11}$$

Let each pair of control points represent one segment of the curve. Each curve segment is a cubic polynomial with its own coefficients. Between each control point pair is a function, which is numbered identically to the index of its leftmost point. In general, $t_i(x)$ in (G.11) is the function representing the curve between control points i and i+1. Because each curve segment is represented by a cubic polynomial function, we have to solve for four coefficients for each segment. We require that each curve segment pass through its control points. This enforces C^0 continuity - that is where the curves meet each other:

$$t_i(x_i) = y_i \ \text{ and } \ t_i(x_{i+1}) = y_{i+1} \tag{G.12}$$

Additionally we require that the curve segments have the same slope where they join together. Thus:

$$\frac{dt_i(x_{i+1})}{dx_{i+1}} = \frac{dt_{i+1}(x_{i+1})}{dx_{i+1}} \tag{G.13}$$

This enforces C^1 continuity - that is that slopes match where the curves join. Finally we require that the curve segments have the same curvature where they join together. That means:

$$\frac{d^2t_i(x_{i+1})}{dx_{i+1}^2} = \frac{d^2t_{i+1}(x_{i+1})}{dx_{i+1}^2} \tag{G.14}$$

This enforces C^2 continuity - that curvatures match at the join. Note that at the left end of the curve we are missing the C^1 and C^2 equations since there is no

segment on the left. So, we are missing two equations needed to solve the entire system. We can get these by having the user supply the slopes at the two ends. Let us call these slopes s_0 and s_1

G.3. Parameterization of splines

The control points can define as piecewise polynomial curves, using cubic functions to define curve segments between control points and enforcing various levels of continuity where segments join. In particular, we employed C^0 continuity, meaning that the two segments match values at the join, C^1 continuity, meaning that they match slopes at the join and C^2 continuity, meaning that they match curvatures at the join.
We were able to determine coefficients for the curve segments via a set of linear equations $\mathbf{A}\cdot\mathbf{x} = \mathbf{b} => \mathbf{x} = \mathbf{A}^{-1}\mathbf{b}$, where $\mathbf{x}$ is the vector of all coefficients, $\mathbf{b}$ is the vector of constants on the right-hand side of the linear equations, and $\mathbf{A}$ is a matrix encoding the C^0, C^1 and C^2 conditions. This approach can be modified to specify each curve segment in parametric form. In the parametric form on the right, we have defined parameters ε_i that vary between 0 and 1 as we step along the x axis between control points. We could write equations

$$\varepsilon_i = \frac{x - x_i}{x_{i+1} - x_i} \text{ with } \frac{d\varepsilon_i}{dx} = \frac{1}{x_{i+1} - x_i}, \ i \in [1,..n] \tag{G.15}$$

relating the ε_i to the original x coordinate. The derivatives indicate how quickly ε_i varies as we move in the x direction.
Now we specify each curve segment by a parametric cubic curve

$$f_i(\varepsilon) = a_i + b_i \cdot \varepsilon_i + c_i \cdot \varepsilon_i^2 + d_i \cdot \varepsilon_i^3, \quad \varepsilon_i \in [0,1] \ \wedge \ i \in [1,..n] \tag{G.16}$$

Notice, that in this form the a_i coefficients are simply the y coordinates of the i^{th} control points, and do not have to be solved for.
For C^1 continuity we differentiate once with respect to x using the chain rule:

$$\frac{df_i}{dx} = \frac{df_i}{d\varepsilon_i} \cdot \frac{d\varepsilon_i}{dx} = \frac{1}{x_{i+1} - x_i} \cdot \frac{df_i}{d\varepsilon_i}, \quad i \in [1,..n] \tag{G.17}$$

and for C^2 continuity we differentiate twice:

$$\frac{d^2 f_i}{d^2 x} = \frac{d^2 f_i}{d\varepsilon_i^2} \cdot \frac{d^2 \varepsilon_i}{dx^2} = \frac{1}{(x_{i+1} - x_i)^2} \cdot \frac{d^2 f_i}{d\varepsilon_i^2}, \quad i \in [1,..n] \tag{G.18}$$

If we normalise the y_i values, we have to introduce at transition parameter

(γ), to adjust the forcing slopes (s_0 and s_1) at the left and right boundary, hence

$$\gamma = \frac{y_{max} - y_{min}}{x_n - x_1} \tag{G.19}$$

where y_{max}= max(y_i) and y_{min}= min(y_i) for i $\in$ [1,..n].

G.4. Single spline

For some purposes, where to smooth two adjacent two functions like g_0 and g_1 in (G.1), it may be sufficient to use a single spline function. The boundary

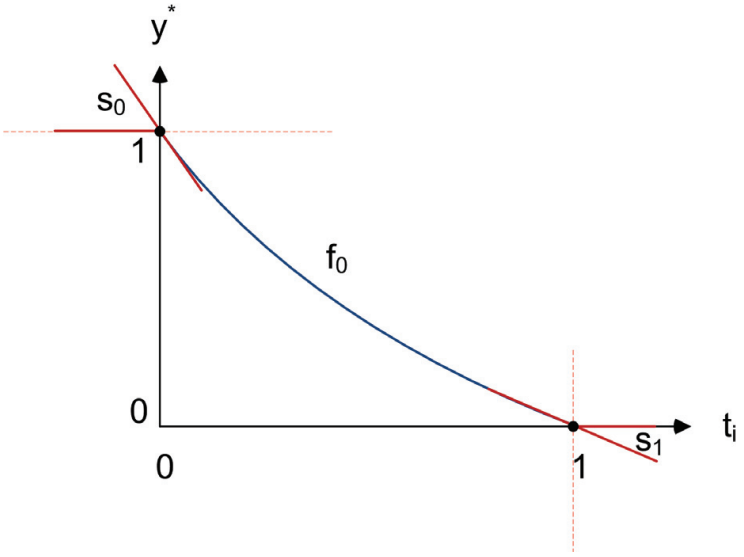

Figure G.2.: A single spline model as transition function.

conditions for at normalised spline function $f(\varepsilon)$ and its derivative $f^{'}(\varepsilon)$ can be given as:

$$\begin{aligned} f_0(0) &= y_0 \\ f_0(1) &= y_1 \\ f_0^{'}(0) &= s_0 \\ f_0^{'}(1) &= s_1 \end{aligned} \tag{G.20}$$

where the function and its derivative are given as

$$\begin{aligned} f_0(\varepsilon) &= a_0 + b_0 \cdot \varepsilon + c_0 \cdot \varepsilon^2 + d_0 \cdot \varepsilon^3 \\ f_0^{'}(\varepsilon) &= b_0 + 2c_0 \cdot \varepsilon + 3d_0 \cdot \varepsilon^2 \end{aligned} \tag{G.21}$$

which leads to the following linear system of equations

$$\mathbf{A} \cdot \mathbf{x} = \mathbf{b} \tag{G.22}$$

where **x**=(a_0, b_0, c_0, d_0), **b**=(y_0, y_1, s_0, s_1) and

$$\mathbf{A} = \begin{pmatrix} 1 & 0 & 0 & 0 \\ 0 & 1 & 1 & 1 \\ 0 & 1 & 0 & 0 \\ 0 & 1 & 2 & 3 \end{pmatrix}$$

Hence **x**=$\mathbf{A}^{-1} \cdot$ **b** which gives

$$\begin{aligned} a_0 &= y_0 \\ b_0 &= s_0 \\ c_0 &= 3(y_1 - y_0) - s_0 - 2s_1 \\ d_0 &= 2(y_0 - y_1) + s_0 + s_1 \end{aligned} \tag{G.23}$$

Note that the two slope coefficients s_0 and s_1 must be corrected for the transformation that occurs from the physical system to the normed system. Therefore, s_0 and s_1 are multiplied by a correction factor γ obtained by the coordinate transformation (x $\Rightarrow \varepsilon$ and y $\Rightarrow$ f), see (G.19).

G.5. Two spline system

A two spline system has the advantage of getting one more parameter to adjust the same curves, and thus may have more control over the process path. It is typically the intention of getting a smoothly as possible curve, so it is often worthwhile to develop two or more contiguous spline functions. For two spline functions, we get 8 boundary conditions, 4 C^0 conditions, 3 C^1 conditions and one C^2 condition, which can be formulated in a system like (G.22) where **x**=($a_0, b_0, c_0, d_0, a_1, b_1, c_1, d_1$), **b**=($y_0, y_1, y_1, y_2, s_0, 0, s_2, 0$) and

$$\mathbf{A} = \begin{pmatrix} 1 & 0 & 0 & 0 & 0 & 0 & 0 & 0 \\ 1 & 1 & 1 & 1 & 0 & 0 & 0 & 0 \\ 0 & 0 & 0 & 0 & 1 & 0 & 0 & 0 \\ 0 & 0 & 0 & 0 & 1 & 1 & 1 & 1 \\ 0 & 1 & 0 & 0 & 0 & 0 & 0 & 0 \\ 0 & 1 & 2 & 3 & 0 & -1 & 0 & 0 \\ 0 & 0 & 0 & 0 & 0 & 1 & 2 & 3 \\ 0 & 0 & 2 & 6 & 0 & 0 & -2 & 0 \end{pmatrix}$$

and the solution is

$$
\begin{aligned}
a_0 &= y_0 \\
b_0 &= s_0 \\
c_0 &= (-3y_2 + 12y_1 - 9y_0 + s_2 - 7s_0)/4 \\
d_0 &= (-3y_2 + 8y_1 - 5y_0 + s_2 - 3s_0)/4 \\
a_1 &= y_1 \\
b_1 &= (-3y_2 + 3y_0 + s_2 + s_0)/4 \\
c_1 &= (-3y_2 + 6y_1 - 3y_0 + s_2 - s_0)/2 \\
d_1 &= (-5y_2 + 8y_1 - 3y_0 + 3s_2 - s_0)/4
\end{aligned}
\tag{G.24}
$$

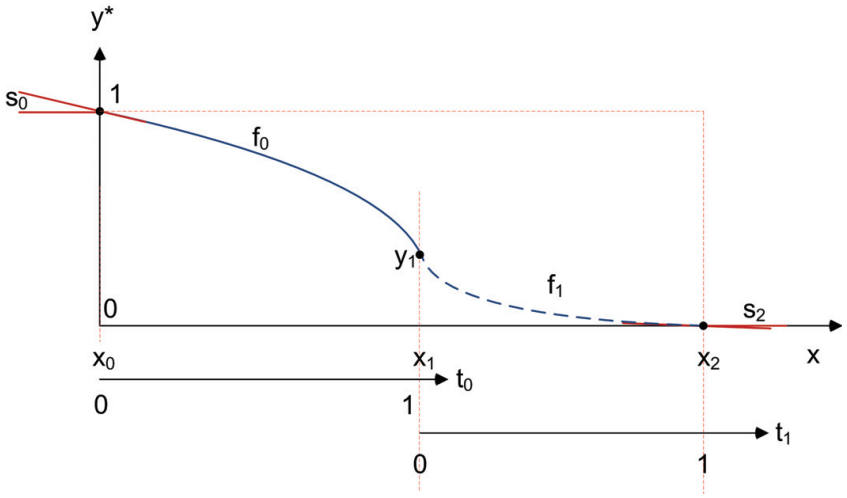

Figure G.3.: A double spline system as transition function.

G.6. Comments

In this section we have worked through two methods for building Smooth Transition Functions. The higher order smooth function based on trigonometric functions have many advantages as a third order single spline function. The spline function of third degree has in principle three zeros, so that the function can generate non smooth shapes, while the trigonometric smooth function is fully controllable and no surprises around the curve course. In general the Spline functions are based on an interpolating spline curve through a set of control points by using continuity C^0, slope C^1 and curvature C^2 constraints, where spline segments join. This is the method for computing natural cubic splines.

and the solution is

$$
\begin{aligned}
a_0 &= y_0 \\
b_0 &= s_0 \\
c_0 &= (-3y_2 + 12y_1 - 9y_0 + s_2 - 7s_0)/4 \\
d_0 &= (-3y_2 + 8y_1 - 5y_0 + s_2 - 3s_0)/4 \\
a_1 &= y_1 \\
b_1 &= (-3y_2 + 3y_0 + s_2 + s_0)/4 \\
c_1 &= (-3y_2 + 6y_1 - 3y_0 + s_2 - s_0)/2 \\
d_1 &= (-5y_2 + 8y_1 - 3y_0 + 3s_2 - s_0)/4
\end{aligned}
\tag{G.24}
$$

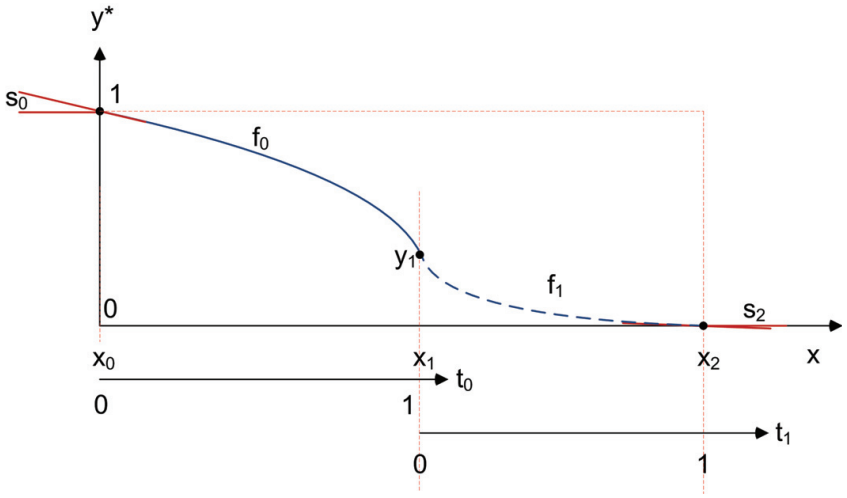

Figure G.3.: A double spline system as transition function.

G.6. Comments

In this section we have worked through two methods for building Smooth Transition Functions. The higher order smooth function based on trigonometric functions have many advantages as a third order single spline function. The spline function of third degree has in principle three zeros, so that the function can generate non smooth shapes, while the trigonometric smooth function is fully controllable and no surprises around the curve course. In general the Spline functions are based on an interpolating spline curve through a set of control points by using continuity C^0, slope C^1 and curvature C^2 constraints, where spline segments join. This is the method for computing natural cubic splines.

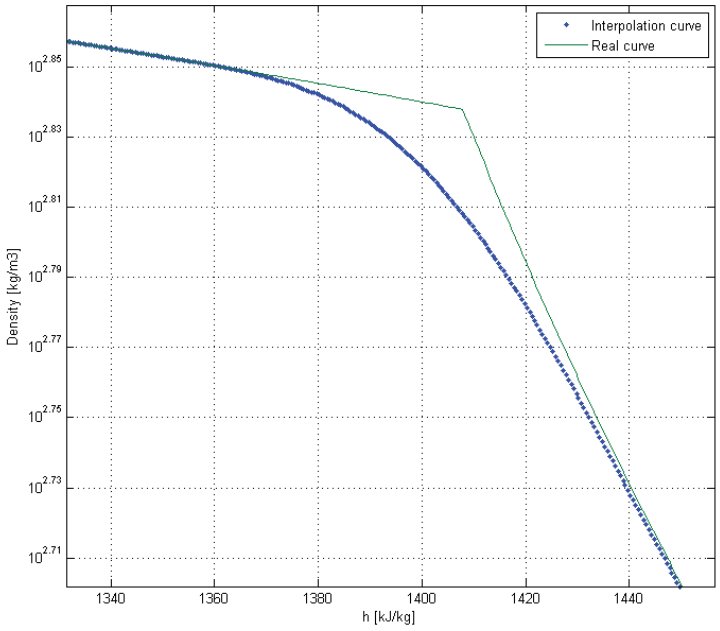

Figure G.5.: A second order trigonometric smooth function for smoothing the density through in the IAPWS-97 water steam table.

H. Maldistribution - curves

In this appendix is given selected curves of maldistribution, in two parallel evaporator tubes, where the power consumption of the tubes is regulated, assuming the total power consumption is constant. The relationship between the relative friction loss, the relative mass flow and relative outlet enthalpy through pipes 1 and 2 as a function of q_2/q_1 are shown.

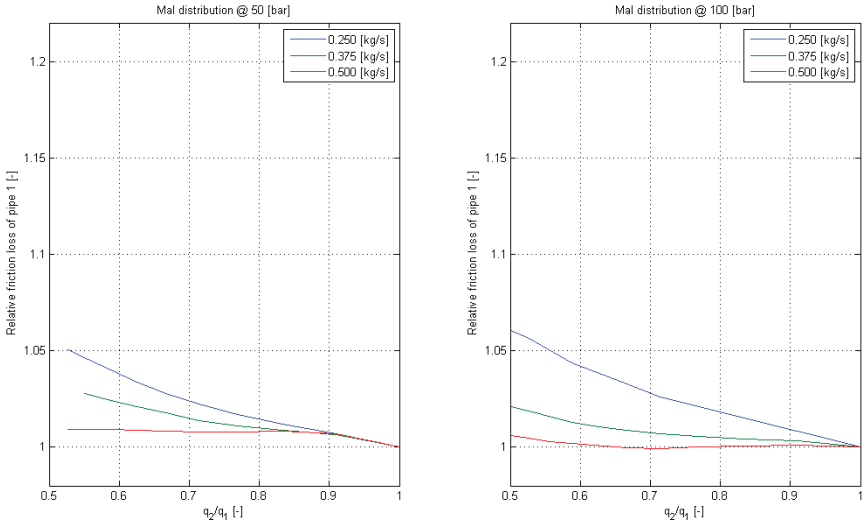

Figure H.1.: Mal distribution in panel wall.

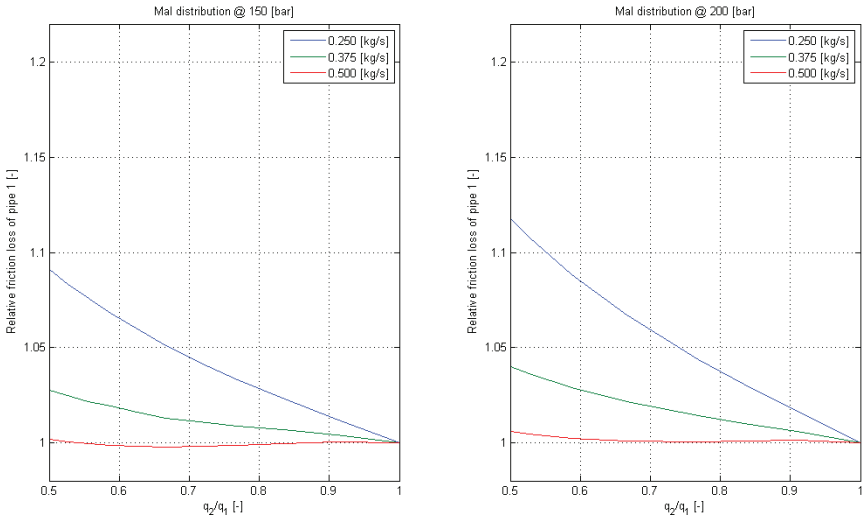

Figure H.2.: Mal distribution in panel wall.

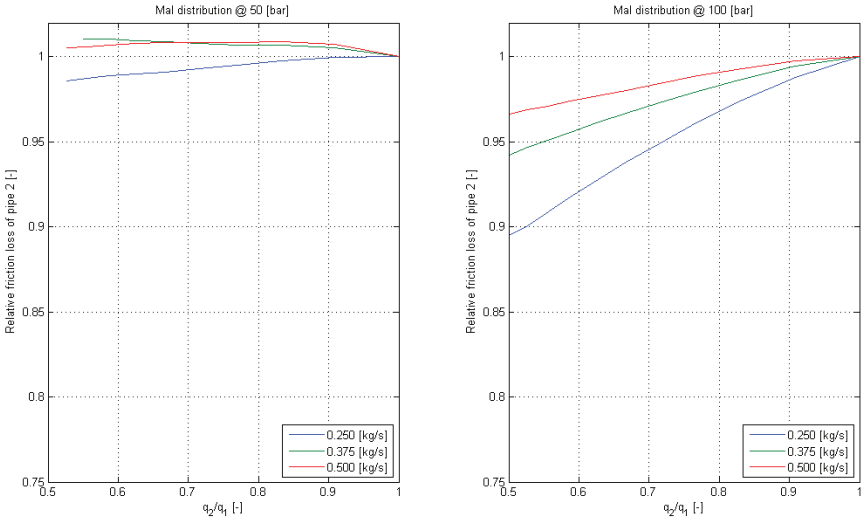

Figure H.3.: Mal distribution in panel wall.

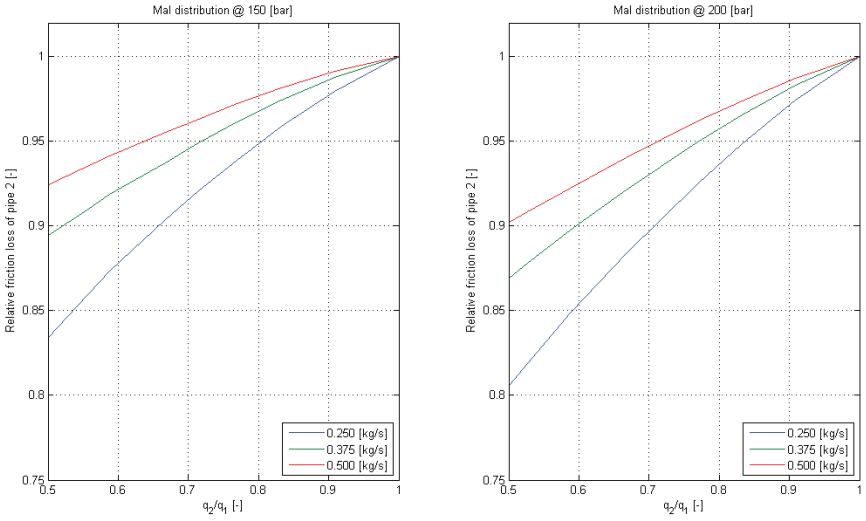

Figure H.4.: Mal distribution in panel wall.

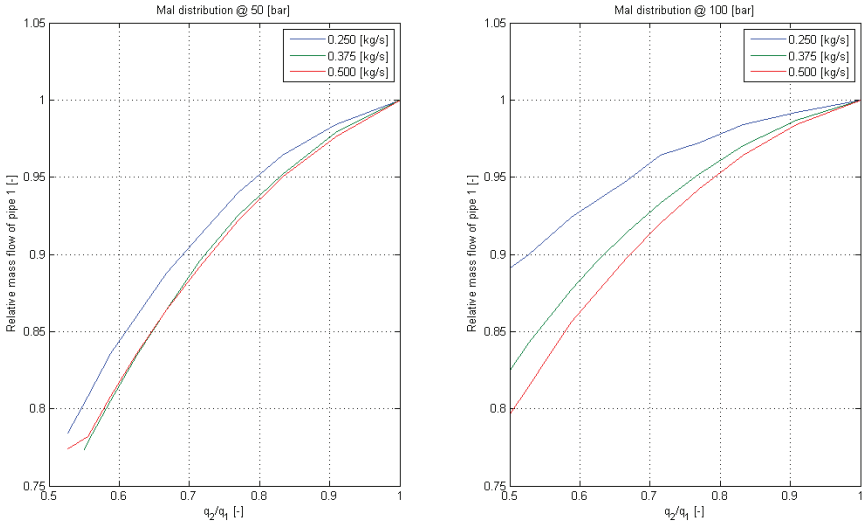

Figure H.5.: Mal distribution in panel wall.

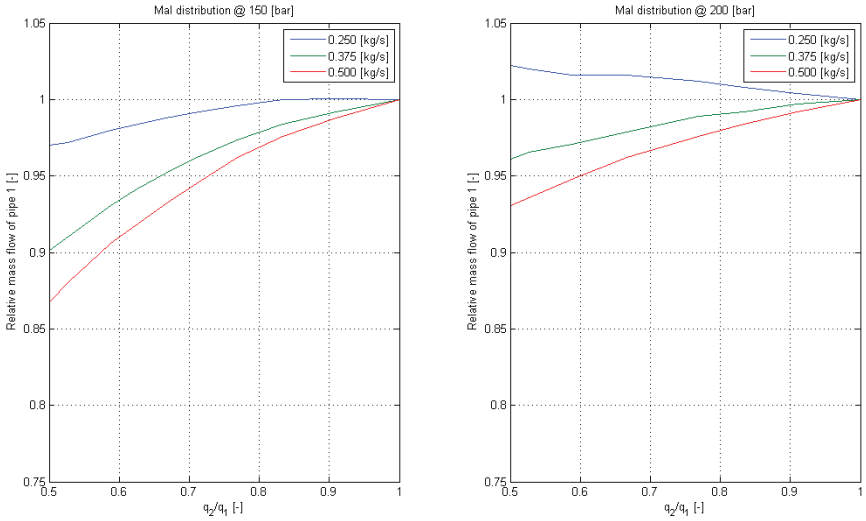

Figure H.6.: Mal distribution in panel wall.

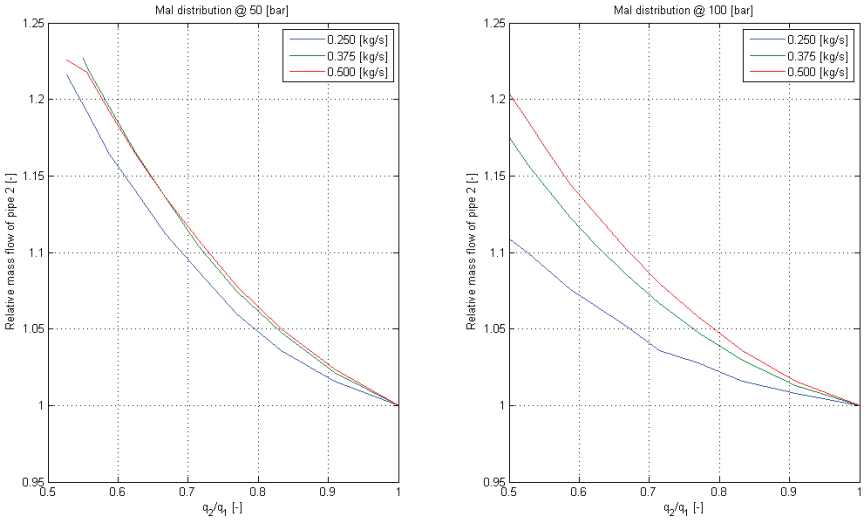

Figure H.7.: Mal distribution in panel wall.

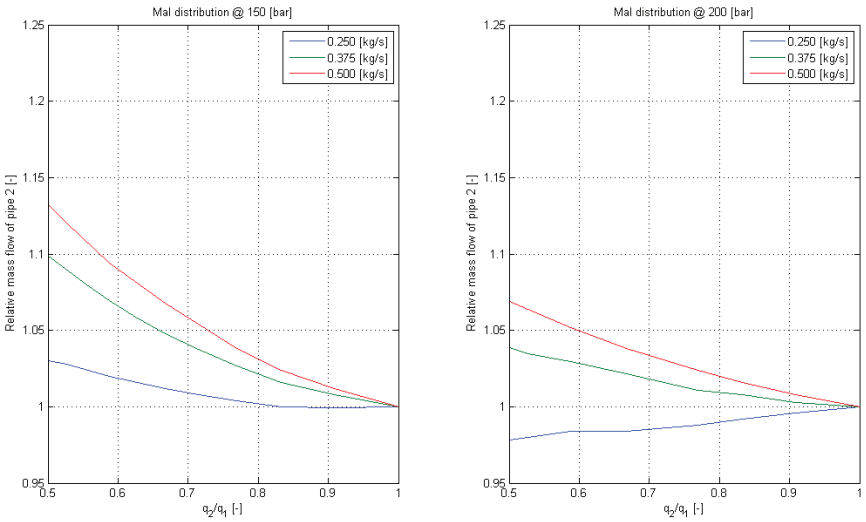

Figure H.8.: Mal distribution in panel wall.

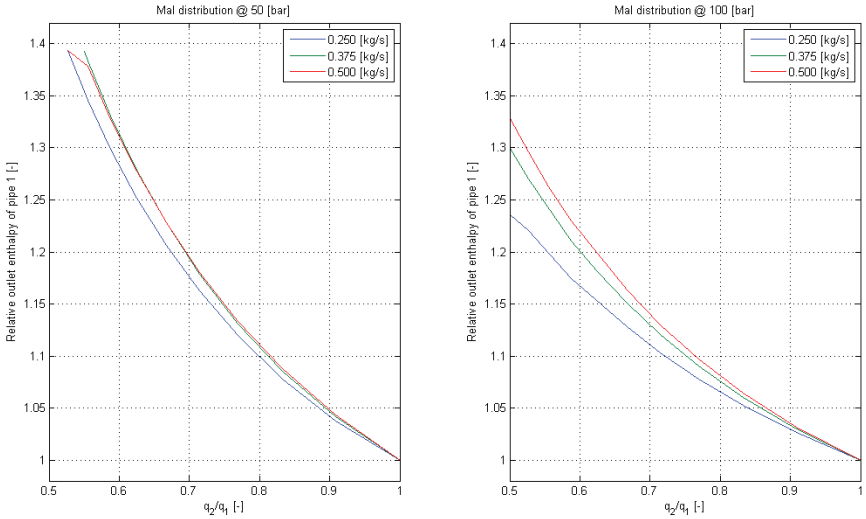

Figure H.9.: Mal distribution in panel wall.

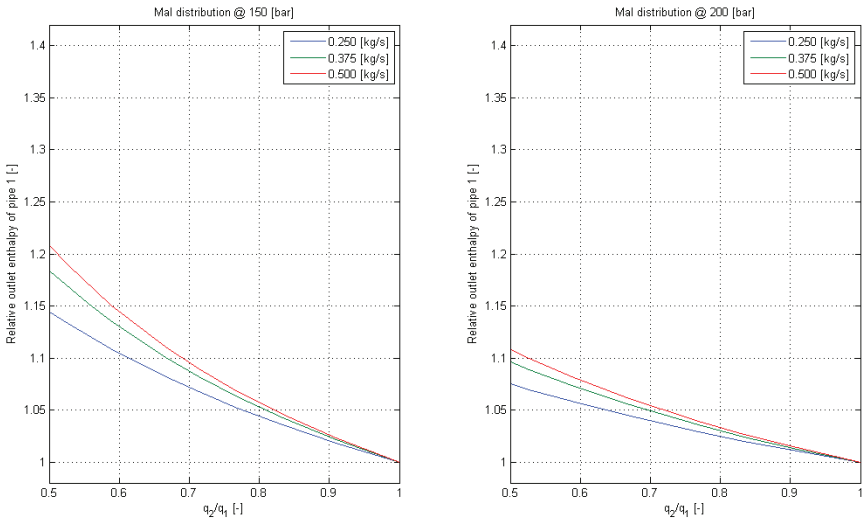

Figure H.10.: Mal distribution in panel wall.

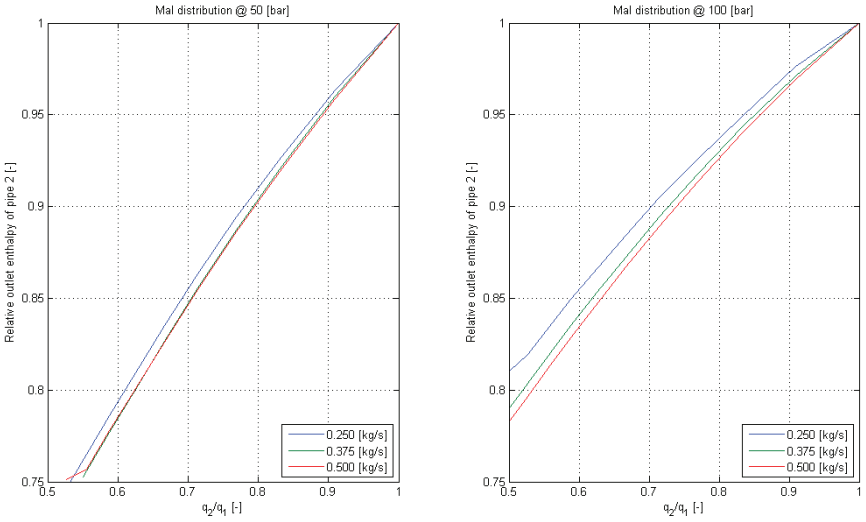

Figure H.11.: Mal distribution in panel wall.

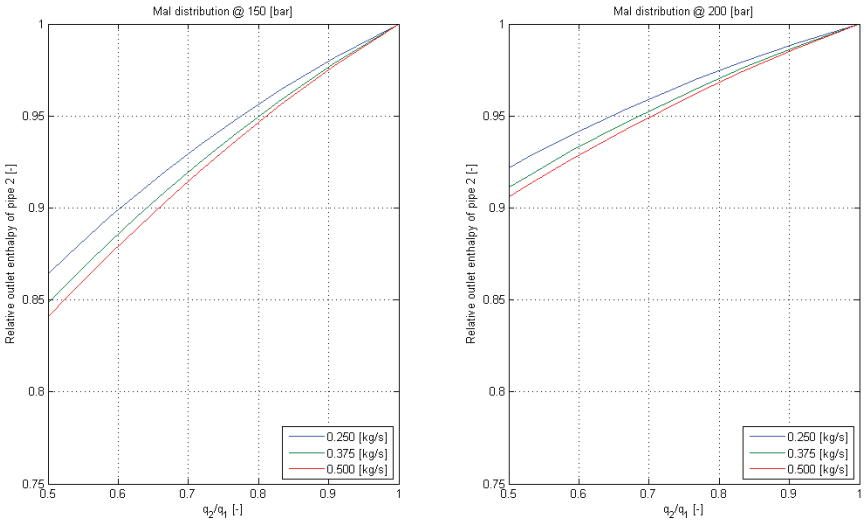

Figure H.12.: Mal distribution in panel wall.

I. EOS - interpolation functions

In the following are three different setup of interpolations are compared.

1. Bilinear (4 node) elements in Region R_5+R_6
2. Bilinear (4 node) and triangular 3 node elements in Region R_1 to R_5
3. Triangular (6 node) iso-parametric elements in Region R_1 to R_5

The first setup is based on a case using two main regions, R_6 which covers regions R_1 to R_4, and R_5 using a pure bilinear 4 node element. The second case is based on five regions using bilinear elements, supplied with a linear triangular element in the vicinity of the saturation line. Finally, a setup is using the five regions by applying an iso parametric triangular element (6-node). The simulation are identified by a number (N_s). Meshes based on different element sizes in the five regions has been created for the individual simulations. The number of elements in each case are listed in tables; table (7.3) for the two region case, table (7.4) for the five-region case with bilinear elements and table (7.5) for the five-region case with triangular elements. The total number of nodes and elements are listed in the last column.
The corresponding figures are shown in the section on interpolation of thermodynamic state variables (7.4).

N_s	N_p	P [Bar]	ε_{max}	ε_{min}	ε_{ave}	Sdev.	$T_{Intp}[s]$
1	10	1.00	0.6351E+03	0.3376E-04	0.4783E+02	0.1583E+01	0.1151E-06
2	10	10.00	0.2895E+03	0.5720E-04	0.9510E+01	0.3491E+00	0.1131E-06
3	10	50.00	0.2256E+02	0.8737E-04	0.1655E+01	0.4422E-01	0.1151E-06
4	10	100.0	0.2407E+02	0.8904E-05	0.7763E+00	0.2707E-01	0.1131E-06
5	10	220.0	0.3816E+00	0.1576E-08	0.1746E-01	0.6711E-03	0.1092E-06
6	10	300.0	0.3209E+00	0.1645E-03	0.6664E-01	0.1020E-02	0.1151E-06
7	10	700.0	0.9952E-01	0.1053E-04	0.3224E-01	0.3303E-03	0.1248E-06
8	25	1.00	0.7266E+02	0.4100E-05	0.9250E+00	0.4758E-01	0.1131E-06
9	25	10.00	0.1323E+03	0.2687E-04	0.2508E+01	0.1187E+00	0.1170E-06
10	25	50.00	0.2564E+02	0.4693E-04	0.5859E+00	0.2534E-01	0.1151E-06
11	25	100.0	0.9988E+01	0.1128E-05	0.1585E+00	0.7662E-02	0.1112E-06
12	25	220.0	0.1718E+00	0.7997E-06	0.3228E-02	0.1597E-03	0.1112E-06
13	25	300.0	0.5539E-01	0.7047E-04	0.9994E-02	0.1657E-03	0.1151E-06
14	25	700.0	0.2084E-01	0.5856E-04	0.4340E-02	0.4311E-04	0.1229E-06
15	50	1.00	0.7483E+02	0.8894E-05	0.2463E+00	0.2760E-01	0.1151E-06
16	50	10.00	0.4188E+02	0.1385E-04	0.8970E+00	0.4789E-01	0.1229E-06
17	50	50.00	0.1470E+02	0.2756E-04	0.1701E+00	0.9523E-02	0.1151E-06
18	50	100.0	0.1867E+01	0.7543E-05	0.1074E-01	0.7158E-03	0.1151E-06
19	50	220.0	0.1342E+00	0.4406E-05	0.2435E-02	0.1075E-03	0.1112E-06
20	50	300.0	0.1143E-01	0.4493E-07	0.1819E-02	0.3120E-04	0.1131E-06
21	50	700.0	0.1217E-01	0.3837E-04	0.8836E-03	0.8227E-05	0.1229E-06
22	100	1.00	0.1103E+03	0.5499E-05	0.5884E+00	0.4895E-01	0.1131E-06
23	100	10.00	0.3987E+02	0.1439E-05	0.3366E+00	0.2455E-01	0.1131E-06
24	100	50.00	0.5258E+01	0.2025E-04	0.3783E-01	0.2469E-02	0.1131E-06
25	100	100.0	0.2874E+01	0.2130E-04	0.1742E-01	0.1238E-02	0.1151E-06
26	100	220.0	0.7624E-01	0.5978E-05	0.1571E-02	0.4768E-04	0.1092E-06
27	100	300.0	0.1277E-01	0.6995E-06	0.6773E-03	0.7363E-05	0.1151E-06
28	100	700.0	0.9522E-02	0.3878E-07	0.3482E-03	0.4274E-05	0.1229E-06
29	200	1.00	0.1061E+03	0.1308E-05	0.5185E+00	0.5169E-01	0.1131E-06
30	200	10.00	0.1087E+02	0.2226E-06	0.4156E-01	0.3840E-02	0.1131E-06
31	200	50.00	0.4391E+01	0.1870E-04	0.1889E-01	0.1645E-02	0.1151E-06
32	200	100.0	0.1741E+01	0.1870E-04	0.8115E-02	0.6253E-03	0.1151E-06
33	200	220.0	0.3406E-01	0.1087E-04	0.1210E-02	0.2069E-04	0.1092E-06
34	200	300.0	0.1344E-01	0.1807E-06	0.7784E-03	0.9472E-05	0.1131E-06
35	200	700.0	0.9653E-02	0.2079E-08	0.3163E-03	0.4008E-05	0.1229E-06

Table I.1.: Bilinear (4 node) elements in Region 1-5.

N_s	N_p	P [Bar]	ε_{max}	ε_{min}	ε_{ave}	Sdev.	$t_{Intp}[s]$
36	10	1.00	0.1108E+03	0.7203E-05	0.1528E+02	0.3030E+00	0.1697E-06
37	10	10.00	0.7830E+02	0.2155E-04	0.6050E+01	0.1628E+00	0.1911E-06
38	10	50.00	0.3098E+02	0.3814E-04	0.9873E+00	0.2957E-01	0.1911E-06
39	10	100.0	0.1380E+02	0.1471E-04	0.7126E+00	0.2266E-01	0.1950E-06
40	10	220.0	0.1223E+01	0.2751E-06	0.6425E-01	0.2617E-02	0.1911E-06
41	10	300.0	0.3209E+00	0.1645E-03	0.6664E-01	0.1020E-02	0.1170E-06
42	10	700.0	0.9952E-01	0.1053E-04	0.3224E-01	0.3303E-03	0.1248E-06
43	25	1.00	0.8374E+02	0.5837E-05	0.7093E+00	0.5331E-01	0.1833E-06
44	25	10.00	0.6184E+02	0.2576E-05	0.1808E+01	0.7462E-01	0.1950E-06
45	25	50.00	0.1274E+02	0.1436E-04	0.4132E+00	0.1546E-01	0.1970E-06
46	25	100.0	0.3421E+01	0.2007E-05	0.1188E+00	0.4021E-02	0.1970E-06
47	25	220.0	0.5405E+00	0.2021E-06	0.1208E-01	0.7002E-03	0.1911E-06
48	25	300.0	0.5539E-01	0.7047E-04	0.9994E-02	0.1657E-03	0.1131E-06
49	25	700.0	0.2084E-01	0.5856E-04	0.4340E-02	0.4311E-04	0.1229E-06
50	50	1.00	0.7441E+02	0.4792E-07	0.2413E+00	0.3659E-01	0.1872E-06
51	50	10.00	0.4427E+02	0.2106E-06	0.5920E+00	0.3219E-01	0.1950E-06
52	50	50.00	0.4947E+01	0.5287E-05	0.1223E+00	0.5118E-02	0.2009E-06
53	50	100.0	0.1293E+01	0.1128E-05	0.1289E-01	0.9235E-03	0.1970E-06
54	50	220.0	0.1242E+00	0.4903E-06	0.2514E-02	0.1151E-03	0.1950E-06
55	50	300.0	0.1143E-01	0.4493E-07	0.1819E-02	0.3120E-04	0.1131E-06
56	50	700.0	0.1217E-01	0.3837E-04	0.8836E-03	0.8227E-05	0.1209E-06
57	100	1.00	0.8298E+02	0.4148E-06	0.9186E+00	0.8431E-01	0.2009E-06
58	100	10.00	0.2744E+02	0.5275E-06	0.2746E+00	0.1979E-01	0.2009E-06
59	100	50.00	0.1749E+01	0.1681E-05	0.2971E-01	0.1389E-02	0.2028E-06
60	100	100.0	0.3090E+00	0.3664E-06	0.1104E-01	0.3529E-03	0.2009E-06
61	100	220.0	0.6737E-01	0.2499E-08	0.1140E-02	0.3535E-04	0.1989E-06
62	100	300.0	0.1277E-01	0.6995E-06	0.6773E-03	0.7363E-05	0.1248E-06
63	100	700.0	0.9522E-02	0.3878E-07	0.3482E-03	0.4274E-05	0.1229E-06
64	200	1.00	0.6971E+02	0.2952E-07	0.4372E+00	0.4871E-01	0.2126E-06
65	200	10.00	0.1344E+02	0.3666E-07	0.5522E-01	0.6762E-02	0.2126E-06
66	200	50.00	0.6311E+00	0.1516E-06	0.1062E-01	0.5174E-03	0.2145E-06
67	200	100.0	0.2396E+00	0.2916E-06	0.4855E-02	0.1752E-03	0.2223E-06
68	200	220.0	0.2018E-01	0.2898E-07	0.5730E-03	0.1242E-04	0.2067E-06
69	200	300.0	0.1344E-01	0.1807E-06	0.7784E-03	0.9472E-05	0.1112E-06
70	200	700.0	0.9653E-02	0.2079E-08	0.3163E-03	0.4008E-05	0.1209E-06

Table I.2.: Bilinear (4 node) and triangular 3 node elements in Region 1-5.

N_s	N_p	P [Bar]	ε_{max}	ε_{min}	ε_{ave}	Sdev.	$t_{Intp}[s]$
71	10	1.00	0.4535E+04	-0.3484E+04	0.4612E+01	0.1773E+01	0.6845E-06
72	10	10.00	0.1548E+05	-0.3744E+05	0.6399E+01	0.6159E+01	0.5441E-06
73	10	50.00	0.1143E+02	0.2879E-07	0.2604E+00	0.1192E-01	0.7001E-06
74	10	100.0	0.1577E+01	0.2500E-09	0.4809E-01	0.2240E-02	0.3140E-06
75	10	220.0	0.1025E+01	0.3350E-08	0.3733E-01	0.1622E-02	0.9731E-06
76	10	300.0	0.2304E-01	0.1941E-06	0.4529E-02	0.6152E-04	0.4680E-06
77	10	700.0	0.1279E-01	0.4543E-07	0.5105E-03	0.6212E-05	0.5714E-06
78	25	1.00	0.7595E+02	0.1906E-05	0.4723E+00	0.3729E-01	0.1047E-05
79	25	10.00	0.1084E+03	0.6143E-08	0.9703E+00	0.7251E-01	0.5324E-06
80	25	50.00	0.1818E+01	0.3127E-09	0.1509E-01	0.1155E-02	0.6299E-06
81	25	100.0	0.2437E+00	0.3767E-10	0.2359E-02	0.1408E-03	0.4758E-06
82	25	220.0	0.3036E+00	0.2234E-06	0.6521E-02	0.3904E-03	0.5967E-06
83	25	300.0	0.7384E-02	0.1246E-07	0.3433E-03	0.4770E-05	0.6123E-06
84	25	700.0	0.1445E-01	0.2579E-08	0.4471E-04	0.3611E-05	0.5324E-06
85	50	1.00	0.5103E+02	0.3262E-07	0.9474E-01	0.1782E-01	0.8561E-06
86	50	10.00	0.1793E+02	0.2462E-09	0.1104E+00	0.1207E-01	0.6396E-06
87	50	50.00	0.4897E+00	0.4591E-08	0.1244E-02	0.1454E-03	0.5129E-06
88	50	100.0	0.5582E-01	0.8189E-11	0.2944E-03	0.3598E-04	0.4056E-06
89	50	220.0	0.3367E-01	0.2235E-07	0.3164E-03	0.1833E-04	0.5948E-06
90	50	300.0	0.6497E-02	0.2778E-08	0.5253E-04	0.2121E-05	0.6260E-06
91	50	700.0	0.1018E-01	0.2690E-09	0.2037E-04	0.2387E-05	0.4934E-06
92	100	1.00	0.6215E+03	-0.2754E+05	-0.4041E+01	0.3452E+01	0.4641E-06
93	100	10.00	0.6139E+01	0.4261E-09	0.1901E-01	0.3045E-02	0.5285E-06
94	100	50.00	0.8725E-01	0.8258E-10	0.3707E-03	0.3629E-04	0.4641E-06
95	100	100.0	0.1914E-01	0.3540E-11	0.6441E-04	0.5530E-05	0.5343E-06
96	100	220.0	0.1407E-01	0.2915E-08	0.9136E-04	0.6483E-05	0.6435E-06
97	100	300.0	0.6470E-02	0.2671E-09	0.1700E-04	0.2004E-05	0.5148E-06
98	100	700.0	0.1602E-01	0.3055E-10	0.1918E-04	0.4443E-05	0.5519E-06
99	200	1.00	0.1454E+04	-0.2294E+04	-0.5369E+00	0.4136E+00	0.4875E-06
100	200	10.00	0.2147E+01	0.2983E-09	0.5196E-02	0.9699E-03	0.4368E-06
101	200	50.00	0.1651E-01	0.5182E-10	0.8987E-04	0.7941E-05	0.6026E-06
102	200	100.0	0.2168E+00	0.1081E-11	0.1098E-03	0.4410E-04	0.5460E-06
103	200	220.0	0.6795E-02	0.8910E-09	0.2177E-04	0.1922E-05	0.5109E-06
104	200	300.0	0.6526E-02	0.1827E-09	0.1221E-04	0.1980E-05	0.3335E-06
105	200	700.0	0.8118E-02	0.1356E-09	0.1112E-04	0.2161E-05	0.4953E-06

Table I.3.: Triangular (6 node) iso-parametric elements in Region 1-5.

J. Sparse solver

Solution of linear equation systems

The solution of implicit partial differential equations involve a robust solver that can handle many degrees of freedom stored in a sparse system of data structure. In addition to this, the equation solver must handle systems of equations with low condition numbers. The partial differential equations (PDE) can be discretized using *finite volume* (FV) methods, which leads to a discretization process is a system of algebraic equations, with a linear or non-linear nature according to the type of the PDE, from which they are derived. In the non-linear case, the discretized equations must be solved by an iterative technique, that involves guessing a solution, linearising the equations about that solution, and improving the solution. This process is repeated until a converged result is obtained. For a 2D problem the algebraic equation, for one CV or grid node, is given by J.1 and the matrix version of the complete numerical problem is given by J.2.

$$a_n\Phi_n + a_s\Phi_s + a_p\Phi_p + a_e\Phi_e + a_w\Phi_w = b_p \tag{J.1}$$

The so-called *conjugated gradient* (CG) methods provide a quite general means for solving the n x n linear system

$$\mathbf{A}\cdot\Phi = \mathbf{b}, \quad \mathbf{A} \in R^{nxn}, \quad \Phi, \mathbf{b} \in R^n \tag{J.2}$$

The simplest CG algorithms solves J.2 only in the case that A is symmetric and positive definite. It is based on the idea of minimizing the function

$$f(\Phi) = \frac{1}{2}\Phi\cdot\mathbf{A}\cdot\Phi - \mathbf{b}\cdot\Phi \tag{J.3}$$

This function is minimized when its gradient

$$\nabla f = \mathbf{A}\cdot\Phi - b \tag{J.4}$$

is zero, which is equivalent to J.2. The matrices derived from partial differential equations are always sparse. Consider the matrix problem represented by J.2 which might result from a FD or FV approximation of a mathematical problem. After n iterations we have an approximate solution Φ^n which does not satisfy these equations exactly. Instead, there is a non-zero residual δ^n:

$$\mathbf{A}\cdot\Phi^n = \mathbf{b} - \delta^n \tag{J.5}$$

By subtracting this equation from J.2, we obtain a relation between the iteration error defined by:

$$\varepsilon^n = \Phi - \Phi^n \tag{J.6}$$

where Φ is the converged solution, and the residual:

$$\mathbf{A} \cdot \varepsilon^n = \delta^n \tag{J.7}$$

The purpose of the iteration procedure is to drive the residual to zero, which lead to ε also becomes zero. To see how this can be done, consider an iterative scheme for a linear system:

$$\mathbf{M} \cdot \Phi^{n+1} = \mathbf{N} \cdot \Phi^n + \mathbf{L} \tag{J.8}$$

An obvious property that must be demanded of an iterative method is that the converged results satisfy J.2. Since, at convergence, $\Phi^{n+1} = \Phi^n = \Phi$, we must have:

$$\mathbf{A} = \mathbf{M} - \mathbf{N} \;\; \& \;\; \mathbf{L} = \mathbf{b} \tag{J.9}$$

or more generally

$$\mathbf{P}\,\mathbf{A} = \mathbf{M} - \mathbf{N} \;\; \& \;\; \mathbf{L} = \mathbf{P}\,\mathbf{b} \tag{J.10}$$

where $\mathbf{P}$ is a non-singular *pre-conditioning matrix*. Non-linear solvers can be grouped into two broad categories: Newton-like methods and global methods. The former converge very quickly if an accurate estimate of the solution is available, but may fail catastrophically if the initial guess is far from the exact solution. The CG method provide a quite general means for solving the n x n linear system like J.2. The attractiveness of these methods for large sparse systems is, that they reference $\mathbf{A}$ only through its multiplication of a vector, or the multiplication of its transpose and a vector. These operations can be very efficient for properly stored sparse matrix. The most general and 'ordinary' conjugate gradient algorithm solves J.2, where $\mathbf{A}$ is not necessarily positive definite or symmetric. The simplest form of preconditioning is the scaling of the matrix $\mathbf{A}$, by rows or by columns, in order to obtain a unit diagonal matrix. For some problems this transformation alone is enough to render a slow iteration to a fast one. The CG method is an effective method for symmetric positive definite systems. It is the oldest and best known non-stationary method, but is not suitable for non-symmetric systems as the residuals cannot be made orthogonal employing short recurrences. The *bi-conjugate gradient* method (Bi-CG) approaches this difficulty differently by replacing the orthogonal sequence of residuals by two mutually orthogonal sequence, one for $\mathbf{A}$ and the other for $\mathbf{A}^{-T}$. This is a great advantage as it involves only three term recurrences enabling the work per iteration step and the storage requirements to remain under control even when many iteration steps are needed. Generally the Bi-CG method requires

four sequences of vectors, $\mathbf{r}_k$, $\bar{\mathbf{r}}_k$, $\mathbf{p}_k$ and $\bar{\mathbf{p}}_k$. Hence the following recurrence is performed:

$$\alpha_k = \frac{\bar{\mathbf{r}}_k \cdot \mathbf{r}_k}{\bar{\mathbf{p}}_k \cdot \mathbf{A} \cdot \mathbf{p}_k} \tag{J.11}$$

$$\mathbf{r}_{k+1} = \mathbf{r}_k - \alpha_k \mathbf{A} \cdot \mathbf{p}_k \tag{J.12}$$

$$\bar{\mathbf{r}}_{k+1} = \bar{\mathbf{r}}_k - \alpha_k \mathbf{A}^T \cdot \bar{\mathbf{p}}_k \tag{J.13}$$

$$\beta_k = \frac{\bar{\mathbf{r}}_{k+1} \cdot \mathbf{r}_{k+1}}{\bar{\mathbf{r}}_k \cdot \mathbf{r}_k} \tag{J.14}$$

$$\mathbf{p}_{k+1} = \mathbf{r}_k + \beta_k \mathbf{p}_k \tag{J.15}$$

$$\bar{\mathbf{p}}_{k+1} = \bar{\mathbf{r}}_k + \beta_k \bar{\mathbf{p}}_k \tag{J.16}$$

This sequence of vectors satisfies the *bi-orthogonally* condition:

$$\bar{\mathbf{r}}_i \cdot \mathbf{r}_j = \mathbf{r}_i \cdot \bar{\mathbf{r}}_j = 0, \quad j < i \tag{J.17}$$

and the *biconjugacy* condition:

$$\bar{\mathbf{p}}_i \cdot \mathbf{A} \cdot \mathbf{p}_j = \mathbf{p}_i \cdot \mathbf{A} \cdot \bar{\mathbf{p}}_j = 0, \quad j < i \tag{J.18}$$

and there is also a mutual orthogonally,

$$\bar{\mathbf{r}}_i \cdot \mathbf{p}_j = \mathbf{r}_i \cdot \bar{\mathbf{p}}_j = 0, \quad j < i \tag{J.19}$$

To use the algorithm to solve J.2, make an qualified initial guess Φ_1 for the solution and choose $\mathbf{r}_1$=δ_l in J.5 and choose $\bar{\mathbf{r}}_1 = \mathbf{r}_1$. Then get an improved estimate from:

$$\Phi_{k+1} = \Phi_k + \alpha_k \cdot \mathbf{p}_k \tag{J.20}$$

while carrying out the recurrence of J.11 to J.16. J.20 guarantees that r_{k+1} from the recurrence is in fact the residual $\mathbf{b} - \mathbf{A} \cdot \Phi_{k+1}$ corresponding to Φ_{k+1}. Since $\mathbf{r}_{m+1}$=0 then Φ_{m+1} is the solution to J.2. The ordinary CG algorithm is the special case of the Bi-CG algorithm when $\mathbf{A}$ is symmetric, and we choose $\bar{\mathbf{r}}_1$=$\mathbf{r}_1$. Then $\bar{\mathbf{r}}_k$=$\mathbf{r}_k$ and $\bar{\mathbf{p}}_k$=$\mathbf{p}_k$ for all k; we can omit computing them and halve the work of the algorithm. This CG version has the interpretation of minimizing J.3. If $\mathbf{A}$ is positive definite as well as symmetric, the algorithm is in theory stable and cannot break down. The stop criteria can be based on J.6, where $|\varepsilon^n| = |\Phi^n - \Phi^{n-1}| < |\varepsilon_{stop}|$.

Sparce technique

The physical problems, which are treated in this work, leads to numerical problems, with very sparsely populated matrices, which results in the use of a compact matrix technique. This technique is implemented in the CFD solver to improve

the computational speed and minimize the memory storage. The method operates with a pointer technique, where each coefficient in the main matrix like J.2 are stored row by row in an **Array**, dictated by a local pointer on row level. Each row has also a pointer to describe the end position of each row. All pointers are stored in a pointer array named **Pointer**. J.1 illustrates how the equation system is organized in a square matrix of n_z x n_z elements (zero elements are not shown). The red cells in in J.1 are referring to the pointer storage scheme in J.2. Note

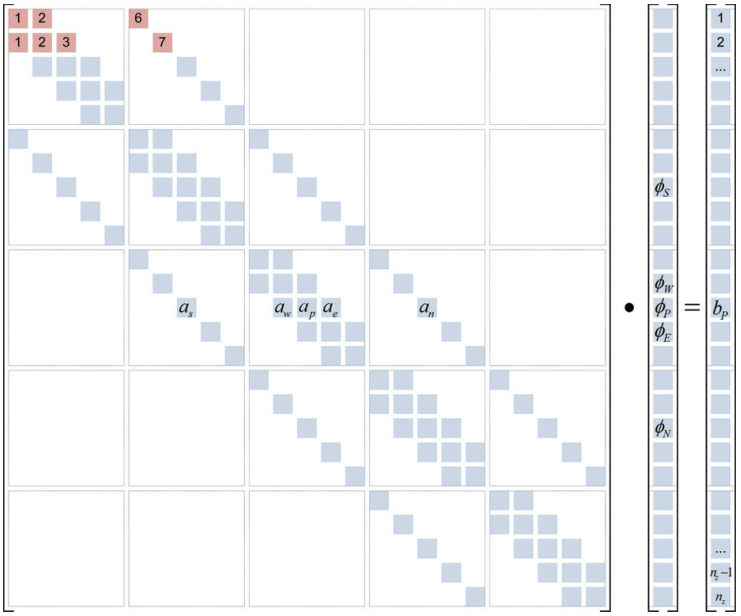

Figure J.1.: Sparse matrix, structure of the matrix for a five-point computational molecule.

that the first n_z elements contains the pointer of a_e^i coefficient, for i=1 to n_z. The following pointers contain the row position counting from 1 to n_z for each row in the matrix system. The organization of the equation system coefficients are

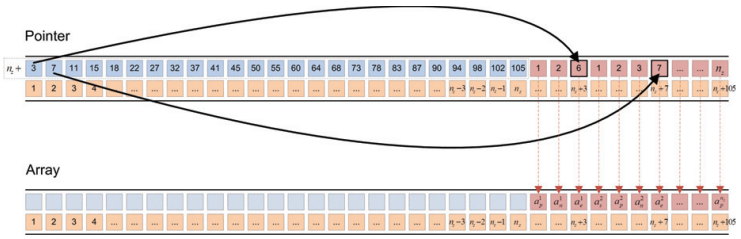

Figure J.2.: Structure of the Pointer and Array for sparse storage of matrix.

described by the following pseudo code: n=Neq

```
for i=1 to Neq

if(a_s(i) != Null & i-nz > 0) then      ! Store a_s coefficient
  n=n+1;   Array(n) = a_s(i);   Pointer(n) = i-nz
endif

if(a_w(i) != Null & i-1 > 0) then      ! Store a_w coefficient
  n=n+1;   Array(n) = a_w(i);   Pointer(n) = i-1
endif

if(a_p(i) != Null) then      ! Store a_p coefficient
  n=n+1;   Array(n) = a_p(i);   Pointer(n) = i
endif

if(a_e(i) != Null & i+1 <= Neq) then      ! Store a_e coefficient
  n=n+1;   Array(n) = a_e(i);   Pointer(n) = i+1
endif

if(a_n(i) != Null & i+nz <= Neq) then      ! Store a_n coefficient
  n=n+1;   Array(n) = a_n(i);   Pointer(n) = i+nz
endif

Array(i) = 1.0D0
Pointer(i) = n

EndDo
```

where Neq is the number of CV's in the model and a_n, a_s, a_e, a_w and a_p are similar to the coefficients in J.1.

Time differentiation

The applied time differentiation scheme is fully implicit backward. This means the solution at step n is a function of the derivatives at step n and the solution at step n-1. Since the derivatives at step n are unknown, this results in a large system of linearised equations to be solved.

K. Further partial derivatives

In this appendix is listed the most important partial derivatives due to an EOS for the one- and two-phase region of a fluid. For the temperature we can derive the below equations for one-phase

$$\left(\frac{\partial T}{\partial h}\right)_p = \frac{1}{c_p} \tag{K.1}$$

$$\left(\frac{\partial T}{\partial p}\right)_h = \frac{\beta T v - v}{c_p} \tag{K.2}$$

and for two-phase region we have

$$\left(\frac{\partial T}{\partial h}\right)_p = 0 \tag{K.3}$$

$$\left(\frac{\partial T}{\partial p}\right)_h = \frac{dT}{dp} \tag{K.4}$$

For the enthalpy we can list the analogue derivatives. For one-phase:

$$\left(\frac{\partial s}{\partial h}\right)_p = \frac{1}{T} \tag{K.5}$$

$$\left(\frac{\partial s}{\partial p}\right)_h = -\frac{v}{T} \tag{K.6}$$

and for two-phase region we have

$$\left(\frac{\partial s}{\partial h}\right)_p = \frac{s_g - s_l}{h_g - h_l} \tag{K.7}$$

$$\left(\frac{\partial s}{\partial p}\right)_h = \frac{ds_l}{dp} + \frac{x}{dp}(s_g - s_l) + x\left(\frac{ds_g}{dp} - \frac{ds_l}{dp}\right) \tag{K.8}$$

where

$$\frac{ds_l}{dp} = \frac{c_{p,l}}{T}\frac{dT}{dp} - \beta_l v_l \quad \text{and} \quad \frac{ds_g}{dp} = \frac{c_{p,g}}{T}\frac{dT}{dp} - \beta_g v_g \tag{K.9}$$

L. Fluent flow and combustion model

L.1. Fluent Flow model

For the simulation of the combustion processes in a furnace, FLUENT® 13.0 is used as the CFD solver. The general mass conservation equation is

$$\frac{\partial}{\partial x_i}(\rho U_i) = 0, \tag{L.1}$$

where ρ is the density of the fluid, U_i are the Cartesian velocity component (i = 1, 2 and 3), x_i are the coordinate axes, and the repeated indices imply summation over 1-3. The Reynolds averaged momentum equations are defined as

$$\rho\left(\frac{\partial U_i}{\partial t} + U_j\frac{\partial U_i}{\partial x_j}\right) = -\frac{\partial p}{\partial x_i} + \frac{\partial}{\partial x_j}\left(\mu\frac{\partial U_i}{\partial x_j}\right) + \frac{\partial R_{ij}}{\partial x_j} \tag{L.2}$$

where p is the pressure, μ is the dynamic viscosity. The Reynolds Stresses are defined as

$$R_{ij} = \mu_t\left(\frac{\partial U_i}{\partial x_j} + \frac{\partial U_j}{\partial x_i}\right) - \frac{2}{3}\rho k\delta_{ij} \tag{L.3}$$

Here μ_t is the eddy viscosity, k is the turbulent kinetic energy, δ_{ij} is the Kronecker symbol. The turbulence model used in this investigation is the realizable variant of the k-ε model (where ε is energy dissipation rate). The eddy viscosity is defined as

$$\mu_t = C_\mu\rho\frac{k^2}{\varepsilon} \tag{L.4}$$

where C_μ is computed from:

$$C_\mu = \frac{1}{A_0 + A_s\frac{ku^*}{\varepsilon}} \tag{L.5}$$

where

$$u^* \equiv \sqrt{S_{ij}S_{ij} + \tilde{\Omega}_{ij}\tilde{\Omega}_{ij}} \tag{L.6}$$

and

$$\tilde{\Omega_{ij}} = \Omega_{ij} - 2\varepsilon_{ijk}\omega_k \tag{L.7}$$

$$\Omega_{ij} = \overline{\Omega_{ij}} - 2\varepsilon_{ijk}\omega_k \tag{L.8}$$

Note that $\overline{\Omega_{ij}}$ is the mean rate of rotation tensor viewed in a moving reference frame with the angular velocity ω_k. The model constants A_0 and A_s are given by: A_0=4.04, A_S=$\sqrt{6}\cos(\phi)$ and ϕ=1/3$\cos^{-1}(\sqrt{6}W)$ and

$$W = \frac{S_{ij}S_{jk}S_{ki}}{\tilde{S}^3}, \quad \tilde{S} = \sqrt{S_{ij}S_{ij}} \tag{L.9}$$

and S_{ij} is given below in relation to the transport equations of k and ε. The turbulence kinetic energy k and its rate of dissipation ε are obtained from the following transport equations:

$$\rho\frac{\partial k}{\partial t} + \rho U_j \frac{\partial k}{\partial x_j} = \frac{\partial}{\partial x_j}\left(\left(\mu + \frac{\mu_t}{\sigma_k}\right)\frac{\partial k}{\partial x_j}\right) + \mu_t S^2 - \rho\varepsilon \tag{L.10}$$

$$\rho\frac{\partial \varepsilon}{\partial t} + \rho U_j \frac{\partial \varepsilon}{\partial x_j} = \frac{\partial}{\partial x_j}\left(\left(\mu + \frac{\mu_t}{\sigma_\varepsilon}\right)\frac{\partial \varepsilon}{\partial x_j}\right) + \frac{\varepsilon}{k}\left(C_{\varepsilon 1}\mu_t S^2 - \rho C_{\varepsilon 2}\varepsilon\right)$$

where S=$\sqrt{2S_{ij}S_{ij}}$ and S_{ij}=$\frac{1}{2}(\frac{\partial U_i}{\partial x_j}+\frac{\partial U_j}{\partial x_i})$, and closure coefficients, $C_{\varepsilon 1}$ = 1.44, $C_{\varepsilon 2}$ = 1.92, σ_k = 1.0, σ_ε = 1.3.
In the present study, second-order upwind scheme has been applied for all numerical simulations. A second order upwind scheme was used to avoid numerical oscillations and instability associated with central differencing for convective terms in the transport equation and to increase the accuracy of solutions. The coupling between the velocity field and pressure field is strong for incompressible flows. The SIMPLE algorithm was employed to relate velocity and pressure corrections to enforce mass conservation and to obtain the pressure field, see ([150]).

L.2. Combustion reaction model

The combustion reaction is modelled by solving an additional set of transport equations for the species involved in the reaction. The transport equation for each mass fraction of species i (Y_i) is of the form, where $D_{i,m}$ is the laminar diffusion coefficient of species i and Sc_t is the turbulent Schmidt number:

$$\frac{\partial}{\partial t}(\rho Y_i) + \nabla\cdot(\rho U_j Y_i) = \nabla\cdot\left(\left(\rho D_{i,m} + \frac{\mu_t}{Sc_t}\right)\nabla\cdot Y_i\right) + R_i + S_i \tag{L.11}$$

$$\text{Transient} + \text{Convection} = \quad \text{Diffusion} \quad + \quad \text{Source/Sink terms}$$

The first term is zero as the model is steady state and the next two is due to

convective flow and diffusion respectively. The source term can be divided into two parts; the rate of production of species i (R_i) from chemical reaction and the rate of creation of species i (S_i) stemming from e.g. a dispersed phase like de-volatilization or char burnout from coal or straw.

L.3. Gas phase reaction setup

The combustion reaction is modelled as a two-step-global reaction mechanism as shown below:

$$\begin{aligned} &\text{I: } CH_4 + \frac{3}{2}O_2 \longrightarrow CO + 2H_2O \\ &\text{II: } CO + \frac{1}{2}O_2 \longrightarrow CO_2 \end{aligned} \tag{L.12}$$

which is a modified implementation following [151]. The gas phase reaction rates are modelled using the finite-rate/eddy dissipation (FR/ED) model setup in FLUENT 13.0. Using this method, it is possible to account for conditions where a given reaction is either kinetically or mixing limited. In turbulent combustion flames the reactions are often mixing controlled and the kinetic reaction rate acts as a "thermal switch" ensuring that reaction does not inadvertently take place before the reactants enter the hot near-burner region (flame region). The kinetic reaction rates for the two reactions are expressed as:

$$\begin{aligned} r_i^f &= k_i^f(T)\,[CH_4]^{0.7}\,[O_2]^{0.8} \\ r_{ii}^f &= k_{ii}^f(T)\,[CO]\,[O_2]^{0.25} \end{aligned} \tag{L.13}$$

where the rate coefficients follow Arrhenius type expressions:

$$k_i^f = A_i T^{\beta_i} \exp\left(\frac{-E_{a,i}}{R_U T}\right) \tag{L.14}$$

The Arrhenius parameters are shown in table L.1: In the mixing controlled region,

Reaction	rate constant	A	β	E_a
Units	[kmol/m^3s]	for β=0:[kmol/s]	[−]	[J/kmol]
(i)	k_i^f	$5.012 \cdot 10^{11}$	0.0	$2 \cdot 10^8$
(ii)	k_{ii}^f	$2.239 \cdot 10^{12}$	0.0	$1.7 \cdot 10^8$

Table L.1.: Arrhenius rate parameters.

the eddy dissipation model (EDM) relates the reaction rate to the dissipation rate of the turbulent eddies containing reactants or products. The governing parameter

in the rate expressions (shown below) is the large-eddy mixing scale (k/ε), where k and ε are the turbulent kinetic energy and turbulent dissipation rate respectively, given by equation (L.10). The first expression is the reaction rate as a function of the eddies containing reactants (r) and the following is a function of the product (p) containing eddies. A and B are empirical constants. In this case A = 2 and B = 0.5.

$$r_r^{ED} = A\rho\frac{\varepsilon}{k}\min_R\left(\frac{Y_R}{\nu'_{R,i}M_{w,R}}\right) \tag{L.15}$$

$$r_p^{ED} = A\rho\frac{\varepsilon}{k}B\left(\left(\frac{\sum_P Y_P}{\sum_j^N \nu''_{j,r}M_{w,j}}\right)\right) \tag{L.16}$$

The FR/ED model will always assume the governing reaction rate to be the smallest of either the kinetic (Arrhenius) expression or one of the two mixing rates for the given reaction. The radiation model applied is the DO radiation model (Chui & Raithby, 1990), (Raithby & Chui, 1993) implemented in the Fluent ® CFD code. Likewise, turbulence closure has been modelled using the realizable variant of the k-ε two-equation turbulence model (Shih, Liou, Shabbir, Yang, & Zhu, 1995) as implemented in the Fluent ® CFD code.

M. Four field model

In this appendix are derived a four-layer flow model, also called four field model. For simplicity the one-dimensional flow is assumed incompressible and a time-averaging of the velocity fluctuations are considered similar to the known averaging turbulent fluctuations from single-phase fluid dynamics. The pipe channel is considered a uniform channel with constant cross sectional area (A) and no internal heat production. For vertical flow, a non-isotherm stratification of the flow fields is caused by the a swirl initiated by the IRBT.

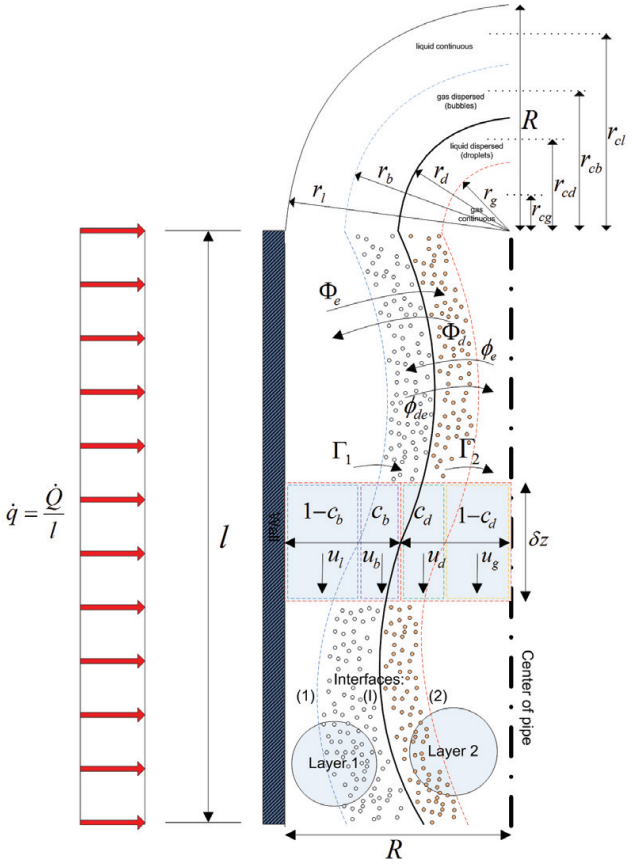

Figure M.1.: Illustration of the four different control volumes in the two-phase fluid. The fluid is flowing in a cylindrical channel with uniform radius R.

M.1. Conservation of mass

The volume fraction of total liquid can be described as the sum of a continuous phase (ε_l) and a dispersed liquid phase as droplets (ε_d):

$$\varepsilon_L = \varepsilon_l + \varepsilon_d \tag{M.1}$$

Correspondingly the volume fraction of total gas or steam can be describes as the sum of a continuous phase (ε_g) and a dispersed gas phase as bubbles (ε_b):

$$\varepsilon_G = \varepsilon_g + \varepsilon_b \tag{M.2}$$

Hence, the sum of ε_L and ε_G must be unity.

$$\varepsilon_L + \varepsilon_G = 1 \tag{M.3}$$

An interface zone (with the perimeter named S_i) is separating the flow into two phases named layer 1 and layer 2. The densities can be formulated as:

$$\rho_1 = \frac{\varepsilon_l \rho_l + \varepsilon_b \rho_b}{\varepsilon_l + \varepsilon_b},\ \varepsilon_1 = \varepsilon_l + \varepsilon_b \tag{M.4}$$

and

$$\rho_2 = \frac{\varepsilon_g \rho_g + \varepsilon_d \rho_l}{\varepsilon_g + \varepsilon_d},\ \varepsilon_2 = \varepsilon_g + \varepsilon_d \tag{M.5}$$

The corresponding centre of mass velocity of the two mixture layers are

$$u_1 = \frac{c_b \rho_g u_b + (1 - c_b)\rho_l u_l}{\rho_1} \tag{M.6}$$

for field 1, and

$$u_2 = \frac{c_d \rho_l u_d + (1 - c_d)\rho_g u_g}{\rho_2} \tag{M.7}$$

for field 2. In equation (M.6) and (M.7) c_b and c_d denote the ration of the dispersed field volume fraction to the mixture volume fraction of the layer:

$$c_b = \frac{\varepsilon_b}{\varepsilon_b + \varepsilon_l},\ c_d = \frac{\varepsilon_d}{\varepsilon_d + \varepsilon_g}, \tag{M.8}$$

A corresponding expression can be written for the pressure P_1 and P_2 as well as for the enthalpy. Pressure correlations:

$$P_1 = \frac{c_b \rho_g P_b + (1 - c_b)\rho_l P_l}{\rho_1} \tag{M.9}$$

$$P_2 = \frac{c_d \rho_l P_d + (1 - c_d)\rho_g P_g}{\rho_2} \tag{M.10}$$

and the enthalpy correlations:

$$h_1 = \frac{c_b \rho_g h_b + (1 - c_b)\rho_l h_l}{\rho_1} \tag{M.11}$$

$$h_2 = \frac{c_d \rho_l h_d + (1 - c_d)\rho_g h_g}{\rho_2} \tag{M.12}$$

The mass flux G_k is defined for both layers (k=1,2)

$$\begin{aligned} G_1 &= \rho_1 u_1 \\ &= G_1(1 - \dot{x_1}) + G_1 \dot{x_1} \\ &= \rho_l (1 - c_b) u_l + \rho_g c_b u_b \end{aligned} \tag{M.13}$$

Where $\dot{x_1}$ is the flow quality given by (M.19). Hence the liquid and bubble velocities are given as:

$$u_l = G_1 \frac{1 - \dot{x_1}}{\rho_l (1 - c_b)} \tag{M.14}$$

$$u_b = G_1 \frac{\dot{x_1}}{\rho_g c_b} \tag{M.15}$$

In analogy withe layer 1, we find for layer 2:

$$\begin{aligned} G_2 &= \rho_2 u_2 \\ &= G_2(1 - \dot{x_2}) + G_2 \dot{x_2} \\ &= \rho_g (1 - c_d) u_g + \rho_l c_d u_d \end{aligned} \tag{M.16}$$

and the gas and droplet velocities are given as:

$$u_g = G_2 \frac{1 - \dot{x_2}}{\rho_g (1 - c_d)} \tag{M.17}$$

$$u_d = G_2 \frac{\dot{x_2}}{\rho_l c_d} \tag{M.18}$$

The flow quality $\dot{x}$ is purely hydrodynamic and must not be compared with the thermodynamic equilibrium quality x. The flow quality for the two layers are given by M.19 and M.20

$$\begin{aligned} \dot{x_1} &= \frac{\rho_g u_b c_b A}{\rho_g u_b c_b A + \rho_l u_l [1 - c_b] A} \\ &= \frac{\dot{m}_b}{\dot{m}_b + \dot{m}_l} \end{aligned} \tag{M.19}$$

$$\begin{aligned} \dot{x_2} &= \frac{\rho_l u_d c_d A}{\rho_l u_d c_d A + \rho_g u_g [1 - c_d] A} \\ &= \frac{\dot{m}_d}{\dot{m}_d + \dot{m}_g} \end{aligned} \tag{M.20}$$

The mass conservation equations are derived for a slice of a pipe element as illustrated in (M.2). Let us define Φ and ϕ as the rates of bubble entrainment and disengagement rates, and droplet entrainment and deposition rates respectively, measured as per unit mixture volume. Additionally, we have Γ representing the rate of phase changes with positive sign for evaporation. The mass transport due to phase changes is represented along two interface layers, i.e. Γ_1 describing the rate of phase changes of liquid continuous to gas dispersed (bubbles) in region 1 and Γ_2, describing the phase change of liquid dispersed (droplets) to gas continuous. Both phase change terms are measured per unit volume per second. The mass flow terms are depicted in M.1 and M.2 for a slice of the flow channel, where z and t are the spatial and time coordinates. The mass flow at z+δz is described by a Taylor series expansion around z. Phase conservation equations, including bubble entrainment, disengagement rates as well as droplet entrainment and deposition rates, can now be derived by applying the mass continuity principle to the four fields (liquid continuous, liquid dispersed, gas continuous and gas dispersed) as occupied portions of a control volume and taking the limit of δz $\rightarrow$ 0.

$$\frac{\partial}{\partial t}(\varepsilon_l \rho_l) + \frac{\partial}{\partial z}(\varepsilon_l \rho_l u_l) = -\Phi_e + \Phi_d - \Gamma_1 \tag{M.21}$$

$$\frac{\partial}{\partial t}(\varepsilon_b \rho_g) + \frac{\partial}{\partial z}(\varepsilon_b \rho_g u_b) = \phi_e - \phi_{de} + \Gamma_1 \tag{M.22}$$

$$\frac{\partial}{\partial t}(\varepsilon_g \rho_g) + \frac{\partial}{\partial z}(\varepsilon_g \rho_g u_g) = -\phi_e + \phi_{de} + \Gamma_2 \tag{M.23}$$

$$\frac{\partial}{\partial t}(\varepsilon_d \rho_l) + \frac{\partial}{\partial z}(\varepsilon_d \rho_l u_d) = \Phi_e - \Phi_d - \Gamma_2 \tag{M.24}$$

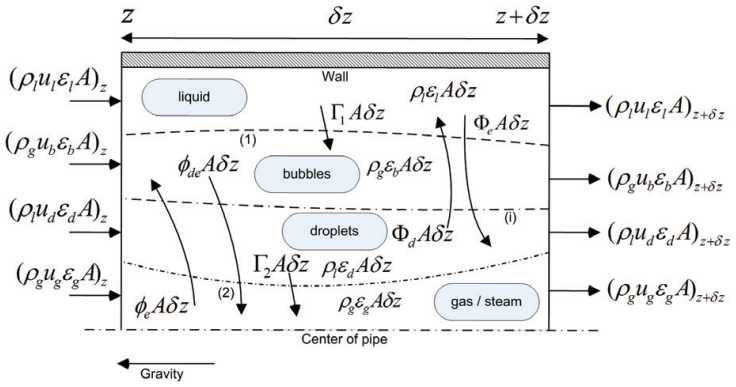

Figure M.2.: Mass transfer terms for the four layers on a slice of a pipe-element.

The mass conversation equations for the total liquid and gas volume fractions are obtained by summing the equations (M.21) and (M.24), (M.23) and (M.22), respectively:

$$\frac{\partial}{\partial t}(\varepsilon_L \rho_l) + \frac{\partial}{\partial z}(\varepsilon_1 G_1) - \Gamma_1 - \Gamma_2 = 0 \tag{M.25}$$

$$\frac{\partial}{\partial t}(\varepsilon_G \rho_g) + \frac{\partial}{\partial z}(\varepsilon_2 G_2) + \Gamma_1 + \Gamma_2 = 0 \tag{M.26}$$

For an isotherm model, the rate of phase change Γ would be zero.

M.2. Momentum equations

The formulation of the momentum equations are derived on the basis of Newton's second law to each layer control volume. This formulation is a minor modification of the momentum equation developed by [103]. The momentum transfer terms are illustrated in (M.3) and the forces acting on the layers are illustrated in (M.4) on a slice of a pipe-element. The momentum balance is set up for each field (l, b, d and g). The interfacial velocities are given as u_{i1} and u_{i2}. $\tau_{drag,k}$ denotes the drag forces in between the dispersed bubbles in the liquid continuous layer and droplets in the gas continuous layer respectively. τ_i represents the interfacial drag along the interface I with the perimeter S_i. The forces are defined per unit area. The principals of conservation of momentum expresses that at any instant of change of momentum of a volume moving with the fluid is equal to the sum of surface forces and volume forces acting on the volume. The momentum transport out of the control volume is illustrated on (M.3) and is located at $z + \delta z$. At the same location we have the corresponding pressure force acting on the downstream boundary of the control volume illustrated in M.4. Those contributions in the momentum balance are described in analogy to the mass continuity equations as

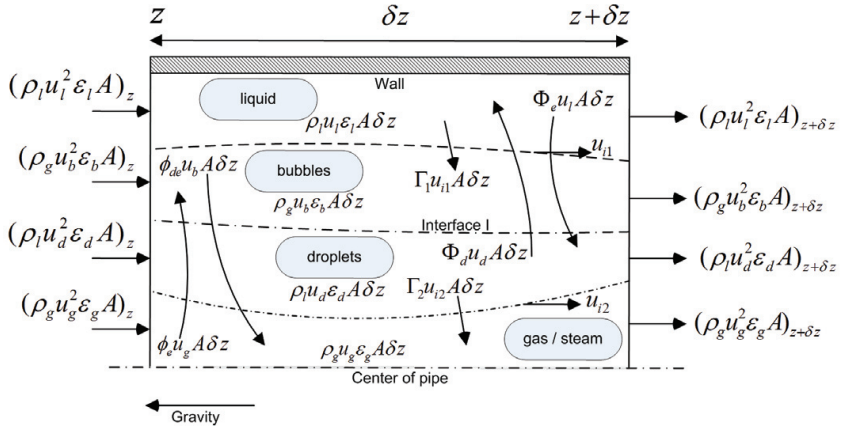

Figure M.3.: Momentum transfer terms for the four fields on a slice of a pipe-element.

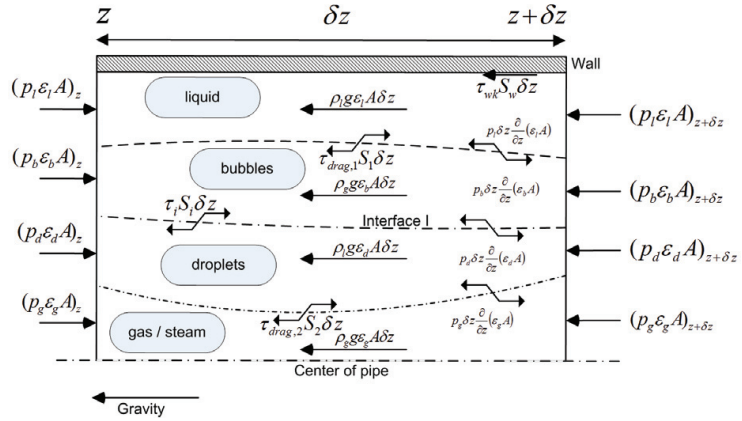

Figure M.4.: Forces acting on the four fields on a slice of a pipe-element.

Taylor expansions around z. The mathematical formula of the above principle can be written for the four momentum equations presenting the four fields by letting $\delta z \to 0$:

$$\begin{aligned}\frac{\partial}{\partial t}\left(\varepsilon_l u_l \rho_l\right) + \frac{\partial}{\partial z}\left(\varepsilon_l \rho_l u_l^2\right) = &-\frac{\partial}{\partial z}\left(P_l \varepsilon_l\right) \\ &- \tau_{wk}\frac{S_w}{A} + \tau_{drag,1}\frac{S_1}{A} \\ &- \rho_l g \varepsilon_l - \Gamma_1 u_{i1} - \Phi_e u_l + \Phi_d u_d\end{aligned} \tag{M.27}$$

$$\begin{aligned}\frac{\partial}{\partial t}\left(\varepsilon_g u_g \rho_g\right) + \frac{\partial}{\partial z}\left(\varepsilon_g \rho_g u_g^2\right) = &-\frac{\partial}{\partial z}\left(P_l \varepsilon_g\right) \\ &- \tau_{drag,2}\frac{S_2}{A} - \rho_g g \varepsilon_g \\ &- \Gamma_2 u_{i2} - \Phi_{de} u_g + \Phi_e u_b\end{aligned} \tag{M.28}$$

$$\begin{aligned}\frac{\partial}{\partial t}\left(\varepsilon_d u_d \rho_l\right) + \frac{\partial}{\partial z}\left(\varepsilon_d \rho_l u_d^2\right) = &-\frac{\partial}{\partial z}\left(P_d \varepsilon_d\right) \\ &- \tau_i\frac{S_i}{A} + \tau_{drag,2}\frac{S_2}{A} \\ &- \rho_l g \varepsilon_d - \Gamma_2 u_{i2} + \Phi_e u_l - \Phi_d u_d\end{aligned} \tag{M.29}$$

$$\begin{aligned}\frac{\partial}{\partial t}\left(\varepsilon_b u_b \rho_g\right) + \frac{\partial}{\partial z}\left(\varepsilon_b \rho_g u_b^2\right) = &-\frac{\partial}{\partial z}\left(P_b \varepsilon_b\right) \\ &+ \tau_i\frac{S_i}{A} - \tau_{drag,1}\frac{S_1}{A} \\ &- \rho_g g \varepsilon_b + \Gamma_1 u_{i1} - \Phi_{de} u_b + \Phi_e u_g\end{aligned} \tag{M.30}$$

The source/sink terms described by (M.29) and (M.30) expresses the non-condensing momentum transport of mass from the specific fields, whereas the phase change rates con tributes with momentum exchange (Γ_1 and Γ_2), caused by the surrounding evaporation or condensation. The τ_{drag} is representing the interfacial drag acting on the dispersed field. The flow pattern is assumed rotating along the main axis of the pipe, as a consequence of the internal rifles in the pipe channel. This causes an acceleration due to the centrifugal force of the fluid particles for the dispersed droplets and bubbles respectively, and is represented by a radial pressure gradient, which is outlined in the section of Rotating flow. The momentum equations can be expressed by a mixture of the continuous liquid layer and the

dispersed bubble layer by adding (M.27) and (M.30) where the conservation of momentum across the interfacial terms cancels out.

$$\begin{aligned}\frac{\partial}{\partial t}\left(\varepsilon_l u_l \rho_l\right)+\frac{\partial}{\partial t}\left(\varepsilon_b u_b \rho_g\right)+\frac{\partial}{\partial z}\left(\varepsilon_l \rho_l u_l^2\right)+\frac{\partial}{\partial z}\left(\varepsilon_b \rho_g u_b^2\right)& \\ =-\frac{\partial}{\partial z}\left(P_l \varepsilon_l\right)-\frac{\partial}{\partial z}\left(P_b \varepsilon_b\right)& \\ -\tau_{wk}\frac{S_w}{A}+\tau_i\frac{S_i}{A}& \\ -\rho_l g \varepsilon_l-\rho_g g \varepsilon_b& \\ -\Phi_e u_l-\Phi_{de} u_b+\Phi_d u_d+\Phi_e u_g&\end{aligned} \tag{M.31}$$

The drag forces $\tau_{drag,1}\frac{S_1}{A}$ as well as the evaporation terms $\Gamma_1 u_{i1}$ are eliminated. Additionally, we find by adding (M.28) and (M.29) the momentum equation for layer 2:

$$\begin{aligned}\frac{\partial}{\partial t}\left(\varepsilon_g u_g \rho_g\right)+\frac{\partial}{\partial t}\left(\varepsilon_d u_d \rho_l\right)+\frac{\partial}{\partial z}\left(\varepsilon_g \rho_g u_g^2\right)+\frac{\partial}{\partial z}\left(\varepsilon_d \rho_l u_d^2\right)& \\ =-\frac{\partial}{\partial z}\left(P_l \varepsilon_g\right)-\frac{\partial}{\partial z}\left(P_d \varepsilon_d\right)& \\ -\tau_i\frac{S_i}{A}& \\ -\rho_g g \varepsilon_g-\rho_l g \varepsilon_d& \\ -\Phi_{de} u_g+\Phi_e u_b+\Phi_e u_l-\Phi_d u_d&\end{aligned} \tag{M.32}$$

Again, we see that the drag force $\tau_{drag,2}\frac{S_2}{A}$ as well as the evaporation terms $\Gamma_2 u_{i2}$ are eliminated. With help of (M.4) and (M.5) the momentum equations for the fields (layers) 1 and 2 can be written as (M.33) and (M.34), where the subscripts are listed in (**??**).

$$\begin{aligned}\frac{\partial}{\partial t}\left(\varepsilon_1 G_1\right)+\frac{\partial}{\partial z}\left(\varepsilon_1 \acute{\rho}_1 G_1^2\right)& \\ =-\frac{\partial}{\partial z}\left(P_l \varepsilon_l\right)-\frac{\partial}{\partial z}\left(P_b \varepsilon_b\right)& \\ -\tau_{wk}\frac{S_w}{A}+\tau_i\frac{S_i}{A}& \\ -\rho_l g \varepsilon_l-\rho_g g \varepsilon_b& \\ -\Phi_e u_l-\Phi_{de} u_b+\Phi_d u_d+\Phi_e u_g&\end{aligned} \tag{M.33}$$

and

$$\begin{aligned}\frac{\partial}{\partial t}(\varepsilon_2 G_2)+\frac{\partial}{\partial z}\left(\varepsilon_2\acute{\rho_2}G_2^2\right)&\\ =-\frac{\partial}{\partial z}(P_l\varepsilon_g)-\frac{\partial}{\partial z}(P_d\varepsilon_d)&\\ -\tau_i\frac{S_i}{A}&\\ -\rho_g g\varepsilon_g-\rho_l g\varepsilon_d&\\ -\Phi_{de}u_g+\Phi_e u_b+\Phi_e u_l-\Phi_d u_d&\end{aligned} \tag{M.34}$$

where $\acute{\rho_1}$ and $\acute{\rho_2}$ is the 1. order momentum density defined as (M.35) and (M.36), respectively. The flow quality is given by (M.19) and (M.20). In M.33 and M.34 the LHS terms expresses the dynamic rate of increase of momentum per volume plus the rate of momentum gain by convection per unit volume. On the RHS we have the pressure force per volume, the interfacial drag along the interface I measured per area, the gravitational force on the element per volume, the rate of momentum gain by viscous transfer per unit volume and the entrainment and disengagement rates for the dispersed fields added as production and dissipation of momentum, i.e. droplet entrainment/deposition for the dispersed liquid field and gas entrainment rate and disengagement. The momentum contribution caused by the phase changes in the fluid is not included in these two momentum equations.

$$\acute{\rho_1}=\frac{(1-\dot{x_1})^2}{\rho_l(1-c_b)}+\frac{\dot{x_1}^2}{\rho_g c_b} \tag{M.35}$$

$$\acute{\rho_2}=\frac{(1-\dot{x_2})^2}{\rho_g(1-c_d)}+\frac{\dot{x_2}^2}{\rho_l c_d} \tag{M.36}$$

The axial flow is expressed by u, the volume fraction by ε, P is the interfacial pressure at each layer, g is acceleration due to gravity and τ is the shear stress, ρ is the density, A the cross sectional area, S_1, S_2 and S_i denotes the perimeter wetted by interface 1, interface 2 and the interfacial I perimeter, respectively, given by (M.37) to (M.39). The pipe inclination with respect to the horizontal line is given by θ. For vertical pipes θ=$\pi/2$.

$$S_1=2\pi r_b=2\pi R\sqrt{1-\varepsilon_l} \tag{M.37}$$

$$S_i=2\pi r_d=2\pi R\sqrt{\varepsilon_g+\varepsilon_d} \tag{M.38}$$

$$S_2=2\pi r_g=2\pi R\sqrt{\varepsilon_g} \tag{M.39}$$

The layer thickness of 1 and 2 is expressed by (M.40) and (M.41):

$$\delta_1 = r_d = R\sqrt{\varepsilon_g + \varepsilon_d} \tag{M.40}$$

and

$$\delta_2 = R - r_d = R(1 - \sqrt{\varepsilon_g + \varepsilon_d}) \tag{M.41}$$

The wall shear stress is typically expressed as:

$$\tau_{wk} = \frac{1}{2} f_{wk} \rho_k \left| u_k \right| u_k \Pi^2, \; k = l \vee g \tag{M.42}$$

where the f_{wk} denotes the wall friction factor, which can be determined by i.e. the Colebrook and White formula. The shear stress between the wall and the phase k is described by τ_{wk}, where the case (k=1) denotes the wall shear stress calculated at layer 1 (Single phase liquid to annular flow) and the case (k=2) denotes the case where layer 2 is the outer layer and layer 1 is non-existing (drop flow to superheated steam). The interface velocity is given by u_i and can be estimated as u_i=$(u_1 + u_2)/2$ [76]. The shear stress is adjusted according to the effect of swirl, by multiplying u_k with Π equation (8.25) to account for the increased wall slip velocity caused by the swirl. In this formula, the fin geometry does not contribute to any correction of the pipe cross section area, because we make the assumption that the fins have an infinitesimal thickness. The fins are periodic with a length of l_p in the axial direction (**k**) of the pipe. For $\gamma = \pi/2$ the fins are perpendicular to the cross section and hence parallel to the main axis of the pipe (no swirl effect). The subscript k denotes the phase in contact with the wall, i.e. u_g if it is the gas and u_l if it is the liquid. Similarly, the interfacial shear stress in between the phases can be formulated as:

$$\tau_i = \frac{1}{2} f_i \rho_i \left| u_g - u_l \right| (u_g - u_l) \tag{M.43}$$

The source/sink terms described in the momentum equations, ϕ_e, ϕ_{de}, Φ_e and Φ_d denote bubble entrainment and disengagement rates, and droplet entrainment and deposition rates respectively. The velocities of the dispersed fields (u_d - droplet velocity, and u_b - bubble velocity) are determined from the momentum equations written for the dispersed phase equations (M.29) and (M.30).

M.3. Energy equations

The total enthalpy of flow region k is defined as the sum of the intrinsic enthalpy, the potential energy, the axial kinetic energy (axial velocity) and the rotation energy caused by the swirl (generated by the internal rifles in the boiler tube). In

the derivation the total specific energy e_t and the total specific convected energy e will be used:

$$e_{tk} = \widetilde{u_k} + \frac{u_k^2}{2} - gz\sin(\theta) + r_{ck}a_{ck} \tag{M.44}$$

and

$$e_k = h_k + \frac{u_k^2}{2} - gz\sin(\theta) + r_{ck}a_{ck} \tag{M.45}$$

where $\widetilde{u_k}$ is the specific internal energy and h_k is the specific enthalpy, related by (M.46). The inclusion of $gz\sin(\theta)$ in the definition of e_{ti} and e_i is general. Often we deal with the difference of total energy along the interface $e_{ti} - e_i$, whereby the $gz\sin(\theta)$ term cancels out.

$$\widetilde{u_k} = h_k - p_k/\rho_k \tag{M.46}$$

The swirl generates an centrifugal acceleration given as:

$$a_{ck} = \frac{1}{2}\omega^2 r_{ck}\Theta \tag{M.47}$$

where index k=l, g, b and d, is referring to liquid continuous, gas continuous, bubbles and droplets. The influence coefficient Θ is depending on the fin geometry in the IRBT as well as the helix angel γ, stated in equation (8.19). A qualified guess, Θ is assigned to 0.5. The rotation speed is given by ω. The area-based centre radius r_{ck}, is calculated in analogy to the momentum of inertia for mechanical objects surrounded by two cylinders (r_i and r_j) where

$$r_{ck} = \sqrt{\frac{r_i^2 + r_j^2}{2}} \tag{M.48}$$

The area-based center radius r_{ck} is expressed by equation M.49 to M.52.

$$\begin{aligned} r_{cg} &= \sqrt{\frac{r_g^2 + 0^2}{2}} \\ &= R\sqrt{\varepsilon_g/2} \end{aligned} \tag{M.49}$$

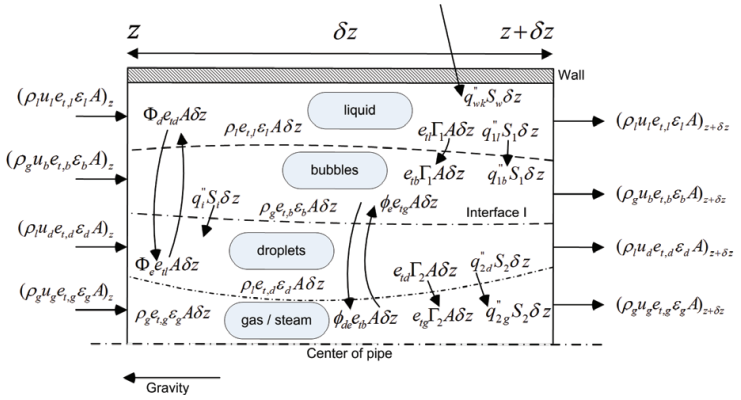

Figure M.5.: Energy transfer and heat flow terms on a slice of a pipe-element.

$$r_{cd} = \sqrt{\frac{r_g^2 + r_d^2}{2}} = R\sqrt{\varepsilon_g + \varepsilon_d/2} \tag{M.50}$$

$$r_{cb} = \sqrt{\frac{r_d^2 + r_b^2}{2}} = R\sqrt{\varepsilon_g + \varepsilon_d + \varepsilon_b/2} = R\sqrt{1 - \varepsilon_b/2 - \varepsilon_l} \tag{M.51}$$

$$r_{cl} = \sqrt{\frac{r_b^2 + r_l^2}{2}} = R\sqrt{1 - \varepsilon_l/2} \tag{M.52}$$

The energy transfer includes the contribution from the basic transport processes of the entrainment and disengagement rates for the dispersed fields added as production and dissipation of energy (i.e. droplet entrainment/deposition for the dispersed liquid field and gas entrainment rate and disengagement in the energy balance equations). The mass transfer caused by phase changes is represented along the two interfaces 1 and 2 represented by Γ_1 and Γ_2, see figure (M.5). The heat flow across the wall is defined positive for $T_w > T_l$. Additionally, the heat transfer along the three interfaces is defined positive according to the illustration in figure (M.5) and is positive, as long as the driving temperature across the

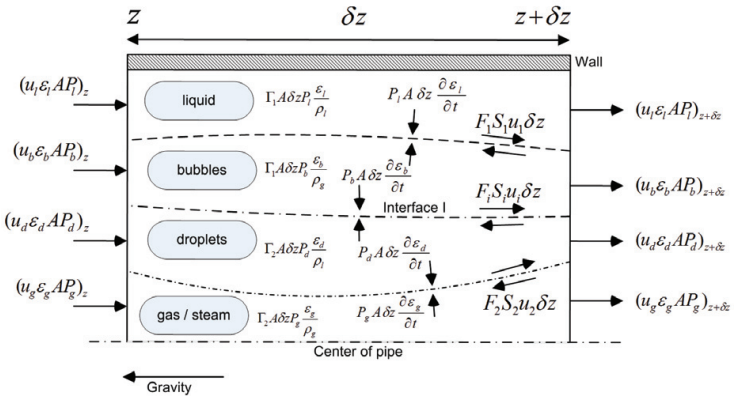

Figure M.6.: work terms on a slice of a pipe-element.

interface is going from high to low temperature. The work terms are illustrated in figure (M.6) and are represented by pressure forces from the surrounding layers. The pressure force per area also contributes with work on the surrounding layers and the interfacial drag along the interfaces performs a work as well. The friction forces allocated to the interface cross sections are also performing a work as well. The coupling between the rotation speed and the axial speed of the fluid is described in (8.25).

To derive the energy conservation equations for the flow fields, one should apply the first law of thermodynamics to the control volumes of the four layers and derive the terms referring to the axial direction at $z+\delta z$ by a Taylor expansion around z. By taking the limit of $\delta z \to 0$, we got the energy conservation equation for the continuous liquid layer (l), given by equation (M.53).

$$\begin{aligned}\frac{\partial}{\partial t}\left(\rho_l e_{tl}\varepsilon_l A\right)+\frac{\partial}{\partial z}\left(\rho_l u_l e_{tl}\varepsilon_l A\right)&\\ =-q''_{wl}S_w+\Gamma_1 A e_{tl}+q''_{1l}S_1-\frac{\partial}{\partial z}\left(u_l\varepsilon_l A P_l\right)&\\ +\Phi_e e_{tl}A-\Phi_d e_{td}A-\frac{\Gamma_1 A P_l\varepsilon_l}{\rho_l}&\\ -P_l\frac{\partial\varepsilon_l}{\partial t}+P_b\frac{\partial\varepsilon_b}{\partial t}-F_1S_1u_1&\end{aligned} \tag{M.53}$$

By substituting e_{tl} in equation (M.53) by equation (M.46) and eliminating the cross sectional area under the assumption that the cross sectional area is constant in time and space, we have:

$$\begin{aligned}
&\frac{\partial}{\partial t}(\rho_l e_l \varepsilon_l) + \frac{\partial}{\partial z}(\rho_l u_l e_l \varepsilon_l) \\
&\qquad = -\frac{q_{wl}'' S_w}{A} - \Gamma_1\left(\frac{P_l}{\rho_l}(l+\varepsilon_l) - e_l\right) \\
&\qquad + \frac{q_{1l}'' S_1}{A} + \Phi_e e_{tl} - \Phi_d e_{td} \\
&\qquad + P_b \frac{\partial \varepsilon_b}{\partial t} + \varepsilon_l \frac{\partial P_l}{\partial t} - F_1 \frac{S_1}{A} u_1
\end{aligned} \tag{M.54}$$

Additionally, we get for the dispersed bubble layer (b):

$$\begin{aligned}
&\frac{\partial}{\partial t}(\rho_g e_b \varepsilon_b) + \frac{\partial}{\partial z}(\rho_g u_b e_b \varepsilon_b) \\
&\qquad = \Gamma_1\left(\frac{P_b}{\rho_g}(1+\varepsilon_b) - e_b\right) \\
&\qquad - \frac{q_{1b}'' S_1}{A} - \phi_e e_{tg} + \phi_{de} e_{tb} \\
&\qquad + P_l \frac{\partial \varepsilon_l}{\partial t} + P_d \frac{\partial \varepsilon_d}{\partial t} \\
&\qquad + \varepsilon_b \frac{\partial P_b}{\partial t} + F_1 \frac{S_1}{A} u_1 - F_i \frac{S_i}{A} u_i
\end{aligned} \tag{M.55}$$

By using the same mathematical manipulations as in equation (M.53), the energy equations for the dispersed droplet layer (d) and the continuous gas layer (g) are given as:

$$\begin{aligned}
&\frac{\partial}{\partial t}(\rho_l e_d \varepsilon_d) + \frac{\partial}{\partial z}(\rho_l u_d e_d \varepsilon_d) \\
&\qquad = \frac{q_{2d}'' S_2}{A} - \Gamma_2\left(\frac{P_d}{\rho_l}(1+\varepsilon_d) - e_d\right) \\
&\qquad - \frac{q_i'' S_i}{A} - \Phi_e e_{tl} + \Phi_d e_{td} \\
&\qquad + P_b \frac{\partial \varepsilon_b}{\partial t} + P_g \frac{\partial \varepsilon_g}{\partial t} \\
&\qquad + \varepsilon_d \frac{\partial P_d}{\partial t} + F_i \frac{S_i}{A} u_i + F_2 \frac{S_2}{A} u_2
\end{aligned} \tag{M.56}$$

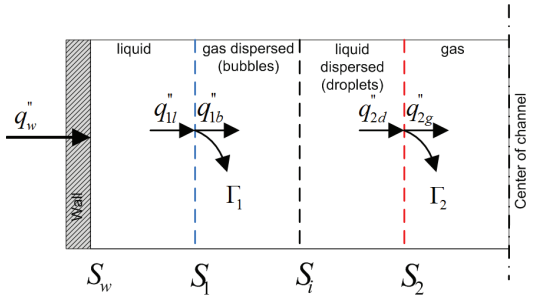

Figure M.7.: Illustration of heat exchange rates in the four field regions

$$\begin{aligned}
&\frac{\partial}{\partial t}(\rho_g e_g \varepsilon_g) + \frac{\partial}{\partial z}(\rho_g u_g e_g \varepsilon_g) \\
&\qquad = -\frac{q''_{wg} S_w}{A} - \Gamma_2\left(\frac{P_g}{\rho_g}(1+\varepsilon_g) - e_g\right) \\
&\qquad - \frac{q''_{2g} S_2}{A} - \Phi_{de} e_{tb} + \Phi_e e_{tg} \\
&\qquad + P_d \frac{\partial \varepsilon_d}{\partial t} \\
&\qquad + \varepsilon_g \frac{\partial P_g}{\partial t} + F_2 \frac{S_2}{A} u_2
\end{aligned} \tag{M.57}$$

Note that it is only in the liquid and gas layers that can allow heat transfer through the wall. The dispersed layers receive energy transfer through the interfacial boundaries, which never will be coincident with the wall boundary. The energy equations can be transformed into a mass flux formulation, by introducing a second order density moment equation $\ddot{\rho}_k$. By adding (M.53) and (M.55), we get an equation describing the layer 1, where the $\Gamma_1 S_1 e_{tl}$ is eliminated:

$$\begin{aligned}
&\frac{\partial}{\partial t}(\varepsilon_l \rho_l (e_l - P_l/\rho_l)) + \frac{\partial}{\partial t}(\varepsilon_b \rho_g (e_b - P_b/\rho_g)) = \frac{\partial}{\partial z}(\varepsilon_l \rho_l e_{tl} u_l) \\
&\qquad + \frac{\partial}{\partial z}(\varepsilon_b \rho_g e_{tb} u_b) - \frac{q''_{1l} S_1}{A} + \frac{q''_{1b} S_1}{A} \\
&\qquad + \frac{q''_w S_w}{A} - \frac{q''_i S_i}{A} - \Phi_e e_{tl} + \Phi_d e_{tl} + \phi_e e_{tg} + \phi_{de} e_{tb} \\
&\qquad - P_l \frac{\partial \varepsilon_l}{\partial t} + P_l \frac{\partial \varepsilon_l}{\partial t} - P_b \frac{\partial \varepsilon_b}{\partial t}
\end{aligned} \tag{M.58}$$

Additionally, we got an expression for the layer 2, which is a result of adding equation (M.56) and equation (M.57). Here source term: $\Gamma_2 S_2 e_{td}$ is eliminated.

$$\begin{aligned}\frac{\partial}{\partial t}\left(\varepsilon_d\rho_l(e_d-P_d/\rho_l)\right)+\frac{\partial}{\partial t}\left(\varepsilon_g\rho_g(e_g-P_g/\rho_g)\right)\\ +\frac{\partial}{\partial z}\left(\varepsilon_d\rho_l e_{td}u_d\right)+\frac{\partial}{\partial z}\left(\varepsilon_g\rho_g e_{tg}u_g\right)=\\ -\frac{q_{2d}^{''}S_2}{A}+\frac{q_{2g}^{''}S_2}{A}\\ +\frac{q_i^{''}S_i}{A}\\ +\Phi_e e_{tl}S_1-\Phi_d e_{td}S_i-\phi_e e_{tg}S_i+\phi_{de}e_{tb}S_i\\ -P_d\frac{\partial\varepsilon_d}{\partial t}+P_b\frac{\partial\varepsilon_b}{\partial t}+P_g\frac{\partial\varepsilon_g}{\partial t}\end{aligned} \tag{M.59}$$

By rearranging the expressions by using equation (M.44), (M.45) and (M.19) and (M.20), we get the energy equations for layer 1 and layer 2:

$$\begin{aligned}\frac{\partial}{\partial t}\left(\varepsilon_1\rho_1 e_1\right)+\frac{\partial}{\partial z}\left(\varepsilon_1 G_1(\dot{x}_1 h_b+(1-\dot{x}_1)h_l)\right)=\\ -\frac{q_{1l}^{''}S_1}{A}+\frac{q_{1b}^{''}S_1}{A}\\ +\frac{q_w^{''}S_w}{A}-\frac{q_i^{''}S_i}{A}\\ -\Phi_e e_{tl}S_1+\Phi_d e_{tl}S_i+\phi_e e_{tg}S_2+\phi_{de}e_{tb}S_i\\ +\frac{\partial}{\partial t}\left(\varepsilon_1 p_1\right)-P_b\frac{\partial\varepsilon_b}{\partial t}\end{aligned} \tag{M.60}$$

and

$$\begin{aligned}\frac{\partial}{\partial t}(\varepsilon_2\rho_2 e_2) - \frac{\partial}{\partial t}(\varepsilon_1 P_2) + \frac{\partial}{\partial z}(\varepsilon_2 G_2(\dot{x}_2 h_d + (1-\dot{x}_2)h_g)) = \\ - \frac{q''_{2d} S_2}{A} + \frac{q''_{2g} S_2}{A} \\ + \frac{q''_i S_i}{A} \\ + \Phi_e e_{tl} S_1 - \Phi_d e_{td} S_i - \phi_e e_{tg} S_i + \phi_{de} e_{tb} S_i \\ - P_d \frac{\partial \varepsilon_d}{\partial t} + P_b \frac{\partial \varepsilon_b}{\partial t} + P_g \frac{\partial \varepsilon_g}{\partial t}\end{aligned} \tag{M.61}$$

Note that e_1 and e_2 is determined by equation (M.62) and (M.62), which express the mass flux weighted average of the bulk energy's at the respective layers. This underlines that it is not weighted by the steady state amount of mass in a fixed control volume.

$$e_1 = \dot{x}_1 e_{tb} + (1-\dot{x}_1) e_{tl} \tag{M.62}$$

$$e_2 = \dot{x}_2 e_{td} + (1-\dot{x}_2) e_{tg} \tag{M.63}$$

M.4. Rotating flow

In the Four Field model we have four pressure levels along the radial direction in the channel flow. The pressure levels are strongly coupled to the swirl generated by the internal rifles. Outside the slip boundary of the near wall region, the velocity is already adjusted according to the increased path through the helix. The radial velocity in a rotating flow can be expressed by equation (8.26), where V_r is the radial velocity and is assume to be proportional to ω. r is the distance from a fluid particle to the centre axis of the tube ($\mathbf{k}$). The distribution of V_r may be estimated, see (8.8). Two boundary conditions may exist: $V_r(0) = 0$ and $V_r(R) = R\omega$, hence the flow distribution is given by:

$$V_r(r) = \omega r \tag{M.64}$$

By integrating equation (8.26) above the four layers, we get the below relationships:

$$\begin{aligned}\Delta P_{lb} &= P_l - P_b \\ &= \int_{r_i}^{R} \frac{1}{\rho}\frac{\partial V_r}{\partial r} dr \\ &= \int_{r_i}^{r_b} \frac{\omega}{\rho_g} dr + \int_{r_b}^{R} \frac{\omega}{\rho_l} dr \\ &= \omega\left(\frac{r_b - r_i}{\rho_g} + \frac{R - r_b}{\rho_l}\right) \\ &= \omega R\left(\frac{\sqrt{1-\varepsilon_l} - \sqrt{\varepsilon_g + \varepsilon_d}}{\rho_g} + \frac{1-\sqrt{\varepsilon_l}}{\rho_l}\right)\end{aligned} \tag{M.65}$$

$$\begin{aligned}\Delta P_{bd} &= P_b - P_d \\ &= \int_{r_g}^{r_b} \frac{1}{\rho}\frac{\partial V_r}{\partial r} dr \\ &= \int_{r_g}^{r_d} \frac{\omega}{\rho_l} dr + \int_{r_d}^{r_b} \frac{\omega}{\rho_g} dr \\ &= \omega\left(\frac{r_d - r_g}{\rho_l} + \frac{r_b - r_d}{\rho_g}\right) \\ &= \omega R\left(\frac{\sqrt{\varepsilon_g + \varepsilon_d} - \sqrt{\varepsilon_g}}{\rho_l} + \frac{\sqrt{1-\varepsilon_l} - \sqrt{\varepsilon_g + \varepsilon_d}}{\rho_g}\right)\end{aligned} \tag{M.66}$$

$$\begin{aligned}\Delta P_{dg} &= P_d - P_g \\ &= \int_{0}^{r_d} \frac{1}{\rho}\frac{\partial V_r}{\partial r} dr \\ &= \int_{0}^{r_g} \frac{\omega}{\rho_g} dr + \int_{r_g}^{r_d} \frac{\omega}{\rho_l} dr \\ &= \omega\left(\frac{r_g}{\rho_g} + \frac{r_d - r_g}{\rho_l}\right) \\ &= \omega R\left(\frac{\sqrt{\varepsilon_g}}{\rho_g} + \frac{\sqrt{\varepsilon_g + \varepsilon_d} - \sqrt{\varepsilon_g}}{\rho_l}\right)\end{aligned} \tag{M.67}$$

M.5. Jump conditions

Evaporation and the belonging mass and energy transport is related to the interface lines 1 and 2, see figure (M.7). The interfacial heat flux and the mass exchange rate Γ_1 across the interface section covered by the perimeter S_1 are linked through the following jump condition at the interface:

$$\Gamma_1(h_{1G} - h_{1L}) + \frac{S_1}{A}(q''_{1l} - q''_{1b}) = 0 \tag{M.68}$$

where h_{1G} and h_{1L} are the enthalpies of the phases at the interface cross sectional line, usually assumed to be at saturation. The thermal jump appears when the fluid is entering the two-phase region in the water/steam table [80]. The following assumptions are made: The thermal hydraulic conditions along the interface are saturated fluids and any contribution from kinetic energies were ignored, hence we have a simple relationship between mass transfer and latent heat of evaporation h_{LG} at the interface formulated by M.69.

$$\Gamma_1 h_{LG} + \frac{S_1}{A}(q''_{1l} - q''_{1b}) = 0 \tag{M.69}$$

If we consider a control volume enclosing the interface and having an infinitesimal thickness, equation (M.69) constitutes an energy balance of this control volume. In the presence of superheated steam and sub cooled liquid, there will be heat transfer from the steam to the interface, where a fraction of the heat flux penetrates into the liquid and is used to heat up the sub cooled liquid. The remaining fraction produces saturated steam at the interface. Additionally we have for the interface section 2:

$$\Gamma_2 h_{LG} + \frac{S_2}{A}(q''_{2d} - q''_{2g}) = 0 \tag{M.70}$$

M.6. Summary

This four layer model has been developed with a view to obtain a better understanding of the internal processes, occurring within a two-phase flow, impacted by a high heat flux. The flow typically starts as a sub-cooled fluid, with only one active layer, as time passes and the fluid is approaching the saturation temperature, the formation of bubbles is starting, which now is transported to the dispersed gas layer. As heating progresses, the formed profile of moisture in the form of bubbles, forms a third layer (dispersed droplets), which contains droplets of liquid, which is established as a result of simple entrainment from the liquid layer, or as a result of local condensation, due to local pressure changes. Finally, the fourth layer is created as a pure gas layer, where the fluid may be superheated. Based on these mechanisms, the model could be used to describe

various flow regimes. In reference [103] is already shown positive results formed the basis of isothermal simulations, where the upstream boundary has specified different configurations with air and water at different speeds. The flow field has formed themselves in four layers downstream. There is not much about how the 8-coupled hyperbolic partial differential equations are solved numerical. This work is intended as a starting point for further research in this area and can benefit greatly, complemented by experimental work to verify the many constitutive expression in the model complex.

N. Paper 1

Axel Ohrt Johansen, Brian Elmegaard, Jens Nørkær Sørensen

Implementation and test of a higher order hybrid solver for hyperbolic and parabolic balance laws

Computers & Mathematics with Applications

Implementation and test of a higher order hybrid solver for hyperbolic and parabolic balance laws

Axel Ohrt Johansen[a,b], Brian Elmegaard[b], Jens Nørkær Sørensen[b]

[a] *DONG Energy - Thermal Power, Kraftværksvej 53, Dk-7000, Fredericia, Denmark*
[b] *Technical University of Denmark, Nils Koppels Allé, Building 403, DK-2800 Kgs. Lyngby, Denmark*

Abstract

In this article a detailed description of the theory and the implementation of a general dynamic Partial Differential Equation (PDE) solver is given. The implementation includes both source and sink terms as well as diffusion terms, which can act locally in the solution space as a function of the physical or chemical process. The numerical method is based on a fifth order Central WENO scheme, with simplified first order weight functions and a fourth order central diffusion term. It is the intention to describe a general hybrid solver with all the components necessary for building a complete numerical solver, including different types of boundary conditions. A number of tests cases for both scalar and vector problems are solved and shows good agreement with the expected results. Moreover, solution of coupled partial differential equations, including source- and diffusion terms, is illustrated by modelling a full scale evaporator model of *Skærbækværket* unit 3 (SKV3) in Fredericia, Denmark. The evaporator is described as a homogeneous flow model with subcooled water on the upstream boundary and superheated steam on the downstream boundary.

Keywords: Central WENO, Black box solver, Evaporator modelling, WENO, Weighted interpolation, Smoothness indicator, Source/Sink, Diffusion, Hyperbolic balance laws, Euler equation, Burgers equation.

1. Motivation

The starting point for this article is the challenge of developing a robust numerical solver, to handle the very strong thermal-hydraulic transients, that can occur in a power plant evaporator. In this context, a one-dimensional pipe wall model is used to ensure the transport of energy from the furnace to the water / steam circuit. The homogeneous thermo hydraulic flow model provides us with some numerical challenges, in the sense that there occurs a singularity in the first derivative of the fluid density, around the saturation lines in the equation

Email address: aoj@addedvalues.dk (Axel Ohrt Johansen)

of state (EOS), see figure (1). This means that strong pressure waves is induced to compensate for sudden sharp negative gradients. Two techniques have been applied to control this pressure oscillation. The first approach concerns a local smoothing of the density around saturation curves, which is implemented in the EOS. The next approach is to impose artificial diffusion, whose strength is estimated from a Boussinesq equation, modelled as heat transfer in a rotating fluid in a pipe, see [1]. Many numerical challenges are brought into play. Choices of

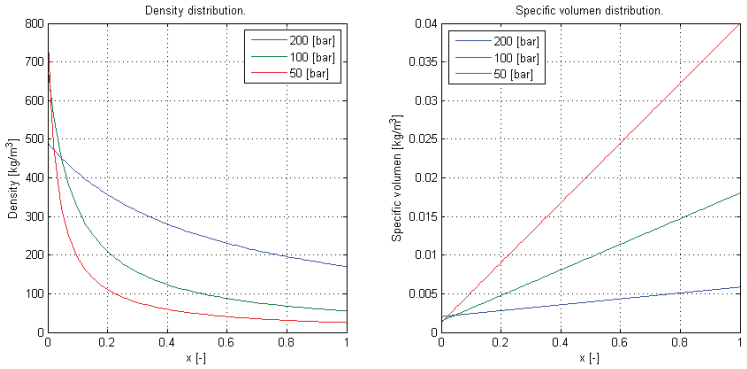

Figure 1: Variations in density and specific volume of water as a function of the steam dryness.

solution strategy including choice of grid (staggered/non-staggered/nested), solution method (explicit/implicit), time integration method, initial- and boundary conditions are just a few of the many challenges, the developer is confronted with, in the construction of a numerical solver. Therefore it is important to explain the entire process and clarify the most necessary components to be included in the implementation of a dynamic numerical solver. An additional challenge is to determine a numerical scheme, that can handle steep gradients without numerical diffusion and over-and under-shooting in the solution domain. Significant efforts are done to remove the numerical oscillations created by higher order numerical schemes of hyperbolic conservation laws near discontinuities, e.g. [2]. A successful numerical method should resolve discontinuities with correct positions, sharp non-oscillatory profiles and retain high order accuracy in smooth parts. A prominent class of such methods is **w**eighted **e**ssentially **n**on-**o**scillatory (WENO) schemes, see e.g. [3] and [4]. The WENO scheme is suitable for solving convection dominated partial differential equations, containing potential discontinuities in the solution, [5]. Examples of such problems are the Euler or Navier-Stokes equations in computational fluid dynamics. WENO is an extension of the **e**ssentially **n**on-**o**scillatory (ENO) scheme, which was introduced by [6]. The essential idea in the WENO methodology is to make a linear combination of lower order reconstructions to obtain a higher-order approximation. The combination coefficients, also called linear weights or ideal weights, are obtained from the local geometry of the mesh and the order of accuracy.

1.1. Aims

In this paper we formulate a numerical solution method for solving the partial differential equations for modelling a full scale evaporator model of *Skærbækværket* unit 3 . The approach is based on a homogeneous evaporator model, as described in [7] and [8], which can summarize by the *system of balance laws* (SBL) as given in (1), where the time dependent variabel Φ and the corresponding flux vector are given below respectively. The dependent variables are $\bar{\rho}$, $\dot{m}$, e and T_w meaning the fluid density, mass flow, total energy of the conserved fluid and wall mean temperature, respectively. The pressure can be determined iteratively by water steam tables: $p = \mathrm{p}(e, \bar{\rho})$, A is the tube cross section area, measured in $[m^2]$. The wall friction coefficients f_w and the convective heat transfer coefficient h is outlined in [7] and [8]. The source term g_s consists of both source/sink terms related to gravity- and wall friction forces. The diffusion term g_d include contributions from the thermal diffusion in the pipe wall, as well as the mixing length eddy viscosity (l^2=0.01 $[m^2/s]$), working as a damping term in the vicinity of the saturation line of water, controled by the steam quality based on an enthalpt approach (x=$\frac{h-h(x=0)}{h(x=1)-h(x=0)}$) in a certain interval eg. ($x \in [-0.01, 0.01]$). The independent variables t represents the time in [s] and z is the spatial coordinate referring to the flow direction of the fluid given in [m].

$$\frac{\partial \Phi(z,t)}{\partial t} + \frac{\partial \mathrm{f}(\Phi(z,t))}{\partial z} = \mathrm{g}_s(\Phi(z,t)) + \mathrm{g}_d\left(\frac{\partial \Phi}{\partial z}, \Phi(z,t)\right), \tag{1}$$
$$\Phi \in R^m, m = 4,\ t \geq\ 0 \wedge z \in \Omega$$

where the dependent variable Φ and the flux vector f are given as

$$\Phi = \begin{pmatrix} \rho A \\ \dot{m} \\ e \\ T_w \end{pmatrix}, \quad \mathrm{f}(\Phi) = \begin{pmatrix} \dot{m} \\ \frac{m^2}{\bar{\rho} A} + pA \\ \frac{(e+pA)\dot{m}}{\rho A} \\ 0 \end{pmatrix}$$

and the source and diffusion vector are given as:

$$\mathrm{g}_s(\Phi) = \begin{pmatrix} 0 \\ p\frac{\partial A}{\partial z} - \rho g A \cos\theta - \sqrt{\frac{\pi}{A}} f_w \frac{\dot{m}|\dot{m}|}{\rho A} \\ S_w \dot{q}_e - \dot{m} g \cos(\theta) \\ \frac{\dot{q}_r}{\rho_w\ C_{pw}} \frac{S_w}{A} - \frac{\dot{q}_e}{\rho_w\ C_{pw}} \frac{d_i \pi}{A} \end{pmatrix} \quad \text{and} \quad \mathrm{g}_d(\Phi) = \begin{pmatrix} 0 \\ \frac{l^2 S_w}{\bar{\rho} A^3} \frac{\partial^2 \dot{m}}{\partial z^2} \\ 0 \\ \alpha \frac{\partial^2 T_w}{\partial z^2} \end{pmatrix}$$

Other parameters are listed in tabel (1). The numerical scheme is challenging and the convective terms are based on the a WENO scheme using a uniform grid, in which we use a central WENO scheme, formulated by [2]. The scheme uses a reconstruction combined with the smoothness indicators introduced by [9] and [10]. We formulate a model of an evaporator which is based on a central-upwind flux discretization. This is simple, generally applicable and efficient formulation [2]. This formulation results in a discretization method developed of order five.

We formulate the diffusion term by a fourth order central difference from [11]. The reconstruction in [2] is a result of a convex centred combination of quadratic polynomials, combined with a third order TVD Runge-Kutta procedure for the time integration. The method includes so called smoothness indicators to avoid vanishing denominators in the weight definitions, i.e., they are parameters designed to keep the weights bounded [3]. In order to reduce the influence of the smoothness indicators on the convergence, we use a simple smoothness indicator introduced by [9] and [10]. Capdeville [2] has shown that the scheme is fifth order accurate in both smooth parts and non-smooth parts of the solution. The theory

Table 1: Geometrical and numerical specifications.

Parameter	Description	Parameter	Description	Parameter	Description
t	Temporal coordinate [s]	Φ	Unknown solution vector	f	Flux vector function
x	Spatial coordinate [m]	g	Source vector	λ	Eigenvalue vector
l_z	Length of solution domain [m]	Ω	Solution domain	$\mathbf{J}$	Jacobian vector
Γ	Diagonal matrix (diffusion coefficient)	$\mathbf{L}$	Left eigenvector	$\mathbf{R}$	Right eigenvector
IS	Smoothness indicators	F	Flux function	τ_5	Central smoothness function
p_j	Polynomial reconstruction	w_j	Weight function	I_j	Cell element j
A (a), B (b)	West, East boundary	c	Speed of sound [m/s]	**CFL**	Courant-Friedrichs-Lewy number
TVD	Total Variation Diminishing	ρ	Fluid density $[kg/m^3]$	$\mathbf{u}$	Convective fluid velocity [m/s]
WENO	Weighted Essentially Non-Oscillatory	p	Fluid pressure [Pa]	$\mathbf{E}$	Total energy of fluid
ρ	mean fluid density [kg/m^3]	A	Tube cross section area $[m^2]$	$\dot{m}$	Mass flux [kg/s]
e	Internal energy [J/m]	p	Fluid pressure [Pa]	T_w	Tube mean wall temp. $[^oC]$
T_f	Fluid temp. $[^oC]$	g	Gravity $[m/s^2]$	C_{pw}	Specific heat capacity [J/kgK]
$\dot{q}_r$	heat flux - furnace $[w/m^2]$	$\dot{q}_e$	heat flux - to fluid $[w/m^2]$	ρ_w	Density of wall $[kg/m^3]$
k_w	Thermal conductivity of wall [w/m]	f_w	Wall friction coefficient [-]	$\mathbf{h}$	Convective heattransfer coeff. $[w/m^2K]$

and development of the model are introduced briefly and are supplemented by an overview of the implementation strategy, where detailed explanations intends to promote understanding of the actual implementation. The resulting scheme improves the convergence order at critical points in smooth parts of the solution as well as it decrease the numerical diffusion near discontinuities.

We test the solver on three well-known numerical experiments for both one dimensional problems and multi variable problems given by a homogeneous thermo-hydraulic evaporator model. The results demonstrate, that the proposed scheme is superior to solve non-linear hyperbolic transport equations. The WENO solver code is implemented in c++ under MicroSoft Visual Studio 2008.

1.2. Overview

The paper is organized as follows. In Section 2 we focus on the numerical approach. Initially, we define the general system of balance laws and the corresponding initial conditions, as well as boundary conditions in relation to a uniform grid. In section 2.2 is given a description of the polynomial reconstructions in the WENO approach and the corresponding non oscillatory weight functions are described in section 2.3. A subsection on flux splitting is included in section 2.4 and the final estimates of the dependent parameter Φ at the element border (Φ^L and Φ^R) is outlined. Finally the source and diffusion terms are described in section 2.5 and 2.6 respectively. The boundary conditions for Non-staggered grid are discussed in section 2.7 and a last section 2.8 mentioning

the time integration principiels, concluding in a brief description of the TVD Runge Kutta integrator. In Section 3 a brief and straightforward way of implementing the method is described. Subsection 4 includes a numerical validation of two numerical problems. Next, a test of consistency is performed. Finally an example of solving a homogeneous thermo-hydraulic evaporator model is demonstrated. The paper is ended by concluding remarks.

2. Methods

Consider a hyperbolic *system of balance laws* (SBL), formulated using a compact vector notation, given by the conservative law of (1).

The domain Ω is partitioned in n_z non-overlapping cells: $\Omega = \cup_{i=1}^{n_z} I_i \in [0, l_z]$, where l_z is a physically length scale in the spatial direction. This system covers the general transport and diffusion equations used in many physical models, e.g. thermo hydraulic evaporator models.

Consider the corresponding hyperbolic system of balance equations (SBL) given in non-conservative form

$$\frac{\partial \Phi(z,t)}{\partial t} + \mathbf{J}\frac{\partial \Phi(z,t)}{\partial z} = \mathrm{g}_s(\Phi(z,t)) + \mathrm{g}_d\left(\frac{\partial \Phi}{\partial z}, \Phi(z,t)\right), \quad t \geq 0 \wedge \quad z \in \Omega \quad (2)$$

were $\mathbf{J}$ is the Jacobian matrix, given by: $\mathbf{J} = \frac{\partial f(\Phi(z,t))}{\partial \Phi}$, and all the eigenvalues $\lambda^{(k)}$ of $\mathbf{J}$ are real numbers. Let $\mathbf{L}$ and $\mathbf{R}$ be the left and right eigenvector matrices of $\mathbf{J}$, then $\mathbf{J} = \mathbf{R} \cdot \Gamma \cdot \mathbf{L}$, $\mathbf{R} = \mathbf{L}^{-1}$ and Γ is the diagonal matrix containing $\lambda^{(k)}$.

The development of a general numerical scheme for solving *PDE*'s may serve as a universal finite-difference method for solving non-linear convection-diffusion equations, in the sense that they are not tied to the specific eigenstructure of a problem, and hence can be implemented in a straightforward manner as black-box solvers for general conservation laws and related equations governing the spontaneous evolution of large gradient phenomena.

2.1. Central Schemes

The definition of hyperbolicity only concerns (2) above; it means that the Jacobian matrix $\mathbf{J}$ has real eigenvalues and a set of associated eigenvectors forming a basis of $\Re^m$, where m is the dimension of vector Φ. The following approach to construct a numerical flux based ENO and WENO reconstructions is simple to implement. The resulting schemes work resonably well for many applications, in particular if the order of the reconstruction is not high. If the order of the reconstruction is high or a demanding test problem shall be solved, a higher order system is recommend worthy. Consider an uniform non-staggered spatial grid, where the cell $I_j = \left[z_{j-1/2}, z_{j+1/2}\right]$ has a cell width Δz, and let Δt be the time step. We denote the spatial grid points by $z_j = \mathrm{j}\Delta z$, $t^n = \mathrm{n}\Delta t$ and $\Phi_j^n = \Phi(z_j, t^n)$. Since the solution of (1), with initial conditions and the two types of boundary conditions given by (Neumann and Dirichlet boundary conditions) can develop discontinuities even for smooth initial data,

the quantities that will be used on the discrete level are cell averages. The numerical approximation of the cell averages in the cell I_j is denoted by $\bar{\Phi}_j^n$:

$$\bar{\Phi}_j^n = \frac{1}{\Delta z} \int_{I_j} \Phi(z, t^n) dz \tag{3}$$

Integration of (2) with respect to z over the volume element I_j at time t we obtain a semi-discrete finite volume scheme formulated as a system of ordinary differential equations (ODEs). The semi-discrete central-upwind scheme presented in [12] can be written as:

$$\frac{d\Phi_j(t)}{dt} = -\frac{1}{\Delta z} \left[F_{j+1/2} - F_{j-1/2} \right] = L_j(\Phi). \tag{4}$$

where the numerical flux at time z=$z_{j+1/2}$ is given by

$$F_{j+1/2} = F(\Phi_{j+1/2}). \tag{5}$$

where we use one of the simplest shock-capturing schemes, the HLL (Harten, Lax and Van Leer) approximate Riemann solver [13]. The steps to follow in the implementation of the numerical scheme (4) can be describes as follows:

1. The first step in the derivation of the approximate solution is to generate a picewise global polynomial reconstruction from the cell averages as

$$\Phi(z, t^n) = P_j^n(z), z \in I_j \tag{6}$$

   where $\Phi(z, t^n)$ is polynomial of a suitable degree. In general the reconstruction should be conservative formally r-th order accurate and non-oscillatory. Based on the reconstruction left and right limit $\Phi_{j+1/2}^L$, $\Phi_{j+1/2}^R$ at location $z_{j+1/2}$, a monotone first order flux is used to establish an essentially non-oscillating higher-order numerical flux. The left extrapolated value is given as:

$$\Phi_{j+1/2}^L = P_j(z_{j+1/2}) \tag{7}$$

   and the right value as:

$$\Phi_{j+1/2}^R = P_{j+1}(z_{j+1/2}) \tag{8}$$

   In this article we use the WENO reconstruction, where the numerical flux at time t is given as

2.

$$F_{j+1/2} = F(\Phi_{j+1/2}) = F(\Phi_{j+1/2}^L, \Phi_{j+1/2}^R). \tag{9}$$

   and we use the central-upwind flux, introduced in [12], where the flux is based on information on the local speed of information. In section 2.4 we review the derivation of this flux.

3. The source term $g_s(\Phi(z,t))$ is added in the expectation that the *system of closure law* (SCL) for a thermo hydraulic fluid flow includes source terms of a given strength. By integrating system (1) over a finite space-time control volume $I_j, \Delta t$ one obtains a finite volume formulation for the system of balance laws, which is outlined in section 2.5.
4. By introducing a diffusion term of (1), we have the ability to change the nature of the differential equation. From pure hyperbolic or partially parabolic system controled by a diffusion term for smoothing a subset of the solution domain. In section 2.6 we review the derivation of this diffusion term.
5. The semi-discrete scheme (2) is solved by a stable (TVD) solver, which retain the spatial accuracy of the scheme. Nonetheless we have choosen to integrate (2) by a third order TVD time integrator instead of a fifth order Strong Stability Preserving (SSP) time discretization method, because the present numerical setup constitute the framework for a dynamic model of an evaporator, which is a cumbersome calculation process, as the equation of state (EOS) is based on an industry standard (IAPWS-97) for the sake of precise expression.

2.2. Polynomial Reconstruction

A fifth order WENO reconstruction of the point values uses a five-points stencil, S_5 which is subdivided into three sub-stencils, $\{S_1; S_2; S_3\}$ as shown in figure (2). To ensure a fifth order accuracy, we chose an optimal polynomial of degree r=4, denoted $\tilde{\Phi}_{opt}$, on the central stencil $S_5 = \{I_{i-2}, I_{i-1}, I_i, I_{i+1}, I_{i+2}\}$. Capdeville [2] introduced this technique and improved the fifth order accuracy also to occur in non smooth solutions. An optimal polynomial covering S_5 off

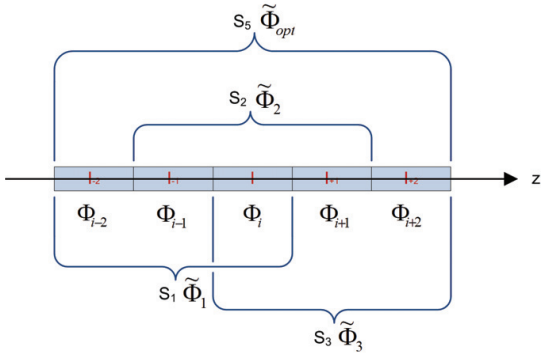

Figure 2: Discrete stencils for the Central WENO procedure.

degree 4 can be expressed as:

$$\tilde{\Phi}_{opt} \equiv \sum_{j=1}^{5} a_{j-1}(z - z_i)^{j-1} \tag{10}$$

where the coefficients a_j can be determinde by solving a 5×5 linear system of Φ_j on a uniform grid (S_5). The coefficients are outlined in [2] and the corresponding reconstruction is for convenience given here:

$$\begin{aligned}
\Phi_{j+1/2} &= P_j(x_{j+1/2}) \\
&= \sum_{k=1}^{4} w_k \cdot \tilde{\Phi}_{j+1/2}^{+^{(k)}}, \\
\Phi_{j-1/2} &= P_j(x_{j-1/2}) \\
&= \sum_{k=1}^{4} w_k \cdot \tilde{\Phi}_{j-1/2}^{-^{(k)}}, \qquad \sum_{k=1}^{4} w_k = 1,
\end{aligned} \tag{11}$$

where the reconstruction polynomials now can be determined at the face values of I_j, which for j+1/2 is:

$$\begin{aligned}
\tilde{\Phi}_{j+1/2}^{+^{(1)}} &= \frac{1}{6}\left[2\bar{\Phi}_{j-2} - 7\bar{\Phi}_{j-1} + 11\bar{\Phi}_j\right] \\
\tilde{\Phi}_{j+1/2}^{+^{(2)}} &= \frac{1}{6}\left[-\bar{\Phi}_{j-1} + 5\bar{\Phi}_j + 2\bar{\Phi}_{j+1}\right] \\
\tilde{\Phi}_{j+1/2}^{+^{(3)}} &= \frac{1}{6}\left[2\bar{\Phi}_j + 5\bar{\Phi}_{j+1} - \bar{\Phi}_{j+2}\right] \\
\tilde{\Phi}_{j+1/2}^{+^{(4)}} &= \frac{1}{120}\left[-2\bar{\Phi}_{j-2} - 7\bar{\Phi}_{j-1} + 73\bar{\Phi}_j + 63\bar{\Phi}_{j+1} - 7\bar{\Phi}_{j+2}\right]
\end{aligned} \tag{12}$$

and for j-1/2 we find:

$$\begin{aligned}
\tilde{\Phi}_{j-1/2}^{-^{(1)}} &= \frac{1}{6}\left[-\bar{\Phi}_{j-2} + 5\bar{\Phi}_{j-1} + 2\bar{\Phi}_j\right] \\
\tilde{\Phi}_{j-1/2}^{-^{(2)}} &= \frac{1}{6}\left[2\bar{\Phi}_{j-1} + 5\bar{\Phi}_j - \bar{\Phi}_{j+1}\right] \\
\tilde{\Phi}_{j-1/2}^{-^{(3)}} &= \frac{1}{6}\left[11\bar{\Phi}_j - 7\bar{\Phi}_{j+1} + 2\bar{\Phi}_{j+2}\right] \\
\tilde{\Phi}_{j-1/2}^{-^{(4)}} &= \frac{1}{120}\left[-7\bar{\Phi}_{j-2} + 63\bar{\Phi}_{j-1} + 73\bar{\Phi}_j - 7\bar{\Phi}_{j+1} - 2\bar{\Phi}_{j+2}\right]
\end{aligned} \tag{13}$$

To derive an essentially non-oscillatory reconstruction, we need to define three supplementary polynomials ($\tilde{\Phi}_1$, $\tilde{\Phi}_2$, $\tilde{\Phi}_3$), approximating $\Phi(z)$ with a lower accuracy on I_j. Thus, is define a polynomial of second-order accuracy, $\tilde{\Phi}_1(z)$, on the reduced stencil S_1: (I_{j-2}, I_{j-1}, I_j), $\tilde{\Phi}_2(z)$ is defined on the stencil S_2: (I_{j-1}, I_j, I_{j+1}), whereas $\tilde{\Phi}_3(z)$ is defined on the stencil S_3: (I_j, I_{j+1}, I_{j+2}), see figure (2). Now, we have to invert a 3×3 linear system similar to the aforementioned 5×5 linear system, for the unknown coefficients $\{a_k\}, k \in \{0, 1, 2\}, k \in \{1, 2, 3\}$ and $k \in \{2, 3, 4\}$, defining $\tilde{\Phi}_1, \tilde{\Phi}_2, \tilde{\Phi}_3$ respectively. The coefficients are outlined in [2].

To implement a specific solution technique, we extend the principle of the central WENO interpolation defined in [14]. First is constructed an ENO interpolant as a convex combination of polynomials, based on different discrete

stencils. For the discrete cell I_j :

$$\tilde{\Phi}^j(z) \equiv \sum_k w_k \times \tilde{\Phi}_k(z), \quad \sum_k w_k = 1 \quad \text{for} \quad w_k \geq 0 \quad \text{for} k \in \{1, .., 4\}, \tag{14}$$

and $\tilde{\Phi}_1$, $\tilde{\Phi}_2$ and $\tilde{\Phi}_3$ are the previously defined polynomials. $\tilde{\Phi}_4$ is the second-order polynomial, defined on the central stencil S_5 which is calculated so that the convex combination in (14) is fifth-order accurate in smooth regions. Therefore we have from [2]:

$$\tilde{\Phi}_{opt}(z) = \sum_k C_k \times \tilde{\Phi}_k(z) \ \ \forall z \in I_j, \quad \sum_k C_k = 1 \quad \text{for} \quad C_k \geq 0 \ \text{ for } \quad k \in \{1, .., 4\}, \tag{15}$$

The constants C_k represent ideal weights for (14) and we make the choice as in [2]:

$$C_1 = C_3 = 1/8, C_2 = 1/4 \text{ and } C_4 = 1/2. \tag{16}$$

Then the central polynomial, $\tilde{\Phi}_4(z)$, can be calculated from (15):

$$\tilde{\Phi}_4(z) = \frac{1}{C_4}\left[\tilde{\Phi}_{opt}(z) - C_1\tilde{\Phi}_1(z) - C_2\tilde{\Phi}_2(z) - C_3\tilde{\Phi}_3(z)\right] \quad \forall z \in I_j. \tag{17}$$

Note that, although the stencil defining $\tilde{\Phi}_4(z)$ is the five-points stencil S_5, this polynomial is only a second-order approximation to $\Phi(z)$ and ensure that we achieve a high-order of accuracy in smooth regions.

2.3. Non-oscillatory weights

To calculate the weights, we review another technique to improve the classical smoothness indicators to obtain weights, that satisfy the sufficient conditions for optimal order of accuracity. It is well known from [2], that the original WENO is fifth order accurate for smooth parts of the solution domain except near sharp fronts and shocks. This idea is taken from [10] and uses the hole five point stencil S_5 to define a new smoothness indicator of higher order than the classical smoothness indicator IS_i. For estimating the weights w_k, k $\in \{1, 2, 3, 4\}$, we find from [9] and [10]:

$$IS_k^* = \frac{IS_k + \epsilon}{IS_k + \epsilon + \tau_5} \tag{18}$$

where IS_k, k $\in \{1, 2, 3\}$ are given by (21), IS_4 given by (22). A modication to the WENO scheme was proposed in [9] using the whole 5-point stencil S_5 to estimate a new smoothness indicator of higher-order than the classical smoothness indicators IS_k. The higher-order information denoted τ_5 is defined as τ_5=$|IS_1 - IS_3|$. The constant ϵ is a small number. In some articles $\epsilon \approx$ from $1 \cdot 10^{-2}$ to $1 \cdot 10^{-6}$, see [14]. Here we use much smaller values of ϵ for the schemes in order to force this parameter to play only its original role of

disallowing vanishing denominators at the weight definitions. The weights w_k are defined as:

$$w_k = \frac{\alpha_k^*}{\sum_{l=1}^{4} \alpha_l^*}, \quad \alpha_k^* = \frac{C_k}{IS_k^*}, \quad k \in \{1,2,3,4\} \tag{19}$$

where C_k are given by (16). When the grid is uniform or smoothly varying, the linear weights remain positive. For the one-dimensional context, the WENO procedure has been defined on a five-point uniform stencil and designed to be fifth-order accurate in regions of smoothness. To this end, we define a finite-difference discretisation (1D) in which we consider the cell averages of the variable as the discrete unknowns. The general indicators of smoothness, defined in [14]:

$$IS_j^i = \frac{1}{\Phi_{max}^2} \sum_{k=0}^{2} \Delta z^{2k-1} \times \int_{I_i} \left(\frac{d^k \tilde{\Phi}_j}{dz^k} \right)^2 dz, \quad j \in \{1,2,3,4\}. \tag{20}$$

where Φ_{max} is calculated over the whole calculation domain Ω: $\Phi_{max}{=}max|\Phi|_{z\in\Omega}$ and k describes the number of equations. These indicators describe the smoothness of the solution over the cell I_j, according to the particular stencil, selected to define $\tilde{\Phi}_k(z)$ on that cell. In regions of smoothness, $IS_k^j << 1$, whereas $IS_k^j = O(\Delta z)$ in cells with strong gradients or discontinuities. Specifically, (20) can be explicated for $\tilde{\Phi}_1$, $\tilde{\Phi}_2$ and $\tilde{\Phi}_3$ on a non-uniform mesh:

$$IS_k^j = a_1^2 \Delta z^2 + \frac{13}{3} a_2^2 \Delta z^4 + O(\Delta z^6), \quad k \in \{1,2,3\}. \tag{21}$$

The general form of IS_4^j is given by [2]:

$$IS_4^j = a_1^2 \Delta z^2 + \left[\frac{13}{3} a_2^2 + \frac{1}{2} a_1 a_3 \right] \Delta z^4 + O(\Delta z^6). \tag{22}$$

2.4. Flux Splitting

In this section we review the derivation of the central-upwind flux presented in [12]. We consider the one dimensional system (1) of m strictly hyperbolic conservation laws. We start with a piecewise polynomial reconstruction $P_j(z)$ with possible discontinuities at the interface points $z_{j+1/2}$. These discontinuities propagate with right- and left-sided local speeds, which can be estimated by

$$c_{j+1/2}^L = \max \left\{ \lambda_N \left(\frac{\partial f(\Phi_{j+1/2}^R)}{\partial \Phi} \right), \lambda_N \left(\frac{\partial f(\Phi_{j+1/2}^L)}{\partial \Phi} \right), 0 \right\}, \tag{23}$$

$$c_{j+1/2}^R = \min \left\{ \lambda_1 \left(\frac{\partial f(\Phi_{j+1/2}^R)}{\partial \Phi} \right), \lambda_1 \left(\frac{\partial f(\Phi_{j+1/2}^L)}{\partial \Phi} \right), 0 \right\}.$$

with $\lambda_1 < ... \lambda_N$ being the eigenvalues of the Jacobian given by $\mathbf{J}{=}\frac{\partial f(\Phi(z,t))}{\partial \Phi}$ given in (2). Here, $\Phi_{j+1/2}^L{=}P_{j+1}(z_{j+1/2})$, and $\Phi_{j+1/2}^R{=}P_j(z_{j+1/2})$ are the corresponding right and left values of the piecewise polynomial interpolant $\{P_j(z)\}$

at the cell interface z=$z_{j+1/2}$. An exact evolution of the reconstruction is followed by an intermediate piecewise polynomial reconstructions which is finally projected back onto the original cells, providing the cell average at the next time step Φ_j^{n+1}. Further details can be found in equation (41). The semi-discrete central-upwind scheme presented in [12] has the numerical flux is given by

$$F_{j+1/2} = \frac{c^L_{j+1/2} f(\Phi^R_{j+1/2}) - c^R_{j+1/2} f(\Phi^L_{j+1/2})}{c^L_{j+1/2} - c^R_{j+1/2}} + \frac{c^L_{j+1/2} c^R_{j+1/2}}{c^L_{j+1/2} - c^R_{j+1/2}} \left[\Phi^L_{j+1/2} - \Phi^R_{j+1/2}\right]. \tag{24}$$

Notice that the accuracy of this scheme is being determined by the accuracy of the reconstruction and the ODE solver. In this chapter the numerical solutions of (4) have advanced in time by means the third order TVD Runge-Kutta method, described by [15] (see section 2.8). By inserting the weights (w_k) in equation (11), the calculation of $\tilde{\Phi}^L_{i+1/2}$,$\tilde{\Phi}^R_{i+1/2}$ produces the key message of this analytical investigation:

$$\begin{aligned}\tilde{\Phi}^L_{i+1/2} = &\left(-\frac{7}{120}w_4 - \frac{1}{6}w_1\right)\bar{\Phi}_{i-2} + \left(\frac{1}{3}w_2 + \frac{5}{6}w_1 + \frac{21}{40}w_4\right)\bar{\Phi}_{i-1} \\ &+ \left(\frac{5}{6}w_2 + \frac{1}{3}w_1 + \frac{11}{6}w_3 + \frac{73}{120}w_4\right)\bar{\Phi}_i + \left(-\frac{1}{6}w_2 - \frac{7}{6}w_3 - \frac{7}{120}w_4\right)\bar{\Phi}_{i+1} \\ &+ \left(\frac{1}{3}w_3 - \frac{1}{60}w_4\right)\bar{\Phi}_{i+2}\end{aligned} \tag{25}$$

$$\begin{aligned}\tilde{\Phi}^R_{i+1/2} = &\left(-\frac{1}{60}w_4 + \frac{1}{3}w_1\right)\bar{\Phi}_{i-2} + \left(-\frac{1}{6}w_2 - \frac{7}{6}w_1 - \frac{7}{120}w_4\right)\bar{\Phi}_{i-1} \\ &+ \left(\frac{5}{6}w_2 + \frac{1}{3}w_3 + \frac{11}{6}w_1 + \frac{73}{120}w_4\right)\bar{\Phi}_i + \left(\frac{1}{3}w_2 - \frac{5}{6}w_3 + \frac{21}{40}w_4\right)\bar{\Phi}_{i+1} \\ &+ \left(-\frac{1}{6}w_3 - \frac{7}{120}w_4\right)\bar{\Phi}_{i+2}\end{aligned} \tag{26}$$

The weights w_k, k$\in \{1,2,3,4\}$ are given by (19).

2.5. Source Term

A source term has been added in the expectation that the *system of closure law* (SCL) for a thermo hydraulic fluid flow includes source terms of a given strength. Let us consider the general SCL given by (1) and restrict our analysis to the source term of the form: $g_s(\Phi(z,t))$ as a continuous source vector function $\neq$ zero. By integrating system (1) over a finite space-time control volume $I_j, \Delta t$ one obtains a finite volume formulation for the system of balance laws, which

usually takes the form

$$\Phi(z,t)_j^{n+1} = \Phi(z,t)_j^n - \frac{\Delta t}{\Delta z}\left(f_{j+1/2} - f_{j-1/2}\right) + \Delta t g_s(\Phi(z,t))_j, \quad t \geq 0, \quad z \in \Omega \tag{27}$$

The integration of (1) in space and time gives rise to a temporal integral of the flux across the element boundaries $f_{j+1/2}$ and to a space-time integral g_s of the source term inside I_j. In practice, one must replace the integrals of the flux and the source in (27) by some suitable approximations, meaning we need to choose a concrete numerical scheme. For SCL, only a numerical flux must be chosen. In this case, the classical properties required are consistency, stability and accuracy. For SBL also a numerical source must be chosen. Here, not only the three classical properties are required, but some additional properties are needed for the global numerical scheme: It should be well-balanced, i.e. able to preserve steady states numerically. It should also be robust on coarse grids, if the source term is stiff. A coarse grid is a grid, whose size does not take into account the source term, i.e. the characteristic space and time steps are based on the associated homogeneous SCL only. Finally, the scheme should be asymptotically consistent or in other words asymptotic preserving, if the source term is stiff. This means that the scheme should give the correct asymptotic behaviour even if the source term is under resolved. We now restrict our analysis to source terms of the form $g_s(\Phi, z)$. Compared with SCL, the presence of a source term generally has consequences on the behaviour of SBL solutions. First of all, SBL may have non-trivial steady solutions, with $\tilde{\Phi}(z)$ given in the following system:

$$\frac{\partial f(\tilde{\Phi}(z,t))}{\partial z} = g_s(\tilde{\Phi}(z,t)), \quad t \geq 0, \quad z \in \Omega \tag{28}$$

Additionally, SBL may tend towards reduced systems as we will explain now. At least two processes are involved in SBL: a conservative process associated to the convective part of (1) (with g_s=0) a characteristic speed u_f , and a dissipative/productive process, associated to the source term g_s, with a characteristic speed u_g. If the time derivative is scaled according to the speed u_f, the dimensionless form (*) of a SBL system reads as:

$$\frac{\partial \Phi^*(z,t)}{\partial t} + \frac{\partial f^*(\Phi(z,t))}{\partial z} = \frac{1}{\epsilon} g_s^*(\Phi(z,t)), \quad t \geq 0, \quad z \in \Omega \tag{29}$$

where all the variables in (29) are dimensionless and where $\epsilon \equiv \frac{u_f}{u_g}$ is the ratio between characteristic speeds. A very small ratio $\epsilon << 1$ means that the dissipative/productive process is too fast, compared to a conservative process, needing to be fully observed. Such a source term is called *stiff* source term. In mathematics, a stiff equation is a differential equation where certain numerical methods for solving the equation are numerically unstable, unless the step size is extremely small. It has proven difficult to formulate a precise definition of stiffness, however, the main idea is to include some terms of rapid variation into the equation, leading to rapid variation in the solution. The presence of a stiff

source term may lead the original system towards an asymptotic reduced system, see [16], which might turn out to be of different mathematical nature than the original one. This situation occurs for instance in the case of an isentropic Euler system with large friction: the asymptotic limit of the original hyperbolic system is a porous media equation, which typical is parabolic of nature.

2.6. Convection-Diffusion equations

By introducing a diffusion part we change the nature of the mathematical problem to a time-parabolic problem. The reason for including this part is that we in a thermo hydraulic evaporator model, gets a sharp change in fluid density, in the moment when a fluid acts as a two-phase fluid. This discontinuity in the derivative of the density, initiate violent pressure waves in the solution, which can be attenuated with local artificial diffusion in the region where this phenomenon occurs. Let us again consider the general SBL, given by equation (1), where the source term g_d is representing by a dissipative flux:

$$g_d(\Phi(z,t), \frac{\partial \Phi}{\partial z}) = \frac{\partial}{\partial z}\left(\Gamma(\Phi(z,t), \frac{\partial \Phi}{\partial z})\right), \quad t \geq 0, \quad z \in \Omega_d, \tag{30}$$

where Ω_d is a subset of Ω and can be given by some physical / chemical requirements of the fluid, where we want to add diffusion to the solution. The gradient of Γ is formulated on the compressed form: $\Gamma(\Phi, \frac{\partial \Phi}{\partial z})_z$ as a nonlinear function $\neq$ zero. This term can degenerate (30) to a strongly parabolic equation, admitting non smooth solutions. Our fifth-order semi-discrete scheme, (4)-(24), can be applied to (1) in a straightforward manner, since we can treat the hyperbolic and the parabolic parts of (30) simultaneously. This results in the following conservative scheme:

$$\frac{d\Phi_j(t)}{dt} = -\frac{1}{\Delta z}\left[F_{j+1/2} - F_{j-1/2}\right] + G_j(\Phi, t). \tag{31}$$

Here $F_{j+1/2}$ is our numerical convection flux, given by equation (24) and G_j is a high-order approximation to the diffusion flux $\Gamma(\Phi, \frac{\partial \Phi}{\partial z})_z$. Similar to the case of the second-order semi-discrete scheme of [17], operator splitting is not necessary for the diffusion term. By using a forth order central differencing scheme, outlined by [11], we can apply our fifth-order semi-discrete scheme, given by (4) and (24), to the parabolic equation (1), where $\Gamma(\Phi, \frac{\partial \Phi}{\partial z})_z$ is a function of ϕ and its derivative in space (diffusion). The diffusion term can be expressed by a high-order approximation from [11]:

$$\begin{aligned} G_j(t) = &\frac{1}{12\Delta z}\left[-G(\Phi_{j+2}, (\Phi_z)_{j+2}) + 8 \cdot G(\Phi_{j+1}, (\Phi_z)_{j+1})\right] \\ &- \frac{1}{12\Delta z}\left[8 \cdot G(\Phi_{j-1}, (\Phi_z)_{j-1}) + G(\Phi_{j-2}, (\Phi_z)_{j-2})\right] \end{aligned} \tag{32}$$

where

$$
\begin{aligned}
(\Phi_z)_{j+2} &= \frac{1}{12\Delta z}\left[25\Phi_{j+2} - 48\Phi_{j+1} + 36\Phi_j - 16\Phi_{j-1} + 3\Phi_{j-2}\right] \\
(\Phi_z)_{j+1} &= \frac{1}{12\Delta z}\left[3\Phi_{j+2} + 10\Phi_{j+1} - 18\Phi_j + 6\Phi_{j-1} - \Phi_{j-2}\right] \\
(\Phi_z)_{j-1} &= \frac{1}{12\Delta z}\left[\Phi_{j+2} - 6\Phi_{j+1} + 18\Phi_j - 10\Phi_{j-1} - 3\Phi_{j-2}\right] \text{ and} \\
(\Phi_z)_{j-2} &= \frac{1}{12\Delta z}\left[-3\Phi_{j+2} + 16\Phi_{j+1} - 36\Phi_j + 48\Phi_{j-1} - 25\Phi_{j-2}\right]
\end{aligned} \tag{33}
$$

and Φ_j are the point-values of the reconstructed polynomials.

2.7. Boundary conditions for Non-staggered grid

This hybrid solver, is as a starting point hyperbolic, but we apply quite generally up-and downstream boundary conditions in this setup, depending on the nature of the system of equations. If we select a globally dominant diffusion part (parabolic system), we need two boundary conditions for each dependent variable in the system, while in hyperbolic systems the boundary condition are related to the number of eigenvalues of the problem.

The hyperbolic system in eq. (1) is defined on a bounded interval a≤z≤b and forms an *Initial Boundary Value Problem*, for which we need initial conditions and boundary data values. For a system of m equations we need a total of m boundary conditions. Typically some conditions must be prescribed at the left boundary (z=A) and some times at the right boundary (z=B). The amount of conditions, required at the boundary's, depends on the number of eigenvalues of the Jacobian **J** that are positive and negative, respectively and whether the information is marching in or out of the boundaries.

So far, we have only described methods for updating cell averages $\bar{\Phi}_j$ assuming that we have neighbouring cell values $\bar{\Phi}^n_{j-1}$ and $\bar{\Phi}^n_{j+1}$ and perhaps values further away as needed in order to compute the cell fluxes $F^n_{j+1/2}$ and $F^n_{j-1/2}$. In practice we must always compute on some finite set of grid cells, covering a bounded domain. In the first and last cells we will not have the required neighbouring information. Instead we must have some set of physical boundary conditions, that must be used in updating these cell values. The computational domain is extended to include a few additional ghost cells on either end of the solution domain. In figure (3) illustrates a grid with three ghost cells at each boundary. These values provide the neighbouring-cell values needed in updating the cells near the physical domain. The updating formula is then exactly the same in all cells, and there is no need to develop a specifically flux limiter method in order to work with boundary instead of initial data. Suppose the mathematical problem is on the physical domain [a,b], which is subdivided into cells I_1,I_2,...,I_{n_z} with $z_{1/2}$=a and $z_{n_z+1/2}$=b, so that Δz= (b-a)/n_z. If we use a method where $F^n_{j-1/2}$ depends only on Φ^n_{j-1} and Φ^n_j, then we need only one

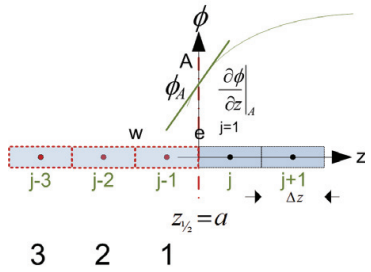

Figure 3: Boundary conditions at the West boundary (up-stream). Example with three Ghost points are marked with red dots.

ghost point on either end. The ghost cell I_0=[a-Δz,a] allows us to calculate the flux $\Phi^n_{1/2}$ at the left boundary A, while the ghost cell I_{n_z+1}=[b,b+Δz] is used to calculate the flux $\Phi^n_{n_z+1/2}$ at the right boundary B. With a flux limiter method or a fifth order WENO approach of the type developed above, we will generally need two ghost cells at each boundary, since a jump in Φ^n_0-Φ^n_{-1} will be needed in limiting the flux correction in $F^n_{1/2}$. For a method with an even higher order of accuracy, additional ghost points would be needed. Consider again the WENO scheme, where the maximal fifth order polynomial reconstruction requires a five point stencil S_5, involving the nodes of I_{j-2}, I_{j-1}, I_j, I_{j+1} and I_{j+2}, for each computational cell in the space of j=1 to n_z. Far away form the boundaries the problem is trivial, as illustrated in figur (4). In the following we are focusing on the non-staggered grid for developing a method to predict the values of Φ on the boundaries, whether we are talking about Dirichlet or Neumann boundaries.

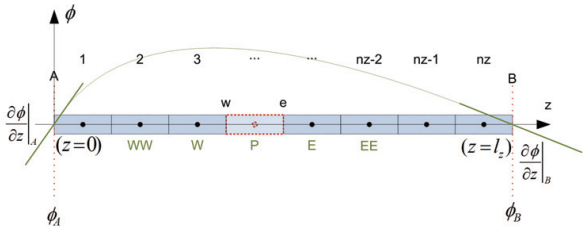

Figure 4: Boundary conditions in pipe model.

If we look at the very first computational cell along the West boundary, we need to be able to predict the values of Φ, for the five point stencil, beginning with the I_{j-2},I_{j-1} and I_j node, which is outside the solution domain (for j=0) (three Ghost points), see figure (3). The idea behind the ghost point approach is to express the value of the solution at control points outside the computational domain in terms of the values inside the domain plus the specified boundary condition. This allows the boundary condition to be imposed by a simple modification of the internal coefficients, using the coefficients of the fictitious external point. This can result in a weak imposition of the boundary condition, where

the boundary flux might not exactly agree with the boundary condition. The three Ghost points are here successive calculated by a third order Taylor expansion around the boundary A, involving I_{-2}, I_{-1} and I_0, and can be used to predict the connection between the I_j cell, marked by red in figure (3), and the boundary condition, given by Φ_A, where Δz is the size of the CV's (uniform grid spacing), see the below figure (3).

Recall now that the Taylor series expansion of the function f(z) about the point z=z_0 is given by

$$f(z) = \sum_{m=0}^{\infty} \frac{(z - z_0)^m}{m!} f_0^{(m)} \tag{34}$$

By establishing a Taylor expansion around the boundary A (or B), we can express a relationship between the ghost points outside the solution domain and grid points inside the domain:

$$\begin{aligned}
\Phi_0 &= \Phi_A - \frac{1}{2}\Delta z \Phi_A^{(1)} + \frac{1}{8}\Delta z^2 \Phi_A^{(2)} - \frac{1}{48}\Delta z^3 \Phi_A^{(3)} + ... \\
\Phi_1 &= \Phi_A + \frac{1}{2}\Delta z \Phi_A^{(1)} + \frac{1}{8}\Delta z^2 \Phi_A^{(2)} + \frac{1}{48}\Delta z^3 \Phi_A^{(3)} + ... \\
\Phi_2 &= \Phi_A + \frac{3}{2}\Delta z \Phi_A^{(1)} + \frac{9}{8}\Delta z^2 \Phi_A^{(2)} + \frac{9}{16}\Delta z^3 \Phi_A^{(3)} + ... \\
\Phi_3 &= \Phi_A + \frac{5}{2}\Delta z \Phi_A^{(1)} + \frac{25}{8}\Delta z^2 \Phi_A^{(2)} + \frac{125}{48}\Delta z^3 \Phi_A^{(3)} + ...
\end{aligned} \tag{35}$$

(36)

The above system can be solved for fixed Φ_A and $\Phi_A^{(1)}$ coresponding to a Dirichlet- and an Neumann boundary conditions. Follow the above procedure, the boundaries can be expressed in terms of Φ_0, Φ_{-1} and Φ_{-2}:
Dirichlet BC at A:

$$\begin{aligned}
\Phi_{-2} &= 32\Phi_A - 50\Phi_1 + 25\Phi_2 - 6\Phi_3 \\
\Phi_{-1} &= \frac{64}{5}\Phi_A - 18\Phi_1 + 8\Phi_2 - \frac{9}{5}\Phi_3 \\
\Phi_0 &= \frac{16}{5}\Phi_A - 3\Phi_1 + \Phi_2 - \frac{1}{5}\Phi_3
\end{aligned} \tag{37}$$

Neumann at A:

$$\begin{aligned}
\Phi_{-2} &= \frac{1}{23}\left[-240\Delta z \frac{\partial \Phi}{\partial z}\|_A - 250\Phi_1 + 375\Phi_2 - 102\Phi_3\right] \\
\Phi_{-1} &= \frac{1}{23}\left[96\Delta z \frac{\partial \Phi}{\partial z}\|_A - 54\Phi_1 + 104\Phi_2 - 27\Phi_3\right] \\
\Phi_0 &= -\frac{1}{23}\left[24\Delta z \frac{\partial \Phi}{\partial z}\|_A - 21\Phi_1 - 3\Phi_2 + \Phi_3\right]
\end{aligned} \tag{38}$$

Similar we find for the downstream boundary B:
Dirichlet BD at B:

$$\begin{aligned}\Phi_{n_z+3} &= 32\Phi_B - 50\Phi_{n_z} + 25\Phi_{n_z-1} - 6\Phi_{n_z-2} \\ \Phi_{n_z+2} &= \frac{64}{5}\Phi_B - 18\Phi_{n_z} + 8\Phi_{n_z-1} - \frac{9}{5}\Phi_{n_z-2} \\ \Phi_{n_z+1} &= \frac{16}{5}\Phi_B - 3\Phi_{n_z} + \Phi_{n_z-1} - \frac{1}{5}\Phi_{n_z-2}\end{aligned} \tag{39}$$

Neumann BC at B:

$$\begin{aligned}\Phi_{n_z+3} &= \frac{1}{23}\left[-240\Delta z\frac{\partial\Phi}{\partial z}\|_B - 250\Phi_{n_z} + 375\Phi_{n_z-1} - 102\Phi_{n_z-2}\right] \\ \Phi_{n_z+2} &= \frac{1}{23}\left[96\Delta z\frac{\partial\Phi}{\partial z}\|_B - 54\Phi_{n_z} + 104\Phi_{n_z-1} - 27\Phi_{n_z-2}\right] \\ \Phi_{n_z+1} &= -\frac{1}{23}\left[24\Delta z\frac{\partial\Phi}{\partial z}\|_B - 21\Phi_{n_z} - 3\Phi_{n_z-1} + \Phi_{n_z-2}\right]\end{aligned} \tag{40}$$

The idea behind the ghost point approach is to express the value of the solution at a control point outside of the computational domain in terms of the values inside the domain plus the specified boundary condition.

2.8. Time discretization

Strong Stability Preserving (SSP) time discretization methods were developed to address the need for nonlinear stability properties in the time discretization, as well as the spatial discretization, of hyperbolic PDE's. The research in the field of SSP methods centres around the search for high order SSP methods where the CFL timestep restriction leads to an as large as possible timestep. These methods include the case where there are more stages than required for the order, in order to maximize the CFL coefficient. Although the additional stages increase the computational cost, this is usually more than offset by the larger stepsize that may be taken. In this article is to present the numerical setup which constitute the framework for a dynamic model of an evaporator, which is a cumbersome calculation process, as the equation of state (EOS) is based on an industry standard (IAPWS-97) for the sake of precise expression. With a formulation given on a conservative form (flux-based), we must iterate on the pressure as a function of density and enthalpy, which is very time consuming. In principle we should use a time integrator of the same order as WENO reconstruction, such as an SSP RK(5,5) solver, see [18], but experience shows that these higher order integrators are much more time consuming as e.g. a third-order TVD time integrator used in both [2] and [19]. The semi-discrete (4) is a system of time dependent ODE's, which can be solved by any stable ODE solver, retaining the spatial accuracy of the scheme. Here we use the TVD Runge-Kutta method presented by [15] which can be categorized as an (SSP-RK(3,3):

$$\frac{d\Phi}{dt} = L(\Phi), \tag{41}$$

where $L(\Phi)$ is an approximation to the derivative $-\frac{\partial f(\Phi)}{\partial z} + g_s(\Phi, z, t) + g_d(\frac{\partial \Phi}{\partial z}, \Phi)$ in the differential (1). The optimal third order TVD Runge-Kutta method (SSP-RK(3,3)) is given by

$$\begin{aligned}
\Phi_j^{(1)} &= \Phi_j^n + \Delta t L(\Phi_j^n), \\
\Phi_j^{(2)} &= \frac{3}{4}\Phi_j^n + \frac{1}{4}\Phi_j^{(1)} + \frac{1}{4}\Delta t L(\Phi_j^{(1)}), \\
\Phi_j^{n+1} &= \frac{1}{3}\Phi_j^n + \frac{2}{3}\Phi_j^{(2)} + \frac{2}{3}\Delta t L(\Phi_j^{(2)}), \quad \text{for } j \in [1, n_z].
\end{aligned} \tag{42}$$

as an alternative, we could have used a (SSP-RK(5,4)), which is a fourth order method consisting of 5 stages and is given by [15]. Furthermore in [15], it has been shown that even a very nice second order TVD spatial discretization may give an oscillatory result, depending whether the time discretization is by a non-TVD, however, linearly stable Runge-Kutta method. Thus it would always be safer to use TVD Runge-Kutta methods for hyperbolic problems. The stability condition for the above schemes is

$$CFL = \max\left(u_j^n \frac{\Delta t}{\Delta z}\right) \leq 1, \tag{43}$$

where CFL stands for the *Courant-Friedrichs-Lewy* condition and u_j^n is the maximum propagation speed in cell I_j at time level n.

3. Implementation

The implementation of the WENO approach is implemented in five stage process ending with the time integration loop. In Step 1 is the model, reading the model specifications and allocating array structures, Step 2 is initializing the time integration loop. In Step 3 the time step is being evaluated due to the CFL number specified. Step four is covering the entire Runge Kutta time integration, which is divided into three parts, due to the third order TVD integrator. In the Boundary module the up- and down stream boundaries are being updated. They can be constant or varying in time. In general there are three possibilities of specifying boundary conditions; Dirichlet, Neumann or non condition. In the method of *Indicators* we are calculating the four indicators IS_i, i∈[1..4]. The *Reconstruction* module is dealing with the weight functions as well as calculating the corresponding reconstructed polynomials. In the module named; *Fluxes* is estimated the Flux vector including both contributions from the source/sink term and diffusion term as well. In the last step 5 is calculation info is being estimated and stored in files. The time loop is running until the time t is exceeding the end of simulation time t_{end}.

4. Numerical validation of hyperbolic solvers

In this section we compare numerical results of both a scalar and a system of hyperbolic equations and compare the results with analytical results from the

literature as well as other published results. The scalar models will focus on solving the inviscid Burger equation, which is a standard test example in the literature for solving hyperbolic equations. Finally the well-known Sod problem is solved by system of Euler equations and is evaluated according to numerical results in literature and the shock strength is compared to a theoretical value.

4.1. Consistency

A consistency test is made by solving (44) numerically and compare the solution to an analytical solution given by (45) for varying grid spacing.

$$\frac{\partial(\rho\Phi)}{\partial t} + \frac{\partial f(\rho\Phi)}{\partial z} = \frac{\partial}{\partial z}\left(\Gamma\frac{\partial(\rho\Phi)}{\partial z}\right), \quad t \geq 0 \ \wedge \ z \in \Omega \tag{44}$$

The governing equation (44) is forced by an *Initial Boundary Value Problem* given by two Dirichlet boundary conditions; $\Phi_A = 1$ for z=0 and $\Phi_B = 0$ for z=1 and an initial field of Φ(z,t=0)=0. The number of computational cells is varying form:n_z=10 to 320. The convective velocity is constant u=1.0 [m/s] (f(Φ) = $u \cdot \Phi$), the length l_z=1 [m] and the density is constant; $\rho = 1$ $[kg/m^3]$. The diffusion coefficient Γ=0.2 $[m^2 s^{-1}]$ in $g_d(\Phi) = \frac{\partial}{\partial z}\left(\Gamma \cdot \frac{\partial(\rho\Phi)}{\partial z}\right)$.

The steady state simulation results are compared with a corresponding analytical solution, given by:

$$\frac{\Phi - \Phi_A}{\Phi_B - \Phi_A} = \frac{\exp\left(\rho \cdot u \cdot z/\Gamma\right) - 1}{\exp\left(\rho \cdot u \cdot l_z/\Gamma\right) - 1}, \quad t \geq 0 \ \wedge \ z \in \Omega \tag{45}$$

The numerical solution to (44) is illustrated in figur (5), where different solution profiles are shown during time and the steady state solution is the basis of the consistancy test by recalculation the numerical model for varying grid spacing. The results are shown in figur (6) and are compared with more simpler numerical schemes as Van Leer and a Central Difference scheme.

Numerical tests show, with no surprise, varying accuracy, dependence on the numerical solution strategy used. The classical Van Leer TVD scheme and a Central Difference scheme (CD) provides a familiar second and first order accuracy respectively, while the central WENO scheme, with a reduced fourth-order diffusions term, give a close to fourth-order accuracy (WENO4) for the steady state solution. The central WENO without diffusion term has a fifth-order accuracy, with reference to [2] and [10].

4.2. Burgers equation

In this example we simulate the pre- and post chock solution to the inviscid Burgers equation given by

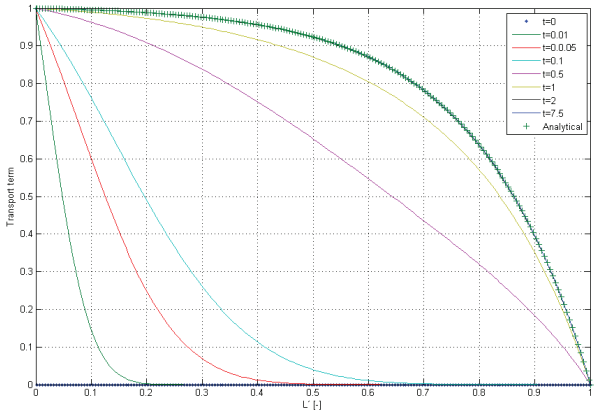

Figure 5: Numerical and analytical solutions to (44).

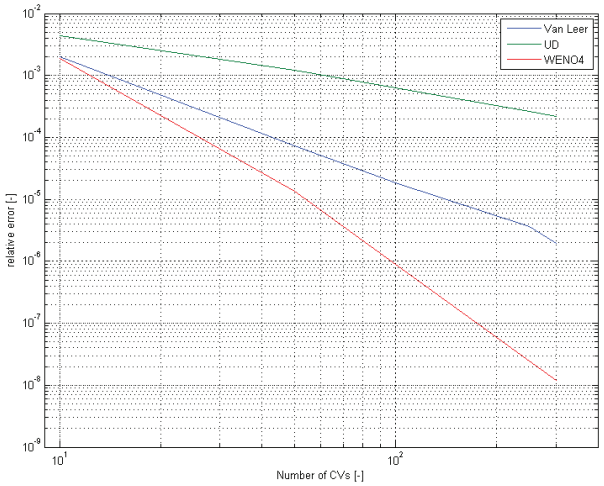

Figure 6: Consistancy.

$$\frac{\partial \Phi}{\partial t} + \frac{\partial}{\partial z}\left(\frac{1}{2}\Phi^2\right) = 0, \quad t \geq 0 \ \wedge \ z \in \Omega \tag{46}$$

and the corresponding initial condition is given by u(z,0)=sin $(\pi z/l_z)$. Ω is partitioned in n_z non-overlapping cells: $\Omega = \cup_{i=1}^{n_z} I_i \in [0, l_z]$, where l_z is a physically

length scale in the spatial direction. The simulation results are based on the fifth order central WENO formulation and the outcome is illustrated in figure (7) and is similar to what is observed in [4] and [17].

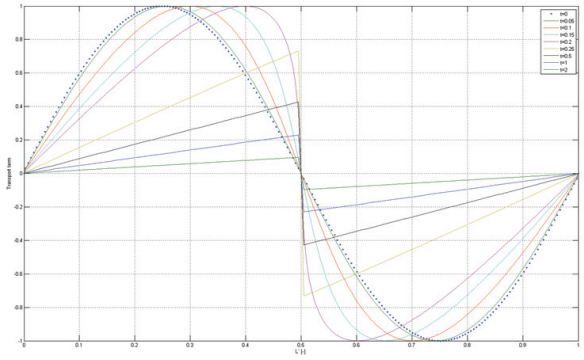

Figure 7: Burgers equation with N=200 and l_z=1.

The results indicates that the solution is perfect symmetric and a planar disturbance is propagating outward at the characteristic speed for the artificial medium, as expected. We can see a shock formation centered at z=0.5.

4.3. Euler equation

We extend the fifth order WENO scheme to envolve the solution of Euler's equations of gas dynamics:

$$\frac{\partial \Phi}{\partial t} + \frac{\partial f(\Phi)}{\partial z} = 0, \quad t \geq 0 \ \wedge \ z \in \Omega \tag{47}$$

where

$$\Phi = \begin{pmatrix} \rho \\ \rho \cdot u \\ E \end{pmatrix}$$

and the flux vector is given as:

$$F(\Phi) = \begin{pmatrix} \rho \cdot u \\ \rho \cdot u^2 + p \\ u \cdot (E + p) \end{pmatrix}$$

Here ρ, u, p and E are respectively the fluid density, velocity, pressure and total energy of the conserved fluid. The ideal gas law (polytropic gas) is used as the equation of state, to derive the speed of sound c, given as: c=$\sqrt{\frac{\gamma p}{\rho}}$. The ration of the specific heats is: $\gamma = \frac{c_p}{c_v} = 1.4$ and the pressure p=$(\gamma - 1)(E - \frac{1}{2}\rho u^2)$.

The linearised Euler equations are obtained by linearisation of the Euler equations in non-conservation form, as in (2), with flux Jacobians:

$$\frac{\partial \mathbf{M}}{\partial t} + \mathbf{A} \cdot \frac{\partial \mathbf{M}}{\partial z} = 0, \quad t \geq 0 \ \wedge \ z \in \Omega \tag{48}$$

where $\bar{\mathbf{M}} = \mathbf{P}^{-1} \cdot \Phi$ and $\mathbf{P}$ is the eigenvector corresponding to the eigenvalues. The matrix $\mathbf{A}(\Phi)$ is diagonalizable, which means it can be decomposed into: $\mathbf{A}$=$\mathbf{P} \cdot \Gamma \cdot \mathbf{P}^{-1}$, where

$$\mathbf{P} = [r_1, r_2, r_3]^T = \begin{pmatrix} 1 & 1 & 1 \\ u-c & u & u+c \\ H-uc & 1/2u^2 & H+uc \end{pmatrix}$$

and

$$\Gamma = \begin{pmatrix} \gamma_1 & 0 & 0 \\ 0 & \gamma_2 & 0 \\ 0 & 0 & \gamma_3 \end{pmatrix}$$

Here $r_1 = [1, u-c, H-uc]^T$, $r_2 = [1, u, \frac{1}{2}u^2]^T$, $r_3 = [1, u+c, H+uc]^T$ are the right eigenvectors of the matrix $\mathbf{A}$ corresponding with the eigenvalues $\gamma_1 = u-c$, $\gamma_2 = u$ and $\gamma_3 = u+c$. We solve the Sod problem up to t=0.01 [s] for a spatial length of l_z=20 [m], with the following initial conditions:

$$\Phi(z,0) = \begin{cases} (1, 0, 2.5 \cdot 10^5)^T & 0 \leq z < \frac{l_z}{2} \\ (0.125, 0, 0.25 \cdot 10^5)^T & \frac{l_z}{2} \leq z \leq l_z. \end{cases} \tag{49}$$

The simulation results are based on CFL=0.90 and the distribution of the density, pressure and velocity are illustrated in the following figures (8), (9) and (10) respectively.

The figure (8) represents five regions (R_1, R_2, R_3, R_4 and R_5) in the normalized spatial space of $z^* \in$ [0,1], which have different density's. Region $R_1 \in$ [0,0.3[, $R_2 \in$ [0.3,0.5[, $R_3 \in$ [0.5,0.63[, $R_4 \in$ [0.63,0.78[and $R_5 \in$ [0.78,1[]. Two regions R_1 and R_5 are in constant state equals the initial state and both fluids are initially in rest. R_2 is representing a rarefaction wave moving to the left. Although the density and pressure is continuous in this region, some of the derivatives of the fluid quantities may not be continuous. The front in-between Region R_3 and R_4 represents the so-called contact discontinuity, where the pressure and the specific energy are not a continuous function. The front in-between Region R_4 and R_5 represents the location of the shock wave moving to the right with the sound of speed. Assuming the same gas in the two chambers, the ration of the specific heats are identical: $\gamma = \gamma_1 = \gamma_5$, hence the two local speeds of sound can be determined and inserted in formula (50), which is taken from [20], p 225, and gives the shock strength to $p_4/p_5 = 3.031$, which fits with the results in figure (9).

$$\frac{p_1}{p_5} = \frac{p_4}{p_5} \left[1 - \frac{(\gamma-1)(a_5/a_1)(p_4/p_5 - 1)}{\sqrt{2\gamma}\sqrt{2\gamma + (\gamma+1)(p_4/p_5)}} \right]^{\frac{-2\gamma}{\gamma-1}} \tag{50}$$

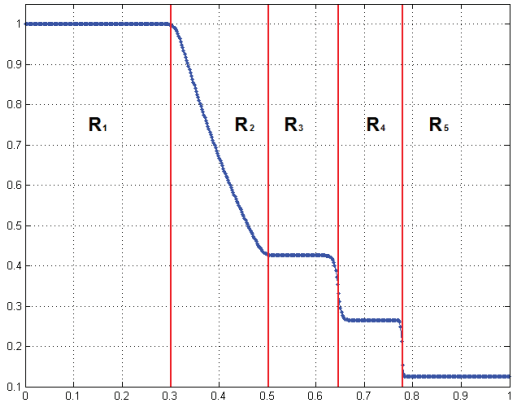

Figure 8: Sod problem with N=400 - Density [kg/m^3] distribution at t=0.01 [s].

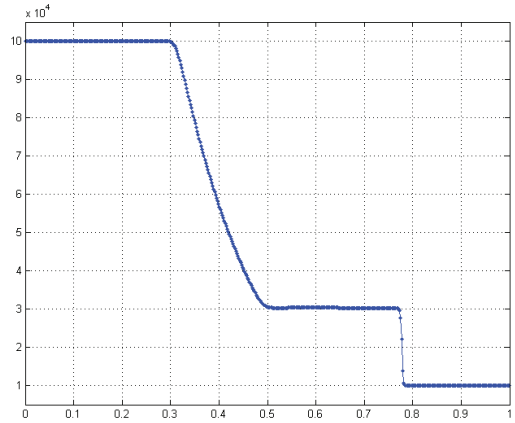

Figure 9: Sod problem with N=400 - Pressure [Pa] distribution at t=0.01 [s].

Across a shock all of the quantities (ρ, m, e and p) will in general be discontinuous. The simulation results shows oscillation free properties. The corners at the endpoints of the rarefaction are almost perfectly sharp and the constant states of R_1 and R_5 are well defined matching the initial state. In general the distribution of the density, pressure and velocity fit very well with similar cases in the literature, see [17]. The timing results are improved with up to 20% by use of the modified weight functions given by [19] compared to the traditional

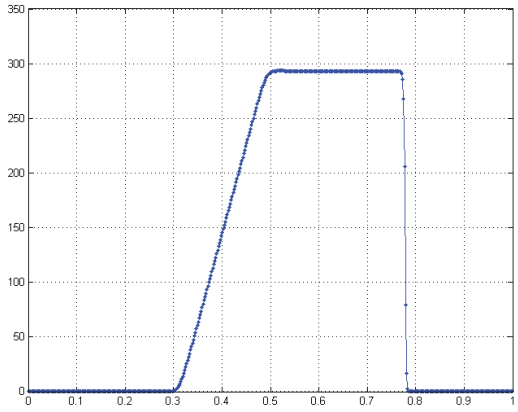

Figure 10: Sod problem with N=400 - Velocity [m/s] distribution at t=0.01 [s].

squared weight factors from [2].

4.4. Homogeneous evaporator model

The homogeneous evaporator model is briefly described in the introduction to this paper and is given by (1), with the time dependent variabel Φ and the corresponding flux, source and diffusion terms given on vector form. The internal energy e is given as: $e = (\rho\bar{E} - p) \cdot A$, which is measured in [J/m]. k_w is the thermal conductivity measured in [w/mK]. The radiation from the furnace is given by $\dot{q_r}$ and $\dot{q}_e$ is the convective heat transfer between the flowing fluid in the pipe and the pipe wall inner surface, $\dot{q}_e$=$h(T_w - T_f)$ and $S_w = a_w A$ is the perimeter of the heated domain and a_w has the physical meaning of the wall area per unit volume. The convective heat transfer coefficient is named h and the driving temperature difference is given by the temperature difference between the wall mean temperature (T_w) and the mixture fluid temperature (T_f). Here the fluid temperature T_f is a function of $\bar{\rho}$ and h. The constitutive relations due to the thermodynamic properties are based on IAPWS 97, and are interpolated in a bilinear scheme, described in [21]. Other constitutive relations for the pipe wall properties are given by [7] and [8]. The model data are listed below in table (1). Note that the gravity is reduced according to the heat pipe inclination ($\sin(11.4^o)$). For isotropic materials, we have expressions of C_{pw}, k_w and ρ_w as function of temperature in Kelvin from [22] and [23]:

$$\begin{aligned} C_{pw} &= 6.683 + 0.04906 \cdot T + 80.74 \cdot \ln(T) \text{ [J/kgK]} \\ k_w &= 9.705 + 0.00176 \cdot T - 1.60 \cdot 10^{-6} \cdot T^2 \text{ [W/mK]} \\ \rho_w &= 7850 \text{ [kg/}m^3\text{]} \text{ at } 20^\circ C \text{ for 13CrMo44} \end{aligned} \tag{51}$$

For isotropic materials, we use the thermal diffusivity given by equation: $\alpha = \frac{k_w}{\rho_w C_{pw}}$ in $[m^2/s]$, which in a sense is a measure of thermal inertia and expresses

how fast heat diffuse through a piece of solid. For a typical panel wall, the thermal diffusivity is approximately $1.98 \cdot 10^{-6}$ $[m^2/\text{s}]$ at $200°C$.

The model consists of 400 computational points with a CFL number of 0.8. A third order TVD time integrator is used, for reasons of ensure a high numerical stability as well as minimizing the time consumption in the calculations. Three Dirichlet boundary conditions are applied for the hydraulic case and two Neumann boundaries are applied for the thermal pipe wall model, given as zero gradients in the wall temperature at each pipe end (No heat loss). The intention is to model an evaporator, which can induce pressure and density oscillations initiated by the compressibility, which arise as a result of a phase shift in the lower part of the evaporator. Therefore, we apply a constant downstream Dirichlet pressure boundary condition, that corresponds to a stiff system downstream the evaporator tube, meaning without any pressure absorption effects in the downstream turbine system due to compressibility. A good analogy for this is a geyser, with a constant surface pressure and an intense heat absorption in the bottom region, whereby an oscillating pressure wave is initiated due to the compressibility and density reduction of the fluid, caused by intense heat from the underground. Additionally we force the model with both a constant enthalpy and mass flux located on the upstream boundary, supplied by a heat flux profile along the entire heat pipe. The model is soft started in two steps, at t=0 [s] is the pure hydraulic model soft started during 4 seconds, without heat flux. After 10 seconds of simulation, the heat flux is build-up during four seconds to $\dot{q}_r$=100 [kW/m^2], in accordance with the operating observations obtained at the site of SKV3. This is done to avoid heavy shock waves moving forward and back in the entire solution domain. The computational results are stored as line series for an equidistant time step and as time series at two stations, located at $z_A = \frac{l_z}{8}$ and $z_B = \frac{7l_z}{8}$, named station A and B respectively. Note that

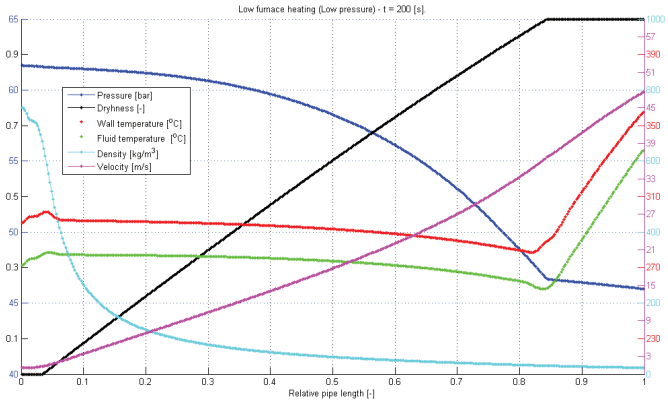

Figure 11: Bottom heating in SKV3 boiler, after 200 [s].

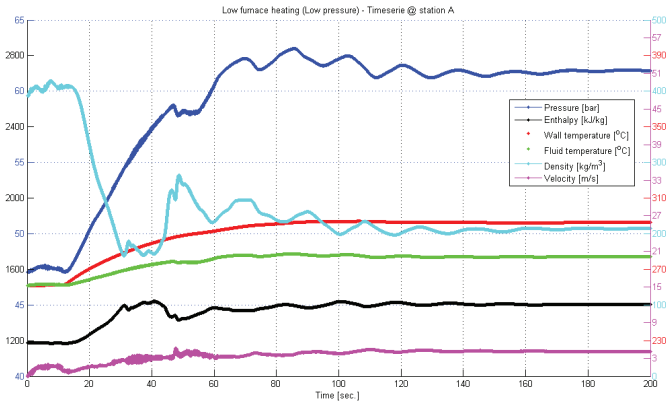

Figure 12: Time series of bottom heating in SKV3 evaporator model at location A.

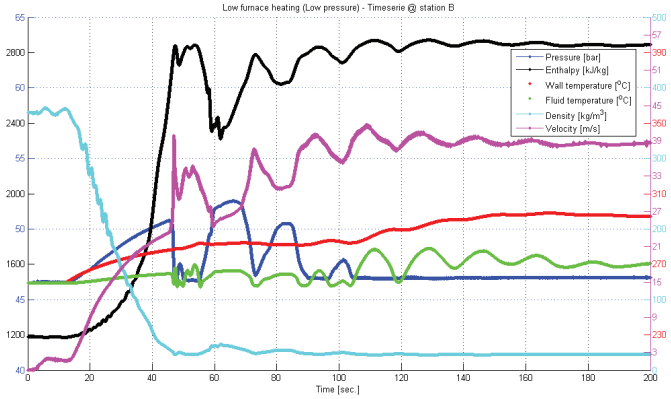

Figure 13: Time series of bottom heating in SKV3 evaporator model at location B.

the temperature curves for the fluid and the pipe wall both refer to the same temperature scale corresponding to the red fluid temperature scale on the right side of the following figures (11), (12) and (13). The soft start model is based on a third order theory outlined in [24], which gives a C^2 continuous sequence, which means zero gradients of the first derivative at both ends of the soft start period. This simulation has shown that there is a dynamic instability in the evaporator during start up. After 200 [s] we see a steady state picture of the axial profile of the thermo hydraulic properties, see figure (11). As shown in figure (13), the system falls in a steady state condition after more than 160 [s] from start. At the upstream station we see the same tendencies, but with less oscillations, see figure (12). The dynamic transients in station B are significant,

while the fluid velocity fluctuates dramatically (up to 15 [m/s] in less than one second). The pressure fluctuates violently too, but falls quickly into a plateau after only 100 [s] from the start. The fluid velocity and enthalpy oscillations are damped gradually, until a steady state situation is reached after160 [s] from start. It is interesting to note the presence of thermo slugs in the homogeneous evaporator model and that its able to establish the sometimes sharp gradients in the solution, which demonstrates that there really exist violent slugs at low operating pressures in steam power plant evaporators. We have now developed a tool that can be used in further studies of the evaporator stability. For further details, see [7] and [8].

4.5. Conclusions

We have developed a robust numerical tool, that is highly flexible in terms of configuration, so that the application can handle source / sink terms, diffusion terms and initial fields as line data and finally two types of boundary conditions can be specified, one Neumann and Dirichlet condition on both up - and down stream boundaries. The WENO solver has a 5. order of accuracy, which is shown by several authors, see e.g. [10] and [2]. The diffusion term can only be dissolved in a fourth order accuracy and with respect to the time integrator, we here have several options, but for our purposes, we find a the third order TVD Runge Kutta integrator for appropriate, which leads to a final order of 4, for the entire steady state system. The Central WENO schemes are designed for problems with piecewise smooth solutions containing discontinuities. The Central WENO scheme have been quite successful in the above applications, especially for solving the test examples containing shocks as well as the homogenious evaporator model, which contains complicated smooth solution structures. The conclusion is that both the scalar and system based versions are non-oscillatory in the sense of satisfying the total-variation diminishing property in the one-dimensional space.

5. References

[1] Sørensen J.N. and Kristensen S.A. and Christensen L.K. . Direct and large eddy simulations of thermo-convective flows. Lecture Notes in Computer Science, Department of Energy Engineering, Fluid Mechanics Section Technical University of Denmark, DK-2800 Lyngby 1995;1 (2):631–40.

[2] Capdeville G. A central weno scheme for solving hyperbolic conservation laws on non-uniform meshes. J Comp Phys 2008;(227):2977–3014.

[3] Jiang GS, Shu CW. Efficient implementation of weighted eno schemes. J Comput Phys 1996;(126):202–28.

[4] Qiu J, Shu CW. On the construction, comparison and local characteristic decomposition for high-order central weno schemes. J Comput Phys 2002;(183):187–209.

[5] Liu Y. and Shu C. W. and Zhang M. . High order finite difference weno schemes for nonlinear degenerate parabolic equations. SIAM Journal on Scientific Computing 2011;33(2):939–65.

[6] Harten A, Engquist B, Osher S, Chakravarthy S. Uniformly high order essentially non-oscillatory schemes. III J Comput Phys 1987;(71):231–303.

[7] Johansen AO, B. E. A homogeneous two-phase flow model of an evaporator with internally rifled tubes. SIMS 2012 2013;(1):1–21.

[8] Johansen AO, B. E. Homogeneous two-phase flow model of a vertical steam evaporator implemented in a fifth order central weno scheme for hyperbolic balance laws. Heat and Fluid Flow 2013;(1):1–25.

[9] Borges R, B. C, Costa W, Don S. An improved weighted essentially non-oscillatory scheme for hyperbolic conservation laws. J Comput Phys 2008;(227):3191–211.

[10] Castro M, Costa B, Don WS. High order weighted essentially non-oscillatory weno-z schemes for hyperbolic conservation laws. Journal of Computational Physics 2010;(230):1766–92.

[11] Kurganov A, Levy D. A third-order semidiscrete central scheme for conservation laws and convection-diffusion equations. SIAM J Sci Comp 2000;4(22):1461–88.

[12] Kurganov A, Noelle S, Petrova G. Semi-discrete central-upwind schemes for hyperbolic conservation laws and hamilton-jacobi equations. SIAM J Sci Comp 2001;(23):707–40.

[13] Harten A. On a class of high resolution total-variation-stable finite-difference schemes. SIAM J Numerical Anal 1983;21(1.):1–23.

[14] Levy D, Pupo G, Russo G. Compact central weno schemes for multidimensional conservation. SIAM J Sci Comput 2000;(22):656–72.

[15] Gotlieb S, Shu C. Total variation diminishing runge-kutta schemes. Math Comp 1998;(67):73–85.

[16] Chen GQ, Levermore CD, Liu T. Hyperbolic conservation laws with stiff relaxation terms and entropy. Communications on Pure and Applied Mathematics 1994;6(47):787–830.

[17] Kurganov A, Tadmor E. New high-resolution central schemes for nonlinear conservation laws and convection-diffusion equations. J Comput Phys 2000;(160):241–82.

[18] Sigal Gottlieb . On high order strong stability preserving rungekutta and multi step time discretizations. Journal of Scientific Computing 2004;25(1):105–28.

[19] Zahran YH. An efficient weno scheme for solving hyperbolic conservation laws. App Math and Comp 2009;(212):37–50.

[20] Bjørnø L, Hartig A. Strømningslære. 2 ed.; Polyteknisk Forlag; 1984.

[21] Johansen, A. O. and Elmegaard B. . Finite element method interpolation scheme for fast calculation of water/steam properties. Applied Thermal Engineering 2013;(1):1–25.

[22] Bentz PD, Prasad Kuldeep R. Thermal performance of fire resistive materials i. characterization with respect to thermal performance models. NIST, Building and Fire research Laboratory, Gaithersburg 2007;(MD 20899-8615).

[23] Rohrenwerke M. Rohre aus warmfesten und hochwarmfesten Stahlen Werkstoffblatter. 1 ed.; MannesMann Rohrenwerke; 1988.

[24] Richter CC. Proposal of New Object-Oriented Equation-Based Model Libraries for Thermodynamic Systems; vol. 1. 1 ed.; Von der Fakultät für Maschinenbau, der Technischen Universität Carolo-Wilhelmina zu Braunschweig; 2008.

O. Paper 2

Axel Ohrt Johansen, Brian Elmegaard

Finite Element Method Interpolation Scheme for Fast Calculation of Water/Steam Properties

Journal of Computational Physics

Finite Element Method Interpolation Scheme for Fast Calculation of Water/Steam Properties

Axel Ohrt Johansen[a,b], Brian Elmegaard[b]

[a] *DONG Energy - Thermal Power, Kraftværksvej 53, Dk-7000, Fredericia, Denmark*
[b] *Technical University of Denmark, Nils Koppels Allé, Building 403, DK-2800 Kgs. Lyngby, Denmark*

Abstract

In engineering practice, where performance monitoring and optimisation of power plants in real time, it is often necessary to obtain very accurate but simple relationships between water and steam properties with a minimum of computational time. In this article a number of compact numerical interpolation schemes for fast calculation of the thermodynamic properties have been developed. The schemes are based on the IAPWS-97 (International Association for the Properties of Water and Steam). The method is based on dividing the complete range of properties into unique regions, which in turn are constructed by interpolation element. We compare the use of linear, bilinear or second order interpolation elements. The thermodynamic properties of water and steam show significant discontinuitues at the saturation curves between liquid and two-phase conditions and two-phase and vapor conditions. We resolve this property by using triangular elements in the vicinity of the saturation line. This improves the resolution of the saturation line to far better accuracy.

The different interpolation schemes have been tested in order to identify the optimum form with background in the desired accuracy and table lookup speed. The accuracy and computing speed of the interpolation schemes have been compared to those widely used in IAPWS-97 standard, which is the reference application in this work. The fastest, averaged lookup speed was found to be 1/33 of the reference calculation, referring to the pure bilinear scheme. The accuracy is varying, dependant of the area of interest, order of the element and the resolution of the interpolation grid, but it is determined to be sufficient for the application of the methods in accurate dynamic modeling of steam plants. The computing time is dependent of the region. It is found that the highest accuracy is achieved in the superheated region, where we have the smoothest function values, which make it possible to use a simple and fast look up function.

Keywords: Two phase flow, interpolation, linear, bilinear, iso parametric, elements, IAPWS-97.

Email address: aoj@addedvalues.dk (Axel Ohrt Johansen)

1. Introduction

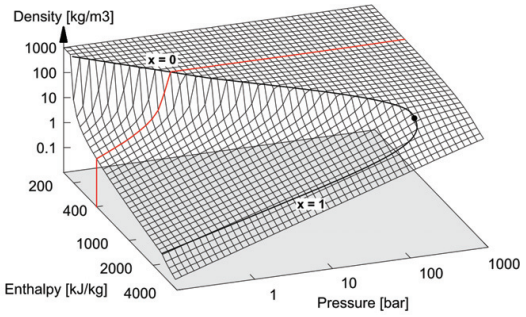

Figure 1: Density as function of Pressure and Enthalpy, [1]

Brereton [2] is motivated by Callandar's enthalpy function for dry steam. It is based on the observation that over a given pressure range density at constant enthalpy is a nearly linear function of pressure within the tolerance of the skeleton steam tables. This is illustrated by the red curve in figure 1. Simple algebraic equations can thus provide dry-steam density within 0.05 % accuracy over a range of 50 to 200 bar and from saturation temperature to 690 ^oC. Reference [3] describes the necessity of fast water/steam calculations for dynamic simulations of boiler tubes. Here, Siemens uses look-up tables, where a large set of interpolation values of state variables has been stored for each necessary property function together with its first order partial derivative. Thus for an arbitrary argument input the corresponding property function can be determined rapidly by the help of the next surrounding interpolation value.

In most cases the interpolation is processed linearly, which is the easiest alternative. Several other authors have written about methods for improving the calculation speed of determining the thermodynamic properties of water and steam, including [4], where a package for the computation of water and steam properties has been developed. This package combines several aims: fast calculation, a good level of accuracy, consistency and high accuracy of the saturated liquid and gas states. The general results is a compromise where the advantage of sophisticated cubic interpolation and the optimum node/grid selection is partly reduced by the computational effort required to meet the severe restrictions of smooth derivatives and high accuracy at the saturation line. The package does not lead to a high-speed, general-purpose package, but to a highly sophisticated package with many special features. In [5] a reconstruction of the fluids properties of refrigerants in the REFPROP database [6] is presented. This method is closely related to the method we describe below. We introduce an effort on decreasing the computation time significantly by developing an advanced interpolation scheme for the steam properties without compromising the accuracy of the overall results. The presented method is based on the

IAPWS 97 formulation and thus retains the accuracy of the recent formulation of steam properties. The method is based on the Finite Element Method[**?**]. We further investigate which type of interpolation elements (linear, bilinear and isoparametric) are best suited for the steam property calculations.

1.1. Motivation for the Interpolation Approach

One of the main advantages of using an interpolation scheme on the IAPWS-97, is fast calculations of the properties with high accuracy for the complete definition range. By using a low order interpolation element, it allows for an unambiguous reverse calculation of the dependent property as a function of any two independent properties. By using higher order interpolation elements, both the interpolation and reverse calculations are based on iteration, extending the lookup time, but also increasing the accuracy.

Additionally the stability of a numerical method including derivatives, e.g., a Newton method, can be improved and may converge easier, with fewer iterations, if the Jacobian matrix consists of smooth derivatives, based on interpolation. These derivatives typically occurs in mathematical models of power plants, where there are major requirements for both speed of calculation and numerical stability, which both are accommodated by use of an interpolation scheme.

1.2. Outline

This paper is organized as follows. In Section 2 we are focusing on the definition area of the interpolated domain. Firstly, in section 2.1.1, we define the general regions and the corresponding interpolation mesh in relation to a uniform Cartesian coordinate system. Secondly, in section 2.2, the principles of the three different types of interpolation elements are outlined. Section 3 is dealing with the timing of an application in general, pointing out the most important considerations to be made. In section 3.2 a numerical validation of the linear interpolation schemes is given. Finally, in section 3.2.1 to 3.2.3 tests of accuracy are performed for three test cases. Our recommendations are outlined on the basis of the discussion of the test cases, and final concluding remarks are included in section 5.

2. Methods

2.1. Interpolation in Steam table

An algorithm has been developed approximate one (or more) properties of water and steam as function of two given properties by interpolation. In this case we focus on the density as function of the enthalpy and pressure of water and steam in the operation range of 0.1 to 4000 [kJ/kg] and 0.1 to 800 [bar], respectively. Below the theory of the interpolation scheme is outlined, supplied with the basic algorithm, discretised nodes and corresponding elements for each region.

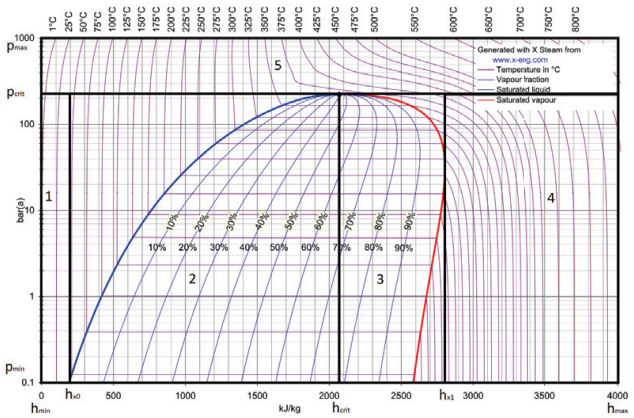

Figure 2: Five Regions in the Pressure and Enthalpy diagram of water/steam.

2.1.1. Steam Table Regions

The interpolation grid is divided into 5 regions, as shown in figure (2). Regions R_1, R_4 and R_5 covers ranges consist only of uniform squared elements with four nodes placed in a rectangular Cartesian grid. Regions R_2 and R_3 instead consist of both squared and triangular elements to be able to construct the saturation curve more accurately. The five regions are defined due to the need to determine the density of a fluid, which is a challenging task, especially for water / steam at low pressure levels where the it exhibits significant discontinuity at the saturation curve. We can easily change the number and location of the regions in order to accommodate other thermodynamic properties. The triangular elements are used in areas, where we need to resolve the saturation curve. These triangular elements are linear or iso-parametric elements, with one side covering the saturation curve, which is assumed to be linear or curved along the border of each element, depending on the order of shape function. This ensures an accurate resolution of the saturation curve, which cannot be handled by a rectangular bi-linear element, without increasing the number of elements substantially.

With the assumption that the interpolation table is dedicated to the interpolation of a water and steam model like IAPWS-97, we define two independent parameters p (pressure) and h (enthalpy) measured in [bar] and [kJ/kg], respectively and cover five regions. The definition area for each of the five regions is given in table (1), where the threshold values are given by: h_{crit}=2084.26 [kJ/kg], p_{crit}=220.19 [bar], $h_{\mathrm{sat,liq}}(p_{\mathrm{min}})$=191.81 [kJ/kg] and $h_{\mathrm{sat,vap}}(p_{\mathrm{min}})$=2803.28 [kJ/kg], due to figure (2). Enthalpy, h, and pressure, p are the coordinates of the abscissa and ordinate axes. They are thus denoted x and y, respectively, in the general implementation described below. The dependent variable ρ is denoted by z.

The algorithm for finding the correct region is shown in figure (3)

Table 1: Definition areas of each region in the general interpolation scheme.

Region	$h_{min}[kJ/kg]$	$h_{max}[kJ/kg]$	$p_{min}[bar]$	$p_{max}[bar]$
1	0.10	191.81	0.1	220.19
2	191.81	2084.26	0.1	220.19
3	2084.26	2803.28	0.1	220.19
4	2803.28	4000.00	0.1	220.19
5	0.10	4000.00	220.19	800.00

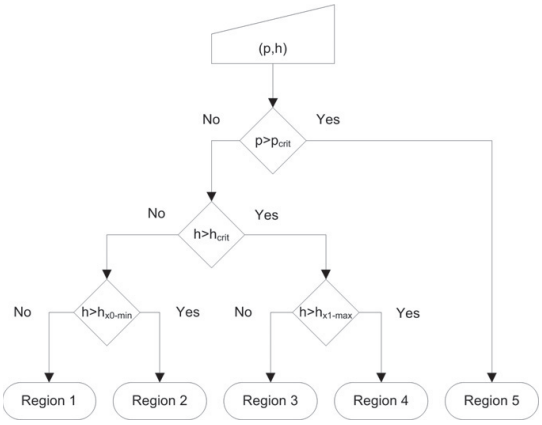

Figure 3: Flow chart diagram for finding region.

2.1.2. Creation of mesh

The creation of a compact grid has been implemented as a generic algorithm, and is specifically adapted to regions R_2 and R_3 in the two-phase region, by establishing a series of pressure lines or isobars (N_p). These are fundamental for the construction of the elements. The specific place, where a rectangular element crosses a saturation line, a linear triangular element is established in order to preserve the function value along the saturation line. Figure (5) illustrates how the element structure is established between two pressure levels. A book keeping system is generally saving a pointer to the very first element in each row, except for the pure Cartesian bilinear grid, where we use a simple integer truncation to find the nearest grid points around the calculated point $P(x, y)$, see equation (9) below.

In regions R_2 and R_3, where the two-phase region of the fluid is described, we consider the saturation curve. Hence the element resolution in the x-direction is no longer equidistant in the vicinity of the saturation line, because the size of the element depends on the slope of the saturation curve ($\frac{\partial \rho}{\partial h}$), which leads to the above-mentioned book keeping system. The very first element in each row

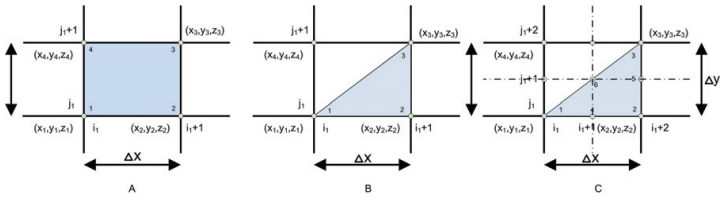

Figure 4: Grids for bilinear (A), linear (B) interpolation and second order (C) interpolation.

is saved, for later speeding up the table lookup procedure, which is illustrated in figure (5). An algorithm is developed to obtain a fast and flexible way to establish a mesh and to search into it. It works in the following way for 3, 4 and 6 node-element systems, but is similar for a higher order elements.

Algorithm:

1) Choose the pressure levels (Not necessarily equidistant).
2) Calculate the definition area in h: h_{min} and h_{max}.
3) Establish a loop from j = 1 to N_p.
4) Calculate the saturation lines h_{sat}^{max} and h_{sat}^{min} for $p(j)$, $p(j+1)$ and possibly $p(j+2)$.
5) Start a main loop holding the pressure level given by $p(j)$ and $p(j+1)$ and $p(j+2)$.
6) Store pointer to the very first element in the main loop.
7) Initialise the two very first local nodes (n_1 and n_4) at h_{min}.
8) Start an inside loop with h=h+Δh.
9) Evaluate which element is restricting the size of h and update it on the basis of h and the type of element (3, 4 or 6 node), see figure (5).
10) Update local nodes n_2 and n_3.
11) Evaluate if h > h_{max}. If true, update the new node n_1 and n_4 and jump to 4) else set $n_1 = n_2$ and $n_4 = n_3$ and continue.

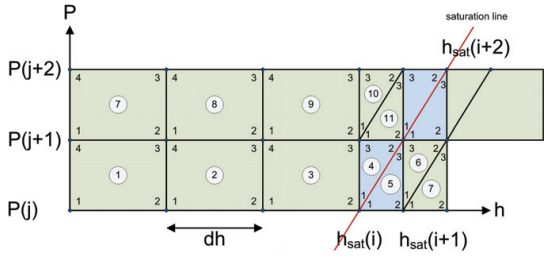

Figure 5: Elements in Region 2 or 3 with local nodes (two phase region with saturation line).

The above algorithm is generic for all regions, except for the evaluation

step 9), which is unique for the three types of regions: Two-phase regions R_2, R_3,single-phase, subcritical regions R_1, R_4 and the supercritical region R_5. For Region R_2 we have to take into consideration that the very first element is a triangular element, because the marching loop is going from low- to high pressure. In R_3 we have the opposite situation, with a triangular element at the very last element. Both R_2 and R_3 are a triangular element and placed at both sides of the saturation line, to ensure optimal resolution of the saturation line. The look up system is based on look up arrays for each element row at fixed pressure, which stores the very first element of each row. Regions R_1, R_4 and R_5 are based on a solely equidistant grid structure, based on bilinear interpolation of four-node square elements. This look up system is determined to bee fast and simple.

2.1.3. Order of Interpolation scheme

Conceptually, the simplest element form of two-dimensional kind is a rectangle, with sides parallel to the x and y axes in a Cartesian coordinate system. Let us assume that the function value $z(x, y)$ is expressed in a polynomial form in x and y. To ensure inter-element continuity of z along the top and bottom sides, the variation must be linear. In general, we seek element expansions which possess the highest order of a complete polynomial for a minimum of degrees of freedom. In this context it is useful to recall the Pascal triangle [7] from which the number of terms occurring in a polynomial in two variables x, y can be readily determined. We use Pascal's triangle which is a triangular array of the binomial coefficients in a triangle, and determines the coefficients arising in binomial expansions.

$$(x+y)^n = \sum_{k=0}^{n} \left(\begin{array}{c} n \\ k \end{array} \right) x^{n-k} y^k \tag{1}$$

$$= a_0 x^n + a_1 x^{n-1} y + a_2 x^{n-2} y^2 + ... + a_{n-1} x y^{n-1} + a_n y^n, \tag{2}$$

for any non-negative integer n and any integer k between 0 and n.

The coefficients are the numbers in row n of Pascal's triangle. In general, when a binomial like $x+y$ is raised to a positive integer power n, the coefficients a_i in the expansion are precisely the numbers on row n of Pascal's triangle.

A first order bilinear shape function can then be expressed as:

$$z(x, y) = a_0 + a_1 x + a_2 y + a_3 xy \tag{3}$$

matching four nodes in a square bilinear element. The interpolated function should not use the term of x^2 or y^2, but $x \cdot y$, which is the bilinear form of x and y. The corresponding second order shape function is given as:

$$z(x, y) = a_0 + a_1 x + a_2 y + a_3 xy + a_4 x^2 + a_5 y^2 \tag{4}$$

which is associated with a six node triangular element.

2.1.4. Lookup table

In a Cartesian equidistant grid system, with the grid spacing of Δx and Δy, it is very fast to calculate the neighbour grid points in an element. Typically we use a simple expression to find the nearest grid points involved in the bilinear interpolation, given by equations (5 to 9):

$$(x_1, y_1) = (\Delta x \cdot i_1, \Delta y \cdot j_1) \tag{5}$$
$$(x_2, y_2) = (\Delta x \cdot (i_1 + 1), \Delta y \cdot j_1) \tag{6}$$
$$(x_3, y_3) = (\Delta x \cdot (i_1 + 1), \Delta y \cdot (j_1 + 1)) \tag{7}$$
$$(x_4, y_4) = (\Delta x \cdot i_1, \Delta y \cdot (j_1 + 1)) \tag{8}$$

where the indices i_1,j_1 are given as

$$(i_1, j_1) = \left(\left| \frac{x - x_{min}}{\Delta x} \right|, \left| \frac{y - y_{min}}{\Delta y} \right| \right) \tag{9}$$

For a non-equidistant grid, we use a look up vector to find the first and last element in a row of elements defined by a pressure level. A marching loop is testing whether the calculated point is in a the given element limited by two nodes.

2.2. Interpolation elements

In this section three types of interpolation elements are outlined, which can be used in combination with each other. The theory is outlined in the following subsections.

2.2.1. Linear interpolation elements

In the context of a triangle, we introduce the so-called barycentric coordinates [7], which are also known as area coordinates, because the coordinates of a point P with respect to triangle ABC are proportional to the areas of PBC, PCA and PAB, which are always positive as long as P is inside the element, see figure (6).

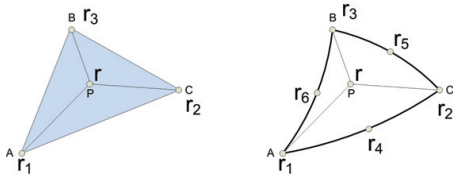

Figure 6: Triangular elements T with 3 and 6 nodes used in Regions 2 or 3 in the vicinity of the saturation line.

Barycentric coordinates are extremely useful in engineering applications involving triangular subdomains. These make analytic integrals often easier to evaluate, and Gaussian quadrature tables are often presented in terms of area coordinates.

First let us consider a triangle T defined by three vertices (nodes) r_1 , r_2 and r_3. Any point $\mathbf{r}$ located on this triangle may then be written as a weighted sum of these three vertices, i.e.

$$\mathbf{r} = \xi_1 \cdot \mathbf{r}_1 + \xi_2 \cdot \mathbf{r}_2 + \xi_3 \cdot \mathbf{r}_3 \tag{10}$$

$$\xi_1 + \xi_2 + \xi_3 = 1 \tag{11}$$

where

$$\mathbf{r}_1 = (x_1, y_1, z_1), \quad \mathbf{r}_2 = (x_2, y_2, z_2) \quad \textit{and} \quad \mathbf{r}_3 = (x_3, y_3, z_3) \tag{12}$$

Inserting $\xi_3 = 1 - \xi_1 - \xi_2$ in (10) gives a plane, defined by two vectors $\mathbf{r}_{12}$ and $\mathbf{r}_{13}$ and the corresponding normal vector is defined by: $\mathbf{n}$=$\mathbf{r}_{12} \times \mathbf{r}_{13}$. This plane can be expressed by the matrix $\mathbf{T}$:

$$\mathbf{T} = \begin{pmatrix} x_{13} & x_{23} \\ y_{13} & y_{23} \end{pmatrix}$$

and the corresponding area of the triangular element is

$$A = \frac{1}{2} \det(\mathbf{T}) \tag{13}$$

where x_{ij}=$x_i - x_j$ and y_{ij}=$y_i - y_j$.

Hence the barycentric coordinates can be formulated as

$$\mathbf{T} \cdot \overline{\xi} = \mathbf{r} - \mathbf{r}_3 \tag{14}$$

which gives

$$\begin{aligned} \overline{\xi} &= \mathbf{T}^{-1} \cdot (\mathbf{r} - \mathbf{r}_3) \\ &= \frac{1}{\det(\mathbf{T})} \begin{pmatrix} y_{23} & -x_{23} \\ -y_{13} & x_{13} \end{pmatrix} \cdot (\mathbf{r} - \mathbf{r}_3) \\ &= \frac{1}{(x_{13} \cdot y_{23} - x_{23} \cdot y_{13})} \begin{pmatrix} y_{23} & -x_{23} \\ -y_{13} & x_{13} \end{pmatrix} \cdot (\mathbf{r} - \mathbf{r}_3) \end{aligned} \tag{15}$$

or

$$\begin{aligned} \xi_1 &= \frac{y_{23} \cdot (x - x_3) - x_{23} \cdot (y - y_3)}{(x_{13} \cdot y_{23} - x_{23} \cdot y_{13})} \\ \xi_2 &= \frac{y_{13} \cdot (x - x_3) + x_{13} \cdot (y - y_3)}{(x_{13} \cdot y_{23} - x_{23} \cdot y_{13})} \\ \xi_3 &= 1 - \xi_1 - \xi_2 \end{aligned} \tag{16}$$

Since barycentric coordinates are a linear transformation of Cartesian coordinates, it turns out that they vary linearly along the edges and over the area of the triangle. If a point lies in the interior of the triangle T, all of the Barycentric coordinates lie in the open interval (0,1). This can be summarized by the following statements:

A point $\mathbf{r}$ lies inside the triangle T if and only if $0 \leq \xi_i \leq 1 \; \forall \; i \; \in [1,2,3]$. Now, we interpolate the value of z given by (x, y) in T as: $\mathbf{n} = \mathbf{r}_{12} \times \mathbf{r}_{13}$ and $\mathbf{n} \cdot (\mathbf{r} - \mathbf{r}_1) = 0$ which is similar to

$$n_1 \cdot (x - x_1) + n_2 \cdot (y - y_1) + n_3 \cdot (z - z_3) = 0 \tag{17}$$

where $\mathbf{n}$ is the normal vector to the triangle ABC:

$$\begin{aligned} \mathbf{n} &= \begin{pmatrix} n_1 \\ n_2 \\ n_3 \end{pmatrix} \\ &= \begin{pmatrix} y_{21} \cdot z_{31} - z_{21} \cdot y_{31} \\ z_{21} \cdot x_{31} - x_{21} \cdot z_{31} \\ x_{21} \cdot y_{31} - y_{21} \cdot x_{31} \end{pmatrix} \end{aligned} \tag{18}$$

Hence

$$z(x, y) = z_1 - \frac{1}{n_3} \cdot [(x - x_1) \cdot n_1 + (y - y_1) \cdot n_2] \tag{19}$$

$$y(x, z) = y_1 - \frac{1}{n_2} \cdot [(x - x_1) \cdot n_1 + (z - z_1) \cdot n_3] \tag{20}$$

$$x(y, z) = x_1 - \frac{1}{n_1} \cdot [(y - y_1) \cdot n_2 + (z - z_1) \cdot n_3] \tag{21}$$

If one of the barycentric coordinates is zero, this means that $\mathbf{r}$ lies on a line segment, defining T, and $\mathbf{r}$ is placed in the opposite direction of the barycentric coordinate, i.e., if ξ_1 equals zero, then $\mathbf{r}$ lies on the segment BC or on the line given by the vector: $\mathbf{r}_{23} = \mathbf{r}_3 - \mathbf{r}_2$. Correspondingly, if one of the barycentric coordinates is less than zero, $\mathbf{r}$ is not inside the triangle T, but positioned outside T in the opposite direction of ξ_i. This technique is useful when we want to traverse from one element to the neighbouring element.

2.2.2. Bilinear interpolation elements

The key idea behind the bilinear interpolation is to perform linear interpolation first in one direction, and then again in the other direction. It is an extension of the linear interpolation for interpolating functions of two variables (e.g., x and y) on a regular grid [7]. Although each step is linear in the sampled values and in the position, the interpolation as a whole is not linear but rather quadratic in the sample location. Nevertheless, one can make an inverse calculation of the dependent parameter z by use of bilinear interpolation, so the function $z(x, y)$ can be expressed explicitly as $y(x, z)$ or $x(y, z)$.

Having a Cartesian rectangular coordinate system in which the four equidistant vertices (nodes), are given by: $\mathbf{r}_1 = (x_1, y_1)$, $\mathbf{r}_2 = (x_2, y_2)$, $\mathbf{r}_3 = (x_3, y_3)$,

and $\mathbf{r}_4 = (x_4, y_4)$, where z is known for all nodes, then the interpolation formula simplifies to

$$z(x,y) = [1-x, x] \begin{pmatrix} z_1 & z_4 \\ z_2 & z_3 \end{pmatrix} \cdot \begin{bmatrix} 1-y \\ y \end{bmatrix} \tag{22}$$

$$z(x,y) = \frac{z_1}{\Delta x \Delta y} \cdot (x_2 - x) \cdot (y_2 - y) + \frac{z_2}{\Delta x \Delta y} \cdot (x - x_1) \cdot (y_2 - y) \tag{23}$$

$$+ \frac{z_4}{\Delta x \Delta y} \cdot (x_2 - x) \cdot (y - y_2) + \frac{z_3}{\Delta x \Delta y} \cdot (x - x_1) \cdot (y - y_2) \tag{24}$$

$$= a_1 + a_2 \cdot x + a_3 \cdot y + a_4 \cdot x \cdot y \tag{25}$$

where

$$\begin{aligned} a_1 &= \frac{1}{\Delta x \Delta y} \cdot [x_2 y_2 z_1 - x_1 y_2 z_2 - x_2 y_1 z_4 + x_1 y_2 z_3] \\ a_2 &= \frac{1}{\Delta x \Delta y} \cdot [-y_2 z_1 + y_2 z_2 + y_1 z_4 - y_1 z_3] \\ a_3 &= \frac{1}{\Delta x \Delta y} \cdot [-x_2 z_1 + x_1 z_2 + x_2 z_4 - x_1 z_3] \\ a_4 &= \frac{1}{\Delta x \Delta y} \cdot [z_1 - z_2 - z_4 + z_3] \end{aligned}$$

and $\Delta x{=}x_2 - x_1$ and $\Delta y{=}y_4 - y_1$. Alternatively, we can express $x(y,z)$ and $y(x,z)$ explicitly as:

$$x(y,z) = \frac{-1}{a_2 + a_4 \cdot y} \cdot [z - a_1 + a_3 \cdot y] \tag{26}$$

and

$$y(x,z) = \frac{-1}{a_3 + a_4 \cdot x} \cdot [z - a_1 + a_2 \cdot x] \tag{27}$$

2.2.3. Iso-Parametric Triangles

If the triangle has variable metric, as in the curved sided 6-node triangle geometries shown in Figure (6), the foregoing formulas need adjustment because the element of area Ω becomes a function of position. It can be shown that the differential area element is given by

$$\begin{aligned} d\Omega &= \mathbf{J} d\xi_1 d\xi_2 d\xi_3 \\ &= \frac{1}{2} \det \begin{bmatrix} 1 & 1 & 1 \\ \sum_{i=1}^n x_i \frac{\partial N_i}{\partial \xi_1} & \sum_{i=1}^n x_i \frac{\partial N_i}{\partial \xi_2} & \sum_{i=1}^n x_i \frac{\partial N_i}{\partial \xi_3} \\ \sum_{i=1}^n y_i \frac{\partial N_i}{\partial \xi_1} & \sum_{i=1}^n y_i \frac{\partial N_i}{\partial \xi_2} & \sum_{i=1}^n y_i \frac{\partial N_i}{\partial \xi_3} \end{bmatrix} \end{aligned} \tag{28}$$

where ξ_i, $i \in$[1,2,3] are normalized coordinates and the shape function N_i is given by equation (30). Above, $\mathbf{J}$ is the Jacobian determinant. The following theory is based on the considerations described in reference [7].

Consider the more general case of an iso-parametric element with n nodes and shape functions N_i. The element geometry is defined by the corner coordinates x_i, y_i, with $i \in [1...6]$. Corners are numbered 1, 2, 3 in counter-clockwise sense. Side nodes are numbered 4, 5, 6, opposite to corners 3, 1, 2, respectively as illustrated in figure (6). The triangular normalised coordinates are as above denoted by ξ_1, ξ_2 and ξ_3, which satisfy $\xi_1+\xi_2+\xi_3 = 1$. The quadratic displacement field $u_x(\xi_1, \xi_2, \xi_3), u_y(\xi_1, \xi_2, \xi_3)$ is defined by the 12 node displacements u_{x_i}, u_{y_i} , $i \in$[1...6], as per the iso-parametric quadratic interpolation formula in [7], page 165. That formula is repeated here for convenience:

$$\begin{bmatrix} 1 \\ x \\ y \\ u_x \\ u_y \end{bmatrix} = \begin{bmatrix} 1 & 1 & 1 & 1 & 1 & 1 \\ x_1 & x_2 & x_3 & x_4 & x_5 & x_6 \\ y_1 & y_2 & y_3 & y_4 & y_5 & y_6 \\ u_{x1} & u_{x2} & u_{x3} & u_{x4} & u_{x5} & u_{x6} \\ u_{y1} & u_{y2} & u_{y3} & u_{y4} & u_{y5} & u_{y6} \end{bmatrix} \mathbf{N} \tag{29}$$

where the shape function $\mathbf{N}$ and the belonging gradients in ξ_i are given as

$$\mathbf{N} = \begin{bmatrix} \xi_1(2\xi_1 - 1) \\ \xi_2(2\xi_2 - 1) \\ \xi_3(2\xi_3 - 1) \\ 4\xi_1\xi_2 \\ 4\xi_2\xi_3 \\ 4\xi_3\xi_1 \end{bmatrix}, \quad \frac{\partial N_i}{\partial \xi_1} = \begin{bmatrix} 4\xi_1 - 1 \\ 0 \\ 0 \\ 4\xi_2 \\ 0 \\ 4\xi_3 \end{bmatrix},$$

$$\frac{\partial N_i}{\partial \xi_2} = \begin{bmatrix} 0 \\ 4\xi_2 - 1 \\ 0 \\ 4\xi_1 \\ 4\xi_3 \\ 0 \end{bmatrix}, \quad \frac{\partial N_i}{\partial \xi_3} = \begin{bmatrix} 0 \\ 0 \\ 4\xi_3 - 1 \\ 0 \\ 4\xi_2 \\ 4\xi_1 \end{bmatrix} \tag{30}$$

If the metric is simply defined by the 3 corners, as in figure (6), the geometry shape functions are linear as in equation (16): $N_1 = \xi_1$, $N_2 = \xi_2$ and $N_3 = \xi_3$. Then the foregoing determinant reduces to that of equation (13), and $\mathbf{J} = \frac{1}{2}$A everywhere. But for general (curved) geometries $\mathbf{J} = \mathbf{J}(\xi_1, \xi_2, \xi_3)$, and the triangle area A cannot be factored out of the integration rules according to [7]. Instead we use the above gradients in a simple iteration procedure to estimate the barycentric coordinates for a specific point $P(x, y)$. The bulk of the shape function logic is concerned with the computation of the partial derivatives of the shape functions (30) with respect to x and y at any point in the element. For this purpose consider a generic scalar function $w(\xi_1, \xi_2, \xi_3)$ that is quadratically interpolated over the triangle by

$$w = w_1N_1 + w_2N_2 + w_3N_3 + w_4N_4 + w_5N_5 + w_6N_6 \tag{31}$$

w may stand for 1, x , y, u_x or u_y , which are interpolated in the iso-parametric representation in (29), or other element-varying quantities such as fluid density, temperature, etc. Determining partial derivatives of w in (31) with respect to x and y and applying the chain rule twice yields

$$\begin{aligned}\frac{\partial w}{\partial x} &= \sum_{i=1}^{n} w_i \frac{\partial N_i}{\partial x} = \sum_{i=1}^{n} w_i \left(\frac{\partial N_i}{\partial \xi_1}\frac{\partial \xi_1}{\partial x} + \frac{\partial N_i}{\partial \xi_2}\frac{\partial \xi_2}{\partial x} + \frac{\partial N_i}{\partial \xi_3}\frac{\partial \xi_3}{\partial x} \right) \\ \frac{\partial w}{\partial y} &= \sum_{i=1}^{n} w_i \frac{\partial N_i}{\partial y} = \sum_{i=1}^{n} w_i \left(\frac{\partial N_i}{\partial \xi_1}\frac{\partial \xi_1}{\partial y} + \frac{\partial N_i}{\partial \xi_2}\frac{\partial \xi_2}{\partial y} + \frac{\partial N_i}{\partial \xi_3}\frac{\partial \xi_3}{\partial y} \right) \end{aligned} \tag{32}$$

where all sums are understood to run over i = 1,...6. In matrix form:

$$\begin{bmatrix} \frac{\partial w}{\partial x} \\ \frac{\partial w}{\partial y} \end{bmatrix} = \begin{bmatrix} \frac{\partial \xi_1}{\partial x} & \frac{\partial \xi_2}{\partial x} & \frac{\partial \xi_3}{\partial x} \\ \frac{\partial \xi_1}{\partial y} & \frac{\partial \xi_2}{\partial y} & \frac{\partial \xi_3}{\partial y} \end{bmatrix} \cdot \begin{bmatrix} \sum w_i \frac{\partial N_i}{\partial \xi_1} \\ \sum w_i \frac{\partial N_i}{\partial \xi_2} \\ \sum w_i \frac{\partial N_i}{\partial \xi_3} \end{bmatrix} \tag{33}$$

Transposing both sides of (33) while exchanging sides yields

$$\begin{bmatrix} \sum w_i \frac{\partial N_i}{\partial \xi_1} & \sum w_i \frac{\partial N_i}{\partial \xi_2} & \sum w_i \frac{\partial N_i}{\partial \xi_3} \end{bmatrix} \cdot \begin{bmatrix} \frac{\partial \xi_1}{\partial x} & \frac{\partial \xi_1}{\partial y} \\ \frac{\partial \xi_2}{\partial x} & \frac{\partial \xi_2}{\partial y} \\ \frac{\partial \xi_3}{\partial x} & \frac{\partial \xi_3}{\partial y} \end{bmatrix} = \begin{bmatrix} \frac{\partial w}{\partial x} & \frac{\partial w}{\partial y} \end{bmatrix} \tag{34}$$

Now make $w \equiv (1, x, y)^T$ and stack the results row-wise:

$$\begin{bmatrix} \sum \frac{\partial N_i}{\partial \xi_1} & \sum \frac{\partial N_i}{\partial \xi_2} & \sum \frac{\partial N_i}{\partial \xi_3} \\ \sum x_i \frac{\partial N_i}{\partial \xi_1} & \sum x_i \frac{\partial N_i}{\partial \xi_2} & \sum x_i \frac{\partial N_i}{\partial \xi_3} \\ \sum y_i \frac{\partial N_i}{\partial \xi_1} & \sum y_i \frac{\partial N_i}{\partial \xi_2} & \sum y_i \frac{\partial N_i}{\partial \xi_3} \end{bmatrix} \cdot \begin{bmatrix} \frac{\partial \xi_1}{\partial x} & \frac{\partial \xi_1}{\partial y} \\ \frac{\partial \xi_2}{\partial x} & \frac{\partial \xi_2}{\partial y} \\ \frac{\partial \xi_3}{\partial x} & \frac{\partial \xi_3}{\partial y} \end{bmatrix} = \begin{bmatrix} \frac{\partial 1}{\partial x} & \frac{\partial 1}{\partial y} \\ \frac{\partial x}{\partial x} & \frac{\partial x}{\partial y} \\ \frac{\partial y}{\partial x} & \frac{\partial y}{\partial y} \end{bmatrix} \tag{35}$$

It is obvious that $\frac{\partial x}{\partial x} = \frac{\partial y}{\partial y} = 1$ and $\frac{\partial 1}{\partial x} = \frac{\partial 1}{\partial y} = \frac{\partial x}{\partial y} = \frac{\partial y}{\partial x} = 0$ because x and y are independent coordinates. It is shown in [7] that, if $\sum N_i = 1$, the entries of the first row of the coefficient matrix are equal to a constant of unity, because the first equation in (36) is homogeneous. These entries can be scaled to unity because the first row of the right-hand side is null. Consequently we arrive at a system of linear equations of order 3, with two right-hand sides:

$$\mathbf{J} \cdot \mathbf{P} = \begin{bmatrix} 1 & 1 & 1 \\ J_{x1} & J_{x2} & J_{x3} \\ J_{y1} & J_{y2} & J_{y3} \end{bmatrix} \cdot \begin{bmatrix} \frac{\partial \xi_1}{\partial x} & \frac{\partial \xi_1}{\partial y} \\ \frac{\partial \xi_2}{\partial x} & \frac{\partial \xi_2}{\partial y} \\ \frac{\partial \xi_3}{\partial x} & \frac{\partial \xi_3}{\partial y} \end{bmatrix} = \begin{bmatrix} 0 & 0 \\ 1 & 0 \\ 0 & 1 \end{bmatrix} \tag{36}$$

where $\mathbf{J}$ is called the Jacobian matrix and its determinant is scaled by one half of the Jacobian: $\mathrm{A} = \frac{1}{2}\det(\mathbf{J})$, as used in the expression of the area of an element

in (13). Additionally the sub Jacobians in (36) is given by

$$J_{x1} = \sum x_i \frac{\partial N_i}{\partial \xi_1}, \quad J_{x2} = \sum x_i \frac{\partial N_i}{\partial \xi_2}, \quad J_{x3} = \sum x_i \frac{\partial N_i}{\partial \xi_3}$$
$$J_{y1} = \sum y_i \frac{\partial N_i}{\partial \xi_1}, \quad J_{y2} = \sum y_i \frac{\partial N_i}{\partial \xi_2}, \quad J_{y3} = \sum y_i \frac{\partial N_i}{\partial \xi_3} \tag{37}$$

Solving system (36) gives

$$\begin{bmatrix} \frac{\partial \xi_1}{\partial x} & \frac{\partial \xi_1}{\partial y} \\ \frac{\partial \xi_2}{\partial x} & \frac{\partial \xi_2}{\partial y} \\ \frac{\partial \xi_3}{\partial x} & \frac{\partial \xi_3}{\partial y} \end{bmatrix} = \frac{1}{2A} \begin{bmatrix} J_{y23} & J_{x32} \\ J_{y31} & J_{x13} \\ J_{y12} & J_{x21} \end{bmatrix} = \mathbf{P} \tag{38}$$

with J_{xji}=J_{xj}-J_{xi}, J_{yji}=J_{yj}-J_{yi} and A=$\frac{1}{2}$($J_{x21}J_{y31}$-$J_{y12}J_{x13}$) $\neq 0$. Substituting this into (32), the partial derivatives of the shape functions are

$$\begin{bmatrix} \frac{\partial N_i}{\partial x} \\ \frac{\partial N_i}{\partial y} \end{bmatrix} = \mathbf{P}^T \begin{bmatrix} \frac{\partial N_i}{\partial \xi_1} & \frac{\partial N_i}{\partial \xi_2} & \frac{\partial N_i}{\partial \xi_3} \end{bmatrix}^T \tag{39}$$

where $\mathbf{P}$ is the 3x2 matrix of triangular coordinates defined in (38)

To determine the barycentric coordinates for an iso-parametric element with $n = 6$ nodes, we have two residual functions for a given point $P(x, y)$, which can be incorporated into an external iterative loop, combined with an iterative backtrack loop of ξ_i:

$$R_x = \sum_{i=1}^{6} N_i x_i - x$$
$$R_y = \sum_{i=1}^{6} N_i y_i - y \tag{40}$$

The iterative backtracking loop of ξ_i can be determined by the knowledge of the contributions of $\frac{\partial \xi_i}{\partial x}$ and $\frac{\partial \xi_i}{\partial y}$;

$$\begin{aligned} \xi_i^{n+1} &= \xi_i^n + \frac{\partial \xi_i}{\partial x} R_x + \frac{\partial \xi_i}{\partial y} R_y \\ &= \xi_i^n + \frac{J_{y23} R_x + J_{x32} R_y}{det(J)}, \quad i \in [1, 2] \end{aligned} \tag{41}$$

hence we have

$$\Delta\xi_1 = \frac{J_{y23} R_x + J_{x32} R_y}{det(J)}$$
$$\Delta\xi_2 = \frac{J_{y31} R_x + J_{x13} R_y}{det(J)} \tag{42}$$

2.2.4. Stretching of grid

By introducing a stretching of the pressure grid, we can ensure improvements in the data representation, especially in areas where there are large gradients in the density. Therefore, we define a simple stretching function, which contributes to a moderate stretch of the pressure grid in the vicinity of the saturation line. Thus, the desired data representation is obtained. Figure (7) illustrates how the stretching works. Here the stretching of the network has greatest impact at both ends at $x = 0$ and $x = 1$.

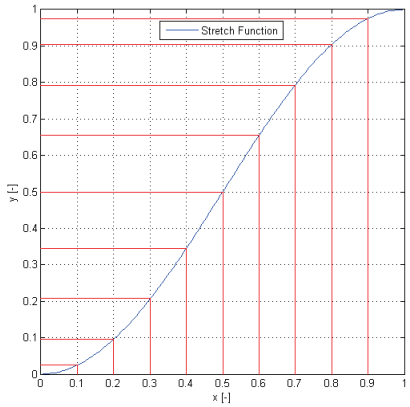

Figure 7: Monotonically increasing stretch function allowing dense grid at boundaries.

A simple monotonically increasing stretch function is given by (43):

$$y = \sin^2(\frac{\pi x}{2}), \quad (x, y) \in [0, ...1] \tag{43}$$

and the reverse function is trivially given by

$$x = \frac{2}{\pi} \sin^{-1}(\sqrt{y}), \quad (x, y) \in [0, ...1] \tag{44}$$

3. Results

3.1. Timing the application

The timing of the simulations is very important because it provides the basis for evaluation of the interpolation elements in terms of time consumption versus effectiveness. One of the performance indicators is the application timing, others can be related to the outcome of the application in terms of numerical results.

Some considerations are important when comparing CPU time: The program timings have to be executed when other users are not active. The timing results can be affected by one or more CPU-intensive processes also running while doing the timings and the application has to be executed under the same

conditions each time in order to provide the most accurate results, especially when comparing execution times of a previous version of the same program. If possible, the same system (processor model, amount of memory, version of the operating system, and so on) has to be used each time. For programs running less than a few seconds, it is important to run several timings to avoid misleading results. Overhead functions like loading libraries might influence short timings considerably. If the program displays a lot of text, redirecting of the output from the program should be considered and will change the times reported because of reduced screen I / O. Timings that show a large amount of system time may indicate a lot of time spent doing I / O, which might be worth investigating. For programs that run for less than a few seconds, several timings shoud be done to ensure that the results are not misleading. The elapsed, real, or "wall clock" time will be greater than the total charged actual CPU time. The total actual CPU time is the sum of the actual user CPU time and actual system CPU time. The computer used is a Lenovo portable PC (T520) with Intel(R) Core (TM) i5-2520M CPU @2.5 GHz 2 Core(s) with 4 logical processors, installed memory (RAM) is 8 GB - 64-bit operation system with Windows 7 Enterprise with service pack 1 Build 7601. Both the test application and the IAPWS-97 water steam table is implemented in C ++ / FORTRAN 90, under Visual studio 2008 - Professional Edition. The applications are compiled with optimiser in order to achieve maximum speed.

3.2. Simulation results

In the following three different setup of interpolations are compared. The first setup is based on a case using two main regions, R_6 which covers regions R_1 to R_4, and R_5 using a pure bilinear 4 node element. The second case is based on five regions using bilinear elements, supplied with a linear triangular element in the vicinity of the saturation line. Finally, a setup is using the five regions by applying an iso parametric triangular element (6-node).

The simulation are identified by a number (N_s). Meshes based on different element sizes in the five regions has been created for the individual simulations. The number of elements in each case are listed in tables; tabel (3) for the two region case, table (4) for the five-region case with bilinear elements and table (5) for the five-region case with triangular elements. The total number of nodes and elements are listed in the last column. We have a linear relationship between the total amount of nodes/elements versus the number of isobars used, N_p, because the step length in enthalpy, h, is approximately fixed and independent of N_p.

For comparison, reference simulations have been performed by running the pure IAPWS-97 water-steam application for pressure $p \in$ (1,10, 50, 100, 220, 300 and 700 [bar]). Corresponding time records are carried out by executing 8 million calculations, varying enthalpy linearly from 0.1 [kJ/kg] up to 4000 [kJ/kg]. The IAPWS 97 is implemented in the same environment as the comparable interpolation scheme. Time consumption is listed in table (2). The averaged simulation time is 1.2248E-6 [s]. The interpolations are performed by stretching isobars in the bottom and top of each region, according to equation (43).

$p[bar]$	1	10	50	100	220	300	700
$t_{ref}[ms]$	0.8775	0.8229	0.7391	0.6923	0.3843	0.7937	0.8054

Table 2: Time consumption of executing IAPWS-97

We notice that it is relatively more time consuming (5-6 times) to perform the interpolation for an isobar passing in the vicinity of the critical pressure (p_{crit}).

N_p	Items	R_6	R_5	$\sum_{i=1}^{5} R_i$
10	Elements:	3600	3600	7200
	Nodes:	4010	3609	7619
25	Elements:	9600	9600	18200
	Nodes:	10025	9624	19649
50	Elements:	19600	19600	39600
	Nodes:	20050	19649	39699
100	Elements:	39600	39600	79600
	Nodes:	40100	39699	79799
200	Elements:	79600	79600	159200
	Nodes:	80200	79799	159999

Table 3: Number of nodes and elements in Region (R_6 covering R_1 to R_4) and R_5 for 4 node elements.

For each simulation setup we perform a traversal with constant pressure and varying enthalpy from 0.5 [kJ/kg] to 3999.5 [kJ/kg] with a step of 0.5 [kJ/kg]). The isobar lines are: (1, 10, 50, 100, 220, 300 and 700 [bar]). Both the maximum, minimum and mean relative error, given by (45) is illustrated, as well as the standard devation, which is a good indicator for how often significant differences in the interpolation occur compared to reference data. Finally, we notice the simulation time for a traversal of h, corresponding to the time records, carried out for the IAPWS-97 reference calculations (t_{Ref}), which is executed for 8 million steps, varying linearly from 0.1 [kJ/kg] up to 4000 [kJ/kg], in order to

N_p	Items	R_1	R_2	R_3	R_4	R_5	$\sum_{i=1}^{5} R_i$
10	Elements:	180	1537	435	1278	3600	7030
	Nodes:	206	2280	525	1420	4009	8440
25	Elements:	600	219	210	2880	9600	19219
	Nodes:	650	4417	1194	3408	10024	21785
50	Elements:	2450	9217	2448	6958	19600	40673
	Nodes:	2512	12907	2557	7100	20049	45125
100	Elements:	9900	18817	9898	14058	39600	92273
	Nodes:	10100	26173	10122	14200	40099	100694
200	Elements:	39800	39957	39798	39800	79600	238955
	Nodes:	40040	55416	40235	40000	80199	255890

Table 4: Number of nodes and elements in Regions 1-5 for 3+4 node elements.

N_p	Items	R_1	R_2	R_3	R_4	R_5	$\sum_{i=1}^{5} R_i$
10	Elements:	360	3074	1142	2160	7200	13936
	Nodes:	920	8437	3068	5520	18418	36363
25	Elements:	1800	8834	3358	6730	9600	13362
	Nodes:	3074	23956	8913	14520	19200	14131
50	Elements:	4900	18434	7048	11760	39200	81342
	Nodes:	12300	49824	18647	29520	98498	208789
100	Elements:	19800	37634	19892	23760	79200	180286
	Nodes:	49799	101540	52557	59520	198598	462014
200	Elements:	79600	79914	79794	79600	159200	478108
	Nodes:	199201	215443	210667	199199	398798	1223308

Table 5: Number of nodes and elements in Region 1-5) for 6 node elements.

evaluate the impact of using different types of elements.

$$\epsilon = \frac{\Phi_{Intp} - \Phi_{ref}}{\Phi_{ref}} \cdot 100\% \tag{45}$$

3.2.1. Bilinear 4 node element

The first simulation setup includes a series of calculations based on the 4 node bilinear element with varying mesh fineness for different pressure levels (isobars). In figure (9) and (10) we illustrate results for density interpolation based on constant pressure and varying enthalpy from 0.5 [kJ/kg] up to 3999.5 [kJ/kg] with a step length of 0.5 [kJ/kg], for different N_p. Additionally, the accuracy of each interpolation is illustrated on figure (8). In general the maximum error is located in the vicinity of the saturation curve for saturated water and is very high, even for N_p=200. Here the density has very large negative gradients $\frac{\partial \rho}{\partial h} << 0$, specially for low pressures (p < 10 [bar]), which is very difficult to resolve in a bilinear scheme. By using a bilinear interpolation scheme, one avoids phenomena such as over and under shoot of the interpolated values, this is only true for higher order polynomial elements. In general we see a stable and fast interpolation scheme, with a standard deviation below 10^{-3} for $p > 50$ [bar] for all N_p, but if we need to resolve the steep gradients, many more elements would be needed. This would not affect the lookup time, only the initial mesh creation. The averaged interpolation time for one point is 0.115 [μ s] which is 10.65 times faster than IAPWS-97 and for the isobars in the vicinity of the critical pressure, we find an even higher performance, up to 33.4 times faster.

3.2.2. Bilinear 4 node combined with triangular 3 node elements

The second simulation setup is similar to the first, except that triangular linear elements are used in the vicinity of the saturation curve. The purpose of using triangular elements is to achieve a better resolution of the saturation curve, in spite of the fact that the triangular element is linear. In figure (12) and (13) the results for density interpolation are illustrated, based on constant

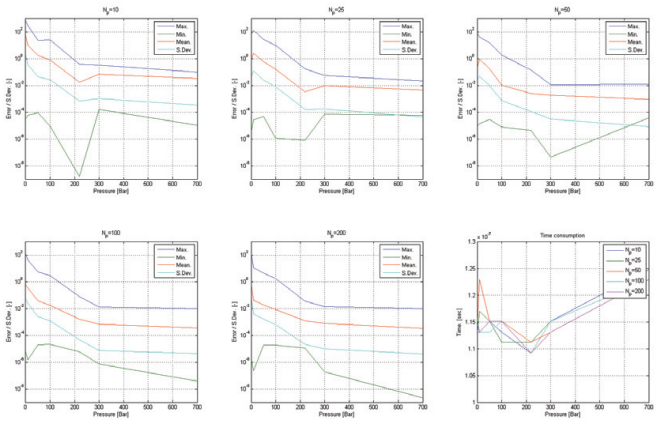

Figure 8: Bilinear interpolation: Relative errors and standard deviation for different resolution of the pure bi-linear grid (N_s).

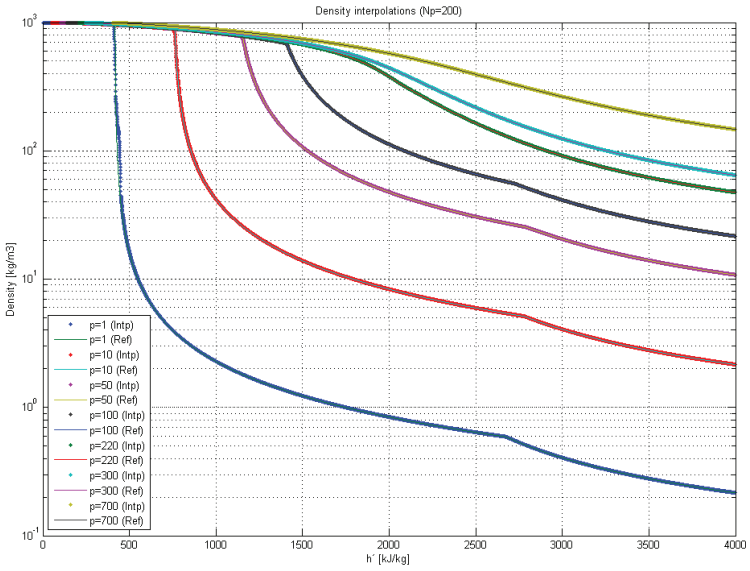

Figure 9: Bilinear interpolation: Density as function of Enthalpy for fixed pressure of 1.0 [bar]. N_p is varying from 10, 100 and 200.

pressure and varying enthalpy from 0.5 [kJ/kg] up to 3999.5 [kJ/kg] with a step length of 0.5 [kJ/kg], for different values of N_p. Additionally, the accuracy of

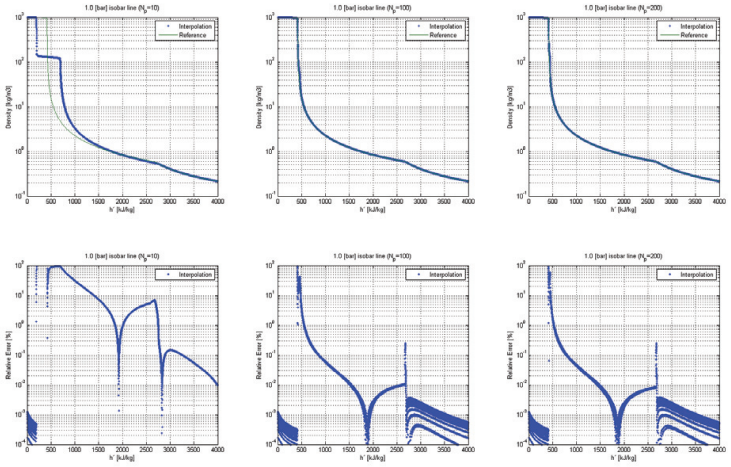

Figure 10: Bilinear interpolation: Density as function of Enthalpy for isobars varying from 1.0 to 700 [bar]. N_p=200.

each interpolation is illustrated in figure (11). In general the maximum error is also here located in the vicinity of the saturation line for saturated water and is very high, even for N_p=200. We observe a minor improvement in the standard deviation for pressures below the critical pressure compared to the case without triangular elements. The density is again found to be very difficult to resolve, even by linear triangular elements. By using a linear interpolation scheme, we avoid the over and under shoot of the interpolated value. This is only possible in higher order polynomial elements. In general we see a stable and fast interpolation scheme, with a standard deviation below 10^{-3} for all $p > 100$ [bar] and $N_p > 25$. The averaged interpolation time for one point is 0.1899 [μs] for the two-phase region and 0.1180 [μs] for the superheated region (R_5). This is 7.3 and 6.7 times faster, respectively, than the reference IAPWS-97. We have an increased time consumption since we use a lookup table, containing the start and end elements of each row of elements. This implementation involves a possible risk in running through a large table before the correct item is found for interpolation. In the pure bilinear interpolation, we can use the form described in equation (9).

3.2.3. Triangular 6 node elements

The last simulation setup uses iso-parametric triangular elements for all regions. Here we operate with five regions as in the previous setup. The purpose of using triangular iso-parametric elements is to achieve a better resolution of the saturation curve as well as increasing the accuracy all over the domain, in spite of the fact that the triangular element is only of second order. Figure (15) and (16) illustrate the results for density interpolation based on constant pressure

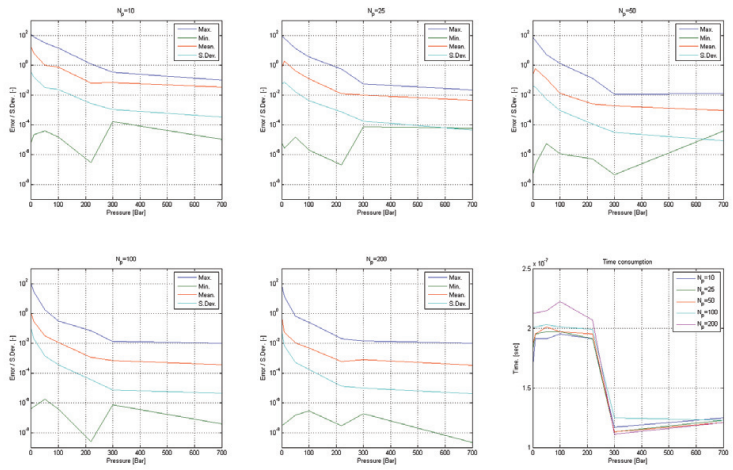

Figure 11: Relative errors and standard deviation for different resolution of the Bilinear grid with triangular elements in the vicinity of the saturation line.

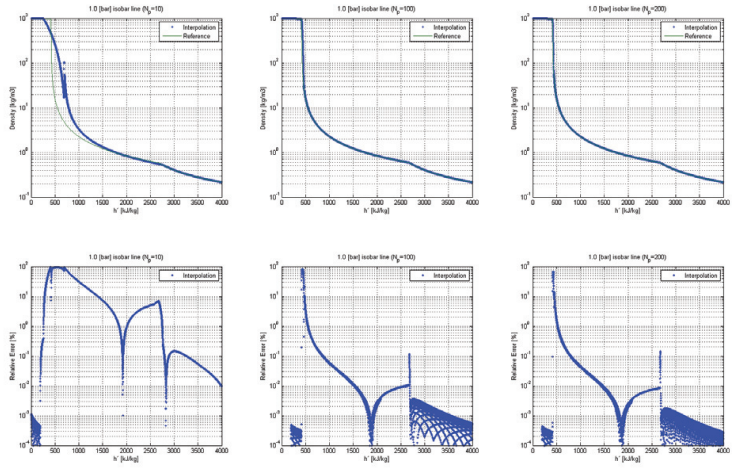

Figure 12: Bilinear and triangular elements: Density as function of Enthalpy for fixed pressure of 1.0 [bar]. N_p is varying from 10, 100 and 200.

and varying enthalpy from 0.5 [kJ/kg] up to 3999.5 [kJ/kg] with a step length of 0.5 [kJ/kg] for different N_p. Additionally, the accuracy of each interpolation is illustrated in figure (14). In general the maximum error is still considerable, up to 400 %, and is also here located in the vicinity of the saturation line

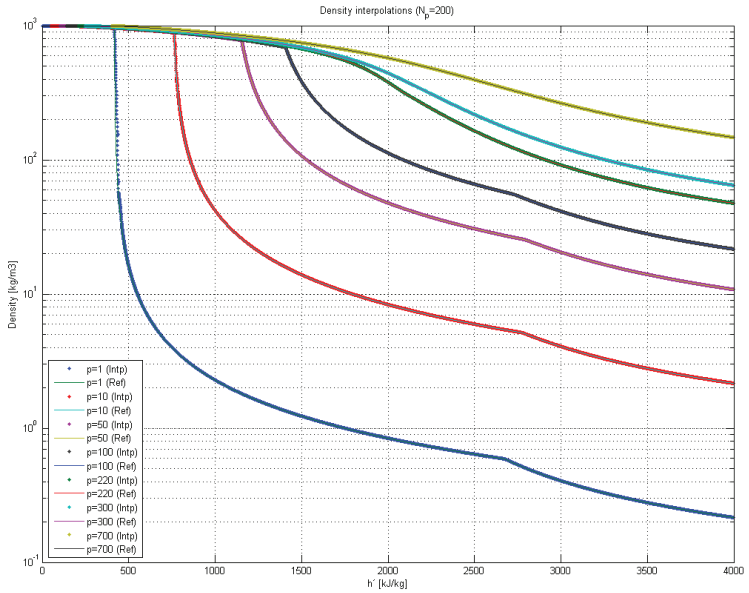

Figure 13: Bilinear and triangular elements: Density as function of Enthalpy for isobars varying from 1.0 to 700 [bar]. N_p=200.

for saturated water, even for N_p=200. However, it is significantly lower than observed in the priviously shown results. We find a significant improvement in the standard deviation for pressures below the critical pressure, compared to the case without triangular elements. Again the density trough for low pressure is still very difficult to resolve - even by an iso parametric triangular element. A second-order element is not necessarily monotonically increasing or decreasing, indicating we have a risk, that the interpolation can be influenced by a numerical over- or under-shoot. We see this clearly for $N_p = 10$ and, more surprisingly, also for $N_p = 200$. In the latter event we observe a sharp jump in function values inside the element nodes, for example, is $\rho_1 = 989$, $\rho_2 = 0.32$, $\rho_3 = 903$, $\rho_4 = 1.30$, $\rho_5 = 10.9$ and $\rho_6 = 974$. The interpolated value is $\rho_{Intp} = 0.18$, while the IAPWS-97 gives 8.19. All ρ values are measured in [kg/m^3]. Here we experience a huge relative error as a result of the inability of the second-order elements to dissolve the very large gradients, that we experience at the density trough for low pressure. The averaged interpolation time for the entire domain is 5.6925 [ms] which is 4.6 times slower than the original IAPSW-97 implementation. The increased time consumption is first of all due to the need to calculate the barycentric coordinates according to algorithm (40) to (42) for each point $P(x, y)$. Secondly, it is due to the lookup table we use, which contains start and end elements of each row of elements, due to a non-equidistantly mesh

in enthalpy, h.

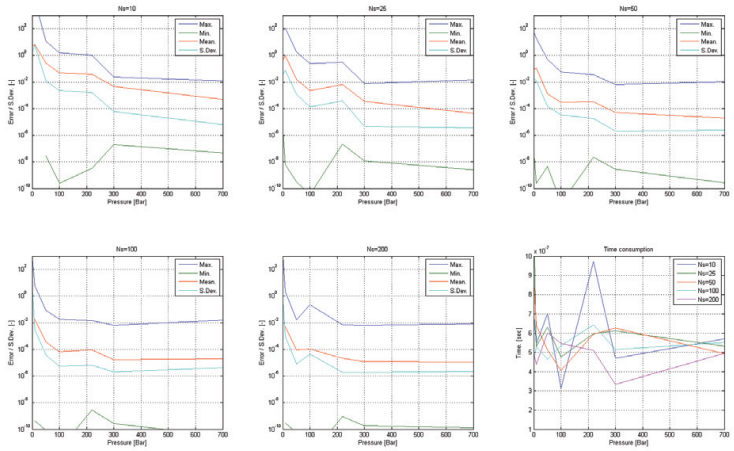

Figure 14: Relative errors and standard deviation for different resolution of the second order iso-parametric elements.

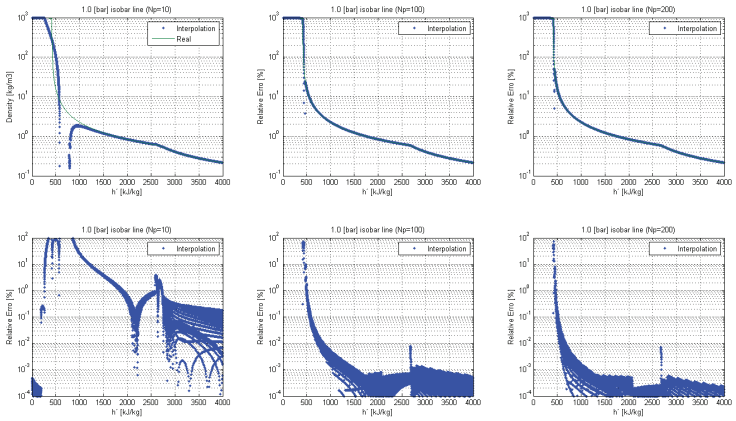

Figure 15: Iso-parametric elements: Density as function of Enthalpy for fixed pressure of 1.0 [bar]. N_p is varying from 10, 100 and 200.

4. Discussion

The benefits in using the iso-parametric elements are minimal in this case, since they are time consuming and not able to resolve the density trough at low

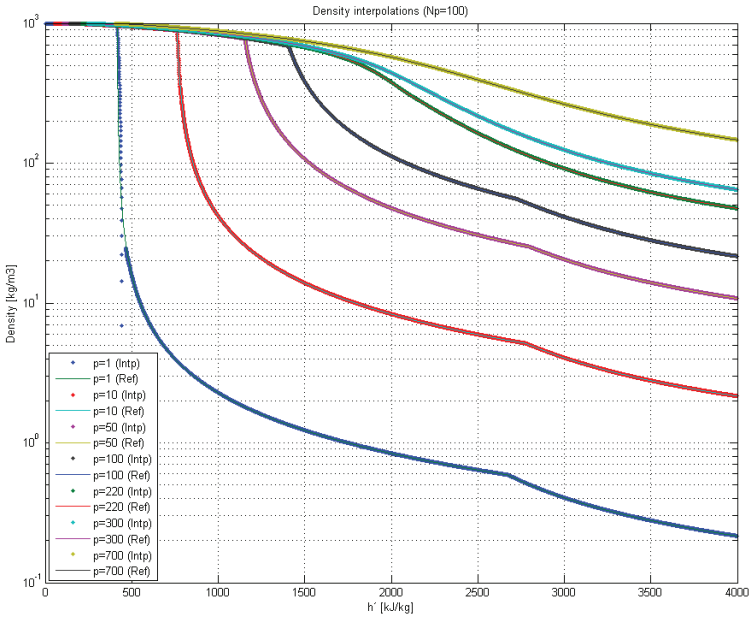

Figure 16: Iso-parametric elements: Density as function of Enthalpy for isobars varying from 1.0 to 700 [bar]. N_p=200.

pressures. We have chosen to interpolate the density, because this thermodynamic property contains very sharp gradients, especially for low pressure, which in this way uncovers an absolute worst case with respect to interpolation. Other state properties would yield significantly better results, such as heat capacity, entropy and temperature. For these reasons we recommend to use this element type in the scope of smoothing the thermodynamic properties, calculated in individual regions in the IAPWS-97 Industrial Standard. We observed also the possibility of inaccurate interpolation along the saturation curve for water at low pressure levels. One example was $N_p = 200$, $p = 1$ [bar] and $h = 578.75$ [kJ/kg]. In this iso parametric element there are large differences in the function values of the nodes, ranging from 989.83 [kg/m^3] down to 0.32 [kg/m^3] by an exponential decrease in density, meaning a second-order element is not suffcient to resolve the functional sequence of the element. If we use regions R_2 and R_3 with a higher minimum pressure ($p_m in$), the iso parametric element gives very high accuracy and reproduces the results with a maximum relative error below 0.5

When modeling a dynamic two-phase flow process, it is not evident what happens in practice to the density when passing the saturation line. The spatial location of the saturated liquid will not be well-defined but will vary over time

and space. Under normal circumstances, it is thus a well-known numerical trick to smoothe the crossing from the subcooled liquid to the two-phase mixture. This blurs the steep gradient, which will be an inherent outcome of using the interpolation scheme. If one uses an interpolation scheme with a suitably large number of pressure lines, a high degree of accuracy is assured in the interpolated state variable, because it will in reality vary over the extent of a control volume. In practice all necessary thermodynamic properties can be saved in each node in the interpolation table. A simple way to enhance the iso-parametric interpolation, is by modifying the surface function which is included in the interpolation element. If we introduce a contribution, which replaces the quadratic relation with a reciprocal relation to the variable, we get a better resolution of the density trough, as we see in the vicinity of saturation curve for water. However, this solution will give less accurate results for other quantities, which are better represented by the second-order relation with respect to variations in pressure or enthalpy. The challenge with the method is that the interpolation table is bulky. An example of $N_p = 200$ isobar lines with 17 state variables stored in each node generates a binary file of approximately 50 MB.

The method is based on the pre-defined range of the problem of interest and thereby the size and number of regions in the interpolation model. The used definition is not optimized and should be seen as one reasonable representation. The regions may be optimized to reach higher accuracy or lower computational time.

5. Conclusion

The paper presents the results of investigating three different methods of using interpolation based on a finite volume methodology to represent thermodynamic states of water / steam instead of the complete formulation defined by IAPWS-97. The results show that significantly reduced computation time may be observed, but also that there are challenges by using the suggested approach. One is that we find low accuracy of the results in parts of the calculation range, but also that even higher time consumption may be found by inappropriate selection of the elements. We recommend bilinear schemes for interpolating the water steam table of IAPWS-97. For pure bilinear interpolation we recommend at least $N_p = 200$ or higher, since no look up table is required in this case. Modern computers do not restrict the amount of data storage significantly, so in practice we do not have to take memory into consideration. The improvements in introducing the triangular elements are too insignificant to justify the more intensive implementation of such scheme, however, the results are more accurate and we can reduce some memory demands. However, in the two-phase region, we need a look up table, which can be time consuming for large grid arrangements. The iso parametric triangular elements cannot be recommended for the entire domain and especially, if the argument is to save CPU costs. Alternatively the iso parametric elements can with advantage be used when calculating first-order derivative of the thermodynamic properties. Thereby we ensure continuity in the first order derivative. If the iso parametric elements

should be used near the density trough, a more dedicated shape function should be implemented. In such case, we can reduce the number of elements drastically and the computational costs as well. However, the barycentric coordinates will be costly to compute. It will be a challenge to find reasons to use the iso-parametric elements.

References

[1] Muhlthaler G. Anwendung objektorientierter Simulationssprachen zur Modellierung von Kraftwerkskomponenten. Technische Universitt Hamburg: PhD thesis; 2000.

[2] Brereton DH. Approximate equations for the properties of dry steam from a generalization of callendar's equation. Int J heat and Fluid Flow, Glasgow College of Technology, UK 1983;(1).

[3] Butterlin A, Schiesser D, Steuer H. Usage of water & steam properties in computational intensive dynamic simulations. Siemens Energy, Power Generation 2008;(47).

[4] Müller W. Fast and accurate water and steam properties programs for two-phase flow calculations. Nuclear Engineering and Design 1994;51149:449–58.

[5] Xia G, Li D, Merkle CL. Consistent properties reconstruction on adaptive cartesian meshes for complex fluids computations. Journal of Computational Physics 2007;225(1):1175 –97.

[6] Lemmon EW, Huber ML. NIST Standard Reference Database 23; 4 ed. NIST National Institute of Standards and Technology; ????

[7] Zienkiewich OC, Taylor JL. The Finite Element Method; vol. 1. 4 ed.; London: McGraw-Hill; 1989.

P. Paper 3

Axel Ohrt Johansen, Brian Elmegaard

Homogeneous two-phase flow model of a vertical steam evaporator implemented in a fifth order Central WENO scheme for hyperbolic balance laws

Applied Thermal Engineering

Homogeneous two-phase flow model of a vertical steam evaporator implemented in a fifth order Central WENO scheme for hyperbolic balance laws

Axel Ohrt Johansen[a,b], Brian Elmegaard[b]

[a] *DONG Energy - Thermal Power, Kraftværksvej 53, Dk-7000, Fredericia, Denmark*
[b] *Technical University of Denmark, Nils Koppels Allé, Building 403, DK-2800 Kgs. Lyngby, Denmark*

Abstract

We develop a numerical model for the transient operation of a steam power plant boiler. The model is based on one-dimensional, compressible flow and a homogeneous two-phase model which is based on a two-layer thermo-hydraulic formulation for predominantly one-dimensional flows in a vertical, heated pipe element. The homogeneous model is based on the assumption of both hydraulic- and thermal equilibrium between the two fluid phases. The consequences and aspects are discussed in that context. The flow model consists of three hyperbolic fluid conservation equations, i.e., mass, momentum and energy balances. The pipe wall is modelled as a one-dimensional heat balance equation in the radial direction. The models can be reformulated in the four independent degrees of freedom pressure, p, enthalpy, h, velocity, u, and wall temperature, T_w. The constitutive relations for the thermodynamic properties are limited to water/steam and are given by the IAPWS 97 standard. Wall friction and heat transfer coefficients are formulated by commonly used methods. The two-layer model has been discussed and used for building a homogenious model for analysing the thermo hydraulic conditions in two phase flow.

The numerical method for solving the homogeneous fluid equations is presented. It is based on a fifth-order Central WENO (Weighted Essentially Non-Oscillatory) scheme with simplified weights functions. The model is able to describe the entire evaporation process from sub cooled water to super heated steam at the outlet. There is constructed a model of the evaporates string of Skærbæk Power Station Unit 3, which is modeled as a dynamic jump in in the feed water temperature, caused by a high pressure feed water heater cutout. This is becoming a natural instrument for achieving rapid load gradients in upper direction. Calculation results reveal strong temperature fluctuations in the evaporator, which can initiate fatigue.

Keywords: Two phase flow, Vertical evaporator, dynamic load, Central

Email address: aoj@addedvalues.dk (Axel Ohrt Johansen)

Operating flexibility is therefore of great importance for the business economics of the plants and also a prerequisite for a stable electrical system. No matter how strong focus is put on this operational flexibility, power plants, however, will always be subject to technical limitations - e.g. boiler dynamics, coal mill dynamics, flame stability and material constraints. The ability of the power plants to stabilize the electrical system can be increased substantially, if we get a better understanding of processes that occur in the evaporation process in the boiler. The evaporator transfers the heat from the flame in the furnace to the evaporating water/steam in the water wall. The state change from liquid water to superheated steam in a once-through process involves large variation in flow and thermodyanmic conditions. Numerous work on evaporators with special focus on the dynamic control features of the power plant boilers is available in the literature. However, less literature is available on dynamic modelling of the evaporation process in the power plant boiler and the consequent load limits. In 1985 Harald Griem, [1] covered the subject and both KEMA [2] and Siemens have performed considerable experimental work that is considered company secrets. Other authors who have dealt with the experimental topic with special focus on internally rifled boiler tubes are [3], [4], [5] and [6]. They have developed consistent algebraic function terms for frictional pressure drop and heat transfer in internally rifled boiler tubes. J. Pan [7] presents a thermo-hydraulic analysis of an ultra supercritical boiler at full load, but does not cover part load conditions.

The present work covers modeling the complete evaporation process at all loads from initial heating to full steam production. The model has been developed with focus on numerical accuracy and stability. The result of this analysis has been an implementation of a WENO solver that handles the system of partial differential-algebraic equation robustly. The WENO solver code is implemented in c++ under MicroSoft Visual Studio 2008, and the solver is validated in [8]. The water/steam table is based on a fast bilinear interpolation scheme which uses the lookup table for improved calculation speed. It is based on the IAPWS97 steam property formulation, which is implemented in FORTRAN 90. This procedure is described in [8].

1. Evaporation in steam power boilers

A power plant boiler is a heat exchanger which includes several units, economizer, evaporator, superheaters, reheaters and air preheater. In the evaporator part, the fuel is burned on the furnace side and the combustion products is a hot gas exchanging radiant heat to the water on the other side of the heat exchanger. The boiler is traditionally built as a tower, inside the hot gas is produced and the walls of the boiler are made of pipes welded together in which the water flows. Frequent start/stop of ultra super critical (USC) plants, which in fact is what is requested, is unfortunately not a realistic scenario, due to the

costs related to start/stop. A more promising track is thus the operation of the thermal power plant at lowest possible load during those hours where the generation from thermal capacity is in fact not requested and furthermore, can the load following capability of the plant be improved or at least retained at low load ("micro load"). The answer to this problem is among other to be found in the water walls surrounding the furnace, these tubes (panel walls), as the water walls are composed of, must at all times be sufficiently cooled with feed water to avoid tube material damage.

The heat flux is approximately 200-400 kW/m^2 in the lower sections of the evaporator and appears as radiation. At the upper part of the tower, the radiation is still dominating, but it is also necessary to take convective heat transfer into account. At the bottom section, where the radiation from gas to the pipe wall is dominating, the heat transfer on the outside is so massive that it is not restriction the heat transfer. Instead, the limit is set by the heat transfer rate from the pipe-wall to the water inside the pipe.

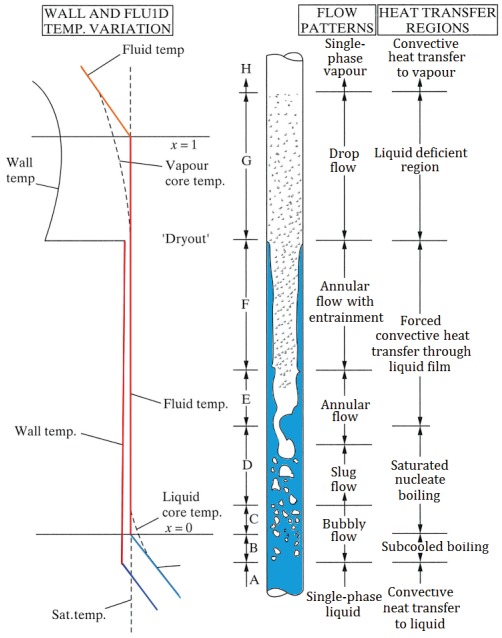

Figure 1: Flow Regimes in vertical pipe.

1.1. Scope of study

Danish central power plants are all once-through boilers of the Benson type. The water walls are typical constructed of some 200 tubes connected in parallel, running from hopper to furnace outlet with an inclination angle of approx 15 degrees. Each of these tubes must be at any instant be sufficiently cooled

at any location along the tube. Normally this corresponds to a tube mass flux rate of 700-800 [kg/s/m^2] at minimum stabel generation and 2000-2500 [kg/s/m^2] at rated capacity. If cooling fails for a certain time, the tube in question will be damaged (material creep and cyclic hoop stress) and eventually burst. Consequently, each power plant has a minimum water fall flow rate which must be respected in order to avoid trip of the plant - however, because there is presumably a 'however'. The plants were designed during the 1980-1990'ties when the extreme low load was not an issue at all and this leaves the belief that further low load optimisation is possible. One of the easier instruments to rapidly load control, is about to cut the high-pressure preheater, whereby the amount of steam through the turbine train is increased, and thus the delivered electricity production. This happens at the cost of the block efficiency and a considerable stress on the evaporator in the form of temperature fluctuations. This can be compensated for by controlling the feed water flow quickly. In this paper, we examine the consequences of only lowering the feed water temperature over 4 seconds from 270.7 [^{o}C] to 220 [^{o}C] at part load. The purpose of this study is to demonstrate that it is possible to develop a robust numerical model, which is able to dissolve the excessive dynamics that occur in connection with an evaporation process. Based on other hard-cored problems in power plants that have been solved with succes, it is our belief that a through understanding of the thermo-hydraulic problems - paired with our existing knowledge on material creep and fatigue (FEM calculations), furnace load (CFD calculations) and more intelligent furnace control in the feed water, fuel and combustion control systems, restricted by an intelligent distributed control system (DCS) - will further improve the low or micro load properties of a plant and eventually lead to enhanced low load operation. This again may allow for further wind penetration. All aspects related to this optimisation, except for the through comprehension of the thermo-hydraulics of the water walls, have been throughly studied by DONG Energy - Thermal Power / DTU thermal Energy Systems during the past decade.

2. Methods

In this section we describe the dominating phenomena in a tube of a power plant boiler. We outline a two layer model for predominantly one-dimensional flows in a vertical pipe element. The model uses a non-equilibrium approach and consists of two continuity equations, two momentum equations and two energy equations. The model is further simplified to a homogeneous formulation.

2.1. Non-Thermal Equilibrium Situations

Some degree of thermal non-equilibrium arises in practically all situations and especially in dynamic situations, thermal non-equilibrium will be present to make heat and mass transfer take place. Thermodynamic equilibrium does exist between a liquid and its vapour separated by a flat interface e.g., water and steam in a closed vessel. But, in the classical case of stationary vapour bubble in

large volume of liquid, the vapour and liquid temperatures are equal. However, due to the effect of surface tension, even in this equilibrium situation, the system temperature must be slightly above the saturation temperature corresponding to the pressure of the liquid due to [9]. It is only in the case of the flat interface, that both phases can be exactly at saturation conditions.

In the equally classical case of nucleate boiling (NB) there must be a certain superheat of the liquid near the wall for a bubble to nucleate and grow. In the case of strong temperature gradients near the wall, one may have subcooled nucleate boiling (SNB) where bubbles nucleate, grow and even detach from the wall and survive for a while in the bulk of subcooled liquid.

In annular flow (forced convection) there is a temperature gradient in the liquid film on the wall, since the liquid layer immediately adjacent to the wall is at the wall temperature, while the interface is near saturation. This temperature gradient drives a heat flux to the interface where evaporation takes place. In dispersed flow film boiling regime, a two-stage heat transfer phenomenon exists, from the wall to the vapour and from the vapour to the liquid droplets, where temperature gradients are the driving mechanisms for these heat exchange processes. The vapour gets superheated from the hot wall, while there is still water in the form of droplets in the flow channel, [9].

Thermal non-equilibrium is present in flashing load situations, i.e. when changes in the evaporator pipes result in superheating of the liquid and thereby production of vapour. An example of absence of thermal equilibrium for this case is a rapid depressurization of a liquid system. In this case the pressure may drop well below the saturation pressure that corresponds to the temperature of the liquid. The causes of this pressure undershoot is clear, it takes time for bubbles to nucleate and grow by transferring heat from the surrounding fluid. Consequently there is a departure from equilibrium, i.e. the liquid tends to remain at its original temperature, whereas the vapour that is being generated is close to saturation. Similarly, a subcooled discharge through a leakage or an orifice may expose fluid particles to a rapid change in pressure. If the outside pressure is below the saturation pressure corresponding to the temperature of the liquid, the fluid flashes in a process similar to that of a rapid depressurization, which results in a similar departure from equilibrium. Flashing is of importance for critical flow situations that affect the safety of various processes in steam power boilers.

2.2. Two-fluid model of power plant boiler evaporation

The above considerations leads to formulation of a model of the evaporation which includes the two phases of the fluid as separate parts in each control volume.

2.2.1. Conservation laws

In a two-fluid model, the field equations are expressed in six conservation equations consisting of mass, momentum and energy balances for each phase. Since these field equations are obtained from an appropriate averaging of local

instantaneous balance equations, the phasic interaction term appears in each of the averaged balance equations. These terms represent the mass, momentum and energy transfer through the interface between the two phases. These terms determine the rate of phase changes and the degree of mechanical and thermal non-equilibrium between the phases, thus they are essentially closure relations for the model system. A pipe channel is considered as a uniform channel with constant cross sectional area, A, and no internal heat production. The model resolves stratified flow transport of fluid between the layers, caused by condensation or evaporation. The field equations take the form as formulated in [10], [11] and [12], where we here describe the source/sink terms in more detail.

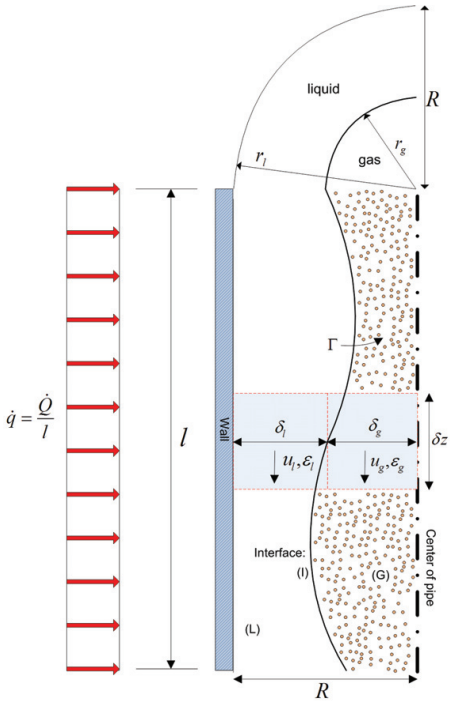

Figure 2: Illustration of the two control volumes in the two-phase fluid. The fluid is flowing in a cylindrical channel with uniform radius R.

2.2.2. Conservation of mass

Conservation of mass for the gas and liquid, respectively, is formulated by:

$$\frac{\partial\left(\epsilon_g \rho_g\right)}{\partial t} + \frac{\partial\left(\epsilon_g \rho_g u_g\right)}{\partial z} = \Gamma_g \tag{1}$$

$$\frac{\partial\left(\epsilon_l \rho_l\right)}{\partial t} + \frac{\partial\left(\epsilon_l \rho_l u_l\right)}{\partial z} = \Gamma_l \tag{2}$$

Here the independent variables t represents the time in [s] and z is the spatial coordinate referring to the flow direction of the fluid given in [m]. The rates of the interfacial mass transport processes caused by evaporation are signified by Γ_k, defined here as the rate of phase change per unit mixture volume. For the gas phase it is positive for evaporation, i.e., $\Gamma_g > 0$. In the equations, ϵ_k stands for the phase volume fractions and ρ_k and u_k are the density and velocity for the k'th ($k \in \{g, l\}$) phase, respectively. For an adiabatic model, the rate of phase change (Γ_k) would be zero. The volume fraction of the fluid can be described as the sum of a continuous liquid phase (ϵ_l) and a continuous gas phase (ϵ_g):

$$\epsilon_l + \epsilon_g = 1 \tag{3}$$

and the rate of phase change can be expressed by

$$\Gamma_l + \Gamma_g = 0 \tag{4}$$

2.2.3. Conservation of momentum

The formulation of the momentum equations is derived on the basis of Newton's 2^{nd} law for each layer in the control volume. The momentum transfer terms have to balance the forces acting on the fluid layers. The momentum balance is derived for each field (gas and liquid phase). The interfacial velocity is given as u_i and is acting parallelly to the pipe main axis. The interfacial force along the interface I is represented by F_i per unit mixture volume. Interfacial drag and friction both contribute to this force. The forces are orientated positive in the direction of the pipe z-axis. The wall friction force is represented by $F_{w,k}$ for the fluids belonging to the wall measured per unit mixture volume. The parameter F_{vm} is the virtual mass force [11] and occurs only when one of the phases accelerates with respect to the other phase. It is caused by the fact that the motion of the accelerating phase results in acceleration of the other phase as well. $F_{g,k}$ are gravitational forces.

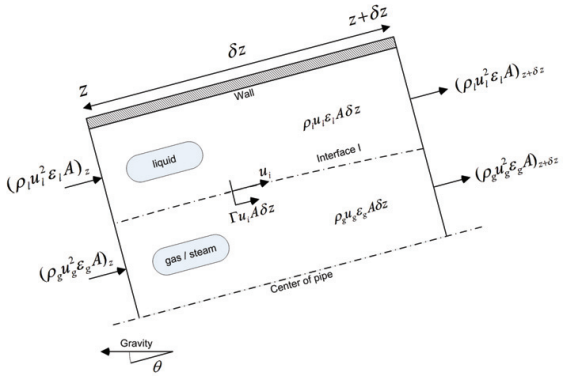

Figure 3: Momentum transfer terms for the two fields on a slice of a pipe-element.

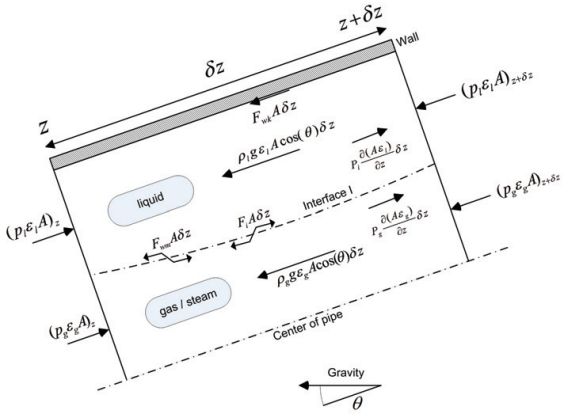

Figure 4: Forces acting on the two fields on a slice of a pipe-element.

$$\frac{\partial\left(\epsilon_g \rho_g u_g\right)}{\partial t} + \frac{\partial\left(\epsilon_g \rho_g u_g^2 + \epsilon_g p_g\right)}{\partial z} = -p_i \frac{\partial \epsilon_g}{\partial z} - F_{w,g} - F_i - F_{g,g} + \Gamma_g u_i + F_{vm} + F_{s,g} \tag{5}$$

$$\frac{\partial\left(\epsilon_l \rho_l u_l\right)}{\partial t} + \frac{\partial\left(\epsilon_l \rho_l u_l^2 + \epsilon_l p_l\right)}{\partial z} = -p_i \frac{\partial \epsilon_l}{\partial z} - F_{w,l} + F_i - F_{g,l} + \Gamma_l u_i - F_{vm} + F_{s,l} \tag{6}$$

The pressure for the k'th fluid is given by p_k and the interfacial pressure is given by: $p_i = \epsilon_g p_g + \epsilon_l p_l$. A simple and widely used choice for the interfacial velocity is u_i=$(u_g + u_l)/2$ given by [10], but a more accurate estimate is given by [12] as:

$$u_i = \frac{\epsilon_g \rho_g u_g + \epsilon_l \rho_l u_l}{\epsilon_g \rho_g + \epsilon_l \rho_l} \tag{7}$$

The first term on the *left hand side* (LHS) of the momentum equations (5) and (6) is the dynamic rate of creation of momentum, the second term is responsible for the axial convection of momentum. On the *right hand side* (RHS) we have the pressure force, the rate of momentum gained by wall shear stresses, the rate of momentum gained by interfacial drag along the interface (I) and the gravitational force acting on the fluid. All the forces are expressed per unit volume. Finally the two last source/sink terms denote the momentum contribution, caused by the phase changes in the fluid and the virtual mass force. In principle, we have excluded the contribution from the shear stresses in the two-layer momentum equations, under the assumption that the fluid is non-Newtonian. The contribution from the shear stress could be $F_{s,k}$=$\frac{\partial \tau_{f,k}}{\partial z}$, where $\tau_{f,k}$ represents the shear stress generated in a gradient field of the fluid velocity. This shear stress will act as artificial diffusion in the area between subcooled liquid and two-phase area - an area which basically has a singularity in the density gradient with respect to z.

2.2.4. Conservation of energy

To derive the energy conservation equations for the flow fields, we apply the first law of thermodynamics to the liquid and gas layer control volumes. The temperatures T_l and T_g are the bulk liquid and gas temperature, T_i is the temperature at the interface layer, surrounding the gas phase, which is related to a physical length scale a_i expressing the interfacial area per unit volume. The mass transfer caused by phase changes is represented along the interface by Γ_g. It is assumed that no heat generation occurs within the control volume and that axial heat diffusion ($E_{d,k}$) is negligible in the convection dominated flow of forced evaporation (or condensation). Other parameters are as follows: $q''_{i,l}$ and $q''_{i,g}$ are the heat fluxes between liquid and gas phases and the interphases, measured in [W/m^2], controlled by the temperature difference in-between the two layers.

The total enthalpy of flow region k is defined as the sum of the intrinsic enthalpy, the potential energy, and the axial kinetic energy. In the derivation the total specific energy E_{tk} and the total specific convected energy E_k, we define the below terms:

$$E_{tk} = \widetilde{h}_k + \frac{u_k^2}{2} - gz\cos(\theta) \tag{8}$$

and

$$E_k = h_k + \frac{u_k^2}{2} - gz\cos(\theta) \tag{9}$$

where $\widetilde{h}_k$ is the specific internal energy and h_k is the specific enthalpy, related by:

$$\widetilde{h}_k = h_k - p_k/\rho_k \tag{10}$$

The inclusion of $gz\cos(\theta)$ in the definition of E_{tk} and E_k is for generality. Often we deal with the difference of total energy along the interface $E_{ti} - E_i$, whereby the $gz\cos(\theta)$ terms cancel out.

The heat flow across the wall is defined positive for $T_w > T_l$ or $T_w > T_g$. Additionally the heat transfer across the interface is defined positive and is positive as long as the driving temperature across the interface is going from high to low temperature. The mass transfer across the interface due to evaporation is represented by $\Gamma_g > 0$ or condensation $\Gamma_l > 0$. The work terms highlight the pressure forces from the neighbour layer. The interfacial drag (friction force) as well as the virtual mass force along the interface perform work along the interface cross section, too. Outflow of energy is defined positive. The two-phase energy conservation equation can now be expressed in [W/m^3] as:

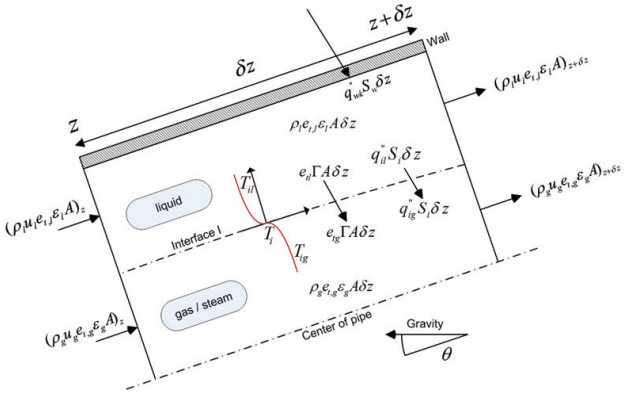

Figure 5: Energy transfer and heat flow on a slice of a pipe-element.

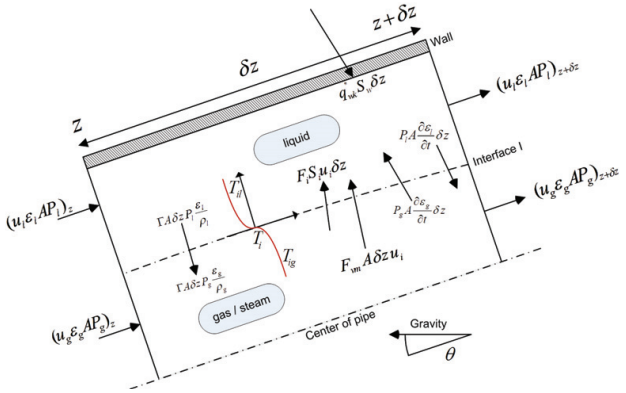

Figure 6: Work terms on a slice of a pipe-element.

$$\frac{\partial\left(\epsilon_g \rho_g h_g\right)}{\partial t}+\frac{\partial\left(\epsilon_g \rho_g h_g u_g\right)}{\partial z}=\epsilon_g\left(\frac{\partial p_g}{\partial t}+\frac{\partial\left(p_g u_g\right)}{\partial z}\right)+\Gamma_g h_{i,g}+\epsilon_g a_w q_{w,g}^{''} \quad (11)$$
$$-a_i q_{i,g}^{''}+F_i u_i-F_{vm} u_i+E_{d,g}$$

$$\frac{\partial\left(\epsilon_l \rho_l h_l\right)}{\partial t}+\frac{\partial\left(\epsilon_l \rho_l h_l u_l\right)}{\partial z}=\epsilon_l\left(\frac{\partial p_l}{\partial t}+\frac{\partial\left(p_l u_l\right)}{\partial z}\right)+\Gamma_l h_{i,l}+\epsilon_g a_w q_{w,l}^{''} \quad (12)$$
$$+a_i q_{i,l}^{''}-F_i u_i+F_{vm} u_i+E_{d,l}$$

The specific enthalpy h_k for the k'th fluid is given by (10) and (9). The dynamic transport term is described by the first part on the LHS in (11) and (12) and is expressing the rate of increase in the specific enthalpy per measured unit of

per volume. The second term is the axial transport of specific enthalpy. On the RHS the first term expresses the work done by the pressure forces at the interface, the second term is the energy transport due to mass transfer caused by evaporation or condensation. The third term represents the rate of heat flux across the wall $\dot{q}_e = q''_{w,g} + q''_{w,l}$ and is defined positive for $T_w > T_l$ and $T_w > T_g$, respectively, see figure (7). The fourth term is the heat flow across the interface and is positive for $T_l > T_g$ due to conduction in-between the two layers. The fifth and six terms are accounting for the friction work done at the interface and the work done by the virtual mass force along the intercase due to the acceleration of one phase with respect to the other phase. The last term is the heat diffusion ($E_{d,k}$), which is assumed negligible in the convection dominated flow. Note that $1/a_i$ denotes the length scale at the interface and a_i has the physical meaning of the interfacial area per unit volume. In a similar manner, a_w is expressing the heated wall surface area per unit volume.

2.2.5. Constitutive relations

The wall friction force acting on the liquid element is $F_{w,k}$. It is the force acting on the fluid in contact with the wall by the length scale a_w, i.e., $F_{w,l}$ for the liquid layer and $F_{w,g}$ for the gas phase. The wall friction force is given by (13):

$$F_{w,k} = \frac{\tau_{w,k}}{a_w} \tag{13}$$

where $\tau_{w,k}$ is the wall shear stress, where subscript k denotes the phase in contact with the wall (k=l or g). The wall shear stress is typically expressed as:

$$\tau_{wk} = \frac{1}{2} f_{wk} \rho_k \left| u_k \right| u_k, \;\; k = l \vee g \tag{14}$$

where the f_{wk} denotes the wall friction factor, which can be determined by i.e. the Colebrook and White formulation. The shear stress between the wall and the fluid is described by τ_{wk}, where the subscript k denotes the phase in contact with the wall, i.e., u_g for the gas and u_l for the liquid. The term F_i represents the interface force per unit mixture volume and is positive for $u_g > u_l$. The parameter F_{vm} is the virtual mass force and occurs only when one of the phases accelerates with respect to the other phase. A simple and widely used expression for one-dimensional separated flow is given by [13] and is:

$$F_{vm} = -C_{vm} \cdot \left(\frac{\partial u_g}{\partial t} + u_g \frac{\partial u_g}{\partial z} - \frac{\partial u_l}{\partial t} - u_l \frac{\partial u_l}{\partial z} \right) \tag{15}$$

where $C_{vm} = C \cdot \epsilon_g \cdot \epsilon_l \cdot \bar{\rho}$ and C$\approx$1. In terms of magnitude F_{vm} is significant only if the gas phase is dispersed. The exact form of the virtual mass force term is only known from theory for some simple and idealized conditions, see [14]. Similarly the interfacial shear stress between the phases can be formulated as:

$$\tau_i = \frac{1}{2} f_i \rho_i \left| u_g - u_l \right| (u_g - u_l) \tag{16}$$

where $\rho_i = \rho_g \cdot \epsilon_g + \rho_l \cdot \epsilon_l$ is expressing the density of the mixing fluid at the interface (I). Correspondingly the friction factor, $f_i = f_g \cdot \epsilon_g + f_l \cdot \epsilon_l$, is given as an averaged value of the respective friction factors of pure liquid and gas.

2.2.6. Jump Conditions

The interfacial heat flux and the mass exchange rate Γ_k across the interface section are linked through the following jump condition at the interface, where any contribution from kinetic energy is ignored:

$$\left(\Gamma_g h_{i,g} - a_i q_{i,g}^{''}\right) + \left(\Gamma_l h_{i,l} + a_i q_{i,l}^{''}\right) = 0 \tag{17}$$

The thermal jump appears when the fluid is entering the two phase region and the following assumptions are made: The thermal hydraulic conditions along the interface are saturated fluids, hence we may have a simple relationship between mass transfer and latent heat of evaporation h_{lg} at the interface formulated by:

$$\Gamma_g \cdot h_{lg} = a_i \left(q_{i,g}^{''} - q_{i,l}^{''}\right) \tag{18}$$

If we consider a control volume enclosing the interface and having an infinitisimal thickness, (18) constitutes an energy balance of this control volume. In the presence of superheated steam and subcooled liquid, there will be no heat transfer initiated by convective transport of evaporated fluid by Γ_l. Instead there will be an intense heat transfer created by the temperature gradient in-between the two layers. Here $q_{i,g}^{''}$ and $q_{i,l}^{''}$ will be responsible for the heat transfer from the subcooled liquid to the interface, where a fraction of the heat flux penetrates into the liquid and is used to heat up the gas. The remaining fraction produces saturated steam at the interface.

2.3. Homogeneous model

In this section we derive a homogeneous dynamic flow model based on the two layer flow model outlined in section (2). The homogeneous model is based on the assumption of both hydraulic and thermal equilibrium and the consequences and aspects of this will be discussed in that context. The assumption of thermal equilibrium is very useful in the treatment of the governing equations for two-phase flow. For the case of boiling water and steam we assume that both phases are at the saturation temperature $T^s(p)$ corresponding to the local pressure p. Based on that assumption it is straightforward to calculate a local equilibrium quality x_e, which is a very useful, but not necessarily a real quantity, compared to the true flow quality based on the ratio of the gas to total flow rates:

$$\begin{aligned} x &= \frac{\dot{m}_g}{\dot{m}_g + \dot{m}_l} \\ &= \frac{\rho_g u_g \epsilon_g A}{\rho_g u_g \epsilon_g A + \rho_l u_l \epsilon_l A} \end{aligned} \tag{19}$$

The local equilibrium quality, x_e, can be calculated by (20), under the assumption that the saturation enthalpies correspond to the local pressure, h_l=$h_l^s(p)$ and h_g=$h_g^s(p)$:

$$x_e = \frac{h - h_l^s}{h_g - h_l} \tag{20}$$

For a two-layer fluid, the mixture density $\bar{\rho}$ and the mass flux G are defined as:

$$\bar{\rho} = \rho_g \cdot \epsilon_g + \rho_l \cdot \epsilon_l \tag{21}$$

and

$$\begin{aligned} G &= \bar{\rho}\bar{u} \\ &= G(1 - \dot{x}) + G\dot{x} \\ &= \rho_l u_l \epsilon_l + \rho_g u_g \epsilon_g \end{aligned} \tag{22}$$

The slip ratio ($S = \frac{u_g}{u_l}$) between the two phases can be expressed by the void fractions and thereby lead to the below expression for the void fraction as function of S:

$$\epsilon_g = \left[1 + \frac{\rho_g}{\rho_f}\frac{1-x}{x}S\right]^{-1} \tag{23}$$

In homogeneous two-phase flow, there is no slip between the phases ($S = 1$), which leads to:

$$\bar{\rho} = \left[\frac{x}{\rho_g^s} + \frac{1-x}{\rho_l^s}\right]^{-1} \tag{24}$$

The interfacial mass transfer model assumes that total mass transfer is partitioned along the vapour/liquid interface (i).

2.3.1. Conservation of mass

The mass conservation equation is derived for a pipe element. The mass conversation equation for the total liquid and gas volume fractions are obtained by summing (1) and (2):

$$\frac{\partial}{\partial t}\left(\epsilon_l \rho_l\right) + \frac{\partial}{\partial t}\left(\epsilon_g \rho_g\right) + \frac{\partial}{\partial z}\left(\epsilon_l \rho_l u_l\right) + \frac{\partial}{\partial z}\left(\epsilon_g \rho_g u_g\right) = 0 \tag{25}$$

which can be recast as:

$$\frac{\partial}{\partial t}\left(\bar{\rho}\right) + \frac{\partial}{\partial z}\left(G\right) = 0 \tag{26}$$

where the mixture density $\bar{\rho}$=$f(\bar{p}, \bar{h})$ for a homogeneous fluid.

2.3.2. Conservation of Momentum

The mixture momentum equation can be obtained by adding (5) and (6). As expected, all the interfacial force terms cancel out, leaving:

$$\frac{\partial}{\partial t}(G) + \frac{\partial}{\partial z}\left(\frac{G^2}{\rho'}\right) = -\frac{\partial \bar{p}}{\partial z} - F_w - F_s - \bar{\rho} g \cos\theta \tag{27}$$

where $\bar{\rho}$ is given by (21) and $\bar{p} = p_l \epsilon_l + p_g \epsilon_g$ and ρ' is named the momentum density and is defined as

$$\rho' = \left(\frac{(1-\dot{x})^2}{\rho_l \epsilon_l} + \frac{\dot{x}^2}{\rho_g \epsilon_g}\right)^{-1} \tag{28}$$

For a homogeneous flow, one assumes $u = u_g = u_l$, which leads to $\bar{\rho} = \rho'$. Hence we have:

$$\frac{\partial}{\partial t}(G) + \frac{\partial}{\partial z}\left(\frac{G^2}{\bar{\rho}}\right) = -\frac{\partial \bar{p}}{\partial z} - \frac{S_w}{A}\tau_w - F_s - \bar{\rho} g A \cos\theta \tag{29}$$

where τ_w is given by (31) and F_s via τ_f is a calibration term, due to axial shear stresses, modelled by for example by the Van Driest mixing length theory, which here is assumed proportional to a diffusion term, see Kinney et al. [15] and Gill et all ([16],[17]), where measurements shows that the logarithmic law for an isotherm two phase flow follows the mixing length theory with a mixing length scale less than observed for a single phase fluid. Normally a homogeneous two-phase flow is assumed to be non-Newtonian, which means that the eddy viscosity is not proportional to the second derivative of the fluid velocity with respect to space. Nevertheless we introduce this term as a way to avoid heavy pressure oscillations, initiated by the very high density gradients in the spatial direction which occurs due to the evaporation of water. This eddy viscosity is only introduced in the transition area from liquid water to the two phase regime ($x \approx 0$).

2.3.3. Closure laws

The axial shear stress is modelled by for example the Van Driest mixing length theory:

$$\begin{aligned} \tau_f &= -\frac{\partial}{\partial z}\left(\rho \bar{u'v'}\right) \\ &\approx l^{\,2} \bar{\rho} \frac{\partial u^2}{\partial z^2} \end{aligned} \tag{30}$$

where u' og v' are the velocity components due to turbulent fluctuation. The corresponding wall shear stress is given by

$$\begin{aligned} \tau_w &= f_w \bar{\rho} \frac{u \cdot |u|}{2} \\ &= f_w \frac{G \cdot |G|}{2\bar{\rho}} \end{aligned} \tag{31}$$

The term f_w is a dimensionless coefficient based on the Darcy friction factor. It can be found from a Moody diagram or more precisely by solving the Colebrook equation:

$$f_w : \begin{cases} \frac{1}{\sqrt{f_w}} = -2\log_{10}\left(\frac{k}{3.7\ d_i} + \frac{2.51}{\mathrm{Re}\ \sqrt{f_w}}\right) & \text{for } Re > 4000 \\ f_w = \frac{64}{\mathrm{Re}} & \text{for } Re \leq 2000 \end{cases} \tag{32}$$

where k is the pipe inner roughness thickness, measured in meter and the Reynolds number, Re=$\frac{d_i u_i}{\mu_i}$. In the two-phase region the friction factor is adjusted according to a two-phase multiplier formulated by ([18]). In that case f_w is based on fluid properties for saturated liquid. The model that is based on [18] calculates the two phase multiplier as:

$$\phi^2 = 1 + B \cdot x \cdot \left(\frac{\rho_l}{\rho_f} - 1\right) \tag{33}$$

Where the coefficient B is:

$$B = 1.58 - 0.47\frac{p}{p_c} - 0.11 \cdot \left(\frac{p}{p_c}\right)^2 \tag{34}$$

Note that the critical pressure (p_c) is 221.2 [bar] for water/steam. If $x \geq 0.9$ B is adjusted linearly as $B = B - (B-1)\cdot(10\cdot x - 9)$ to obtain continuity between the two-phase fluid and the steam phase.

2.3.4. Conservation of Energy

The mixture energy equation is obtained by adding (11) and (12), where conservation of energy across the interface means that all the interfacial terms cancel out, hence

$$\begin{aligned} \frac{\partial}{\partial t}\left(\epsilon_l \rho_l E_{tl} + \epsilon_g \rho_g E_{tg}\right) + \frac{\partial}{\partial z}\left(\epsilon_l \rho_l E_{tl} u_l + \epsilon_g \rho_g E_{tg} u_g\right) = \\ + a_w \dot{q}_e + \frac{\partial}{\partial z}\left(u_l \epsilon_l p_l + u_g \epsilon_g p_g\right) + E_d \end{aligned} \tag{35}$$

The heat flux $\dot{q}_e$ is illustrated on figure (7). By using (8) and neglecting the last term due to potential energy, we have

$$\frac{\partial}{\partial t}\left(\bar{\rho}h + \frac{1}{2\rho'}G^2 - \bar{p}\right) + \frac{\partial}{\partial z}\left(G\bar{h} + \frac{1}{2\rho'^2}G^3\right) = a_w \dot{q}_e - Ggcos(\theta) + E_d \tag{36}$$

where $\bar{\rho} = \rho_l \epsilon_l + \rho_g \epsilon_g$, ρ' is given by (28). The heat diffusion can be included into the energy equation and the thermal diffusivity of the fluid can be estimated by the fluid properties. It is a measure of the diffusion coefficient. The mixture

pressure is given by $\bar{p} = p_l\epsilon_l + p_g\epsilon_g$. ρ'' is named the second order momentum density and is defined as

$$\rho'' = \left[\frac{(1-\dot{x})^3}{(\rho_l\epsilon_l)^2} + \frac{\dot{x}^3}{(\rho_g\epsilon_g)^2}\right]^{-1} \tag{37}$$

Both h and $\bar{h}$ appear in (36), where h is referring to a frozen flow field picture and $\bar{h}$ is the dynamic mixture enthalpy. The former can be developed from the thermodynamic equilibrium quality as shown by

$$\begin{aligned} \bar{\rho}h &= \rho_l h_l \epsilon_l + \rho_g h_g \epsilon_g \\ m\bar{h} &= m_l h_l + m_g h_g \\ \bar{h} &= (1-x_e)h_l + x_e h_g \end{aligned} \tag{38}$$

where the thermodynamic equilibrium quality x_e is given by (20).

By assuming thermodynamic equilibrium, we have $\bar{\rho} = \rho'' = \rho' = \mathrm{f}(\bar{p}, h)$, which leads to

$$\frac{\partial}{\partial t}\left(\bar{\rho}h + \frac{1}{2\bar{\rho}}G^2 - \bar{p}\right) + \frac{\partial}{\partial z}\left(G\bar{h} + \frac{1}{2\bar{\rho}^2}G^3\right) = a_w\dot{q}_e - Gg\cos(\theta) + E_d \tag{39}$$

2.3.5. Homogeneous model setup

The homogeneous model consists of three conservation equations given by (26), (27) and (36), which can be reformulated in the three independent variables density, ρ, mass flow, $\dot{m}$ and internal energy, E. For $\dot{m} = \bar{\rho}uA$ we find:

Continuity equation:

$$\frac{\partial}{\partial t}(\bar{\rho}A) + \frac{\partial}{\partial z}(\dot{m}) = 0 \tag{40}$$

Momentum equation:

$$\frac{1}{A}\frac{\partial}{\partial t}(\dot{m}) + \frac{1}{A}\frac{\partial}{\partial z}(\dot{m}u) = -\frac{\partial \bar{p}}{\partial z} - \bar{\rho}g\cos(\theta) - F_w \tag{41}$$

where $F_w = \frac{S_w}{A}\tau_w$ and τ_w is given by (31).

Energy equation:

$$\frac{\partial}{\partial t}\left(\bar{\rho}A\bar{h} + \frac{1}{2}\bar{\rho}Au^2 - pA\right) + \frac{\partial}{\partial z}\left(\dot{m}\bar{h} + \dot{m}\frac{1}{2}u^2\right) = Aa_w\dot{q}_e - \dot{m}g\cos(\theta) \tag{42}$$

where the independent variables are $z \in [0\ ,...,\ l_z]$ and $t \in [0\ ,...,\ \infty[$.

Then equation (42) can be reformulated by use of the definition of the total specific convected energy: $\bar{E} = \bar{h} + 1/2u^2 + gz\cos(\theta)$ and by using the continuity equation to eliminate the gravitational terms on the left hand side, we find:

$$\frac{\partial}{\partial t}\left(A(\bar{\rho}\bar{E} - \bar{p})\right) + \frac{\partial}{\partial z}\left(\dot{m}\bar{E}\right) = \dot{q}_e S_w - \dot{m}g\cos(\theta) \tag{43}$$

where $\dot{q}_e$ represents the heat flux per unit surface area through the inner wall and $S_w = a_w A$ is the perimeter of the heated domain and a_w has the physical meaning of the wall area per unit volume. The internal energy e is given as: $e = (\bar{\rho}\bar{E} - \bar{p}) \cdot A$, which is measured in [J/m].

2.4. Pipe Wall Model

The heat transfer processes from a combustion process (radiation and convection) to the water and steam curcit in a power plant, is using the pipe wall as the transfer medium, to transport the energy from the furnace to the cooling media, which in this case is water/steam flowing in the panel wall. The solution of problems involving heat conduction in solids can, in principle, be reduced to the solution of a single differential equation, the heat conduction equation. The equation can be derived by formulating an energy balance for a differential volume element in the solid. A volume element for the case of conduction only in the z-direction is illustrated in figure (7). The balance equation for the volume element is:

$$\begin{aligned}(\text{rate of accumulation of internal energy}) = &(\text{rate of heat in})\\ &-(\text{rate of heat out})\\ &+(\text{net rate of internal}\\ &\quad\text{energy generation } (=0))\end{aligned} \tag{44}$$

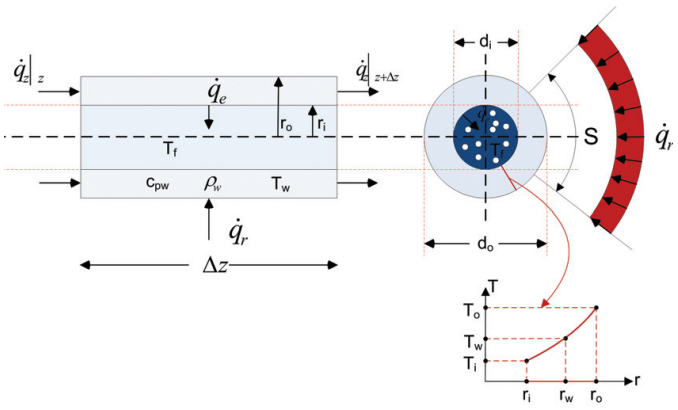

Figure 7: Energy transfer and heat flow terms on a slice of a pipe wall element.

The generation term appears in the equation because the balance is made on internal energy, not total energy. For example, internal energy may be generated within a solid by an electric current or by decay of a radioactive material. The rate at which heat enters the volume element across the face at z is given by the product of the heat flux and the uniform cross-sectional area, $\dot{q}_z|_z A_c$, where $A_c = \pi(d_o^2 - d_i^2)/4$. Similarly, the rate at which heat leaves the element across the face at $z + \Delta z$ is $\dot{q}_z|_{z+\Delta z} A_c$. For a homogeneous heat source/sink of strength $\dot{q}_r$ per unit area, the net rate of generation is $\dot{q}_r S \Delta z$, where S is the pipe perimeter of impact. Finally, the rate of accumulation is given by the time derivative of the internal energy of the volume element, which is $C_{pw}\rho_w(T - T_{\text{ref}})A_c$, where T_{ref} is an arbitrary reference temperature. Thus, the balance equation becomes:

$$\begin{aligned} \Delta z \ \rho_w \ C_{pw} A_c \frac{\partial T_w}{\partial t} &= \left(\dot{q}_z|_z - \dot{q}_z|_{z+\Delta z}\right) A_c \\ &\quad + \dot{q}_r S \Delta z - \dot{q}_e d_i \pi \Delta z \end{aligned} \tag{45}$$

where C_{pw} and ρ_w are the heat capacity and the density of the pipe wall, given below by (69). By dividing (45) by Δz and letting $\Delta z \to 0$, we get a 1. order PDE describing the energy balance in the pipe element as a function of t and z.

$$\rho_w \ C_{pw} A_c \frac{\partial T_w}{\partial t} = -A_c \frac{\partial \dot{q}}{\partial z} + \dot{q}_r S - \dot{q}_e d_i \pi \tag{46}$$

The heat flux $\dot{q}$ per unit area can be expressed via the Fourier equation: $\dot{q} = -k_w \frac{\partial T_w}{\partial z}$, where k_w is the thermal conductivity measured in [W/m K]. For isotropic materials, we introduce the thermal diffusivity given by $\alpha = \frac{k_w}{\rho_w C_{pw}}$ in $[m^2/s]$, which in a sense is a measure of thermal inertia and expresses how fast heat diffuses through a solid. For a typical panel wall, the thermal diffusivity is approximately $1.98 \cdot 10^{-6}$ [m^2/s] at 200° C, see [19]. Hence the energy balance for the isotropic pipe wall can be described by:

$$\frac{\partial T_w}{\partial t} = \alpha \frac{\partial^2 T_w}{\partial z^2} + \frac{\dot{q}_r}{\rho_w \ C_{pw}} \frac{S}{A_c} - \frac{\dot{q}_e}{\rho_w \ C_{pw}} \frac{d_i \pi}{A_c}, \quad z \in [0, l_z] \wedge t \geq 0 \tag{47}$$

where $\dot{q}_r$ is the radiation from the furnace and $\dot{q}_e$ is the convective heat transfer between the flowing fluid in the pipe and the pipe wall inner surface, $\dot{q}_e = h_e(T_w - T_f)$. The convective heat transfer coefficient is named h_e and the driving temperature difference is given by the temperature difference between the wall mean (T_w) and the mixture fluid temperature (T_f). For isotropic materials, we have expressions of C_{pw}, k_w and ρ_w as function of temperature in Kelvin from [19] and [20]:

$$\begin{aligned} C_{pw} &= 6.683 + 0.04906 \cdot T + 80.74 \cdot \ln(T) \ \text{[J/kgK]} \\ k_w &= 9.705 + 0.00176 \cdot T - 1.60 \cdot 10^{-6} \cdot T^2 \ \text{[W/mK]} \\ \rho_w &= 7850 \ [\text{kg}/m^3] \ \text{ at } \ 20°C \ \text{ for 13CrMo44} \end{aligned} \tag{48}$$

A simple, fast and robust model of the heat transfer in film boiling is given by [21]. The heat transfer coefficient h_{fb} is given as

$$h_{fb} = c_f \dot{q}^{0.673} \quad [\mathrm{W/m^2K}] \tag{49}$$

where the coefficient c_f is given by the below expression, which is a function of the saturation temperature (T_s), measured in $[^oC]$

$$c_f = \frac{0.06136}{\left[1 - \left(\frac{T_s}{378.64}\right)^{0.0025}\right]^{0.73}} \tag{50}$$

The single phase laminar heat transfer coefficient is calculated from

$$\begin{aligned} Nu_s &= \frac{h_s d_i}{k_f} \\ &= 4.36 \end{aligned} \tag{51}$$

and is valid for $L/d_i > 50$ and $\frac{d_i G}{\mu} < 2000$. For turbulent single phase flow and $\frac{d_i G}{\mu} > 10{,}000$ we use

$$\begin{aligned} Nu_s &= \frac{h_s d_i}{k_f} \\ &= 0.023 \left(\frac{d_i G}{\mu_l}\right)^{0.8} \left(\frac{C_p \mu_f}{k_f}\right)^{1/3} \end{aligned} \tag{52}$$

The total heat transfer coefficient is given by (53), and consists of two contributions; one from the convective heat transfer boundary layer associated to the flowing fluid inside the pipe and one that relates to conduction through the pipe wall material.

$$h_e = \frac{1}{\frac{1}{h_c} + \frac{r_i}{k_w} \cdot \ln\left(r_w / r_i\right)} \tag{53}$$

where h_c is expressing the heat transfer coefficient due to the thermal boundary on the inner side of the pipe wall and r_w is defined by $T_w = T(r_w)_z$. h_c is smoothed in-between h_s and h_{fb} depending of the dryness of the fluid.

$$h_c = \begin{cases} h_s & \text{for } x > 1 \vee x < 0 \\ \\ h_{fb} & \text{for } 0 \geq x \leq 1 \end{cases} \tag{54}$$

Since we use the calculated average wall tube temperature as driver in the calculation of the total heat transport to the fluid, we must know r_w. Due to the knowledge of radial conduction in the pipe, we use an analytical wall temperature profile for estimating the inner wall temperature. It is expressed by the average wall temperature (T_w), based on the heat transfer through the isotropic

pipe wall to the flowing fluid. Let $T(r)_z$ represent the radial temperature distribution by

$$\begin{aligned} T(r)_z &= \frac{T_i - T_o}{\ln\left(\frac{r_i}{r_o}\right)} \ln\left(\frac{r}{r_o}\right) + T_o \\ &= a_0 \ln(\frac{r}{r_o}) + T_o \end{aligned} \tag{55}$$

where r is the pipe radius with suffix (i inner) and (o outer). Hence, for small values of the thermal diffusivity, the average wall temperature can reasonably be estimated by:

$$\begin{aligned} T_w &= \frac{1}{A_c} \int_{r_i}^{r_o} 2\pi r \cdot T(r) dr \\ &= \frac{2\pi}{A_c} \left[a_0 \left[x^2 \ln(x)/2 - x^2/4 \right]_{r_i}^{r_o} - a_0 \ln(r_o) \left[x^2/2 \right]_{r_i}^{r_o} \right] + T_o \cdot \left[x^2/2 \right]_{r_0}^{r_1} \\ &= a_1 \cdot T_i + (1 - a_1) \cdot T_o \end{aligned} \tag{56}$$

where a_1 is given by

$$a_1 = \frac{r_i^2}{r_i^2 - r_o^2} - \frac{1}{2\ln(r_i/r_o)} \tag{57}$$

Hence the entire heat transfer can be estimated for the temperature range between the wall mean temperature (T_w) and the fluid mixture temperature (T_f), which is assumed homogeneous and well mixed with a temperature boundary layer represented by h_c. The one-dimensional pipe wall model only consists of an axial heat transfer term, and has no spatial resolution in the radial dimension.

The inner wall temperature can be determined by use of the equation for pure conduction through the pipe:

$$\dot{q}_r S = \frac{2\pi k_w}{\ln(r_o/r_i)}(T_o - T_i) = \frac{2\pi k_w}{\ln(r_w/r_i)}(T_w - T_i). \tag{58}$$

Hence we find T_i by insertion (56) in (58):

$$T_i = T_w + \frac{\dot{q}_r S \ln(\frac{r_o}{r_i})(1 - a_1)}{2\pi k_w} \tag{59}$$

and hence r_w in (53) can be determined from (56) and (59) and we find

$$h_e = \frac{1}{\frac{1}{h_c} + \frac{r_i(a_1 - 1)}{k_w} \cdot \ln(r_i/r_o)} \tag{60}$$

Additionally h_c is adjusted on the basis of a smoothing between laminar and turbulent single phase flow as well as for two-phase flow. The simplest way to find a suitable function is according to [22] to look at the fundamental trigonometric function. The smoothing function is due to table (1) for $n = 2$. The associated

slopes are determined numerically. The heat flux is positive for $T_i > T_f$. Using the model parameters from table (2) we find a_1=0.423 and the temperature decrease above the pipe wall is T_o-T_i=27.9 [^oC], which gives a temperature gradient of dT/dr = 3930 [$^oC/m$] for a heat flux of $\dot{q}_r$=100 [kW/m^2]. The heat conduction in the material is a significant barrier for an effective cooling of the tube wall.

2.5. System of balance laws

Based on the above we can summarize the *system of balance laws* (SBL) into a compact vector notation, given by:

$$\frac{\partial \Phi(z,t)}{\partial t} + \frac{\partial \mathrm{f}(\Phi(z,t))}{\partial z} = \mathrm{g}(\Phi(z,t)) + \mathrm{h}\left(\frac{\partial \Phi}{\partial z}, \Phi(z,t)\right), \quad \Phi \in R^m, m = 4, \quad t \geq 0 \wedge \quad z \in \Omega \tag{61}$$

where the dependent variable Φ and the flux vector f are given as

$$\Phi = \begin{pmatrix} \bar{\rho}A \\ \dot{m} \\ e \\ T_w \end{pmatrix}, \quad \mathrm{f}(\Phi) = \begin{pmatrix} \dot{m} \\ \frac{\dot{m}^2}{\bar{\rho}A} + pA \\ \frac{(e+pA)\dot{m}}{\bar{\rho}A} \\ 0 \end{pmatrix}$$

and the source and diffusion vector are given as:

$$\mathrm{g}(\Phi) = \begin{pmatrix} 0 \\ p\frac{\partial A}{\partial z} - \bar{\rho}gA\cos\theta - \sqrt{\frac{\pi}{A}} f_w \frac{\dot{m}|\dot{m}|}{\bar{\rho}A} \\ S_w q_w'' - \dot{m} g \cos(\theta) \\ \frac{\dot{q}_r}{\rho_w} \frac{S}{C_{pw}} \frac{S}{A_c} - \frac{\dot{q}_e}{\rho_w} \frac{d_i \pi}{C_{pw}} \frac{}{A_c} \end{pmatrix} \quad \text{and} \quad \mathrm{h}(\Phi) = \begin{pmatrix} 0 \\ \frac{l^2 S_w}{\bar{\rho}A^3} \frac{\partial \dot{m}^2}{\partial z^2} \\ 0 \\ \alpha \frac{\partial^2 T_w}{\partial z^2} \end{pmatrix}$$

The dependent variables are $\bar{\rho}$, $\dot{m}$, e and T_w meaning the fluid density, mass flow, total energy of the conserved fluid and wall mean temperature, respectively. The pressure can be determined iteratively by water steam tables: $p = \mathrm{p}(e, \rho)$. The source term g consists of both source/sink terms and the diffusion term h include contributions from the mixing length eddy viscosity, working as a damping term in the vicinity of $x = 0$, and the thermal diffusion in the pipe wall, as well.

2.6. Smoothing functions

Smoothing is a core concept in mathematical modelling and is well described by [22]. It is in particular used in the dynamic modelling of physical problems where, for example, material constants and material data are defined in a static and idealized world. Smoothing is used both in start-up of dynamic models, in order to avoid undesirable transient phenomena, but is also used to ensure a natural continuous transition between different constitutive relations (jump from laminar to turbulent flow for friction or heat transfer), so that discontinuities are replaced and a stable solution can be found. Even in the water steam

table, we smooth the density in the vicinity of the saturation line(s) to avoid discontinuities. These smoothing functions $\mathrm{T}(x)$, can be used in the following way to switch between the two functions $\mathrm{g}_0(x)$ and $\mathrm{g}_1(x)$, wherein $\mathrm{T}(x)$ is a normalized function and is provided with boundary conditions at $x = x_0$ and $x = x_1$, corresponding to the slope at each end of the range of the definition.

$$\mathrm{G}(x) = \mathrm{g}_0(x) \cdot \mathrm{T}(x) + \mathrm{g}_1(x) \cdot (1 - \mathrm{T}(x)), \quad x \in \Re \tag{62}$$

where

$$\mathrm{T}(x) \equiv \begin{cases} 1 & \text{for } x < x_0, \\ \mathrm{t}(x) & \text{for } x_0 \leq x \leq x_1, \\ 0 & \text{for } x > x_1. \end{cases} \tag{63}$$

In order to ensure that $\mathrm{T}(x)$ is smooth, the following restrictions apply for $\mathrm{t}(x)$

$$\frac{\mathrm{dt}(x)}{dx}|_{x=x_0} = 0 \quad \text{and} \quad \frac{\mathrm{dt}(x)}{dx}|_{x=x_1} = 0 \tag{64}$$

According to [22] a natural choice is the following trigonometric function

$$\mathrm{t}(\varphi) = a \left(\frac{\cos^{n-1}(\varphi) \sin(\varphi)}{n} + \frac{n-1}{n} \int \cos^{n-2}(\varphi) d\varphi \right) + b \tag{65}$$

where φ is the phase defined by

$$\varphi = \left(\frac{x - x_0}{\Delta x} - 1/2 \right) \pi, \quad \text{where} \quad \Delta x = x_1 - x_0 \tag{66}$$

and n is a positive integer yielding the following function for $\mathrm{t}(\varphi)$. The two parameters a and b can be computed from equation (64). The resulting function $\mathrm{t}(\varphi)$ is continuous of order $n - 1$. Table (1) shows the functions $\mathrm{t}(\varphi)$, its derivatives and values of a and b for $n = 1, 2, 3, 4$.

Table 1: Function $\mathrm{t}(\varphi)$ used in smooth functions $\mathrm{T}(x)$ for n=(1,2,3,4).

n	$\mathrm{t}(\varphi))$	$\frac{dt(\varphi))}{d\varphi}$	a	b
1	$a \sin(\varphi) + b$	$a \cos(\varphi)$	-1/2	1/2
2	$\frac{a}{2}(\cos(\varphi)\sin(\varphi) + \varphi) + b$	$a\left(1 - \sin^2(\varphi)\right)$	$-2/\pi$	1/2
3	$\frac{a}{3}\left(\cos^2(\varphi)\sin(\varphi) + 2\sin(\varphi)\right) + b$	$\frac{a}{3}\left(\cos^2(\varphi)(2 - \cos^2(\varphi)) + 2\cos(\varphi)\right)$	-3/4	1/2
4	$\frac{a}{8}\left(2\cos^3(\varphi)\sin(\varphi) + 3\cos(\varphi)\sin(\varphi) + 3\varphi\right) + b$	$\frac{a}{8}\left(2\cos^2(\varphi)(4\cos^2(\varphi) - 3) + 3(2\cos^2(\varphi) - 1) + 3\right)$	$-8/3\pi$	1/2

2.7. Auxiliary relations

The Water / Steam library IAPWS 97 by [23] is used as a general equation of state, to derive the speed of sound and the thermodynamic properties of water and steam. In some relations we need a relationship for pressure as

function of density and enthalpy: $p = \mathrm{p}(\rho, \bar{h})$. This can be done by a simple Newton Raphson solver, where we iterate on p by given h and ρ. To improve the computational speed it is recommended to use a bilinear interpolation, see [8]. We create a look up table covering approximately 160000 nodes, which ensure an accuracy below 0.3% as an absolute maximum, because we smooth the density in the vicinity of the saturation line of water, where we experience the highest significant error, due to [8].

2.8. Boundary conditions

With the aim to analyse the dynamic stability of vertical evaporators, we have chosen to apply a fixed downstream pressure boundary condition, so that pressure oscillations can be reflected downstream. This will represent an absolute worst-case situation, but for the situation of an intense warm-up in the bottom of a vertical evaporator and the overlying heavy water mass compressing the compressible fluid around the evaporation zone in the evaporator. This will result in pressure oscillations in the evaporator, initiated where the fluid has the largest gradient in density. Upstream, we will apply a fluid velocity and an inlet enthalpy boundary condition. The evaporator is influenced by a uniform heat flux as well as a constant gravitational force. Therefore, the following properties are used as boundary conditions; velocity (u), pressure (p) and enthalpy (h). This allows us to rewrite the boundary conditions to those properties, which are described by Φ, see (61). The Dirichlet boundary conditions are given by (67) and the corresponding Neumann boundary conditions are obtained by applying the chain rule for differentiation of complex functions as given by (68).

$$\text{Dirichlet BC}: \begin{cases} \rho A \\ \rho A u \\ \rho A(h + \frac{u^2}{2} + gz\cos(\theta)) - pA \end{cases} \tag{67}$$

where θ is the angle of the pipe inclination with respect to the horizontal.

$$\text{Neumann BC}: \begin{cases} A\frac{\partial \rho}{\partial z} + \rho\frac{\partial A}{\partial z} \\ uA\frac{\partial \rho}{\partial z} + \rho u\frac{\partial A}{\partial z} + \rho A\frac{\partial u}{\partial z} \\ \frac{\partial(\rho A)}{\partial z}\left[h + \frac{u^2}{2} + gz\cos(\theta)\right] + \rho A\left[\frac{\partial h}{\partial z} + u\frac{\partial u}{\partial z} + g\cos(\theta)\right] \\ -A\frac{\partial p}{\partial z} - p\frac{\partial A}{\partial z} \end{cases} \tag{68}$$

2.9. Numerical Solution of Hyperbolic Transport Equation

The developed model is solved by a fifth order Central WENO scheme for particularly developed with focus on solving hyperbolic balance laws. The scheme is tested for consistency and stability with respect to both a scalar and vector based system of hyperbolic equations and is compared to analytical results from the literature as well as other published results. This work is outlined in [8]. The semi-discrete ODE system is based on a semi-discrete central-upwind

scheme presented in [24] and uses a five point stencil. The system is a time dependent, which can be solved by any stable ODE solver, which retain the spatial accuracy of the scheme. Here we usea third order TVD Runge-Kutta method presented by [25].

2.10. Model setup

Three boundary conditions are applied for the hydraulic case and two Dirichlet boundaries are applied for the pipe wall model, with zero gradients at each pipe end, i.e., we assume no heat loss by conduction outside the pipe. The computational results are stored as line series for an equidistant time step and time series at two positions located at $z_A = \frac{l_z}{8}$ and $z_B = \frac{7l_z}{8}$, named station A and B respectively.

2.11. Simulation

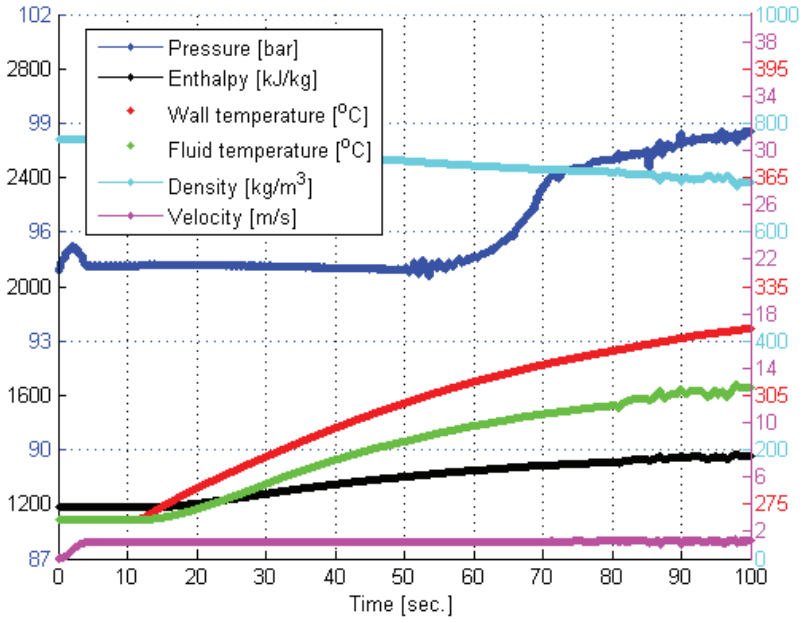

Figure 8: Soft start response of SKV3 evaporator model @ station A.

The model is soft-started in two steps; At $t = 0$ the hydraulic part of the model is soft-started from rest during 4 seconds, without heat flux. After 10 seconds the heat flux is build-up during 4 seconds to 100 [kW/m^2]. This is done to avoid heavy shock phenomena and gives a smotth and robust startup of the simulation as illustrated in figure (8 and 9). The figure illustrates the development of pressure, enthalpy, density, fluid velocity and wall- and fluid

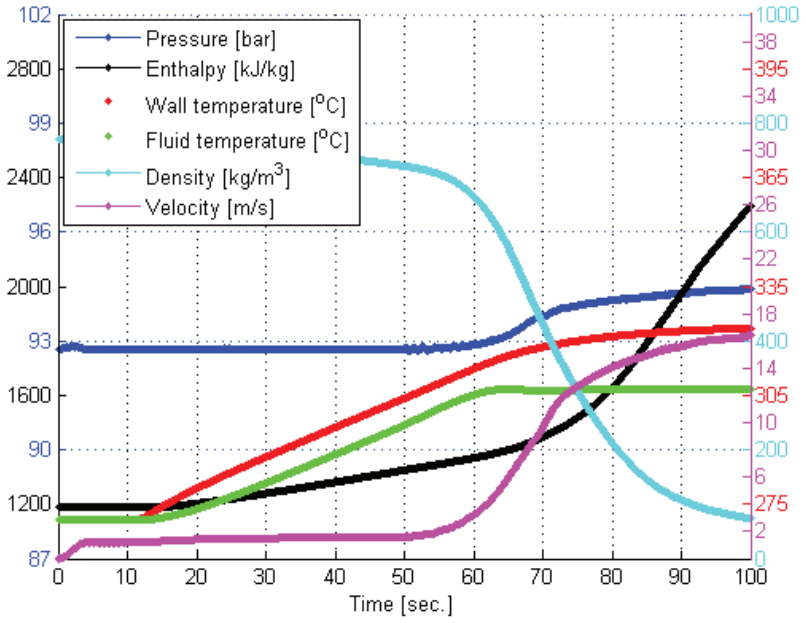

Figure 9: Soft start response of SKV3 evaporator model @ station B.

temperature. I general is the curves for wall- and fluid temperature reffering to the same scale, meaning the red wall temperature scale.

If the soft-start period is reduced to only 1 second heavy pressure oscillations occur, which will be damped during 15 seconds of simulation, see figure (10). The soft start model is based on the theory outlined in section (2.6), which gives a C^2 continuous sequence, with zero gradients in the first derivative at both ends of the soft start period.

3. Results

In this section we solve the homogeneous evaporator pipe model for $\Omega \in [0,\, l_z]$, defined by the system of balance laws given by equation (61) combined with the pipe wall model given by equation (47). The model is compared to measurements performed by a full-scale evaporator at Skærbækværket Unit 3, see [26] (SKV3) in Fredericia, Denmark. Secondly, a scenario is performed, where a high pressure preheater is closed during 4 seconds.

The model data are listed below in table (2). The dynamic start-up process is shown in figure (11), where the density is given in [kg/m^3], pressure in [bar], Temperature in [^{o}C], enthalpy in [kJ/kg] and mixture velocity in [m/s]. Note that the acceleration of gravity, is ajusted according to the pipe inclination of 12 degree (1.9399 $[m^2/s]$)

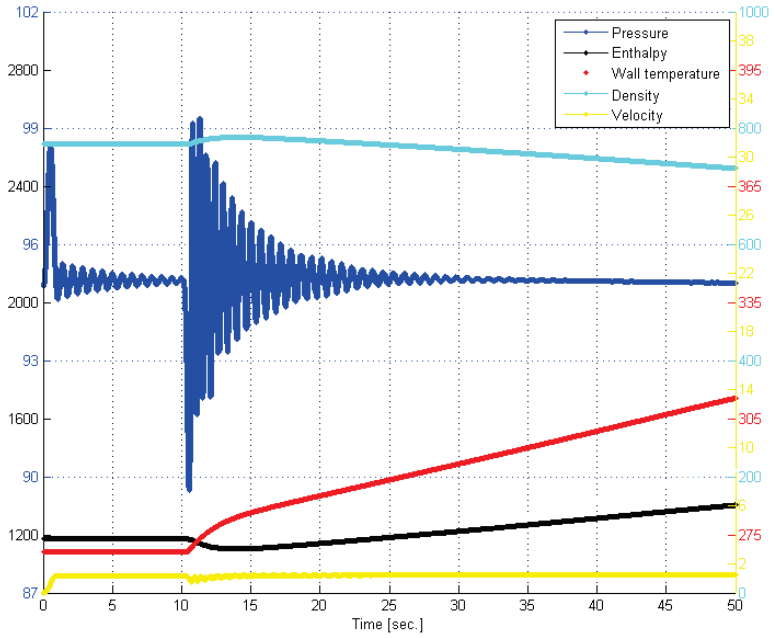

Figure 10: Time series for short dynamic soft start start-up process @ station A.

3.1. Evaporator Startup

Figure (11) illustrates the output results for each 25 seconds of the simulation, referring to the solution of both the homogeneous flow equations as well as the wall tube model. The spiral wounded furnace have tubes that are wound at an angle of 12^o around the furnace perimeter from the lower furnace inlet headers to above the burner zone, see [26]. This arrangement means that each tube in the furnace passes through the various heat zones so that the heat absorption for adjacent tubes is reasonably uniform. By wrapping each furnace enclosure tube through each of the four furnace enclosure walls, each tube goes through approximately the same variation in heat absorption, both axially and radially. A high mass flux is required to maintain effective heat transfer across the boiler load range as well as to avoid stratification of the two phases of water and steam at minimum load. The potential of stratification or inadequate heat transfer at low loads limits the minimum once-trough load (*Benson load*) of spiral furnaces. Also the high mass flux causes a high pressure drop in the tubes, which means feed water pump power is correspondingly high, which leads to a high dynamic friction loss compared to the static pressure loss (hydrostatic loss). Additionally the spiral wound furnace have a negative flow response characteristic for a high mass flux system. The water flow must decrease with higher

Table 2: Geometrical and numerical specifications.

Parameter	Value	Unit	Parameter	Value	Unit
Gravity (g)	1.9399	[m/s^2]	Spatial start position	0.000	[m]
Spatial end position (L)	193.499	[m]	Inner diameter of pipe (d_i)	23.8	[mm]
Outer diameter of pipe (d_o)	38.0	[mm]	Heat conductivity in wall (k_w)	10.139	[w/mK]
Wall density (ρ_w)	7850.0	[kg/m^3]	Specific heat capacity of pipe wall (Cp_w)	527.21	[J/kg/K]
Heat flux ($\dot{q}_e$)	100.000	[W/m^2]	Wall roughness (λ)	10^{-6}	[m]
Initial Enthalpy - left side	1187.6988	[kJ/kg]	Initial Enthalpy - right side	1187.6988	[kJ/kg]
Initial Pressure - left side	92.3762	[Bar]	Initial Pressure - right side	92.3762	[Bar]
Initial Velocity - left side	0.0	[m/s]	Initial Velocity - right side	0.0	[m/s]
Pressure BC (Dirichlet - right side)	92.3762	[Bar]	Enthalpy BC (Dirichlet - left side)	1187.6988	[kJ/kg]
Velocity BC (Dirichlet - left side)	1.1711	[m/s]	Simulation time	1000.0	[s]
Output frequency	0.1	[s]	CFL number	0.80	[-]
Number of computational grids (N_p)	400	[-]	Slip Correction Factor	1.0	[-]

heat input to maintain system pressure loss, which illustrate that the furnace wall tube metal temperature are adversely affected as tube flow is reduced when there is an above-averaged heat supply. The response time of a spiral wound furnaces is restricted by the way the furnace is supported. Because spiral wound tubes can not support their own weight, vertical support straps are required on the outside of the furnace, which leads to thermal stresses between the tubes and the support straps during dynamic load conditions, which limit the start up speed of the boiler as strap temperature lags behind the tube temperature. Departure from nucleate boiling (DNB) occurs when a heat flux is applied to a boiler tube and steam film forms between the water and the tube. The result is increased tube metal temperature due to lower steam conductivity and much reduced furnace tube life. Under certain simplified conditions under which we look at a long evaporator tube, feeded by subcooled water and deliver superheated steam at a fixed pressure to the turbine system, gives a steady state solution, obtained after approximately 500 seconds, and is depicted in figure (12). The model consists of 400 differential elements, thus ensuring a smooth continuous solution. By reducing the number of computational cells to only 50 elements, one would observe a more intensive standing wave at the entrance of two-phase region, which is due to intensive heating of the differential cell in the vicinity of the boiling zone, where we have an intensive negative slope in the density as function of the enthalpy, hence the density change becomes so dramatic that a pressure wave is established to ensure momentum balance. A steady state of general sense is not existing here, because the model successively experiences pressure oscillations created from the transition zone between subcooled and two-phase fluid, where the very large density gradients occurs. The results show how the outlet state of the fluid gradually moves from the inlet condition, in the form of subcooled water, to two-phase conditions, in which the boiling is starting, and finally reaches the superheated state, where the dry steam is at about 385 ^oC. The pressure is fixed downstream in the form of a Dirichlet boundary condition, corresponding to the measured pressure levels from (SKV3). This pressure boundary condition has an aggravating circum-

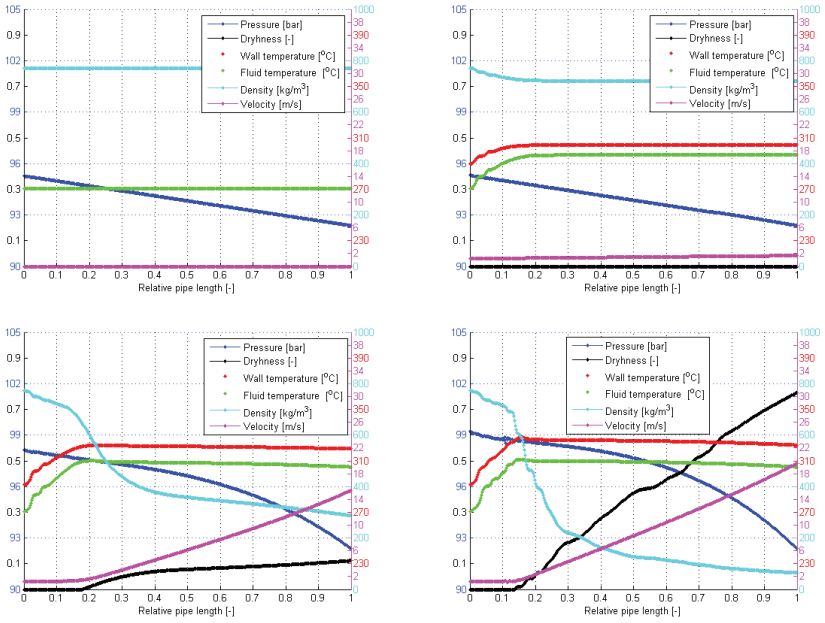

Figure 11: Initial conditions and the solution of SKV3 evaporator model after 50, 75 and 100 sec.

stance, but needed to provoke instabilitets phenomena in the evaporator. The pressure distribution along the evaporator reflects the pressure gradient of single and two-phase regions, respectively. The two-phase region is modeled by the two phase multiplier outlined in (33), which scales the pressure gradient up to 16 times relative to the pressure gradient for saturated water. The inlet velocity is specified as an upstream Dirichlet boundary condition, and is soft started by use of the before mentioned smoothing function, having a soft start period of 4 seconds. This ensures a smooth hydraulic flow condition of the cold evaporator. Next the heating is built up smoothly, by the same smoothing technique, so that undesirable thermal shock phenomena are avoided. The superheated steam leaves the downstream boundary at steady state flow conditions with a speed of 24 m/s. Pressure-drop oscillations could occur, if larger upstream compressibility existed in the flow boiling system, see ([27], [28]). These oscillations in, e.g., pressure can be generated in the form of a standing wave in the front of the boiling zone of the fluid. This phenomenon is also present in horizontal evaporators. The dryness line in figure (11) expresses the mass based percentage of the steam flowing in the evaporator tube, not surprisingly, this process corresponds linearly to a constant heat flux along the tube.

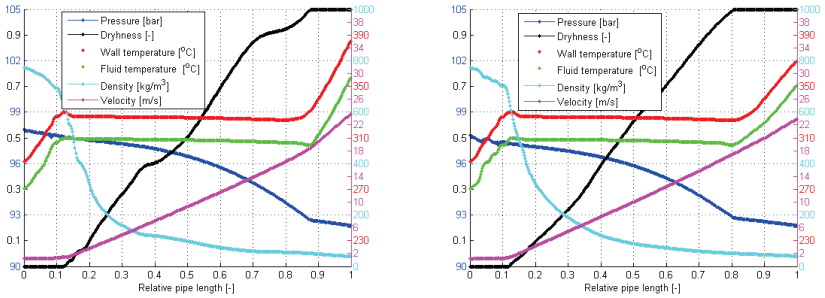

Figure 12: Solutions of SKV3 evaporator model after 210 [s] and 400 [s].

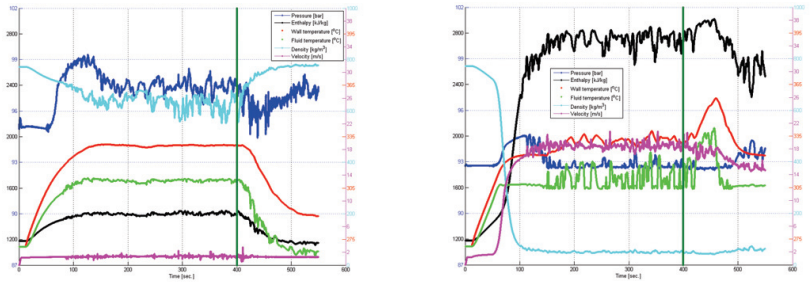

Figure 13: Preheater failure after 400 [s]. Left and right figures represents time series at station A and B respectively.

3.2. Preheater failure

A high pressure preheater improves the electrical efficiency of a power plant, by recuperating heat from a fraction of the steam from the steam turbine. Thus, the feed water temperature is raised before entering the economizer and subsequently the evaporator. With a preheater failure, the plant experiences an rapid decrease in feedwater temperature to the evaporator. By smoothly changing the feed water temperature on the SKV3 model on the upstream Dirichlet boundary from 1187 [kJ/kg] to 750 [kJ/kg] during 4 [s], the outlet temperature changes from 270.7 [^{o}C] to 220 [^{o}C]. The model responds promptly and by observing time series located up- and downstream the evaporator (station A and B), we can see a response as a function of time. Not surprisingly, we see a response in the upstream station, which is very similar to the boundary condition, while in the downstream station B, we experience a peak in the steam temperature, despite the fact, that we are feeding the system with less energy. This is due to the compressibility in the evaporator, so that the fluid now takes up less space in the upstream section and the residence time of down stream fluid becomes

greater, for a short while, so as to achieve a higher super heating of the superheated fluid. After a certain period, this superheated fluid is advected out of the down stream boundary and we will see a reduced superheating.

4. Discussion

The Central WENO schemes are designed for problems with piecewise smooth solutions containing discontinuities. The Central WENO scheme has been quite successful in the above applications, especially for solving the pressure distribution downstream of an evaporator. The inlet conditions is subcooled water and the outflow is superheated steam. Minor pressure waves are initiated in the transition zones to the two phase region ($x = 0$), which creates pressure waves marching downstream the pipe reaching the downstream pressure boundary condition. Normally dynamic models using traditional numerical schemes will have problems, and create instabilities in the transition zone between subcooled- and two-phase fluid, but the higher order WENO schemes are perfect for handling oscillations and steep gradients without introducing over-under shooting or numerical diffusion, although numerical diffusion will be a calming measures here.

A very interesting phenomenon that we can see in figure (13), is the appearance of flashing (temperature oscillations) induced by pressure and enthalpy oscillations. During periods the fluid temperature assumes a temperature corresponding to the local saturation temperature, and at other times the pressure increases (and enthalpy), so that the fluid is being superheated. This results in a short-term temperature rise, which takes a size of typically 10 $[^oC]$. This will affect the small metal structures on the inner side of the tube and can eventually result in microscopic cracks.

The operational staff on SKV3 has by their own vision experienced dramatic dynamic stresses on the boiler, particularly at cold start can be observed dramatic dynamic stresses, which are able to move the boiler outlet pipes up to half a meter out of their natural position. Fortunately, these tubes are mounted in the straps, attached to the top of the boiler construction, so that they have the necessary flexibility. But in the long run, there is violent impacts that should be analyzed in order to fatigue of boiler tubes.

We find that the WENO solver is able to solve such an strong, nonlinear, physically complex system of PDE in a mixture of hyperbolic fluid equations and a parabolic model of the wall with respect to the transformed independent solution parameters. The model is very time consuming in solving the system, because the total energy is determined iteratively as well as the density is a function of pressure and enthalpy. The solution time is up to a couple of hours, runnung on a portable PC (Lenovo T520 i5-2520M CPU @2.5GHz with 8GB memory). The iteration accuracy for calculating the pressure is set to 10^{-13}, which is very low and is an obvious target for optimization. The model is stable as long as the CFL number is less than one and the speed of sound is below the highest calculated speed of sound along the entire spatial solution area of the fluid, which is determined at each time step. The observed oscillations are

caused by the compressibility of the fluid and are initiated in the transition zone between the subcooled- and the two-phase boiling zone. This is thus due to the physical properties of the evaporator and is not caused by numerical instabilities, as shown in by investigations and test cases performed in [29]. If we reduce the degree of subcooling to a minimum, we will see a much smoother solution that will achieve a steady state solution much faster. We can conclude that the solution procedure is non-oscillatory in the sense of satisfying the total-variation diminishing property in the one-dimensional space. No numerical wiggles are observed in the hyperbolic models and smooth solutions are observed in the continuous zones of the flow regimes.

5. Conclusion

I this article is developed a numerical model of a complete evaporator, which can handle a fluid in different thermodynamic conditions, as subcooled liquid, saturated liquid, two-phase fluid, saturated gas and as a superheated gas. The model is developed on the basis of a two-layer model, which is a good approach to the understanding of the thermal hydraulic conditions in an evaporator. This model is solved numerically by means of a fifth-order WENO scheme that uses a five point stencil in the semi-explicit solution method. It is the same scheme used in all the thermodynamic conditions. Time integration is handled by a third-order TVD time integrator. Model simulations show that it is possible to demonstrate the very dynamic and oscillatory conditions, which occur in a vertical evaporator with a fixed back pressure. The model also respond adequately to dynamic changes in the upstream boundary. In connection with the analysis of the consequences of a preheater failure, we see that the fluid with a momentary change of inlet temperature, get changed the specific volume, so that the residence time of the fluid in the downstream part of the evaporator increases, with a short-term increase in superheat to follow. We can conclude that the WENO scheme is robust and suitable for further studies in two-phase flows.

References

[1] H. Griem, Untersuchung zur thermohydraulik innenberippter verdampferohre., PhD thesis, Technische Universitat Munchen, Lehrstuhl fur Termische Kraftanlagen. (1).

[2] Anonymous, Garantee test results of steam turbine SVS3 - 98550369-KPG/TCM 99-6907 Confidential, KEMA, Arnhem, 25 January 1999, Arnhem, The Netherlands, 1999.

[3] J. Pan, D. Yang, Z. Dong, T. Zhu, Q. Bi, Experimental investigation on heat transfer characteristics of low mass flux rifled tube upward flow., International Journal of Heat and Mass Transfer. 54 (2011) 2952–2961.

[4] D. Yang, J. Pan, C. Zhou, X. Zhu, Q. Bi, T. Chen, Experimental investigation on heat transfer and frictional characteristics of vertical upward rifled tube in supercritical cfb boiler., Experimental Thermal and Fluid Science. 35 (2011) 291–300.

[5] X. Zhu, Q. Bi, Q. Su, D. Yang, J. Wang, G. Wu, S. Yu, Self-compensating characteristic of steam-water mixture at low mass velocity in vertical upward parallel internally ribbed tubes., Applied Thermal Engineering. 30 (2010) 2370–2377.

[6] X. Fan, S. Wu, Heat transfer and frictional characteristics of rifled tube in a 1000 mw supercritical lignite-fired boiler., School of Energy Science and Engineering, Harbin Institute of Technology, China. 1 (2010) 1–5.

[7] J. Pan, Y. Dong, H. Yu, Q. Bi, H. Hua, F. Gao, Z. Yang, Mathematical modeling and thermo-hydraulic analysis of vertical water wall in an ultra supercritical boiler., Applied Thermal Engineering. 29 (2009) 2500–2507.

[8] A. O. Johansen, E. B., J. N. Sørensen, Implementation and test of a fifth order central weno scheme for solving hyperbolic balance laws., Applied Thermal Engineering ,1-25. (1).

[9] M.-S. Chung, K.-S. Chang, S.-J. Lee, Numerical solution of hyperbolic two-fluid two-phase flow model with non-reflecting boundary conditions, Int. J. Engineering Science 40 (1) (2002) 789 – 803.

[10] G. B. Wallis, One dimensional two phase flow., 3rd Edition, McGraw-Hill., 1969.

[11] S. M. Ghiaasiaan, Two-Phase Flow, Boiling, and Condensation in Conventional and Miniature Systems, 1st Edition, Cambridge University Press, Georgia Institute of Technology, 2008.

[12] J. Zhou, L. Cai, J. Feng, W. Xie, Numerical simulation for two-phase flows using hybrid scheme., Applied Mathematics and Computation. 186 (2007) 980–991.

[13] T. Watanabe, M. Hirano, F. Tanabe, H. Kamo, The effect of virtual mass on the numerical stability and efficiency of system calculations., Nucl. Eng. Design, 120, 181-192.

[14] G. Hewitt, J. Delhave, N. Zuber, Inertial coupling in two-phase flow: Macroscopic properties of suspension in an inviscid fluid., vol 5, chapter 4 Edition, In Multiphase Science and Technology., 1969.

[15] G. R. Kinney, A. E. Abramson, J. L. Sloop., Internal-liquid-film cooling experiments with air-steam temperatures to 2000 ^{o}f in 2-inch and 4-inch diameter horizontal tubes., NACA Report no. 1087. 1 (1) (1952) 1.

[16] L. E. Gill, G. Hewitt, J. W. Hitchon., Sampling probe studies of the gas core in annular two-phase flow, part 1. the effect of length of phase and velocity distribution., Chem. Eng. Sci. 18 (1) (1963) 525–535.

[17] L. E. Gill, G. Hewitt, J. W. Hitchon., Sampling probe studies of the gas core in annular two-phase flow, part 2. studies of the effect of phase flow rates on phase and velocity distributions., U.K. Report AERE-R 3955. (1).

[18] F. Jirous, Analytische methode der berechnung des naturumlaufes bei dampferzugern, VGB Heft 5 (1978) 366–372.

[19] P. D. Bentz, R. Prasad, Kuldeep, Thermal performance of fire resistive materials i. characterization with respect to thermal performance models., NIST, Building and Fire research Laboratory, Gaithersburg. (MD 20899-8615).

[20] Anonymous, Rohre aus warmfesten und hochwarmfesten Stahlen Werkstoffblatter., 1st Edition, Vol. 1, MannesMann Rohrenwerke., 1988.

[21] F. Brandt, FDBR-FACHBUCHREIHE - warmeubertragung in Dampferzeugern und Warmeaustauschern., band 2 Edition, Vulkan-Verlag, Essen., 1985.

[22] C. C. Richter, Proposal of New Object-Oriented Equation-Based Model Libraries for Thermodynamic Systems., 1st Edition, Vol. 1, Von der Fakultät für Maschinenbau, der Technischen Universität Carolo-Wilhelmina zu Braunschweig., 2008.

[23] W. Wagner, H.-J. Kretzschmar, International Steam Tables - Properties of Water and Steam Based on the Industrial Formulation IAPWS-IF97, 2nd Edition, Springer, Berlin Heidelberg, 2008.

[24] A. Kurganov, S. Noelle, G. Petrova, Semi-discrete central-upwind schemes for hyperbolic conservation laws and hamilton-jacobi equations., SIAM J. Sci. Comp. ,707-740. (23).

[25] S. Gotlieb, C. Shu, Total variation diminishing runge-kutta schemes., Math. Comp., 73-85 (67).

[26] A. O. Johansen, Simulation and optimisation of thermal power stations by use of turabs., Proceedings of the 17th International Conference on ECOS 3 (2004) 1267–1277.

[27] A. Bergles, e. a. J.H. Lienhard, Boiling and evaporation in small diameter channels., Heat Transf. Eng. 24 (2003) 18–40.

[28] S. Kakac, B. Bon., A review of two-phase flow dynamic instabilities in tube boiling system., Int. J Heat Mass Transfer. 51 (2008) 399–433.

[29] A. O. Johansen, E. B., Finite element method interpolation scheme for fast calculation of water/steam properties., Journal of Computational Physics ,1-25. (1).

Q. Paper 4

Axel Ohrt Johansen, Brian Elmegaard

A homogeneous two-phase flow model of an evaporator with internally rifled tubes, modelled by a fifth order Central WENO scheme for solving hyperbolic balance laws

SIMS 2012, Reykjavik, Iceland.

Available online at www.sciencedirect.com
ScienceDirect
SIMS 00 (2012) 1–21
SIMS 2012
www.elsevier.com/locate/procedia

A homogeneous two-phase flow model of an evaporator with internally rifled tubes☆

Axel Ohrt Johansen[a,b], Brian Elmegaard[b]

[a]DONG Energy - Thermal Power, Kraftværksvej 53, Dk-7000, Fredericia, Denmark
[b]Technical University of Denmark, Nils Koppels Allé, Building 403, DK-2800 Kgs. Lyngby, Denmark

Abstract

In this article a numerical model for solving a transient one dimensional compressible homogeneous two phase model is developed. It is based on a homogeneous model for predominantly one-dimensional flows in a vertical pipe element with internal rifles. The homogeneous model is based on the assumption of both hydraulic- and thermal equilibrium. The consequences and aspects will briefly be discussed in that context. The homogeneous flow model consists of three hyperbolic fluid conservation equations; continuity, momentum and energy and the pipe wall is modelled as a one dimensional heat balance equation. The models can be reformulated in the four in-dependant parameters p(pressure), h(enthalpy) u(velocity) and T_w(wall temperature). Constitutive relations for the thermodynamic properties are limited to water/steam and is given by the IAPWS 97 standard. Wall friction and heat transfer coefficients are based on the Blasius friction model for rifled boiler tubes and the correlation by Jirous respectively. The numerical method for solving the homogeneous fluid equations is presented and the method is based on a fifth order Central WENO scheme, with simplified weight functions. Good convergence rate is established and the model is able to describe the entire evaporation process from sub-cooled water to super-heated steam at the outlet.

1. Introduction/motivation

Along with the liberalization of electricity markets in Northern Europe and Denmark, there is an increasing need to quickly regulate the large central power plants to cover the current supply of electricity and district heating. Much focus has been put in optimizing the individual power plants, so they can meet the requirements to stabilize the power supply and district heat production, caused by the stochastic nature of wind farms. Electricity generation based on wind has primacy in terms of production and the central power plants have to fill the gap between producing and consuming power. In periods of very high wind generation, the central power plants are thus forced to run down into low load and maintain a contingency in case the wind unexpectedly fails to come. In these situations, there may still be a need for district heating production, why we might consider turbine bypass in the steam power plants and directly produce district heating from the boiler at moderate pressure.

Keywords: Two phase flow, Vertical evaporator, Dynamic load, Internal Rifled Boiler Tubes, Central WENO, Hyperbolic balance laws.

☆Modelled by a fifth order Central WENO scheme for solving hyperbolic balance laws.

Email address: axejo@dongenergy.dk (Axel Ohrt Johansen)

Operating flexibility is therefore of great importance for the business economics of the plants and also a prerequisite for a stable electrical system. No matter how strong focus is put on this operational flexibility, power plants, however, will always be subject to technical limitations - e.g. boiler dynamics, coal mill dynamics, flame stability and material constraints. The power plants' ability to stabilize the electrical system can be increased substantially if we get a better understanding of the thermodynamic and flow changes, which occur in the evaporation process. Siemens has spent years developing a new evaporator concept, in brief; it has developed an evaporator with vertical boiler tubes lined with internal rifles. The system is called the SLMF principle (Siemens Low Mass Flux), see [1], which can be used for very specific evaporator systems. One of the advantages of using SLMF is that the boiler's primary operating area (Benson minimum) can be moved from the traditional 35-40% load. In new constructions this transition point is to around 20% load. In this way we avoid the very expensive and time consuming Benson transition, when an installation must adapt to the free electricity market and drive down the load. There is very little literature on the subject and there is a modest material relating to the mathematical description of heat transfer and pressure drop in rifled boiler tubes. Back in 1985 Harald Griem, [1] wrote on the subject, and both KEMA and Siemens have performed considerable experimental work that is considered company secrets. Other authors who have dealt with the topic experimentally are [2], [3], [4] and [5]. They have developed consistent algebraic expressions for frictional pressure drop and heat transfer in internally rifled boiler tubes. A Weighted Essentially non-oscillatory (WENO) solver code is implemented in c++ under MicroSoft Visual Studio 2008, and the solver is validated in [6]. The water/steam table is based on a fast bi-linear interpolation scheme, where the lookup table are based on the IAPWS97 standard, which is implemented in FORTRAN 90. The lookup table is described in [7].

2. Evaporation in steam power boilers

A power plant boiler works as a heat exchanger. On one side the fuel is burned and the product of combustion is a hot gas exchanging radiant heat to the water on the other side of the heat exchanger. The boiler is traditionally built as a tower, inside the hot gas is produced and the walls of the boiler are made of pipes welded together, in these pipes the water flows.

The heat flux is approximately 200-400 kW/m^2 in the lower sections of the boiler and is represented as radiation. At the upper part of the tower, the radiation is still dominating, but it is also necessary to take convective heat transfer into account. At the bottom section, where the radiation from gas to the pipe wall is dominating, the heat transfer on the outside is so massive that it is no longer setting the restriction for the optimal heat transfer. Instead, the limit is set by the heat transfer rate from the pipe-wall to the water inside the pipe.

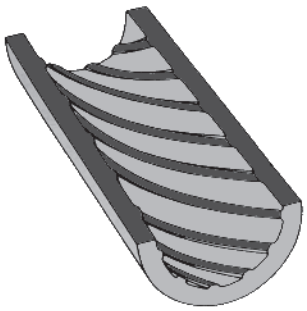

Fig. 1. Center cutting of an internal rifled boiler tube

One parameter that determines the heat transfer rate on the inside of the pipe is the fluid velocity near the inner pipe wall. If the velocity can be increased without increasing the net mass flux through the boiler, the heat transfer rate can be increased. With that assumption it is possible to build a more compact boiler,

by taking into account the specific type of combustion processes (Coal, Gas Wood pellets ect.). Internally rifled boiler tubes (IRBT) are an attempt to speed up the velocity at the wall and keep the vertical tube of a boiler construction. The mass flux through the IRBT are usually in the range of 1000 kg/m^2s and is less than the half as is seen in traditional Benson boiler panel walls, with a moderate pipe inclination.

In addition to the increase in heat transfer, the IRBTs are characterised by an excellent performance concerning two phase flow. The swirl is very good for separation of liquid from gas. The centrifugal force will increase the rate of light fluid to the centre of the pipe and force the heavy fluid components to near the wall, which will improve the cooling of the pipe and thereby increase the heat transfer and decrease the wall temperature of the pipe. Additionally the IRBT have the following advantages: The rifles will enlarge the surface of convective heat transfer, increasing the turbulent intensity in the boundary layer and increase the relative velocity between the wall and core fluid by rotational flow.

The advantages of the IRBT have a price. The pressure loss is higher than in the traditional boiler tubes, but it can be used in a constructive way. When super critical boilers operate at part load, stability problems can occur. The problem is usually solved by building individual pressure loss at each pipe inlet section. Thus the increased pressure loss in the IRBT can be utilized to replace the traditional built in pressure loss and thereby not increase the pumping power

3. Methods

Although the assumptions of thermodynamic equilibrium are often made in two-phase flow models, the phases rarely find themselves at thermal equilibrium. Some degree of thermal non-equilibrium arises in practically all situations and specially in dynamic situations, thermal non equilibrium must always be present so that heat and mass transfer can take place. Thermodynamic equilibrium does exist between a liquid and its vapour separated by a flat interface e.g., water and steam in a closed vessel. In the classical case of stationary vapour / bubble in large amount of liquid, the vapour and liquid temperatures are equal. However, due to the effect of surface tension, even in this equilibrium situation, the system temperature must be slightly above the saturation temperature corresponding to the pressure of the liquid. It is only in the case of the flat interface, that both phases can be exactly at saturation. Thus, the absence of hydraulic and thermal equilibrium is the rule rather than the exception in multi phase flows. In this chapter we outline a homogeneous dynamic flow model, based on the two layer flow model outlined in [8].

3.1. Thermo-Hydraulic model

The homogeneous model is based on the assumption of both hydraulic and thermal equilibrium and consists of three conservation equations, which can be reformulated in the three in-dependant variables ρ(density), $\dot{m}$(mass flow) and E(internal energy), where the dependant variables z (axial position in the pipe) $\in [0\ ,..., l_z]$ and t(time) $\in [0\ ,..., \infty[$. The pipe length is l_z. For the massflow given by: $\dot{m} = \bar{\rho} u A$ we find:

Continuity equation:

$$\frac{\partial}{\partial t}\left(\bar{\rho}A\right) + \frac{\partial}{\partial z}\left(\dot{m}\right) = 0 \tag{1}$$

where $A{=}\pi r_i^2$ is the cross section area of the pipe and r_i is the inner radius of the pipe. The mixture density is given by $\bar{\rho}$.

Momentum equation:

$$\frac{1}{A}\frac{\partial}{\partial t}\left(\dot{m}\right) + \frac{1}{A}\frac{\partial}{\partial z}\left(\dot{m}u\right) = -\frac{\partial \bar{p}}{\partial z} - \bar{\rho} g \cos\left(\theta\right) - F_w - F_s \tag{2}$$

where the mixture fluid velocity is given by u, g is the gravity and θ is the angle of pipe inclination measured from the vertical direction. The mixture pressure is given as $\bar{p}$ and the shear forces due to wall friction is given by: $F_w{=}\frac{S_w}{A}\tau_w$ and τ_w is given by (6) and S_w is the perimeter. The turbulent Reynolds stresses in the mixing fluid is given by $F_s = \frac{S_w}{A}\tau_s$.

Energy equation:

$$\frac{\partial}{\partial t}\left(\bar{\rho}A\bar{h} + \frac{1}{2}\bar{\rho}Au^2 - pA\right) + \frac{\partial}{\partial z}\left(\dot{m}\bar{h} + \dot{m}\frac{1}{2}u^2\right) = S_w q_e^{''} - \dot{m} g \cos\left(\theta\right) \tag{3}$$

Here the mixture enthalpy is given as $\bar{h}$. Equation (3) can be reformulated by use of the definition of the total specific convected energy: $\bar{e} = \bar{h} + 1/2u^2 + gz\cos\left(\theta\right)$ and by using the continuity equation to eliminate the gravitational terms on the left side, we find:

$$\frac{\partial}{\partial t}\left(A(\bar{\rho}\bar{e} - \bar{p})\right) + \frac{\partial}{\partial z}\left(\dot{m}\bar{e}\right) = q_e^{''} S_w - \dot{m} g \cos\left(\theta\right) \tag{4}$$

where $q_e^{''}$ represents the heat flux per unit surface area through the inner wall and S_w is the perimeter of the heated domain. The internal energy E is given as: $E{=}(\bar{\rho}\bar{e} - \bar{p}) \cdot A$, which is measured in [J/m].

3.2. Hydraulic closure laws

Closure laws in relation to the momentum equation is presented here. The axial shear stress is modelled by for example the Van Driest mixing length theory, see [9]:

$$\begin{aligned}\tau_s &= -\frac{\partial}{\partial z}\left(\rho \bar{u'v'}\right) \\ &\approx l^2 \bar{\rho} \frac{\partial u^2}{\partial z^2}\end{aligned} \tag{5}$$

and is used as an damping in the solution domain where we experienced transients initiated by large gradients in the density (compressibility). This is only applied for a restricted domain where the steam quality $x \in$ [-0.02,0.02]. The corresponding wall shear stress is given by

$$\begin{aligned}\tau_w &= f_w \bar{\rho} \frac{u \cdot |u|}{2} \\ &= f_w \frac{G \cdot |G|}{2\bar{\rho}}\end{aligned} \tag{6}$$

The term f_w is the dimensionless friction coefficient based on the single phase frictional coefficient in heated rifled tubes: $f_w = \frac{a}{Re^b} + c$. In table (1) we propose coefficients given by [1], for different rifled profiles. In [3] the same formulation of f_w is used and the author has for specific rifled pipes reported an absolute relative error less than 6.3 %.

Table 1. Algebraic relations of f_w for different profiles. [1]

type	RR6	RR5	RR4	RR2
a	1702	0.56	16.26	1.65
b	1.18	0.32	0.71	0.44
c	0.032	0.01309	0.01509	0.02344

In the two-phase region the friction factor is adjusted according to a two-phase multiplier, formulated by [10]. In that case f_w is based on fluid properties for saturated liquid. The model that is based on [10] calculates the two phase multiplier as:

$$\phi^2 = 1 + B \cdot x \cdot \left(\frac{\rho_l}{\rho_f} - 1\right) \tag{7}$$

Where the coefficient B is:

$$B = 1.58 - 0.47\frac{p}{p_c} - 0.11 \cdot \left(\frac{p}{p_c}\right)^2 \tag{8}$$

Note that the critical pressure (p_c) is 221.2 [bar] for water/steam. B is adjustment as: B = B - (B - 1)·(10· x - 9). The correlation of (7) is compared to the well known and more computation intensive model of Friedel and is illustrated in figure (2).

3.3. Pipe Wall Model

The heat transfer processes from a combustion process (radiation and convection) to the water and steam circuit in a power plant, is using the pipe wall as the transfer median, to transport the energy from the furnace to the cooling media, in this case water / steam flowing in the panel wall. The solution of problems involving heat conduction in solids can, in principle, be reduced to the solution of a single differential equation, by Fourier's law. The equation can be derived by making a thermal energy balance on a differential volume element in the solid. A volume element for the case of conduction only in the z-direction is illustrated in figure (3).

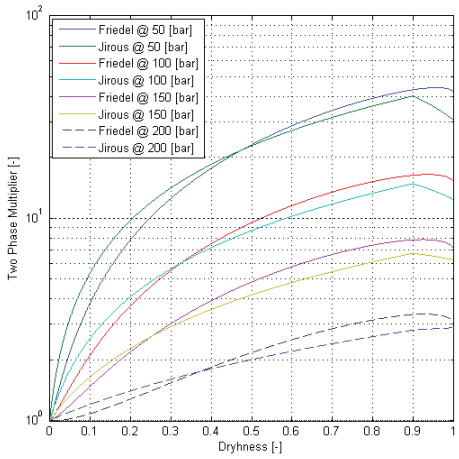

Fig. 2. Comparison of two-phase-multipliers of Jirous and Friedel.

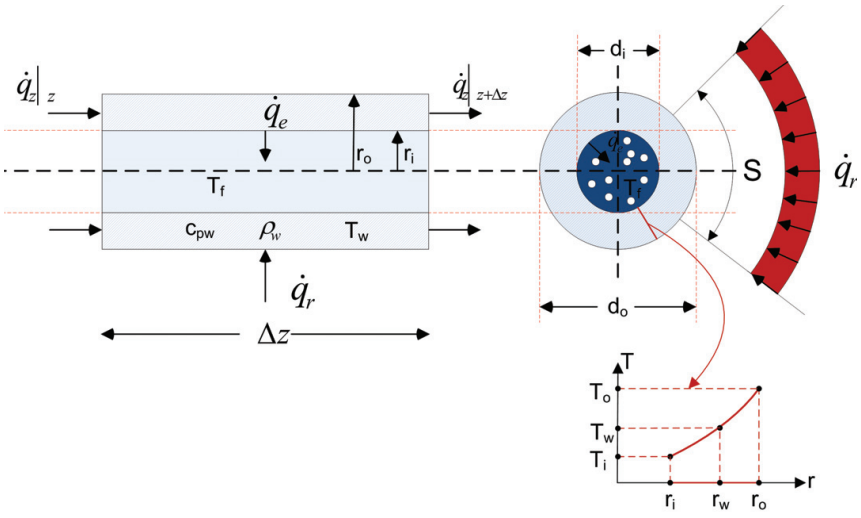

Fig. 3. Energy transfer and heat flow terms on a slice of a pipe wall element.

The balance equation becomes:

$$\frac{\partial T_w}{\partial t} = \alpha \frac{\partial^2 T_w}{\partial z^2} + \frac{\dot{q}_r}{\rho_w C_{pw}} \frac{S}{A_c} - \frac{\dot{q}_e}{\rho_w C_{pw}} \frac{d_i \pi}{A_c}, \quad z \in [0, l_z] \wedge t \geq 0 \tag{9}$$

where C_{pw} and ρ_w are the heat capacity and the density of the pipe wall and $A_c = \pi(r_o^2 - r_i^2)$ is the cross section area of the pipe wall. T_w is the mean wall temperature forced by the heat fluxes $\dot{q}_r$ and $\dot{q}_e$ expressing the heat flux from the furnace and the heat flux to the cooling fluid respectively.

Hence we can summarize the *system of balance laws* (SBL), given by (1), (2), (4) and (9), into a compact vector notation, given by:

$$\frac{\partial \Phi(z,t)}{\partial t} + \frac{\partial f(\Phi(z,t))}{\partial z} = \mathbf{g}(\Phi(z,t)) + \mathbf{h}(\frac{\partial \Phi}{\partial z}, \Phi(z,t)), \quad \Phi \in R^m, m = 4, \quad t \geq 0 \wedge \quad z \in \Omega \tag{10}$$

where the dependent variable Φ and the flux vector $\mathbf{f}$ are given as

$$\Phi = \begin{pmatrix} \bar{\rho}A \\ \dot{m} \\ E \\ T_w \end{pmatrix}, \quad f(\Phi) = \begin{pmatrix} \dot{m} \\ \frac{\dot{m}^2}{\bar{\rho}A} + pA \\ \frac{(E+pA)\dot{m}}{\bar{\rho}A} \\ 0 \end{pmatrix}$$

and the source and diffusion vectors are given as:

$$\mathbf{g}(\Phi) = \begin{pmatrix} 0 \\ p\frac{\partial A}{\partial z} - \bar{\rho}gA\cos\theta - \sqrt{\frac{\pi}{A}}f_w\frac{\dot{m}|\dot{m}|}{\bar{\rho}A} \\ S_w q_w'' - \dot{m}g\cos(\theta) \\ \alpha\frac{\partial^2 T_w}{\partial z^2} + \frac{\dot{q}_r}{\rho_w C_{pw}}\frac{S}{A_c} - \frac{\dot{q}_e}{\rho_w C_{pw}}\frac{d_i\pi}{A_c} \end{pmatrix} \text{ and } \mathbf{h}(\Phi) = \begin{pmatrix} 0 \\ \frac{l^2 S_w}{\bar{\rho}A^3}\frac{\partial \dot{m}^2}{\partial z^2} \\ 0 \\ \alpha\frac{\partial^2 T_w}{\partial z^2} \end{pmatrix}$$

Here the dependent variables are $\bar{\rho}$, $\dot{m}$, E and T_w meaning the fluid density, mass flow, total energy of the conserved fluid and wall mean temperature respectively. The pressure can be determined iteratively by water steam tables: p=$p(E, \rho)$. The source term $\mathbf{g}$ consists of both source/sink terms and the diffusion term $\mathbf{h}$ includes contributions from the mixing length eddy viscosity (5), working as a damping term in the vicinity of x=0, and the thermal diffusion in the pipe wall as well.

3.4. Constitutive relations for the heat pipe model

For isotropic materials, we introduce the thermal diffusivity given by: $\alpha = \frac{k_w}{\rho_w C_{pw}}$ given in $[m^2/s]$, which in a sense is a measure of thermal inertia and expresses how fast heat diffuses through a piece of solid. For a typical panel wall, the thermal diffusivity is approximately $1.98 \cdot 10^{-6}$ $[m^2/\mathrm{s}]$ at $200°C$, see [11]. The radiation from the furnace to the pipe surface is given by the heat flux $\dot{q}_r$. The heat flux $\dot{q}_e$ represents the convective heat transfer between the pipe wall inner surface and the flowing fluid in the pipe, and is given as: $\dot{q}_e$=$h_t(T_w - T_f)$, where h_t is the convective heat transfer coefficient and $T_w - T_f$ is the driving temperature difference, which is positive for boiling. For isotropic materials (pipe wall), we have expressions for specific heat capacity C_{pw}, heat conductivity k_w and density ρ_w as function of temperature in Kelvin from [11] and [12].

A simple, fast and robust model of the heat transfer in film boiling, is given by [13]. The heat transfer coefficient h_{fb} is given as

$$h_{fb} = c_f \dot{q}_r^{\,0.673} \quad [W/m^2K] \tag{11}$$

where the coefficient c_f is given by the below expression, which is a function of the saturation temperature (T_s), measured in $[^oC]$

$$c_f = \frac{0.06136}{\left[1 - (\frac{T_s}{378.64})^{0.0025}\right]^{0.73}} \tag{12}$$

The single phase laminar heat transfer coefficient (h_s) is calculated from

$$\begin{aligned} Nu_s &= \frac{h_s d_i}{k_f} \\ &= 4.36 \end{aligned} \tag{13}$$

and is valid for $L/d_i > 50$ and $\frac{d_i G}{\mu} < 2000$. For turbulent single phase flow and $\frac{d_i G}{\mu} > 10{,}000$ we use

$$\begin{aligned} Nu_s &= \frac{h_s d_i}{k_f} \\ &= 0.023\left(\frac{d_i G}{\mu_l}\right)^{0.8}\left(\frac{c_p \mu_f}{k_f}\right)^{1/3} \end{aligned} \tag{14}$$

The total heat transfer coefficient is given by (15), and consists of two contributions; one from the convective heat transfer boundary layer associated to the flowing fluid inside the heat pipe and one that relates to conduction through the pipe wall material.

$$h = \frac{1}{\frac{1}{h_c} + \frac{r_i}{k_w} \cdot \ln(r_w/r_i)} \tag{15}$$

where h_c is expressing the heat transfer coefficient due to the thermal boundary on the inner side of the pipe wall and r_w is defined by $T_w = T_r(r_w)$. Since we use the calculated average wall tube temperature as driver in the calculation of the total heat transport to the fluid, we must know r_w.

Due to the knowledge of radial conduction in the pipe, we use a simple analytical wall temperature profile, for estimating the inner wall temperature, expressed by the averaged wall temperature (T_w), based on the heat transfer through the isotropic pipe wall to the flowing fluid. Let $T_r(r)$ represent the radial temperature distribution by

$$\begin{aligned} T_r(r) &= \frac{T_i - T_o}{\ln(\frac{r_i}{r_o})} \ln(\frac{r}{r_o}) + T_o \\ &= a_0 \ln(\frac{r}{r_o}) + T_o \end{aligned} \tag{16}$$

where r is the pipe radius with suffix (i=inner) and (o=outer). This temperature profile for radial isotropic pipes, is the steady state solution to the 1D Fourier's law of heat transfer. Hence, for small values of the thermal diffusivity, the averaged wall temperature can reasonable be estimated by:

$$\begin{aligned} T_w &= \frac{1}{A_c} \int_{r_i}^{r_o} 2\pi r \cdot T_r(r) dr \\ &= \frac{2\pi}{A_c} \left[a_0 \left[x^2 \ln(x)/2 - x^2/4 \right]_{r_i}^{r_o} - a_0 \ln(r_o) \left[x^2/2 \right]_{r_i}^{r_o} \right] + T_o \cdot \left[x^2/2 \right]_{r_0}^{r_1} \\ &= a_1 \cdot T_i + (1 - a_1) \cdot T_o \end{aligned} \tag{17}$$

where a_1 is given by

$$a_1 = \frac{r_i^2}{r_i^2 - r_o^2} - \frac{1}{2ln(r_i/r_o)} \tag{18}$$

Hence the entire heat transfer can be estimated for the temperature range in between the wall mean temperature (T_w) and the fluid mixture temperature (T_f), which is assumed homogeneous and well mixed with a temperature boundary layer represented by h_c. The one dimensional pipe wall model does only consists of axial heat transfer term, and have no spatial resolution in the radial dimension.
The inner wall temperature can be determined by use of the equation for pure conduction through the pipe:

$$\dot{q}_r S = \frac{2\pi k_w}{\ln(r_o/r_i)}(T_o - T_i) = \frac{2\pi k_w}{\ln(r_w/r_i)}(T_w - T_i). \tag{19}$$

Hence we find T_i by insertion (17) in (19):

$$T_i = T_w + \frac{q_r S \ln(\frac{r_o}{r_i})(1 - a_1)}{2\pi k_w} \tag{20}$$

and hence r_w in (15) can be determined from (17) and (20) and we find

$$h = \frac{1}{\frac{1}{h_c} + \frac{r_i(a_1 - 1)}{k_w} \cdot \ln(r_i/r_o)} \tag{21}$$

where h_c is smoothed in-between h_s and h_{fb} depending of the dryness of the fluid. Additionally h_c is adjusted on the basis of a smoothing between laminar and turbulent single phase flow as well as for two-phase

flow. The smoothing function is based on a third order function and the associated slopes are determined numerically. Note that the heat flux is positive for $T_i > T_f$. Using the model parameters from table (2) we find a_1=0.423 and the temperature fall above the thermal boundary is: T_o-T_i=27.9 [^oC], which gives a temperature gradient in the pipe wall of dT/dr= 3930 [$^oC/m$] for a heat flux of q_e=100 [kW/m^2]. The heat conduction in the material is the most significant barrier for an effectively cooling of the tube wall.

3.5. Auxiliary relations

The Water / Steam library IAPWS 97 by [14] is used as a general equation of state, to derive thermodynamic properties of water and steam. In some relations we need a relationship for the pressure as function of density and enthalpy: p=p(ρ,$\bar{h}$). This can be done by a Newton Rapson solver. To improve the computational speed, we recommended to use a look up table within at least 200000 nodes, based on bilinear interpolation, see [7]. Here we create a look up table to ensure water/steam properties within an accuracy below 0.3% as an absolute maximum, due to [7]. Note that the density is smoothed in the vicinity of the saturation line of water to avoid heavy gradients and discontinuities.

3.6. Boundary conditions

It is convenient to use boundary conditions to the model which are physically measurable. Therefore, the following properties are used as boundary conditions; velocity (u), pressure (p) and enthalpy (h). This allows us to rewrite the boundary conditions to those properties, which are described by Φ, see (10). The Dirichlet boundary conditions are given by (22) and the corresponding Neumann boundary conditions are obtained by applying the chain rule for differensation of complex functions, and are given by (23).

$$\text{Dirichlet BC}: \begin{cases} \rho A \\ \rho A u \\ \rho A(h + \frac{u^2}{2} + gz\cos(\theta)) - pA \\ \rho T_w \end{cases} \tag{22}$$

where θ is the angle of the pipe inclination with respect to the horizontal.

$$\text{Neumann BC}: \begin{cases} A\frac{\partial \rho}{\partial z} + \rho\frac{\partial A}{\partial z} \\ uA\frac{\partial \rho}{\partial z} + \rho u\frac{\partial A}{\partial z} + \rho A\frac{\partial u}{\partial z} \\ \frac{\partial(\rho A)}{\partial z}\left[h + \frac{u^2}{2} + gz\cos(\theta)\right] + \rho A\left[\frac{\partial h}{\partial z} + u\frac{\partial u}{\partial z} + g\cos(\theta)\right] - A\frac{\partial p}{\partial z} - p\frac{\partial A}{\partial z} \\ \frac{\partial T_w}{\partial z} \end{cases} \tag{23}$$

3.7. Numerical Solution of Hyperbolic Transport Equation

Let us consider a hyperbolic *system of balance laws* (SBL) formulated on a compact vector notation, given by (10), where Φ is the unknown m-dimensional vector function, $\mathbf{f}(\Phi)$ the flux vector, $\mathbf{g}(\Phi)$ a continuous source vector function on the right hand side (RHS), with z as the single spatial coordinate and t the temporal coordinate, Ω is partitioned in n_z non-overlapping cells: $\Omega = \cup_{i=1}^{n_z} I_i \in [0, l_z]$, where l_z is a physically length scale in the spatial direction. This system covers the general transport and diffusion equations used in many physical aspects and gas dynamics as well. The SBL system is subjected to the initial condition:

$$\Phi(z, 0) = \Phi_0(z) \tag{24}$$

and the below boundary conditions given by:

Dirichlet boundaries:

$$\Phi(z = 0, t) = \Phi_A(t) \text{ and } \Phi(z = l_z, t) = \Phi_B(t) \tag{25}$$

and

Neumann boundaries:

$$\frac{\partial \Phi(z = 0, t)}{\partial z} = \frac{\partial \Phi_A(t)}{\partial z} \text{ and } \frac{\partial \Phi(z = l_z, t)}{\partial z} = \frac{\partial \Phi_B(t)}{\partial z} \tag{26}$$

The above boundary conditions can be given by a combination of each type of boundaries. The Dirichlet condition is only specified, if we have ingoing flow conditions at the boundaries.

The development of a general numerical scheme for solving *PDE*'s may serve as universal finite-difference method, for solving non-linear convection-diffusion equations in the sense that they are not tied to the specific eigenstructure of a problem, and hence can be implemented in a straightforward manner as black-box solvers for general conservation laws and related equations, governing the spontaneous evolution of large gradient phenomena. The developed non-staggered grid is suitable for the modelling of transport of mass, momentum and energy and is illustrated in figure (4),where the cell $I_j = \left[z_{j-1/2}, z_{j+1/2}\right]$ has a cell width Δz and Δt the time step.

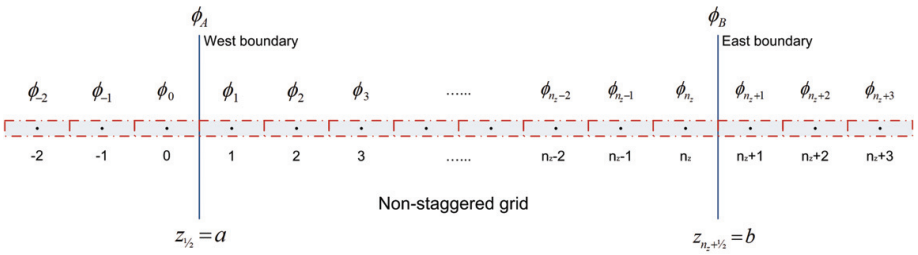

Fig. 4. The computational grid $[0,l_z]$ is extended to a set of ghost points for specifying boundary conditions.

In this section, we review the central fifth order WENO schemes in one spatial dimension, developed by [15] with uses modified weight functions outlined by [16]. We recall the construction of the non-staggered central scheme for conservation laws. The starting point for the construction of the semi-discrete central-upwind scheme for (10) can be written in the following form:

$$\frac{d\Phi_j(t)}{dt} = -\frac{1}{\Delta z}\left[F_{j+1/2} - F_{j-1/2}\right] + S_j(\Phi). \tag{27}$$

where the numerical fluxes $F_{j+1/2}$ are given by

$$F_{j+1/2} = \frac{a^+_{j+1/2} f(\Phi^-_{j+1/2}) - a^-_{j+1/2} f(\Phi^+_{j+1/2})}{a^+_{j+1/2} - a^-_{j+1/2}} + \frac{a^+_{j+1/2} a^-_{j+1/2}}{a^+_{j+1/2} - a^-_{j+1/2}}\left[\Phi^+_{j+1/2} - \Phi^-_{j+1/2}\right]. \tag{28}$$

Notice that the accuracy of this scheme is determined by the accuracy of the reconstruction of Φ and the ODE solver. In this chapter the numerical solutions of (27) is advanced in time by mean of third order TVD Runge-Kutta method described by [17]. The local speeds of propagation can be estimated by

$$a^+_{j+1/2} = \max\left\{\lambda_N\left(\frac{\partial f(\Phi^-_{j+1/2})}{\partial\Phi}\right), \lambda_N\left(\frac{\partial f(\Phi^+_{j+1/2})}{\partial\Phi}\right), 0\right\}, \tag{29}$$
$$a^-_{j+1/2} = \min\left\{\lambda_1\left(\frac{\partial f(\Phi^-_{j+1/2})}{\partial\Phi}\right), \lambda_1\left(\frac{\partial f(\Phi^+_{j+1/2})}{\partial\Phi}\right), 0\right\}.$$

with $\lambda_1 < ... \lambda_N$ being the eigenvalues of the Jacobian given by $\mathbf{J}=\frac{\partial f(\Phi(z,t))}{\partial\Phi}$. Here, $\Phi^+_{j+1/2}=p_{j+1}(z_{j+1/2})$, and $\Phi^-_{j+1/2}=p_j(z_{j+1/2})$ are the corresponding right and left values of the piecewise polynomial interpolant $\{p_j(z)\}$ at the cell interface $z=z_{j+1/2}$.

To derive an **e**ssentially **n**on-**o**scillatory reconstruction (ENO), we need to define three supplementary polynomials $(\tilde{\Phi}_1, \tilde{\Phi}_2, \tilde{\Phi}_3)$, approximating $\Phi(z)$ with a lower accuracy on I_i. Thus, we define the polynomial of second-order accuracy, $\tilde{\Phi}_1(z)$, on the reduced stencil S_1: (I_{i-2}, I_{i-1}, I_i), $\tilde{\Phi}_2(z)$ is defined on the stencil S_2: (I_{i-1}, I_i, I_{i+1}), whereas $\tilde{\Phi}_3(z)$ is defined on the stencil S_3: (I_i, I_{i+1}, I_{i+2}). Now, we have to invert a 3×3 linear system for the unknown coefficients $\{a_j\}$, $j \in \{0, ..., 2\}$, defining $\tilde{\Phi}_1, \tilde{\Phi}_2, \tilde{\Phi}_3$. Once again, the constants determining the interpolation are pre-computed and stored before solving the PDEs. When the grid is uniform, the values of the coefficients for $\tilde{\Phi}_1, \tilde{\Phi}_2$ and $\tilde{\Phi}_3$ can be explicitly formulated. It is left to the reader to read [15] or [6] for further details about determining the coefficients in the reconstructed polynomials. To implement a specific solution technique, we extend the principle of the central WENO interpolation defined in [18]. First, we construct an ENO interpolant as a convex combination of polynomials that are based on different discrete stencils. Specifically, we define in the discrete cell I_i:

$$\tilde{\Phi}^i(z) \equiv \sum_j w_j \times \tilde{\Phi}_j(z), \quad \sum_j w_j = 1 \quad \text{for} \quad w_j \geq 0 \ \text{ for} j \in \{1, .., 4\}, \tag{30}$$

and $\tilde{\Phi}_1$, $\tilde{\Phi}_2$ and $\tilde{\Phi}_3$ are the previously defined polynomials. $\tilde{\Phi}_4$ is the second-order polynomial defined on the central stencil S_5: $(I_{i-2}, I_{i-1}, I_i, I_{i+1}, I_{i+2})$ and is calculated such that the convex combination in (30), will be fifth-order accurate in smooth regions. Therefore, it must verify:

$$\tilde{\Phi}_{opt}(z) = \sum_j C_j \times \tilde{\Phi}_j(z) \ \ \forall z \in I_i, \quad \sum_j C_j = 1 \quad \text{for} \quad C_j \geq 0 \ \text{ for } j \in \{1, .., 4\}, \tag{31}$$

The calculation of $\tilde{\Phi}^+_{i+1/2}$,$\tilde{\Phi}^-_{i+1/2}$ produces the following simplified result:

$$\begin{aligned}\tilde{\Phi}^+_{i+1/2} =& \left(-\frac{7}{120}w_4 - \frac{1}{6}w_1\right)\bar{\Phi}_{i-2} + \left(\frac{1}{3}w_2 + \frac{5}{6}w_1 + \frac{21}{40}w_4\right)\bar{\Phi}_{i-1} \\ &+ \left(\frac{5}{6}w_2 + \frac{1}{3}w_1 + \frac{11}{6}w_3 + \frac{73}{120}w_4\right)\bar{\Phi}_i + \left(-\frac{1}{6}w_2 - \frac{7}{6}w_3 - \frac{7}{120}w_4\right)\bar{\Phi}_{i+1} + \left(\frac{1}{3}w_3 - \frac{1}{60}w_4\right)\bar{\Phi}_{i+2}\end{aligned} \tag{32}$$

$$\begin{aligned}\tilde{\Phi}^-_{i+1/2} =& \left(-\frac{1}{60}w_4 + \frac{1}{3}w_1\right)\bar{\Phi}_{i-2} + \left(-\frac{1}{6}w_2 - \frac{7}{6}w_1 - \frac{7}{120}w_4\right)\bar{\Phi}_{i-1} \\ &+ \left(\frac{5}{6}w_2 + \frac{1}{3}w_3 + \frac{11}{6}w_1 + \frac{73}{120}w_4\right)\bar{\Phi}_i + \left(\frac{1}{3}w_2 - \frac{5}{6}w_3 + \frac{21}{40}w_4\right)\bar{\Phi}_{i+1} + \left(-\frac{1}{6}w_3 - \frac{7}{120}w_4\right)\bar{\Phi}_{i+2}\end{aligned} \tag{33}$$

To calculate the weights w_j, j$\in \{1, 2, 3, 4\}$, we review another technique to improve the classical smoothness indicators to obtain weights that satisfy the sufficient conditions for optimal order of accuracy. It is well known from [15], that the original WENO is fifth order accurate for smooth parts of the solution domain

except near sharp fronts and shocks. The idea here is taken from [16] and uses the hole five point stencil S_5 to define a new smoothness indicator of higher order than the classical smoothness indicator IS_i. The general form of indicators of smoothness are defined in [18]:

$$IS^i_j = a_1^2\Delta z^2 + \frac{13}{3}a_2^2\Delta z^4 + O(\Delta z^6), \quad j \in \{1,2,3\}. \tag{34}$$

and the form of IS^i_4 is given by [15]:

$$IS^i_4 = a_1^2\Delta z^2 + \left[\frac{13}{3}a_2^2 + \frac{1}{2}a_1a_3\right]\Delta z^4 + O(\Delta z^6). \tag{35}$$

where a_0 and a_1 can be determined by solving the coefficients to reconstructed polynomial $\tilde{\Phi}_4$ on S_5. For estimating the weights w_k, k $\in \{1,2,3,4\}$, we proceed as follows: Define

$$IS^*_k = \frac{IS_k + \epsilon}{IS_k + \epsilon + \tau_5} \tag{36}$$

where IS_k, k $\in \{1,2,3\}$ are given by (34), IS_4 given by (35) and τ_5=$|IS_1 - IS_3|$. The constant ϵ is a small number. In some articles $\epsilon \approx$ from $1\cdot 10^{-2}$ to $1\cdot 10^{-6}$, see [18]. Here we use much smaller values of ϵ for the mapped and improved schemes in order to force this parameter to play only its original role of not allowing vanishing denominators at the weight definitions. The weights w_k are defined as:

$$w_k = \frac{\alpha^*_k}{\sum_{l=1}^4 \alpha^*_l}, \quad \alpha^*_k = \frac{C_k}{IS^*_k}, \quad k \in \{1,2,3,4\} \tag{37}$$

The constants C_j represent ideal weights for (30). As already noted in [18], the freedom in selecting these constants has no influence on the properties of the numerical stencil; any symmetric choice in (31), provides the desired accuracy for $\tilde{\Phi}_{opt}$. In what follows, we make the choice as in [15]:

$$C_1 = C_3 = 1/8, C_2 = 1/4 \text{ and } C_4 = 1/2. \tag{38}$$

3.7.1. Convection-Diffusion equations

Let us again consider the general System of Conservation Laws (SCL), given by equation (10), where the source term g is replaced by a dissipative flux:

$$\frac{\partial\Phi(z,t)}{\partial t} + \frac{\partial f(\Phi(z,t))}{\partial z} = \frac{\partial}{\partial z}\left(g(\Phi(z,t), \frac{\partial\Phi}{\partial z})\right), \quad t \geq 0, \quad z \in \Omega \tag{39}$$

The gradient of g is formulated on the compressed form: $g(\Phi, \frac{\partial\Phi}{\partial z})_z$ as a nonlinear function $\neq$ zero. This term can degenerate (39) to a strongly parabolic equation, admitting non smooth solutions. To solve it numerically is a highly challenging problem. Our fifth-order semi-discrete scheme, (27)-(28), can be applied to (10) in a straightforward manner, since we can treat the hyperbolic and the parabolic parts of (39) simultaneously. This results in the following conservative scheme:

$$\frac{d\Phi_j(t)}{dt} = -\frac{1}{\Delta z}\left[F_{j+1/2} - F_{j-1/2}\right] + G_j(\Phi, t). \tag{40}$$

Here $F_{j+1/2}$ is our numerical convection flux, given by equation (28) and G_j is a high-order approximation to the diffusion flux $g(\Phi, \frac{\partial\Phi}{\partial z})_z$. Similar to the case of the second-order semi-discrete scheme of [19], operator splitting is not necessary for the diffusion term. By using a forth order central differencing scheme, outlined by [20], we can apply our fifth-order semi-discrete scheme, given by (27) and (28), to the parabolic equation (10), where $g(\Phi, \frac{\partial\Phi}{\partial z})_z$ is a function of ϕ and its derivative in space (diffusion). The diffusion term can be expressed by a high-order approximation:

$$G_j(t) = \frac{1}{12\Delta z}\left[-G(\Phi_{j+2}, (\Phi_z)_{j+2}) + 8\cdot G(\Phi_{j+1}, (\Phi_z)_{j+1}) - 8\cdot G(\Phi_{j-1}, (\Phi_z)_{j-1}) + G(\Phi_{j-2}, (\Phi_z)_{j-2})\right] \tag{41}$$

where

$$(\Phi_z)_{j+2} = \frac{1}{12\Delta z}\Big[25\Phi_{j+2} - 48\Phi_{j+1} + 36\Phi_j - 16\Phi_{j-1} + 3\Phi_{j-2}\Big], \tag{42}$$
$$(\Phi_z)_{j+1} = \frac{1}{12\Delta z}\Big[3\Phi_{j+2} + 10\Phi_{j+1} - 18\Phi_j + 6\Phi_{j-1} - \Phi_{j-2}\Big],$$
$$(\Phi_z)_{j-1} = \frac{1}{12\Delta z}\Big[\Phi_{j+2} - 6\Phi_{j+1} + 18\Phi_j - 10\Phi_{j-1} - 3\Phi_{j-2}\Big] \quad \text{and}$$
$$(\Phi_z)_{j-2} = \frac{1}{12\Delta z}\Big[-3\Phi_{j+2} + 16\Phi_{j+1} - 36\Phi_j + 48\Phi_{j-1} - 25\Phi_{j-2}\Big]$$

and Φ_j are the point-values of the reconstructed polynomials.

3.7.2. Source Term

Next, let us consider the general SCL given by (10) and restrict our analysis to the source term of the form: $g(\Phi, t)$ as a continuous source vector function $\neq$ zero. By integrating system (10) over a finite space-time control volume $I_i, \Delta t$ one obtains a finite volume formulation for the system of balance laws, which usually takes the form

$$\Phi(z,t)_j^{n+1} = \Phi(z,t)_j^n - \frac{\Delta t}{\Delta z}\Big(f_{j+1/2} - f_{j-1/2}\Big) + \Delta t g(z,t)_j, \quad t \geq 0, \quad z \in \Omega \tag{43}$$

The integration of (10) in space and time gives rise to a temporal integral of the flux across the element boundaries $f_{j+1/2}$ and to a space-time integral g_i of the source term inside I_i. In practice, one must replace the integrals of the flux and the source in (43) by some suitable approximations, that is to say one must choose a concrete numerical scheme. For SBL a numerical source must be chosen. Here, not only the three classical properties are required, but some additional properties are needed for the global numerical scheme: It should be well-balanced, i.e. able to preserve steady states numerically. It should be robust also on coarse grids if the source term is stiff.

3.7.3. Boundary conditions for Non-staggered grid

For a system of m equations we need a total of m boundary conditions. Typically some conditions must be prescribed at the inlet boundary (z=a) and some times at the outlet boundary (z=b). How many are required at each boundary depends on the number of eigenvalues of the Jacobian $\mathbf{A}$ that are positive and negative, respectively and whether the information is marching in or out for the boundaries.

By extending the computational domain to include a few additional cells on either end of the solution domain, called ghost cells, whose values are set at the beginning of each time step in some manner that depends on the boundary condition. In figure (4) is illustrated a grid with three ghost cells at each boundary. The idea behind the ghost point approach is to express the value of the solution at control points outside the computational domain in terms of the values inside the domain plus the specified boundary condition. This allows the boundary condition to be imposed by a simple modification of the internal coefficients using the coefficients of the fictitious external point. This can result in a weak imposition of the boundary condition, where the boundary flux not exactly agree with the boundary condition. By establishing a Taylor expansion around the boundary a or (b), we can express a relationship between the ghost points outside the solution domain and grid points inside the domain. For further details see [6].

3.7.4. Time discretization

The semi-discrete ODE given by (27) is a time dependent system, which can be solved by a TVD Runge-Kutta method presented by [17]. The optimal third order TVD Runge-Kutta method is given by

$$\Phi_j^{(1)} = \Phi_j^n + \Delta t L(\Phi_j^n), \tag{44}$$
$$\Phi_j^{(2)} = \frac{3}{4}\Phi_j^n + \frac{1}{4}\Phi_j^{(1)} + \frac{1}{4}\Delta t L(\Phi_j^{(1)}),$$
$$\Phi_j^{n+1} = \frac{1}{3}\Phi_j^n + \frac{2}{3}\Phi_j^{(2)} + \frac{2}{3}\Delta t L(\Phi_j^{(2)}), \quad \text{for } j \in [1, n_z].$$

The stability condition for the above schemes is

$$CFL = \max\left(u_j^n \frac{\Delta t}{\Delta z}\right) \leq 1, \tag{45}$$

where CFL stands for the *Courant-Friedrichs-Lewy* condition and u_j^n is the maximum propagation speed in cell I_j at time level n.

4. Results

In this section we setup and solve a homogeneous boiler tube model for two cases; one without IRBT and one with Siemens RR5 pipes. The governing equations are defined by the system of balance laws given by equation (10) including the pipe wall model given by equation (9) for the solution domain given by $\Omega \in [0,l_z]$.

4.1. Numerical setup

Three Dirichlet boundary conditions are applied for the hydraulic case and two Neumann boundaries are applied for the pipe wall model, given as zero gradients in the wall temperature at each pipe end (No heat loss). The intention is to model an evaporator, which can induce oscillations initiated by the compressibility, which arise as a result of a phase shift in the lower part of the evaporator. Therefore, we apply a constant downstream Dirichlet pressure boundary condition, that is corresponding to a stiff system, without any pressure absorption effects in the down stream turbine system due to compressibility. An analogy to this is a geyser, where there is a constant surface pressure and an intense heat absorption in the bottom region, whereby an oscillating pressure wave is initiated due to the compressibility of the fluid, caused by intense heat from the underground. Additionally we force the model with both a constant enthalpy and mass flux located on the upstream boundary, supplied by a constant heat flux along the entire heat pipe. The numerical scheme is the fifth order WENO scheme outlined in chapter (3.7) and consists of 400 computational points with CFL number of 0.8. The numerical scheme is tested for consistency and stability with respect to both a scalar- and a system of hyperbolic equations and has been successfully compared to analytical results from the literature as well as other published results. This work is outlined in [7].

The model is soft started in two steps, at t=0 [s] is the pure hydraulic model soft started during 4 seconds, without heat flux. After 10 seconds the heat flux is build-up during four seconds. This is done to avoid heavy shock waves moving forward and back in the entire solution domain. If the soft start period is reduced to only 1 second, heavy pressure oscillations occur. The soft start model is based on a third order theory [21], which gives a C^2 continuous sequence, which means zero gradients of the first derivative at both ends of the soft start period. The model data are listed below in table (2). The dynamic start-up process can be seen in figure (6), where the density is given in $[kg/m^3]$, pressure in [bar], Temperature in $[^oC]$, enthalpy in [kJ/kg] and mixture velocity in [m/s].

4.2. Model consistency

The model consists of 400 differential elements, thus ensuring a smooth continuous solution. By reducing the number of computational cells to only 50 elements, one would observe a more intensive standing wave at the entrance of two-phase region, which is due to intensive heating of the differential cell in the vicinity of the boiling zone, where we have an intensive negative slope in the density as function of the enthalpy, hence the density change becomes so violent that a pressure wave is established to ensure momentum balance. Using a CFL number higher than 1.0 is leading to instabilities due to the semi implicit scheme.

4.3. Simulation results - without IRBT

In figure (5) we illustrate the output results for each 25 sec. of simulation, referring to the solution of the full-scale evaporator at Skærkækværket unit 3 (SKV3) in Fredericia (Denmark), without IRBT. Here we have a tower boiler which consists of 4x56 parallel boiler tubes representing an entire mass flow of 90 [kg/s] flowing in 193.5 meter long heat pipes with an inclination of 12 degree. A steady state solution is obtained after approximately 250 seconds, and is depicted in figure (6) together with the initial conditions. The entire pressure drop and heat uptake fit (± 5 %) with steady state experiments performed at (SKV3). The simulation results shows how the state of the fluid gradually moves from the inlet condition, in the form of subcooled water, to the two phase zone, in which the boiling is starting, and finally reaches the super heating zone, where the dry steam is superheated to approximately 360 $[^oC]$. The pressure drop is fixed downstream in the form of a Dirichlet boundary condition, corresponding to measured pressure level from (SKV3). The Pressure distribution along the evaporator reflects different pressure loss models, the pressure

Table 2. Geometrical and numerical specifications. Data in parentheses are referring to simulation without IRBT.

Parameter	**Value**	**Unit**	**Parameter**	**Value**	**Unit**
Gravity (g)	9.81	[m/s^2]	Spatial start position	0.000	[m]
Spatial end position (L)	38.25 (193.40)	[m]	Inner diameter of pipe (d_i)	23.8	[mm]
Outer diameter of pipe (d_o)	38.0	[mm]	Heat conductivity in wall (k_w)	10.139	[w/mK]
Wall density (ρ_w)	7850.0	[kg/m^3]	Specific heat capacity of pipe wall (Cp_w)	527.21	[J/kg/K]
Heat flux ($\dot{q}_e$)	100.000	[W/m^2]	Wall roughness (λ)	1.0E-6	[m]
Initial Enthalpy - Inlet	1187.6988	[kJ/kg]	Initial Enthalpy - Outlet	1187.6988	[kJ/kg]
Initial Pressure - Inlet	92.3762	[Bar]	Initial Pressure - Outlet	92.3762	[Bar]
Initial Velocity - Inlet	0.0	[m/s]	Initial Velocity - Outlet	0.0	[m/s]
Pressure BC (Dirichlet - Outlet)	92.3762	[Bar]	Enthalpy BC (Dirichlet - Inlet)	1187.6988	[kJ/kg]
Velocity BC (Dirichlet - Inlet)	0.200(1.1711)	[m/s]	Simulation time	200.0	[s]
Output frequency	0.1	[s]	CFL number	0.80	[-]
Number of computational grids (N_p)	400	[-]	Riffle type	RR5 1.5994(No rifels)	[-]

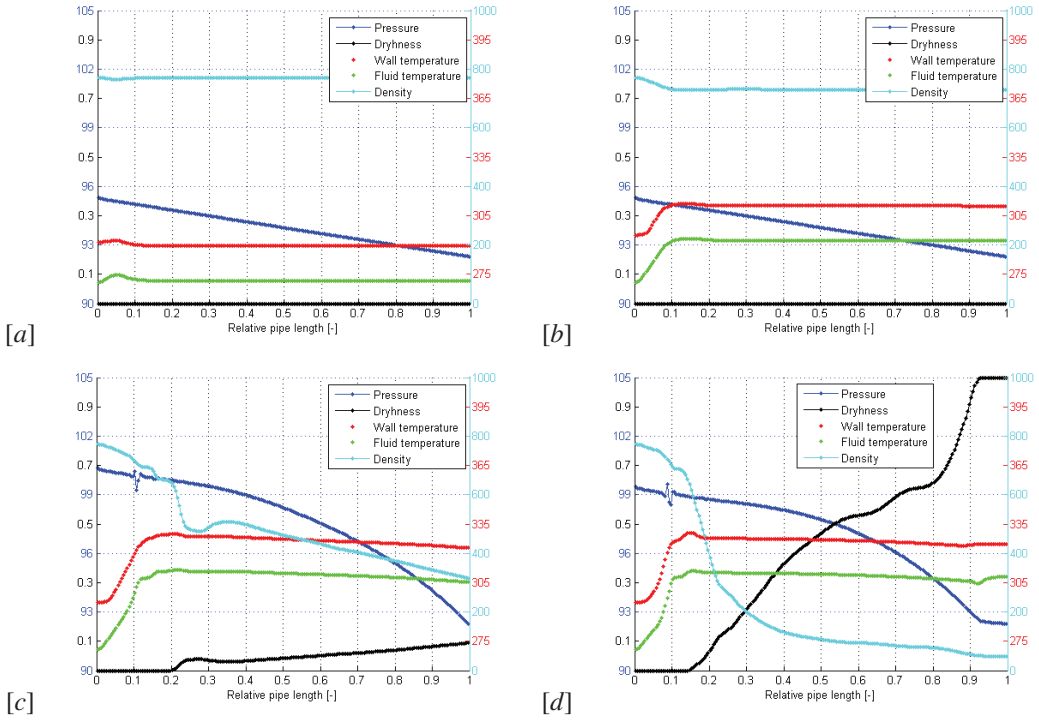

Fig. 5. Solution of SKV3 evaporator model without IRBT after (a):25, (b):50, (c):75 and (d):100 sec.

gradient of single and two-phase regions respectively. The pressure drop in the two-phase region involves the two phase multiplier, outlined in (7), which multiplies the pressure gradient with up to 16 times relative to the pressure gradient for saturated water. The inlet velocity is specified as an upstream Dirichlet boundary condition, and is soft started by use of the before mentioned smooth function, having a soft start period of four seconds. The super heated steam leaves the down stream boundary at steady state flow condition with a speed of app. 24 [m/s]. This ensures a smooth hydraulic flow condition of a cold evaporator. After words the heating is build up smoothly, applied by the same smoothing technique, so that undesirable thermal shock phenomena is reduced to a minimum. A standing pressure wave in the front of the boiling zone of the fluid is created by the very intense negative slope in the fluid density at the entrence to the two phase region. This

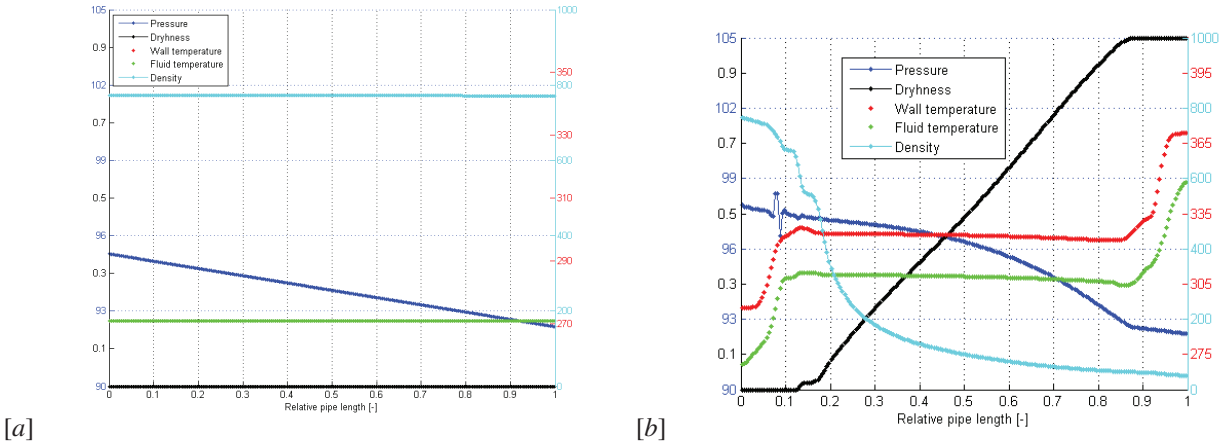

Fig. 6. Initial (a) and steady state solution (b) of SKV3 evaporator model without IRBT.

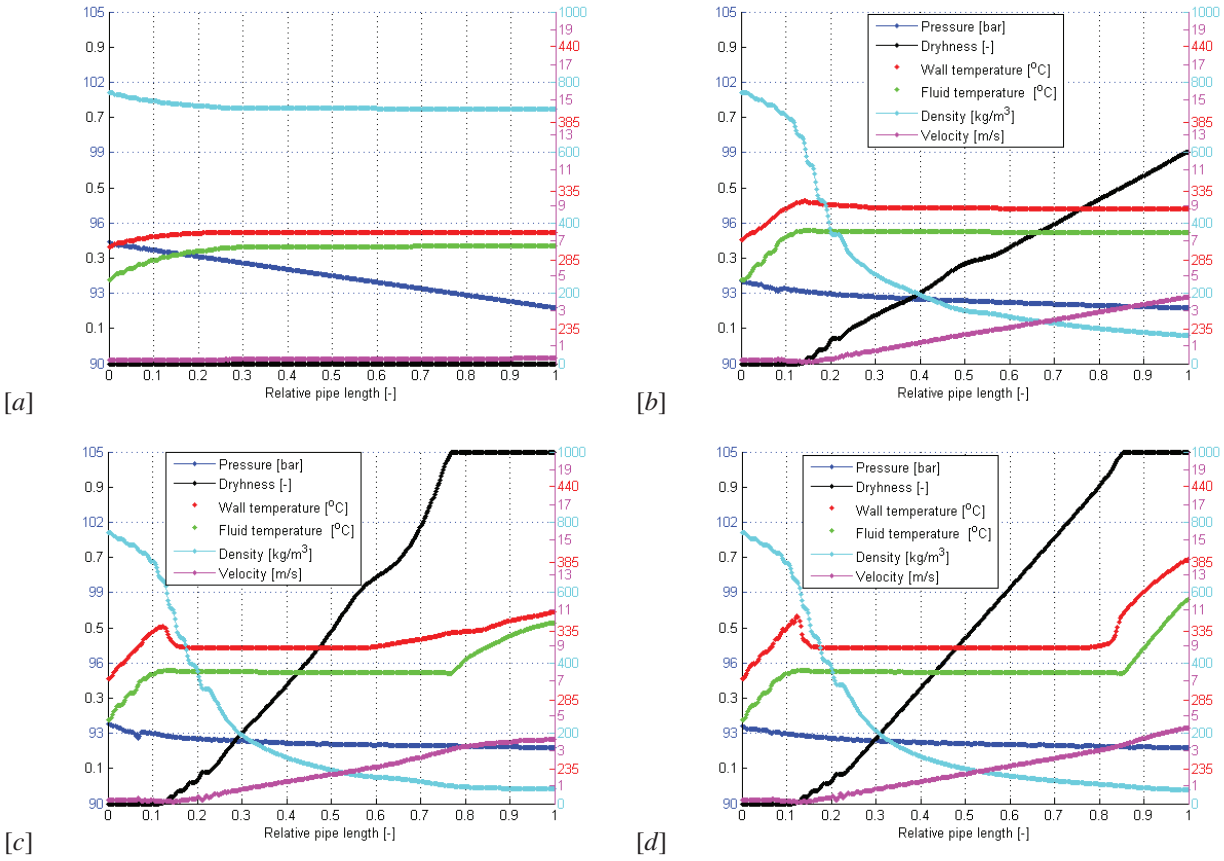

Fig. 7. Solution of Modified SKV3 vertical evaporator model with SLMF after (a):50, (b):100, (c):150 and (d):200 [s].

pressure-drop oscillations could occur, when there exists large upstream compressibility in the flow boiling system, see ([22], [23]). This phenomenon is increased in a vertical evaporator where the heating phase has

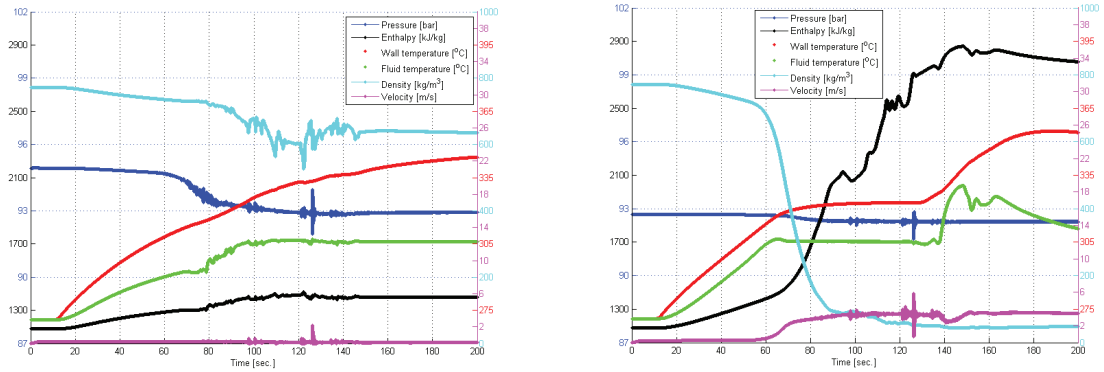

Fig. 8. Modified SKV3 vertical evaporator model with IRBT at station A(left) and B(right).

a heavy column of liquid to be transported out of the solutions area, which can initiate stability problems. This phenomenon occurs at low operating pressure in the evaporator or low firing, ie. heating the bottom of the evaporator. The dryness line in figure (5) expresses the mass based percentage of the steam flowing in the evaporator tube, not surprisingly, this process linearly corresponding to a constant heat flux along the tube.

Pressure-drop oscillations can be characterised as a secondary phenomenon of dynamic instability, which is triggered by a static instability phenomenon. Pressure-drop oscillations occur in systems having a compressible volume upstream of, or within, the heated section. Pressure-drop oscillations have been studied in considerable details by Maulbetsch [24] and Griffith [25], for sub cooled boiling of water, and by Stenning et al. [26], [27], for bulk boiling of freon-11. Maulbetsch and Griffith found that the instability was associated with operation on the negative sloping portion of the pressure-drop - flow curve.

4.4. Simulation results - with IRBT

By converting the SKV3 boiler to a system equipped by RR5 internal rifled boiler tubes (IRBT), this will normally lead to a complete redesign of both the furnace- and the evaporator system, but in this fictive case we use the same heat transfer area, despite the fact, that the IRBT considerably improve the heat transfer in the boiling zone. In this new setup, the length of the boiler tubes are reduced from 193.5 [m] to 38.25 [m] and the number of parallel tubes are increased from the original 4 x 56 to 4 x 270 parallel tubes. We have proved used a very low mass flux (corresponding to approx. 10% load), specifically to analyze the effects of the wall temperature distribution. It should be emphasized that this simulation event is a fictional setup and is rather a calculation example of what can happen in an evaporator tubes, if near zero flow momentarily occurs.

The vertical IRBT leads to an decrease in the mass flux, which is illustrated in (7) for instant pictures of 100, 150, 175 and 200 [s] of simulation. The wall temperature are varying in time and reach a peak while the flow locally is approaching zero, caused by local pressure oscillations initiated by the compressibility at the entrance of the two phase region. The bad cooling caused by near zero flow can have disastrous consequences for the pipe material and may ultimately lead to a meltdown of the evaporator tube. In practice, this is avoided by increasing the circulation through the evaporator. The pressure drop through the evaporator tube is unrealistically low, due to the very low mass flux (105 [kg/m^2s]). Normally, the mass flux of IRBT is approx. 1200 [kg/m^2s] at 100% load. In figure (8) is listed timeseries of the thermo hydraulic data at two stations located at A(z=$\frac{1}{8}l_z$) and B(z=$\frac{7}{8}l_z$). The thermo hydraulic conditions in station A is situated in the subcooled region while the station B is situated in the super heated region. Both stations are affected by the compressibility effect, initiated in the entrance to the boiling zone. Pressure waves are approaching up- and down stream due to the eigenvalues of the hyperbolic governing equations (λ_1=c, λ_2=u+c and λ_3=u-

c) where λ_i, i=1,3 is the eigenvalues and c is the local speed of sound for the two phase mixture. In the downstream station B we can also see minor slugs of enthalpy for t=100 [s], which also is referring to the compresibility phenomena.

4.5. Model consistency

The model consists of 400 differential elements, thus ensuring a smooth continuous solution. By reducing the number of computational cells to only 50 elements, one would observe a more intensive standing wave at the entrance of two-phase region, which is due to intensive heating of the differential cell in the vicinity of the boiling zone, where we have an intensive negative slope in the density as function of the enthalpy, hence the density change becomes so violent that a pressure wave is established to ensure momentum balance. Using a CFL number higher than 1.0 is leading to instabilities due to the semi implicit scheme.

4.6. Discussion

The two simulation cases shows two very different thermo hydraulic conditions. The simulation of (SKV3) without IRBT is verified against steady state measurements and the pressure drop and heat uptake fits quite well (± 5 %). The case of IRBT does not reach a steady state condition after 200 [s] and is illustrating an absolute worst case of boiler layout. It is interesting to see that it is possible to initiate local temperature spikes in an evaporator tubes - even before the boiling region - caused by the compressibility phenomena. The above results show that the numerical model is able to simulate the pressure drop and heat transfer in evaporator tubes (with and without IRBT), in both a time and spatial resolution. However, despite the extremely large in-linearities in the fluid density, and the hyperbolic nature of the governing equations, the model is capable to calculate a dynamic response over the saturation zones in the evaporator. Under normal conditions, the sub-cooled section of the evaporator will be separated from the two-phase section, to ensure numerical stability, but by use of the WENO technique, this can be handled in one setup. It is unfortunately not possible to compare the numerical calculations with measured data, since the IRBT evaporator model is a hypothetical example, but the boundary data are taken from measurements from SKV3.

It is interesting to see how the tube wall temperature may be increased, as a result of poor heat transfer due to the low flow rate in the subcooled section of the evaporator. Further downstream, where the flow speed increases, progressively better heat transfer are observed and a more homogeneous axial temperature distribution all the way down to the superheated section, where the material temperature rises again.

Similarly, we can observe that there are several different models of the wall friction into play, which is revealed by considering the slope of the pressure downstream in figure (7). The pressure gradient is ultimately the greatest in the two-phase region, due two-phase multiplier. we see also that the pressure gradient for superheated steam also, not surprisingly, are larger than sub-cooled liquid.

The Central WENO schemes are designed for problems with piecewise smooth solutions containing discontinuities. The Central WENO scheme has been successful in the above applications, especially for solving the pressure distribution down streams an evaporator. The inlet conditions is sub cooled water and the out flow is superheated steam. Minor pressure waves are initiated in the transition zones to the two phase region (x=0), because of the compressibility of the fluid. The pressure oscillations generated in the entrance to the boiling zone is controlled by the shear stresses in the momentum equation (0.01 $[m^2/s]$, which smooth the oscillations due to diffusion of momentum. The model is very time consuming in solving the system, because the total energy is determined iteratively as well as the density is a function of pressure and enthalpy. The model is stable as long as the CFL number is less than one and the speed of sound is below the highest calculated speed of sound in the fluid domain, determined at each time step. We can conclude that the solution procedure is non-oscillatory in the sense of satisfying the total-variation diminishing property in the one-dimensional space. No numerical wiggles are observed in the hyperbolic models and smooth solutions are observed in the continuous zones of the flow regimes.

4.7. Conclusion

In this article we have solved the dynamic flow equations and associated wall model for a boiler tube, by use of a fifth order WENO scheme. Simulations with and without a model of the inner rifling of the boiler tube has been carried out. The calculations include the entire evaporation process from sub-cooled water to super-heated steam, which includes a massive change in fluid density downstream. The simulations show that there is a very large pressure drop across the boiler tube without rifling, while the tube with rifling has a significantly lower pressure drop, due to the lower mass flux, although the relative pressure drop in the rifle tube is significantly higher compared to the smooth boiler tube. We also see that the mass flux in IRBT for design reasons are significantly lower. The model handles perfect the pressure oscillations occurring in the two phase region, as a result of the increased compressibility of the fluid. This instability generates minor enthalpy slugs downstream in the calculations. In the IRBT simulations we experience very low mass flux just before the entrance to the two-phase region, which locally gives a very poor cooling of tube wall and rising wall temperature. We can generally conclude that WENO scheme both numerically and in terms of stability is well suited to solve such an complicated hyperbolic system of PDE's with respect to the transformed independent solution parameters.

5.

References

[1] H. Griem, Untersuchung zur thermohydraulik innenberippter verdampferohre., PhD thesis, Technische Universitat Munchen, Lehrstuhl fur Termische Kraftanlagen. (1).

[2] J. Pan, D. Yang, Z. Dong, T. Zhu, Q. Bi, Experimental investigation on heat transfer characteristics of low mass flux rifled tube upward flow., International Journal of Heat and Mass Transfer. 54 (2011) 2952–2961.

[3] D. Yang, J. Pan, C. Zhou, X. Zhu, Q. Bi, T. Chen, Experimental investigation on heat transfer and frictional characteristics of vertical upward rifled tube in supercritical cfb boiler., Experimental Thermal and Fluid Science. 35 (2011) 291–300.

[4] X. Zhu, Q. Bi, Q. Su, D. Yang, J. Wang, G. Wu, S. Yu, Self-compensating characteristic of steam-water mixture at low mass velocity in vertical upward parallel internally ribbed tubes., Applied Thermal Engineering. 30 (2010) 2370–2377.

[5] X. Fan, S. Wu, Heat transfer and frictional characteristics of rifled tube in a 1000 mw supercritical lignite-fired boiler., School of Energy Science and Engineering, Harbin Institute of Technology, China. 1 (2010) 1–5.

[6] A. O. Johansen, E. B., J. N. Sørensen, Implementation and test of a fifth order central weno scheme for solving hyperbolic balance laws., Applied Thermal Engineering ,1-25. (1).

[7] A. O. Johansen, E. B., Implementation scheme for water steam properties., Applied Thermal Engineering ,1-25. (1).

[8] S. M. Ghiaasiaan, Two-Phase Flow, Boiling, and Condensation in Conventional and Miniature Systems, 1st Edition, Cambridge University Press, Georgia Institute of Technology, 2008.

[9] E. V. Driest, On turbulent flow near a wall., Journal of the Aeronautical Sciences. 23 (1956) 1007–1011.

[10] F. Jirous, Analytische methode der berechnung des naturumlaufes bei dampferzugern, VGB Heft 5 (1978) 366–372.

[11] P. D. Bentz, R. Prasad, Kuldeep, Thermal performance of fire resistive materials i. characterization with respect to thermal performance models., NIST, Building and Fire research Laboratory, Gaithersburg. (MD 20899-8615).

[12] M. Rohrenwerke, Rohre aus warmfesten und hochwarmfesten Stahlen Werkstoffblatter., 1st Edition, MannesMann Rohrenwerke, 1988.

[13] F. Brandt, FDBR-FACHBUCHREIHE - warmeubertragung in Dampferzeugern und Warmeaustauschern., band 2 Edition, Vulkan-Verlag, Essen., 1985.

[14] W. Wagner, H.-J. Kretzschmar, International Steam Tables - Properties of Water and Steam Based on the Industrial Formulation IAPWS-IF97, 2nd Edition, Springer, Berlin Heidelberg, 2008.

[15] G. Capdeville, A central weno scheme for solving hyperbolic conservation laws on non-uniform meshes., J. Comp. Phys.,2977-3014. (227).

[16] M. Castro, B. Costa, W. S. Don, High order weighted essentially non-oscillatory weno-z schemes for hyperbolic conservation laws., Journal of Computational Physics 230 ,1766-1792.

[17] S. Gotlieb, C. Shu, Total variation diminishing runge-kutta schemes., Math. Comp., 73-85 (67).

[18] D. Levy, G. Pupo, G. Russo, Compact central weno schemes for multidimensional conservation., SIAM J. Sci. Comput. ,656-672. (22).

[19] A. Kurganov, E. Tadmor, New high-resolution central schemes for nonlinear conservation laws and convection-diffusion equations., J. Comput. Phys. ,241-282. (160).

[20] A. Kurganov, D. Levy, A third-order semidiscrete central scheme for conservation laws and convection-diffusion equations., SIAM J. Sci. Comp. No.4 ,1461-1488. (22).

[21] C. C. Richter, Proposal of New Object-Oriented Equation-Based Model Libraries for Thermodynamic Systems., 1st Edition, Von der Fakultat fur Maschinenbau, der Technischen Universitat Carolo-Wilhelmina zu Braunschweig., 2008.

[22] A. Bergles, e. a. J.H. Lienhard, Boiling and evaporation in small diameter channels., Heat Transf. Eng. 24 (2003) 18–40.

[23] S. Kakac, B. Bon., A review of two-phase flow dynamic instabilities in tube boiling system., Int. J Heat Mass Transfer. 51 (2008) 399–433.

[24] J.S.Maulbetsch, P.Griffith, A Study of System-Induced Instabilities in Forced-Convection Flows With Subcooled Boiling., 1st Edition, no. 5382-35, NIT Engineering Projects Lab Report, 1965.

[25] J.S.Maulbetsch, P.Griffith, Prediction of the onset of System-Induced Instabilities in Subcooled Boiling., 1st Edition, no. 799-825, EURATOM Report, Proc. Symp. on Two-phase flow dynamics at Eindhoven, 1967.

[26] A.H.Stenning, T.N.Veziroglu, Flow Oscillations Modes in Forced Convection Boiling., 1st Edition, no. 301-316, Heat Transfer and Fluid Mech. Inst., Stanford Univ. Press., 1965.

[27] T. A.H.Stenning, G.M.Callahan, Pressure-Drop Oscillations in Forced Convection Flow with Boiling., 1st Edition, no. 405-427, EURATOM Report, Proc. Symp. on Twophase flow dynamics., 1967.

DTU Mechanical Engineering
Section of Thermal Energy
Technical University of Denmark

Nils Koppels Allé, Bld. 403
DK- 2800 Kgs. Lyngby
Denmark
Phone (+45) 4525 4131
Fax (+45) 4588 4325
www.mek.dtu.dk
ISBN: 978-87-7475-383-4

DCAMM
Danish Center for Applied Mathematics and Mechanics

Nils Koppels Allé, Bld. 404
DK-2800 Kgs. Lyngby
Denmark
Phone (+45) 4525 4250
Fax (+45) 4593 1475
www.dcamm.dk
ISSN: 0903-1685